



Journal of Fluids Engineering

Published Bimonthly by ASME

VOLUME 126 • NUMBER 4 • JULY 2004

FLUIDS ENGINEERING DIVISION

Editor

JOSEPH KATZ (2005)

Assistant to the Editor

LAUREL MURPHY (2005)

Associate Editors

MALCOLM J. ANDREWS (2006)
S. BALACHANDAR (2005)
KENNETH S. BREUER (2006)
STEVEN L. CECCIO (2004)
GEORGES L. CHAHINE (2006)
WILLIAM W. COPENHAVER (2004)
THOMAS B. GATSKI (2006)
SIVIRAM GOGINENI (2006)
FERNANDO F. GRINSTEIN (2005)
HAMID JOHARI (2006)
JINKOOK LEE (2006)
M. VOLKAN OTUGEN (2004)
MICHAEL W. PLESNIAK (2004)
DENNIS SIGINER (2005)
KYLE D. SQUIRES (2005)
YOSHINOBU TSUJIMOTO (2006)

OFFICERS OF THE ASME

President, HARRY ARMEN

Exec. Director

V. R. CARTER

Treasurer

R. E. NICKELL

PUBLISHING STAFF

Managing Director, Engineering

THOMAS G. LOUGHLIN

Director, Technical Publishing

PHILIP DI VIETRO

Managing Editor, Technical Publishing

CYNTHIA B. CLARK

Production Coordinator

CARMEN WALKER

Production Assistant

MARISOL ANDINO

Transactions of the ASME, Journal of Fluids Engineering (ISSN 0098-2202) is published bimonthly (Jan., Mar., May, July, Sept., Nov.) by The American Society of Mechanical Engineers, Three Park Avenue, New York, NY 10016. Periodicals postage paid at New York, NY and additional mailing offices.

POSTMASTER: Send address changes to Transactions of the ASME, Journal of Fluids Engineering, c/o THE AMERICAN SOCIETY OF MECHANICAL ENGINEERS, 22 Law Drive, Box 2300, Fairfield, NJ 07007-2300.

CHANGES OF ADDRESS must be received at Society headquarters seven weeks before they are to be effective. Please send old label and new address.

STATEMENT from By-Laws. The Society shall not be responsible for statements or opinions advanced in papers or ... printed in its publications (B7.1, Par. 3).

COPYRIGHT © 2004 by the American Society of Mechanical Engineers. Authorization to photocopy material for internal or personal use under those circumstances not falling within the fair use provisions of the Copyright Act, contact the Copyright Clearance Center (CCC), 222 Rosewood Drive, Danvers, MA 01923, tel: 978-750-8400, www.copyright.com. Request for special permission or bulk copying should be addressed to Reprints/Permission Department.

INDEXED by Applied Mechanics Reviews and Engineering Information, Inc. Canadian Goods & Services Tax Registration #126148048.

- 505 8th International Symposium on Gas-Liquid Two-Phase Flows
Dimitris E. Nikitopoulos
- 508 Panelist Comments on: Open Questions and New Directions in Gas-Liquid Flows


TECHNICAL PAPERS


- 516 Aerobreakup in Rarefied Supersonic Gas Flows
T. G. Theofanous, G. J. Li, and T. N. Dinh
- 528 Interfacial Structures and Regime Transition in Co-Current Downward Bubbly Flow
S. Kim, S. S. Paranjape, M. Ishii, and J. Kelly
- 539 Local Liquid Velocity in Vertical Air-Water Downward Flow
Xiaodong Sun, Sidharth Paranjape, Seungjin Kim, Hiroshi Goda, Mamoru Ishii, and Joseph M. Kelly
- 546 Two-Phase Flow Through Square and Circular Microchannels—Effects of Channel Geometry
Peter M.-Y. Chung, Masahiro Kawaji, Akimaro Kawahara, and Yuichi Shibata
- 553 Oil-Water Separation in a Novel Liquid-Liquid Cylindrical Cyclone (LLCC[®]) Compact Separator—Experiments and Modeling
C. Oropeza-Vazquez, E. Afanador, L. Gomez, S. Wang, R. Mohan, O. Shoham, and G. Kouba
- 565 The Modeling of Thin Liquid Films Along Inclined Surfaces
Michael Z. Podowski and Anela Kumbaro
- 573 The Modeling of Lift and Dispersion Forces in Two-Fluid Model Simulations of a Bubbly Jet
M. Lopez de Bertodano, F. J. Moraga, D. A. Drew, and R. T. Lahey, Jr.
- 578 An Improved Three-Dimensional Level Set Method for Gas-Liquid Two-Phase Flows
Hiroyuki Takahira, Tomonori Horiuchi, and Sanjoy Banerjee
- 586 The Characteristics-Based Matching (CBM) Method for Compressible Flow With Moving Boundaries and Interfaces
R. R. Nourgaliev, T. N. Dinh, and T. G. Theofanous
- 605 Application of Preconditioning Method to Gas-Liquid Two-Phase Flow Computations
Byeong Rog Shin, Satoru Yamamoto, and Xin Yuan

ADDITIONAL TECHNICAL PAPERS

- 613 The Influence of Small Particles on the Structure of a Turbulent Shear Flow
David I. Graham
- 620 A Stochastic Model for Gravity Effects in Particle-Laden Turbulent Flows
Z. Gao and F. Mashayek
- 626 On the Criterion for the Determination Transition Onset and Breakdown to Turbulence in Wall-Bounded Flows
J. Jovanović and M. Pashtrapanska
- 634 Modeling the Rapid Part of the Pressure-Diffusion Process in the Reynolds Stress Transport Equation
Kazuhiko Suga

(Contents continued on inside back cover)

This journal is printed on acid-free paper, which exceeds the ANSI Z39.48-1992 specification for permanence of paper and library materials. 

 85% recycled content, including 10% post-consumer fibers.

- 642 **Loss Reduction Using Riblets on a Supersonic Through-Flow Fan Blade Cascade**
Todd Ninnemann and Wing F. Ng
- 650 **Secondary Flow Control Using Vortex Generator Jets**
R. K. Sullerey and A. M. Pradeep
- 658 **The Design of a New Flow Meter for Pipes Based on the Drag Force Exerted on a Cylinder in Cross Flow (Drag Force Flow Meter: DFFM)**
C. Ruppel, T. Funke, and F. Peters
- 665 **Momentum Flux in Plane, Parallel Jets**
Robert E. Spall, Elgin A. Anderson, and Jeffrey Allen
- 671 **Measurement and Modeling of Propeller Cavitation in Uniform Inflow**
Francisco Pereira, Francesco Salvatore, and Fabio Di Felice
- 680 **An Experimental Study on the Influence of Flow Maldistribution on the Pressure Drop Across a Plate Heat Exchanger**
B. Prabhakara Rao and Sarit K. Das
- 692 **Effects of Inclination Angle of Ribs on the Flow Behavior in Rectangular Ducts**
Xiufang Gao and Bengt Sundén

TECHNICAL BRIEFS

- 700 **Aerodynamic Entropy Generation Rate in a Boundary Layer With High Free Stream Turbulence**
Philip C. Griffin and Mark R. D. Davies
- 704 **Discussion: Criticisms of the "Correction Factor" Verification Method**
Robert Wilson, Jun Shao, and Fred Stern
- 707 **Erratum**
S. Garimella, J. D. Killion, and J. W. Coleman
- 708 **Erratum**
S. Garimella, J. D. Killion, and J. W. Coleman

The ASME Journal of Fluids Engineering is abstracted and indexed in the following:

Applied Science & Technology Index, AMR Abstracts Database, Chemical Abstracts, Chemical Engineering and Biotechnology Abstracts (Electronic equivalent of Process and Chemical Engineering), Civil Engineering Abstracts, Computer & Information Systems Abstracts, Corrosion Abstracts, Current Contents, Ei EncompassLit, Electronics & Communications Abstracts, Engineered Materials Abstracts, Engineering Index, Environmental Engineering Abstracts, Environmental Science and Pollution Management, Excerpta Medica, Fluidex, Index to Scientific Reviews, INSPEC, International Building Services Abstracts, Mechanical & Transportation Engineering Abstracts, Mechanical Engineering Abstracts, METADEX (The electronic equivalent of Metals Abstracts and Alloys Index), Petroleum Abstracts, Process and Chemical Engineering, Referativnyi Zhurnal, Science Citation Index, SciSearch (The electronic equivalent of Science Citation Index), Shock and Vibration Digest, Solid State and Superconductivity Abstracts, Theoretical Chemical Engineering

8TH INTERNATIONAL SYMPOSIUM ON GAS-LIQUID TWO-PHASE FLOWS

Dimitris E. Nikitopoulos, Center for Turbine Innovation and Energy Research (TIER), College of Engineering, Louisiana State University, Baton Rouge, LA 70803, USA

Tohru Fukano, Department of Mechanical Engineering Science, Kyushu University, 6-10-1, Hakazaki, Higashi-ku, Fukuoka, 812-8581, Japan

Michel Lance, Lab. Mec. des Fluides et d'Acoustique, Ecole Central de Lyon, 36 Av. Guy de Collongue, 69 130 Ecully, France

Theofanis G. Theofanous, Center for Risk Studies and Safety, Departments of Chemical Engineering and Mechanical & Environmental Engineering, University of California, Santa Barbara, CA 93106, USA

Yoichiro Matsumoto, Department of Mechanical Engineering, The University of Tokyo, Hongo, Bunkyo-ku, Tokyo 113-8656, Japan

Timothy J. O'Hern, Sandia National Laboratories, Engineering Sciences Center, MS 0834, Dept 9112 Albuquerque, NM 87185-0834, USA

Upendra K. Rohatgi, Energy Sciences and Technology Department, Brookhaven National Lab., Bldg. 475-B, PO Box 5000, Upton, NY 11973-5000, USA

The 8th International Symposium on Gas-Liquid Two-Phase Flows took place during the ASME/JSME Joint Fluids Engineering Division Summer Meeting held July 6-10, 2003 at the Sheraton Waikiki Hotel, Honolulu, Hawaii, and was sponsored by the Multiphase Flow Technical Committee of the ASME Fluids Engineering Division and the Japan Society of Mechanical Engineers (JSME). Over the last 18 years, this symposium has regularly appeared, approximately every other year, in ASME conferences. Its scope has been as broad as its name implies, offering a forum for the presentation and discussion of gas-liquid research work covering the range of the spectrum from theory and fundamentals to experimentation and applications.

During this eighth incarnation, the symposium included 49 papers distributed over 11 sessions and an additional panel discussion session dedicated to "Open Questions and New Directions in Gas-Liquid Flows." As in the past, a broad range of topics was covered. Among these, Bubbly Flows had a prominent presence with 13 papers (3 sessions) predominantly covering experimental work on single-bubble or bubble-chain dynamics, bubbly flows in pipes, channels and bubble columns, as well as bubbly flows in more complex geometries such as sudden duct expansions and around cylinders confined in channels. Two keynote papers in this area addressed issues of bubble clustering near the walls in bubbly channel flows (So et al., FEDSM2003-45387) and a review of modern imaging and pulsed-light velocimetry measuring techniques in bubbly flows (Sommerfeld and Bröder, FEDSM2003-45794). A substantial group of eight papers (two sessions) addressed Computational Methods for the Simulation of gas-liquid flows and their applications, covering novel schemes that incorporated level-set, characteristics-matching and preconditioning methodologies and offering numerical simulation results on the motion of free-surfaces and flows of practical interest and complexity such as boiling flows during the quenching of engine blocks. A keynote paper in this area discussed an improved implementation of a level-set method in three dimensions (Takahira et al., FEDSM2003-45389). Applications of gas-liquid flows to Complex and Industrial Systems were strongly represented by 10 papers (two sessions) covering phase-separation technology and swirling flows relevant to the oil industry, flows in rod-bundle geometries relevant to the nuclear industry, two-phase flow development during depressurization of liquid filled industrial vessels, flow measurement in automotive air-conditioning heat exchangers and in rapidly rotating annular systems as well as two-phase flow characteristics in helically coiled tubes. Gas-Liquid flows in micro-scale geometries are a rapidly emerging area of research interest and were addressed by five papers (one session) predominantly dealing with flows in micro-channels. Three papers dealing with the stochastic representation of droplet motion in annular flows, swirling spray combustion LES and wake disappearance in multiphase flow, represented droplet flows. A keynote paper completed

one session in this area (Theofanous and Dinh, FEDSM2003-45371) providing a review of the aerobreakup field while presenting interesting new insights into the mechanisms occurring under rarified supersonic conditions. Theory and Modeling of gas-liquid flows was covered by one session with four papers that addressed modeling of thin liquid films on inclined surfaces, lift and dispersion forces in bubbly flows, and liquid film formation and entrainment generation in horizontal annular flows (keynote paper by Fukano, FEDSM2003-45815). The five papers of the last session of the symposium addressed issues in non-bubbly flow regimes such as turbulence modification in annular flows, application of real time electrical tomography to phase detection and measurement, air-oil flows through sudden expansions, the effect of surfactants on the slug flow regime, and measurement of interfacial area concentration in this regime.

During the symposium review process, a group of papers was recommended by the symposium reviewers for an accelerated review towards publication in the Journal of Fluids Engineering. Ten of these papers follow this introductory editorial in this special issue of the Journal of Fluids Engineering, and cover the breadth of experimental, computational and modeling work in gas-liquid flows.

The first group of papers consists of predominantly experimental investigations. The leading paper by Theofanous et al. provides original observations of interfacial phenomena and mixing patterns during the breakup of Newtonian liquid drops, when these are impulsively subjected to a high-Mach number rarified airflow environment. This study covers a wide range of Weber numbers, identifies several breakup regimes and associated transition criteria, and offers qualitative and quantitative insights into interfacial phenomena and breakup mechanisms occurring during the aerobreakup of liquid drops.

Air-water downward flow is the object of the second and third papers. Kim et al. identify regime transitions in such flows by employing a novel combination of an impedance-based void meter and neural network method. They demonstrate that, unlike vertical upwards flow, regime transition boundaries in co-current downward flows are strongly dependent on pipe diameter. The paper also presents local measurements of void fraction, interfacial area concentration and bubble velocity and size. Experimental results are analyzed in the perspective of the drift flux model and the authors present new correlations for the distribution parameter that can be useful in applying the drift flux model in practical gas-liquid flow systems. The paper by Sun et al. focuses on local measurements in vertical-downwards, dilute air-water bubbly flows through the use of Laser Doppler Velocimetry for the liquid velocity and miniaturized conductivity probes for the bubble velocity and void fraction. They observe off-center liquid mean velocity maxima and flatter mean liquid velocity profiles in two-phase flow relative to the single-phase flow counterpart. The liquid fluctuation intensity is shown to increase with increasing average void fraction especially at low superficial liquid velocities. An estimate of the distribution parameter and drift velocity is also provided as relevant to a practical application of the drift flux model.

The fourth paper of this group investigates two-phase flow in micro-channels, a topic of recent and growing research interest. Chung et al. identify flow regimes and transition boundaries for both square- and circular-cross section micro-channels, demonstrating a significant dependence of the regime transition boundaries on the shape of the channel cross section. Although gas and liquid superficial velocities are varied over two orders of magnitude, bubbly, churn and purely annular flows are not observed. Measurements of void fraction indicate that an empirical correlation developed from circular micro-channel data is equally successful in predicting void fraction from volumetric flow ratio in the square micro-channel. Measurements of frictional pressure drop are used to verify that the Lockhart-Martinelli correlation with a modified correlation constant performs well in predicting the experimental data for both circular and square micro-channels.

The last paper of this group by Oropeza-Vasquez et al. presents the experimental investigation and evaluation of a liquid-liquid cylindrical cyclone separator developed for oil-water separation as needed by the oil-industry. The device achieves effective water content

reduction of an oil-water mixture. A mechanistic model for the prediction of separation efficiency is presented for use in design and performance analysis of such industry-relevant systems. The performance of this model is successfully validated through comparisons with the results of experimental tests.

The second group of papers covers theoretical and computational aspects of gas liquid flows. The first paper of this group by Podowski and Kumbaro addresses theoretically both stationary and moving liquid films on inclined solid surfaces from vertical to horizontal. The authors develop analytical expressions for the distribution of the thin liquid film thickness on inclined solid surfaces on the basis of first principles. Their results cover the full range from the liquid free surface to the disjoining-pressure-dominated (asymptotic) region. In the case of moving surfaces, an elegant derivation of an analytical solution for the thin film evolution is presented and a clear explanation of why liquid film thickness is normally beyond the range of Van der Waals forces is given.

The second paper of this group focuses on the modeling of dispersion and lift forces for use in simulations based on a two-fluid model. The turbulent dispersion model of Lopez de Bertodano et al. is based on a Boltzmann-type kinetic transport equation. The two-fluid model is tested for a bubbly jet with 1-mm bubbles and shown to yield satisfactory results in the jet far field through comparisons with experimental data. The sensitivity of the results to the lift coefficient is shown not to be significant. This work provides a first assessment of the performance of the two-fluid model in a free shear dispersed gas-liquid flow.

Takahira et al. present a three-dimensional level set method for the simulation of high-density ratio flows in the third paper of this group. The conservation equations are solved using a fractional step method on a non-staggered grid and a semi-implicit time stepping scheme. The authors improve the stability of the algorithm by improving the treatment of the convection terms, the interpolation method used to obtain the volume flux on the computational cell faces, as well as the Poisson solver for the pressure. The mass conservation performance of the algorithm is also enhanced through an improved reinitialization procedure for the level set function. The scheme is shown to perform very well for test problems involving bubble coalescence and a bubble bursting through a free surface, and holds good promise for high-density ratio two-phase flow simulations.

The fourth paper of the group by Nourgaliev et al. pursued the same goal as the previous paper for compressible multi-fluid, high density-ratio problems by introducing an original and very promising approach. The authors introduce a novel algorithm referred to as “characteristics-based matching” (CBM) to capture a moving boundary condition. The scheme is based on a level set method and a “Ghost Fluid Method” strategy to tag computational nodes. The boundary conditions are implemented through a characteristic decomposition in the direction normal to the boundary. The CBM method suppresses over and under-heating errors and is shown to yield very good results in a broad variety of multi-phase test problems.

Shin et al. present a two-dimensional numerical algorithm for the simulation of gas-liquid flows in the last paper of the series. The authors use a finite-difference Runge-Kutta method employing Roe’s flux difference splitting and MUSCL-TVD schemes. Preconditioning is used to extend the functionality of the algorithm to nearly incompressible flows. Simulation of several cavitating test flow problems are carried out using a homogeneous cavitation model. The algorithm performance is successfully validated at low Mach numbers through comparison of the computational cavitation results with experimental data.

The co-organizers of the eighth international gas-liquid flow symposium would like to thank the authors of the papers in this special issue of the Journal of Fluids Engineering for their interesting contributions, as well as the reviewers who contributed their time, experience and constructive criticism towards the improvement of the quality of these papers.

On behalf of the symposium co-organizers,
Dimitris E. Nikitopoulos

PANELIST COMMENTS ON: OPEN QUESTIONS AND NEW DIRECTIONS IN GAS-LIQUID FLOWS

Summaries of the ideas and discussion contributed by the panelists are presented in this article. Each panelist has contributed under a separate title in order to preserve the individuality of the opinions and visions expressed on the subject.

Tickling Gas-Liquid Flows

Andrea Prosperetti

Department of Mechanical Engineering

The Johns Hopkins University

Baltimore, MD 21218, USA.

Faculty of Applied Physics, Twente Institute of Mechanics, and Burgerscentrum,
University of Twente, AE 7500 Enschede, The Netherlands

While certainly there are many new important and promising directions into which multiphase flow research can be extended (micro-devices, processing, the environment), in my mind flow regimes still remain the key unsolved problem. For perfectly legitimate reasons, much of the past research has been centered on the study of processes occurring in flows and under conditions of direct practical interest. It is my impression that it would be useful to adopt the approach used in medical animal research in which, in order to understand the system, the organism is perturbed so much as to be often killed. In other words, it may be profitable to shift attention from situations encountered in practice to highly artificial ones, which are not of direct interest in themselves, but may nevertheless reveal the underlying physics. It is in this spirit that I propose the following experiments.

Bubbly/slug flow transition. According to some scenarios, a bubbly flow transitions to slug flow when the void fraction exceeds a certain threshold. A way to cause this void fraction increase is to generate a bubbly flow in a pressurized tube and release the pressure to expand the bubbles. Is there a threshold for transition? How long does it take? What is the role of bubble size? Bubble size can be controlled pretty well e.g. by simply using salt water. Another worthwhile experiment (which has already been attempted, but which could probably stand repetition and extension) is to generate void fraction and pressure waves at the bottom of a bubbly column.

Slug stability. The same device can be used to study the stability of long bubbles: when the pressure falls, the bubble will elongate. What happens then? Does it break up? Two bubbles would both expand: do they get closer? Do they coalesce?

Horizontal stratified/slug transition. In a stratified flow, one could use a wave-maker submerged in the liquid to investigate the role of surface roughness in the transition. An insert could taper the available gas space and gradually increase its velocity. A long time ago, Jean Fabre (Toulouse) suggested that this transition could be affected by secondary flows generated in the cross-section of the tube due to the roughening influence of surface waves. These secondary flows may in some sense be similar to the Langmuir cells at the ocean surface. The surface roughness would be dependent on the local liquid depth, which could be controlled in a number of ways, e.g. by an insert on the bottom of the tube shaped so as to vary the wave amplitude in different parts of the cross section.

Atomization. The onset of atomization is likely related to the amplitude of surface waves. In a horizontal flow, rather than relying on naturally occurring waves, one could artificially generate them with a submerged wave-maker, or small, submerged vertical jets. For example, for the same gas velocity, it should be possible to investigate whether a threshold exist for the onset of entrainment.

Flow regime transition has proven to depend on very subtle physical mechanisms which are not easily understood or identified. Progress in Science has often relied on the generation of unusual situations in the laboratory studied not because they actually occur in practice, but because they help elucidate the mechanisms at work in the systems of interest. It may be time to have a greater recourse to this attitude than has perhaps prevailed in the past. Learn from the doctors: kill the patient!

Towards Strategic Research

Theofanis G. Theofanous

Center for Risk Studies and Safety

Departments of Chemical Engineering

and Mechanical & Environmental Engineering

University of California

Santa Barbara, CA 93106

Gas-liquid flow is at a critical juncture of its development as a subject. Knowledge islands created during the past fifty years have brought us to a point where sporadic, often practice-driven studies are unlikely to significantly improve basic

understanding, generalization and predictive capability. The opportunity is open to enter the phase of development of the subject as a scientific discipline. What is needed is a new vision and a research agenda that can rise to the challenge. We can expect that opinions on how to best accomplish this, colored by interests, would differ. Here are my views on what is important at this high level of definition. I will address it in terms of conceiving, nurturing, and keeping on track such an endeavor.

(a) *Conception.* The essence of the subject is Flow Regimes – the space-time distribution of phases and their length scales. This has always been, and remains THE Open Question.

(b) *Nurturing.* Viewed as Flow Regimes the subject falls into the realm of complexity – self organization, adaptation, emergent behavior. Accordingly resolution requires very special efforts. Never having been realized as THE main thrust, this should be the dominant consideration in defining New Directions.

(c) *Operational Framework.* Even if we all were to agree on the above, we would still have to face the choice of strategic steps appropriate to achieving a pertinent degree of focus over such a broad domain of scientific and practical needs. And even if this was agreed upon, we would still need effective means for communication and debate, appropriate incentives both for synergisms and independence, and track records that would foster responsibility and accountability over the whole spectrum of activity, from providing advice to making decisions.

In my opinion it is this third aspect that has been, and is likely to remain, a critical missing link to success. To put it differently, in an otherwise favorable technical situation (however hard, but enabled with modern advances in physics, mathematics, and digital technologies – computation, instrumentation) the principal impediment I see is human factors related, over the whole spectrum of those involved, from the researcher to administrative personnel in various industries and governmental agencies.

Significant change in this respect would require the great and focused attention arising from an overwhelming need, such as that of Nuclear Safety in power reactors in the seventies. Rather, the situation now is one of comparatively low level, but highly diversified/diffuse needs, of commercial significance for the most part. To create a focus in this environment, a focus that is helpful to all, would require an enormous amount of leadership and risk taking. Previous sporadic efforts indicate that odds for success are not favorable.

To address Flow Regimes properly we would need an unrestricted view of the multidimensional, multiscale, and in some cases (boiling and burnout, cavitation, etc.) even multiphysics aspects of multiphase flow. This in turn would require the synergistic, adaptable use of precise and detailed measurements and a panoply of theoretical and computational tools (from direct numerical simulation to effective field models), in wisely-conceived, scrupulously-controlled, and independently verified experiments. The task of uncovering the organizing principles, that is, the dominant features of the flow that create organization, involves much, much more than showing the agreement of an analytical or numerical model with selected features of a flow, in selected experiments. It needs a much more developed (than what has been the case in the past) sensibility on matters of falsification (as Karl Popper would say), for this is just as powerful a force for progress as are new ideas or concepts that purport to explain nature. This is the path to resolving complexity, and it is for this reason that an Operational Framework, as noted above, is absolutely essential.

Let us call this strategic research. It could be an important complement to individual investigator, ad hoc inspired efforts that marked the landscape in the past. A recent DOE Basic Energy Science workshop [1] came up with a whole list of such specific scientific issues in multiphase flow. It also led to a vision for pursuing strategic research on Flow Regimes [2]. Briefly, the idea is that consideration of “steady, fully-developed gas-liquid flows in conduits”, and “mixing flows” (including heat transfer and phase change) can be viewed as the canonical elements, and starting points, of an approach for anchoring a general quest for capability that would eventually address multidimensional, unsteady flows in general.

In my view, the overwhelming need is that we do not continue to lose the forest for the trees, and this is why I chose to approach the subject of this panel in the manner outlined above. In these metaphorical terms, complexity, that is, the forest being much more than the sum total of its trees, makes this view even more imperative. For completeness I should conclude by noting that key influences on these views are recent experiences in the very old subject of Boiling and Burnout [3], and a rather new one on Compressible Multihydrodynamics [4], as well as my experiences with the Institute for Multifluid Science and Technology (IMuST, www.crss.ucsb.edu/imust)

Multi-Scale Dynamics in Bubbly Flow

Yoichiro Matsumoto

Department of Mechanical Engineering

The University of Tokyo Hongo, Bunkyo-ku

Tokyo 113-8656, Japan

Bubbly flow has multiple structures in terms of time and spatial scales. The macro-scale flow structure in bubbly flow is affected by both mezzo-scale and micro-scale phenomena. A multi-scale analysis is required to solve bubbly flows reasonably. It is well known that a very small amount of surfactant can drastically change the terminal velocity of a bubble. When the liquid is contaminated, the bubble motion is affected by the Marangoni effect due to the variation of surface tension along the bubble surface caused by the gradient of the contaminant concentration. Numerical results reveal that the flow pattern around the contaminated bubble becomes similar to that of a rigid particle and the drag coefficient increases from that of clean bubble to that of rigid particle.

An example of a bubbly flow where the mezzo-scale phenomena can be clearly observed is the rise of bubbles in quiescent contaminated water. There is much to be learnt on the subject by conducting Direct Numerical Simulations (DNS) on fundamental flows such as this. We have adopted this approach, and the Navier-Stokes equations by the finite difference method and tracking the bubble motion within a rectangular grid system. The relation between drag coefficient, Reynolds number and void fraction is thus investigated at moderate Reynolds numbers. Present results on void fraction dependence on the drag coefficients show good agreement with experiment and theory. Information on the turbulence structure and related averaged quantities in a multi-bubble system is obtained from simulations of the flow around swarms of spherical bubbles rising in a periodic box, leading to conclusions such as that the turbulent energy in the surrounding liquid increases with the void fraction.

To simulate large-scale, more realistic turbulent bubbly flows Large Eddy Simulations (LES) become necessary. This requires application of Sub-Grid Scale (SGS) modeling in bubbly flows. Currently we are carrying out two-fluid LES under the same conditions as the DNS of bubble swarm motion in quiescent liquid for

comparisons and validation. Constitutive equations, where not only SGS stresses but also boundary conditions of the pressure and the vorticity on the interface are taken into account, are derived for the LES. The energy spectrum obtained by the present bubbly flow model reproduces the DNS result well. In contrast, the result by the conventional model, where the SGS stress and the boundary conditions on the interface are neglected, shows considerable differences relative to the DNS one.

The development of SGS models for conducting LES in bubbly flows is a topic of considerable interest and still an open problem. Conducting DNS on simpler bubbly flows including the essential physics is a very useful tool in aiding this development.

Drag and Lift Forces Acting on Bubbles

Akio Tomiyama

Faculty of Engineering, Kobe University

Rokkodai, Nada, Kobe 657-8501

Japan

Drag and lift forces acting on single bubbles are of fundamental importance in modeling gas-liquid two-phase flow phenomena. Even after several decades' efforts, our knowledge on them is still rudimentary due to the presence of time-dependent gas-liquid interfaces and the nonlinearity intrinsic to fluid motion. As an example, it has been believed that the balance between the drag and buoyancy forces uniquely determines the terminal velocity of a single bubble in stagnant liquid. However, it has emerged out of recent experimental works [5], [6] that one can easily obtain various terminal velocities and shapes just by slightly changing the way of bubble release. It has been also pointed out that the instantaneous bubble shape uniquely determines the instantaneous rise velocity of a bubble in a low viscosity system [5]. Though a single bubble is a trifle entity in practical bubbly flow systems, the presence of multiple states in terminal velocity and shape might be one of the dominant sources of the diversity in bubbly flow. Physical explanation of multiple terminal conditions, therefore, has to be made in the near future.

The same applies to the lift force, which plays a significant role in the transverse motion of a bubble. Due to the highly complex nature of the lift force, most of the research on it has been restricted to the simplest case, i.e., the lift force acting on a bubble in a simple shear flow. According to a semi-theoretical model for a spherical bubble [7], the lift coefficient C_L increases up to more than 10 as the bubble Reynolds number decreases. On the other hand, measured data showed an opposite tendency [8]. It is recently confirmed by our recent experiments that the cause of this discrepancy is

the bubble shape, that is, a slight departure from spherical bubble shape results in a large difference from C_L of a spherical bubble.

The aforementioned two examples clearly demonstrate that the time-dependent bubble shapes and nonlinearity would cause the diversity even for the motion of a single bubble in a simple flow condition. Despite the fact that the problems with respect to single bubbles and drops are old, it is also true that they are still open to question due to the diversity.

Two-Phase Flow in Microchannels

Masahiro Kawaji

University of Toronto

200 College Street

Toronto, Ontario M5S 3E4

Canada

Microchannels with 1 ~ 200 μm diameters embedded in thin plastic and glass plates or silicon wafers are used in lab-on-a-chip devices, micro-reactors, Micro Total Analysis Systems (μTAS), MEMS, micro-heat exchangers, and so on. Many novel applications are being developed, e.g., insulin delivery by atomization, sperm selection, and various types of sensors and analytical systems for use in biomedical engineering, health care, chemical production, environmental analyses, among others. It is a new field that bridges the gap between the conventional technology and nanotechnology. Fortunately, our current knowledge of transport phenomena and reaction engineering is applicable to microchannels, however, some new physico-chemical phenomena need to be better understood including the effects of an Electric Double Layer, wall roughness, and greater heat dissipation in channel walls. In addition, microchannel flows are predominantly laminar for both phases, lack mixing which may be both problematic and advantageous.

At the First International Conference on Microchannels and Minichannels held in Rochester, NY, in April, 2003, 185 participants came from around the world. There were more than 100 papers presented that covered adiabatic two-phase flow, boiling, condensation, micro heat exchangers, microfluidics, and device fabrication. The activity level is high, and more papers are expected at the next Conference in 2004.

The challenges facing the microfluidics and microchannel two-phase flow research include the development of microscale devices such as pumps, valves, heat exchangers, as well as new measurement principles, sensors and control devices. Due to the small size, many conventional technologies are not directly applicable, and new

methods based on optical and microfabrication techniques need to be fully utilized. For gas-liquid two-phase flow studies in microchannels, measurement of extremely low gas and liquid flow rates is challenging, and for heat transfer studies, measurements of local fluid and channel wall temperatures and heat flux require advanced instrumentation. The effects of surface wettability and fluid properties on two-phase flow characteristics as well as flow rate distributions in micro heat exchangers, thermal and hydraulic aspects of PEM fuel cells with small flow channels are additional topics that need to be investigated in connection with the microchannels.

References

- [1] Hanratty T.J., Theofanous T., Delhaye J.M., Eaton J., McLaughlin J., Prosperetti A., Sundaresan S., Tryggvason G. (2003) Workshop on scientific issues in multiphase flow. Workshop findings. *International Journal of Multiphase Flows*, Vol. 29(7), p. 1047-1059, 2003.
- [2] Theofanous T.G. and T.J. Hanratty (2003). "Appendix 1: Report of study group on flow regimes in multifluid flow", *International Journal of Multiphase Flows*, Vol. 29(7), p.1061-1068, 2003
- [3] Theofanous, T.G., T.N. Dinh, J.P. Tu, and A.T. Dinh (2002). "The Boiling Crisis Phenomenon – Part 1: Nucleation and Nucleate Boiling Heat Transfer", V.26 (6-7), pp.775-792. Part 2: Dryout Dynamics and Burnout", *J. Experimental Thermal and Fluid Science*, V.26 (6-7), pp.793-810.
- [4] Theofanous, T.G., R.R. Nourgaliev, and T.N. Dinh (2004). "Compressible Multi-Hydrodynamics: Emergent Needs, Approaches and Status", IUTAM Symposium "Computational Approaches to Disperse Multiphase Flow".
- [5] A. Tomiyama, G. P. Celata, S. Hosokawa and S. Yoshida, "Terminal velocity of single bubbles in surface tension force dominant regime", *Int. J. Multiphase Flow*, 28, 1497 (2002).
- [6] M. Wu and M. Gharib, "Experimental studies on the shape and path of small air bubbles rising in clean water", *Phys. Fluids*, 14, L49 (2002).
- [7] D. Legendre and J. Magnaudet, "The lift force on a spherical bubble in a viscous linear shear flow", *J. Fluid Mech.*, 368, 81 (1998).
- [8] A. Tomiyama, H. Tamai, I. Zun and S. Hosokawa, "Transverse migration of single bubbles in simple shear flows, *Chemical Engineering and Science*, 57, 1849 (2002).

T. G. Theofanous
Professor,
e-mail: theo@engr.ucsb.edu

G. J. Li
Post-Graduate Researcher,
e-mail: li@engr.ucsb.edu

T. N. Dinh
Associate Adjunct Professor,
e-mail: nam@engr.ucsb.edu

Center for Risk Studies and Safety,
University of California, Santa Barbara,
6740 Cortona Drive, Goleta, CA 93117

Aerobreakup in Rarefied Supersonic Gas Flows

We present new experimental results on the interfacial instabilities and breakup of Newtonian liquid drops suddenly exposed to rarefied, high-speed (Mach 3) air flows. The experimental approach allows for the first time detailed observation of interfacial phenomena and mixing throughout the breakup cycle over a wide range of Weber numbers. Key findings are that Rayleigh-Taylor instability alone is the active mechanism for freestream Weber numbers as low as 28 for low viscosity liquids and that stripping rather than piercing is the asymptotic regime as $We \rightarrow \infty$. This and other detailed visual evidence over $26 < We < 2,600$ are uniquely suitable for testing Computational Fluid Dynamics (CFD) simulations on the way to basic understanding of aerobreakup over a broad range of conditions. [DOI: 10.1115/1.1777234]

Introduction

When a liquid drop is suddenly exposed to a gas flow it deforms and breaks up into a cloud of smaller droplets at rates and sizes that depend principally on the Weber number; $We = \rho_g u^2 d / \sigma$, where u is the gas velocity, ρ_g the gas density, d the droplet diameter, and σ the surface tension. The process is amazingly rich in phenomena, which again depends principally on the magnitude of the Weber number, above some critical value of ~ 10 needed for instability [1]. The various regimes and key investigations that led to their definition are summarized in Fig. 1. Brief explanations are provided in Appendix A.

Remarkable is that all these studies were carried out at pressures not significantly varying from normal atmospheric pressure. Also to be noted is that the high Weber number shock tube experiments involved mildly supersonic flow speeds (typically $M \sim 1.3$), very high temperatures (up to 1,000 K) due to compression behind the shock, and very small drops. As shown in Fig. 1, the time scales for breakup involved in the high- We regimes (stripping and catastrophic) are in the 100 s of microseconds, and the resulting droplets are of such small scale and large number density as to obscure the view in what appears (at the edges at least) as a very fine mist.

Several attempts have been made toward a basic understanding through analysis but without definitive results. The difficulties consist of accounting for competing phenomena. For example, Harper et al. [2] in a very elaborate analysis tried to account for aerodynamic deformation together with Rayleigh-Taylor (R-T) penetration on the windward surface, but they ignored the shear/stripping phenomena found experimentally to precede, and in fact, co-participate with what was thought to be their "shattering" or "catastrophic" mode. The same can be said about the work of Joseph et al. [3], who tried to match apparent wavelengths such as those shown in Fig. 1 to a straightforward R-T analysis on a planar interface (without shear). Probably the only attempts to identify regimes through competing processes were those of Gel'fand [4] and of Patel and Theofanous [5]; the former is empirical and inconclusive, while the latter remained at the very rough conceptual level.

Attempts via direct numerical simulations at the low Weber number "bag" breakup regime, while tentative at this time, show promise. The difficulty here is in that the inevitable interfacial smearing interferes with the proper coupling of tangential stress at the interface. Thus, it is well known that rather than "bag," such

simulations produce an inverted "cup" shape [6]. A most recent attempt by Han and Tryggvason [7] seems to have produced a bag, but their simulations were limited to systems with small liquid/gas density ratios, from 1.15 to 10. At higher Weber numbers, direct numerical simulations face the significant challenges of resolution (wavelengths decrease) and changes in topology at a very fine scale (local pinch offs and entrainment).

The work reported here developed as an aside from the main purpose of our experimental facility which was to study aerobreakup of viscoelastic liquids at highly rarefied, highly supersonic conditions. It benefited greatly from the pursuit of the needs of our main task for high visual resolution, larger masses, and long observation times. It also benefited in more subtle ways from operating at extremely low pressures and supersonic speeds. We were suddenly, and unexpectedly confronted with results that did not conform to long-held beliefs. We are now in a position to question these beliefs. More importantly, we think our data and interpretations provide a new entry point for basic understanding. Our experimental approach provides a convenient pair of parameters (flow density and Mach number) for working incrementally to the more complex domain of competing processes, and towards a comprehensive understanding. We expect that direct numerical simulations will provide a key aid to experiments in this quest.

The Alpha Facility

Our experiments were carried out in a supersonic wind tunnel especially constructed to study aerobreakup of viscoelastic liquids. As illustrated in Fig. 2, the tunnel consists of a supply tank and two receiving tanks connected via a vertical, transparent test section (101.6 mm in diameter). A converging-diverging nozzle accelerates the flow to supersonic speeds—in the setup discussed here, a pressure ratio greater than ~ 50 produces a flow Mach number 3. The system can operate at any pressure level from $\sim 10^{-2}$ down to $\sim 10^{-4}$ atm.

At the tee-junction, on the top, we can see the drop generator. It can produce a single, well-defined drop, in the size range from ~ 2 mm up to 20 mm. Depending on the fluid and our interest this device is selected among several options developed for this purpose. Thanks to the very low pressures, rather large drops can reach the nozzle exit in perfectly stable spherical shape.

When the drop crosses a location in the test section, sensed by a photocell, the automatic sequencing of the experiment is set in action. A plunger, consisting of an array of very sharp knives, is set in motion to break the diaphragm, and concurrently the pressure transducer signal monitoring equipment is activated. After some appropriate delay, the high-speed camera (Kodak Motion Corder Analyzer, Model SR-Ultra, PS-110), and a synchronized copper-vapor laser are switched on. The camera typically operates

Contributed by the Fluids Engineering Division for publication in the JOURNAL OF FLUIDS ENGINEERING. Manuscript received by the Fluids Engineering Division May 27, 2003; revised manuscript received February 18, 2004. Associate Editor: J. Katz.

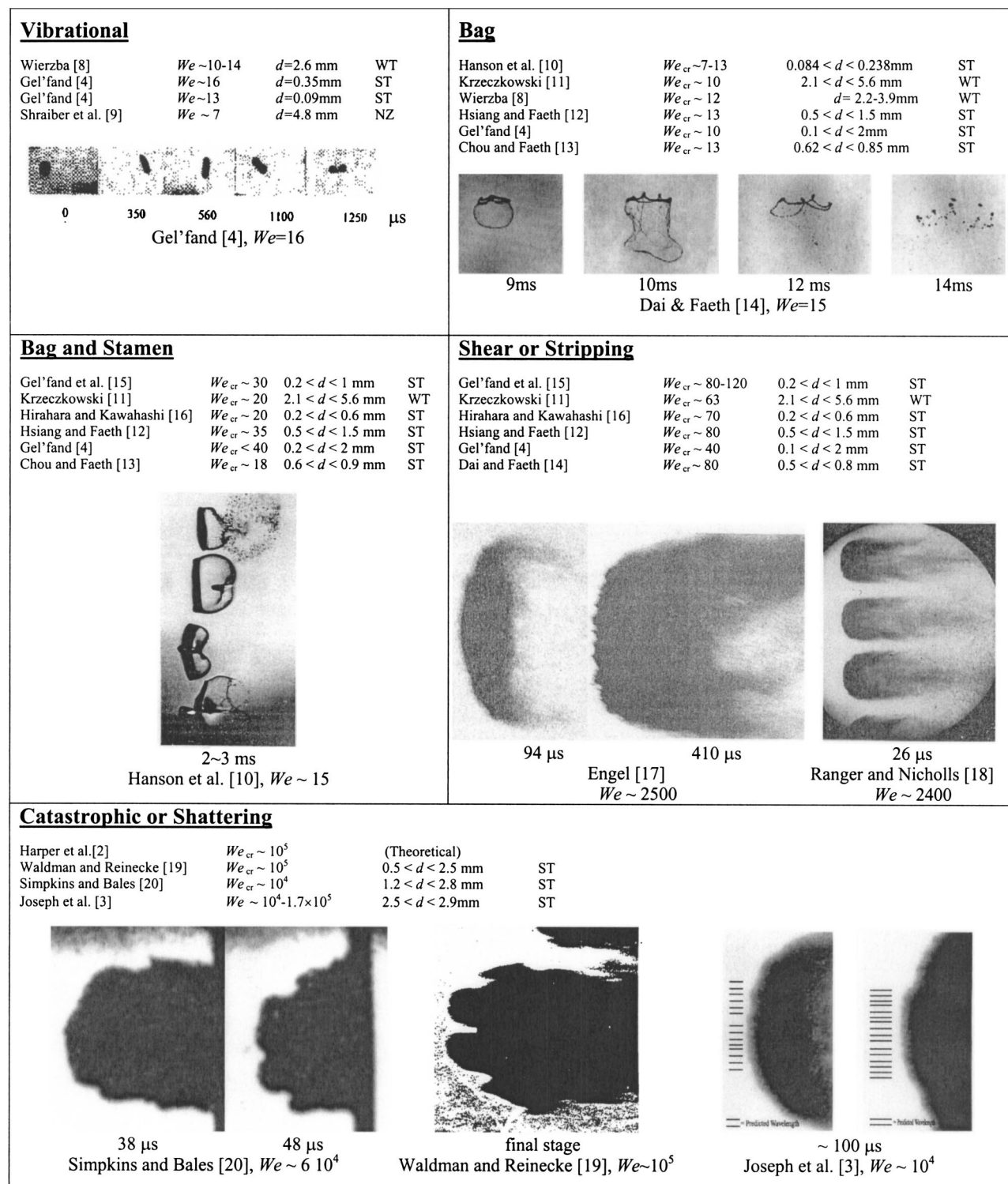


Fig. 1 Breakup regimes obtained at or near atmospheric conditions. All experiments were carried out at subsonic or mildly supersonic flow conditions. ST—shock tube, WT—Wind tunnel, NZ—Nozzle

at 2 kHz, while each frame is exposed to a single 15–30 ns laser pulse of extremely intense light (Oxford Lasers, LS20–50). A steady flow duration of $\sim 100 \text{ ms}$ is obtained, while a typical run time at the low pressure conditions considered here is $\sim 40 \text{ ms}$. The overall physical arrangement of the facility can be seen in the photograph of Fig. 3.

The flow behavior obtained in ALPHA has been characterized by means of detailed mapping of the stagnation pressure field, and

the static pressure measured at the wall of the test section. The measurements were carried out with piezoelectric transducers (Kistler, Model 206), whose natural frequency is no less than 130 KHz. Stagnation pressures were measured by holding the transducer so that its face is normal to the flow direction. Both axial and radial traverses were possible with the help of a probe-like arrangement (a rigid steel tube) supported from the top te-junction.

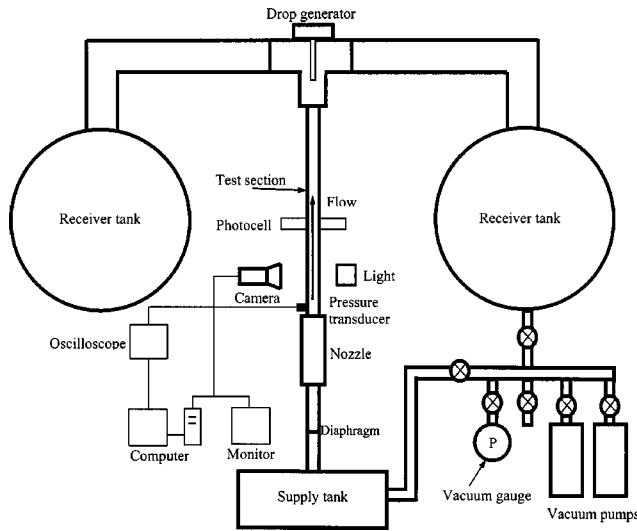


Fig. 2 Schematic of the ALPHA facility

The stagnation pressure is related to static pressure and flow Mach number of the freestream by the theoretical result,

$$\frac{P_s}{P_0} = \left(\frac{(1 + \gamma)^2 M^2}{4\gamma M^2 + 2(1 - \gamma)} \right)^{\gamma(\gamma-1)} \frac{1 - \gamma + 2\gamma M^2}{1 + \gamma} \quad (1)$$

which was found to accurately predict all our measurements [21].

A typical flow history based on the measured static and stagnation pressures, and Eq. (1), is shown in Fig. 4. Both radial and azimuthal variations in a central cylinder within radius of one-half the test section radius were found to be negligible. In the axial direction, the flow was found to decrease slowly (due to friction) from a $M \sim 3$ at the nozzle exit to a $M \sim 2.7$ (or 2 for the low end of the pressure range tested) just upstream of the tee-junction at a distance of 1.8 m. The flow characterization work covered the pressure range $144 < P_0 < 4 \times 10^3$ Pa. For lower pressures, we use detailed CFD simulations (of the whole tunnel) benchmarked against the experimental data over the pressure range for which they are available.

The static pressure is monitored in all experimental runs so as to positively qualify against spurious diaphragm/cutter operation.

Experimental Results

The experiments reported here were run with Tributyl-Phosphate (TBP) and Glycerin, both having a sufficiently low

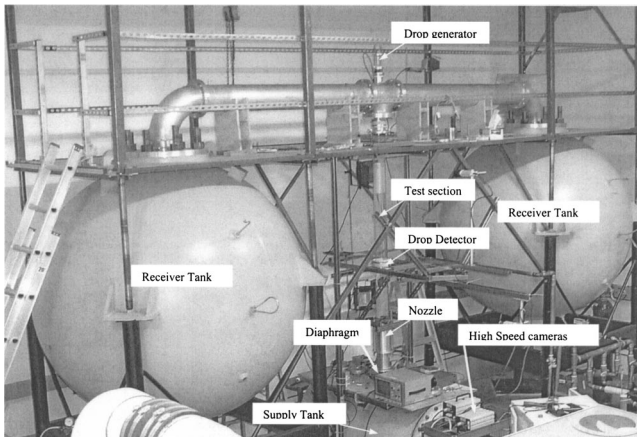


Fig. 3 The ALPHA facility

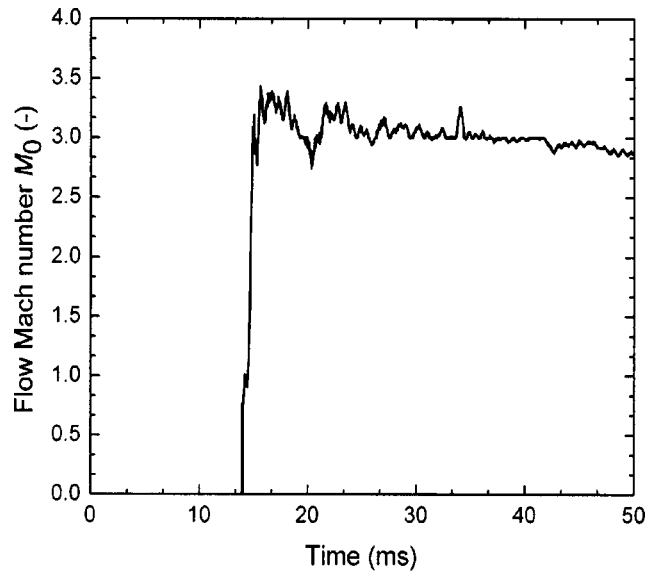


Fig. 4 A typical flow transient in ALPHA as deduced from measurements of static and stagnation pressures

vapor pressure to be suitable for the highly rarefied conditions of interest here. TBP is a Newtonian, water-like liquid with density/viscosity of $0.978 \text{ g}\cdot\text{cm}^{-3}/4\text{cp}$, while for Glycerin we have $1.26 \text{ g}\cdot\text{cm}^{-3}/13 \text{ p}$. The drop diameter was held essentially constant at $3.5 < d < 4.0 \text{ mm}$ for TBP drops and $3.7 < d < 4.5 \text{ mm}$ for Glycerin drops, and so was the flow speed at Mach ~ 3 . The sonic speed for all test conditions was 200 m/s. Besides the two viscosities, the principal experimental variable was the gas density. This density, defined by the static pressure was controlled by the supply pressure, and by ensuring an initial pressure ratio (supply/receiver) of at least 50; that is somewhat greater than the theoretical value of 37 needed for Mach 3 flow. The ranges covered in these experiments are $5 \cdot 10^{-4} < \rho_g < 10^{-1} \text{ kg/m}^3$ and $15 < P_0 < 2600 \text{ Pa}$.

The Weber number based on free stream conditions turns out to be within a few percent of the Weber number based on the flow stagnation pressure (the pressure actually acting on the drop)

$$We = \frac{\rho_g u^2 d}{\sigma} = \frac{\gamma M^2 d}{\sigma} P_0 \approx \frac{P_s d}{\sigma} \quad (2)$$

hence, we believe it to be appropriate for the supersonic conditions considered here as well. The Reynolds number, based on free stream velocity and the drop diameter,

$$Re = \frac{\rho_g u d}{\mu_g} = \sqrt{\frac{\gamma}{RT}} \frac{M d}{\mu_g} P_0 \quad (3)$$

was ~ 200 at the low end of the pressure range and increased to $\sim 31,600$ at the upper end. The Knudsen number

$$Kn = \frac{M}{\sqrt{Re}} \quad (4)$$

varies correspondingly in the range of $0.02 < Kn < 0.22$, which is squarely in the slip flow regime known to extend over

$$10^{-2} < Kn < 10^{-1} \quad (5)$$

Thus we can expect slip flows, and basically laminar boundary layers.

We carried out a total of 64 runs, at conditions as summarized in Fig. 5. The TBP runs identified in Fig. 5 as "preliminary," were carried out with a slightly different inlet geometry, and prior to the detailed characterization discussed above. These runs are included

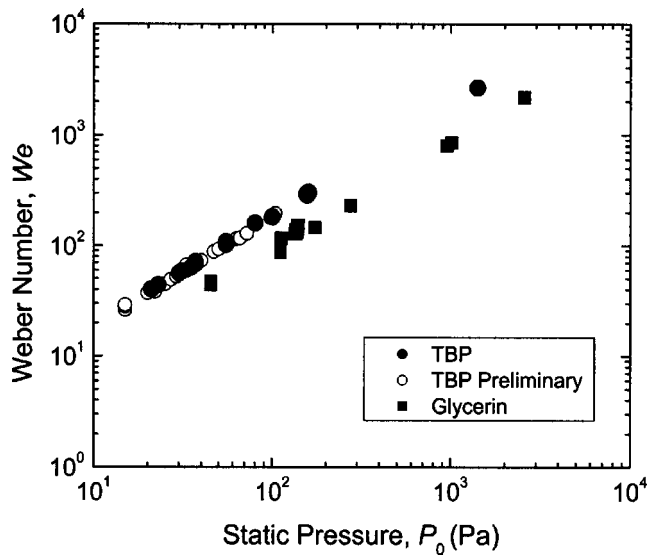


Fig. 5 Summary of test conditions considered in this work

because except for slight differences in timing they produced basically the same results as those found in the main part of the program. The intent of Fig. 5 is to show the extent of the experimental coverage, including resolution on the Weber number scale.

The overall results for TBP are summarized in Fig. 6. In these images as well as all other images shown in this paper, the direction of the gravity is from left to right, and the air flow (upward in reality) is from right to left. We can see that instability sets in by what appears as a gradual extension of the drop in the flow direction. This “pulling” regime is quite narrow and quickly gives way to the development of “bags” and “multibags.” This regime is comparatively narrow too, as it gives way to a multiwave “piercing” mechanism, in what appears as an actual manifestation of the Rayleigh-Taylor waves originally envisioned by Harper et al. [2]. At significantly higher values of the Weber number we see manifestation of shear-induced “stripping.” Remarkable are the following:

- (a) Piercing appears to be “pure.” Starting from a single “bubble” (“bag”), the number increases as the Weber number increases.

- (b) The “pure” above refers to the absence of the coupling (and obscuring) effects of shear/stripping. As a consequence, we have the first clear record of the mechanism, as well as the first quantitative characterization of the relevant parameters, from inception to full development and ultimate disposition into daughter drops (see below).
- (c) The presently found piercing regime sets in at Weber numbers that are lower by several orders of magnitude compared to previously stated experimental (suspected piercing), or theoretical (predicted piercing) regime-onset values ($We \sim 10^4 - 10^5$).
- (d) Rather than building to a piercing regime dominance, envisioned previously, as $We \rightarrow \infty$, the present results suggest the reverse; that is, piercing giving way to stripping.

As illustrated in Fig. 7 the above are further supported by the results obtained with Glycerin. The effect of high viscosity is to eliminate the extremely narrow “pulling” regime, and translate the various transitions (from single bag to multiwave piercing) to higher Weber numbers. In the next section, we show that this effect of viscosity is quantitatively predictable within a mechanism that encompasses the behavior found with low viscosity.

Records of the detailed evolutions from representative runs are collected in Appendix B. These records make available for the first time the internal length scales involved in the mixing process, the fine structure of the process itself, and the ultimately resulting daughter drop length scales.

Discussion

Evidently, the picture that emerged from the ALPHA experiments is quite different, and in a way reverse, of what was believed to be the case previously (Fig. 1). Specifically, the difference consists of:

- (a) The “pulling” and “multibag” regimes are new.
- (b) “Piercing” appears as a series of transitions with increasing number of waves/bubbles (reducing the mixing length scales) as the Weber number increases from a lower limit of ~ 26 (where a single wave—the bag—appears).
- (c) “Stripping” becomes quite evident at a Weber number of $\sim 10^3$, and is seen to become increasingly more important (than piercing) as the Weber number increases beyond this value.

The reversal is in that previously it was thought that stripping (or shear) breakup precedes piercing, and that piercing is the ter-

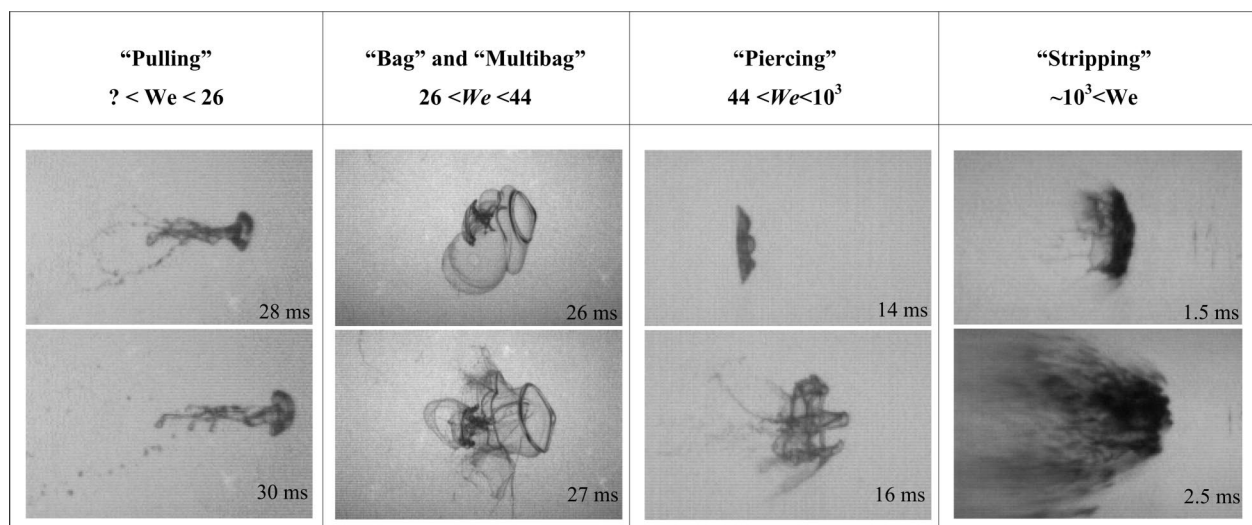


Fig. 6 Summary illustration of breakup regimes found in low pressure ALPHA tests for TBP drops ($M=3$)

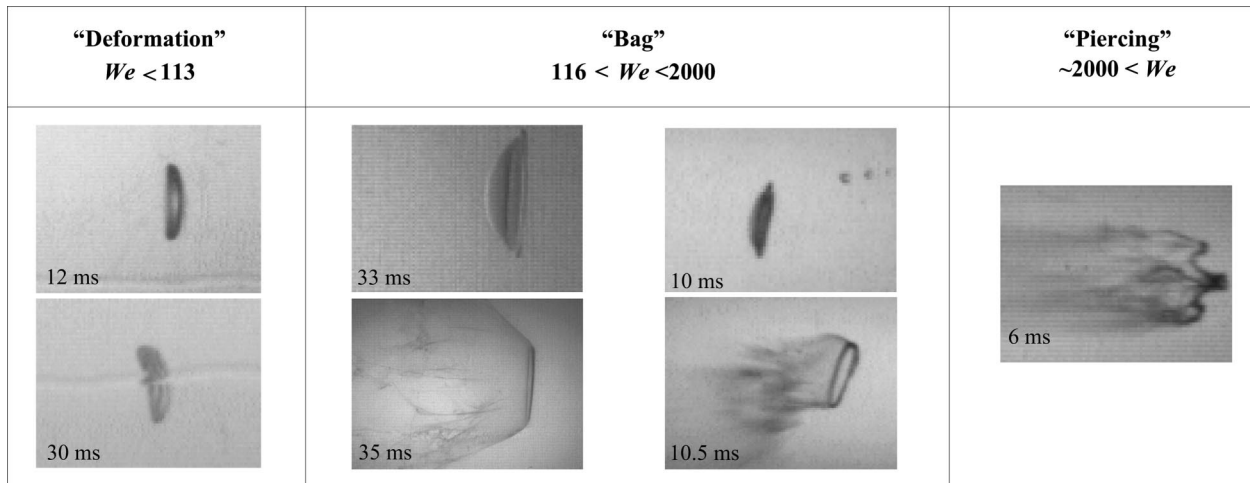


Fig. 7 Summary illustration of breakup regimes found in low pressure ALPHA tests for Glycerin drops ($M=3$)

minal regime obtained at Weber number greater than 10^4 or 10^5 , while here we see clearly the piercing set in at a Weber number of 26, and that stripping enters and becomes increasingly more important at Weber number beyond about 2×10^3 .

The discussion that follows consists of two parts. The first is to set up a conceptual/theoretical framework aimed to interpret the present experimental results. In the second, and with the help of the first part, we attempt to reconcile the differences with previous work, and the reversal, noted above. Our main point on this is that previous interpretations of experimental data were hampered by the small drop sizes involved, insufficient spatial resolution in visualizations, and in addition they were unduly influenced by the related-to-each-other theoretical/experimental works of Harper et al. [2] and Simpkins and Bales [20], respectively.

As the drop flattens, due to the aerodynamics, it becomes immediately susceptible to Rayleigh-Taylor piercing at the accelerated upstream-facing interface. The acceleration can be obtained from (the gravitational acceleration is negligible here)

$$a = \frac{3}{4} C_D \Phi_1 \Phi_2 \frac{\rho_g}{\rho_l} \frac{u^2}{d} \quad (6)$$

where C_D is the appropriate drag coefficient on a sphere (of diameter d) at the relevant flow conditions. The Φ_1 and Φ_2 are to account for deformation effects, the Φ_1 on C_D , and Φ_2 on the cross-sectional area of the drop. With increasing deformation ($1 < d_{\max}/d < 2$) both these factors increase from 1 to ~ 4 . On the other hand, the fastest-growing wave from the classical inviscid analysis can be written as [22]

$$\lambda_d = 2\pi \sqrt{\frac{3\sigma}{a\rho_l}} \quad (7)$$

where we have neglected the gas density relative to that of the liquid. Thus, we can express the number of waves (an odd number of $1/2\lambda_d$'s) that would fit on a “disc” of diameter d_{\max} as

$$n = \frac{2d_{\max}}{\lambda_d} = \frac{1}{2\pi} (C_D \Phi_1)^{1/2} \Phi_2 We^{1/2} \quad (8)$$

Evaluated in this way the n 's for all our TBP experiments are shown in Fig. 8.

The relation of such predictions with TBP data is shown in Fig. 9. The number of waves (the so-called bubbles in the non-linear development of R-T waves) is deduced from the values of n , recognizing that for $n=1$ we have one wave (the “bag”), and that for each increase in n by two (one wavelength) we have to add one more wave. When the number of waves is small, we can see that the visual images support the predictions quantitatively. At

higher Weber numbers, the quantitative measure in the images is lost, but the gradual transition to smaller and small mixing length scales, in agreement with prediction is unmistakable (we will return to these length scales momentarily).

The Glycerin runs were added to the experimental program as a further test of the above—in fact one might say they were “pre-predicted.” Here we use the classical results of Chandrasekhar [22] for viscous liquids (see also a simpler derivation by Joseph et al. [3], using viscous potential flow theory). The exponential growth constant η in the linear regime can be obtained from (we have neglected the gas density relative to that of the liquid, and the gas viscosity):

$$1 - \frac{ak}{\eta^2} = -\frac{k^3 \sigma}{\eta^2 \rho_l} - \frac{4k^2 \mu_l}{\eta \rho_l} + \frac{4k^3 \mu_l^2}{\eta^2 \rho_l^2} \left(\sqrt{k^2 + \frac{\eta \rho_l}{\mu_l}} - k \right) \quad (9)$$

and λ_d was found as the value of $k = 2\pi/\lambda_d$ that maximizes it. The predicted numbers of waves for conditions corresponding to

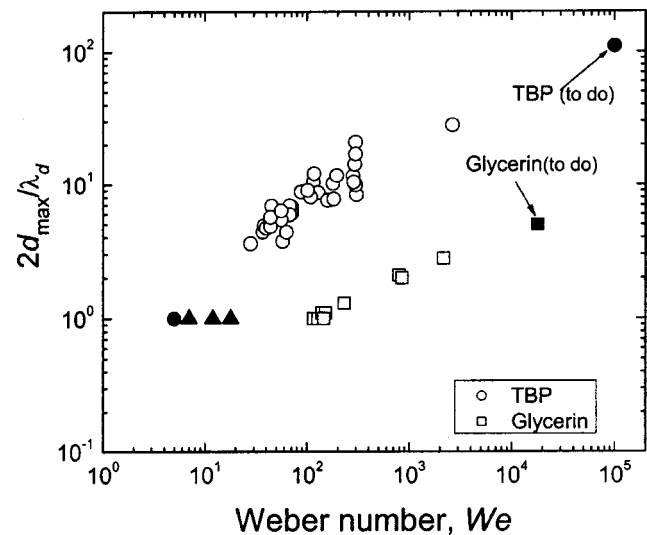


Fig. 8 Estimation of the number of piercing waves possible on an accelerating drop as a function of the Weber number. All ALPHA runs are represented. The scatter for TBP is due to small variation in diameter and degree of deformation (Φ_1, Φ_2) observed. The solid points are explained in the text. The “to do” refers to key new conditions yet to be attained in future experiments.

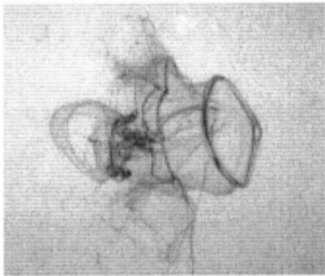
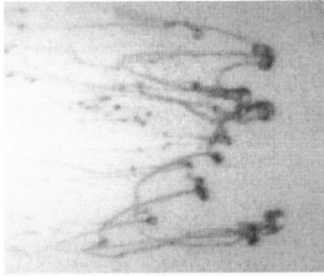
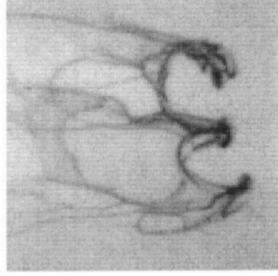
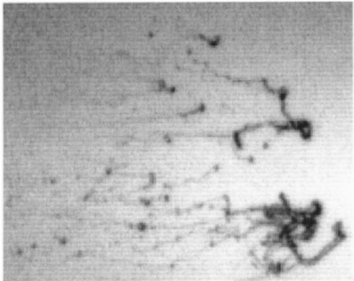
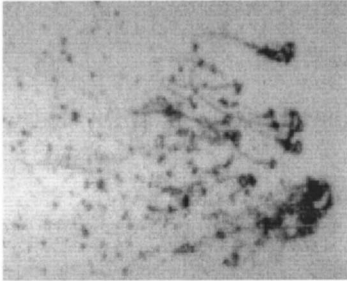
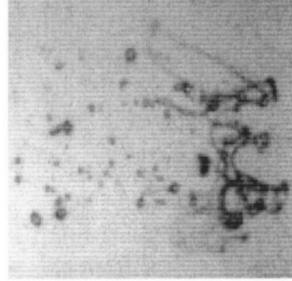
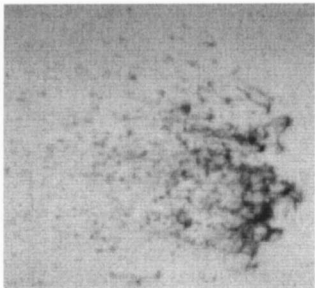
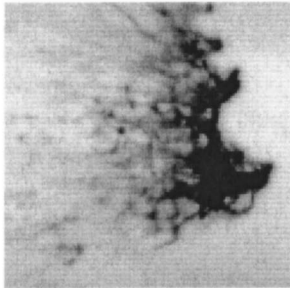
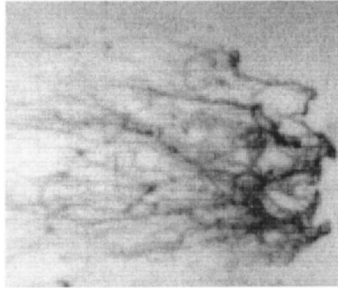
 <p>$We=28$, $d=3.8\text{mm}$, $P_0=15\text{pa}$</p> <p>R-T Instability Prediction $n_{0.5}=3.6$, $\lambda_d=3.2\text{ mm}$, Number of waves predicted 2</p>	 <p>$We=44$, $d=3.7\text{mm}$, $P_0=23\text{pa}$</p> <p>R-T Instability Prediction $n_{0.5}=4.8$, $\lambda_d=2.44\text{ mm}$, Number of waves predicted 3</p>	 <p>$We=56$, $d=3.7\text{mm}$, $P_0=30\text{pa}$</p> <p>R-T Instability Prediction $n_{0.5}=6.4$, $\lambda_d=1.97\text{ mm}$, Number of waves predicted 4</p>
 <p>$We=58$, $d=3.7\text{mm}$, $P_0=31\text{pa}$</p> <p>R-T Instability Prediction $n_{0.5}=3.8$, $\lambda_d=2.76\text{ mm}$, Number of waves predicted 2-3</p>	 <p>$We=63$, $d=3.7\text{mm}$, $P_0=35\text{pa}$</p> <p>R-T Instability Prediction $n_{0.5}=4.4$, $\lambda_d=2.46\text{ mm}$, Number of waves predicted 3</p>	 <p>$We=68$, $d=3.7\text{mm}$, $P_0=37\text{pa}$</p> <p>R-T Instability Prediction $n_{0.5}=5.9$, $\lambda_d=2.0\text{ mm}$, Number of waves predicted 3~4</p>
 <p>$We=109$, $d=3.9\text{mm}$, $P_0=55\text{pa}$</p> <p>R-T Instability Prediction $n_{0.5}=8.0$, $\lambda_d=1.6\text{ mm}$, Number of waves predicted 4~5</p>	 <p>$We=183$, $d=3.7\text{mm}$, $P_0=100\text{pa}$</p> <p>R-T Instability Prediction $n_{0.5}=7.8$, $\lambda_d=1.43\text{ mm}$, Number of waves predicted 4~5</p>	 <p>$We=299$, $d=3.7\text{mm}$, $P_0=160\text{pa}$</p> <p>R-T Instability Prediction $n_{0.5}=17.0$, $\lambda_d=0.8\text{ mm}$, Number of waves predicted 9</p>

Fig. 9 The “piercing” regime in ALPHA and relationship to the predictions of Eq. (8)

our Glycerin runs are shown in Fig. 8. Accordingly, we predict that breakup should initiate by a single wave (“bag”) at $We \sim 100$, and that this should persist up to $We \sim 2,000$, at which point a double wave should appear. As seen in Fig. 7, these predictions are fully supported by the experimental results in ALPHA. Further, in Fig. 8, we can see that for a triple wave piercing the Weber number must reach $\sim 2 \cdot 10^4$ (this test is for our future, upgraded ALPHA).

Now let us consider the “pulling” regime. For a laminar boundary layer, the average shear stress can be expressed as

$$\tau \sim \sqrt{\frac{\sigma \mu_g c}{d^2}} M^{1/2} We^{1/2} \quad (10)$$

Compared to normal pressure/temperature conditions, the square root in the above equation for our experiments is 2.2 times smaller, while the $M^{1/2}$ (at the low Weber number end) would be 9.2 larger. Thus at the same Weber number the shear effect on the drop should be 4.2 times larger, and the “pulling” regime is a clear manifestation of this increase. In fact the pulling regime can

be seen also to be active in the early development of instability at conditions appropriate for single wave piercing (Fig. B.1). This may be responsible for the hourglass shape and the multibag morphology that follows. It appears that in this case, $We \sim 26$, viscous-drag-induced motion just about balances the tendency to penetrate. Thus, the predicted single bag ($n=1$) at $5 < We < 26$ cannot really materialize (with low viscosity liquids, see Fig. 8) in supersonic flow. On Fig. 8, we also show (solid triangles) predictions of the onset of bag breakup in subsonic flow. For a maximum deformation of 1.5 to 1.3, we predict critical Weber numbers of 7 to 18, which is in agreement with data from previous work (see Fig. 1) at normal P/T conditions. Further, pulling is evident in the subsequent behavior of daughter drops found at the low end of multiwave piercing (see Fig. B.2). Preliminary investigation shows that the effect of slip flow on the above results is negligible.

On the other hand, shearing motions are slow relative to piercing, so for $26 < We < \sim 10^3$ the primary mechanism remains piercing. At still higher Weber numbers, as nonlinear piercing slows down because of the decrease in length scales (see below), and shear increases (see Eq. (10)), shear, and accompanying stripping should become increasingly more important and this is quite evident at the upper end of the Weber number range investigated here (see Figs. 6 and B.4). Finally, it is worth pointing out that the internal (liquid) length scales in Fig. 9 are what is left of the so-called R-T “spikes,” broken up into drops, and although related, they should *not* be expected to correspond to the λ_d of the piercing waves—rather they should be much smaller, as indeed seems to be the case in Fig. 9.

Now we apply this understanding to the previous available data and predictions. The pulling regime was not seen previously, and in light of Eq. (10) this is not surprising. What was known as bag breakup is consistent with present findings although not recognized as the inception of piercing process, prevalent over a rather large span of Weber numbers. This piercing regime was missed in previous work, and one reason can be found in Eq. (8). While the Φ_1 and Φ_2 are approximately the same at subsonic or slightly supersonic (previous) and highly supersonic (ours) flow conditions the drag coefficient increases by as much as a factor of 3 to 4. Thus, for the same Weber number the number of waves obtained in supersonic flow would be increased by a factor of 2, which makes them more visible at the low end of the Weber number range. Alternatively, at the same number of waves (same value of $C_D We$), a larger value of d (and d_{\max}) produces a greater, easier to visualize, value of λ_d .

Another reason is that following the works of Harper et al. [2], Simpkins and Bales [20] and Waldman and Reinecke [19] (which appear to have been closely related to each other), the expectation was that piercing (or catastrophic) breakup becomes prevalent at $We \sim 10^4$ to 10^5 , so more attention was focused at the very low (bag breakup) and the upper end of the Weber number range. Applying Eq. (8) with $We \sim 10^5$, and slightly supersonic flow ($M \sim 1.2$), we find $n = 110$, and for a drop of typical size in previous experiments $d \sim 1$ mm, the λ_d is $27 \mu\text{m}$. One implication is that such a wavelength is impossible to visually resolve (see Fig. 1).

Another and perhaps more important implication is that in the nonlinear regime such waves would penetrate with a velocity (inviscid approximation)

$$U \sim \sqrt{\lambda_d a} \sim \sqrt{2\pi \frac{3}{2} \frac{\sigma}{\rho_l d_{\max}}} (C_D \Phi_1)^{1/4} \Phi_2^{1/2} We^{1/4} \quad (11)$$

that is, a velocity that is rather slowly increasing with Weber number. As we can see from Eq. (10), shear increases considerably faster, and this would be further accentuated by interfacial

roughness due to the development of waves (also Kelvin-Helmholtz instability and perhaps turbulence may have to be included). Liquid viscosity, active at such small length scales, would further retard the penetration velocity, thus shifting even more the balance in favor of shear. In particular using Eqs. (8) and (11) a bounding estimate of the Reynolds number can be obtained as

$$Re = \frac{\rho_l U \lambda_d}{\mu_l} \sim 4\pi \sqrt{3} \pi \sqrt{\frac{\rho_l d_{\max} \sigma}{\mu_l^2}} (C_D \Phi_1)^{-1/4} \Phi_2^{-1/2} We^{-1/4} \quad (12)$$

which clearly shows $Re \rightarrow 0$ as $We \rightarrow \infty$. For example, at $We = 10^6$, $Re \sim 210$ and 0.2 , for 1 mm water and Glycerin drops, respectively.

In the same vein, it should also be noted that, as Eq. (8) indicates, when n is of order unity penetration occurs in the linear-growth regime and it is exponential (this is why bag and multibags appear to “explode”), while when n is very large (large Weber numbers) the penetration should enter the nonlinear regime (Eq. 11), well before penetration, and should proceed at a constant rate, as by Eq. (11), or some appropriate modification of it, when viscosity becomes important.

A similar conclusion is reached by comparing the penetration velocity (in the nonlinear regime), U , with the shear-induced interfacial velocity, U_s obtained from a coupled laminar boundary layer analysis. For an 1 mm water drop at $We = 10^2$, $U/U_s = 1.5$, while at $We = 10^6$, we obtain $U/U_s = 0.2$, and would expect this to be even smaller if account is taken of interfacial roughness.

Thus, as $We \rightarrow \infty$ we would expect shear and stripping, rather than piercing to prevail. Actually, as noted already, such stripping is quite evident in our experiments already at $We \sim 10^3$, and also it can be seen in previous data (Fig. 1), especially well in the data of Ranger and Nicholls [18]. The question remains, is piercing present at all of this very high end of Weber numbers (practically $We \rightarrow \infty$)? On the basis of the above, we think it may be not.

Finally, it is worth noting that behavior of fuel droplets behind a shock wave in transonic and supersonic gas flow plays an important role in supersonic combustors and liquid-fuel pulse detonation engines operating on a multiphase principle. Under normal-to-high pressures and high-flow velocities, small sizes of fuel droplets in these applications lead us to an exotic regime of high Mach, low Weber and high Knudsen numbers. Due to the prohibitive difficulty to visually observe and quantify breakup phenomena of microscopic droplets in high-speed flows, analyses of supersonic combustion systems made use of drop breakup data obtained for low Weber number conditions but in low Mach and low Knudsen number flow. Results presented in this paper shows that the Mach scaling is important. The ALPHA facility, with its supersonic rarefied conditions, offers the possibility to simultaneously satisfy the Weber, Mach and Knudsen scaling needed [23].

Conclusions and Implications

1. The regimes of drop breakup in highly rarefied, highly supersonic gas flows, are for the first time quantified (transition criteria, evolving morphologies, mixing length scales, daughter drops sizes), and theoretically elucidated including effects of liquid viscosity.

2. With increasing Weber number the regime sequence is, Pulling (by viscous drag), Piercing (by Rayleigh-Taylor instability, in succession from one wave, a bag, to multiple waves), and Stripping (by shear). Further confirmation of the piercing regime, perhaps by frontal three-dimensional imaging would seem desirable. Evidence is presented that the present scheme of interpretation is also consistent with all normal P/T data, quite unexpectedly in

light of all previous interpretations; however, this issue requires further investigation, directly by experiments at such conditions.

3. The experimental approach developed in this work provides for unprecedented access to interfacial breakup and mixing phenomena to a detail (and conditions) that is quite appropriate for benchmarking direct numerical simulations (qualitative comparisons of key features of breakup regimes). This would be crucial on the way to predicting more complex and experimentally inaccessible situations; for example the effect of “structuring” the flow history.

4. The importance of breakup regime on resulting distribution of length scales and mixing morphologies is clearly demonstrated, thus providing the means to tailoring condition to desired behaviors. More detailed characterization of these aspects merits further investigation.

5. Consideration in this framework of even larger masses would be very significant (theoretical as well as practical interest).

Acknowledgments

The ALPHA facility was built under support from Lawrence Livermore National Laboratory (LLNL), thanks to the vision and cooperation of Drs. F. Handler and G. Nakafuji. This Newtonian fluids work was carried out as a preamble to considering viscoelastic liquids, which is the principal purpose of ALPHA. We are grateful to our collaborators at CRSS, Dr. K. Gasljevic, Mr. T. Salmassi and Mr. R. Khalafi for help with building and operating ALPHA, and Drs. R. Nourgaliev, S. Sushchikh, and D. L. Dalal for CFD support using the MuSic code, that was quite essential in refining the design, and operation of the facility.

Nomenclature

a	= acceleration
c	= speed of sound
C_D	= drag coefficient of sphere
d	= spherical drop diameter
Kn	= Knudsen number
M	= Mach number
P_0	= static pressure
P_s	= stagnation pressure
Re	= Reynolds number
T	= temperature
u	= free stream velocity
We	= Weber number
Φ_1	= shape coefficient on drag, Eq. (6)
Φ_2	= shape coefficient on area, Eq. (6)
γ	= gas specific heat ratio
λ	= wavelength of R-T instability
μ_g, μ_l	= gas, liquid viscosities
ρ_g, ρ_l	= gas, liquid densities
σ	= surface tension
τ	= shear stress

Appendix A: Brief Explanations on Fig. 1

An influential review and synthesis on the subject was provided by Pilch and Erdman [24], and recently we have the extensive critical review of Gel'fand [4]-200 papers cited. The most recent, extensive experimental works were carried out by Faeth and co-workers [12-14] focusing on the low end of the Weber number range (~ 10 to 10^2) and by Joseph and co-workers [3,25] who focused on the high end ($\sim 10^4$ to 10^5). Classic references are those of Engel [17], Ranger and Nicholls [18], Simpkins and Bales [20], Waldman and Reinecke [19], and the theoretical work of Harper et al. [2]. The experiments were carried out mainly in shock tubes and at pressures near atmospheric, but in a few cases wind tunnels were also employed. Because of their great length, shock tubes are positioned horizontally, and this creates limitations on the injection method and the drop sizes obtainable. A wind tunnel, operating at steady state, requires that the liquid be injected through the wall boundary layer; this introduces complications in interpretation, and limits the conditions accessible for such experiments. Except for slight and usually undocumented differences, the overall regime classification scheme that emerges from all this work is as shown in Fig. 1.

The “Vibrational,” “Bag,” and “Bag-and-stamen” regimes, as illustrated, are easily recognizable, and rather well defined in terms of the critical Weber number required for their inception. The “Bag” regime was studied most extensively, and it is known that the resulting droplet distribution is bimodal: one size coming from the shattering of the bag, and another much bigger size coming from the capillary breakup of the rim (see Fig. 1). No robust theoretical interpretation of these regimes has been previously available.

The “shear,” or “stripping,” and “catastrophic” or “shattering” regimes were thought to evolve at higher Weber numbers, but data, definitions and interpretations are partial and to a significant degree speculative. As indicated in Fig. 1, the former is stated to evolve from $We \sim 10^2$, until $We \sim 10^4$ to 10^5 , where the latter is thought to set in as the dominant mechanism. As visualized in Fig. 1, the former involves a fine mist of liquid emanating from the equator, presumably due to a shear-induced boundary layer on the liquid surface. A simplified viscous description of it (ignoring all other effects such as interfacial instabilities and of thus-resulting roughness) was given by Taylor [26] and Ranger and Nicholls [18]. The catastrophic regime, first introduced theoretically by Harper et al. [2], is thought to involve piercing by Rayleigh-Taylor waves, and it was recently analyzed, on the same basis, also by Joseph et al. [3]. Harper et al. [2] argued that at a $We \sim 10^5$ the growth of instabilities changes character, from algebraic to exponential. Joseph et al. [3] argued that waves seen on visual images (such as those in Fig. 1) are consistent with most rapidly growing Rayleigh-Taylor waves at the Weber number range of their experiments (10^4 to $\sim 2 \cdot 10^5$). Waldman and Reinecke [19] and Simpkins and Bales [20] related their experimental results qualitatively to the catastrophic regime of Harper et al. Just as Taylor [26] and Ranger and Nicholls [18] considered shear without interfacial instability, so Harper et al. [2] and Joseph et al. [3] considered interfacial instability without shear. No fragment length scales or mixing morphologies are available in these high-Weber-number regimes.

Appendix B. Detailed Evolutions from Selected ALPHA Tests

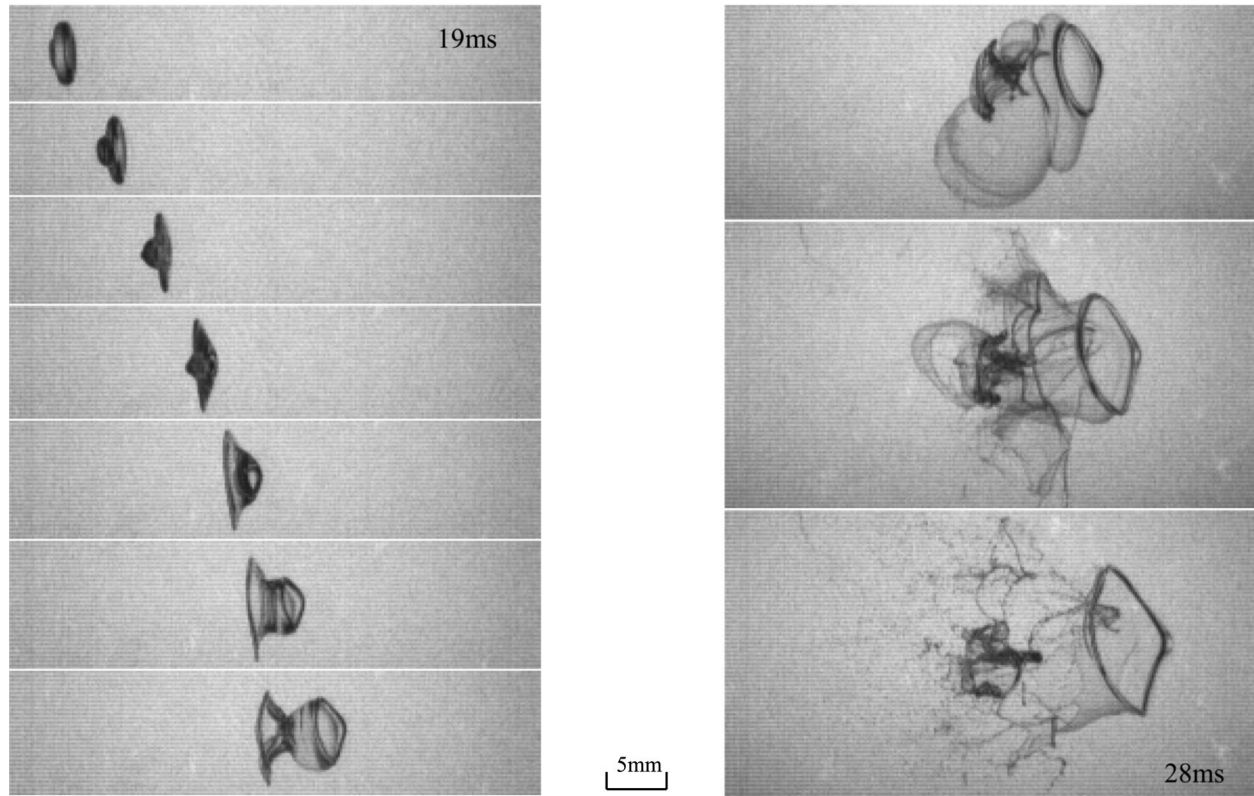


Fig. B.1 “Multibag” breakup of a TBP drop in ALPHA ($We=28, d=3.8$ mm). Time interval between two adjacent images is 1 ms.

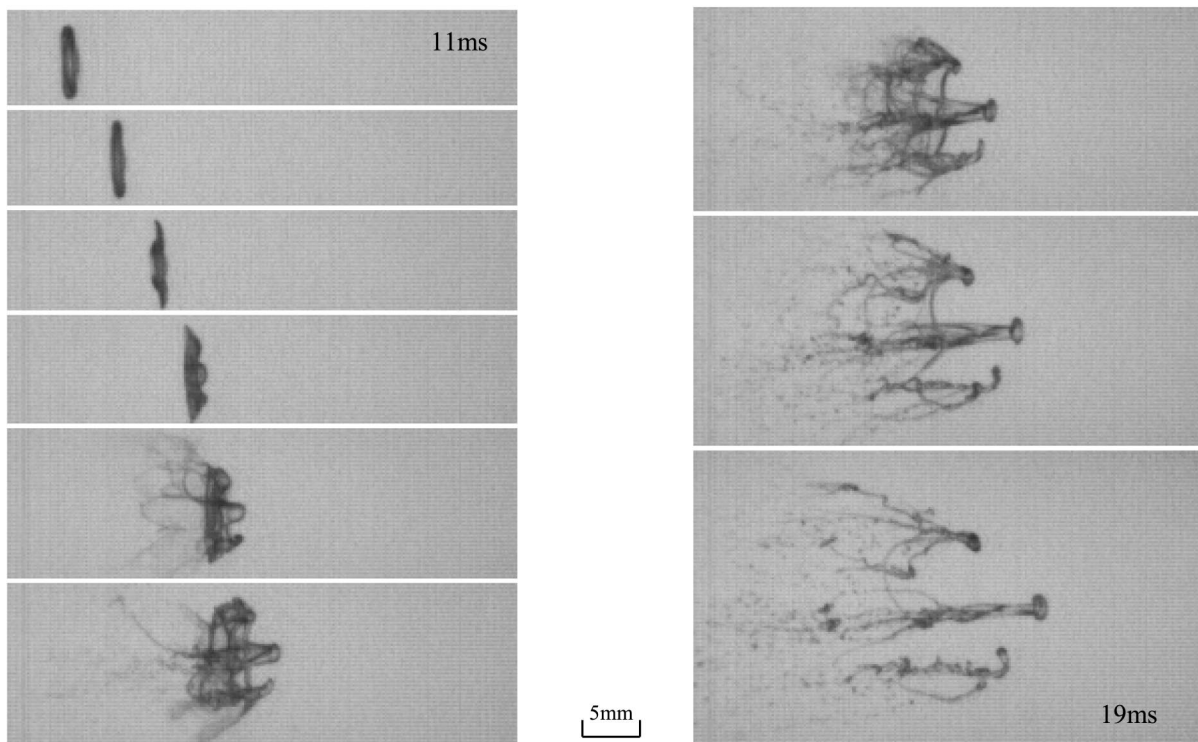


Fig. B.2 “Piercing” breakup of a TBP drop in ALPHA ($We=57, d=3.7$ mm). Time interval between two adjacent images is 1 ms.

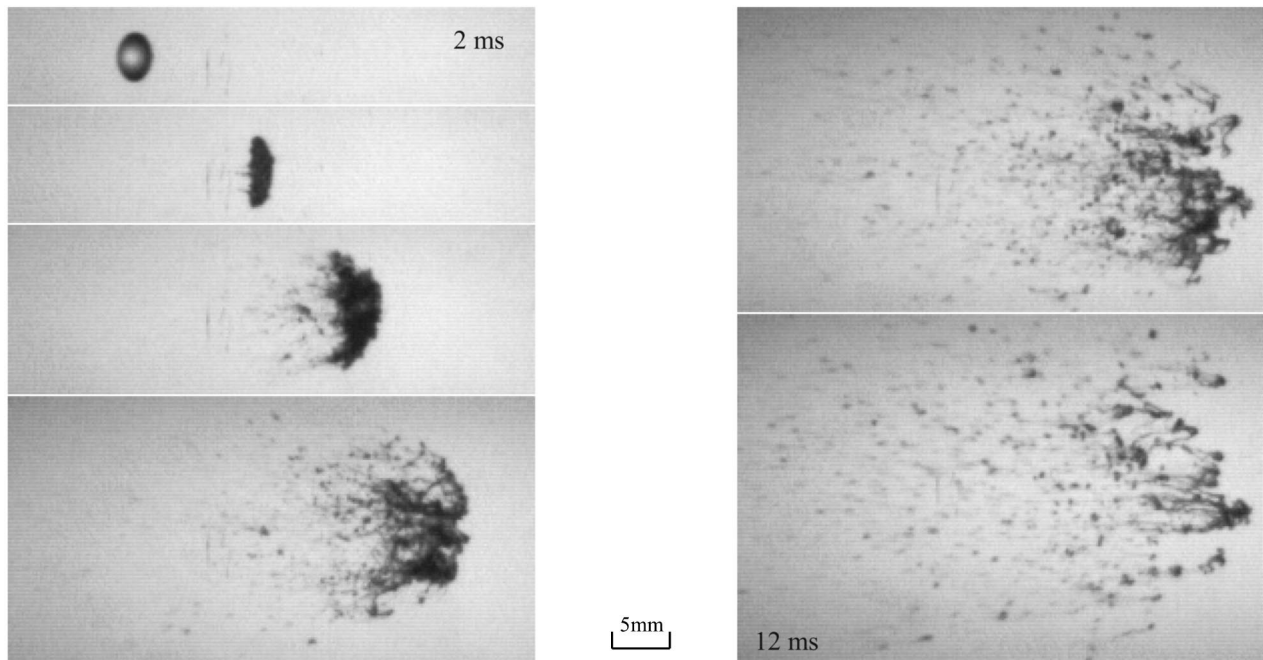


Fig. B.3 “Piercing” breakup of a TBP drop in ALPHA ($We=109, d=3.9$ mm). Time interval between two adjacent images is 2 ms.

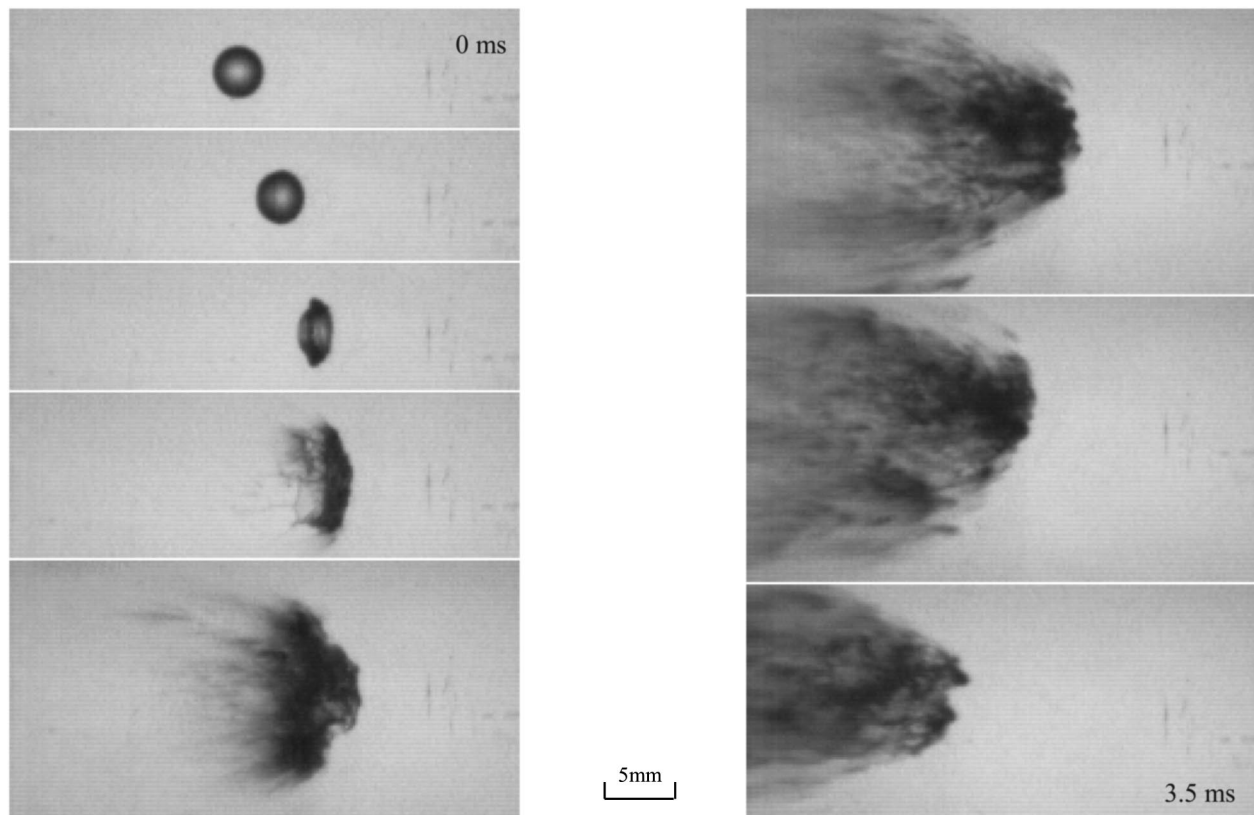
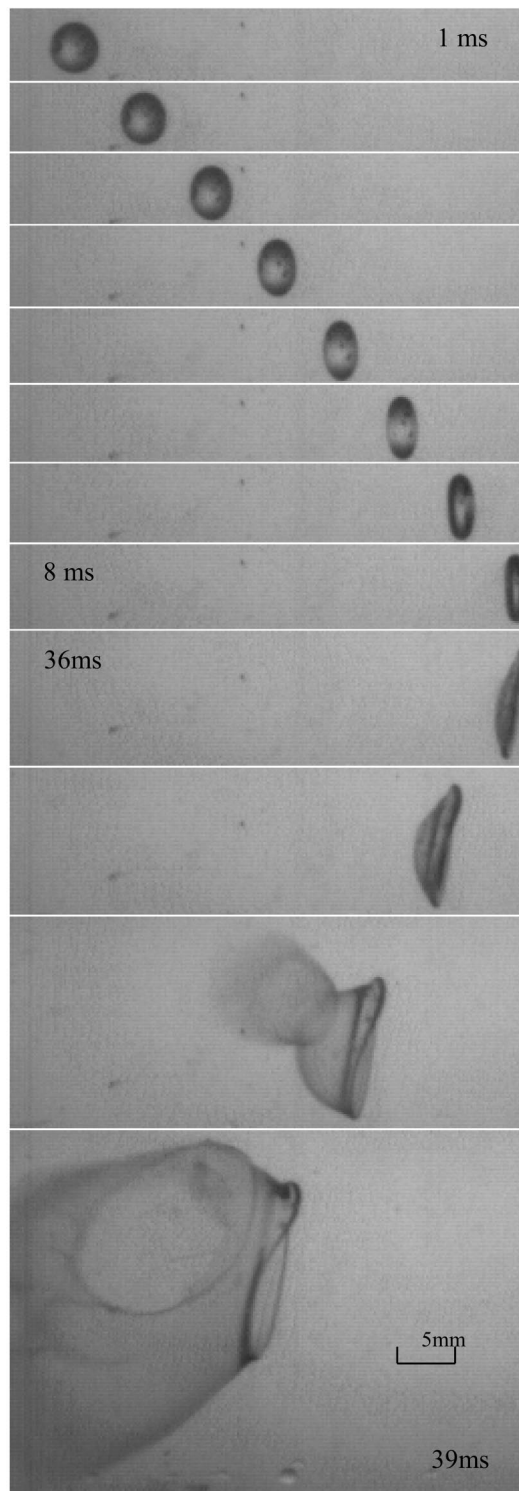
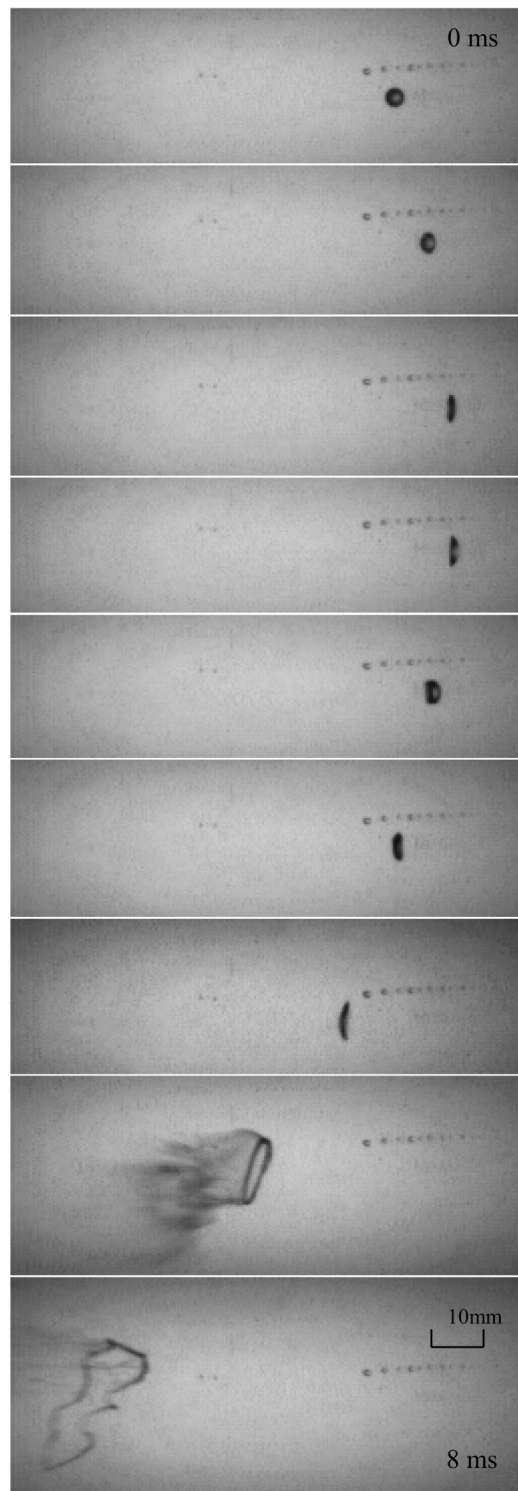


Fig. B.4 Mostly “Stripping” breakup of a TBP drop in ALPHA ($We=2643, d=3.7$ mm). Time interval between two adjacent images is 0.5 ms.



$We=140, d=4.5 \text{ mm}$



$We = 852, d=3.7 \text{ mm}$

Fig. B.5 “Bag” breakup of Glycerin drops in ALPHA. Time interval between two adjacent images is 1 ms.

References

- [1] Hinze, J. O., 1955, “Fundamentals of the hydrodynamic mechanism of splitting in dispersion processes,” *AIChE J.*, **1**, pp. 289–295.
- [2] Harper, E. Y., Grube, G. W., and Chang, I.-D., 1972, “On the breakup of accelerating liquid drops,” *J. Fluid Mech.*, **52**, pp. 565–591.
- [3] Joseph, D. D., Belanger, J., and Beavers, G. S., 1999, “Breakup of a liquid suddenly exposed to a high-speed airstream,” *Int. J. Multiphase Flow*, **25**, pp. 1263–1303.
- [4] Gel’fand, B. E., 1996, “Droplet breakup phenomena in flows with velocity lag,” *Prog. Energy Combust. Sci.*, **22**, pp. 201–265.
- [5] Patel, B. D., and Theofanous, T. G., 1981, “Hydrodynamic fragmentation of drops,” *J. Fluid Mech.*, **103**, pp. 207–223.
- [6] Seghal, B. R., Nourgaliev, R. R., and Dinh, T. N., 1999, “Numerical simulation of droplet deformation and break-up by a Lattice-Boltzman method,” *Progress in Nuclear Energy*, **34**, pp. 471–488.
- [7] Han, J., and Tryggvason, G., 1999, “Secondary breakup of axisymmetric liq-

- uid drops. I. Acceleration by a constant body force," *Phys. Fluids*, **11**, pp. 3650–3668.
- [8] Wierzbna, A., 1990, "Deformation and Breakup of liquid drops in a gas stream at nearly critical Weber number," *Exp. Fluids*, **9**, pp. 59–64.
- [9] Shraiber, A. A., Poduystotsky, A. M., and Dubrovsky, V. V., 1996, "Deformation and breakup of drops by aerodynamic forces," *Atomization Sprays*, **6**, pp. 667–692.
- [10] Hanson, A. R., Domich, E. G., and Adams, H. S., 1963, "Shock tube investigation of the breakup of drops by air blasts," *Phys. Fluids*, **6**, pp. 1070–1080.
- [11] Krzeczkowski, S. A., 1980, "Measurement of liquid droplet disintegration mechanisms," *Int. J. Multiphase Flow*, **6**, pp. 227–239.
- [12] Hsiang, L.-P., and Faeth, G. M., 1992, "Near-limit drop deformation and secondary breakup," *Int. J. Multiphase Flow*, **18**, pp. 635–652.
- [13] Chou, W.-H., and Faeth, G. M., 1998, "Temporal properties of secondary drop breakup in the bag breakup," *Int. J. Multiphase Flow*, **24**, pp. 889–912.
- [14] Dai, Z., and Faeth, G. M., 2001, "Temporal properties of secondary drop breakup in the multimode breakup regime," *Int. J. Multiphase Flow*, **27**, pp. 217–236.
- [15] Gel'fand, B. E., Gubin, S. A., and Kogarko, S. M., 1974, "Various forms of drop fractionation in shock waves and their special characteristics," *Inzh.-Fiz. Zh.*, **27**, pp. 119–126.
- [16] Hirahara, H., and Kawahashi, M., 1992, "Experimental investigation of viscous effects upon a breakup of droplets in high-speed air flow," *Exp. Fluids*, **13**, pp. 423–428.
- [17] Engel, O. G., 1958, "Fragmentation of water drops in the zone behind an air shock," *J. Res. Natl. Bur. Stand.*, **60**, pp. 245–280.
- [18] Ranger, A. A., and Nicholls, J. A., 1969, "Aerodynamic shattering of liquid drops," *AIAA J.*, **7**, pp. 285–290.
- [19] Waldman, G. D., and Reinecke, W., 1972, "Raindrop breakup in the shock layer of a high-speed vehicle," *AIAA J.*, **10**, pp. 1200–1204.
- [20] Simpkins, P. G., and Bales, E. L., 1972, "Water-drop response to sudden accelerations," *J. Fluid Mech.*, **55**, pp. 629–639.
- [21] Anderson, Jr, J. D., 2001, *Fundamentals of aerodynamics*, Third Edition, McGraw-Hill, London, pp. 495–497.
- [22] Chandrasekhar, S., 1981, *Hydrodynamic and hydromagnetic stability*, Dover Publication, Inc., New York, pp. 441–443.
- [23] Dinh, T. N., Li, G. J. and Theofanous, T. G., 2003, "An Investigation of Droplet Breakup in a High Mach, Low Weber Number Regime," *41st Aerospace Sciences Meeting*, Reno, Nevada, January 5–8, 2003. Paper AIAA-2003-0317.
- [24] Pilch, M., and Erdman, C. A., 1987, "Use of breakup time data and velocity history data to predict the maximum size of stable fragments for acceleration-induced breakup of a liquid drop," *Int. J. Multiphase Flow*, **13**, pp. 741–757.
- [25] Joseph, D. D., Beavers, G. S., and Funada, T., 2002, "Rayleigh-Taylor instability of viscoelastic drops at high Weber numbers," *J. Fluid Mech.*, **453**, pp. 109–132.
- [26] Taylor, G. I., 1949, "The shape and acceleration of a drop in a high-speed air stream," *The Scientific Papers of Sir Geoffrey Ingram Taylor*, 3, Batchelor, G. K. (Ed.), University Press, Cambridge, 1963.

S. Kim*

Assistant Professor
Nuclear Engineering, University of
Missouri-Rolla
Rolla, MO 65409-0170

S. S. Paranjape

Graduate Student
School of Nuclear Engineering, Purdue
University,
West Lafayette, IN 47907-1290

M. Ishii

Walter H. Zinn Distinguished Professor
School of Nuclear Engineering, Purdue
University,
West Lafayette, IN 47907-1290

J. Kelly

U.S. Nuclear Regulatory Commission
Washington D.C., 20555

Interfacial Structures and Regime Transition in Co-Current Downward Bubbly Flow

The vertical co-current downward air-water two-phase flow was studied under adiabatic condition in round tube test sections of 25.4-mm and 50.8-mm ID. In flow regime identification, a new approach was employed to minimize the subjective judgment. It was found that the flow regimes in the co-current downward flow strongly depend on the channel size. In addition, various local two-phase flow parameters were acquired by the multi-sensor miniaturized conductivity probe in bubbly flow. Furthermore, the area-averaged data acquired by the impedance void meter were analyzed using the drift flux model. Three different distributions parameters were developed for different ranges of non-dimensional superficial velocity, defined by the ration of total superficial velocity to the drift velocity. [DOI: 10.1115/1.1777229]

1 Introduction

The significance of the co-current downward flows can be easily found in some transient conditions in the reactor system. Some examples in the Light Water Reactor (LWR) systems can be found in cases of Loss of Heat Sink (LOHS) by feedwater loss or secondary pipe break. In such scenario, the steam generator may go into the two-phase co-current down flow condition. This can also happen when the primary coolant is discharged through the relief valve. It is also possible that the two-phase flow may go through the SG in cases of small break LOCA or relieve valve open, and thus creating both the co-current up and co-current down flows. In Boiling Water Reactor (BWR), the co-current downward two-phase flow can be encountered in the later stage of the ECCS injection, signified by the Counter Current Flow Limitation (CCFL) phenomena.

Even though, there exist some previous studies focused on co-current downward two-phase flow, most of the researches were focused mainly on the flow regime identification by flow visualization method [1–4]. However, due to the subjective nature of the flow visualization method, the regime transition boundaries are not only inconsistent, but they are not reliable. Furthermore, there is hardly any research on interfacial structures or interfacial area transport in co-current downward two-phase flow.

2 Experimental Facilities

The schematic diagram of the adiabatic vertical air-water experimental loop employed in this study is shown in Fig. 1. The two test sections were made with round acrylic pipes of 25.4 and 50.8 mm ID. The total length of each test section is $z/D = 150$ and 75 for 25.4 and 50.8 mm ID pipes, respectively. The water and air flow rates are measured by an electro-magnetic flow meter and rotameters, respectively. The accuracies are within $\pm 3\%$ and $\pm 8\%$ when the measured flow rate is more than 50% of the full scale. Throughout the experiment, the air pressure is maintained

by a pressure regulator at 690 kPa (100 psia), and both the water and air flow rates are measured by flow meters whose scale yield more than 50% of the full scale. A sparger with porous tip with 10 micron pores is employed as a bubble generator. The present injection unit produces uniform bubbles of approximately 1–2 mm in diameter at the inlet of the test section. An air-water mixture injection unit is employed at both the top and the bottom of each test section so that the loop is capable of operating in both upward and downward flow experiments. In operating the loop, single-phase water flow was created as the initial condition, and thereafter, gas was gradually supplied into the test section. The free-falling condition was not investigated. In some flow conditions, falling film annular flow was observed near the inlet, followed by a very chaotic mixing region due to kinematic shock. After the mixing region, the flow eventually reaches either bubbly or slug flows depending on the inlet conditions.

In the flow visualization study, a high-speed digital motion analyzer was employed which is capable of operating at the maximum of 1,000 frames per second and 1/20,000 s of shutter speed. A transparent acrylic square box filled with water was attached onto the test section to minimize the image distortion due to the curved surface of the test section.

An impedance void meter was employed in order to obtain the area-averaged impedance signals [5]. An impedance void meter is a non-intrusive conductance type probe that utilizes the difference in electrical conductivity between the air and water. Two-pairs of stainless steel plates are employed as an electrode, and they are flush mounted against the inner wall of the test section. The electrodes span 90 deg of the cross section with thickness of 0.953 cm. The thickness was chosen so as to be larger than the dimension of a typical bubble, yet shorter than the length of a cap or a slug bubble. At one measurement port, two-pairs of electrodes, which are 100 mm apart, are installed so that the void propagation velocity can be acquired. An alternating current is supplied to the electrodes at 100 kHz, and the electrodes are connected to the electrical circuit, which is specially designed so that the output voltage of the circuit becomes proportional to the measured impedance; i.e., $V_{out} \propto G_m$. These impedance signals were employed

*The author was at Purdue University when this research was performed.

Contributed by the Fluids Engineering Division for publication in the JOURNAL OF FLUIDS ENGINEERING. Manuscript received by the Fluids Engineering Division May 27, 2003; revised manuscript received September 16, 2003. Associate Editor: J. Katz.

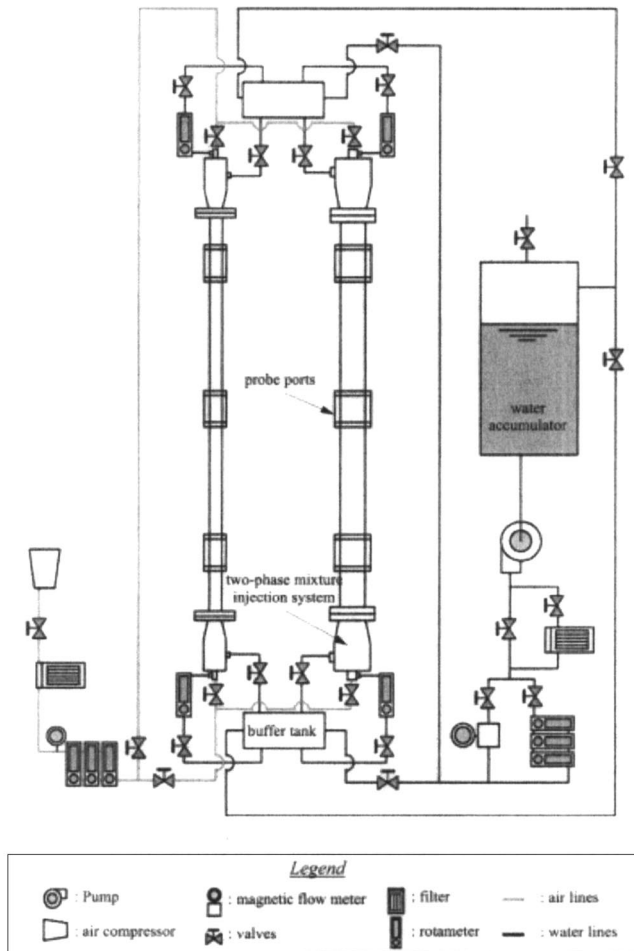


Fig. 1 Schematic diagram of the present experimental loop

in both acquiring the area-averaged void fraction with the specific impedance-void fraction correlation and identifying the flow regime.

The four-sensor conductivity probe was employed to acquire the local two-phase flow parameters [6]. The local parameters were acquired by traversing the probe from the center to the wall of the test section with a smallest increment of $r/R=0.1$. Accounting for the interfacial structures, more detailed measurements were made near the wall than near the center of the test section. The measurement error of the present probe is estimated to be less than $\pm 7\%$ [7].

3 Experimental Results and Discussions

3.1 Flow Regime Identification

Flow Visualization Method. The flow was observed at $z/D = 116$ and 58 from the inlet, for the 25.4 mm ID loop and the 50.8 mm ID loop, respectively. The experimental flow conditions were varied within $j_f = -1.25 \sim -3.11$ m/s, $j_g = -0.01 \sim -22.9$ m/s for the 25.4 mm ID loop, and $j_f = -0.47 \sim -3.42$ m/s, $j_g = -0.003 \sim -5.46$ m/s for the 50.8 mm ID loop. In general, the frame rate of a high-speed motion analyzer was set at 500 frames per second with the shutter speed of $1/2,000$ s. Figures 2(a)–(d) show the photographic images of four typical flow regimes observed in the co-current downward two-phase flow in 25.4 mm ID test section. No significant difference was observed in the flow regime characteristics between the 25.4 mm ID and 50.8 mm ID loop. The following observations were made for each regime:

a. The bubbly flow is essentially similar to that in the upward flow. The major difference can be observed in that the bubbles in downward flow tend to migrate towards the center of the tube, which was also reported in previous studies [8,9].

b. The slug flow observed in the co-current downward flow is quite different from that observed in the upward flow. The characteristic bullet-shaped gas slug (also known as the Taylor bubble)

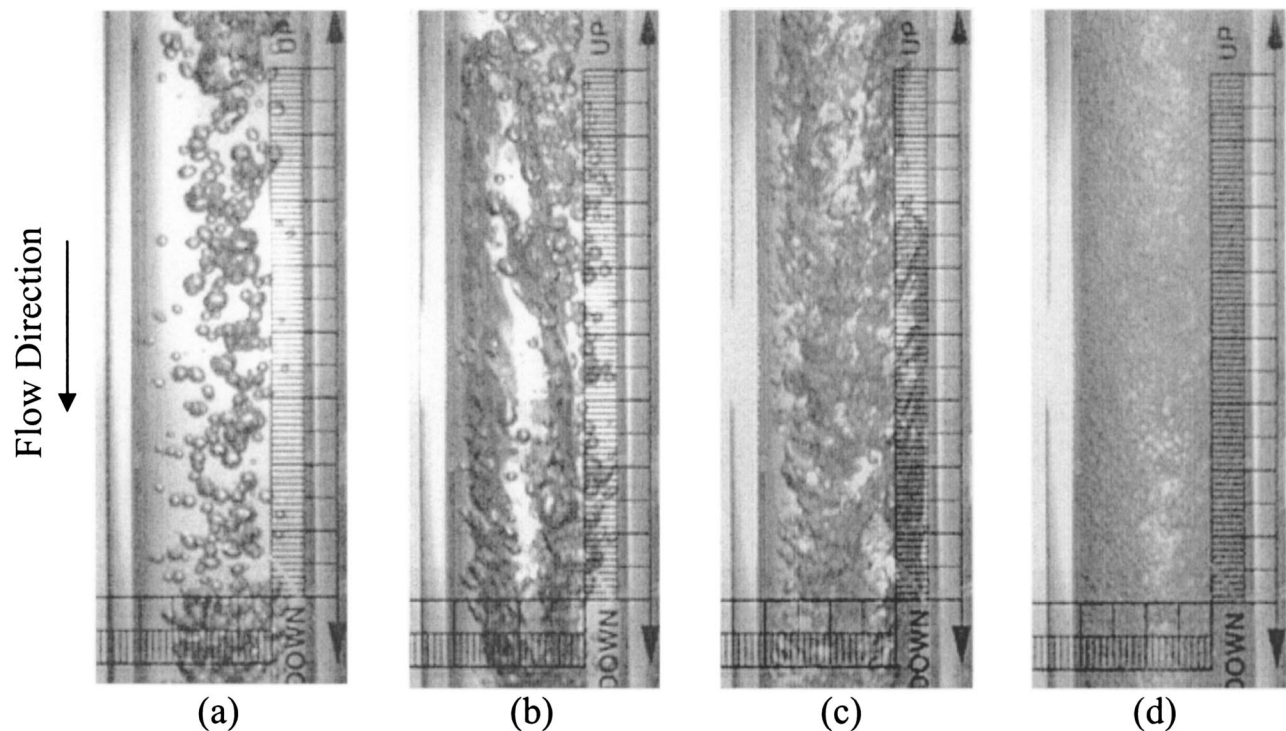


Fig. 2 Characteristic images acquired for each flow regime. (a) Bubbly flow: $j_f = -2.12$ m/s & $j_g = -0.21$ m/s, (b) Slug flow: $j_f = -2.12$ m/s & $j_g = -0.42$ m/s, (c) Churn-turbulent flow: $j_f = -2.12$ m/s & $j_g = -1.07$ m/s and (d) Annular flow: $j_f = -2.12$ m/s & $j_g = -9.17$ m/s.

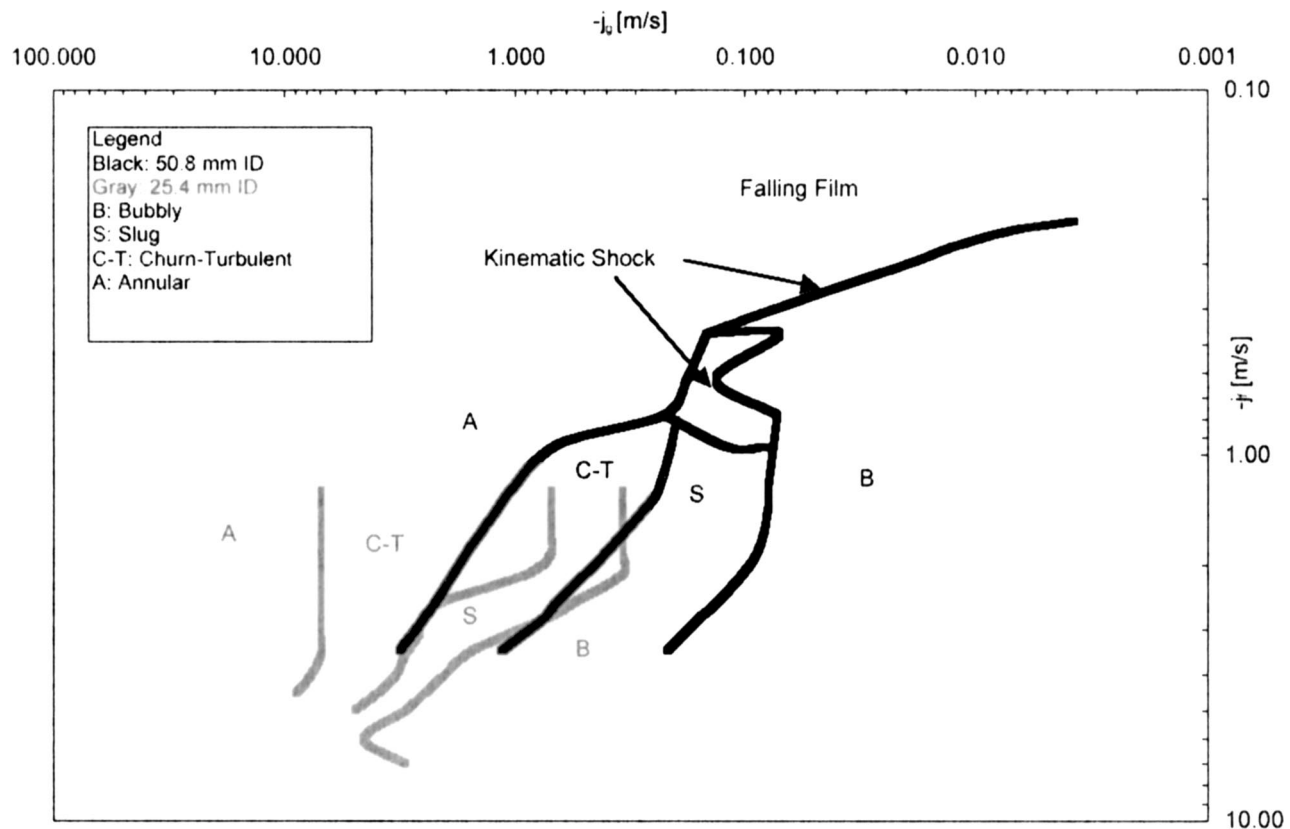


Fig. 3 Flow regime transition boundaries for co-current downward two-phase flow in 25.4 mm ID and 50.8 mm ID pipes

with its nose directing toward the flow direction and staying near the center of the flow channel was not observed. In the co-current downward two-phase flow gas, the slug is highly distorted and its nose is always off-centered toward the wall of the test section, forming a wedge shape. In addition, the nose faces opposite to the flow direction in the downward co-current two-phase flow.

c. The churn-turbulent flow can be considered as a transition condition between the slug and annular flow. It is characterized by the highly distorted cap bubbles varying in size and shape, and by highly turbulent flow field. It is noted that some previous studies [4] do not categorize churn-turbulent flow as an independent flow regime; it was instead included within slug flow. The present study categorizes the churn-turbulent flow as an independent flow regime in view of distinctive interfacial structures and difference in bubble interaction mechanisms as shown in Fig. 2(c).

d. The annular flow is characterized by wavy liquid film along the pipe inner wall with gas core. The Annular flow for downward flow can be categorized into two categories, that is; the falling film flow and the annular drop flow. As expected, in the flow visualization, the identification of the boundary between the churn-turbulent and annular flow regime was quite difficult simply due to the unclear images in the transition condition. In the present study, the flow was categorized as an annular flow when the images of continuous ripples due to the wavy liquid film were observed.

Impedance Void Meter With Neural Network Classification Technique. An impedance void meter is capable of acquiring the area-averaged signals that represent the structural characteristics of the flow. Hence, various statistical moments of the impedance signal would reflect the characteristics of the flow regimes [5]. The mean, standard deviation, and skewness derived from the impedance signals were adopted to train the neural network in this investigation. These statistical parameters are defined as follows:

$$\text{Mean: } \bar{x} = \frac{1}{n} \sum_{i=1}^n x_i \quad (1)$$

$$\text{Standard Deviation: } \sigma = \sqrt{\frac{1}{n(n-1)} \left[n \sum_{i=1}^n x_i^2 - \left(\sum_{i=1}^n x_i \right)^2 \right]} \quad (2)$$

$$\text{Skewness: } \gamma = \frac{n}{(n-1)(n-2)} \sum_{i=1}^n \left(\frac{x_i - \bar{x}}{\sigma} \right)^3 \quad (3)$$

These three statistical parameters derived from the impedance signals were set into the self-organizing neural network as an input matrix. In processing the signal, the MATLAB was employed. The neural network was trained by these input parameters and classified them into four categories. The classification categories adopted in this investigation were four flow regimes; namely, bubbly, slug, churn-turbulent, and annular flow regimes. The selection of training samples based on subjective judgment may hamper the reliability of present approach. Therefore, particular attention was paid in choosing sample images, such that the selected training sample obviously belongs to one flow regime. In general, the samples from 50 flow conditions were used in training process, and approximately 5,000 iterations were allowed in training the network. The resulting flow regime map for both flows in 25.4 and 50.8 mm ID pipes are shown in Fig. 3. Unlike the upward two-phase flow, it was found that the flow regime transition in co-current downward two-phase flow strongly depends on the flow channel size.

3.2 Data Analysis. To study the details of the interfacial structures, 15 flow conditions were chosen in the bubbly flow regime for 25.4 mm ID loop and 10 flow conditions in the bubbly

Table 1 Flow conditions for local measurement

Run No.	Flow Conditions for 25.4 cm ID loop		Flow Conditions for 50.8 cm ID loop	
	j_g [m/s]	j_f [m/s]	j_g [m/s]	j_f [m/s]
1	0.015	1.250	0.004	0.620
2	0.087	1.250	0.004	1.250
3	0.085	2.120	0.028	1.250
4	0.086	3.110	0.023	2.490
5	0.404	3.110	0.040	0.620
6	0.243	1.250	0.048	1.260
7	0.317	2.120	0.071	2.490
8	0.068	4.000	0.078	3.480
9	0.068	5.070	0.158	3.470
10	0.253	3.970	0.078	1.250
11	0.248	4.980	—	—
12	0.595	4.030	—	—
13	0.570	4.960	—	—
14	1.974	3.990	—	—
15	1.977	4.970	—	—

flow regime for 50.8 mm ID loop. These flow conditions are shown in Table 1. The local two-phase flow parameters are acquired by the state-of-the-art four-sensor conductivity probe [6]. The signal obtained from the probe is fed to a signal processing program, which calculates the local parameters from the raw data. These local parameters include void fraction (α), interfacial area concentration (a_i), and bubble velocity (v_b). These parameters are measured at three axial locations in each loop. In 25.4 mm ID loop, the local parameters are measured at $z/D = 13, 68$ and 133 , while in 50.8 mm ID loop, these are measured at $z/D = 7, 34$ and

67. At each axial measurement location, the probe is traversed in the radial direction to take measurements at different r/R locations, ($r/R = 0, 0.2, 0.4, 0.5, 0.6, 0.7, 0.8, 0.9$) where r is the radial distance from the center of the pipe and R is the inner radius of the pipe. The spacing between the measurement points is chosen such that it is coarser near the center of the pipe and finer near the wall of the pipe, considering the fact that the variation of the local two-phase flow parameters is higher near the pipe wall. The area-averaged parameters are calculated from the local parameters, by integrating them over the pipe cross-section, assuming radial symmetry. To have the statistical error within $\pm 7\%$ of the measured values, at each location, the data acquisition time is adjusted so that at least 2,000 bubbles are encountered by the probe tip [7]. To assess the accuracy of the probe measurement, the area averaged value of the product of local α and v_b , (i.e., $\langle \alpha v_b \rangle$) is compared with $\langle j_g \rangle$, obtained from gas flow meter and local pressure measurements. It was observed that the two values agree well within $\pm 10\%$ for most of the flow conditions.

Local Two-phase Flow Parameters. The characteristic results from local parameter measurements are presented in this subsection. The local profiles of the two-phase flow parameters at different axial locations reveal the bubble interaction mechanisms. To highlight the transport characteristics, the results from runs 2, 8 and 14 in 25.4 ID loop and runs 5 and 8 from 50.8 mm ID loop are presented. Figures 4 and 5 show the profiles of α , a_i , and v_b for run 2 in 25.4 mm ID loop and for run 5 in 50.8 mm ID loop, respectively. Figures 6 and 7 show the α and a_i profiles for run 8 in 25.4 mm ID loop and for run 8 in 50.8 mm ID loop, respectively. Figure 8 shows those for the group 1 and group 2 bubbles in run 14.

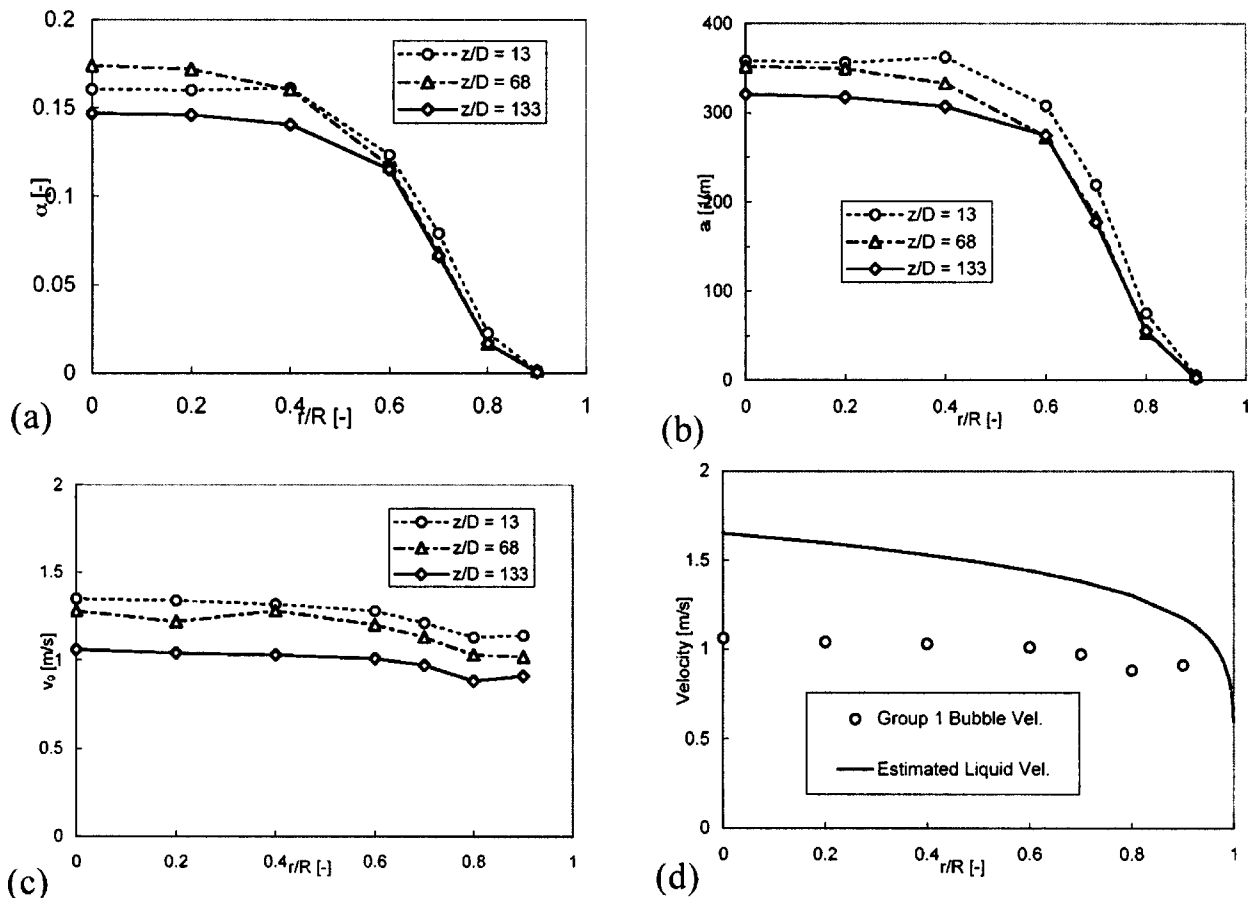


Fig. 4 Local parameter profiles for run 2 in 25.4 mm ID loop. (a) void fraction, (b) interfacial area concentration, (c) bubble velocity, (d) bubble velocity and estimated liquid velocity at port 3.

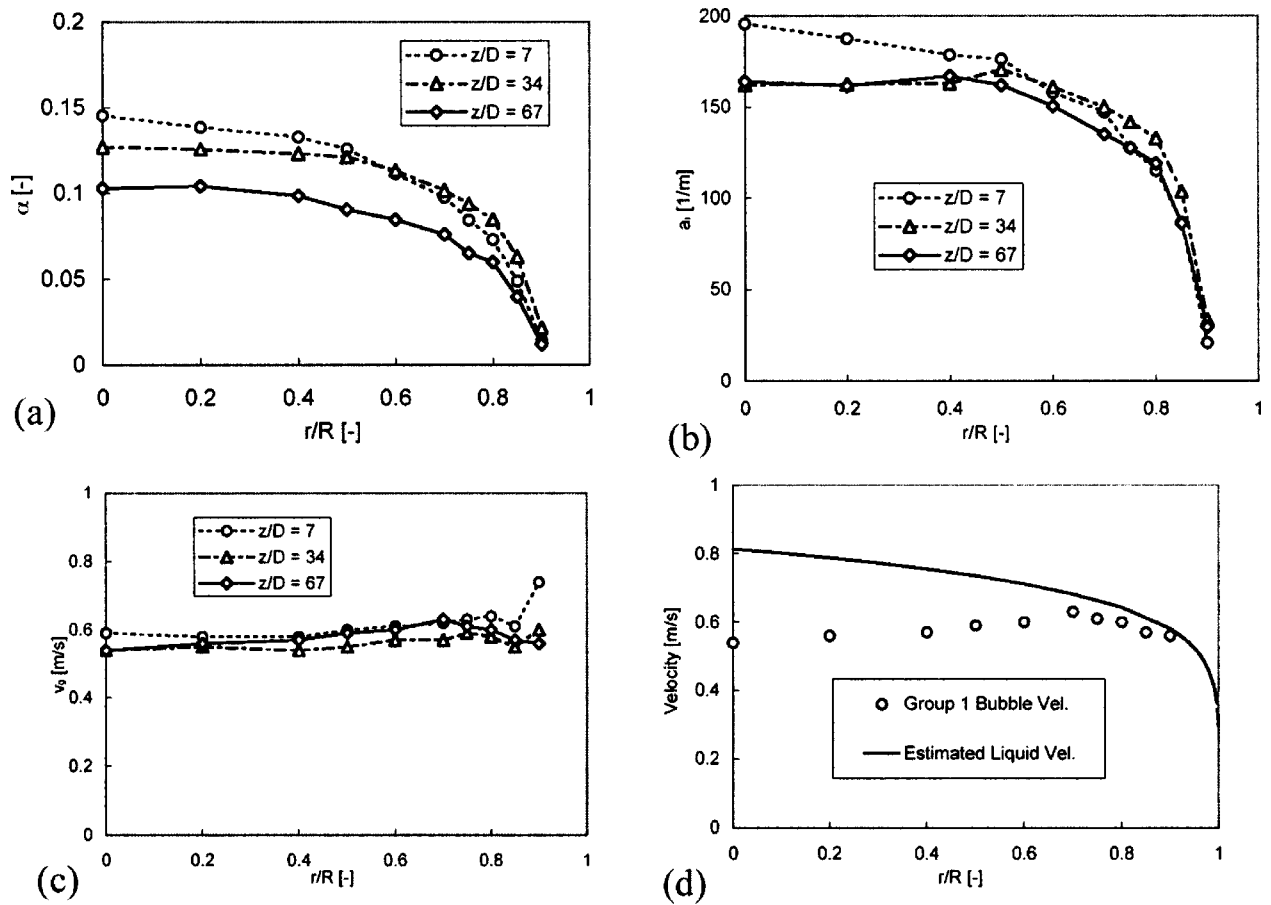


Fig. 5 Local parameter profiles for run 5 in 50.8 mm ID loop. (a) void fraction, (b) interfacial area concentration, (c) bubble velocity, (d) bubble velocity and estimated liquid velocity at port 3.

In most of the bubbly flow conditions, the void fraction profile shows peak in the center of the pipe. This can be explained on the basis of the direction of the lift force acting on the bubbles. In the downward flow, the lift force on the bubbles acts towards the center of the channel. Since the lift force is proportional to the product of the radial gradient of the axial velocity of the continuous phase and the relative velocity, the direction of the lift force is

opposite for upward and downward flow. Hence, the bubbles tend to agglomerate in the center of the channel causing increase in the void fraction in the center. This observation is opposite to that in the upward flow, where wall peak is commonly observed. It is worthwhile to note that in the downward flow, the bubbles move slower than the liquid due to the gravity force acting in the direction opposite to the direction of the flow. Figures 4 and 6 show α

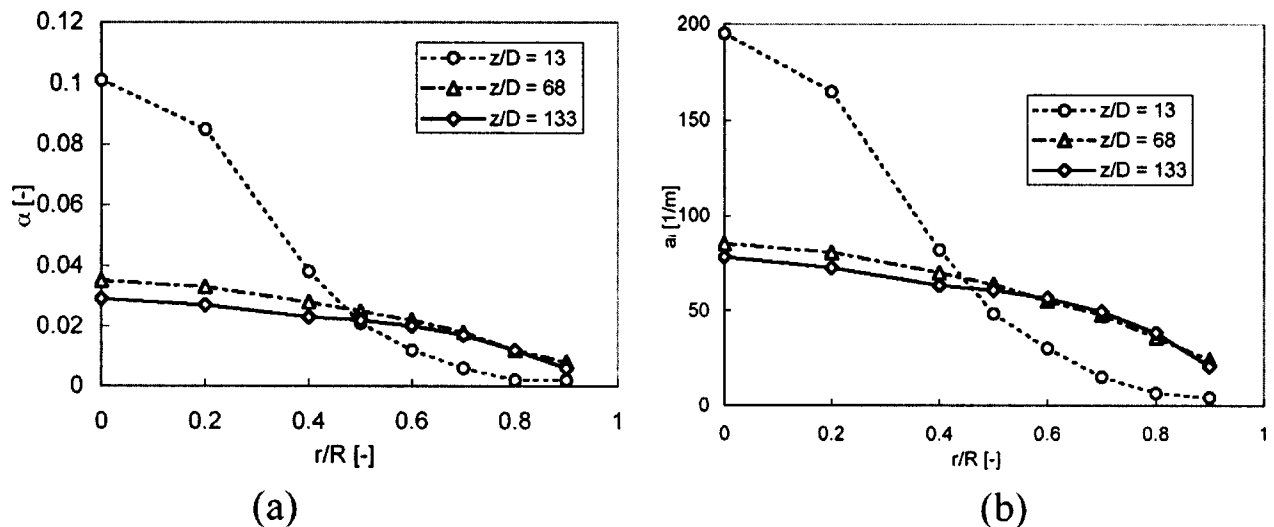


Fig. 6 Radial profiles of (a) void fraction and (b) interfacial area concentration for run 8 in 25.4 mm ID loop

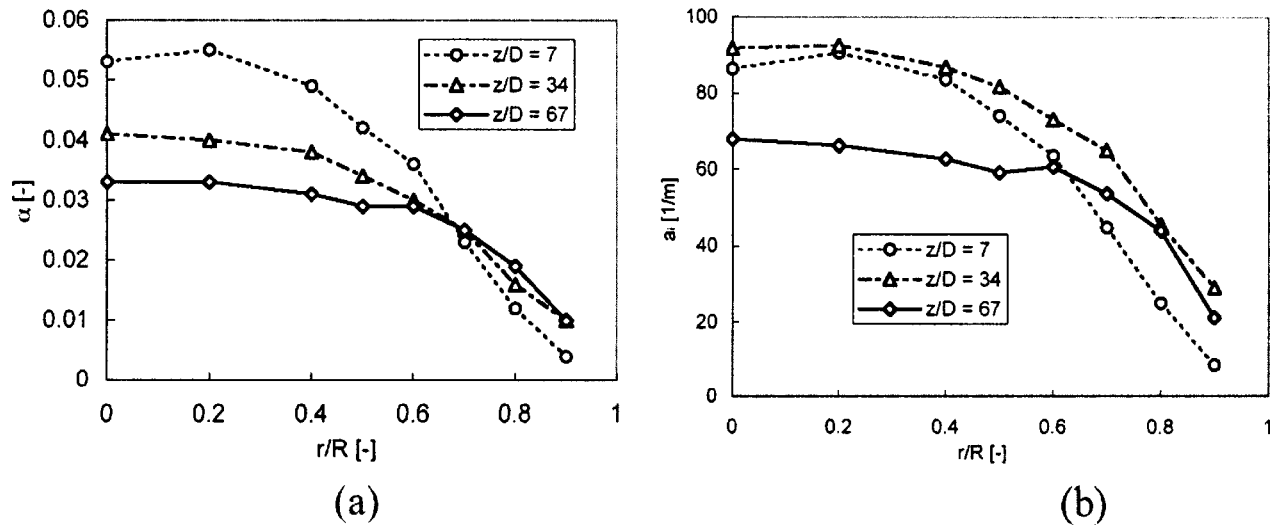


Fig. 7 Radial profiles of (a) void fraction and (b) interfacial area concentration for run 8 in 50.8 mm ID test section

profiles of runs 2 and 8 in the 25.4 mm ID test section respectively. They have similar superficial gas velocity ($j_g = 0.087$ m/s and 0.068 m/s, respectively) but different superficial liquid velocity ($j_l = 1.25$ m/s and 4.00 m/s, respectively). It is interesting to note that, while run 2 shows nearly uniform profile near the central region, the run 8 shows a strong center peak. It can be specu-

lated that the effect of the lift force is higher in the flow condition with higher superficial liquid velocity due to larger axial velocity gradient in the radial direction. The effect of velocity gradient can also be observed by comparing the void profiles in different diameter test sections. In general it was observed that the void profiles are flatter in the central region of 50.8 mm ID loop than that

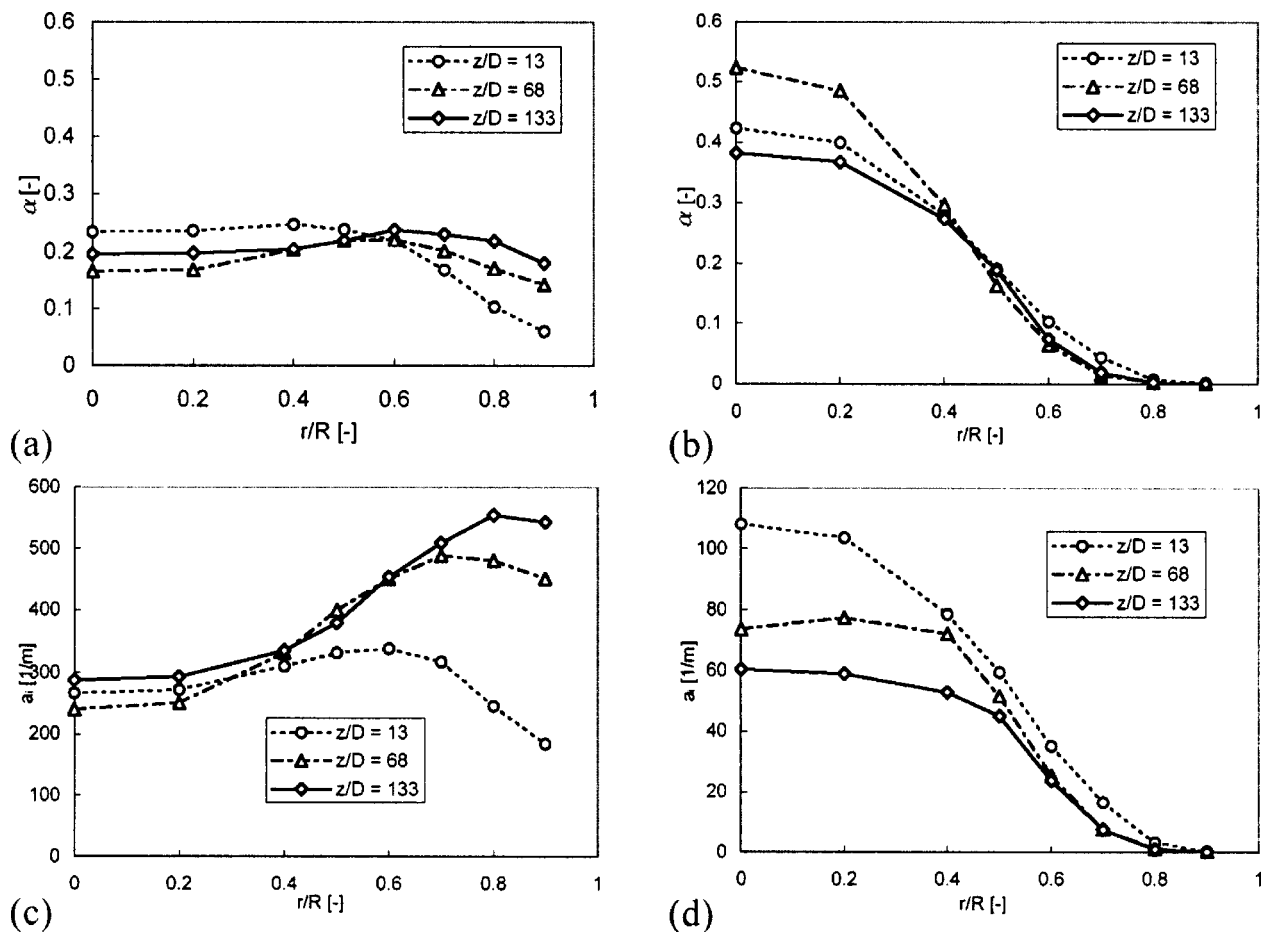


Fig. 8 Local parameter profiles for run 14 in 25.4 mm ID loop. (a) group 1 bubble void fraction, (b) group 2 bubble void fraction, (c) group 1 bubble interfacial area concentration, (d) group 2 bubble interfacial area concentration.

of 25.4 mm ID loop. However, it is interesting to note that in some flow conditions, the void profiles showed off center peak (e.g. at $z/D=13$ of run 2 in 25.4 mm ID test section and at $z/D=7$ of run 8 in 50.8 mm ID test section). This off-center peak distribution of the void fraction is also reported by Wang et al. [8] and Kashinsky and Randin [9]. This phenomenon of the off-center peak void distribution needs further investigation.

The interfacial area concentration is proportional to the void fraction and inversely proportional to the bubble Sauter mean diameter. In most of the flow conditions, the radial distribution of the group 1 bubble Sauter mean diameter was uniform. Hence, the radial profiles of void fraction and the interfacial area concentration are quite similar. As the group 2 bubbles form, the Sauter mean diameter increases and has broad peak at the center. The increase in the Sauter mean diameter tends to reduce the interfacial area concentration in the center. Such flow conditions show dissimilarity in the α and a_i profiles. This is evident from Fig. 8, which shows the α and a_i profiles for run 14, which is in the transition region between the bubbly and the slug flow. The bubbles were classified based on their chord lengths into group 1 (<10 mm) and group 2 (>10 mm). This classification was based on the difference in the bubble interaction mechanisms for the two groups of the bubbles. The difference in the distribution of the two groups of the bubbles is also evident from Fig. 8.

The radial profiles of group 1 bubble velocities are shown in Figs. 4(c) and (d) and Figs. 5(c) and (d) for runs 2 and 5 in 25.4 mm ID and 50.8 mm ID loops respectively. The bubble velocity profiles are compared with the estimated liquid velocity profiles at $z/D=133$. The liquid velocity is estimated with the correlation given by [10]:

$$u_f(r) = u_{f,\max} \left(1 - \frac{r}{R} \right)^{1/n}$$

$$u_{f,\max} = \frac{(n+1)(2n+1)}{2n^2} \frac{\langle j_f \rangle}{1-\langle \alpha \rangle}$$

$$n = 2.95 \text{Re}_f^{0.0805}, \quad \text{Re}_f = \frac{2\rho_f \langle j_f \rangle R}{\mu_f} \quad (4)$$

where u_f is the local liquid velocity, R and r are the radii of the test section and the radial coordinate (originating from the pipe centerline), respectively; ρ_f and μ_f are the density and dynamic viscosity of the liquid phase; and $\langle \alpha \rangle$ is the area-averaged void fraction.

In most of the flow conditions, the bubble velocity profiles are nearly uniform across the flow cross-section or close to the power-law profile. The velocity profiles are similar at different axial locations for most of the flow conditions. However, the velocity profile in run 5 in 50.8 mm ID test section is peaked off-centered. That is bubbles in the central region move slower than those in the surrounding area. This can be explained based on the center peak distribution of the void and the fact that in downward flow, the bubbles tend to move slower than the liquid. Hence, in the flow conditions with low liquid velocities, the liquid velocity in the central part of the channel is lower than that in the surrounding area, which is also reflected in the bubble velocity profiles. Some velocity profiles show higher bubble velocities in the vicinity of the wall. This can be attributed to the measurement error due to insufficient number of bubble samples collected by the probe near the wall.

The comparison of bubble velocity with estimated liquid velocity clearly shows that the bubbles in downward flow move slower than the liquid. The gravity force acts on the bubbles in the upward direction, i.e., opposite to the flow direction. Hence, the bubbles move slower than the surrounding liquid. The drag force by the surrounding downward flowing liquid acts in the downward direction. The balance between the two forces determine the terminal velocity of the bubbles.

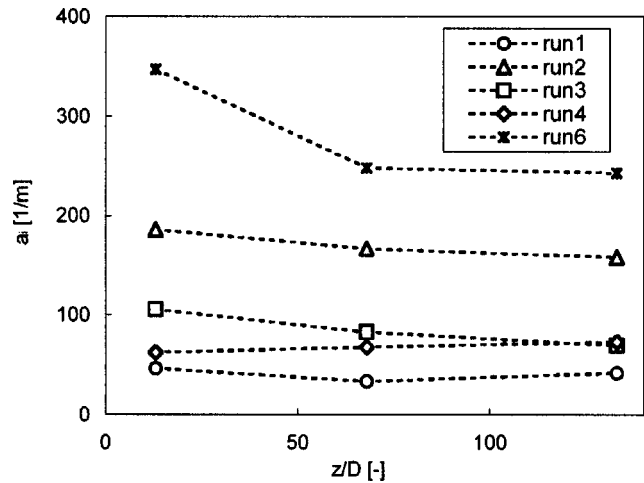


Fig. 9 Axial development of area averaged a_i for runs 1, 2, 3, 4 and 6 in 25.4 mm ID loop.

Interfacial Area Transport. Interfacial area transport model is a dynamic approach for predicting the interfacial area concentration in two phase flow systems, as opposed to the static, algebraic models based on the flow regimes maps. The foundations of the interfacial area transport equation were first established by Kocamustafaogullari and Ishii [11]. The interfacial area transport equation dynamically predicts the interfacial area concentration along a flow field from given boundary conditions. In order to complete the interfacial area transport model, constitutive relations for the source and sink terms appearing in the right hand side of the interfacial area transport equation have to be developed. This is achieved by mechanistically modeling the bubble interaction mechanisms for a given two-phase flow. Recently, interfacial area transport equation for adiabatic air-water two-phase flow was developed for various channel geometries [12–14]. In view of developing the interfacial area transport equation for downward two-phase flow, and of providing an experimental database to evaluate the interfacial area transport model, the present study was carried out.

Figures 9, 10 and 11 show the axial development of the interfacial area concentration for the bubbly flow conditions. In general, it was found that the area averaged void fraction tends to decrease in the downstream direction for flow conditions with low superficial liquid velocity ($j_f < 2.5$ m/s), while it increases for the flow conditions with higher superficial liquid velocities.

Considering air as an ideal gas, void fraction and pressure are inversely proportional to each other. The pressure gradient is the sum of the hydrostatic pressure gradient and the frictional pressure gradient. In downward flow, the hydrostatic pressure tends to increase in the downstream direction while the frictional pressure drop tends to decrease the pressure in the downstream direction. Hence, for low liquid flow rate conditions, the pressure increases at higher z/D locations causing the void fraction to decrease, while the opposite is observed in the case of flow conditions with high liquid flow rates. Interfacial area concentration is proportional to the void fraction. Hence in most of the bubbly flow conditions, the axial development of the interfacial area concentration is similar to that in the void fraction.

However, bubble coalescence mechanisms tend to decrease the interfacial area concentration, while bubble breakup mechanisms tend to increase the interfacial area concentration. The runs 1, 2, and 6 in 25.4 mm ID loop have same superficial liquid velocity ($j_f=1.25$ m/s) but different superficial gas velocities. ($j_g = 0.15$ m/s, 0.087 m/s, 0.243 m/s respectively.). The void fraction in these flow conditions is progressively higher. It can be observed from the Figure 9 that decrease in the interfacial area concentration is higher in run 6 as compared to runs 1 and 2. This is due to

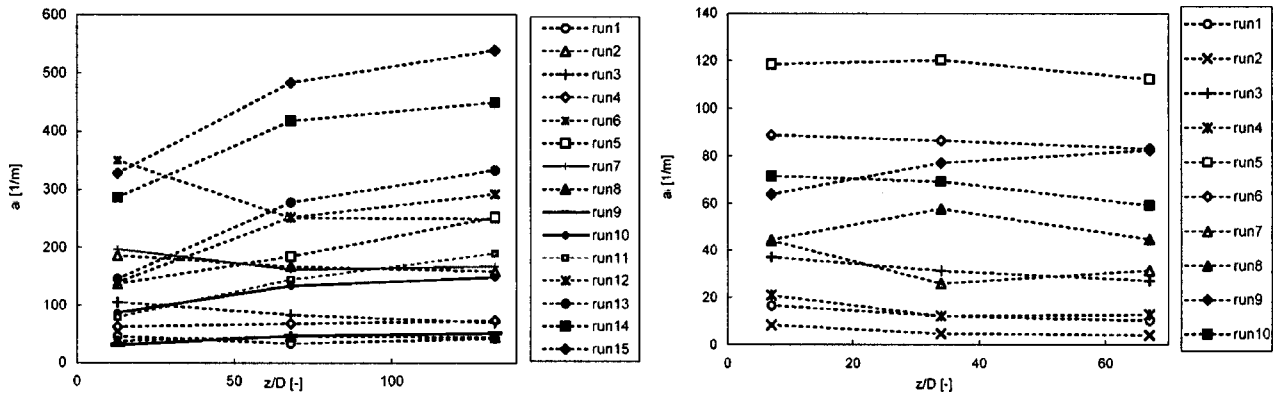


Fig. 10 Axial development of area averaged a_i

the increase in bubble coalescence mechanisms. The effect of the increasing superficial liquid velocity is also evident from Fig. 9. The runs 2, 3, and 4 have similar superficial gas velocities ($j_g = 0.087$ m/s, 0.085 m/s, and 0.086 m/s respectively), while different superficial liquid velocities. ($j_f = 1.25$ m/s, 2.12 m/s, 3.11 m/s) It can be observed that the interfacial area concentration decreases for the run 2 and 3 while increases for the run 4. This can be attributed to the break-up of bubbles due to increased turbulence intensity with increased liquid velocity. The runs 8, 9, 11, 12, 17, and 18 in 25.4 mm ID loop, which have high liquid velocity also

show significant increase in the interfacial area concentration. Similar trends are also observed in the 50.8 mm ID loop.

The runs 7 and 14 in 25.4 mm ID test section are near the bubbly to slug transition boundary. Figures 11 and 12 show the axial development of the void fraction and the interfacial area concentration for group 1 and group 2 bubbles in these flow conditions. In run 7, the void fraction of group 1 bubbles decreases while that of group 2 bubbles increase in the downstream direction. This suggests that the group 2 bubbles are formed by the coalescence of group 1 bubbles. However, run 14 show the oppo-

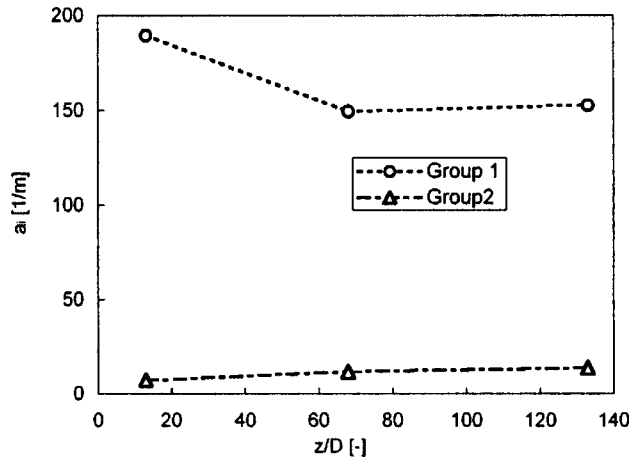
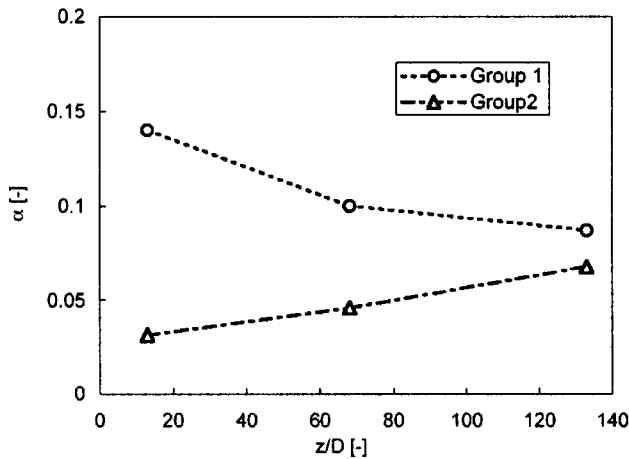


Fig. 11 Axial development of local parameters for run 7 in 25.4 mm ID loop

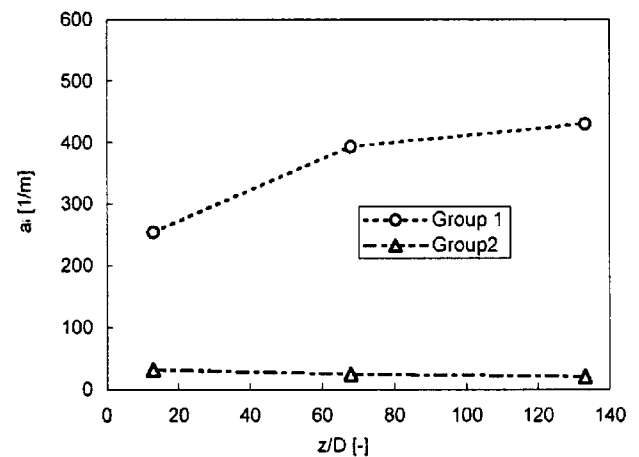
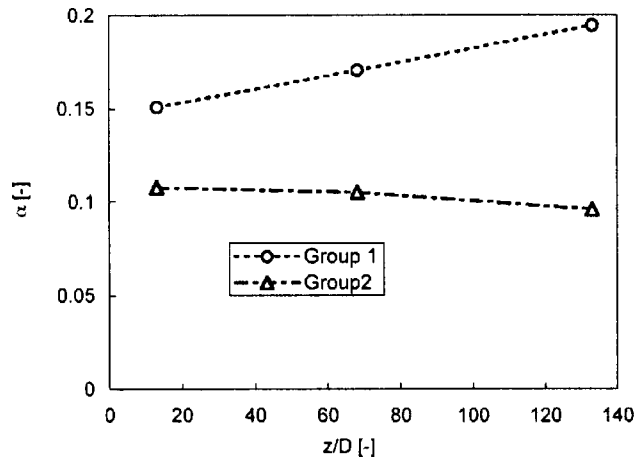


Fig. 12 Axial development of local parameters for run 14 in 25.4 mm ID loop

site trend. In this flow condition, the group 2 bubble void fraction decreases in downstream direction, while that of group 1 bubble increases. The area averaged interfacial area concentration profiles also show similar trends. This shows that there exist break-up mechanisms to form small bubbles. Run 14 has higher superficial liquid velocities ($j_f=3.99$ m/s) as compared to that in run 7 ($j_f=2.12$ m/s). Hence there is increased turbulence intensity in these flow conditions, which leads to increase in bubble disintegration.

Drift Flux Model Analysis. The two-phase flow analysis using the drift flux model by Zuber and Findlay [15] is presented in this paper. They presented the drift flux model, which has been widely accepted for predicting the two-phase flow behavior in a vertical tube. The model takes into account the effect of a nonuniform flow and a concentration distribution between the phases. The drift flux model is formulated by

$$\frac{\langle j_g \rangle}{\langle \alpha \rangle} = \langle v_g \rangle = C_0 \langle j \rangle + \langle V_{gj} \rangle \quad (5)$$

where C_0 is the distribution parameter and V_{gj} is the drift velocity. The distribution parameter, C_0 , generally depends upon the pressure, flow regime and flow path geometry, and is defined as

$$C_0 \equiv \frac{\langle \alpha j \rangle}{\langle \alpha \rangle \langle j \rangle} \quad (6)$$

The drift velocity, V_{gj} , is defined as the gas velocity relative to the superficial velocity of the two-phase mixture, which is given as

$$V_{gj} = v_g - j = (1 - \alpha) v_r \quad (7)$$

where v_r is the relative velocity between the phases.

Hirao et al. [16] and Kawanishi et al. [17] studied a steam-water downward two-phase flow for 19.7 mm ID and 102.3 mm ID round tubes, and proposed correlations based upon their experimental results as well as the previous data. The drift velocity for downward flow was given the same as that for churn-turbulent bubbly flow, given by Ishii [18] as,

$$\langle V_{gj} \rangle = \sqrt{2} \left(\frac{\sigma g (\rho_f - \rho_g)}{\rho_f^2} \right)^{0.25} \quad (8)$$

In their studies, the distribution parameter was empirically determined with respect to the superficial velocity of the two-phase mixture, $\langle j \rangle$, as

$$C_0 = 0.9 + 0.1 \sqrt{\frac{\rho_g}{\rho_f}}, \quad -2.5 \text{ m/s} \leq \langle j \rangle < 0 \text{ m/s} \quad (9)$$

$$C_0 = 0.9 + 0.1 \sqrt{\frac{\rho_g}{\rho_f}} - 0.3 \left(1 - \sqrt{\frac{\rho_g}{\rho_f}} \right) (2.5 + \langle j \rangle); \quad -3.5 \text{ m/s} \leq \langle j \rangle < -2.5 \text{ m/s} \quad (10)$$

$$C_0 = 1.2 - 0.2 \sqrt{\frac{\rho_g}{\rho_f}}, \quad \langle j \rangle < -3.5 \text{ m/s} \quad (11)$$

However, there is one shortcoming in the correlation for $-3.5 \text{ m/s} \leq \langle j \rangle < -2.5 \text{ m/s}$. The distribution parameter, which is originally defined by Eq. (6), must be a nondimensional number; notwithstanding, they determined the formula in a dimensional form, as shown in Eq. (10). This formula was, therefore, nondimensionalized by employing the drift velocity, $\langle V_{gj} \rangle$, given in Eq. 8, in the present study. Hirao et al. [16] developed these correlations for the distribution parameter based upon the constant drift velocity, and this constant drift velocity contributes the distribution parameter quantity as an anchor. In other words, the distribution parameter was solely determined by the constant drift velocity to fit the experimental data. Thus, the correlation might

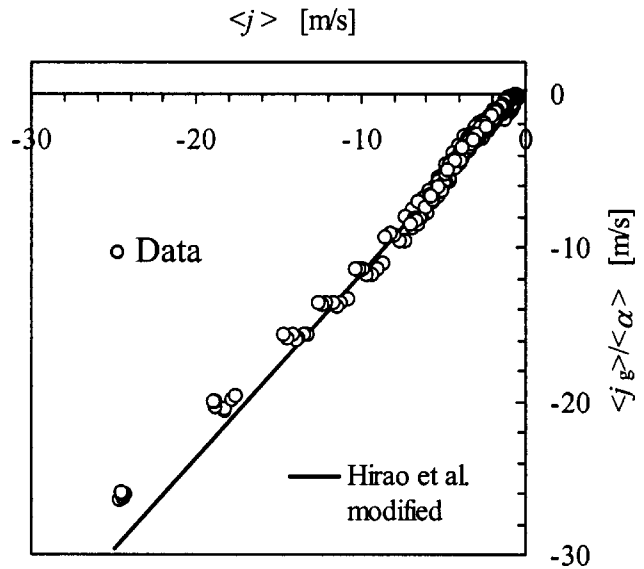


Fig. 13 $\langle j \rangle$ vs. $\langle j_g \rangle / \langle \alpha \rangle$ plot from data with correlations by Hirao et al. [15]

also reflect the effect of the drift velocity. Furthermore, the thresholds, which were also determined with respect to j , were nondimensionalized by applying the constant $\langle V_{gj} \rangle$.

An impedance void meter is capable of measuring the area-averaged void fraction, $\langle \alpha \rangle$, thus the experimental results were plotted on $\langle j \rangle$ vs. $\langle j_g \rangle / \langle \alpha \rangle$ plane. The $\langle j \rangle$ and $\langle j_g \rangle$ were measured by a magnetic flow meter and a rotameter, and $\langle \alpha \rangle$ was acquired by an impedance void meter. Figure 13 shows all the experimental results obtained by an impedance void meter from both the 25.4 mm ID and 50.8 mm ID loops with the correlation proposed by Hirao et al. [16]. It shows reasonably good agreement in general; although the C_0 value for the higher flow rate region is slightly overestimated. This overshoot in C_0 may stem from the fact that Hirao et al. [16] empirically developed the correlations with the data up to $\langle j \rangle = -10$ m/s, and the data in higher flow rate such as -20 or -30 m/s was not available. The present experimental result showed that the distribution parameter, C_0 , tends to decrease as the flow rate increases on the higher flow rate region, such as $\langle j \rangle < -10$ m/s. In view of this, Goda [19] made further modification on the correlations for the distribution parameter. First, C_0 was classified into three regions, such as low, high and intermediate flow rate. Second, some of the coefficients in the formulas and the thresholds with respect to the nondimensionalized superficial mixture velocity, $\langle j^* \rangle$ were modified based on the present database. The resulting correlations are:

$$C_0 = 0.9 + 0.1 \sqrt{\frac{\rho_g}{\rho_f}}, \quad -13 \leq j^* < 0 \quad (12)$$

$$C_0 = 0.9 + 0.1 \sqrt{\frac{\rho_g}{\rho_f}} - \left(1 - \sqrt{\frac{\rho_g}{\rho_f}} \right) (0.45 + 0.035 \langle j^* \rangle); \quad -22 \leq j^* < -13 \quad (13)$$

$$C_0 = 1.26 - 0.26 \sqrt{\frac{\rho_g}{\rho_f}} - 0.26 \left(1 - \sqrt{\frac{\rho_g}{\rho_f}} \right) \left(1 - \exp \left[\frac{j^*}{100} \right] \right); \quad j^* < -22 \quad (14)$$

Where j^* is defined by

$$j^* \equiv \frac{\langle j \rangle}{\langle V_{gj} \rangle} \quad (15)$$

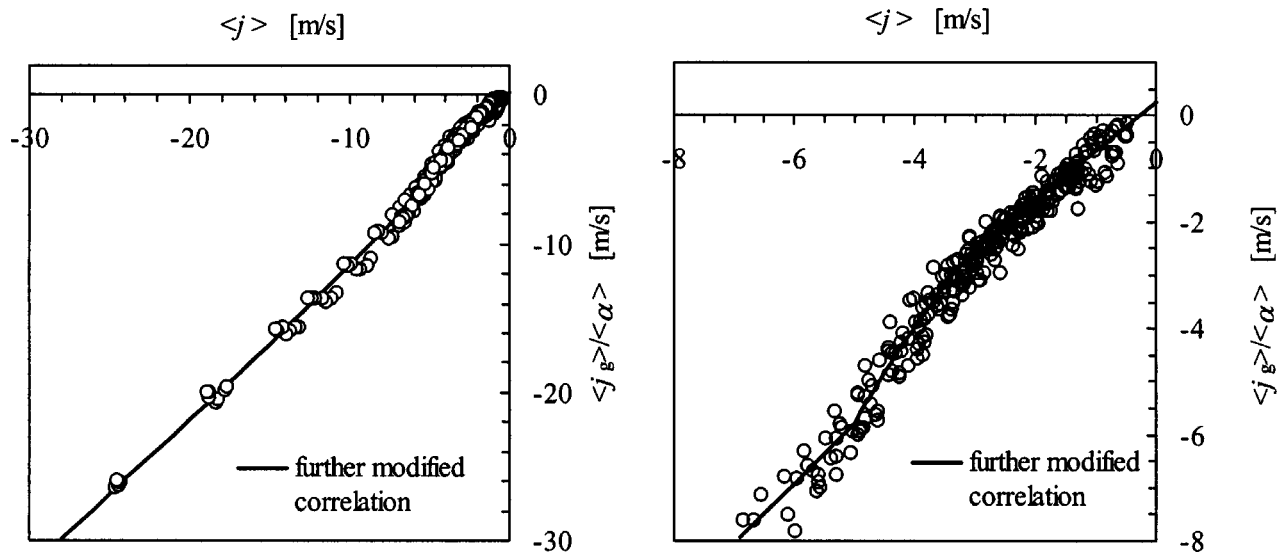


Fig. 14 $\langle j \rangle$ vs. $\langle j_g \rangle / \langle \alpha \rangle$ plot; experimental data with present correlations (Circle: Data, Solid Line: Further modified correlation)

These modified correlations are plotted with the present experimental results, and shown in Figs. 14(a) and (b), for both the entire flow rates and lower flow rates, respectively.

4 Summary

The present research performed detailed experimental studies in the vertical co-current air-water downward two-phase flow. A less subjective and more scientific method is employed in the flow regime identification study by employing an impedance void meter coupled with the self-organized neural network. In the experiment, detailed local two-phase flow parameters were acquired by the state-of-the-art conductivity probe, which included local time-averaged void fraction, interfacial area concentration, bubble velocity and bubble Sauter mean diameter. The area-averaged data acquired by the impedance void meter were analyzed by the drift flux model. Three different distributions parameters were developed for the different ranges of non-dimensional superficial velocity, defined by the ratio of total superficial velocity to the drift velocity. The new correlations can be applied to a co-current downward two-phase flow in a wide range of flow regime spanning from bubbly to annular flow. In summary, following observations were made:

1. Unlike the vertical upward two-phase flow, the flow regime boundaries highly depend on the pipe size (or flow area) in the co-current vertical downward two-phase flow;
2. Interfacial structures in the co-current vertical downward two-phase flow are quite different from that in the upward vertical two-phase flow. In bubbly flow, in particular, the bubbles migrate toward the center of the pipe;
3. In the slug flow regime, the gas slug was highly distorted and its nose was always off-centered toward the wall of the test section, forming a wedge shape.
4. The bubble velocity was smaller than the liquid velocity.
5. Due to the "bubble coring" and slower bubble velocity in the downward bubbly flow, the maximum liquid velocity was not necessary in the center of the pipe
6. In downward bubbly flow, flow visualization and the acquired data suggested that the major bubble interaction mechanisms leading to bubble coalescence or disintegration were similar to those in the vertical upward two-phase flow in bubbly flow;

Acknowledgments

This work was supported by USNRC Office of Nuclear Regulatory Research.

Nomenclature

Latin Symbol

- a_i = interfacial area concentration
- D = pipe diameter
- D_{sm} = Sauter mean diameter
- f = frequency
- G_m = measured impedance
- G^* = non-dimensionalized impedance
- j = mixture volumetric flux
- j_f = superficial liquid velocity
- j_g = superficial gas velocity
- r = radial distance
- v_f = liquid velocity
- v_g = gas velocity

Greek Symbol

- α = void fraction
- σ = standard deviation
- γ = skewness

Operators

- $\langle \cdot \rangle$ = Area averaging operator
- $\langle \langle \cdot \rangle \rangle$ = Void weighted area averaging operator

References

- [1] Oshinowo, T., and Charles, M. E., 1974, "Vertical two-phase flow Part I. Flow pattern correlation," *Can. J. Chem. Eng.*, **52**, pp. 25–35.
- [2] Barnea, D., Shoham, O., and Taitel, Y., 1982, "Flow pattern transition for vertical downward two phase flow," *Chem. Eng. Sci.*, **37**(5), pp. 741–744.
- [3] Yamaguchi, K., and Yamazaki, Y., 1984, "Combinated flow pattern map for cocurrent and countercurrent air-water flows in vertical tube," *J. Nucl. Sci. Technol.*, **21**(5), pp. 321–327.
- [4] Usui, K., and Sato, K., 1989, "Vertically downward two-phase flow, (I) Void distribution and average void fraction," *J. Nucl. Sci. Technol.*, **26**(7), pp. 670–680.
- [5] Mi, Y., 1998, "Two-phase flow characterization base on advanced instrumentation, neural networks, and mathematical modeling," Ph.D. Thesis, Purdue University, West Lafayette, IN, USA.
- [6] Kim, S., Fu, X. Y., Wang, X., and Ishii, M., 2000, "Development of the miniaturized four-sensor conductivity probe and the signal processing scheme," *J. Heat Transfer*, **43**, pp. 4101–4118.

- [7] Wu, Q., and Ishii, M., 1999, "Sensitivity study on double-sensor conductivity probe for the measurement of interfacial area concentration in bubbly flow," *Int. J. Multiphase Flow*, **25**(1), pp. 155–173.
- [8] Wang, S. K., Lee, S. J., Jones, Jr, O. C., and Lahey, Jr., R. T., 1987, "3-D Turbulence structure and phase distribution measurements in bubbly two-phase flows," *Int. J. Multiphase Flow*, **13**, pp. 327–343.
- [9] Kashinsky, O. N., and Randin, V. V., 1999, "Downward bubbly gas-liquid flow in a vertical pipe," *Nucl. Eng. Des.*, **25**, pp. 109–138.
- [10] Hibiki, T., Hogsett, S., and Ishii, M., 1998, "Local measurement of interfacial area, interfacial velocity and liquid turbulence in two-phase flow," *Nucl. Eng. Des.*, **184**(2–3), pp. 287–304.
- [11] Kocamustafaogullari, G., and Ishii, M., 1995, "Foundations of the interfacial area transport equation and its closure relations," *Int. J. Heat Mass Transfer*, **38**(3), pp. 481–493.
- [12] Wu, Q., Kim, S., Ishii, M., and Beus, S. G., 1998, "One-group interfacial area transport in vertical bubbly flow," *Int. J. Heat Mass Transfer*, **41**(8–9), pp. 1103–1112.
- [13] Kim, S., 1999, "Interfacial area transport equation and measurement of local interfacial characteristics," Ph.D. Thesis, Purdue University, West Lafayette, IN, USA.
- [14] Sun, X., 2001, "Two-group interfacial area transport equation for a confined test section," Ph.D. Thesis, Purdue University, West Lafayette, IN, USA.
- [15] Zuber, N., and Findlay, J. A., 1965, "Average volumetric concentration in two-phase flow systems," *ASME J. Heat Transfer*, **87**, pp. 453–468.
- [16] Hirao, Y., Kawanishi, K., and Tsuge, A. and Kohriyama, T., 1986, "Experimental study on drift flux correlation formulas for two-phase flow in large diameter tubes," *Proceedings of second international topical meeting on nuclear power plant thermal hydraulics and operations*, pp. 1-88-1-94.
- [17] Kawanishi, K., Hirao, Y., and Tsuge, A., 1990, "An experimental study on drift flux parameters for two-phase flow in vertical round tubes," *Nucl. Eng. Des.*, **120**, pp. 447–458.
- [18] Ishii, M., 1977, "One-dimensional drift-flux model and constitutive equations for relative motion between phases in various two-phase flow regimes," *Argonne National Laboratory Report ANL-77-47*.
- [19] Goda, H., 2001, "Flow regimes and local parameter measurements for downward two-phase flow," MS Thesis, School of Nuclear Engineering, Purdue University, West Lafayette, IN, USA.

Xiaodong Sun*
Sidharth Paranjape
Seungjin Kim¹
Hiroshi Goda²
Mamoru Ishii

Thermal-Hydraulics
and Reactor Safety Laboratory,
School of Nuclear Engineering,
Purdue University,
400 Central Drive,
West Lafayette, IN 47907, USA

Joseph M. Kelly
U.S. Nuclear Regulatory Commission,
Mail Stop: T10K8, 11545 Rockville Pike,
Rockville, MD 20852, USA

Local Liquid Velocity in Vertical Air-Water Downward Flow

This paper presents an experimental study of local liquid velocity measurement in downward air-water bubbly and slug flows in a 50.8 mm inner-diameter round pipe. The axial liquid velocity and its fluctuations were measured by a laser Doppler anemometry (LDA) system. It was found that the maximum liquid velocity in a downward two-phase flow could occur off the pipe centerline at relatively low liquid flow rates and this observation is consistent with other researchers' results. The comparisons between the liquid flow rates measured by a magnetic flow meter and those obtained from the local LDA and multi-sensor conductivity probe measurements showed good agreement. In addition, based on the local measurements the distribution parameter and the drift velocity in the drift-flux model were obtained for the current downward flow tests.

[DOI: 10.1115/1.1777235]

Introduction

The phase distribution and turbulence structure in gas-liquid two-phase flows are closely related to each other. Experimentally, the local phase distribution can be measured by optical probe, conductivity probe, advanced imaging technique, and thermal anemometry, such as hot film probe; while the local velocity and turbulence structure of the liquid phase can be obtained by laser Doppler anemometry (LDA), hot film probe, and particle image velocimetry. In literature, considerable amount of research have been carried out to investigate the local liquid velocity distribution in two-phase flows [1–10]. Most of the previous investigations focused on co-current upward flow in vertical ducts. Only very limited research has been conducted for downward flow, which can be important in many industrial applications, such as chemical reactors and in particular, nuclear reactors under accidental conditions. A good understanding for the downward two-phase flow is needed for efficient performance and safe operation of various chemical and nuclear power reactors.

Oshinovo and Charles [11] are among the early researchers who studied downward two-phase flows. They performed experiments for downward and upward gas-liquid flows in a 25.4 mm inner-diameter (*ID*) vertical tube coil containing two risers and a downcomer, which were all connected by “U” bends. They found that the liquid holdup in downward flow was always less than that in upward flow, which indicated that the gas velocity in downward gas-liquid flows is smaller. Later, detailed experimental studies were carried out by Clark and Flemmer [12,13] in 50 and 100 mm *ID* pipes for downward bubbly flows. Their primary interest focused on the averaged bubble velocity.

Wang et al. [14] and quite recently, Kashinsky and Randin [15] carried out extensive experiments for the local liquid velocity profiles as well as the turbulence structure in bubbly downward flow. They found that the maximum liquid velocity could occur off the pipe centerline, which is quite different from the upward two-

phase flows. Despite the above mentioned investigations in downward flows, compared to the numerous studies performed in vertical upward and horizontal two-phase flows, however, data of the liquid velocity distribution and turbulence structure in downward flows is still quite limited, in particular in the flow conditions with high liquid flow rates. Furthermore, no detailed information of the local relative velocity between the gas and liquid phases has been revealed for the downward flow.

In the present experimental study, local measurements were performed for a vertical co-current air-water downward flow in a 50.8 mm *ID* round pipe with relatively low void fraction. An LDA system was used to measure the local axial (1-D) velocity and the turbulence of the liquid phase. To enhance the data rate, Titanium dioxide particles with a mean diameter of 2 micron were used as seeding particles. In addition to the local liquid velocity and turbulence, the local time-averaged void fraction and bubble velocity were obtained by miniaturized four-sensor conductivity probes in the previous experiments performed by Goda [16], as well as in the current experiments for additional test runs.

Based on the local LDA and conductivity probe measurements, the liquid superficial velocity can be calculated by the area integration of the local liquid velocity and the void fraction measurements, such as: $\int_A u_f (1 - \alpha) dA / A$. The comparisons between this value and the one obtained from an inlet magnetic flow meter showed quite good agreements. In addition, the distribution parameter, C_o , and the drift velocity, $\langle V_{gj} \rangle$, in the drift flux model [17] were also calculated based on their definitions. It should be mentioned that the current paper is based on a manuscript presented in ASME/JSME 2003 Joint Fluids Engineering Division Summer Meeting [18] and a previously published paper [19].

Experiments

Experimental Loop. Figure 1 shows a schematic of the present vertical co-current downward air-water two-phase loop. Air was supplied via external compressors with a constant back-pressure of 900 KPa. To generate bubbles of nearly uniform size at the inlet of the test section, one sparger unit with a mean pore size of 10 micron was used in the bubble injector. The water was first demineralized, and then a small amount of Morpholine was added to increase the electrical conductance. The test section was a vertical 50.8 mm *ID* acrylic round pipe with an overall length of 3.81 m. Three probe-mount ports for conductivity probes were

*Corresponding author: xsun@ecn.purdue.edu

¹Present address: Nuclear Engineering, University of Missouri-Rolla, 219 Fulton Hall, 1870 Miner Circle, Rolla, MO 65409, USA.

²Present address: Mitsubishi Heavy Industries, Ltd., 3-3-1 Minatomirai Nishi-ku, Yokohama 220-8401, Japan.

Contributed by the Fluids Engineering Division for publication in the JOURNAL OF FLUIDS ENGINEERING. Manuscript received by the Fluids Engineering Division May 27, 2003; revised manuscript received July 15, 2003. Associate Editor: J. Katz.

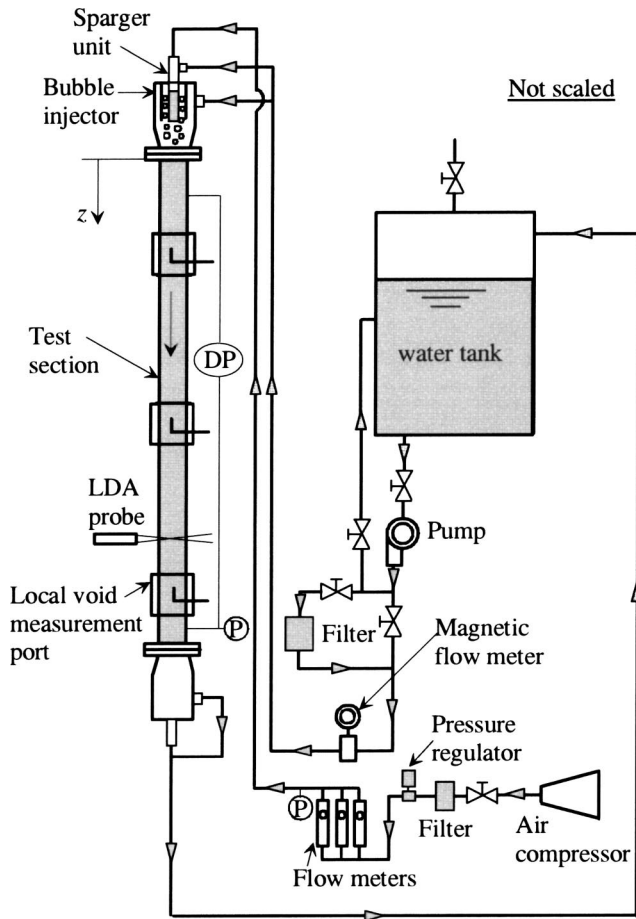


Fig. 1 Schematic of the experimental loop.

installed in the test section at axial locations of $z/D=7, 34,$ and $67,$ respectively [16]. Note that the z -coordinate originated from the inlet of the test section and pointed to the downward direction.

The liquid flow rate was measured by a 50 mm ID magnetic flow meter, which had an accuracy of $\pm 1\%$ of the full-scale read-

ing. This resulted in a maximum of $\pm 1.5\%$ uncertainty for the liquid flow rate measurement. The air flow rate was measured by several rotameters with an accuracy of $\pm 4\%$ of the full-scale reading. The backpressure of the inlet gas and the local pressure at the exit of the test section were measured by pressure gauges with an accuracy of $\pm 3\%$ of the full-scale reading; while the differential pressure (DP) along the test section was measured by a DP transducer with $\pm 1\%$ of span uncertainty.

It is well known that LDA applications in high void fraction two-phase flows can lead to large measurement uncertainty. Due to strong scattering of the beams by bubble surfaces, the intensity of the laser beams decreases significantly along their paths in the mixture at high void fraction, in which large bubbles may appear. The flow visualization showed that cap bubbles were observed at relatively low void fraction ($<10\%$) in the present downward flow facility. Therefore, the current experiments were performed in the flow conditions in which the area-averaged void fraction was less than 10% , so as to reduce the measurement uncertainty. Table 1 shows the current experimental flow conditions in detail. In the table, the test runs with "L" and "T" in the run numbers are single-phase water flows and two-phase air-water flows, respectively. The local air superficial velocity was obtained through the rotameters by considering the local pressure. These flow conditions are also depicted in a flow regime map, which was developed in the current downward flow loop [16], as shown in Fig. 2. From the figure, it can be seen that some flow conditions are in either bubbly-slug flow transition region or slug flow.

LDA Setup. An integrated LDA system from TSI was used in the present experiment to measure the axial liquid velocity. The argon-ion laser of the system has a maximum power of 100 mW. Back-scattering is the available mode to receive scattered light.

The LDA measurement was performed at an axial location of $z/D=52.5$. The increment of the radial movement of the measurement volume in the fluids was set as 2.5 mm in the regions of $r/R < 0.7$ and then 1.25 mm in the region near the wall. Here R and r are the radius of the test section and the radial coordinate (originating from the pipe centerline), respectively. It should be noted that due to the difference of the refractive index between the air and water, the actual movement of the measurement volume in water is about 1.33 times of the probe traversing distance (in air) [20]. The photomultiplier tube (PMT) voltage of the LDA system was set as 1,095 to 1,132; while 2,000 to 150,000 data points were collected at each measurement location depending on the flow

Table 1 Measurement conditions and results.

Run No.	LDA at $z/D=52.5$						Drift-flux Model		
	$\langle j_l \rangle$ [m/s]	$\langle j_g \rangle^1$ [m/s]	$\langle \alpha \rangle^2$ [%]	$\langle u_l \rangle$ [m/s]	$\langle u_l(1-\alpha) \rangle$ [m/s]	Percentage difference [%]	C_o [16]	C_o	$\langle V_{gl} \rangle$ [m/s]
L1	0.630	—	—	—	0.650	3.15	—	—	—
L2	1.263	—	—	—	1.298	2.71	—	—	—
L3	2.532	—	—	—	2.559	1.08	—	—	—
L4	1.015	—	—	—	1.049	3.40	—	—	—
L5	3.510	—	—	—	3.526	0.47	—	—	—
T1	0.621	0.004	0.57	0.658	0.654	5.32	1.139	1.077	-0.14
T2	1.248	0.004	0.24	1.301	1.298	4.01	1.139	1.076	-0.16
T3	1.254	0.031	1.86	1.331	1.306	4.21	1.149	1.080	-0.23
T4	2.489	0.030	0.74	2.603	2.583	3.79	1.188	1.107	-0.05
T5	0.620	0.049	7.10	0.706	0.656	5.82	1.146	1.026	-0.14
T6	1.247	0.084	6.50	1.390	1.300	4.26	1.144	1.062	-0.17
T7	2.487	0.082	2.44	2.618	2.554	2.71	1.182	1.108	-0.04
T8	2.496	0.152	5.08	2.701	2.564	2.71	1.162	1.089	-0.02
T9	1.251	0.052	4.52	1.337	1.277	2.06	—	1.074	-0.25
T10	2.502	0.193	8.21	2.691	2.470	-1.30	—	1.069	-0.08
T11	3.463	0.081	2.29	3.586	3.504	1.16	—	1.085	-0.27
T12	3.468	0.162	4.88	3.681	3.501	0.96	—	1.077	-0.11
T13	3.463	0.321	8.47	3.878	3.549	2.48	—	1.088	-0.06

¹ $\langle j_g \rangle$ values are given at $z/D=52.5$.

² $\langle \alpha \rangle$ values are linearly interpolated from the local conductivity measurements at $z/D=34$ and 67 .

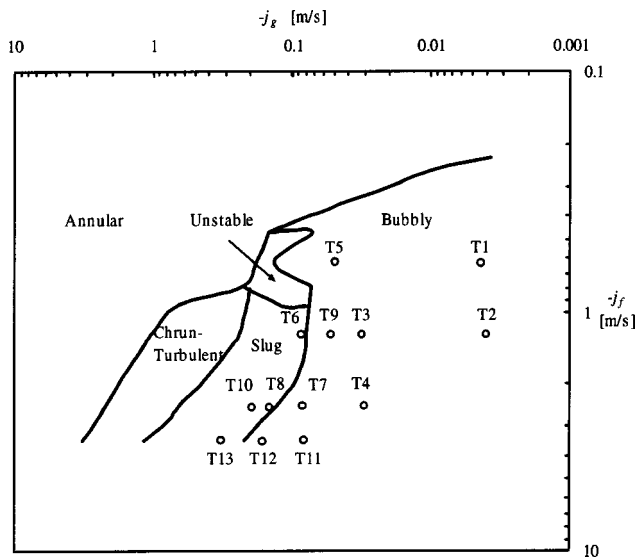


Fig. 2 Flow conditions on a flow regime map for the two-phase flow experiment.

conditions. A maximum of 5-minute data was acquired at each measurement location. Through the TSI software, the velocity information was directly obtained and saved for further data reduction.

To examine the accuracy of the mean axial liquid velocity measurements, the area-averaged liquid superficial velocity was calculated as

$$\langle (1 - \alpha)u_f \rangle = \frac{1}{A} \int_A [1 - \alpha(r)]u_f(r) dA, \quad (1)$$

where A is the cross-sectional area of the pipe; u_f and α are the measured liquid velocity and the void fraction by conductivity probes. This area-averaged value was then compared to the corresponding inlet liquid volumetric flux given by the flow meter as

$$\langle j_f \rangle = \frac{Q_f}{A}, \quad (2)$$

where Q_f is the liquid flow rate measured by the magnetic flow meter. It should be noted that similar comparisons were made to benchmark the measurement accuracy of the void fraction and bubble velocity [16]. The void fraction measurements by the conductivity probe were benchmarked against impedance void meters. The differences between the two instruments were within $\pm 10\%$.

Measurement Approach

The LDA has been a well-established and extensively used instrument for local velocity measurements in transparent single-phase flow because of its high accuracy, good spatial resolution, and nonintrusive features. In general, small seeding particles (around the order of microns) serve as the scattering centers for the laser beams and are assumed to follow the main flow. However, its application in gas-liquid two-phase flow becomes complicated because large particles, such as bubbles, also scatter or reflect laser light; and the burst signals generated by these scattered lights may also be interpreted as effective velocity information by the LDA system under certain criteria. Therefore, to obtain the liquid velocity, it has been considered important to distinguish the liquid signals from the interface signals.

In the past, considerable efforts have been made to distinguish the signals in the continuous liquid phase from those in the bubble-liquid interfaces by many researchers [3–6,20–28]. Several signal discrimination and data reduction approaches have

been developed. However, it was found that those approaches were not practically applicable in the current experiments due to the nature of the integrated LDA system and the relatively high flow rates [18,19].

Velidandla et al. [26] applied a back-scattering LDA system in bubbly flow and found that the bursts of the seeding particles could be separated well from those of the bubbles by using different frequency shift and PMT voltage values. No further data reduction was needed to obtain the liquid velocity. In the current experiment, a similar approach was adopted due to the available instrument. To ensure that the current LDA setup has negligible contribution from the bubble interfaces to all effective burst signals, the following procedures were applied [18]:

1. The current experiment was performed in relatively low void fraction conditions. The maximum area-averaged void fraction in all the flow conditions was about 8.5%, as shown in Table 1.
2. Titanium dioxide particles with a mean diameter of 2 micron were used as seeding particles. In the current flow conditions, the ratio of the seeding particle number concentration to the bubble number density is on the order of 100.
3. A high voltage value was applied to the PMT of the LDA system, usually around 1,100 V. In general, the intensity of the laser light scattered by the bubbles is higher than that scattered by the small seeding particles. Therefore, a relatively low PMT voltage will lead to the situation that the majority of the effective burst signals are from the bubble interfaces other than the seeding particles. However, a high PMT voltage will reverse the above result at low void fractions with the presence of enough seeding particles.
4. The maximum power of the laser beams was used during the experiments, which increased the beam intensity scattered by the seeding particles.

By following the above procedures, Sun et al. [18] were able to obtain the information of the liquid velocity and its fluctuations without any further discrimination process. The mean liquid velocity, u_f , and its mean fluctuation, u_{ft} , were directly obtained from the output of the LDA system as:

$$u_f = \frac{1}{N} \sum_{i=1}^N u_{f,i} \quad \text{and} \quad u_{ft} = \sqrt{u_f'^2} = \sqrt{\frac{1}{N} \sum_{i=1}^N u_{f,i}^2 - u_f^2}, \quad (3)$$

where $u_{f,i}$ is the i th velocity value acquired by the LDA. By applying this approach, the present results showed that the difference between the area-averaged liquid volumetric flux, $\langle (1 - \alpha)u_f \rangle$, and the inlet $\langle j_f \rangle$ measurement was within $\pm 6\%$, as shown in Table 1. The detailed discussions of the measurement results are presented in the following section.

Experimental Results

In the current experiments, repeatability of the experimental results was carefully examined in both single-phase and two-phase flow conditions. Repeated runs were carried out for Runs L1, T1, and T10. In addition to perform complete repeated runs, regular check was randomly made when acquiring data. In all these cases, the differences were within $\pm 2.6\%$, which ensures good repeatability in the current experimental setup.

A benchmark experiment in single-phase liquid flow was first carried out to examine the performance of the LDA system. Good agreement between the area-averaged liquid velocity and volumetric flux $\langle j_f \rangle$ was obtained, within 4% difference, as shown in Table 1. Also, the axial velocity fluctuations showed satisfactory agreement with the experimental data acquired by Laufer [29], as shown in [18,19].

In the two-phase flow experiments, conductivity probes were first used to measure the void fraction and the bubble velocity. The measurement principle of the conductivity probe is based on the difference of the electric conductance between the water and

gas phases. Readers are referred to a paper by Kim et al. [30] for details on the measurement procedure and signal processing scheme. Since the local measurements of the conductivity probe were performed at locations of $z/D=34$ and 67 , the distributions of the void fraction and bubble velocity at the locations where the LDA measurements were carried out, i.e., $z/D=52.5$, were linearly interpolated from the local measurements. This interpolation may introduce additional uncertainty due to the non-linear nature of the flow structure development, especially when a flow regime transition is involved in the flow.

Figure 3 presents the void fraction results acquired by Goda [16] for test Runs 1-8 and obtained in the current experiments for Runs 9-13. In these flow conditions, Runs T1, T2, T4, T5, and T11 were in bubbly flow while cap bubbles or slug bubbles were captured by the conductivity probe in other test runs even though the averaged void fraction was quite low. In general, the void profiles had a center-peaked distribution except Runs T2 and T10, in which the void peak appeared at around $r/R=0.6$. This center-peak void distribution is quite different from the vertical upward flows in which wall-peaked void profiles can be often observed. This may be related to the bubble lateral lift force.

Figure 4 shows the results of the axial liquid velocity for four different superficial liquid velocities, namely, $\langle j_l \rangle = 0.62, 1.25, 2.50,$ and 3.50 m/s. In general, the presence of the bubbles tended to flatten the liquid velocity profile, which was also observed by Wang et al. [14]. For some flows, the maximum liquid velocity occurred slightly off the pipe centerline, for example, $r/R=0.2$ for Run T1, 0.1 for Run T3, and 0.2 for Run T7. In particular, the locations of the maximum liquid velocity were $r/R=0.5$ for Run T6 and 0.8 for Run T5, in which the area-averaged void fraction were 6.5% and 7.10% , respectively. Wang et al. [14] and Kashinsky and Randin [15] had the same observations in their downward bubbly flow experiments. Wang et al. [14] attributed this phenomenon to the bubble "coring" in downflow that retarded the flow in the core due to buoyancy. Thus, the liquid in the core tended to divert into the low void fraction region near the wall. However, the authors have a different viewpoint on this phenomenon. In downward flow, the wake region of the bubbles is in the same direction of the main flow and the liquid velocity in the wake region is smaller than that out of the wake. Also, the void profile in downflow is generally center-peaked. Therefore, the maximum liquid velocity will generally occur off the centerline of the pipe provided that the void fraction is considerably large. Since the magnitude of the wake depression is approximately constant, this effect becomes less significant in the conditions with high liquid flow rates. Moreover, Kashinsky and Randin [15] also showed that the larger the void fraction, the larger possibility this phenomenon would occur. This observation also agreed with the present experimental results and is consistent with the above explanation to this phenomenon. In addition to the local velocity profiles, the holdup-weighted area-averaged liquid velocity, $\langle\langle u_r \rangle\rangle$, is given in Table 1. Here, $\langle\langle u_r \rangle\rangle$ is defined as:

$$\langle\langle u_r \rangle\rangle = \frac{\langle(1-\alpha)u_r\rangle}{1-\langle\alpha\rangle}. \quad (4)$$

Furthermore, Fig. 5 shows the axial liquid velocity fluctuations in two-phase downward flow. At low void fraction conditions ($<1\%$), the axial turbulent fluctuation was not significantly affected by the addition of the gas phase. However, with the larger void fraction, the liquid turbulence increased, especially in the core region, where the liquid was considerably influenced by the presence of the bubbles. This was, in particular, evident in Runs T5, T6, T10, and T13. In these flow conditions except T5, cap bubbles were observed, which may increase the liquid velocity fluctuations. Furthermore, in general, the axial turbulence was quite uniform in the radial direction. This may be attributed to the fact that the bubble-induced turbulence in the core region is much larger than that near the wall region since the void had a core-

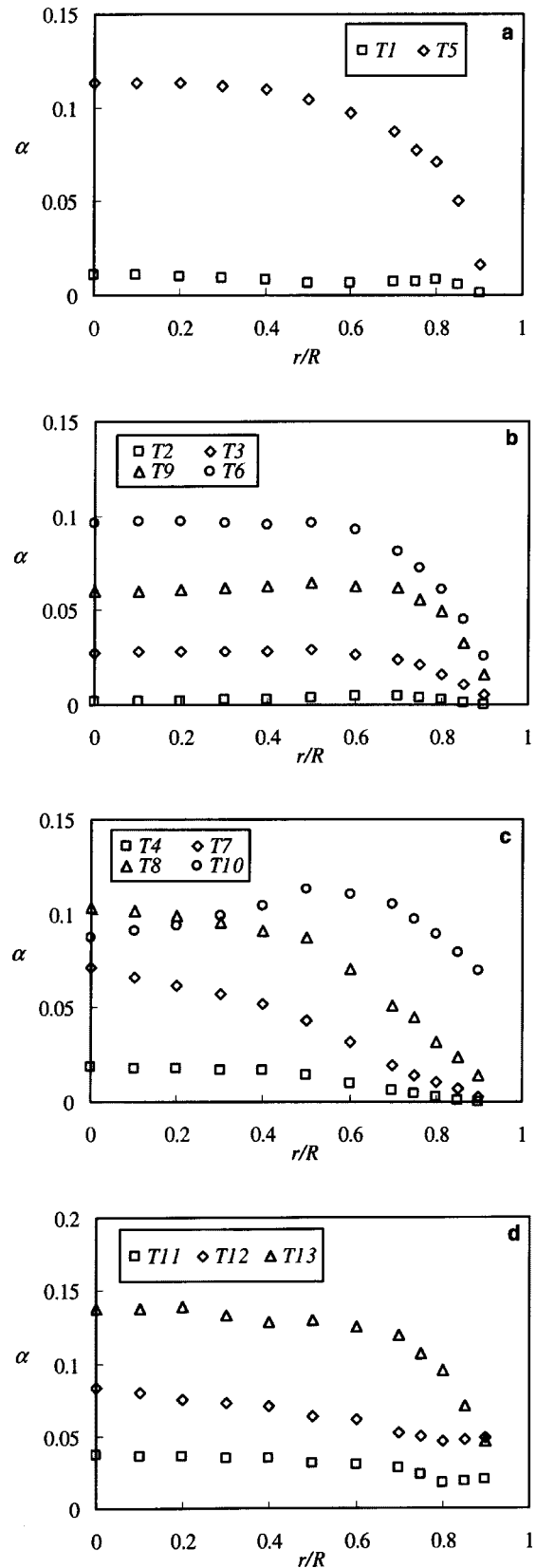


Fig. 3 The void fraction measured by the conductivity probe for $\langle j_l \rangle$: a 0.62 m/s, b 1.25 m/s, c 2.50 m/s, and d 3.50 m/s.

-peaked distribution. Again, this observation agreed with Wang et al. [14] and Kashinsky and Randin [15]. It is also interesting to note that the fluctuating liquid velocity started to decrease around $r/R=0.8$ in Runs T5 and T6.

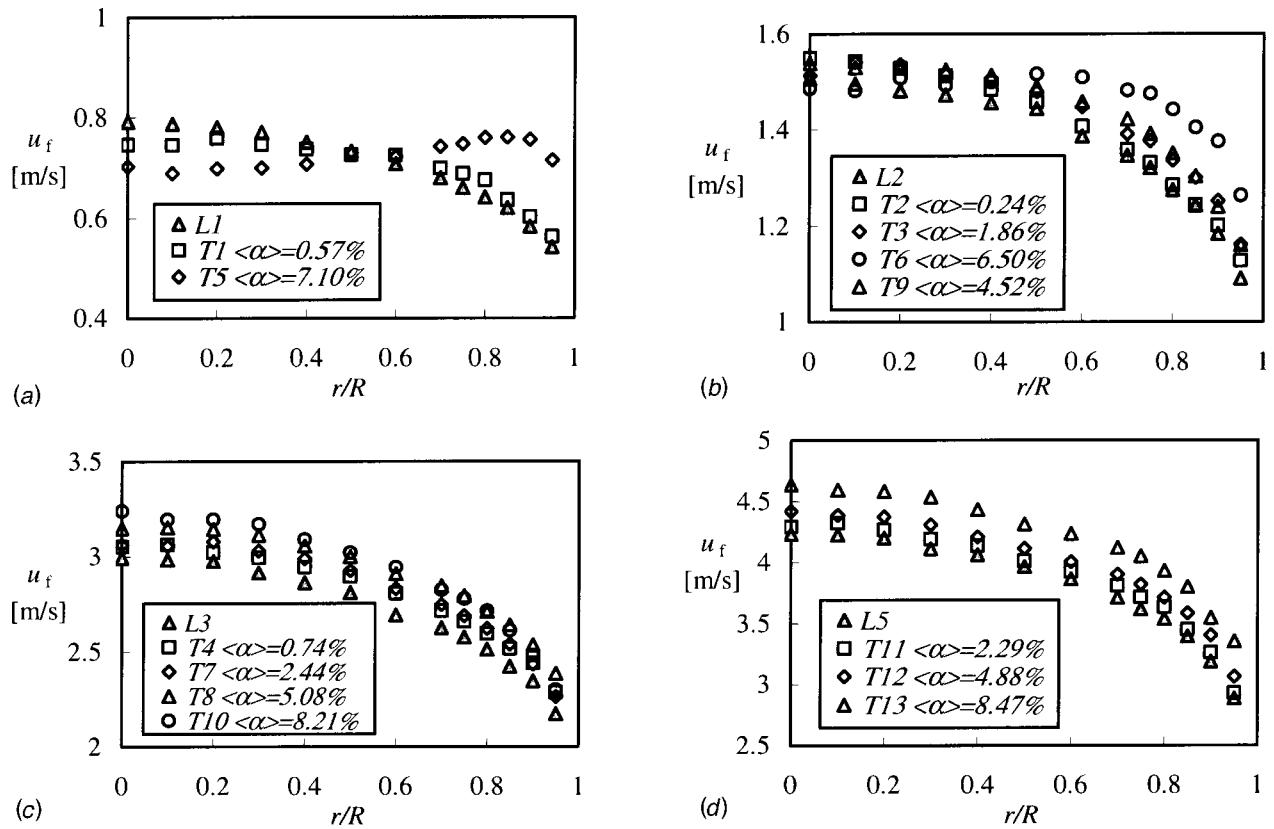


Fig. 4 The mean axial liquid velocity in two-phase flow experiments for $\langle j_f \rangle$: a 0.62 m/s, b 1.25 m/s, c 2.50 m/s, and d 3.50 m/s.

The addition of the gas phase usually increases the turbulent intensity in the continuous liquid phase. However, Serizawa et al. [2], Tsuji et al. [31], Michiyoshi and Serizawa [32], and Wang et al. [14] observed a reduction of the axial liquid turbulence in some two-phase flow conditions. No noticeable turbulent reduction in the current downward flow conditions was observed. This may be related to the relatively larger bubble size and lower void fraction in the current experiment. Nevertheless, a broad database in downward flow is indispensable to investigate this phenomenon in detail.

In addition to the local profiles of the liquid velocity and fluctuations, the liquid superficial velocity calculated based on the local LDA and conductivity probe measurements, i.e., $\langle (1-\alpha)u_f \rangle$, was compared to the boundary condition $\langle j_f \rangle$ based on the inlet flow meter. Table 1 shows the percentage difference of the local measurements with the boundary condition. The percentage difference is defined by

$$\frac{\langle (1-\alpha)u_f \rangle - \langle j_f \rangle}{\langle j_f \rangle} \times 100\%. \quad (5)$$

In most of the flow conditions, the local measurements tended to over-predict the liquid flow rate. This could be due to the over-predictions of the liquid velocity and/or the under-estimation of the void fraction. The errors in the LDA measurements can come from the setup and alignment of the fiberoptic probe and the calibration of the traverse distance. On the other hand, the local conductivity probe generally under-estimates the void fraction due to its intrusiveness. Nevertheless, the agreements between the local measurements and the inlet condition were quite remarkable, within 6%.

Furthermore, in analyzing the uncertainty of the LDA measurement, the error propagation scheme was employed, given by

$$E_A^2 = (\partial A / \partial B)^2 E_B^2 + (\partial A / \partial C)^2 E_C^2 + \dots, \quad (6)$$

where, E_A is the error of quantity A , which is a function of B , C , and etc. The magnetic flow meter had an accuracy of $\pm 1\%$ of the full-scale reading. In the current experiments, the full-scale reading was adjusted to ensure that the actual reading was around 2/3 of the full scale. Then, $\langle j_f \rangle$ may have a maximum uncertainty of about 1.8% if 1.0% measurement uncertainty is assumed for the cross-sectional area of the test section. Therefore, the calculated quantity $\langle (1-\alpha)u_f \rangle$ may have a maximum uncertainty of 7.8% since the difference between $\langle (1-\alpha)u_f \rangle$ and $\langle j_f \rangle$ is within 6%. From Eq. (6), the measurement uncertainty of the LDA can be calculated as about 7.9% for a conservative estimation if the void fraction is assumed to have a maximum of 10% measurement uncertainty.

Distribution Parameter and Drift Velocity in the Drift-Flux Model

The one-dimensional drift-flux model [17] has been widely applied in the two-phase flow analyses for several decades. This model considered the effects to the bubble velocity of the phase distribution and the local relative motion. It can be written as:

$$\left. \begin{aligned} \langle u_g \rangle &= C_o \langle j \rangle + \langle V_{gj} \rangle \\ C_o &= \frac{\langle \alpha j \rangle}{\langle \alpha \rangle \langle j \rangle}, \quad \langle V_{gj} \rangle = \frac{\langle \alpha V_{gj} \rangle}{\langle \alpha \rangle \langle V_{gj} \rangle} \end{aligned} \right\}, \quad (7)$$

where, C_o and $\langle V_{gj} \rangle$ are the distribution parameter and the void-weighted area-averaged drift velocity, while V_{gj} is the local drift velocity, defined by $V_{gj} = u_g - j$. The local superficial velocities for the liquid and gas phases can be obtained by

$$j_f = (1-\alpha)u_f, \quad j_g = \alpha u_g, \quad j = j_f + j_g. \quad (8)$$

Based on the data of the void fraction and bubble velocity by the conductivity probe and the LDA measurements, C_o and $\langle V_{gj} \rangle$ can

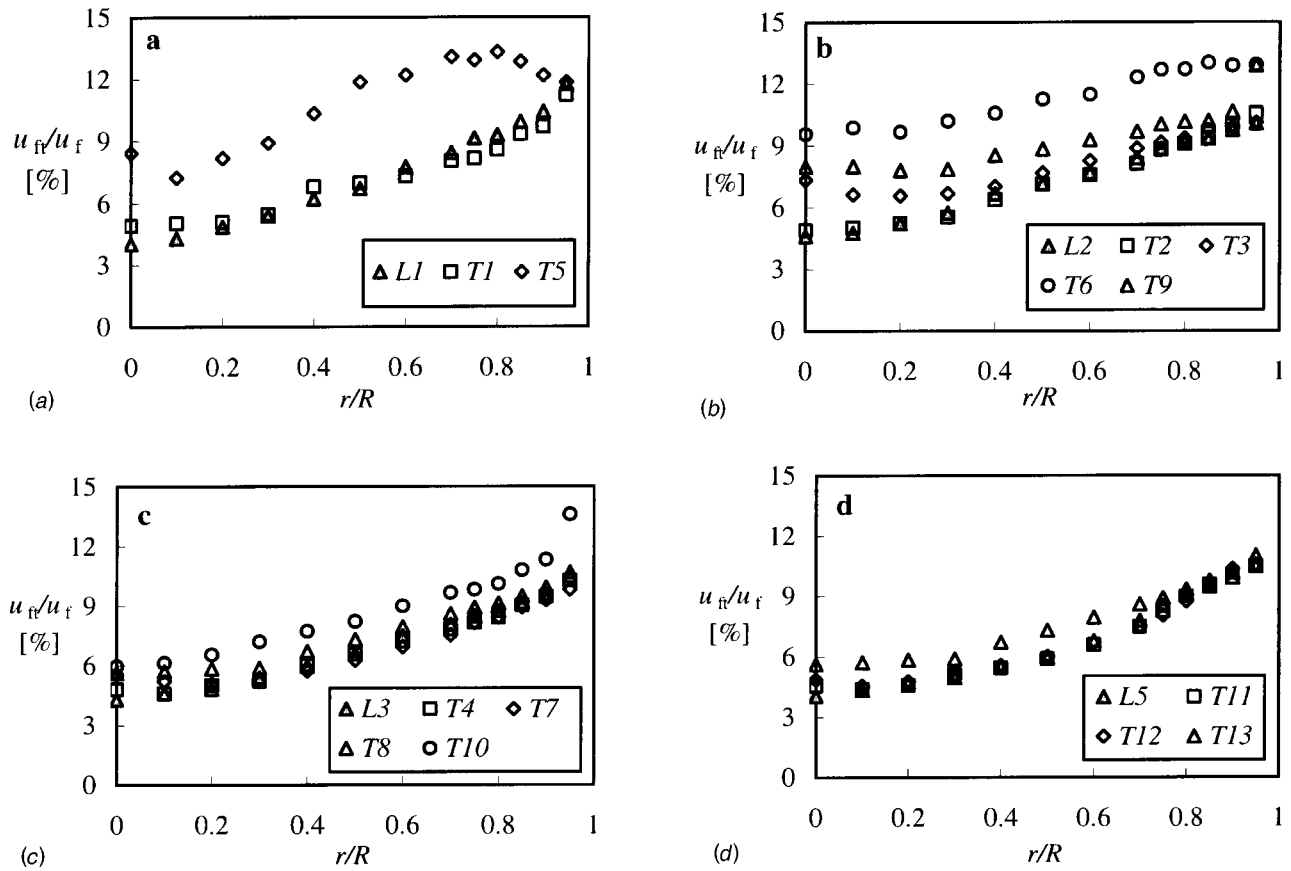


Fig. 5 The liquid turbulence intensity in two-phase flow experiment for $\langle j_l \rangle$: a 0.62 m/s, b 1.25 m/s, c 2.50 m/s, and d 3.50 m/s.

be calculated from their definitions for the current 13 two-phase flow conditions. The results are presented in Table 1. The averaged C_o value for this 13 flow conditions was 1.078. Meanwhile, Goda [16] also estimated the C_o values at $z/D=34$ and 67 for Runs 1-8 by assuming an empirical axial liquid velocity distribution and $\langle V_{gl} \rangle$ as $-\sqrt{2}[\sigma g(\rho_f - \rho_g)/\rho_f^2]^{0.25}$, which is applicable to churn-turbulent flow [33]. For the purpose of comparison, Table 1 also shows the values obtained by linearly interpolating Goda's results to $z/D=52.5$. It was found that Goda's values are always slightly higher than the current ones. Sun et al. [18] attributed this difference to the fact that the actual axial liquid velocity in the current downward flows is flatter than that given by the empirical relation used by Goda.

The void weighted drift velocity was also presented in Table 1 based on its definition in Eq. (7). In most of the flow conditions, $\langle V_{gl} \rangle$ varied from -0.11 to -0.27 m/s, which agreed reasonably with $-\sqrt{2}[\sigma g(\rho_f - \rho_g)/\rho_f^2]^{0.25}(1 - \alpha)^{1.75}$, the correlation of $\langle V_{gl} \rangle$ for bubbly flow [33]. However, for some of the cases, $\langle V_{gl} \rangle$ had much smaller numerical values. Figure 6 shows the axial liquid velocity by the LDA, the bubble velocity from the conductivity probe, and the local relative velocity, u_r for two test runs. Here, the relative velocity has the conventional definition, i.e., $u_g - u_f$. For Run T9, u_r is quite uniform in the radial direction. However, in Run T4, the bubble velocity close to the wall had an unexpected increase, which leads to the result that the gas phase locally moved faster than the liquid phase. It is considered that the resulted small relative velocity value is possibly due to the erroneous measurement of the bubble velocity close to the wall region.

Summary and Conclusions

Local measurements for axial liquid velocity and its fluctuations were performed using the LDA for vertical air-water down-

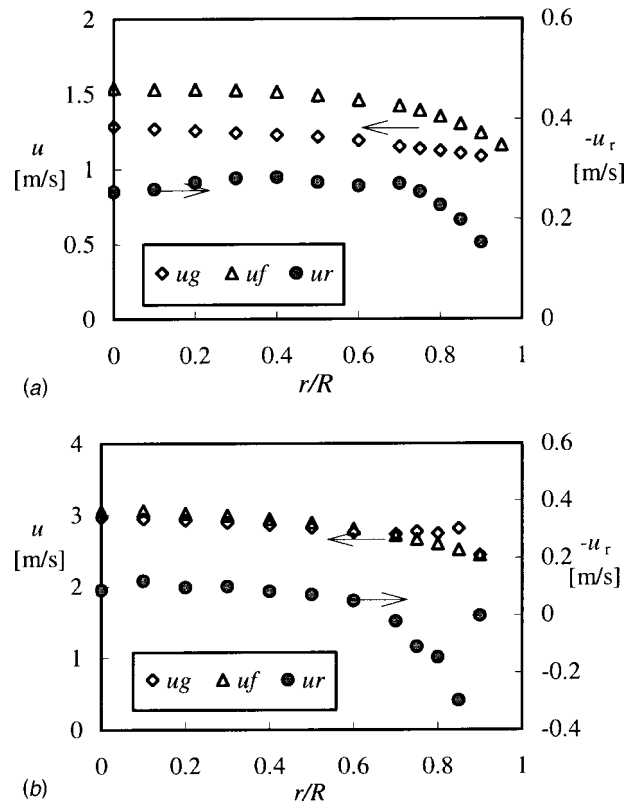


Fig. 6 Gas and liquid velocity profiles and relative velocity between the liquid and gas phase in a Run T9 ($\langle j_l \rangle=1.251$ and $\langle j_g \rangle=0.052$ m/s) and b Run T4 ($\langle j_l \rangle=2.489$ and $\langle j_g \rangle=0.030$ m/s).

ward bubbly and slug flows in a round pipe with a 50.8 mm *ID*. By applying the special setup of the LDA system, it was found that no signal discrimination process be required to obtain the liquid velocity in the present low void fraction conditions.

The benchmark experiments in single-phase liquid flow showed good agreements between the LDA and the magnetic flow meter. The void fraction measured by the conductivity probe generally had a center-peaked profile. The LDA measurement results in the two-phase bubbly flow demonstrated that the presence of the bubbles tended to flatten the liquid velocity profile, and the maximum liquid velocity could occur off the pipe centerline. Furthermore, no noticeable turbulent reduction in the two-phase downward flow was observed in the current flow conditions. The liquid superficial velocity calculated based on the local LDA and the conductivity measurements agreed very well with the magnetic flow meter.

Furthermore, the distribution parameter and the drift velocity in the drift-flux model were calculated based on their definitions. The averaged value for the distribution parameter in the present 13 flow conditions was 1.078; and the drift velocity varied from -0.02 to -0.27 m/s. The relative small drift velocity was considered due to the unreliable local bubble velocity measurement near the wall region by the conductivity probe.

Acknowledgments

This work was performed at Purdue University under the auspices of the U.S. Nuclear Regulatory Commission through the Institute of Thermal-hydraulics.

Nomenclature

A	= cross-sectional area of the test section
C_o	= distribution parameter
D	= inner diameter of the test section
E	= error in Eq. (6)
g	= gravitational acceleration
j	= volumetric flux (superficial velocity)
N	= total number of samples
Q	= volumetric flow rate
R	= inner radius of the test section
r	= radial coordinate
u	= velocity
u'	= instantaneous axial liquid velocity fluctuation
u_{ft}	= mean axial liquid velocity fluctuation
u_r	= relative velocity
V_{gj}	= drift velocity
z	= axial direction coordinate

Greek

α	= void fraction
ρ	= density
σ	= surface tension

Subscripts

f	= liquid
g	= gas

Mathematical symbols

$\langle \rangle$	= area averaging
$\langle\langle \rangle\rangle$	= void-weighted area averaging

References

- [1] Delhay, J. M., 1969, "Hot Film Anemometry in Two-phase Flow," *ASME Symposium on Two-phase Flow Instrumentation*, Le Tourneau, B. W., and Bergles, A. E. (eds.), *11th National Heat Transfer Conference*, pp. 58–69.
- [2] Serizawa, A., Kataoka, I., and Mishigoshi, I., 1975, "Turbulence Structure of Air-water Bubbly Flow-I, II, and III," *Int. J. Multiphase Flow*, **2**, pp. 221–259.
- [3] Theofanous, T. G., and Sullivan, J. P., 1982, "Turbulence in Two-phase Dispersed Flows," *J. Fluid Mech.*, **116**, pp. 343–362.
- [4] Boerner, T., Martin, W. W., and Leutheusser, H. J., 1984, "Comprehensive Measurements in Bubbly Two-phase Flows Using Laser-Doppler and Hot-film Velocimeter," *Chem. Eng. Commun.*, **28**, pp. 29–43.
- [5] Ohba, K., Yuhara, T., and Matsuyama, H., 1986, "Simultaneous Measurements of Bubble and Liquid Velocities in Two-phase Bubbly Flow Using Laser Doppler Velocimeter," *Bull. JSME*, **29**, pp. 2487–2493.
- [6] Lance, B., and Bataille, J., 1991, "Turbulence in the Liquid Phase of a Uniform Bubbly Air-water Flow," *J. Fluid Mech.*, **222**, pp. 95–118.
- [7] Liu, T. J., and Bankoff, S. G., 1993, "Structure of Air-water Bubbly Flow in a Vertical Pipe—I. Liquid Mean Velocity and Turbulence Measurements," *Int. J. Heat Mass Transfer*, **36**, pp. 1049–1060.
- [8] Aloui, F., and Souhar, M., 1996, "Experimental Study of a Two-phase Bubbly Flow in a Flat Duct Symmetric Sudden Expansion-part II: Liquid and Bubble Velocities, Bubble Sizes," *Int. J. Multiphase Flow*, **22**, pp. 849–861.
- [9] Hibiki, T., Hogsett, S., and Ishii, M., 1998, "Local Measurement of Interfacial Area, Interfacial Velocity and Liquid Turbulence in Two-phase Flow," *Nucl. Eng. Des.*, **184**(2-3), pp. 287–304.
- [10] Sharma, S., Lewis, S., and Kojasoy, G., 1998, "Local Studies in Horizontal Gas-liquid Slug Flow," *Nucl. Eng. Des.*, **184**, pp. 305–318.
- [11] Oshinovo, T., and Charles, M. E., 1974, "Vertical Two-phase Flow, Holdup and Pressure Drop," *Can. J. Chem. Eng.*, **52**, pp. 438–448.
- [12] Clark, N. N., and Flemmer, R. L. C., 1984, "On Vertical Downward Two-phase Flow," *Chem. Eng. Sci.*, **39**, pp. 170–173.
- [13] Clark, N. N., and Flemmer, R. L., 1985, "Predicting the Holdup in Two-phase Bubble Upflow and Downflow using the Zuber-Findlay Drift-flux Model," *AIChE J.*, **31**, pp. 500–503.
- [14] Wang, S. K., Lee, S. J., Jones, Jr, O. C., and Lahey, Jr, R. T., 1987, "3-D Turbulence Structure and Phase Distribution Measurements in Bubbly Two-phase Flows," *Int. J. Multiphase Flow*, **13**, pp. 327–343.
- [15] Kashinsky, O. N., and Randin, V. V., 1999, "Downward Bubbly Gas-liquid Flow in a Vertical Pipe," *Int. J. Multiphase Flow*, **25**, pp. 109–138.
- [16] Goda, H., 2001, "Flow Regimes and Local Parameter Measurements for Downward Two-phase Flow," MS Thesis, Purdue University, West Lafayette, IN.
- [17] Zuber, N., and Findlay, J. A., 1965, "Average Volumetric Concentration in Two-phase Flow Systems," *ASME J. Heat Transfer*, **87**, pp. 453–468.
- [18] Sun, X., Paranjape, S., Kim, S., Goda, H., Ishii, M., and Kelly, J. M., 2003, "Local Liquid Velocity in Vertical Air-water Downward Flow," *Proc. of the 8th International Symposium on Gas-Liquid Flows, 4th ASME/JSME Joint Fluids Engineering Division Summer Meeting*, Honolulu, Hawaii, USA, July 6–10, 2003, Paper No.: FEDSM2003-45548.
- [19] Sun, X., Paranjape, S., Ishii, M., and Uhle, J., 2004, "LDA Measurement in Air-water Downward Flow," *Exp. Therm. Fluid Sci.*, **28**, pp. 317–328.
- [20] Sun, X., Kim, S., Smith, T. R., and Ishii, M., 2002, "Local Liquid Velocity Measurements in Air-water Bubbly Flow," *Exp. Fluids*, **33**, pp. 653–662.
- [21] Durst, F., and Zare, M., 1975, "Laser Doppler Measurements in Two-phase Flows," *Proc. of the LDA Symposium*, Copenhagen, Denmark, pp. 403–429.
- [22] Lee, S. L., and Durst, F., 1982, "On the Motion of Particles in Turbulent Duct Flows," *Int. J. Multiphase Flow*, **8**, pp. 125–146.
- [23] Tsuji, Y., and Morikawa, Y., 1982, "LDV Measurement of an Air-solid Two-phase Flow in a Horizontal Pipe," *J. Fluid Mech.*, **120**, pp. 385–409.
- [24] Marie, J. L., and Lance, M., 1983, "Turbulence Measurements in Two-phase Bubbly Flows Using Laser Doppler Anemometry," *Measuring Techniques in Gas-liquid Two-phase Flow*, Delhay, J. M., and Cognet, G., (eds), Springer, New York, pp. 141–148.
- [25] Sheng, Y. Y., and Irons, C. A., 1991, "A Combination Laser Doppler Anemometry and Electrical Probe Diagnostic for Bubbly Two-phase Flow," *Int. J. Multiphase Flow*, **17**, pp. 585–598.
- [26] Velidandla, V., Putta, S., and Roy, R. P., 1996, "Velocity Field in Isothermal Turbulent Bubbly Gas-liquid Flow through a Pipe," *Exp. Fluids*, **21**, pp. 347–356.
- [27] Suzanne, C., Ellingsen, K., Risso, F., and Roig, V., 1998, "Local Measurements in Turbulent Bubbly Flows," *Nucl. Eng. Des.*, **184**(2-3), pp. 319–327.
- [28] Mudde, R. F., Groen, J. S., and Van Den Akker, H. E. A., 1998, "Application of LDA to Bubbly Flows," *Nucl. Eng. Des.*, **184**, pp. 329–338.
- [29] Laufer, J., 1954, "The Structure of Turbulence in Fully Developed Pipe Flow," NACA Report 1174, <http://naca.larc.nasa.gov/reports/1954/naca-report-1174/naca-report-1174.pdf>.
- [30] Kim, S., Fu, X. Y., Wang, X., and Ishii, M., 2000, "Development of the Miniaturized Four Sensor Conductivity Probe and the Signal Processing Scheme," *Int. J. Heat Mass Transfer*, **43**, pp. 4101–4118.
- [31] Tsuji, Y., Morikawa, Y., and Shiomi, H., 1984, "LDV Measurements of an Air-solid Two-phase Flow in a Vertical Pipe," *J. Fluid Mech.*, **139**, pp. 417–434.
- [32] Michiyoshi, I., and Serizawa, A., 1986, "Turbulence in Two-phase Bubbly Flow," *Nucl. Eng. Des.*, **95**, pp. 253–267.
- [33] Ishii, M., 1977, "One-dimensional Drift-flux Model and Constitutive Equations for Relative Motion between Phases in Various Two-phase Flow Regimes," Argonne National Laboratory Report, ANL-77-47, Argonne, IL.

Peter M.-Y. Chung

Dept. of Chemical Engineering & Applied
Chemistry,
University of Toronto,
Toronto, Ontario,
Canada

Masahiro Kawaji

Dept. of Chemical Engineering & Applied
Chemistry,
University of Toronto,
Toronto, Ontario,
Canada

Akimaro Kawahara

Dept. of Mechanical Engineering & Materials
Science,
Kumamoto University,
Kumamoto, Kyushu,
Japan

Yuichi Shibata

Dept. of Mechanical Engineering,
Ibaraki National College of Technology,
Hitachinaka-shi, Ibaraki-ken,
Japan

Two-Phase Flow Through Square and Circular Microchannels—Effects of Channel Geometry

An adiabatic experiment was conducted to investigate the effect of channel geometry on gas-liquid two-phase flow characteristics in horizontal microchannels. A water-nitrogen gas mixture was pumped through a 96 μm square microchannel and the resulting flow pattern, void fraction and frictional pressure drop data were compared with those previously reported by the authors for a 100 μm circular microchannel. The pressure drop data were best estimated using a separated-flow model and the void fraction increased non-linearly with volumetric quality, regardless of the channel shape. However, the flow maps exhibited transition boundaries that were shifted depending on the channel shape. [DOI: 10.1115/1.1777227]

Introduction

Two-phase flow in microchannels is encountered in miniature heat exchangers that cool electronics and biotechnology systems. Advances in electronic packaging and chemical processing have driven the demand to improve thermal-control systems such as micro-heat pipes, miniature heat exchangers and micro-scale thermosyphons (Peng and Wang, [1]). There is now a growing need to remove high heat fluxes from a small area and maintain the desired temperature uniformly. Using phase change as the main means to transfer heat, coolant is circulated in rectangular microchannels on the silicon wafer of the computer chip requiring cooling. Compared to the heat transfer of single-phase forced convection, the temperature gradient is lower in flow boiling because of the phase change phenomena. This fact implies a higher heat transfer coefficient and a lesser demand on the liquid flow (Stanley et al., [2]).

There is no consideration of heat transfer or phase change in this study of adiabatic flow. With the injection of gas into the liquid stream, much can be learned from just the morphology or mechanism of adiabatic two-phase flow in microchannels. Since heat transfer with phase change is related to the flow structure, identifying the two-phase flow pattern will ensure that the appropriate heat transfer or flow model is applied.

The purpose of this paper is to determine the effect of channel shape on adiabatic two-phase flow in a microchannel. In particular, the flow through a microchannel with a square or circular cross section of similar size is compared. The comparison will be made based on the flow pattern transitions, void fraction and two-phase pressure drop. The analysis will start with a detailed study of the two-phase flow structures by flow visualization, followed

by the development of the two-phase flow pattern map and correlations of the void fraction and frictional pressure drop data.

Microchannels. An inspection of the published literature on two-phase flow will easily show that the dimensions of a microchannel can vary considerably, but has been mainly limited to about 1 mm. Here, a channel is labeled a microchannel when its characteristic length is significantly below 1 mm. Strict adherence to this definition would eliminate most previous studies that used the term microchannel. Very few publications are available on studies involving a diameter of 100 μm or less. Guided by the channel size in compact plate-fin evaporators, Kandlikar [3] referred to channels with a hydraulic diameter between 200 μm and 3 mm as minichannels. Based on the size of channels in micro-electro-mechanical systems (MEMS), he proposed a range of 10 to 200 μm to characterize the hydraulic diameter of a microchannel used for flow boiling.

Channel Geometry. Due to the capillary force, Bi and Zhao [4] argued that water would always be retained in the corner of the channel and create the buoyancy force necessary for air bubbles to rise in stagnant water. They had documented the motion of Taylor bubbles in triangular and rectangular channels with a hydraulic diameter as small as $D_h = 0.866$ mm and $D_h = 1.0$ mm, respectively. Carey [5] described an alternating sequence of liquid and gas slugs in a small circular channel. The gas bubble fills the entire cross section of the tube and yields a dry wall. There is a complete separation of the gas phase from the liquid phase, in contrast to that intrinsic to small noncircular channels. Furthermore, Zhao and Bi [6] stated that the flow in the corner of a triangular channel may stay laminar despite a fully turbulent flow in the core.

According to Kolb and Cerro [7], the shape of a gas bubble inside a square channel depends on the magnitude of the capillary number, Ca . For a large Ca , the cross section of the bubble is axisymmetric and circular. For a small Ca , the bubble shape is

Contributed by the Fluids Engineering Division for publication in the JOURNAL OF FLUIDS ENGINEERING. Manuscript received by the Fluids Engineering Division May 27, 2003; revised manuscript received March 17, 2004. Associate Editor: J. Katz.

non-axisymmetric. Here, the cross section of the bubble appears flat alongside the channel walls and displays an arc of constant curvature in the corners of the square channel. Cox [8] attributed the non-axisymmetric shape of the bubble in horizontal flow to the dominating effect of gravity at low Ca . Later, Kolb and Cerro [9] claimed that the flow in the corners contributes to over 95% of the total flow. Clearly, the differences between the flows in noncircular and circular channels can be significant due to the flow at the corners.

Adiabatic two-phase flow in circular microchannels has been reported by Kawahara et al. [10] for $D=100\ \mu\text{m}$, and Serizawa et al. [11] for $D=20, 25,$ and $100\ \mu\text{m}$. The results obtained in this study for a square microchannel of $D_h=96\ \mu\text{m}$ will be compared to those reported previously by Kawahara et al. [10] for a circular microchannel of $D=100\ \mu\text{m}$.

Experimental Details

Experimental Apparatus and Test Section. A schematic of the experimental apparatus is shown in Fig. 1. Liquid was forced through the horizontal microchannel by a pneumatic pump. The pump consisted of a pressure vessel filled with deionized water and connected to a gas cylinder of dry nitrogen gas that pushed the water out. This approach yields a liquid flow that is constant and pulsation-free. For this setup, all tubing and compression-fitting connections were made of stainless steel or brass to avoid any volumetric expansion in the flow loop or leakage under pressure.

A mixture of nitrogen gas and deionized water was pumped into a square microchannel placed horizontally. Nitrogen gas is practically insoluble in water and provided the high pressure source needed to drive the liquid through the microchannel. The effect of channel shape was identified through tests in a square channel with a hydraulic diameter of $96\ \mu\text{m}$. A circular channel with an inner diameter of $100\ \mu\text{m}$ was used earlier for the test section (Kawahara et al., [10]). The actual diameter was determined from the sample average of images taken with an optical or scanning electron microscope. Since the microchannel was entirely constructed from fused silica by a drawing process, the microchannel used was transparent and can be regarded as a smooth channel. Thus, the effect of wall roughness was not explored in this study. Long channels of high L/D ratio were used to minimize the entrance and exit effects. The shape and size of the channels compared are listed in Table 1.

Three pressure transducers covering different ranges ($210 \pm 0.52\ \text{kPa}$, $3,450 \pm 8.6\ \text{kPa}$, and $24.9 \pm 0.037\ \text{kPa}$), were connected to a tee junction upstream of the inlet of the microchannel to measure the pressure drop between the channel inlet and outlet.

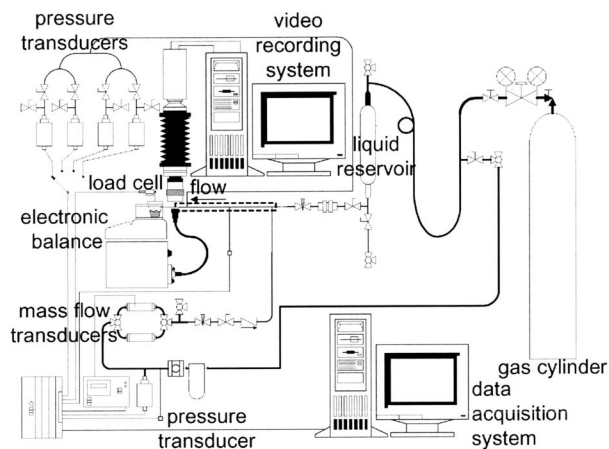
The tee junction had an internal diameter of $250\ \mu\text{m}$ and was connected to the two-phase mixer, the test section and the manifold of pressure transducers. The appropriate pressure sensor was selected by manipulating the plug valves on the manifold. The liquid was discharged freely from the microchannel, so the pressure was atmospheric and temperature ambient at the outlet. A type K (-200 to 1250°C) thermocouple probe provided the fluid temperature upstream of the microchannel.

The liquid flow rate was measured by collecting the liquid in a small container discharged over a sufficient period of time and measuring its weight using an electronic balance ($120 \pm 0.001\ \text{g}$) or load cell ($50.97 \pm 0.255\ \text{g}$). The gas flow rate was read from three mass flowmeters (0–1, 0–10 and 0–50 sccm). A correction was applied to the mass flow readings because the experimental conditions were different from those that existed during calibration. The system was confirmed to be at steady-state by observing the pressure readings. All analog signals for pressure, temperature and mass flow rate readings were recorded with a 16-bit data acquisition system at 100 Hz.

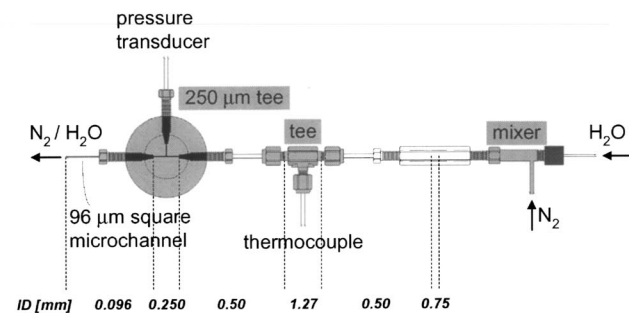
The transparent test section enabled the flow patterns to be recorded with a video camera against a lighted backdrop. Background illumination was provided by a cold lamp and gooseneck light guide placed behind the test section. To observe the structure of the gas-liquid flow inside the microchannel, a 5X microscope objective lens was coupled to the video camera as shown before in Fig. 1. Two monochrome CCD cameras were used depending on the resolution and frame rate required for a given run. The first camera had a resolution of $1024(\text{H}) \times 1024(\text{V})$ pixels and operated at a maximum frame rate of 30 fps and a shutter speed of $1/16,000\ \text{s}$. The second camera offered a resolution of $648(\text{H}) \times 484(\text{V})$ pixels and ran at a maximum frame rate of 125 fps and an exposure period of $66\ \mu\text{s}$.

Experimental Flow Conditions. All experiments on the square microchannel were conducted at room temperature and atmospheric pressure at the discharge of the test section. Sufficient time was allowed for data collection to ensure that steady state would be achieved. Also, a longer sampling time was used for the measurement of the liquid flow rate. The liquid flow rate can be determined more accurately when the water is weighed over an extended period of time. Notwithstanding, some runs warranted a short recording of the data at quasi-steady state due to control difficulties in keeping the flow conditions constant.

Typical of conditions found in the literature for microchannel flow, the Bond number is much smaller than unity ($0.000310 \leq Bo \leq 0.000313$). Flow fields dominated by inertia and surface tension are both encountered, as indicated by the range of superficial Weber number for liquid ($0.00010 \leq We_{LS} \leq 25$) and gas



(a) experimental apparatus



(b) test section

Fig. 1 Experimental apparatus and test section

Table 1 Channel Dimensions

Channel cross section	D [μm] or D_h [μm]	L [mm]
square	95.6	65.05
circular	99.6	63.90, 65.10

($0.000019 \leq We_{GS} \leq 9$). The significance of inertia is shown again by the value of the superficial Reynolds number for liquid ($1 \leq Re_{LS} \leq 438$) and gas ($1 \leq Re_{GS} \leq 612$).

Data Analysis

Frictional Pressure Drop for Single-Phase Liquid Flow

For the square microchannel used in the present study, single-phase flow experiments were first conducted to determine the friction factor using deionized water. The frictional factor data were then compared with the conventional values for laminar flow in a square channel.

If $P_{channel}$ is the atmospheric pressure at the outlet of the microchannel and P_{tee} is the pressure measured by a pressure transducer at the inlet tee section, the pressure drop in the microchannel over the fully developed flow region, $\Delta P_{f,channel}$, would be given by

$$\Delta P_{f,channel} = P_{tee} - P_{channel} + \frac{\rho}{2}(u_{tee}^2 - u_{channel}^2) - \Delta P_{f,tee} - \Delta P_{inlet} - \Delta P_{entrance}, \quad (1)$$

where $\Delta P_{f,tee}$ is the frictional pressure drop in the tee, ΔP_{inlet} is the pressure loss due to sudden contraction at the microchannel inlet ($96 \mu\text{m}$) from the larger tee junction ($250 \mu\text{m}$), $\Delta P_{entrance}$ is the pressure drop in the entrance region, and u_{tee} and $u_{channel}$ are the mean velocities in the tee section and microchannel, respectively. For simplicity, the pressure loss within the tee was assumed to be zero. Further information on computing the single-phase pressure drop is available in Chung et al. [12].

Frictional Pressure Drop for Two-Phase Flow. The overall pressure drop measured in horizontal two-phase flow, $\Delta P_{measured}$, is given by

$$\Delta P_{measured} = \Delta P_{friction} + \Delta P_{contraction} + \Delta P_{acceleration}, \quad (2)$$

where $\Delta P_{friction}$ is the pressure drop due to wall friction, $\Delta P_{contraction}$ is the pressure loss due to contraction from the tee into the microchannel, and $\Delta P_{acceleration}$ is the pressure change due to acceleration. In order to obtain two-phase frictional pressure drop data, the second and third terms on the right hand side of Eq. (2) must be estimated and subtracted from the total two-phase pressure drop measured. Thus, $\Delta P_{contraction}$ and $\Delta P_{acceleration}$ were estimated using a homogeneous and separated flow model, respectively. The void fraction data to estimate the accelerational pressure drop were available from the analysis of the video recordings and fitted to a new empirical correlation developed by Kawahara et al. [10]. The reader is advised to consult Kawahara et al. [10] for a greater elaboration on the data reduction process.

Results and Discussion

Two-Phase Flow Patterns in a Horizontal Microchannel

Images of flow patterns captured during the experiment are shown in Fig. 2. To allow comparison with other investigators, an attempt is made to initially name the flow patterns after those already observed in ~ 1 mm diameter channels by Triplett et al. [13]. They presented bubbly, churn, slug, slug-annular and annular flow in their flow pattern maps. These conventional names will be used, but any departure from the minichannel flow patterns is pointed out and clarified. Images of the flow patterns observed in the present square and circular microchannels are shown in Fig. 2.

Unlike in minichannels, bubbly, churn, slug-annular and annular flow could no longer be identified in these microchannels, and the slug flow regime became more prevalent. Being typically laminar in a microchannel, the liquid flow lacks the kinetic energy to break up the gas phase into small bubbles. With the size of the square channel diminishing, Coleman and Garimella [14] ob-

96 μm square channel ($j_L = 0.26$ m/s, $j_G = 42.18$ m/s)

100 μm circular channel ($j_L = 0.25$ m/s, $j_G = 37.87$ m/s)

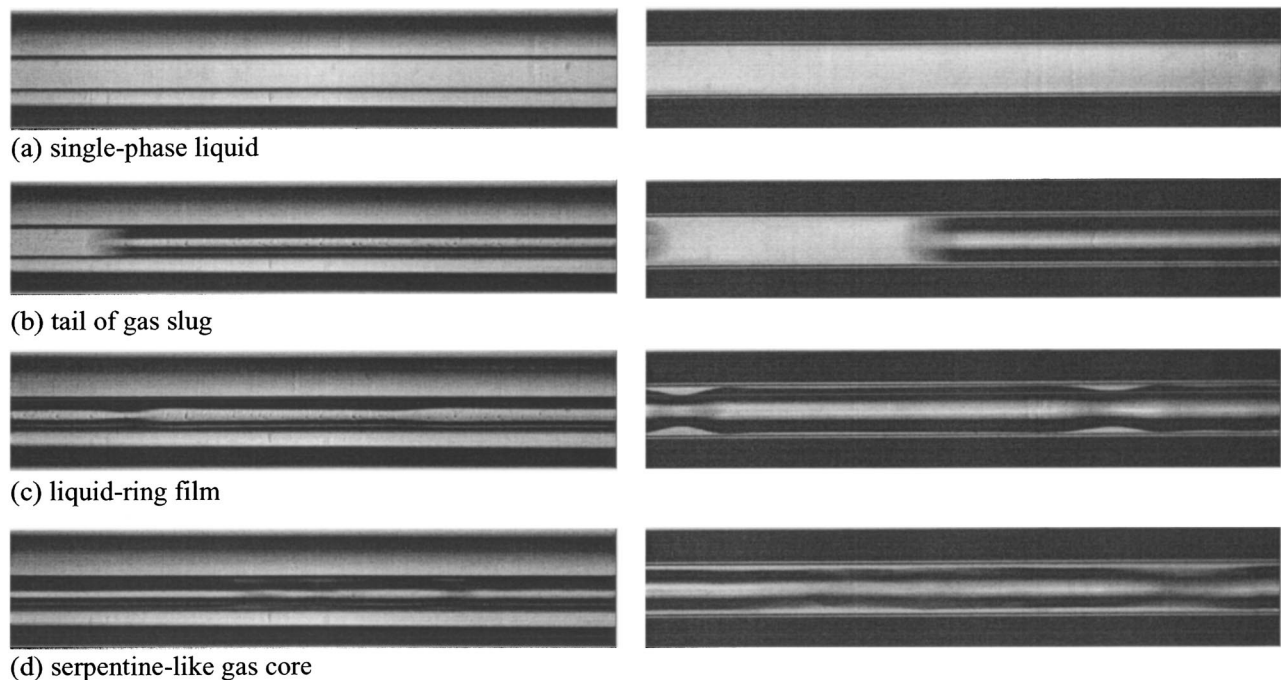


Fig. 2 Flow patterns in the square and circular microchannels under similar flow conditions

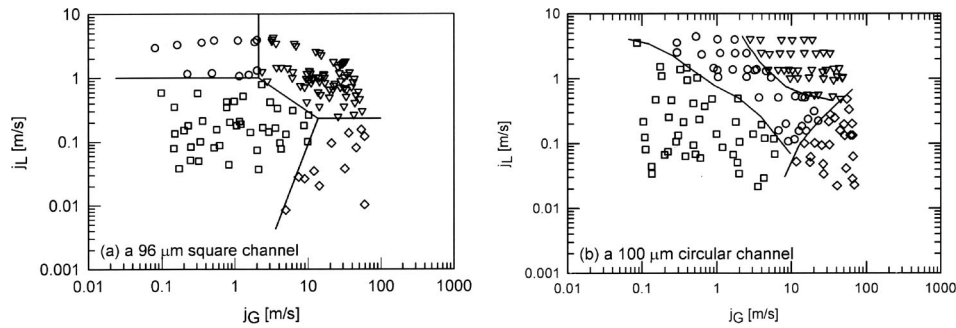


Fig. 3 Two-phase flow pattern maps using flow pattern definitions for microchannels (□ slug-ring; ○ ring-slug; ▽ multiple; ◇ semi-annular; — transition lines)

served the intermittent flow regime become increasingly prevalent during the condensation of the refrigerant R134a. As the hydraulic diameter decreases, the effect of surface tension outweighs the effect of gravity and causes the liquid to be pulled up into the four corners and less liquid would be distributed along the side walls of the square channel. Stanley et al. [2] tested combinations of water with argon, helium or nitrogen gas in rectangular microchannels of hydraulic diameters ranging from 56.0 to 256.9 μm and aspect ratios of 0.492 to 1.548. They observed the flow regime to be composed primarily of slug flow with some annular flow.

When the mixture volumetric flux is increased at low liquid superficial velocities, long bubbles in a minichannel coalesce to form a gas slug with a visible neck. Triplett et al. [13] called this flow pattern slug-annular flow. Note that these interfacial waves comprising the neck of the gas slug can also be found on the liquid film of annular flow, but the waves are not regularly spaced. Conversely, the surface waves in microchannels have regularly-spaced peaks of large amplitude relative to the diameter of the channel. These symmetric waves do not lean in the flow direction. This flow pattern is called liquid-ring flow in Fig. 2(c) and is unique to microchannels (Serizawa et al., [11]; Kawahara et al., [10]), where the effect of surface tension tends to induce symmetry in the capillary waves.

Moreover, the shape and motion of the gas-liquid interface in a microchannel can resemble a serpentine-like gas core moving through the tube and, to our knowledge, this type of flow pattern has not been previously observed in small ($D_h \sim 1 \text{ mm}$) or large ($D_h > 3 \text{ mm}$) flow channels. It is similar to a flow pattern called “disturbed core-annular” or “corkscrew core flow” occurring in liquid-liquid flows (Joseph et al., [15]). Hence, the flow pattern in Fig. 2(d) can be thought of as a gas core flow with a wavy film.

At high gas superficial velocity, gas slugs merge to form a long semi-continuous gas core and bring about a high void fraction. It is called semi-annular flow, since short liquid bridges still exist to separate the long gas slugs and prevent the formation of an annular flow with a fully continuous gas core. On the flow pattern map, the region of semi-annular flow had a visibly higher void fraction than those of the neighboring flow patterns, allowing the void fraction for semi-annular flow to be easily determined for that channel size. Semi-annular flow is identified by its high void fraction and long gas core.

Another unique characteristic of microchannel two-phase flow is the occurrence of multiple flow patterns for a single flow condition. Obviously, some judgment is required to classify a run showing several flow patterns at different times for the same flow condition and location in the channel. Such a flow condition may be represented by the dominant or most probable flow pattern, if not a specific flow pattern.

In developing two-phase flow pattern maps for the 96 μm square and 100 μm circular microchannels, it became clear that new flow patterns need to be defined to fully describe the flow characteristics of the slug flow region for these sizes. The time

fractions of different flow patterns were obtained for each two-phase flow condition because of the simultaneous occurrence of different flow patterns in the channel under any given flow condition. From the observation section of the microchannel, the two-phase flow can be classified as: (A) liquid alone; (B) gas core with a smooth liquid film; (C) gas core with a ring-shaped liquid film and (D) gas core with a deformed liquid film. Note that thick and thin liquid films of smooth interface are grouped together into class (B). This classification deals with the shape of the gas-liquid interface (types B, C and D) on the gas slug. Class (D) includes flows exhibiting a serpentine-like gas-liquid interface and small ripples on the interface. When compared to churn flow in a minichannel, class (D) flow in a microchannel does not display the dispersion of bubbles that trail the tail of the gas slug. Incidentally, the deformed liquid film of a serpentine-like gas core may appear as a liquid lump in an even smaller microchannel of 20 or 25 μm diameter (Serizawa et al., [11]). The number of images containing each flow pattern was then counted and the probability of appearance was computed for a given flow condition. Based on these probabilities and the time-averaged void fraction for each flow condition, four flow patterns were defined as follows:

- “Slug-ring flow” is the flow in which the probability of class (B) is larger than that of (C) and the time-averaged void fraction is less than a prescribed value, 0.8;
- “Ring-slug flow” is the flow in which the probability of class (C) is greater than that of (B) and the time-averaged void fraction is less than a prescribed value, 0.8;
- “Semi-annular flow” is the flow in which the flow mostly alternates between classes (A), (B), and (C) and the time-averaged void fraction is greater than a prescribed value, 0.8;
- “Multiple flow” contains all four flow patterns, (A)-(D), and the time-averaged void fraction is less than a prescribed value, 0.8.

Two-Phase Flow Maps for a Horizontal Microchannel.

Figure 3 shows the overall two-phase flow pattern maps developed for the shapes of microchannels under investigation. The ordinate and abscissa are the superficial velocities of liquid and gas, respectively. Here, the superficial gas velocity was calculated based on the gas density evaluated at the pressure in the observation area, which was determined by assuming a linear pressure variation between the channel inlet and outlet. In Fig. 3, the flow pattern maps are plotted according to the definitions derived earlier for flow patterns in a microchannel. All four of the above flow patterns were observed in both microchannels, although the transition boundaries for slug-ring flow, ring-slug flow, and multiple flow were shifted between the two channel geometries. For a microchannel of 100 μm hydraulic diameter or less, these flow patterns are normally hidden behind those defined for a minichannel.

The region of ring-slug flow pattern in the circular channel collapsed in the square channel. Notwithstanding the slight difference in size, the cross-section geometry is most likely responsible

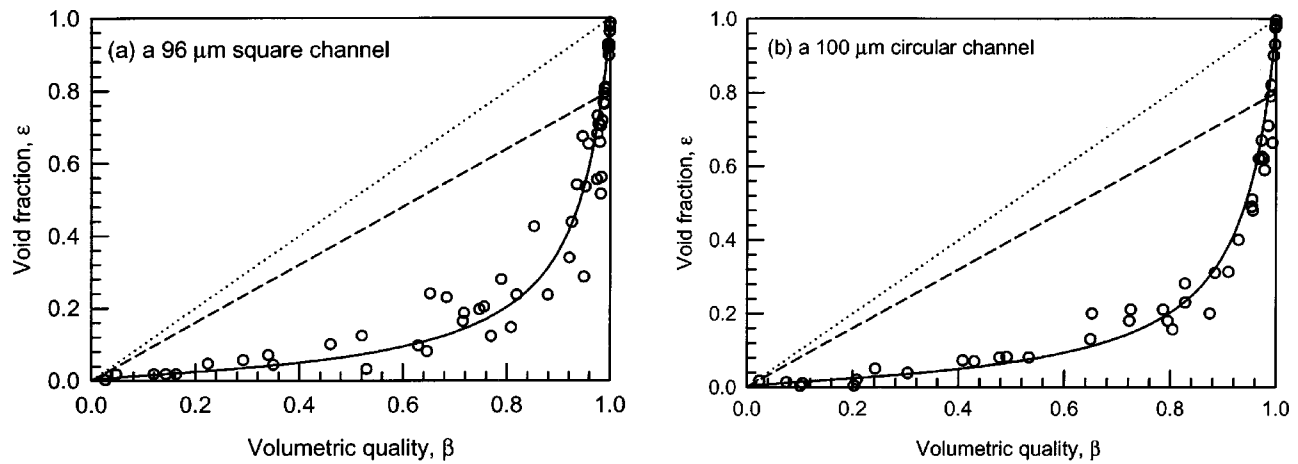


Fig. 4 Volume-averaged void fraction (○ from experiment; — from Eq. (3) with $C_1=0.03$, $C_2=0.97$; ···· for homogeneous flow; - - - - from Ali et al. [16])

for the relocation of the ring-slug flow pattern or shift in flow pattern transition between the square and circular channels. The liquid film in a noncircular microchannel can accumulate in the sharp corners, whereas the liquid film in a circular microchannel can build up in thickness along the channel wall or locally develop into a liquid ring. In the region of ring-slug flow for the circular channel, the liquid in the square channel does not form a ring and is retained instead in the corners. The numerical simulation of Kolb and Cerro [9] showed that the flow was faster in the corners than along the sides of a square channel. They reasoned this finding to be due to the thicker liquid film at the corners.

Void Fraction in a Microchannel. Image analysis was used on the video images of the gas-liquid interface to calculate the void fraction for the 96 μm square channel and 100 μm circular channel. The method used to determine the void fraction in the circular channel is described below and was also applied to the square channel. The computed void fraction is averaged in space and with time.

The void fraction in the 100 μm microchannel was estimated by analyzing the recorded images of the gas-liquid interface in the observation window of the channel. The video images from 46 experimental runs were examined to produce the void fraction database for the circular channel. The total number of images for each run ranged from 201 to 501. Each image covered a distance of about 1 mm in the flow direction. For a given run, all the images were assigned a void fraction. Images showing liquid flowing alone had a void fraction of zero. When the flow pattern depicted a gas core flow with a smooth liquid film or ring-shaped liquid film, the void fraction was assumed to be unity. By summing the void fraction for each image and dividing by the total number of images, the time-averaged void fraction can be determined. The success of this void fraction estimation lies in the gas core flow always occupying the whole field-of-view, i.e., there is no image of a liquid bridge or the nose of a gas slug to contend with. When the smooth liquid film is thick, the gas core volume fraction can be estimated by regarding the gas core as a cylinder of smaller radius than the channel radius and taking the ratio of the squared radii. The issue of optical distortion with this method was addressed by Kawahara et al. [10]. It was later found that the error caused by neglecting the liquid film around the gas slug is slight and the average void fraction is insensitive to the camera frame rate. If the instantaneous void fraction is estimated using values of 0 and 1, instead of values between 0 and 1, the average void fraction is overpredicted by about 11%. In addition, the average void fraction is essentially the same when determined using images captured at 30 or 15 fps. The development of the void fraction uncertainty is omitted in this work due to space limitation.

Figure 4 presents the time-averaged void fraction results for both microchannels. The void fraction is plotted against a volumetric quality or homogeneous void fraction, $\beta [=j_G/(j_G + j_L)]$. Homogeneous flow ($\varepsilon = \beta$) and the correlation recommended by Ali et al. [16] for narrow channels are shown as a dotted and dashed line in the figure, respectively. For narrow rectangular channels with $D_h \sim 1$ mm, Ali et al. [16] reported that the void fraction can be approximately given by a correlation ($\varepsilon = 0.8\beta$) resembling that formulated by Armand [17].

It is clear that the average void fraction for both the square and circular microchannels does not correlate with either the homogeneous flow model or Armand-type correlation. The void fraction remained low for relatively high volumetric quality, $\beta < 0.8$, but increased rapidly for $0.8 < \beta < 1$. The void fraction data indicate a strong deviation from homogeneous flow and a large slip existing between the gas and liquid phases, even at relatively low gas flow rates. The following empirical correlation was employed to best fit the void fraction data and is plotted as a solid curve in the figure:

$$\varepsilon = C_1 \beta^{0.5} / (1 - C_2 \beta^{0.5}), \quad (3)$$

where C_1 and C_2 are constants determined from the experiment. $C_1 = 0.03$ and $C_2 = 0.97$ for both the square and circular microchannels. There were some differences in the flow pattern transition boundaries between the square and circular microchannels, but the void fraction data are quite similar and therefore predictable by the same correlation.

Two-Phase Frictional Pressure Drop. Prior to performing the two-phase flow experiments, single-phase pressure drop data were obtained using de-ionized water in the microchannel. The friction factor was determined from the measured pressure drop. For the analysis of two-phase frictional pressure drop described next, this friction factor was used to calculate the single-phase frictional pressure drop.

According to some previous studies on two-phase frictional pressure drop, the homogeneous flow model can predict experimental data successfully; e.g., for ammonia-steam flow in circular minichannels with $D = 1.46$ to 3.15 mm by Ungar and Cornwell [18], and for air-water flow in circular and semi-triangular minichannels with $D_h = 1.09$ and 1.49 mm by Triplett et al. [19]. However, the two-phase flow patterns were much less homogeneous in the present microchannels, as indicated by the video images and very large slip ratios. Thus, the homogeneous flow model is not expected to correlate effectively the current two-phase pressure drop data.

On the other hand, the development of the Lockhart and Mar-

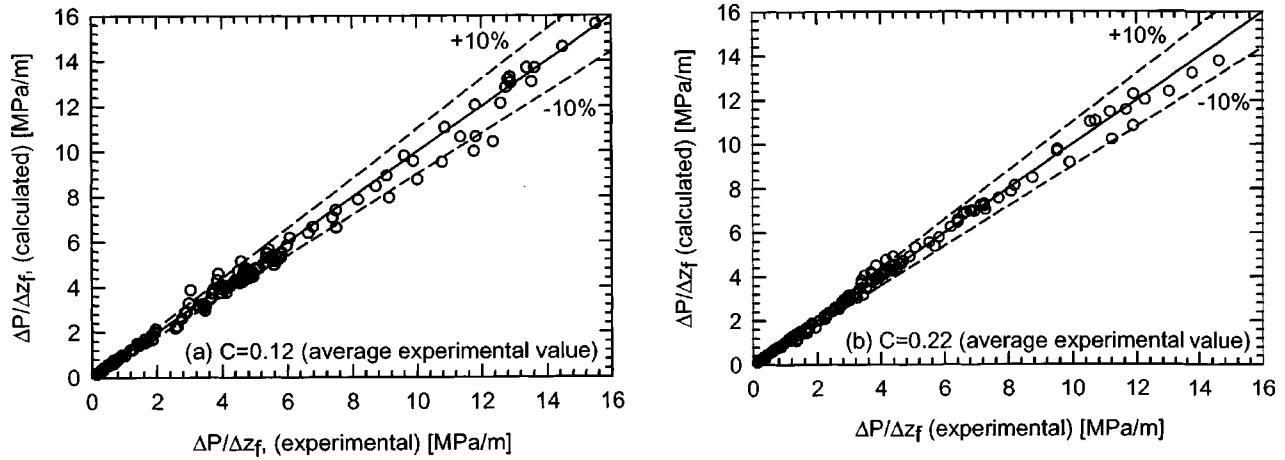


Fig. 5 Prediction of the two-phase frictional pressure gradient in the (a) 96 μm square channel and (b) 100 μm circular channel. The C -value in the Lockhart-Martinelli correlation (Eq. 4) is averaged from experiment.

tinelli [20] correlation was based on a separated flow assumption and can be represented by Chisholm's [21] correlation for the two-phase friction multiplier:

$$\phi_L^2 = 1 + C/X + 1/(X^2), \quad (4)$$

where ϕ_L^2 is the two-phase friction multiplier, C is a constant, and X is the Lockhart-Martinelli parameter. This approach has been found by Zhao and Bi [6] to represent reasonably well their data for vertical air-water flow in miniature triangular channels with $D_h = 0.87$ to 2.89 mm. Figure 5(a) compares the two-phase frictional pressure gradient data from the 96 μm square microchannel with the predictions of the Lockhart-Martinelli correlation using the average experimental C -value of 0.12 in Eq. (4). Although not shown here, the conventional value of $C = 5$ significantly over-predicted the present data, while the correlation of Mishima and Hibiki [22] generally over-predicted the present data by about 10%. Agreement within 10% was obtained with the use of the C -value given by the model of Lee and Lee [23], not depicted here, and the present value of $C = 0.12$. In Fig. 5(b), the same comparison is made with the data from the 100 μm circular channel and identical statements can be made if C is set to 0.22. Hence, the two-phase frictional pressure drop is marginally affected by the shape of the microchannel, square or circular. The Lockhart-Martinelli correlation can sufficiently predict the two-phase frictional pressure drop in both microchannels.

Conclusions

An experimental investigation has been carried out on nitrogen gas-water two-phase flow in a square channel of 96 μm hydraulic diameter and a circular channel of 100 μm diameter. The two-phase flow patterns were identified and the time-averaged void fraction and two-phase frictional pressure drop data were measured. From the results shown, the following conclusions can be made:

- Only slug flow was identified in both of the microchannels. Bubbly, churn and annular flow were not observed for the flow conditions tested. The absence of the bubbly and churn flow patterns can be attributed to the laminar nature of liquid flow in the microchannels.

- An inspection of the liquid film structure in the slug flow pattern revealed a gas core flow with a smooth or ring-shaped liquid film and a serpentine-like gas core flow surrounded by a deformed liquid film. Four new flow patterns were defined on the probability of the interfacial structure appearing: slug-ring flow, ring-slug flow, semi-annular flow and multiple flow.

- Flow pattern maps for both channels were developed based on the new flow pattern definitions in the slug flow region, and compared to each other. The liquid flow in the corner of the square channel can account for the relocation of the ring-slug flow pattern.

- Images of the two-phase flow were analyzed to obtain the time-averaged void fraction. The disagreement with the Armand [17] correlation was attributed to the large slip ratio and weak momentum exchange between the gas and liquid phases in both channel geometries.

- The separated flow model of Lockhart and Martinelli [20] correlated well (within $\pm 10\%$) the pressure drop data from both microchannels.

Acknowledgments

The authors express gratitude to the Natural Sciences and Engineering Research Council of Canada (a Research Grant and an Equipment Grant), the Government of Ontario (a graduate student scholarship for P.M.-Y. Chung) and the Japanese Ministry of Education, Culture, Sports, Science and Technology (a fellowship for A. Kawahara and Y. Shibata).

Nomenclature Symbols

$B_0 = (\rho_L - \rho_G)g(D/2)^2/\sigma$	= Bond number
C	= coefficient in Eq. (4)
C_1	= first coefficient in Eq. (3)
C_2	= second coefficient in Eq. (3)
$Ca = \mu_L u_B/\sigma$	= capillary number
D	= inner diameter [m]
g	= gravitational acceleration [m/s ²]
j	= superficial velocity [m/s]
L	= length [m]
P	= pressure [Pa]
$Re_{LS} = j_L D/\nu_L$	= superficial Reynolds number for liquid
$Re_{GS} = j_G D/\nu_G$	= superficial Reynolds number for gas
u	= axial velocity [m/s]
$We_{LS} = j_L^2 D \rho_L/\sigma$	= superficial Weber number for liquid
$We_{GS} = j_G^2 D \rho_G/\sigma$	= superficial Weber number for gas
X	= Lockhart-Martinelli parameter

Greek

- β = volumetric quality
 Δ = finite difference between two conditions
 ε = void fraction
 μ = dynamic viscosity [Pa·s]
 ν = kinematic viscosity [m²/s]
 ρ = mass density [kg/m³]
 σ = surface tension [N/m]
 ϕ_L = two-phase friction multiplier

Subscripts

- acceleration* = acceleration loss
AVG = average value
B = bubble
channel = in channel
contraction = loss in contraction
entrance = loss due to flow development at entrance
f = loss due to friction
friction = frictional loss
G = gas phase
h = based on hydraulic diameter
inlet = loss due to entrance configuration
L = liquid phase
measured = measured loss
S = superficial
tee = in tee

References

- [1] Peng, X. F., and Wang, B.-X., 1993, "Forced convection and flow boiling heat transfer for liquid flowing through microchannels," *Int. J. Heat Mass Transfer*, **36**(14), pp. 3421–3427.
- [2] Stanley, R. S., Barron, R. F., and Ameen, T. A., 1997, DSC-Vol. 62/HTD-Vol. 354, *Microelectromechanical Systems (MEMS) ASME*, pp. 143–152.
- [3] Kandlikar, S. G., 2002, "Fundamental issues to flow boiling in minichannels and microchannels," *Exp. Therm. Fluid Sci.*, **26**(2–4), pp. 389–407.
- [4] Bi, Q. C., and Zhao, T. S., 2001, "Taylor bubbles in miniaturized circular and noncircular channels," *Int. J. Multiphase Flow*, **27**(3), pp. 561–570.
- [5] Carey, V. P., 1992, *Liquid-vapor phase-change phenomena*. Hemisphere, New York.
- [6] Zhao, T. S., and Bi, Q. C., 2001, "Pressure drop characteristics of gas-liquid two-phase flow in vertical miniature triangular channels," *Int. J. Heat Mass Transfer*, **44**(13), pp.2523–2534.
- [7] Kolb, W. B., and Cerro, R. L., 1991, "Coating the inside of a capillary of square cross section," *Chem. Eng. Sci.*, **46**(9), pp. 2181–2195.
- [8] Cox, B. G., 1964, "An experimental investigation of the streamlines in viscous fluid expelled from a tube," *J. Fluid Mech.*, **20**(2), pp.193–200.
- [9] Kolb, W. B., and Cerro, R. L., 1993, "Film flow in the space between a circular bubble and a square tube," *J. Colloid Interface Sci.*, **159**(2), pp. 302–311.
- [10] Kawahara, A., Chung, P. M.-Y., and Kawaji, M., 2002, "Investigation of two-phase flow pattern, void fraction and pressure drop in a microchannel," *Int. J. Multiphase Flow*, **28**(9), pp. 1411–1435.
- [11] Serizawa, A., Feng, Z., and Kawara, Z., 2002, "Two-phase flow in microchannels," *Exp. Therm. Fluid Sci.*, **26**(6–7), pp. 703–714.
- [12] Chung, P. M.-Y., Kawaji, M., and Kawahara, A., 2002, Characteristics of single-phase flow in microchannels. Proceedings of 2002 Joint US ASME-European FEDSM, July 14–18, Montreal, Quebec, Canada, pp. 1–10.
- [13] Triplett, K. A., Ghiaasiaan, S. M., Abdel-Khalik, S. I., and Sadowski, D. L., 1999a, "Gas-liquid two-phase flow in microchannels Part I: Two-phase flow pattern," *Int. J. Multiphase Flow*, **25**(3), pp. 377–394.
- [14] Coleman, J. W., and Garimella, S., 2000, Two-phase flow regime transitions in microchannel tubes: the effect of hydraulic diameter. Proceedings of the ASME Heat Transfer Division, HTD-Vol. 366-4, pp. 71–83.
- [15] Joseph, D. D., Bai, R., Chen, K. P., and Renardy, Y. Y., 1997, "Core-Annular Flows," *Annu. Rev. Fluid Mech.*, **29**, pp.65–90.
- [16] Ali, M. I., Sadatomi, M., and Kawaji, M., 1993, "Two-phase flow in narrow channels between two flat plates," *Can. J. Chem. Eng.*, **71**(5), pp. 657–666.
- [17] Armand, A. A., 1946, The resistance during the movement of a two-phase system in horizontal pipes. *Izv. Vses. Teplotekh. Inst.*, 1, 16–23 (AERE-Lib/Trans 828).
- [18] Ungar, E. K., and Cornwell, J. D., 1992, Two-phase pressure drop of ammonia in small diameter horizontal tubes. AIAA 17th Aerospace Ground Testing Conf., Nashville, TN, July 6–8.
- [19] Triplett, K. A., Ghiaasiaan, S. M., Abdel-Khalik, S. I., LeMouel, A., and McCord, B. N., 1999, "Gas-liquid two-phase flow in microchannels-Part II: Void fraction and pressure drop," *Int. J. Multiphase Flow*, **25**(3), pp. 395–410.
- [20] Lockhart, R. W., and Martinelli, R. C., 1949, "Proposed correlation of data for isothermal two-phase, two-component flow in pipes," *Chem. Eng. Prog.*, **45**(1), pp. 39–48.
- [21] Chisholm, D., 1967, "A theoretical basis for the Lockhart-Martinelli correlation for two-phase flow. *Int. J. Heat Mass Transfer*, **10**(12), pp. 1767–1778.
- [22] Mishima, K., and Hibiki, T., 1996, "Some characteristics of air-water two-phase flow in small diameter vertical tubes," *Int. J. Heat Mass Transfer*, **22**(4), pp. 703–712.
- [23] Lee, H. J., and Lee, S. Y., 2001, "Pressure drop correlations for two-phase flow within horizontal rectangular channels with small height," *Int. J. Multiphase Flow*, **27**(5), pp. 783–796.

C. Oropeza-Vazquez

E. Afanador

L. Gomez

S. Wang

R. Mohan

O. Shoham

The University of Tulsa,
600 S. College Ave.,
Tulsa, OK 74104

G. Kouba

Senior Staff Research Scientist,
ChevronTexaco Energy Technology Company,
2811 Hayes Road,
Houston, TX 77082

Oil-Water Separation in a Novel Liquid-Liquid Cylindrical Cyclone (LLCC[©]) Compact Separator—Experiments and Modeling

The hydrodynamics of multiphase flow in a Liquid-Liquid Cylindrical Cyclone (LLCC) compact separator have been studied experimentally and theoretically for evaluation of its performance as a free water knockout device. In the LLCC, no complete oil-water separation occurs. Rather, it performs as a free-water knockout, delivering a clean water stream in the underflow and an oil rich stream in the overflow. A total of 260 runs have been conducted, measuring the LLCC separation efficiency for water-dominated flow conditions. For all runs, an optimal split-ratio (underflow to inlet flow rate ratio) exists, where the flow rate in the water stream is maximum, with 100% watercut. The value of the optimal split-ratio depends upon the existing inlet flow pattern, and varies between 60% and 20%. For split-ratios higher than the optimal one, the watercut in the underflow stream decreases as the split-ratio increases. A novel mechanistic model has been developed for the prediction of the complex flow behavior and the separation efficiency in the LLCC. Comparisons between the experimental data and the LLCC model predictions show excellent agreement. The model is capable of predicting both the trend of the experimental data as well as the absolute measured values. The developed model can be utilized for the design and performance analysis of the LLCC. [DOI: 10.1115/1.1777233]

1 Introduction

Oil-water-gas separation technology in the petroleum industry has been based in the past on conventional vessel-type separators. These separators are bulky, heavy and expensive. With the new trend in the petroleum industry toward hydrocarbons production from offshore fields and economic challenges to reduce production costs, the petroleum industry has recently shown keen interest in compact separators that are low weight, low cost and efficient.

One alternative for gas-liquid separation, which is economically attractive, is the Gas Liquid Cylindrical Cyclone (GLCC^{©1}). The GLCC is a simple, compact and low-cost separator. It is a vertical pipe section, with a downward inclined, tangential inlet located approximately at the middle. The separation in the GLCC is achieved by centrifugal and gravity effects. Mechanistic models for design and performance prediction of the GLCC are now available. The GLCC has recently gained popularity in the industry, with more than 700 units installed in the field around the world.

The Liquid-Liquid Cylindrical Cyclone (LLCC^{©2}) is a piece of vertical pipe with a horizontal inlet. The LLCC horizontal inlet promotes oil-water segregation and the liquid phases enter the vertical separator section through a reducing area nozzle, increasing their velocity. The swirling motion in the LLCC produces a centrifugal separation, whereby, an oil-rich stream exits through the top (overflow) and a water-rich stream leaves the system through the bottom (underflow).

Figure 1 shows a schematic of the GLCC and LLCC configured as a two-stage 3-phase compact separator. In this configuration, the three-phase gas-oil-water mixture enters through the inclined

tangential inlet of the GLCC. The gas flows to the top and exits out of the system. The liquid, an oil-water mixture, flows through the GLCC liquid leg into the LLCC, where the separation of oil and water occurs.

2 Literature Review

Most of the studies on liquid-liquid cyclonic separation have been focused on conical liquid hydrocyclones (LLHC). The Liquid-Liquid-Cylindrical Cyclone (LLCC) is a new technology for oil-water flow separation. Thus, very few studies have been published on the LLCC separator. Listewnik [1] reported oil-water separation efficiency in a cylindrical hydrocyclone with four inlets. Gay et al. [2] presented a comparison between a static conical hydrocyclone and a rotary cylindrical cyclone. Bednarski and Listewnik [3] analyzed the effect of the inlet diameter on the separation efficiency of a hydrocyclone. They concluded that small inlets cause droplet break-up and big inlets do not produce enough swirl intensity. Seyda [4] simulated the separation of oil-water dispersions in a small cylindrical tube.

A pioneering study on oil-water separation in the LLCC was presented by Afanador [5], who acquired the original set of data. Follow up and expansion studies were presented by Mathiravedu [6] and Oropeza-Vazquez [7]. The present paper is based on these three studies. Pertinent studies on related topics, namely, swirling flow, oil-water flow patterns and oil droplet size distribution can be found in Oropeza-Vazquez [7].

The above literature review reveals a lack of systematic data and mechanistic models for the LLCC. This is the scope and contribution of the present study.

3 Experimental Program

The experimental program was conducted utilizing a 2-inch ID, fully instrumented oil-water-air three-phase flow loop, where the LLCC test section, described below, was installed.

LLCC Test Section: A schematic and a photo of the LLCC test section are given in Figs. 2 and 3, respectively. The LLCC is a 6.4-foot, 2-inch ID vertical pipe, with 5-foot-long, 2-inch ID hori-

Contributed by the Fluids Engineering Division for publication in the JOURNAL OF FLUIDS ENGINEERING. Manuscript received by the Fluids Engineering Division May 27, 2003; revised manuscript received January 13, 2004. Associate Editor: M. J. Andrews.

¹GLCC©-Gas-Liquid Cylindrical Cyclone-Copyright, The University of Tulsa, 1994.

²LLCC©-Liquid-Liquid Cylindrical Cyclone-Copyright, The University of Tulsa, 1998.

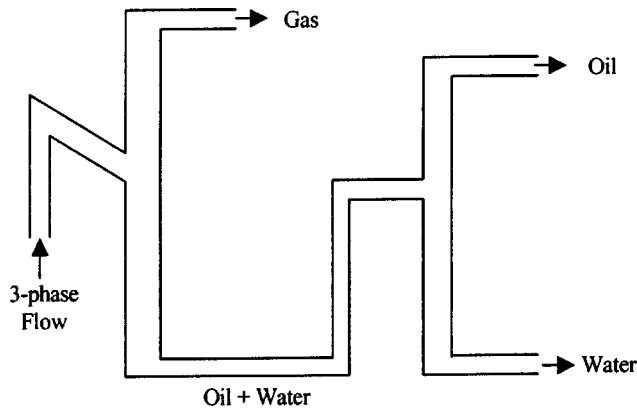


Fig. 1 Schematic of GLCC and LLCC Separation System

zontal inlet. The inlet is attached to the LLCC 3.3 feet below its top. A nozzle is located at the LLCC inlet, causing the flow to enter the LLCC tangentially (see Fig. 2). The inlet slot area is 25% of the inlet full bore cross sectional area. A 1.5-inch ID concentric pipe located at the top is used as the oil outlet (overflow), and the water outlet (underflow) is a radial, 1.5-inch ID pipe located at the bottom. A temperature sensor is located at the inlet and a pressure sensor is located on each outlet. Valves in both the oil outlet and the water outlet allow the control of the flow rates leaving the separator, namely, the split-ratio. The split-ratio is defined as the ratio between the underflow liquid flow rate and the inlet liquid flow rate, as given by

$$SR = \frac{q_{under}}{q_{in}} \quad (1)$$

Experimental Results. Experiments on the LLCC have been conducted by Mathiravedu [6] in order to develop control strategies to maximize the free-water knockout. Only the 260 water-dominated experimental runs ($v_{SW} > v_{SO}$) are analyzed in this study. Several combinations of oil and water superficial velocities are used, varying the split-ratio for every combination of oil and water superficial velocities.

Inlet Flow Patterns. During the experiments, four flow patterns were observed in the horizontal inlet, as shown in Fig. 4.

- At low superficial velocities ($v_{SW} < 0.2$, $v_{SO} < 0.1$ m/s), the oil enters the inlet through the upstream vertical pipe section in the form of large droplets. These oil droplets immediately move to

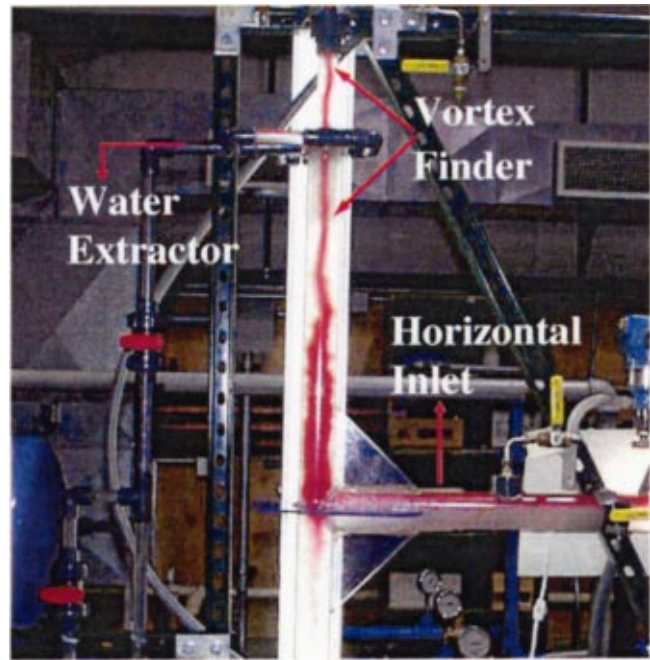
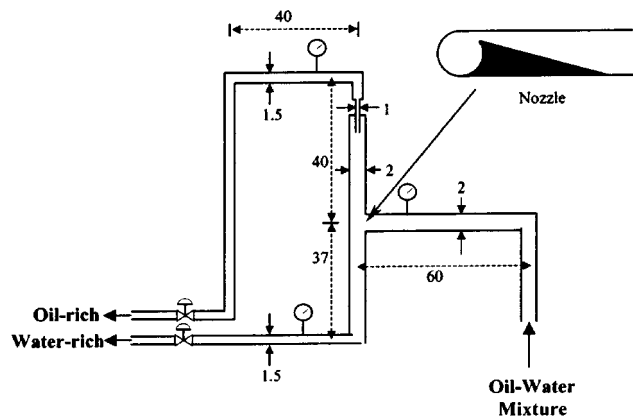


Fig. 3 Photograph of LLCC Test Section

the top of the pipe forming a continuous oil layer. The water remains at the bottom. This flow pattern is called "Stratified" (ST) (Fig. 4a).

- When the superficial water velocity increases ($0.2 < v_{SW} < 0.8$ m/s) and the oil content is low ($v_{SO} < 0.2$ m/s), the droplets entering the inlet are smaller. They still are able to move to the top of the pipe, but they do not form a continuous oil-phase. Thus, an oil in water dispersion flows at the top of the pipe and a free-water layer flows at the bottom. This configuration is called "Oil-in-Water Dispersion and Water Layer" (DO/W&W) (Fig. 4b).

- At intermediate superficial water velocities ($0.2 < v_{SW} < 0.8$ m/s), but increasing the oil content ($v_{SO} > 0.2$ m/s), the bigger oil droplets move to the top and the small ones remain at the bottom, and no free-water layer is observed. However, the oil concentration is increasing from the bottom to the top of the pipe. Dividing the pipe by a horizontal plane parallel to the pipe axis, it



*Units in inches
*Not to scale

Fig. 2 Schematic of LLCC Test Section

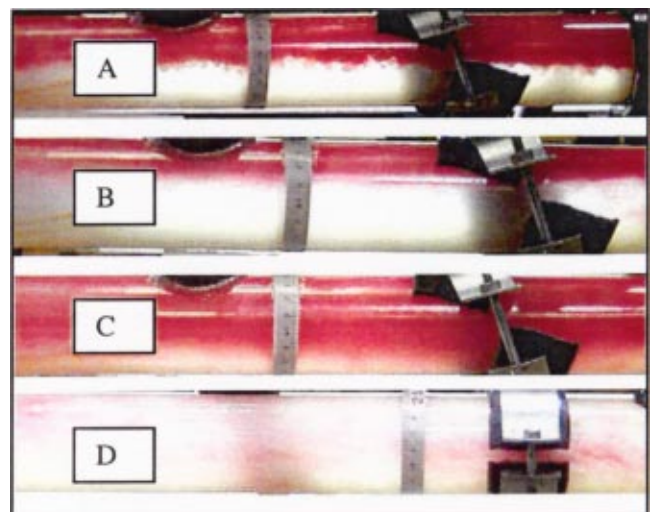


Fig. 4 Horizontal Inlet Flow Patterns

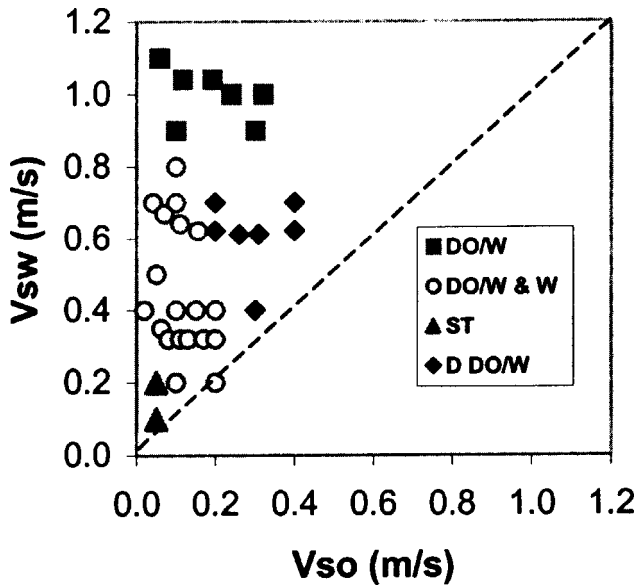


Fig. 5 Experimental Flow Pattern Map for LLCC Inlet

can be considered that two dispersions with different oil content flow in the inlet. This flow pattern is called “double oil in water dispersion” (Double DO/W) (Fig. 4c).

- At higher superficial water velocities ($v_{sw} > 0.8$ m/s), the oil droplets are small and they are evenly distributed in the entire cross-sectional area of the pipe. This flow pattern is called “Oil-in-Water Dispersion” (DO/W), as seen in Fig. 4d.

Figure 5 shows the inlet flow pattern map obtained during the experimental data acquisition. The superficial oil velocity is plotted in the horizontal axis and the superficial water velocity is plotted in the vertical axis. The broken line divides the water-dominated region and the oil-dominated region. As can be observed, all the experimental data points are located in the water-dominated region.

Separation Efficiency. Figure 6 shows the effect of the split-ratio on the purity of the underflow by a sequence of photographs of the lower section of the LLCC (water leg) for Stratified flow pattern at the inlet. The superficial water and oil velocities at the inlet are 0.1 m/s and is 0.05 m/s yielding watercut (or water fraction) of 67%. Under these conditions, the water level in the inlet pipe is 50% of the inlet diameter. For a split-ratio of 50%, only clean water is observed in the water leg. When the split-ratio is increased to 55%, oil droplets are entering the water leg, but they

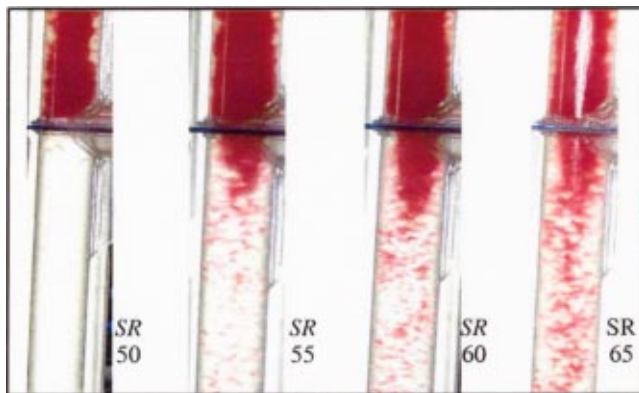


Fig. 6 LLCC Separation Behavior as a Function of the Split-Ratio ($v_{sw}=0.1$ m/s, $v_{so}=0.05$ m/s)

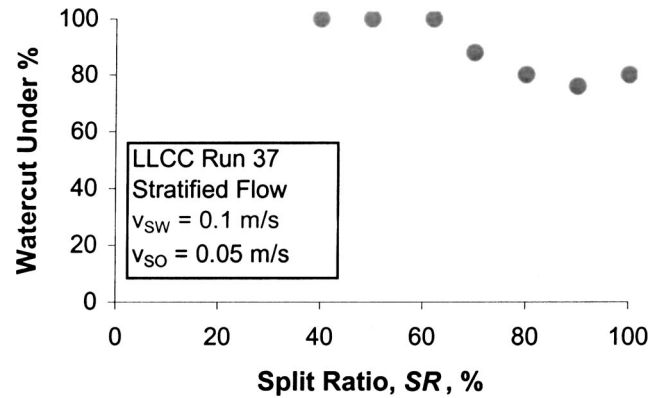


Fig. 7 Experimental Results for Stratified Flow

are separated and go up to the oil leg. At 60%, more oil is entrained, but still only clean water is leaving the water leg. At a split-ratio of 65% the entrained oil in the water leg increases even more and some quantity of oil leaves with the underflow.

The experimental results for this case of Stratified Flow are shown in Fig. 7. The watercut in the underflow outlet is plotted as a function of the split-ratio. As can be observed, for split-ratios lower than 62%, clean water is obtained in the underflow. Increasing the split-ratio beyond 62% the oil-phase starts flowing into the underflow along with the water. It can be observed that as the split-ratio increases, the watercut in the underflow decreases, and at about a split-ratio of 80% the watercut in the underflow reaches the same value as the inlet watercut. At this point, no separation is occurring. Increasing the split-ratio, beyond 80%, the underflow watercut continues decreasing, so for these split-ratios the underflow watercut is smaller than the inlet watercut. Finally, at the split-ratio of 100%, all the liquid is flowing down so the watercut in the underflow is the same as the inlet watercut. Similar behavior is observed for the Oil-in-Water dispersion and Water Layer flow pattern.

The separation behavior in the LLCC for the Double Oil-in-Water Dispersion flow pattern is shown in Fig. 8. For this case, the optimal split-ratio for 100% watercut decreases to 18%. In all the experiments for this flow pattern, the optimal split-ratio is low, decreasing as the inlet oil content increases. For the Oil-in-Water Dispersion flow pattern, the optimal split-ratio is affected strongly by the oil content and the velocity of the mixture. For low oil content, optimal split-ratios around 50% are observed, but values of optimal split-ratio around 20% occur for high oil content.

In summary, from the experimental investigations, it can be concluded that better separation efficiency is achieved for the Stratified and the DO/W & W inlet flow patterns. The Double

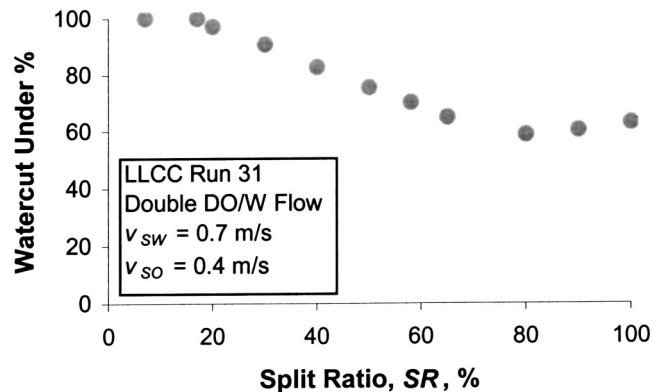


Fig. 8 Experimental Results for Double DO/W Flow

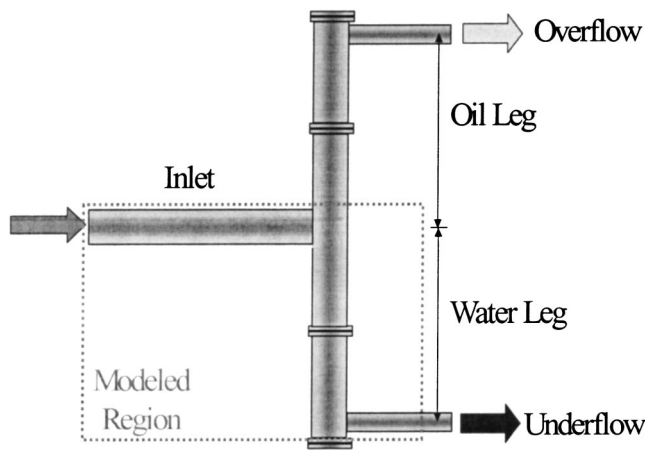


Fig. 9 Schematic of LLCC Mechanistic Model

Dispersion cases show good efficiency near the transition to DO/W & W, but the efficiency decreases as the oil content increases. The Oil-in-Water Dispersion flow pattern is efficient at very low oil contents (less than 10%), and this efficiency decreases, as the oil content in the inlet is higher. This last flow pattern is limited by the emulsification phenomenon.

Watercut Measurement Uncertainty. The watercut was measured in this study utilizing the Starcut[®] watercut meter, which is based on microwave technology. The multiple measurement relative uncertainty for this study was determined using conventional uncertainty analysis techniques, which resulted in an uncertainty of $\pm 2.85\%$. Detailed results are omitted in this paper for brevity; however, Contreras [8] may be referred for further details.

4 Mechanistic Modeling

The LLCC consists of a vertical pipe section (the separator) and a horizontal pipe section (the inlet), as shown in Fig. 9. Both pipes are attached through a reducing area nozzle. The vertical pipe is divided by the nozzle into two sections. The upper section is called the “oil leg” as it delivers oil-rich stream into the oil outlet or overflow. The lower section is called the “water leg” and it delivers water stream into the water outlet or underflow. Valves in the oil and water outlets are used to control the flow rates leaving the LLCC, namely, the split-ratio.

To date, no simple and general definition of the liquid-liquid separation efficiency has been developed. In this study, the separation efficiency is described by means of the split-ratio and the watercut in the water leg. These two parameters give information about how much liquid exits through the water outlet, and the purity of this liquid stream.

Two approaches could be taken for the present study, namely, CFD simulations or mechanistic modeling. Mechanistic modeling was chosen as it enables incorporation of the physical phenomena, compared with the extensive implementation work that would be associated with numerical CFD codes. Also, mechanistic models can be converted into design codes to be used by the industry, as has been done for the GLCC. The mechanistic model presented here is adequate, being capable of predicting the physical phenomena associated with the LLCC.

The LLCC model consists of sub-models for the different components of the separator, namely, the horizontal inlet pipe, the reducing area nozzle (inlet analysis), and the water leg (separation analysis). Note that by analyzing only the water leg, the system behavior is well defined, as the flow into the oil leg is the difference between the flows of the inlet and the water leg. These sub-models are given in the following sections.

Table 1 Modified Coefficients for LLCC Inlet Flow Pattern Prediction

Droplet Diameter	Friction factor	C	n
$d_{od,max}$	f_m	0.33	-3.5
$d_{od,max}$	f_w	0.9	2
$d_{od,min}$	f_w	0.174	-7
$d_{wd,max}$	f_m	37.39	1.832
$d_{wd,max}$	f_o	0.043	0

Inlet Analysis. The inlet consists of the horizontal pipe and the nozzle. Different flow patterns may occur in the inlet, depending upon the oil and water flow rates combination, pipe diameter and fluid properties. The determination of the existing flow pattern for a given set of flow conditions is essential for the analysis, since all the design parameters of the flow depend on the existing flow pattern. These include the spatial distribution of the phases and their corresponding velocities. Models to predict the flow pattern in the inlet pipe, individual models for each of the flow patterns and the nozzle analysis are presented next.

Inlet Flow Pattern Prediction. The starting point for the LLCC modeling is the prediction of the occurring flow pattern in the horizontal inlet. Trallero [9] developed a mechanistic model for liquid-liquid flow pattern prediction, applicable for fully developed flow in horizontal and near horizontal pipes. This model is modified in the present study for the inlet section analysis, to account for the fact that the flow at the inlet section is not fully developed. The modifications are carried out by adjusting the coefficients for the droplet diameter and friction factor, as shown in Table 1.

In order to use the modified model to predict the four flow patterns observed in the LLCC inlet, the Stratified with Mixing flow pattern (defined originally by Trallero [9]) is considered as Oil-in-Water Dispersion–Water Layer, and the Oil-in-Water and Water-in-Oil Dual Dispersion flow pattern is considered as the Oil-in-Water Double Dispersion flow pattern. Figure 10 shows the LLCC experimental data and the boundaries predicted by the modified model. As can be observed, the predicted flow pattern boundaries agree very well with the experimental data.

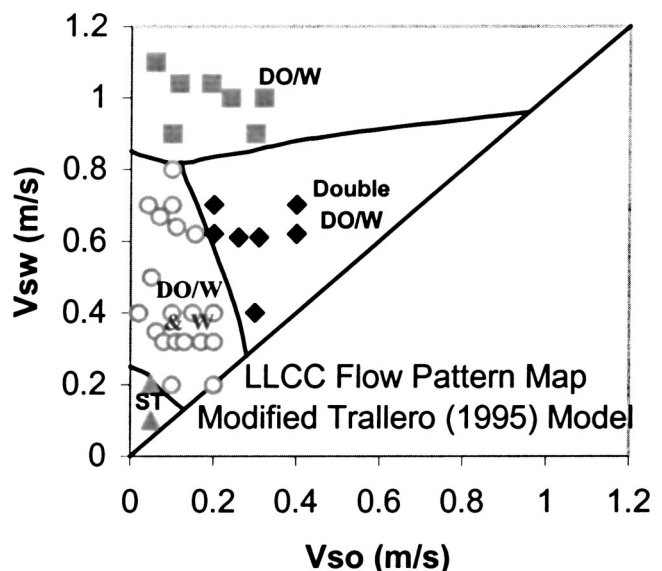


Fig. 10 Comparison between Modified Trallero (1995) Model and Experimental Data

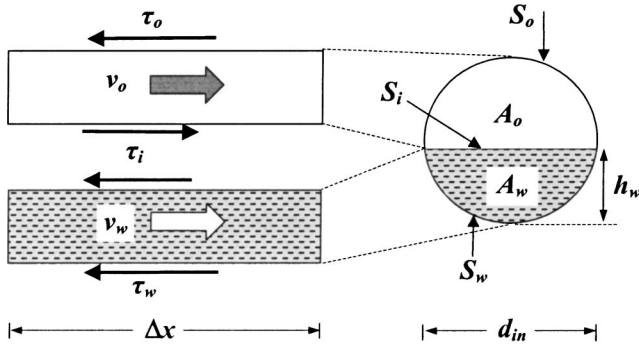


Fig. 11 Stratified Flow Model Geometry and Variables

Stratified Flow Model. For low liquid velocities, stratified flow pattern is observed in the inlet. The water flows at the lower section of the pipe, and a layer of oil travels at the top. A suitable model for this flow configuration is the two-fluid model. Figure 11 shows the geometry and the variables of the stratified flow pattern.

A momentum balance can be written for each of the phases. Eliminating the pressure gradient from both equations, the combined momentum equation can be obtained, as follows:

$$\frac{\tau_o S_o}{A_o} - \frac{\tau_w S_w}{A_w} - \tau_i S_i \left(\frac{1}{A_o} + \frac{1}{A_w} \right) = 0. \quad (2)$$

The shear stresses are calculated as:

$$\tau_o = \frac{f_o \rho_o v_o^2}{2}, \quad \tau_w = \frac{f_w \rho_w v_w^2}{2} \quad (3)$$

$$\tau_i = \frac{f_i \rho_i (v_w - v_o) |v_w - v_o|}{2}. \quad (4)$$

If $v_w > v_o$, $f_i = f_w$ and $\rho_i = \rho_w$; for $v_o > v_w$, $f_i = f_o$ and $\rho_i = \rho_o$. The friction factors are calculated as:

$$f_o = C_o \left[\frac{d_o v_o \rho_o}{\mu_o} \right]^{-n_o}, \quad f_w = C_w \left[\frac{d_w v_w \rho_w}{\mu_w} \right]^{-n_w}. \quad (5)$$

For laminar flow $C_w = C_o = 16$ and $n_w = n_o = 1$. For turbulent flow $C_w = C_o = 0.046$ and $n_w = n_o = 0.2$.

The hydraulic diameters depend on the relative velocity between the phases, as follows:

For $v_o > v_w$

$$d_o = \frac{4A_o}{S_o + S_i}; \quad d_w = \frac{4A_w}{S_w}. \quad (6)$$

For $v_o < v_w$

$$d_o = \frac{4A_o}{S_o}; \quad d_w = \frac{4A_w}{S_w + S_i}. \quad (7)$$

For $v_o = v_w$

$$d_o = \frac{4A_o}{S_o}; \quad d_w = \frac{4A_w}{S_w}. \quad (8)$$

The geometrical variables are functions of h_w , as follows:

$$S_w = d_{in} \left[\pi - \cos^{-1} \left(\frac{2h_w}{d_{in}} - 1 \right) \right], \quad (9)$$

$$S_o = d_{in} \cos^{-1} \left(\frac{2h_w}{d_{in}} - 1 \right), \quad (10)$$

$$S_i = d_{in} \sqrt{1 - \left(\frac{2h_w}{d_{in}} - 1 \right)^2}, \quad (11)$$

$$A_w = \frac{d_{in}^2}{4} \left[\pi - \cos^{-1} \left(\frac{2h_w}{d_{in}} - 1 \right) + \left(\frac{2h_w}{d_{in}} - 1 \right) \sqrt{1 - \left(\frac{2h_w}{d_{in}} - 1 \right)^2} \right], \quad (12)$$

$$A_o = \frac{d_{in}^2}{4} \left[\cos^{-1} \left(\frac{2h_w}{d_{in}} - 1 \right) - \left(\frac{2h_w}{d_{in}} - 1 \right) \sqrt{1 - \left(\frac{2h_w}{d_{in}} - 1 \right)^2} \right]. \quad (13)$$

The actual velocities are calculated as:

$$v_w = \frac{A}{A_w} v_{sw}, \quad v_o = \frac{A}{A_o} v_{so}. \quad (14)$$

The combined momentum equation, Eq. (2), is an implicit function of the water layer height, h_w . The combined momentum equation and the auxiliary relationships, Eqs. (3)–(14), can be solved to determine the water layer height h_w and the actual phase velocities v_o and v_w , for a given set of flow conditions.

Oil droplet-size distribution: The oil droplet size distribution is correlated with the horizontal pipe inlet flow conditions. The same model developed for Oil-in-Water Dispersion–Water Layer flow (to be presented in next section) is used, but by considering the velocity, properties and geometry of the oil layer, instead of the dispersion layer.

Oil-in-Water Dispersion and Water Layer Model. For this flow pattern, an oil-in-water dispersion-layer flows at the top of the pipe with a layer of free water flowing at the bottom. Considering the free-water-layer as a phase and the dispersion-layer as a second-phase, this flow pattern can be analyzed as the case of stratified flow, applying the two-fluid model. The combined momentum equation for this case becomes:

$$\frac{\tau_d S_d}{A_d} - \frac{\tau_w S_w}{A_w} - \tau_i S_i \left(\frac{1}{A_d} + \frac{1}{A_w} \right) = 0. \quad (15)$$

The dispersion-layer properties can be calculated by assuming no-slip condition between the oil droplets and the water in the dispersed-phase (which is a sound assumption for horizontal flow), as follows:

$$\rho_d = \rho_w \lambda_{w,d} + \rho_o (1 - \lambda_{w,d}), \quad (16)$$

$$\mu_d = \mu_w \lambda_{w,d} + \mu_o (1 - \lambda_{w,d}), \quad (17)$$

where $\lambda_{w,d}$ is the local no-slip watercut in the dispersion. A correlation for $\lambda_{w,d}$ is used, developed by Oropeza-Vazquez [7], as follows:

$$\lambda_{w,d} = 1 - \left[\frac{A_{in} v_{SO}}{A_w (v_{SW} + v_{SO})} \right]^{h_w/2}. \quad (18)$$

Equation (18) is a function of the water and oil superficial velocities, which are known, and the height of the water layer. Thus, simultaneous solution of the equation for $\lambda_{w,d}$ and the combined momentum equation, yields the water layer height h_w and the actual velocities of the dispersion layer, v_d , and the water layer, v_w .

Oil droplet-size distribution: The determination of the maximum and minimum oil droplet diameters in the dispersion-layer is performed by using modified Hinze [10] and Levich [11] models, respectively, as follows:

$$d_{od,max} = \left[\frac{\lambda_{w,in}^{0.5}}{1.9} \right] 0.725 \left(\frac{\sigma_{o,w}}{\rho_d} \right)^{0.6} \left(\frac{2f_d v_d^3}{d_d} \right)^{-0.4} \quad (19)$$

$$d_{od,min} = \left[\frac{\lambda_{w,in}^{0.5}}{2.5} \right] 2 \left(\frac{\sigma_{o,w} \mu_d}{25 \rho_d^2 v_d^3 (0.5f_d)^{1.5}} \right)^{1/2}, \quad (20)$$

where $\lambda_{w,in}$ is the no-slip holdup of the water in the inlet flow, and d_d , the hydraulic diameter of the dispersion-layer, is calculated as given in Eqs. (6) to (8).

Oil-in-Water Dispersion Model. For high liquid velocities, the oil droplets entering the inlet pipe cannot coalesce and they move along with the water-phase and no water layer is observed. For this flow pattern, the homogeneous no-slip model is applicable. The oil and water velocities are the same, namely, $v_w = v_o = v_m = v_{SW} + v_{SO}$, and the dispersion properties are averaged based on $\lambda_{w,in}$, the inlet no-slip watercut.

Oil droplet-size distribution: Determination of the maximum and minimum oil droplet diameters for this flow pattern is also performed by using modified Hinze [10] and Levich [11] models, respectively, and considering the mixture velocity and properties, as follows:

$$d_{od,max} = \left[\frac{1}{2.14} \right] 0.725 \left(\frac{\sigma_{o,w}}{\rho_m} \right)^{0.6} \left(\frac{2f_m v_m^3}{d_{in}} \right)^{-0.4} \quad (21)$$

$$d_{od,min} = \left[\frac{1}{1.43} \right] 2 \left(\frac{\sigma_{o,w} \mu_m}{25 \rho_m^2 v_m^3 (0.5f_m)^{1.5}} \right)^{1/2} \quad (22)$$

Double Oil-in-Water Dispersion Model. At intermediate liquid velocities and high oil contents, the bigger oil droplets are able to move to the top while the smaller ones remain at the bottom. Under these conditions, the local watercut increases gradually from the top to the bottom of the pipe. It is assumed that this flow can be divided into two layers of dispersions with different oil concentrations. The division plane is located at the middle of the pipe and the velocities of both layers are considered the same, equal to the mixture velocity.

The water fraction in the upper and lower dispersions is calculated, respectively, as:

$$\lambda_{w,u} = 1 - 2a \left(\frac{v_{SO}}{v_{SO} + v_{SW}} \right), \quad (23)$$

$$\lambda_{w,l} = 1 - 2(1-a) \left(\frac{v_{SO}}{v_{SO} + v_{SW}} \right), \quad (24)$$

where the parameter a , varying in the range $[0, 1]$, is the fraction of oil in the upper dispersion and is correlated with the mixture velocity as follows:

$$a = 1 - 0.4 v_m \quad (25)$$

The maximum and minimum oil droplet diameters are calculated in the same way as in the Oil-in-Water Dispersion model, i.e., by using the mixture velocity and the mixture properties, averaged with $\lambda_{w,in}$, the inlet no-slip watercut.

Nozzle Analysis. The inlet pipe delivers the liquid into the LLCC vertical section through a reducing area tangential nozzle. The effect of the nozzle is to increase the velocity of the flow, and to create the swirling flow in the LLCC.

In the Oil-in-Water Dispersion and the Oil-in-Water Double Dispersion flow patterns no water-layer exists, so the dispersion velocity at the inlet slot is:

$$v_{is} = \frac{(v_{SW} + v_{SO}) A_{in}}{A_{is}} \quad (26)$$

Next, the nozzle analysis for the Stratified flow pattern is presented. The same model is applied to the Oil-in-Water Dispersion–Water Layer case, but the oil-phase is replaced with the dispersion-phase.

Figure 12 shows a schematic of the nozzle geometry and the variables considered. The nozzle is formed by a vertical plate located inside the horizontal inlet. The plate forms the nozzle from the full inlet bore to the reduced inlet-slot-area tangential to the LLCC vertical pipe section. The inlet slot has the shape of a circular sector. In this analysis, however, it is considered as a rectangle, keeping the same height of a circular sector and the same area, which is 25% of the inlet cross-sectional area.

The height of the inlet slot is calculated from:

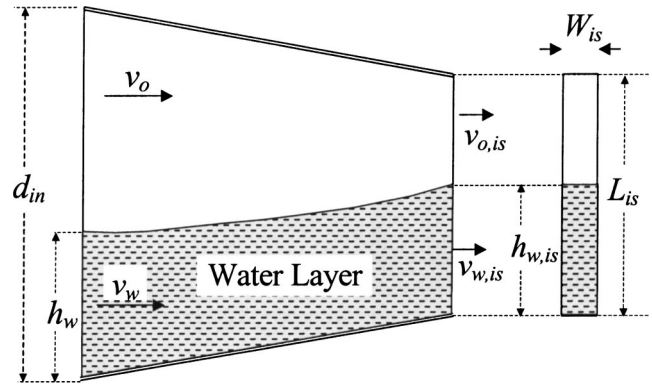


Fig. 12 Nozzle Schematic and Variables

$$L_{is} = \sqrt{1 - \left(\frac{2y}{d_{in}} - 1 \right)^2}, \quad (27)$$

where y is the solution of

$$\frac{A_{is}}{A_{in}} = \frac{1}{\pi} \left[\pi - \cos^{-1} \left(\frac{2y}{d_{in}} - 1 \right) + \left(\frac{2y}{d_{in}} - 1 \right) \sqrt{1 - \left(\frac{2y}{d_{in}} - 1 \right)^2} \right] \quad (28)$$

The inlet slot width is

$$W_{is} = \frac{A_{is}}{L_{is}} \quad (29)$$

Application of Bernoulli's equation to the top of the water layer, between the inlet pipe and the inlet slot, results in:

$$P_{in} + \frac{\rho_w v_w^2}{2} + \rho_o g (d_{in} - h_w) = P_{is} + \frac{\rho_w v_{w,is}^2}{2} + \rho_o g \left(\frac{d_{in}}{2} - \frac{L_{is}}{2} + h_{w,is} \right) \quad (30)$$

Applying Bernoulli's equation to the top of the oil layer yields

$$P_{in} + \frac{\rho_o v_o^2}{2} = P_{is} + \frac{\rho_o v_{o,is}^2}{2} + \rho_o g \left(\frac{d_{in}}{2} - \frac{L_{is}}{2} \right) \quad (31)$$

From continuity, the velocities of the oil and water phases at the inlet slot are:

$$v_{w,is} = \frac{v_{SW} A_{in}}{h_{w,is} W_{is}}, \quad v_{o,is} = \frac{v_{SO} A_{in}}{(L_{is} - h_{w,is}) W_{is}} \quad (32)$$

Eliminating the pressure drop from Eqs. (31) and (32) the following polynomial in $h_{w,is}$ is obtained:

$$C_1 h_{w,is}^5 + C_2 h_{w,is}^4 + C_3 h_{w,is}^3 + C_4 h_{w,is}^2 + C_5 h_{w,is} + C_6 = 0 \quad (33)$$

where the coefficients are:

$$C_1 = 2W_{is}^2 \rho_o g \quad (34)$$

$$C_2 = W_{is}^2 (2\rho_o g (h_w - d_{in}) + \rho_o v_o^2 - \rho_w v_w^2) - 2L_{is} C_1 \quad (35)$$

$$C_3 = L_{is}^2 C_1 - 2L_{is} W_{is}^2 (2\rho_o g (h_w - d_{in}) + \rho_o v_o^2 - \rho_w v_w^2) \quad (36)$$

$$C_4 = \rho_w (v_{SW} A_{in})^2 + L_{is}^2 W_{is}^2 (2\rho_o g (h_w - d_{in}) + \rho_o v_o^2 - \rho_w v_w^2) - \rho_o (v_{SO} A_{in})^2 \quad (37)$$

$$C_5 = -2L_{is} \rho_w (v_{SW} A_{in})^2 \quad (38)$$

$$C_6 = L_{is}^2 \rho_w (v_{SW} A_{in})^2 \quad (39)$$

Solution of Eq. (33) yields the height of the water-layer at the inlet slot location, $h_{w,is}$. Only one root is obtained in the interval

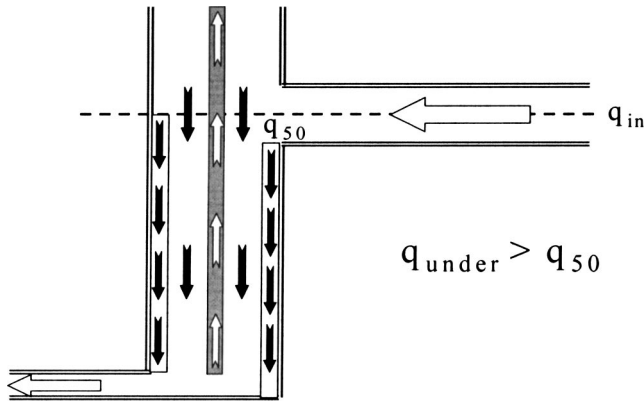


Fig. 13 Local Split at Entry Region and Fluid Transfer for $q_{under} > q_{50}$

$h_{w, is}[0, L_{is}]$. In summary, the nozzle model utilizes the velocities and flow geometry in the inlet to provide the spatial configuration and the velocities of the phases at the inlet slot, which are the input for the separation analysis in the vertical section. This is given in the next section.

Separation Analysis. The liquid coming from the nozzle enters the vertical section of the LLCC tangentially and rotates, creating a swirling flow. The oil droplet separation is achieved by the resulting centrifugal forces.

Entry Region Analysis. A local geometrical flow split is assumed at the inlet slot, as shown schematically in Fig. 13. The middle plane of the inlet (the broken line in Fig. 13) divides the incoming liquid flow locally into two streams. One stream, consisting of the fluid flowing in the inlet above the dividing middle plane, flows upwards into the oil leg, while the other stream, consisting of the fluid flowing in the inlet below the dividing middle plane, flows downward into the water leg.

The local flow rate of the incoming liquid going downward is designated “ q_{50} ” and it is calculated as:

$$q_{50} = \int_0^{A_{is}/2} v_{is} dA_{is} \quad (40)$$

It is important to note that q_{50} describes a local split at the entry region. However, the net flow going downward is dictated by the operation of the valve in the water leg outlet and/or the valve in the oil outlet. This results in re-circulation and rearrangement of the fluid. The actual liquid flow rate going downward through the water leg is determined by the split-ratio, as follows:

$$q_{under} = (v_{SW} + v_{SO}) A_{in} SR \quad (41)$$

In swirling pipe flow, a reverse flow region is generated at the center of the pipe. Thus, the general movement of the liquid in the water leg is downwards, but a core region in the center moves up and delivers additional liquid to the oil leg. The reverse flow region is indicated in Fig. 13 as a central core moving upwards.

It is important to note that the incoming liquid enters tangentially at high velocities and is spread on the pipe wall forming an annular configuration. The centrifugal effect, due to the rotation of the liquid, generates a low potential region between the incoming flow and the reverse flow region. Liquid can be transferred from one leg to the other through this low potential zone. Two cases are considered:

- The liquid flow rate produced through the water outlet is smaller than the liquid flow rate entering the water leg according to the local geometrical split, namely, $q_{under} < q_{50}$. For this case, the flow rate difference is transferred upwards to the oil leg through the low potential zone.

- On the other hand, when the liquid flow rate taken from the water outlet exceeds the flow rate entering the water leg from the inlet, namely, $q_{under} > q_{50}$, the difference is taken from the oil leg into the water leg. The last case is depicted in Fig. 13.

Due to the swirling motion of the liquid in the entry region, the oil droplets tend to concentrate at the center. Thus, the liquid transferred from the oil leg to the water leg, has a modified local watercut that is termed $\lambda_{w,e}$. Expressions for this modified oil content are presented in the next section.

Flow Field. Improved velocity field correlations for swirling flow in a vertical cylinder, presented by Erdal [12], are used in this study, as described next.

The swirl intensity dimensionless number, as a function of the vertical distance from the inlet z , is calculated as:

$$\Omega = 0.1182M^{0.93} Re^{0.13} \exp \left[-0.1355M^{0.35} Re^{-0.36} \left(\frac{z}{d_{wl}} \right)^{0.7} \right]; \quad (42)$$

for $\frac{z}{d_{wl}} \geq 2$.

The Reynolds number is evaluated in terms of the axial liquid superficial velocity v_{SZ} , the mixture properties and the LLCC diameter d_{wl} , namely,

$$Re = \frac{\rho_m v_{SZ} d_{wl}}{\mu_m} \quad (43)$$

The axial liquid superficial velocity in the water leg is a function of the split-ratio and is calculated as:

$$v_{SZ} = \frac{(v_{SO} + v_{SW}) A_{in} SR}{A_{wl}} \quad (44)$$

The momentum flux ratio at the inlet, M , is taken as the ratio of the horizontal (tangential) momentum at the inlet slot to the total axial momentum in the vertical cylinder:

$$M = \frac{M_t}{M_T} \quad (45)$$

where t indicates tangential and T indicates total.

The tangential velocity profile, as a function of the radial position and the swirl intensity, is given by:

$$v_{\theta} = \frac{(0.9\Omega - 0.05)r_{wl}v_{SZ}}{r} \left\{ 1 - \exp \left[- \left(3.6 + 20 \exp \left(- \frac{\Omega}{0.6} \right) \right) \times \left(\frac{r}{r_{wl}} \right)^2 \right] \right\} \quad (46)$$

The axial velocity profile, as a function of the radial position, can be determined from:

$$v_z = v_{SZ} \left\{ 1 + \frac{1}{C} \left[2 \left(\frac{r}{r_{wl}} \right)^3 - 3 \left(\frac{r}{r_{wl}} \right)^2 + 0.7 \right] \right\} \quad (47)$$

The parameter C is a function of r_{rev} , the radius of the reverse flow region, namely,

$$C = \left(\frac{r_{rev}}{r_{wl}} \right) \left[3 - 2 \left(\frac{r_{rev}}{r_{wl}} \right) \right] - 0.7, \quad (48)$$

where the radius of the reverse flow region is a function of the swirl intensity:

$$r_{rev} = 0.023r_{wl}\Omega^{0.33} \quad (49)$$

Inlet Momentum Flux Ratio. The inlet momentum flux ratio is required in order to predict the velocity field in the water leg (Eq.

Table 2 Inlet Momentum Flux Ratio and Initial Watercut Calculation

Oil-in-Water Dispersion—Water Layer	
$q_{under} \leq q_{50}$	No oil flows into water leg
$h_{w,is} > 0.5L_{is}$	$q_{50} = A_{is} v_{w,is} / 2$ $\lambda_{w,e} = 1 - \frac{v_{50} A_{in}}{(v_{50} + v_{sw}) A_{in} - q_{50}} - (1 - \lambda_{w,d})(1 - SR)$
$q_{under} > q_{50}$	$\rho_e = \rho_w \lambda_{w,e} + \rho_o(1 - \lambda_{w,e})$ $M = \frac{2(q_{50} \rho_w)^2 A_{wl}}{(q_{50} \rho_w + (q_{under} - q_{50}) \rho_e)^2 A_{is}}$ $\lambda_{w,ini} = 1 - \frac{(q_{under} - q_{50})(1 - \lambda_{w,e})}{q_{under}}$
$h_{w,is} > 0.5L_{is}$	$q_{50} = v_{w,is} W_{is} H_{w,is} + v_{d,is} W_{is} (0.5L_{is} - h_{w,is})$ $M = \frac{2q_{50}^2 A_{wl}}{q_{under} A_{is}}$ $\lambda_{w,ini} = 1 - \frac{v_{d,is} W_{is} (0.5L_{is} - h_{w,is})(1 - \lambda_{w,d})}{q_{50}}$
$q_{under} > q_{50}$	$q_{50} = v_{w,is} W_{is} h_{w,is} + v_{d,is} W_{is} (0.5L_{is} - h_{w,is})$ $\rho_{50} = \frac{\rho_w v_{w,is} W_{is} h_{w,is} + \rho_d v_{d,is} W_{is} (0.5L_{is} - h_{w,is})}{q_{50}}$ $\lambda_{w,e} = \lambda_{w,d} - (1 - \lambda_{w,d})(1 - SR); \rho_e = \rho_w \lambda_{w,e} + \rho_o(1 - \lambda_{w,e})$ $M = \frac{2(q_{50} \rho_{50})^2 A_{wl}}{(q_{50} \rho_{50} + (q_{under} - q_{50}) \rho_e)^2 A_{is}}$ $\lambda_{w,ini} = 1 - \frac{v_{d,is} W_{is} (0.5L_{is} - h_{w,is})(1 - \lambda_{w,d}) + (q_{under} - q_{50})(1 - \lambda_{w,e})}{q_{under}}$
Oil-in-Water Dispersion	
$q_{under} \leq q_{50}$	$q_{50} = A_{in}(v_{sw} + v_{so})/2$ $M = \frac{2q_{50}^2 A_{wl}}{q_{under} A_{is}}; \lambda_{w,ini} = \lambda_{w,in}$
$q_{under} > q_{50}$	$q_{50} A_{in}(v_{sw} + v_{so})/2$ $\lambda_{w,e} = \lambda_{w,in} - 0.52(1 - SR)\lambda_{w,in}^2$ $\rho_e = \rho_w \lambda_{w,e} + \rho_o(1 - \lambda_{w,e})$ $M = \frac{2(q_{50} \rho_m)^2 A_{wl}}{(q_{50} \rho_m + (q_{under} - q_{50}) \rho_e)^2 A_{is}}$ $\lambda_{w,ini} = 1 - \frac{q_{50}(1 - \lambda_{w,in}) + (q_{under} - q_{50})(1 - \lambda_{w,e})}{q_{under}}$
Double Oil-in-Water Dispersion	
$q_{under} \leq q_{50}$	$q_{50} = A_{in}(v_{sw} + v_{so})/2$ $M = \frac{2q_{50}^2 A_{wl}}{q_{under} A_{is}}$ $\lambda_{w,ini} = 1 - 2\alpha(1 - \lambda_{w,in})$
$q_{under} > q_{50}$	$q_{50} = A_{in}(v_{sw} + v_{so})/2; \rho_{50} = \rho_w \lambda_{w,i} + \rho_o(1 - \lambda_{w,i})$ $\lambda_{w,e} = \lambda_{w,u} - (1 - \lambda_{w,u})(1.05 - SR)\lambda_{w,in}^2$ $\rho_e = \rho_w \lambda_{w,e} + \rho_o(1 - \lambda_{w,e})$ $\rho_{under} = \frac{\rho_{50} q_{50} + (q_{under} - q_{50}) \rho_e}{q_{under}}$ $M = \frac{2(\rho_{50} q_{50})^2 A_{wl}}{(\rho_{under} q_{under})^2 A_{is}}$ $\lambda_{w,ini} = 1 - \frac{2\alpha q_{50}(1 - \lambda_{w,in}) + (q_{under} - q_{50})(1 - \lambda_{w,e})}{q_{under}}$

(42). Following Chang and Dhir [13], the inlet momentum flux ratio for the LLCC is defined as (this definition is applicable to every flow pattern):

$$M = \frac{2(q_{50} \rho_{50})^2 / A_{is}}{(q_{under} \rho_{under})^2 / A_{wl}} \quad (50)$$

The amount of oil entering the water leg depends on the spatial distribution of the fluids at the inlet slot and the split-ratio, and it defines the initial watercut in the water leg ($\lambda_{w,ini}$). This watercut has to be calculated separately for every flow pattern.

The set of equations for calculating M , $\lambda_{w,e}$ and $\lambda_{w,ini}$ for the Oil-in-Water Dispersion and Water Layer flow pattern is given in

the upper part of Table 2. The same equations are used for Stratified flow, replacing the dispersion variables with the oil variables. The second part of Table 2 includes the set of equations for calculating M , $\lambda_{w,e}$ and $\lambda_{w,ini}$ for the Oil-in-Water Dispersion and Double Oil-in-Water Dispersion flow patterns.

It is important to notice that the equations for the watercut in the entry region, $\lambda_{w,e}$, are empirical expressions based on data. On the other hand, the initial watercut in the water leg $\lambda_{w,ini}$ results from mass balances between the oil and water flow rates entering either from the inlet or from the oil leg.

Droplet Trajectory. With the determination of the tangential velocity and the axial velocity profiles, and considering no radial flow of the continuous-phase, the oil droplet trajectory for a given droplet diameter is calculated, as proposed by Mantilla et al. [14].

The relative (slip) velocity between the water-phase and the oil droplet is:

$$v_{o,slip} = \left(\frac{4(\rho_m - \rho_o)d_{od}}{3\rho_w C_D} \right)^{1/2} \left[g^2 + \left(\frac{v_\theta}{r} \right)^2 \right]^{1/4}. \quad (51)$$

The axial and radial components of the slip velocity are:

$$v_{z,o,slip} = \left(\frac{4(\rho_m - \rho_o)d_{od}}{3\rho_w C_D} \right) \frac{g}{v_{o,slip}}, \quad (52)$$

$$v_{r,o,slip} = \left(\frac{4(\rho_m - \rho_o)d_{od}}{3\rho_w C_D} \right) \frac{v_\theta^2}{r v_{o,slip}}. \quad (53)$$

The drag coefficient is calculated as:

$$C_D = 0.36 + \frac{24}{Re_{od}} + 5.48 Re_{od}^{-0.573}. \quad (54)$$

The Reynolds number in this case is defined based on the mixture properties, the relative velocity and the oil droplet diameter, as follows:

$$Re_{od} = \frac{\rho_m v_{o,slip} d_{od}}{\mu_m}. \quad (55)$$

The trajectory of the droplet is computed by the numerical integration of the following equation:

$$z = \int_{r_{wl}}^r \left(\frac{v_z - v_{z,o,slip}}{v_{r,o,slip}} \right) dr. \quad (56)$$

Droplet Size Distribution. Crowe [15] and Karabelas [16] reported the use of the Rosin-Rammler droplet-size distribution expression. The Rosin-Rammler expression provides v_{cum} , the cumulative volume fraction, as a function of the droplet diameter, d_{od} . Using the maximum oil droplet diameter as the droplet char-

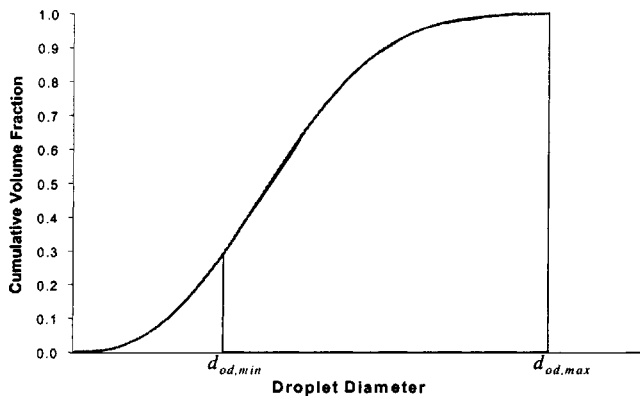


Fig. 14 Rosin-Rammler Droplet Size Distribution

acteristic diameter, considering that $v_{cum}(d_{od,max})$ is 0.999, and taking an average value for the exponent n , the Rosin-Rammler distribution becomes:

$$V_{cum} = 1 - \exp \left[-6.9077 \left(\frac{d_{od}}{d_{od,max}} \right)^{2.6} \right]. \quad (57)$$

Figure 14 shows a typical plot of the oil droplet size distribution, as predicted by Eq. (57). The oil droplet diameter is plotted versus the Rosin-Rammler cumulative oil volume fraction. The maximum droplet diameter defines the entire distribution. In this study, the minimum droplet diameter is used as a limiting value. No droplets smaller than $d_{od,min}$ are considered to exist in the flow, even though the distribution might indicate their existence.

Calculation Procedure. In the water leg, the swirling motion promotes the migration of the oil droplets to the center region of the pipe. The oil droplets that reach the reverse flow region at the center of the pipe are carried upwards, and they are separated into the oil leg. By analyzing oil-droplet trajectories in the water leg, it is possible to determine the droplets that will not be separated but rather carried under, thereby, enabling the determination of the underflow purity.

The liquid flowing in the water leg loses oil continuously, as it moves downward, because the bigger oil droplets migrate to the reverse flow region, separate, and move to the oil leg. Thus, the continuous-phase properties are modified due to the oil removal process. In order to model this phenomenon appropriately, the water leg is divided into small vertical segments, from the middle of the inlet to the middle level of the water outlet, as shown in Fig. 15, and the following procedure is carried out.

The first segment corresponds to the top of the water leg. The local watercut of the liquid entering the water leg, $\lambda_{w,ini}$, is known from the inlet analysis. Thus, the liquid mixture properties in the first segment are calculated as follows:

$$\lambda_w(1) = \lambda_{w,ini}, \quad (58)$$

$$\rho_m(1) = \rho_w \lambda_w(1) + \rho_o (1 - \lambda_w(1)) \quad (59)$$

$$\mu_m(1) = \mu_w \lambda_w(1) + \mu_o (1 - \lambda_w(1)).$$

By applying the droplet trajectory model, a trial and error scheme is used to determine the size of the oil droplet that reaches the reverse flow radius exactly at the lower end of the first segment, $d_{od,sep}(1)$, as shown in Fig. 15. Droplets bigger than this size are able to reach the reverse flow and are separated. Droplets smaller than $d_{od,sep}(1)$ will remain in the flow, going downwards, and will pass to Segment 2. The determined $d_{od,sep}(1)$ is introduced into the droplet-size distribution, Eq. (57), to obtain the volumetric fraction of oil remaining in the flow, $v_{cum}(2)$. This volumetric fraction determines the watercut for Segment 2, as:

$$\lambda_w(2) = 1 - (1 - \lambda_{w,ini}) V_{cum}(2). \quad (60)$$

The properties of the liquid in Segment 2 are calculated based on the watercut $\lambda_w(2)$, as follows:

$$\rho_m(2) = \rho_w \lambda_w(2) + \rho_o (1 - \lambda_w(2)) \quad (61)$$

$$\mu_m(2) = \mu_w \lambda_w(2) + \mu_o (1 - \lambda_w(2)).$$

Again, the droplet trajectory model is applied in order to calculate the diameter of the oil droplet that reaches the reverse flow region exactly at the end of Segment 2, $d_{od,sep}(2)$. The droplets are released at the middle of the inlet slot and they pass through Segment 1 and 2, taking into account the different properties of the continuous medium in each of these segments. Droplets bigger than the diameter calculated $d_{od,sep}(2)$ are separated from the downward liquid flow, while the smaller ones pass to Segment 3. Thus, $d_{od,sep}(2)$ is used in the Rosin-Rammler distribution to calculate the watercut and properties for Segment 3.

This procedure is repeated for all the segments until the bottom of the water leg is reached. At this point, the calculated watercut

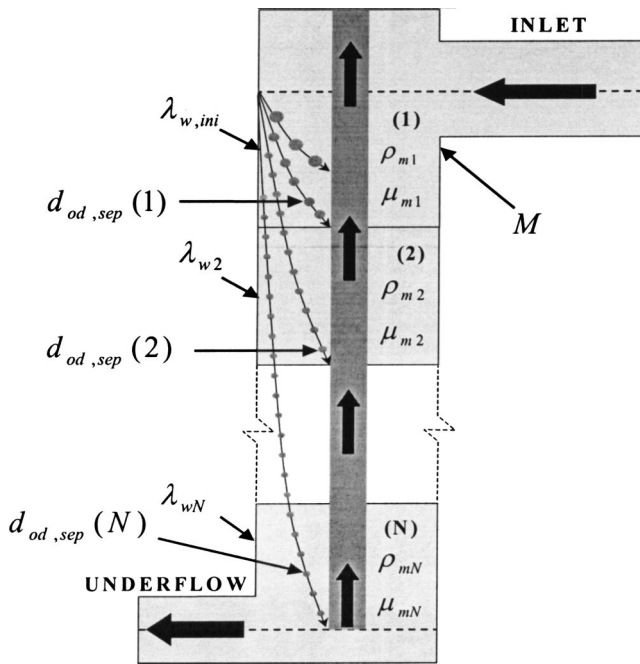


Fig. 15 Schematic of Water Leg Separation Calculation Procedure

of the liquid leaving the LLCC through the water outlet is the watercut in the underflow, determination of which is the objective of the LLCC model.

5 Results and Discussion

Comparison between the experimental data and model predictions for each flow pattern are presented.

Stratified Flow. Figure 16 shows the experimental data along with the results predicted by the LLCC model for superficial water velocities of 0.2 and 0.1 m/s and superficial oil velocity of 0.05 m/s. The points in the figure represent the experimental data and the continuous lines are the model predictions. As can be observed, the agreement between the mechanistic model predictions and the experimental data is very good both with respect to the maximum split-ratio for 100% watercut, around $SR=60\%$, and for higher split-ratios with lower watercuts.

Oil-in-Water Dispersion—Water Layer Flow. This is the most observed flow pattern in the studied operational region. A typical comparison between experimental data and model predictions is shown in Fig. 17 for a water superficial velocity of $v_{SW}=0.4$ m/s and superficial oil velocities between 0.025 and 0.2 m/s. As can be seen the agreement between the model predictions and the experimental data is very good with respect to optimal split-ratio for 100% watercut and higher split-ratios.

Double Oil-in-Water Dispersion Flow. The experimental data versus model predictions comparison for data acquired under this flow pattern is presented in Fig. 18, for superficial water velocity of about 0.6 m/s and several superficial oil velocities. The comparison reveals excellent agreement between the data and the model. This includes the prediction of the maximum split-ratios that yield 100% watercut in the underflow. For the Double Oil-in-Water Dispersion flow pattern, this optimal split-ratio is lower, as compared to the Stratified flow pattern. Also, the model follows well the trend of the data, where the optimal split-ratio decreases with increasing oil superficial velocity, from 50% at $v_{SO}=0.4$ m/s to 20% for $v_{SO}=0.2$ m/s.

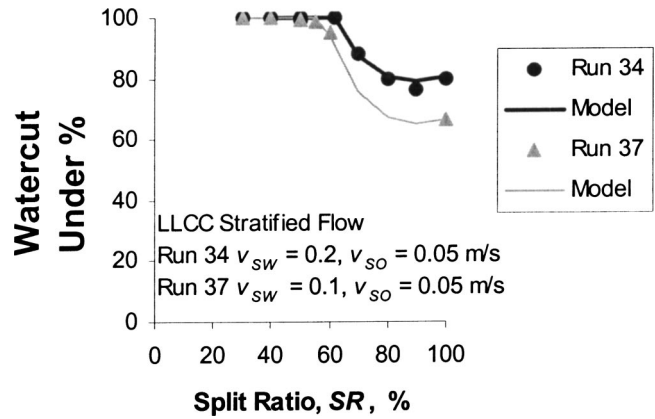


Fig. 16 Comparison between Data and Model Predictions for Stratified Flow

Oil-in-Water Dispersion Flow. Figure 19 shows the comparison results for this flow pattern. The superficial water velocity is about 1 m/s, while the superficial oil velocity varies from 0.058 to 0.32 m/s. The agreement between the data and the model predictions is very good for this case, too. Similar to the Double DO/W flow, with increase in oil superficial velocity, the maximum split-ratio for 100% watercut in the underflow decreases.

6 Conclusions

The following are the conclusions of this study:

- The Liquid-Liquid Cylindrical Cyclone (LLCC) compact separator has been proven to perform as a free water knockout device. No complete oil-water separation occurs in the LLCC. Rather, it delivers a clean water stream in the underflow and an oil rich stream in the overflow.
- A total of 260 runs have been conducted for the LLCC for water-dominated flow conditions. Four different flow patterns in the inlet have been identified, namely: Stratified flow; Oil-in-Water Dispersion and Water Layer flow; Double Oil-in-Water Dispersion flow; and Oil-in-Water Dispersion flow. The reported data includes the watercut in the underflow as function of the split ratio for each of the existing flow pattern.
- There exists an optimal split-ratio, where the underflow water flow rate is maximum, with 100% watercut. The value of the optimal split-ratio varies, depending upon the existing inlet flow pattern. For the Stratified and Oil-in-Water Dispersion—Water Layer flow patterns it is about 60%. For the Double Oil-in-Water

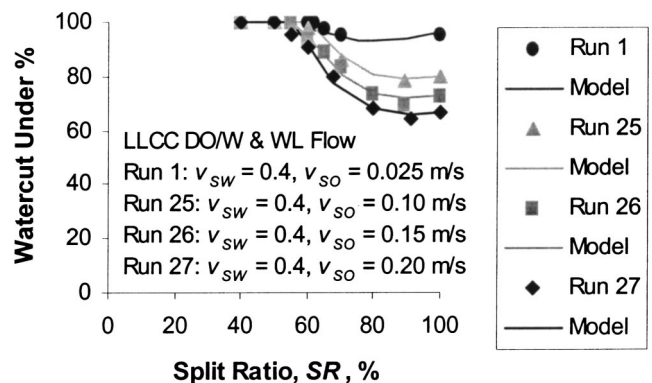


Fig. 17 Comparison between Data and Model Predictions for DO/W and Water Layer Flow

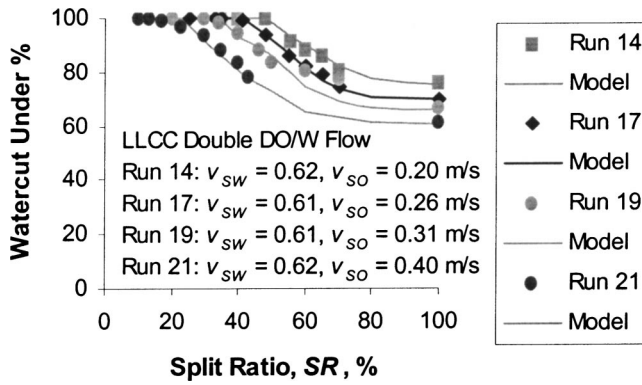


Fig. 18 Comparison between Data and Model Predictions for Double DO/W Flow

Dispersion and Oil-in-Water Dispersion flow patterns, the optimal split-ratio ranges from 50% to 20%, decreasing with the increase of oil content in the inlet.

- A novel mechanistic model, consisting of several sub-models, has been developed for prediction of the complex flow behavior in the LLCC and its separation performance. Comparison between the experimental data and the LLCC model predictions shows an excellent agreement. The model is capable of predicting both the trend of the experimental data as well as the absolute measured values.

Acknowledgments

The authors wish to thank the U.S. Department of Energy (DOE), for the five-year research grant (DE-FG26-97BC15024) and the member companies of Tulsa University Separation Technology Projects (TUSTP) for supporting this study.

Nomenclature

- A = cross sectional area (m^2)
- C = constant or coefficient (-)
- C_D = drag coefficient (-)
- d = diameter (m)
- f = friction factor (-)
- g = acceleration due to gravity ($9.81 m/s^2$)
- h = layer height (m)
- L = length (m)
- M = inlet momentum flux ratio (-)
- n = exponent
- P = pressure (Pa)

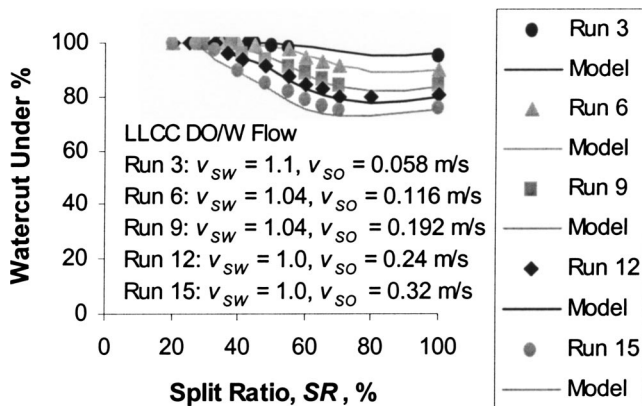


Fig. 19 Comparison between Data and Model Predictions for DO/W Flow

- q = volumetric flow rate (m^3/s)
- r = radius (m)
- Re = Reynolds number (-)
- S = perimeter (m)
- SR = Split-ratio
- V_{cum} = cumulative volume fraction (-)
- v = velocity (m/s)
- W = width (m)
- x = horizontal distance (m)
- z = vertical distance (m)

Greek Letters

- λ = no-slip holdup (-)
- μ = viscosity (Pa-s)
- Ω = swirl intensity (-)
- ρ = density (Kg/m^3)
- σ = interfacial tension (N/m)
- τ = shear stress (N/m^2)

Subscripts

- d = dispersion
- e = entry region
- i = interface
- in = inlet
- is = inlet slot
- l = lower
- m = mixture
- max = maximum
- min = minimum
- N = nozzle
- o = oil phase
- od = oil droplet
- rev = reverse flow region
- sep = separated
- SO = superficial oil
- SW = superficial water
- t = tangential
- T = total
- $under$ = underflow
- w = water phase

References

- [1] Listewnik, J., 1984, "Some Factors Influencing the Performance of De-Oiling Hydrocyclones for Marine Applications," Second International Conference on Hydrocyclones, England, September 19–21.
- [2] Gay, J. C., Triponey, G., Bezar, C. and Schummer, P., 1987, "Rotary Cyclone Will Improve Oily Water Treatment and Reduce Space Requirement/Weight on Offshore Platforms," SPE 16571.
- [3] Bednarski, S. and Listewnik, J., 1988, "Hydrocyclones for Simultaneous Removal of Oil and Solid Particles from Ships' Oily Waters," Filtration and Separation, pp. 92–97.
- [4] Seyda, B., 1991, "Separation of a Light Dispersion in a Cylindrical Vortex Chamber," Report, Michigan State University.
- [5] Afanador E., 1999, "Oil-Water Separation in Liquid-Liquid Cylindrical Cyclone Separators," M.S. Thesis, The University of Tulsa.
- [6] Mathiravedu, R. S., 2001, "Design, Performance and Control Strategy Development of Liquid-Liquid Cylindrical Cyclone (LLCC) Separator," M. S. Thesis, The University of Tulsa.
- [7] Oropeza-Vazquez, C., 2001, "Multiphase Flow Separation in Liquid-Liquid Cylindrical Cyclone and Gas-Liquid-Liquid Cylindrical Cyclone Compact Separators," Ph.D. Dissertation, The University of Tulsa.
- [8] Contreras, W., 2002, "The Effect of Inlet Gas Void Fraction on the Performance of Liquid-Liquid Cylindrical Cyclone (LLCC) Separator," M. S. Thesis, The University of Tulsa.
- [9] Trallero, J. L., 1995, "Oil-Water Flow Patterns in Horizontal Pipes," Ph.D. Dissertation, The University of Tulsa.
- [10] Hinze, J. O., 1955, "Fundamentals of the Hydrodynamic Mechanism of Splitting in Dispersion Processes," AIChE J., 1(3), pp. 289–295.
- [11] Levich, V. G., 1962, "Physicochemical Hydrodynamics," Prentice Hall, Englewood Cliffs, N.J.
- [12] Erdal, F., 2001, "Local Measurements and Computational Fluid Dynamic Simulations in a Gas-Liquid Cylindrical Cyclone Separator," Ph.D. Dissertation, The University of Tulsa.
- [13] Chang, F., and Dhir, V. K., 1995, "Mechanisms of Heat Transfer Enhancement and Slow Decay of Swirl in Tubes Using Tangential Injection," Int. J. Heat Fluid Flow, 16(2), pp. 78–87.

[14] Mantilla, I., Shirazi, S. A., and Shoham, O., 1999, "Flow Field Prediction and Bubble Trajectory Model in GLCC Separators," Proceedings of the ASME Energy Resources Technology Conference and Exhibition, ETCE, Houston, TX, February 1-2 1999, ASME J. Energy Resour. Technol., **121**, pp. 9-14.

[15] Crowe, C. T., Sommerfeld, M. and Tsuji, Y., 1998, "Multiphase Flows with Droplets and Particles," CRC Press, Boca Raton, FL.

[16] Karabelas, A. J., 1978, "Droplet Size Spectra Generated in Turbulent Pipe Flow of Dilute Liquid-Liquid Dispersions," AIChE J., **24**(2), pp. 170-180.

The Modeling of Thin Liquid Films Along Inclined Surfaces

Michael Z. Podowski

Professor
Center for Multiphase Research,
Rensselaer Polytechnic Institute,
Troy, N.Y. USA

Anela Kumbaro

Research Engineer
Commissariat à l'Energie Atomique,
Saclay, France

This paper is concerned with the analysis of thin and ultra-thin liquid films. The results are applicable to various geometrical and kinematic conditions, including both stationary and moving surfaces. The new results obtained in this work include: • the derivation of an analytical solution for the evolution of film thickness over the entire multiscale range, from the liquid free surface to the asymptotic (disjoining-pressure controlled) region, and for any surface inclination angle between 0 deg and 90 deg, • the formulation of a method to deduce the Hamaker constant based on a single measured value of film thickness at the beginning of the disjoining-pressure-controlled region, applicable to any inclination angle, • the explanation of the reasons why the thickness of liquid films on moving surfaces is normally beyond the range of Van der Waals forces, • the formulation of an expression for the nondimensional asymptotic film thickness as a function of the capillary number; this new result explicitly accounts for the effect of gravity on the average film velocity. [DOI: 10.1115/1.1777228]

Introduction

The physics of thin and ultra-thin films formed along solid surfaces has been investigated before by various authors [1–7], including both stationary films and liquid spreading induced by surface motion. In the case of stationary films, the issues of interest include the characteristics of the capillary region and the macroscopic contact angle, the development of ultra-thin (nanometer range) films by fully wetting fluids, and thin-film evaporation. A primary question in the case of surface-motion-induced coating is concerned with the effect of surface velocity on film thickness.

One of the major difficulties in the analysis of thin films spreading at fully wetting conditions is due to the film thickness range that covers scales from millimeters to nanometers. A typical approach is based on making approximations for the transition region and adjusting parameters such as the Hamaker constant, to obtain the ultra-thin film thickness that matches the measured values. A new approach, leading to a consistent theoretical model and the associated computational method, that allows one to accurately predict the film thickness over the entire multi-scale range, for the surface inclination angles from nearly horizontal to vertical, is presented in this paper.

The method utilizing the spreading of a uniform thin liquid layer over a slowly moving solid surface is a widely used coating technology. Because of the small thickness of the moving film, the existing models normally ignore details of liquid flow inside the film. As it is shown in the last section of the present paper, using a rigorous approach to film fluid mechanics, a more complete analytical model can be derived, together with an efficient solution method. This new model proves useful for explaining the effect of surface velocity on the liquid film thickness and, furthermore, shows the importance of accounting for velocity distribution across the film on film thickness predictions.

Problem Formulation

Let consider a solid flat plate partially immersed in a pool of wetting liquid, as shown in Fig. 1.

If the liquid completely wets the substrate material, the entire surface will be coated by a thin film, even if the wall is stationary. In the case of a moving surface, coating is expected even if the wetting conditions are beyond the range of Van der Waals forces. An interesting issue, both theoretically and practically, is con-

cerned with the thickness of the resultant coating, for various wall configurations (inclination angles) and velocities.

The purpose of this paper is to formulate a mathematical model and method, applicable to various geometrical and kinematic conditions over the entire film length, from the liquid surface at the film inception and through the capillary, transition and disjoining-pressure-dominated regions. Also, a general computational approach is presented allowing for accurately determining the film thickness over the entire film spreading range. It is shown that the proposed method allows one to accurately determine the Hamaker constant based on the measured stationary film thickness at the beginning of the asymptotic film region. A rigorous analytical derivation is also shown for the asymptotic (uniform) film thickness along a moving wall, including the effect of gravity. The results for both stationary and moving wall cases are applicable to an arbitrary wall inclination angle, from horizontal to vertical.

The numerical examples shown in the paper to illustrate the proposed approach are based on the properties of Hexane on a Silicone substrate. The specific properties of interest here are:

- density: $\rho = 660 \text{ kg/m}^3$,
- dynamic viscosity: $\mu = 2.8 \cdot 10^{-4} \text{ kg/m-s}$,
- surface tension: $\sigma = 1.84 \cdot 10^{-2} \text{ N/m}$.

Stationary Film on a Vertical Wall

In order to introduce the proposed modeling concepts, let us first consider a liquid film spread along a fully wetted stationary vertical wall, shown in Fig. 2.

A general equation governing the axial thickness distribution of the liquid film along the wall is [2]

$$\frac{d(\sigma K + \Phi)}{dx} = \rho g \quad (1)$$

where K is the curvature of the film surface

$$K = \frac{\delta''}{(1 + \delta'^2)^{3/2}} \quad (2)$$

and Φ represents the disjoining pressure at the liquid-vapor interface, given by

$$\Phi = \frac{B}{\delta^n} \quad (3)$$

where B is the Hamaker constant and n is disjoining pressure exponent (typically, $n = 4$).

Contributed by the Fluids Engineering Division for publication in the JOURNAL OF FLUIDS ENGINEERING. Manuscript received by the Fluids Engineering Division May 27, 2003; revised October 17, 2003. Associate Editor: S. Balachandar.

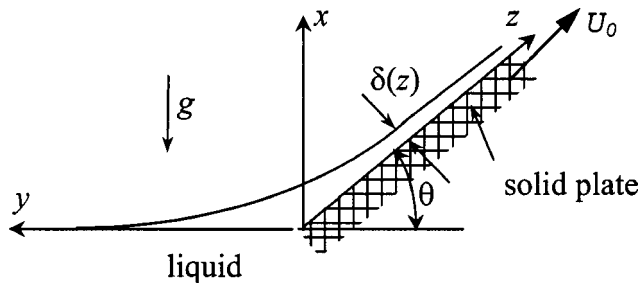


Fig. 1 Fluid in contact with an inclined moving surface

Equation (1) is subject to the following boundary conditions:

$$\lim_{x \rightarrow 0} \delta = \delta_{in}; \quad \lim_{x \rightarrow 0} \delta' = -\infty; \quad \lim_{x \rightarrow 0} \frac{\delta''}{(1 + \delta'^2)^{3/2}} = K_{in} \quad (4)$$

Integrating Eq. (1) with the boundary conditions given by Eq. (4) yields

$$\frac{\delta''}{(1 + \delta'^2)^{3/2}} = \frac{\rho g}{\sigma} x - \frac{B}{\sigma} \left(\frac{1}{\delta'^2} - \frac{1}{\delta_{in}^2} \right) + K_{in} \quad (5)$$

For a large area of the free surface, $\delta_{in} = \lim_{x \rightarrow 0} \delta(x) = \infty$ and $K_{in} = 0$, so that Eq. (5) simplifies to

$$\frac{\delta''}{(1 + \delta'^2)^{3/2}} = \frac{\rho g}{\sigma} x - \frac{B}{\sigma} \frac{1}{\delta'^2} \quad (6)$$

Equation (6) does not have a closed-form analytical solution. Numerical solutions are complicated by the fact that both associated boundary conditions refer to the "infinity" limits

$$\lim_{x \rightarrow 0} \delta(x) = \infty; \quad \lim_{x \rightarrow 0} \delta'(x) = -\infty \quad (7)$$

Alternatively, one of the boundary conditions in Eq. (7) can be replaced by the asymptotic limit of the final film thickness, again at infinity. In particular, the following boundary conditions can be used in place of those in Eq. (7)

$$\lim_{x \rightarrow 0} \delta(x) = \infty; \quad \lim_{x \rightarrow \infty} \delta(x) = 0 \quad (8)$$

Another, even more profound, difficulty of solving Eqs. (6) and (7) (or Eqs. (6) and (8)) is due to the fact that, over the entire range of liquid film, the model encompasses regions of dramatically different scales, from mm (in the initial capillary region) to nm (in the asymptotic region where the Van der Waals forces are

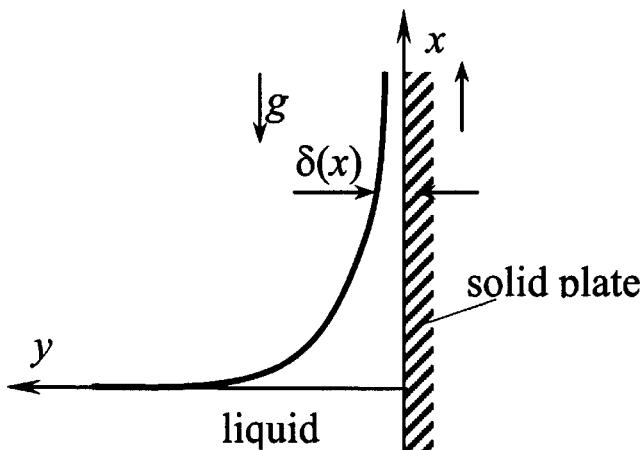


Fig. 2 Stationary film along a stationary vertical wall

dominant). It turns out that a consistent and accurate solution to this problem can be obtained by introducing yet another, intermediate region, where both the capillary and disjoining pressures are important.

Meniscus Region. First, let us take a look at the intrinsic meniscus, which is defined as the portion of meniscus governed by the Young-Laplace equation with the effects of disjoining pressure being negligible. In this case, Eq. (6) simplifies to

$$\frac{\delta''}{(1 + \delta'^2)^{3/2}} = \frac{\rho g}{\sigma} x \quad (9)$$

Integrating Eq. (9) with the boundary condition, $\lim_{x \rightarrow 0} \delta'(x) = -\infty$, yields

$$\frac{d\delta}{dx} = \frac{x^2 - 2a^2}{x\sqrt{4a^2 - x^2}} \quad (10)$$

where $a = \sqrt{\sigma/\rho g}$ is the capillary length.

The limiting range for Eqs. (9) and (10) is determined by the value of x where the slope becomes zero

$$x^* = \sqrt{2}a = \sqrt{\frac{2\sigma}{\rho g}} \quad (11)$$

Integrating Eq. (10), we obtain

$$\delta(x) = \delta_0 - \sqrt{4a^2 - x^2} + a \ln \frac{2a + \sqrt{4a^2 - x^2}}{x} + \sqrt{4a^2 - x_0^2} - a \ln \frac{2a + \sqrt{4a^2 - x_0^2}}{x_0} \quad (12)$$

where $x_0 < x^*$ is a reference distance (yet to be determined) and $\delta_0 = \delta(x_0)$ is the corresponding film thickness.

As can be seen, in order to determine the film thickness in the meniscus region from Eq. (12), the values of x_0 and δ_0 must be found first. On the other hand, Eqs. (9) and (10), respectively, directly provide the slope and curvature of the film in this region.

The result obtained for a Haxane film on a Silicone substrate is shown in Fig. 3.

Transition Region. In order to determine both x_0 and δ_0 , we notice that using Eq. (9) at $x = x_0$ yields

$$K_0 = \frac{x_0}{a^2} \quad (13)$$

On the other hand, including the effect of disjoining pressure, we obtain from the complete model given by Eq. (6)

$$K_0 = \frac{x_0}{a^2} - \frac{B}{\sigma \delta_0^2} \quad (14)$$

Thus, the selected point of reference must be such that

$$\frac{B}{\sigma \delta_0^2} = \varepsilon \frac{x_0}{a^2} \quad (15)$$

where $0 < \varepsilon \ll 1$. As can be seen, the specific choice of ε will control the error of the present method. Thus, the desired accuracy of calculations can be predetermined for any specific case.

Since Eq. (15) includes x_0 and δ_0 , both of which are yet to be determined, the missing boundary condition must be provided by matching the capillary solution with the solution of the full equation, Eq. (6). The difficulty here is in that the boundary condition of interest is referred to an infinite distance from the origin, $\lim_{x \rightarrow \infty} \delta = 0$. Since, as mentioned before, Eq. (6) does not have a

closed-form analytical solution, a practical approach is to develop a numerical method of solution. One possible method is to define the transition location as

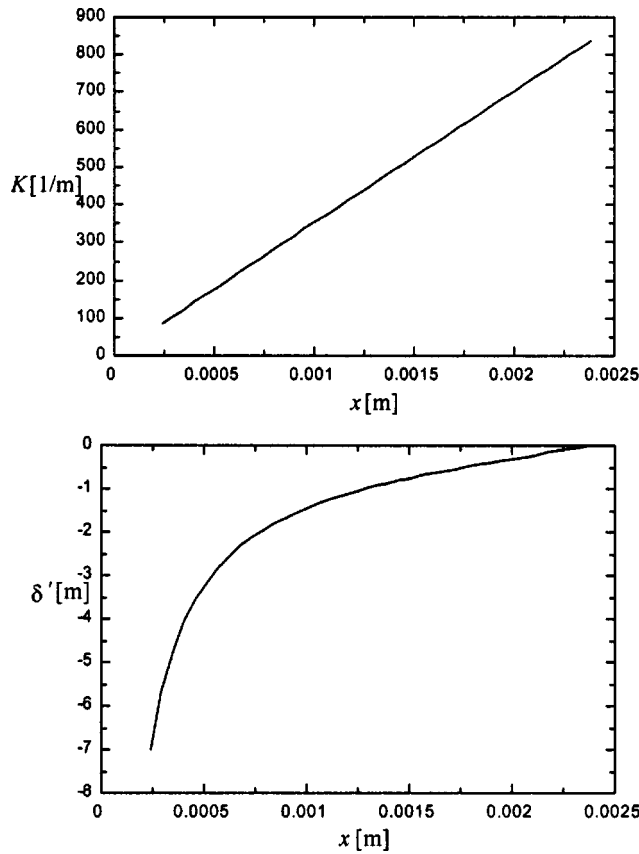


Fig. 3 Meniscus slope and curvature profiles for a Hexane film on Silicone substrate

$$x_0 = x^*(1 - \gamma) = (1 - \gamma) \sqrt{\frac{2\sigma}{\rho g}} \quad (16)$$

and iterate on the values of $0 < \gamma < 1$ until the asymptotic boundary condition is met.

The results obtained for a Hexane film spreading along a vertical Silicone substrate are shown in Fig. 4. In these calculations, the Hamaker constant was, $B = 1.0 \times 10^{-30}$ Jm, The desired accuracy was determined by choosing $\varepsilon = 0.005$ (see Eq. (15)).

In order to demonstrate the accuracy of the proposed method, Fig. 5 shows a comparison between the film thickness calculated using different assumed values of ε in Eq. (15). As can be seen, whereas the location of the onset of the transition region, x_0 , and the corresponding film thickness, δ_0 , depend on the assumed accuracy, the predicted film thickness, $\delta(x)$, is practically the same for all assumed values of ε . In particular, the film thickness at $x = x^* = 0.002385$ m is $\delta(x^*) \approx 190$ Å, and it decreases to $\delta(x_1) \approx 160$ Å when the effect of film curvature becomes negligible (at an approximate distance, $x - x^* = 0.000012$ m).

It is important to point out that a measure of the accuracy of the results shown in Figs. 4 and 5 is the difference between the values of curvature calculated at both sides of $x = x_0$. Specifically: $K(x_0^-) = x_0/a^2$ and $K(x_0^+) = x_0/a^2(1 - \varepsilon)$, so that $[K(x_0^-) - K(x_0^+)]/K(x_0^-) = \varepsilon \ll 1$. Since $|(x_0 - x^*)/x^*| = \gamma \ll 1$, it can be assumed that

$$K(x_0) \approx \frac{x^*}{a^2} \quad (17)$$

However, because of a dramatic reduction in the surface curvature in the transition region, the actual value of curvature at x^* may only be about 50% or less of $K(x_0)$ (see Fig. 4).

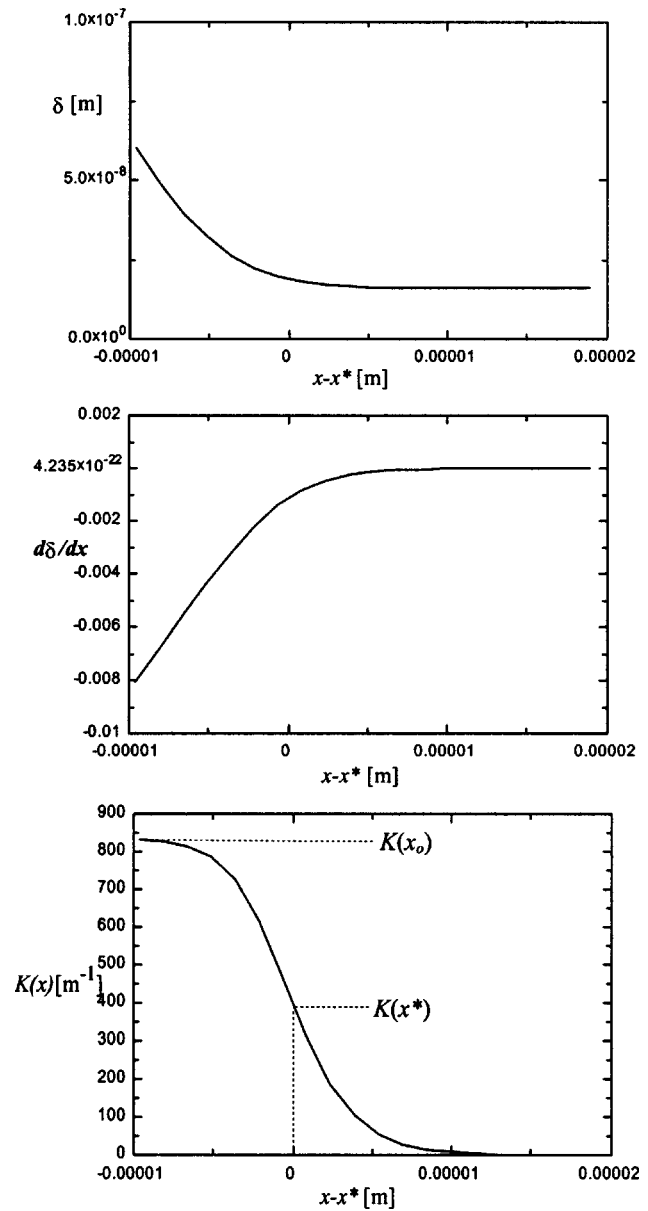


Fig. 4 Film thickness, slope and curvature profiles in the transition region

Furthermore, it is interesting to notice that the rigorous numerical approach to the transition region, presented above, can be replaced by an estimate obtained by rewriting Eq. (6) as

$$\frac{\delta''}{(1 + \delta'^2)^{3/2}} = \frac{\rho g}{\sigma} (x - x_0) - \frac{B}{\sigma} \left(\frac{1}{\delta^n} - \frac{1}{\delta_0^n} \right) + K_0 \quad (18)$$

and assuming that in the transition region $|\delta'| \ll 1$ and $|x - x_0| \ll a^2 K_0$. Consequently, Eq. (18) can be simplified to

$$\delta'' = K_0 - \frac{B}{\sigma} \left(\frac{1}{\delta^n} - \frac{1}{\delta_0^n} \right) \quad (19)$$

Multiplying both sides of Eq. (19) by δ' and integrating, we obtain

$$\frac{(\delta')^2}{2} = \left(K_0 + \frac{B}{\sigma} \frac{1}{\delta_0^n} \right) \delta - \frac{B}{\sigma(n-1)} \frac{1}{\delta^{n-1}} + C \quad (20)$$

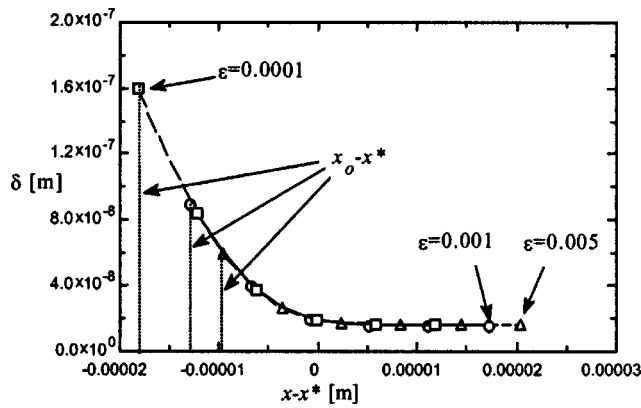


Fig. 5 The effect of assumed accuracy on the calculated film thickness

Assuming that at the end of the transition region (where $\delta(x_1) = \delta_1$), the following conditions are satisfied: $\delta''(x_1) \ll K_0$ and $|\delta'(x_1)| \ll B/[\sigma(n-1)\delta_1^{n-1}]$, Eqs. (19) and (20) yield

$$K_0 - \frac{B}{\sigma} \left(\frac{1}{\delta_1^n} - \frac{1}{\delta_0^n} \right) = 0 \quad (21)$$

$$\left(K_0 + \frac{B}{\sigma} \frac{1}{\delta_0^n} \right) \delta + \frac{B}{\sigma(n-1)} \frac{1}{\delta_1^n} + C = 0 \quad (22)$$

Calculating δ_1 and C from Eqs. (21) and (22), and substituting the results into Eq. (20), we obtain

$$\frac{(\delta')^2}{2} \approx \left(K_0 + \frac{B}{\sigma} \frac{1}{\delta_0^n} \right) \delta + \frac{B}{\sigma(n-1)} \frac{1}{\delta_1^{n-1}} - \frac{4B}{3\sigma} \left(\frac{\sigma K_0}{B} + \frac{1}{\delta_0^n} \right)^{1-1/n} \quad (23)$$

Taking into account that the solutions for the capillary and transition regions should assure the continuity of film thickness and its rate of change at $x = x_0$, and using Eq. (15) for the curvature error control, the combined Eqs. (10), (15) and (23) can now be solved for x_0 , $\delta_0 = \delta(x_0)$, $\delta'(x_0)$ and K_0 . Comparing the results against those shown in Fig. 5 indicates that the simplified approach yields accurate values of film thickness at the end of the transition region, δ_1 (obtained from Eq. (21)). However, this method does not provide information about the length of the transition region itself. Practically, the only way to determine the film thickness distribution in the transition region, $\delta(x)$ for $x_0 < x < x_1$, and in particular, $\delta(x^*)$, is to use the numerical solution illustrated in Fig. 5.

Asymptotic Nano-Region. Although, theoretically speaking, the film calculations along the wall could continue using the full model given by Eq. (6), the accuracy of the numerical solution diminishes as the curvature term (δ'') becomes negligible. Hence, a more efficient, and still very accurate, approach is to use an asymptotic formula obtained from Eq. (18). Specifically, since for $x \geq x_1$, $K(x) \ll K_0$, Eq. (18) can be simplified to

$$\frac{\rho g}{\sigma} (x - x_0) - \frac{B}{\sigma} \left(\frac{1}{\delta^n} - \frac{1}{\delta_0^n} \right) + K_0 \approx \frac{\rho g}{\sigma} (x - x_1) - \frac{B}{\sigma} \left(\frac{1}{\delta^n} - \frac{1}{\delta_1^n} \right) = 0 \quad (24)$$

Solving Eq. (24) for $\delta(x)$, we obtain

$$\delta(x) = \left[\frac{\rho g (x - x_0) + \sigma K_0}{B} + \frac{1}{\delta_0^n} \right]^{-1/n} \approx \left[\frac{\rho g (x - x_1)}{B} + \frac{1}{\delta_1^n} \right]^{-1/n} \quad (25)$$

where x_0 and δ_0 are determined from the analysis discussed in the previous section.

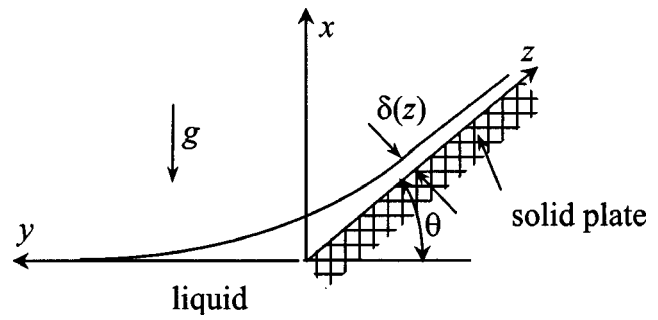


Fig. 6 Fluid in contact with an inclined stationary plate

Stationary Film on an Inclined Wall

The analysis presented in the previous section can be readily extended to the case of a plate inclined at an arbitrary angle with respect to the liquid free surface, as shown in Fig. 6.

For a given plate inclination angle, θ , the limiting value for the extent of the initial capillary region can be determined from Eq. (10) as

$$\frac{(x^*)^2 - 2a^2}{x^* \sqrt{4a^2 - (x^*)^2}} = -\cot \theta = -\Gamma \quad (26)$$

Solving Eq. (26) for x^* yields

$$x^* = \sqrt{2}a \sqrt{1 - \frac{\Gamma}{\sqrt{1 + \Gamma^2}}} \quad (27)$$

Since the film thickness evolution is now considered with respect to z rather than x , an appropriate change of variables is necessary. In particular, the following expression can be derived for the rate of film thickness change

$$\frac{d\delta}{dz} = \frac{\frac{d\delta}{dx} \sin \theta + \cos \theta}{\sin \theta - \frac{d\delta}{dx} \cos \theta} \quad (28)$$

For $x > x_0$, the film thickness in the transition region is governed by a modified Eq. (6), converted from x to z as an independent variable.

The current problem can either be solved numerically using Eq. (15) or, alternatively, an approximated solution can be obtained using the simplified approach discussed before. Typical results of the calculated film thickness at the end of the transition region, δ_1 (see Eq. (21)), for Hexane/Silicone and various plate inclination angles, are shown in Fig. 7. It is interesting to notice that for $B = 1.0 \times 10^{-30}$ Jm and $\theta = 90^\circ$ the predicted value, $\delta_1 = 160$ Å, is the same as that obtained solving numerically a complete model for a vertical wall and shown in Fig. 5.

Figure 7 also shows a comparison between the present model's predictions and the experimental data for a 4° inclination angle [8]. As can be seen, the appropriate value of the Hamaker constant for this case is, $B = 3 \times 10^{-31}$ Jm. It is important to notice that for any given measured value of δ_1 , an accurate estimate of the Hamaker constant can be obtained from Eq. (19). Specifically, taking into account that $\delta_1^n \ll \delta_0^n$, Eq. (21) yields

$$B \approx \sigma K_0 \delta_1^n \quad (29)$$

The calculated values of K_0 for various wall inclination angles are shown in Fig. 8. In fact, the arbitrariness in defining K_0 and difficulties associated with measuring the film curvature seem to be the main reasons for a wide spectrum of values proposed for the Hamaker constant for individual materials (for example, see Refs. [1] and [8]). In particular, it follows from Fig. 8 that the

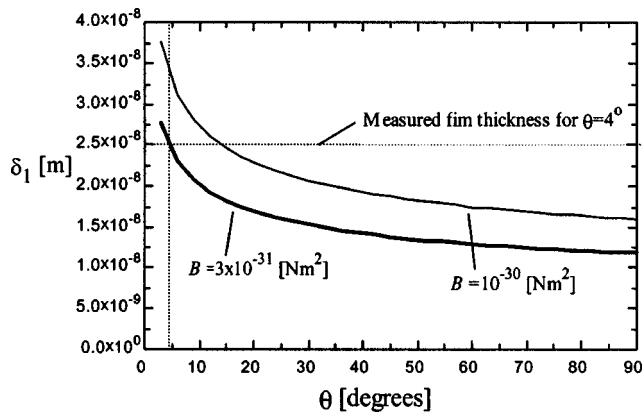


Fig. 7 Film thickness in the transition region for different plate inclination angles

value of K_0 for a 4° inclination angle, corresponding to $B = 3 \times 10^{-31} \text{ Nm}^2$, is $K_0 = 41 \text{ m}^{-1}$. On the other hand, for the value, $K_0 = 95 \text{ m}^{-1}$, that was assumed (rather than calculated) in Ref. [8], the predicted Hamaker constant was $B = 1 \times 10^{-30} \text{ Nm}^2$.

Since K_0 can be determined with a good accuracy in terms of just two fluid properties: surface tension and density (from the combined Eqs. (17), (27), and (29)), it is practically independent of B . Thus, the present method can indeed serve as an accurate vehicle for deducing the Hamaker constant based on the measured film thickness at the end of the transition, and the beginning of the asymptotic, regions.

Flow Conditions

Let us now consider a film-coating problem, where a thin film of fluid clings to the plate which is drawn vertically through a liquid pool with a constant velocity, U_0 . As shown in Fig. 9, starting from the free surface, the overall film length can be divided into two regions. In the initial (normally very short) region above the surface (Region-I, extending from $x = 0$ to $x = x_c$), the motion of the plate has a negligible effect on the shape of the meniscus line. As soon as the liquid layer becomes sufficiently thin, the free surface starts moving (Region-II, for $x > x_c$), following the plate with a gradually increasing average velocity as the film gets thinner.

The meniscus region between the free surface ($x = 0$) and the onset of motion at the film surface ($x = x_c$) is very short (typically, of the order of no more than a few millimeters), whereas its thick-

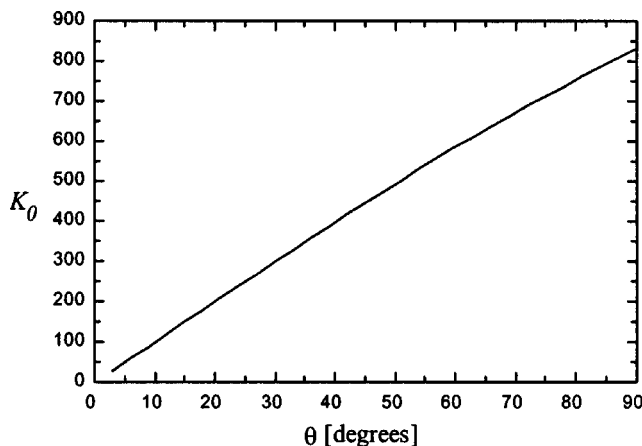


Fig. 8 Effect of plane inclination angle on film surface curvature at the beginning of the transition region

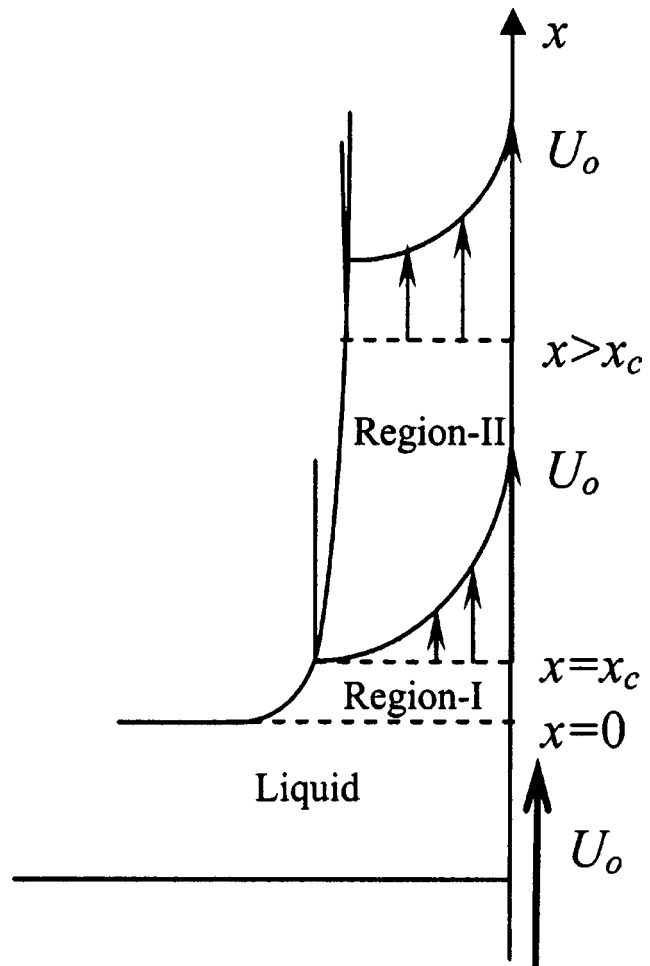


Fig. 9 Schematic of liquid film formation along a vertical moving plate submerged in a liquid pool

ness changes dramatically. The velocity field in the submerged portion of the liquid (for $x < 0$) depends on the liquid depth and the plate velocity, and the net flow in the upward direction is governed by the ability of the combined wall shear and capillary forces to counterbalance the effect of gravity. Although a detailed multidimensional liquid velocity field driven by the moving plate wall (including the boundary layer development) is somewhat complicated, when approaching the onset of motion point ($x = x_c$), the velocity profile gradually assumes the shape shown in Fig. 9.

Since the moving film in Region-II is thin, its motion can be described by a unidirectional momentum equation along the surface. Specifically, we write

$$\frac{\partial \tau_{yx}}{\partial y} = -\frac{\partial(\sigma K + \Phi)}{\partial x} + \rho g \quad (30)$$

As long as the film is sufficiently thin, the flow inside the film is going to be laminar (the validity of this assumption will be confirmed later in this Section). Thus, the shear stress across the film can be expressed as

$$\tau_{yx} = \mu \frac{\partial u(y)}{\partial y} \quad (31)$$

Substituting Eq. (31) into Eq. (30) gives the following equation for the two-dimensional axial film velocity (along the plate wall and across the film)

$$\mu \frac{\partial^2 u}{\partial y^2} = -\frac{\partial(\sigma K + \Phi)}{\partial x} + \rho g \quad (32)$$

Ignoring the gas/liquid interfacial shear at the free surface of the film, yields

$$u(x, y) = U_0 - \frac{3}{2} \left(U_0 - \frac{Q}{\delta(x)} \right) \left[2 \frac{y}{\delta(x)} - \left(\frac{y}{\delta(x)} \right)^2 \right] \quad (33)$$

for $x > x_c$, where Q is the volumetric flow rate of the liquid per unit width of the film (yet to be determined).

It follows from Eq. (33) that

$$u[x_c, \delta(x_c)] = 0 \quad (34)$$

and $u(x, y) > 0$ for $x > x_c$.

Substituting Eq. (33) into Eq. (32), we write

$$\frac{d(\sigma K + \Phi)}{dx} = \rho g - 3\mu \frac{U_0 - \frac{Q}{\delta}}{\delta^2} \quad (35)$$

As x increases, the film thickness approaches a constant asymptotic value that satisfies the equation

$$\frac{\rho g}{3\mu} \delta_\infty^3 - U_0 \delta_\infty + Q = 0 \quad (36)$$

Combining Eqs. (35) and (36), and assuming a constant surface tension, σ , we obtain

$$\delta^3 \frac{d(\sigma K + \Phi)}{dx} = \frac{\rho g}{\sigma} (\delta^3 - \delta_\infty^3) - \frac{3\mu}{\sigma} U_0 (\delta - \delta_\infty) \quad (37)$$

or

$$\delta^3 \frac{d(\sigma K + \Phi)}{dx} = [\rho g (\delta^2 + \delta \delta_\infty + \delta_\infty^2) - 3\mu U_0] (\delta - \delta_\infty) \quad (38)$$

where Φ is given by Eq. (3) with $n=4$.

In the asymptotic region of the flowing film, Eq. (38) can be approximated by

$$\sigma \delta_\infty^3 \frac{d^3 \delta}{dx^3} - \frac{4B}{\delta_\infty^2} \frac{d\delta}{dx} + 3(\mu U_0 - \rho g \delta_\infty^2) (\delta - \delta_\infty) = 0 \quad (39)$$

A general solution of Eq. (39) is

$$\delta(x) = \delta_\infty + C_1 e^{b_1 x} + C_2 e^{b_2 x} + C_3 e^{b_3 x} \quad (40)$$

As can be seen, the properties of the solution given by Eq. (40) depend on the sign of the term, $r = \mu U_0 - \rho g \delta_\infty^2$. Let us first assume that the asymptotic film thickness is driven by the disjoining pressure and, thus, is in the nanometer range. In this case, Eq. (39) simplifies to

$$\frac{4B}{\delta_\infty^2} \frac{d\delta}{dx} - 3(\mu U_0 - \rho g \delta_\infty^2) (\delta - \delta_\infty) = 0 \quad (41)$$

The existence of an asymptotic steady film thickness requires that $r < 0$. Using the material properties given in Section 1, we conclude that for $\delta_\infty \leq 10^{-7}$ m, the corresponding surface velocity would have to be, $U_0 < 2.31 \cdot 10^{-7}$ m/s. Thus, for all practical purposes, it can be assumed that the asymptotic film thickness along a moving (vertical) surface is beyond the range of Van der Waals forces.

The corresponding solution can be obtained by replacing Eq. (39) by

$$\frac{d^3 \delta}{dx^3} + b^3 (\delta - \delta_\infty) = 0 \quad (42)$$

where

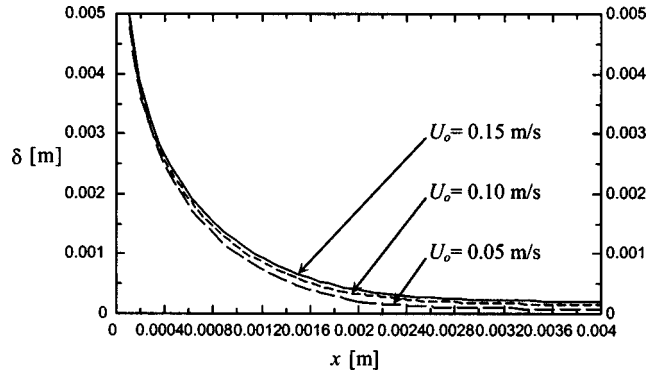


Fig. 10 The effect of surface velocity on liquid film thickness

$$b = \left[\frac{3}{\sigma} \left(\frac{\mu U_0}{\delta_\infty^3} - \frac{\rho g}{\delta_\infty} \right) \right]^{1/3} \quad (43)$$

Now, the exponents in Eq. (40) become

$$b_1 = -b = - \left[\frac{3}{\sigma} \left(\frac{\mu U_0}{\delta_\infty^3} - \frac{\rho g}{\delta_\infty} \right) \right]^{1/3}, \quad b_{2,3} = 0.5(1 \pm \sqrt{3})b \quad (44)$$

Since in the present case, $b > 0$, we conclude that the film can reach an asymptotic constant thickness only if $C_2 = C_3 = 0$. This, in turn, implies that the solution of Eq. (42) is

$$\delta(x) = \delta_\infty + C_1 e^{-bx} \quad (45)$$

The constant, C_1 , can be determined by matching the solutions for the initial capillary region, where the wall velocity has no effect of the film thickness, against that given by Eq. (45) for the flow region.

The film thickness in the static meniscus region is (see Eq. (12))

$$\delta(x) = -\sqrt{4a^2 - x^2} + a \ln \frac{2a + \sqrt{4a^2 - x^2}}{x} + C \quad (46)$$

This solution is valid as long as the motion of the meniscus layer surface is neglected, i.e., for $x \leq x_c$, where x_c satisfies Eq. (34).

Combining Eqs. (33), (34) and (46) yields

$$\delta_c = \delta(x_c) = 3\delta_\infty - \frac{\rho g}{\mu U_0} \delta_\infty^3 \quad (47)$$

Now, the matching conditions can be written as

$$\delta(x_c^-) = \delta(x_c^+), \quad \left. \frac{d\delta}{dx} \right|_{x_c^-} = \left. \frac{d\delta}{dx} \right|_{x_c^+}, \quad \left. \frac{d^2\delta}{dx^2} \right|_{x_c^-} = \left. \frac{d^2\delta}{dx^2} \right|_{x_c^+} \quad (48)$$

Using Eqs. (45), (46), (47) and (48), the integration constants, C and C_1 , can be determined, together with the asymptotic film thickness, δ_∞ , and the location of critical distance, x_c . Thus, the entire film thickness, $\delta(x)$ for $x \in (0, \infty)$, can be determined from Eq. (46) (for $x \leq x_c$) and Eq. (45) (for $x > x_c$). Typical results for different surface velocities are shown in Fig. 10.

The model discussed in this section can be used to obtain non-dimensional characteristics of thin film coatings in the asymptotic region, applicable to any film and surface materials. Specifically, introducing the non-dimensional asymptotic film thickness and the capillary number, respectively, as

$$\Delta = \frac{\delta_\infty}{a} = \delta_\infty \sqrt{\frac{\rho g}{\sigma}} \quad (49)$$

$$Ca = \frac{\mu U_0}{\sigma} \quad (50)$$

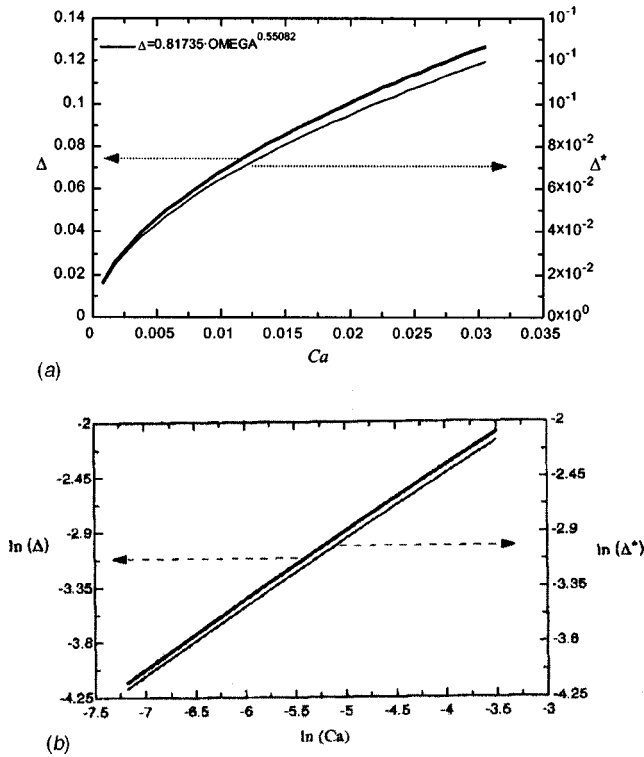


Fig. 11 Nondimensional asymptotic thickness of thin film coating as a function of the capillary number. (a) linear scale; (b) logarithmic scale

the solution of the present model can be plotted as a function, $\Delta = f(Ca)$, as shown in Fig. 11(a). The same function is plotted in Fig. 11(b) using a ln-ln scale.

As can be seen, the result shown in Fig. 11(b) can be described with a very good accuracy by a linear function

$$\ln(\Delta) = -0.1271 + 0.555 \ln(Ca) \quad (51)$$

Eq. (51) can be also rewritten as

$$\Delta = \beta(Ca)^\omega \quad (52)$$

where $\beta = 0.880$ and $\omega = 0.555$.

Equation (41) was obtained from Eq. (39) assuming that $\delta(x) \approx \delta_\infty$ in the asymptotic region. Actually, the film thickness changes gradually from $\delta(x_c)$ to δ_∞ . In the present case, the average value of $\delta(x)$ in the asymptotic region was about $\delta_{av} = 1.25\delta_\infty$, over the entire analyzed range of surface velocities from 0 to 2 m/s. In order to quantify the uncertainty associated with the treatment of the asymptotic region in the present model, and to improve the accuracy of predictions of the average film thickness in this region, another series of calculations was also performed in which the previously used assumption was replaced by

$$\delta^2 + \delta\delta_\infty + \delta_\infty^2 \approx \delta_{av}^2 + \delta_{av}\delta_\infty + \delta_\infty^2 = 3.81\delta_\infty^2 \quad (53)$$

Consequently, Eq. (41) has been modified as follows

$$\frac{4B}{\delta_\infty^2} \frac{d\delta}{dx} - (3\mu U_0 - 3.81\rho g \delta_\infty^2)(\delta - \delta_\infty) = 0 \quad (54)$$

The predicted updated nondimensional asymptotic film thickness, Δ^* , is also shown in Figs. 11(a) and 11(b). The corresponding modified functional form is

$$\ln(\Delta^*) = -0.2017 + 0.551 \ln(Ca) \quad (55)$$

Eq. (55) is equivalent to Eq. (52) with $\beta = 0.817$ and $\omega = 0.551$.

As can be seen, the difference between the modified and original results is about 6%. Thus, the proposed model is not very sensitive to details of the initial film thickness distribution in the asymptotic region.

Integrating Eq. (33) over the film thickness yields the following expression for the volumetric film flow rate (per unit width)

$$Q = U_0 a \Delta \left(1 - \frac{\Delta^2}{3Ca} \right) \quad (56)$$

The corresponding average film velocity can be calculated from

$$U_{f,\infty} = \frac{Q}{\delta_\infty} = U_0 \left(1 - \frac{\Delta^2}{3Ca} \right) \quad (57)$$

In order to determine flow conditions inside the film, one can use the Reynolds number defined with respect to the moving plate wall

$$Re_f = \frac{(U_0 - U_{f,\infty})\delta_\infty}{\nu} = \frac{U_0\delta_\infty}{\nu} \frac{\Delta^2}{3Ca} = \frac{a^3 g \beta^3}{\nu^2} \frac{1}{3} (Ca)^3 \omega \quad (58)$$

Applying a standard criterion for wave-free laminar films as

$$Re_f < Re_c \approx 30 \quad (59)$$

and taking the updated constants, $\beta = 0.817$ and $\omega = 0.551$ (corresponding to Eq. (55)), yields the critical value of the capillary number, $Ca_c = 0.0116$. Using the properties of Hexane, listed on p. 2, the above-given condition translates into the following limiting condition on the plate velocity: $U_0 < 0.76$ m/s. As can be seen, the asymptotic film remains smooth laminar for a broad range of moving plate velocities. However, it should be mentioned that the value of the Reynolds number near the onset of film motion (defined before as $x = x_c$) is larger than that in the asymptotic region. Thus, for some situations satisfying the condition given by Eq. (59), the moving film may assume a wavy laminar initial structure, to eventually reach a smooth waveless laminar flow pattern.

It is interesting to mention that the functional form of Eqs. (52) is similar to the expression reported by Probstein [7]. However, the numerical coefficients are different; according to Probstein, $\beta = 0.946$ and $\omega = 2/3$. One reason for that is that whereas earlier models ignored the effect of gravity (thus, a uniform velocity across the film was assumed, equal to the surface velocity, U_0 , and consequently, the film flow rate was, $Q = U_0\delta_\infty$), the present model explicitly accounts for this effect. As a result, the average film velocity obtained from the parabolic velocity profile is given by Eq. (57).

Using the properties of Hexane and assuming a surface velocity of $U_0 = 0.76$ m/s, the nondimensional asymptotic film thickness obtained from Eq. (55) is $\Delta_{actual} = 0.0701$, whereas the simplified model of Probstein [7] gives $\Delta_{simplified} = 0.0484$. Thus, the error associated with the latter is, $|\Delta_{simplified} - \Delta_{actual}| / \Delta_{actual} \times 100\% \approx 31\%$. As it can be readily noticed, the difference between the simplified model and the present, more detailed, model increases with decreasing wall velocity, to 40% for $U_0 \approx 0.23$ m/s, and to 50% for $U_0 \approx 0.05$ m/s.

Whereas the analysis given in this Section has been performed for a vertical moving plate, it can be readily extended to a surface moving at any inclination angle between 0° and 90° . In particular, if the effect of gravity in Eq. (33) becomes negligible, $U_f \rightarrow U_0$, as in the model given by Probstein [7].

Conclusions

A theoretical model of thin and ultra-thin films has been presented, applicable to various geometrical and kinematic conditions. This model allows one to determine the film thickness over the entire film length, from the liquid surface at the film inception and through the capillary, transition and asymptotic (disjoining-

pressure-dominated) regions. Also, a general computational method has been developed to accurately compute the film thickness along a solid wall submerged in a liquid.

The new results obtained in this work for stationary films include:

- the accurate evaluation of ultra-thin film thickness at the beginning of the asymptotic (disjoining-pressure controlled) region, over the full range of surface inclination angles, from 0 to 90 deg,
- the formulation of a method to deduce the Hamaker constant based on a single measured value of film thickness at the beginning of the disjoining-pressure-controlled region, applicable to any inclination angle.

Furthermore, the fluid mechanics of liquid films over moving surfaces has also been investigated. The major results are:

- the derivation of an analytical solution for the evolution of film thickness over the entire range from the liquid free surface to the asymptotic region,
- the explanation of the reasons why the thickness of liquid films on moving surfaces is normally beyond the range of Van der Waals forces,
- the formulation of a relationship between the nondimensional asymptotic film thickness and the capillary number; this new formula accounts explicitly for the effect of gravity on the average film velocity and can be extended to any surface inclination angle.

Whereas the subject of this paper was concerned with smooth surfaces, where the effects of surface roughness on the spreading of liquid films are negligible, the overall approach should also be useful in the interpretation of experimental data where such effects become important.

References

- [1] Ingram, B. T., 1974, Wetting of Silica by *n*-Alkanes, *J. Chem. Soc., Faraday Transactions I*, **70**, p. 868.
- [2] Renk, F., Wayner, P. C., and Homsy, G. M., 1978, On the Transition Between a Wetting Film and a Capillary Meniscus, *J. Colloid Interface Sci.*, **67**, p. 408.
- [3] Bankoff, S. G., 1990, Dynamics and Stability of Thin Heated Films, *J. Heat Transfer*, **112**, p. 538.
- [4] Wayner, P. C., 1991, The Effect of Interfacial Mass Transport on Flow in Thin Liquid Films, *J. Colloids and Surfaces*, **52**, p. 71.
- [5] Wayner, P. C., 1992, Intermolecular and Surface Forces with Applications in Change-of-Phase Heat Transfer, in *Boiling Heat Transfer: Modern Developments and Advancements* (ed.: R. T. Lahey, Jr.), Elsevier, p. 569.
- [6] Voinov, O. V., 1998, Fine Structure of Meniscus of a Wetting Liquid, *J. Colloid Interface Sci.*, **200**, p. 197.
- [7] Probstein, R. F., 1994, *Physicochemical Hydrodynamics, An Introduction*, 2nd Ed., John Wiley & Sons, Inc.
- [8] Truong, J. G., 1987, *Ellipsometric and Interferometric Studies of Thin Liquid Films Wetting on Isothermal and Nonisothermal Solid Surfaces*, Ph.D. Thesis, RPI.

M. Lopez de Bertodano

Nuclear Engineering Department,
Purdue University, West Lafayette, IN
47907-2017, USA

F. J. Moraga

D. A. Drew

R. T. Lahey, Jr.

Center for Multiphase Research,
Rensselaer Polytechnic Institute,
Troy, NY 12180-3590, USA

The Modeling of Lift and Dispersion Forces in Two-Fluid Model Simulations of a Bubbly Jet

Two-fluid model simulations of a bubbly vertical jet are presented. The purpose of these simulations is to assess the modeling of lift and turbulent dispersion forces in a free shear flow. The turbulent dispersion models used herein are based on the application of a kinetic transport equation, similar to Boltzmann's equation, to obtain the turbulent diffusion force for the dispersed phase [1–4]. They have already been constituted and validated for the case of particles in homogeneous turbulence and jets [5] and for microscopic bubbles in grid generated turbulence and mixing layers [6,7]. It was found that it is possible to simulate the experimental data of Sun [8] (see Figs. 1–6) for a bubbly jet with 1 mm diameter bubbles. Good agreement is obtained using the model of Brucato et al. [9] for the modulation of the drag force by the liquid phase turbulence and a constant lift coefficient, C_L . However, little sensitivity is observed to the value of the lift coefficient in the range $0 < C_L < 0.29$. [DOI: 10.1115/1.1777231]

1 Introduction

The present two-fluid model for turbulent bubbly flows applies recent advances in the development of interfacial forces. They include the general solution of the lift force for a rotating sphere moving through a viscous shear flow by [10] and studies of drag modulation by turbulence [9]. Another important advance has been the application of a kinetic transport equation, similar to the Boltzmann's equation, to obtain the turbulent diffusion force for the dispersed phase [3,4]. This method has been successfully applied in the field of particle flows and provides Eulerian results that are as accurate as the Lagrangian analysis. The magnitude of the turbulent dispersion force is obtained rigorously from the first moment of the kinetic equation and is constituted in terms of the statistics of the turbulence of the continuous liquid phase and the drag law of the dispersed phase, without the need of any ad. hoc. constants. This turbulent dispersion force has already been constituted and validated for the case of particles in homogeneous turbulence and jets [5] and for microscopic bubbles in grid generated turbulence and mixing layers [6,7]. The most important dimensionless number controlling dispersion in these works is the Stokes number, St , which was very large for the particles, $St \approx 100$ at the nozzle entrance [5], and very small for the bubbles, $St \approx 10^{-3}$ [6,7]. Jets are a particularly challenging flow for predicting turbulent dispersion because the characteristic time of the turbulence and consequently the Stokes number change dramatically across the computational domain. In this paper, simulations of the air/water bubbly jet characterized by Sun [8] are presented. By selecting a low void fraction bubbly flow, instead of the gas/solid flow simulated by Lopez de Bertodano [5], we intend to study dispersion in a flow with a completely different turbulence structure and Stokes number distribution. Unlike the previously studied jet the selected bubbly flow is one-way coupled (i.e., the bubbles do not appreciable modulate the continuous phase turbulence) and the Stokes numbers are made larger by selecting large bubbles, yet no so large as to experience helicoidal trajectories. An additional benefit of selecting the data of Sun [8] is that they

have previously been simulated with Lagrangian approaches [11]. Thus, a comparison of performance between Eulerian and Lagrangian formulations is possible.

The organization of the paper is as follows. The next section presents the two-fluid model, while Section 3 covers the simulations and results. Finally, the most relevant conclusions are stated in Section 4.

2 Two-Fluid Model Equations

Conservation of the ensemble-averaged mass and momentum for phase- k , in the absence of phase change, are expressed as [[12], §11.3]:

$$\frac{\partial \alpha_k \rho_k}{\partial t} + \nabla \cdot \alpha_k \rho_k \mathbf{u}_k = 0 \quad (1)$$

and,

$$\frac{\partial \alpha_k \rho_k \mathbf{u}_k}{\partial t} + \nabla \cdot \alpha_k \rho_k \mathbf{u}_k \mathbf{u}_k = \nabla \cdot \alpha_k (\mathbf{T}_k + \mathbf{T}_k^{\text{Re}}) + \alpha_k \rho_k \mathbf{g} + \mathbf{M}_k - \mathbf{T}_{ki} \cdot \nabla \alpha_k, \quad (2)$$

where α_k , ρ_k , \mathbf{u}_k are the void fraction, density and velocities of phase- k , respectively. Also, \mathbf{T}_k , \mathbf{T}_k^{Re} and \mathbf{T}_{ki} are the viscous stress tensor, the Reynolds stress tensor, and the interface stress tensor of phase- k , respectively, and \mathbf{g} is the gravitational acceleration. In the remaining of this work the subscript $k=c, d$ represents the continuous and dispersed phases, respectively, and we may neglect the viscous part of the interface stress tensor. Thus, $\mathbf{T}_{ki} = -p_{ki} \mathbf{I}$. We further assume that the difference $p_k - p_{ki}$, $k=c, d$, is negligibly small. With these two assumptions we achieve closure for the interfacial stress tensor.

3 Bubbly Jet

3.1 Model for the Interfacial Force. The interfacial momentum force density, \mathbf{M}_d , needs to be constituted in order to achieve closure. Thus we write,

$$\mathbf{M}_d \cong \mathbf{M}_d^D + \mathbf{M}_d^{TD} + \mathbf{M}_d^{VM} + \mathbf{M}_d^L \quad (3)$$

where these forces are, respectively, those due to drag (D), turbulent dispersion (TD), virtual mass (VM) and lift (L).

Contributed by the Fluids Engineering Division for publication in the JOURNAL OF FLUIDS ENGINEERING. Manuscript received by the Fluids Engineering Division August 15, 2002; revised manuscript received July 16, 2003. Associate Editor: S. Balachandrar.

The virtual mass force accounts for the effect of acceleration of the liquid displaced by the bubbles, and can be modeled as

$$\mathbf{M}_d^{VM} = \alpha_d \rho_c C_{VM} \left[\left(\frac{\partial \mathbf{u}_c}{\partial t} + \mathbf{u}_c \cdot \nabla \mathbf{u}_c \right) - \left(\frac{\partial \mathbf{u}_d}{\partial t} + \mathbf{u}_d \cdot \nabla \mathbf{u}_d \right) \right], \quad (4)$$

where the virtual volume coefficient, C_{VM} , is 0.5 for the dilute potential flow of spherical bubbles.

The drag force may be expressed as

$$\mathbf{M}_d^D = -\alpha_d \rho_c C_D \frac{3}{8} \frac{|\mathbf{u}_r|}{D_b/2} \mathbf{u}_r, \quad (5)$$

where the drag coefficient C_D is defined after Tomiyama [13], with a void fraction correction based on that of Ishii [14] to include interaction between the bubbles. in tap water:

$$C_D = \frac{1}{\alpha_c} \frac{24}{\text{Re}_D} (1 + 0.15 \text{Re}_D^{0.687}), \quad (6)$$

where Re_D is the bubble Reynolds number based on the bubble diameter, D_b , and the relative velocity, $\mathbf{u}_r = \mathbf{u}_d - \mathbf{u}_c$. We note that for the bubble size range of interest in this work, the Eötvös number correction introduced by Tomiyama [13] is not applicable.

The lift force on a sphere in shear flow can be expressed as [15],

$$\mathbf{M}_d^L = -\alpha_d \rho_c C_L \mathbf{u}_r \times (\nabla \times \mathbf{u}_c), \quad (7)$$

where $C_L = 0.5$ for inviscid flow. Legendre and Magnaudet [16] performed a full computational fluid dynamic (CFD) simulation for viscous shear flow around a spherical bubble with no shear at the surface and obtained a similar result to Eq. (7) for $10 < \text{Re}_D < 1000$, though C_L varies a little. In particular, $C_L = 0.45$ for $\text{Re}_D = 100$ (i.e., a 1 mm bubble) and a dimensionless vorticity, $a = D_b \nabla \times \mathbf{u}_c / u_r = 0.2$.

However, bubbles flowing in tap water behave like rigid spheres and, furthermore, they may rotate as they move through the shear flow. Recently Kurose and Komori [10] solved the problem of a rotating sphere moving in linear shear flow with a full CFD simulation. In this case not only a , but also the dimensionless sphere rotation, $\Omega = \Omega_b / u_r$, were considered. It turns out that assuming $\Omega = a/2$ and $\text{Re}_D = 100$ the result of Kurose and Komori [10] can be reproduced very closely with Eq. (7) and $C_L = 0.28$ for $0 < a < 0.4$, which is the range of the current jet calculations. However, if $\Omega = 0$ as proposed by Bagchi and Balachandar [17] for solid spheres at moderate Re in shear flow the model of Kurose and Komori yields $C_L = -0.07$. So the prediction of the lift coefficient remains uncertain.

Experimental results are in good agreement with the result of Kurose and Komori [10] and the assumption that $\Omega = a/2$. For example, the experiment of Naciri [18] for a bubble in a vortex showed that $C_L = 0.25$ for $10 < \text{Re}_D < 120$ and $a = 0.25$. Tomiyama's experimental data [13] for small bubbles in Couette flow agrees with Eq. (7) when $C_L = 0.288$. Tomiyama's lift coefficient was used in the bubbly jet simulations presented herein.

Physically, turbulent dispersion (TD) is the result of the fluctuating component of the forces acting on the bubbles. In the simplest case the turbulent diffusion force at a point is the ensemble average of the fluctuating component of the drag force on all the bubbles whose trajectories intersect that point. The kinetic equation obtained by Reeks [3,4] describes the evolution of the probability density function (pdf) for the bubbles in phase space and so it implicitly has the information of the bubble trajectories in it. The Eulerian two-fluid momentum equation for the bubbles is obtained from the ensemble-averaged first moment of the kinetic equation. Assuming that the turbulence is homogeneous (though not necessarily isotropic) and that the turbulence autocorrelation function follows the usual Markov law,

$$\overline{\mathbf{u}'_c(\mathbf{x}, 0) \mathbf{u}'_c(\mathbf{x}, t)} = \overline{\mathbf{u}'_c \mathbf{u}'_c} \exp(-t/\tau_c), \quad (8)$$

the turbulent diffusion force comes out of this process in a natural way as [5]:

$$\mathbf{M}_d^{TD} = -\rho_c \frac{1}{St(1+St)} \overline{\mathbf{u}'_c \mathbf{u}'_c} \cdot \nabla \alpha_d, \quad (9)$$

where the Stokes number, St , is defined as the ratio of the relaxation times of the bubble, τ_d , and the eddies, τ_c .

Comparing this homogeneous flow formulation with that of Reeks [2] for a simple shear flow, there are some differences in the derivation of the turbulent diffusion force as well as the Reynolds stresses:

(1) Turbulent diffusion force: The presence of the shear produces extra terms that are a function of the dimensionless product $\tau_c S$ where S is the strain rate, in addition to the Stokes number. However, they are smaller than the corresponding terms in the homogeneous model (at most 30% for the present case) and more importantly, these terms act only in the x-direction. For the jet, the diffusion in the x-direction is much smaller than the convective transport, so it is neglected.

(2) Reynolds stresses of the dispersed phase: Reeks points out that the Boussinesq approximation for the Reynolds shear stress of the dispersed phase is deficient. However, in the present case the Reynolds stresses of the bubbles are proportional to the density of the air, as shown in Eq. (2), so they are neglected. Therefore, this effect as well as others (e.g., turbophoresis) which are significant in the case of particle flows, are negligible for bubbles.

The time constant of the bubbles can be derived using Eqs. (6), (5) and (4) as:

$$\tau_d = \frac{1}{18} \frac{(\rho_d + C_{VM} \rho_c) D_b^2}{\mu_c (1 + 0.15 \text{Re}_D^{0.687})}. \quad (10)$$

Closure is provided by the $k-\epsilon$ model which is used to calculate τ_c and $\overline{\mathbf{u}'_c \mathbf{u}'_c}$. The eddy relaxation time based on the $k-\epsilon$ model is,

$$\tau_c = C_\mu^{3/4} k / \epsilon. \quad (11)$$

Another important effect influencing dispersion is eddy cross over. It is characterized by the time scale $\tau_R = \lambda / |\mathbf{u}_r|$ [5,19], where λ is the Eulerian length scale of the eddies. Estimating this length scale with the $k-\epsilon$ model mixing length it is concluded that, $\tau_R \ll \tau_c$, which implies that eddy cross over has a negligible effect on dispersion [5,19].

The normal Reynolds stress components in Eq. (9) may be obtained from $k = \text{trace}(\overline{\mathbf{u}'_c \mathbf{u}'_c})$. However, for a jet the transverse components are approximately one half the value of the axial component. Specifically, Lopez de Bertodano [5] shows that in the limit of very small particles or bubbles it is possible to reduce the two-fluid conservation of mass and momentum equations of the dispersed phase to a single "convection-diffusion" conservation of mass equation with the diffusivity given by:

$$v_{dij} = \tau_c \overline{v'_{ci} v'_{cj}}. \quad (12)$$

The normal Reynolds stresses are modeled as:

$$\overline{v'_{ci} v'_{cj}} = c_{ij} k. \quad (13)$$

The time constant of the turbulent eddies according to the $k-\epsilon$ model is:

$$\tau_c = 0.165 k / \epsilon. \quad (14)$$

The diagonal components of diffusivity are obtained combining these three equations:

$$v_{dij} = 0.165 c_{ij} k^2 / \epsilon. \quad (15)$$

Comparing this to the $k-\epsilon$ model definition of turbulent diffusivity $v_i = c_\mu k^2 / \epsilon$, and assuming the Schmidt number is unity, one obtains that $c_{ij} = c_\mu / 0.165 = 0.545$. Thus, the transverse normal Reynolds stresses are modeled as

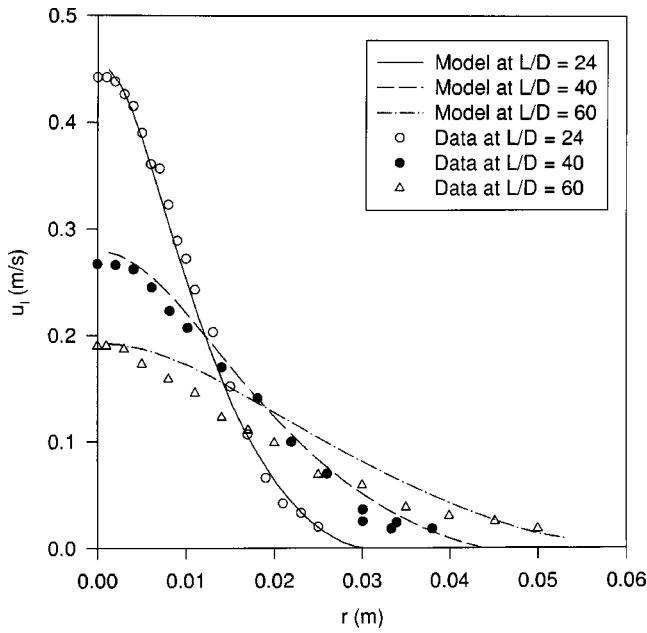


Fig. 1 Average liquid velocity

$$\overline{u'_c u'_c} = 0.545k \quad (16)$$

so that the diffusivity of the bubbles matches the diffusivity of momentum in the $k - \epsilon$ model in the limit when the bubbles are so small that they behave as tracers [5].

3.2 Simulations. Case-I of the data of Sun [8] was selected to test the two-fluid model. This is the case with the lowest bubble flow rate and thus, the turbulence modulation by the bubbles is negligible. The bubbly jet was injected vertically upward from a 5.08 mm nozzle into a still water tank. The bubbles had a diameter of (1 ± 0.11) mm. The inlet jet velocity was 1.65 m/s and the void fraction was 2.4%. Mean and fluctuating properties of both phases were measured using a LDA system while bubble concentration was measured using flash photography. Data were measured at $x/D = 24, 40, 60$.

It was assumed that the mean flow is steady, axisymmetric, incompressible and isothermal, and that both phases have constant physical properties. The governing two-fluid model equations were solved numerically using the PHOENICS code. The equations were discretized on a uniform cylindrical grid, 80 jet diameters long and 20 jet diameters in diameter, using a finite volume procedure. The elliptic formulation implies that conditions at all the boundaries, including the downstream one, need to be specified. The boundary condition on the wall of the cylinder is the free stream condition (i.e., the gradients of the velocities are zero). At the top of the cylinder, the pressure is atmospheric and the boundary conditions at the inlet are specified from the known inflow conditions. Preliminary simulations were performed to test for numerical convergence. The mesh spacing was halved repeatedly until the solution stopped changing. Numerical convergence was achieved for an 80×80 grid.

Another preliminary adjustment was performed because of the well known fact that the standard $k - \epsilon$ model does not fit the data for single-phase axisymmetric jets very closely. Sun and Faeth [11] modified one of the constants in the model, $C_{\epsilon 2}$, from 1.92 to 1.87. This correction has been applied in the present simulation [5]. Figures 1 and 2 show the liquid velocity and turbulent kinetic energy profiles at three axial positions. These results are essentially the same as the single-phase profiles because the void fraction is very low. Therefore they do not reflect any effect due to changes in the bubble interfacial forces. On the other hand the liquid field has a strong effect on these forces (i.e., the lift force is

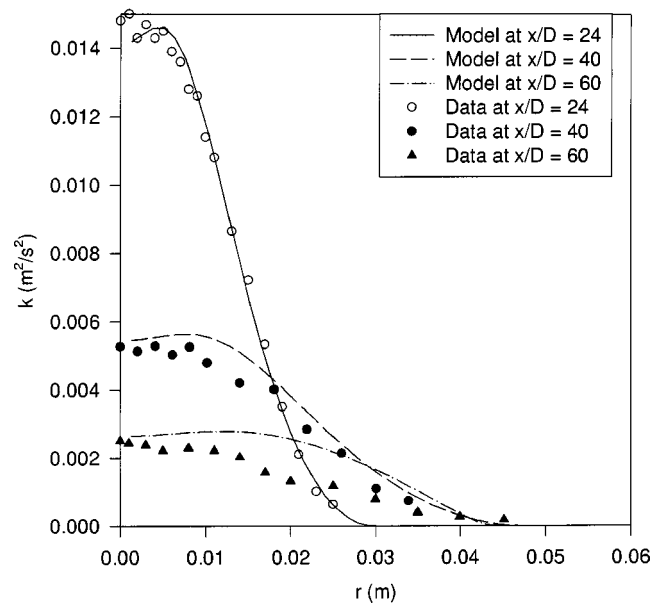


Fig. 2 Kinetic energy of the turbulence

proportional to the vorticity of the liquid flow and the turbulence diffusion force is proportional to the turbulence intensity). Since there is good agreement between the simulation and the liquid flow data the interfacial forces may be assessed properly. The model, described in Section 3, produced too much lateral migration of the bubbles (Fig. 3). After inspection of the solution it was found that near the jet nozzle the drag force (i.e., Eq. (6)) was too small compared to the data (Figs. 4 and 5). It is known that particles in a turbulent fluid have significantly lower relative velocities compared to a still fluid. Brucato et al. [9] were able to correlate their relative velocity data, as well as other's, with:

$$C_D = C_{D\infty} \left[1 + 8.76 \times 10^{-4} \left(\frac{D_b}{\lambda_K} \right)^3 \right] \quad (17)$$

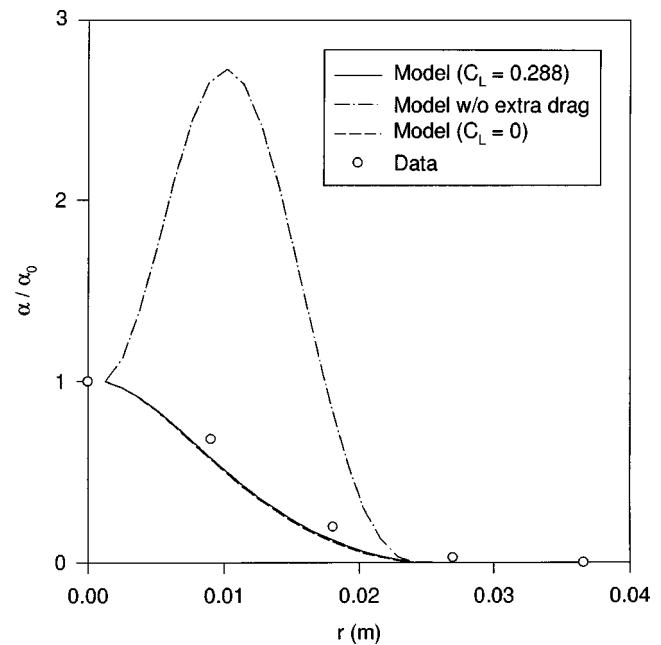


Fig. 3 Normalized void fraction with and without correction for drag modulation by turbulence ($x/D = 24$)

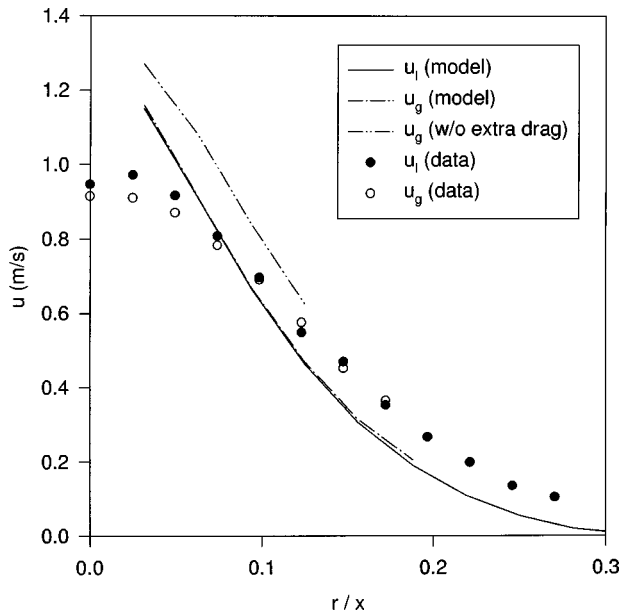


Fig. 4 Average bubble and liquid velocity ($x/D=8$)

where the Kolmogorov length scale of the turbulence is defined as:

$$\lambda_K = \left(\frac{\nu^3}{\epsilon} \right)^{1/4} \quad (18)$$

The void fraction distribution is much closer to the data once this correction is performed. Figure 3 shows that the decrease of the relative velocity has a significant effect in the drift of the bubbles near the nozzle. Figure 4 shows that very near the nozzle ($x/D=8$) the measured relative velocity is practically zero as predicted by Eq. (17). At $x/D=24$, Fig. 5, Eq. (17) predicts the relative velocity correctly near the centerline but not so in the periphery. As a consequence the radial dispersion of the bubbles is also slightly underpredicted. Finally, Fig. 6 shows that the agreement

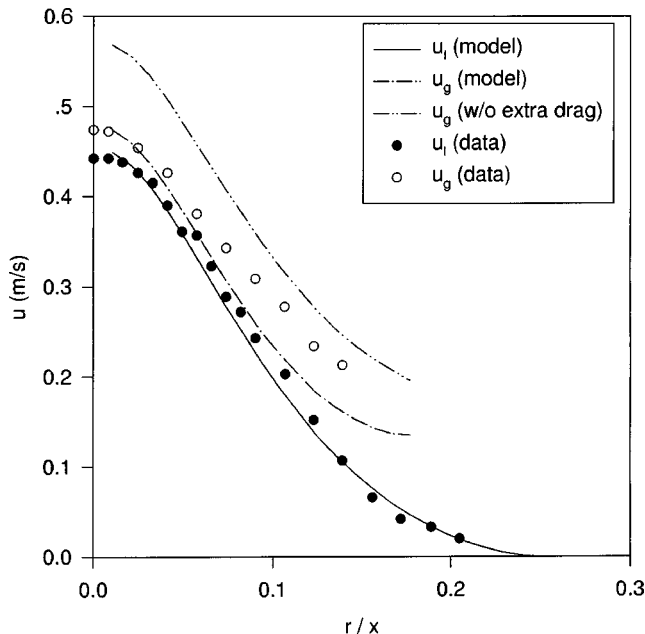


Fig. 5 Average bubble and liquid velocity ($x/D=24$)

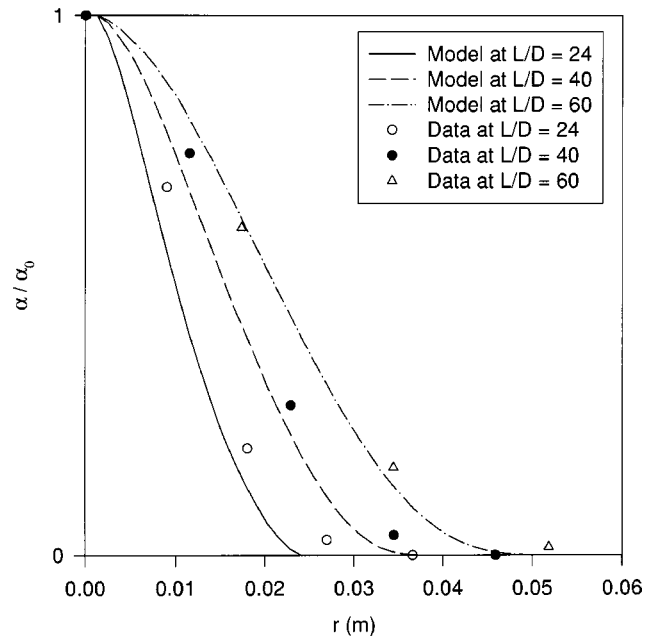


Fig. 6 Final normalized void fraction predictions

of the void fraction distribution predicted by the model and the data along the jet is satisfactory.

It is important to note that once the relative velocity has been corrected, the effect of lift becomes negligible. Figure 3 shows that the calculation results with $C_L=0.288$ and 0 are practically the same. This brings another point: the similarity between the present results and those of Sun and Faeth [11]. It has already been mentioned that our calculations use the same the $k-\epsilon$ model, and in general the same Eulerian formulation for the continuous phase. However, Sun and Faeth used a Lagrangian formulation for the dispersed phase. The other difference is that they did not consider the lift force, but since it is negligible, the results validate the assertion that the present Eulerian formulation is as accurate as the Lagrangian analysis.

4 Conclusions

Simulations of a bubbly jet for which the dominant forces on bubbles are buoyancy, drag, turbulent dispersion and lift were conducted. In particular the turbulent dispersion correlation developed by Lopez de Bertodano [5] was successfully applied here.

It was found that at the jet entrance considerable modulation of the drag coefficient by the turbulence exists. Once the model of [9] is introduced to account for this modulation, good agreement with data was found. Results are insensitive to the value of the lift coefficient in the range, $0 < C_L < 0.29$, where the upper bound correspond to the correlation developed by Tomiyama [13]. It should be noted that the rigorously derived models for turbulent dispersion are applied without any arbitrary constants, except for a few simplifying assumptions discussed in the paper. Equation (17), which is an empirical model, is the largest source of uncertainty in these results.

References

- [1] Drew, D. A., 2001, "A Turbulent Dispersion Model for Particles or Bubbles," *J. Eng. Math.*, **41**(2-3), NOV pp. 259-274.
- [2] Reeks, M. W., 1993, "On the Constitutive Relations for Dispersed Particles in Nonuniform Flows. I: Dispersion in a Simple Shear Flow," *Phys. Fluids A*, **5**(3), pp. 750-761.
- [3] Reeks, M. W., 1992, "On the Continuum Equations for Dispersed Bubbles in Non-Uniform Flows," *Phys. Fluids A*, **4**(6), pp. 1290-1302.
- [4] Reeks, M. W., 1991, "On a Kinetic Equation for the Transport of Bubbles in Turbulent Flows," *Phys. Fluids A*, **3**(3), pp. 446-456.

- [5] Lopez de Bertodano, M., 1998, "Two Fluid Model for Two-Phase Turbulent Jet," *Nucl. Eng. Des.*, **179**, pp. 65–74.
- [6] Moraga, F. J., Larretéguy, A. E., Drew, D. A., and Lahey, R. T., Jr., 2001, "Assessment of Turbulent Dispersion Models for Bubbly Flows," Paper 379, 4th International Conference on Multiphase Flow, New Orleans LA, USA.
- [7] Moraga, F. J., Larretéguy, A. E., Drew, D. A., and Lahey, Jr., R. T., 2003, "Assesment of Turbulent Dispersion Models for Bubbly Flow in the Low Stokes Number Limit," *Int. J. Multiphase Flow*, **29**(4), pp. 655–673.
- [8] Sun, T.-Y., 1985, "A Theoretical and Experimental Study on Noncondensable Turbulent Bubbly Jets," Ph.D. Dissertation, The Pennsylvania State University, University Park, PA.
- [9] Brucato, A., Grisafi, F., and Montante, G., 1998, "Particle Drag Coefficients in Turbulent Fluids," *Chem. Eng. Sci.*, **53**(18), pp. 3295–3314.
- [10] Kurose, R., and Komori, S., 1999, "Drag and Lift Forces on a Rotating Sphere in Laminar Shear Flows," *J. Fluid Mech.*, **384**, pp. 183–206.
- [11] Sun, T.-Y., and Faeth, G. M., 1986, "Structure of Turbulent Bubbly Jets -I. Methods and Centerline Properties, -II. Phase Property Profiles," *Int. J. Multiphase Flow*, **12**, pp. 99–126.
- [12] Drew, D. A., and Passman, S. L., 1998, *Theory of multicomponent fluids*, App. Math. Sci. **135**, Springer.
- [13] Tomiyama, A., 1998, "Struggle With Computational Bubble Dynamics," *Third Int. Conf. on Multiphase Flows, ICMF'98*, Lyon, France.
- [14] Ishii, M., 1987, *Two-Fluid Model for Two-Phase Flow*, 2nd Int. Workshop on Two-Phase Flow Fundamentals, Rensselaer Polytechnic Institute, Troy, NY.
- [15] Auton, T. R., 1987, "The Lift Force on a Spherical Body in a Rotational Flow," *J. Fluid Mech.*, **183**, pp. 199–213.
- [16] Legendre, D., and Magnaudet, J., 1998, "The Lift Force on a Spherical Bubble in Viscous Linear Flow," *J. Fluid Mech.*, **368**, pp. 81–126.
- [17] Bagchi, P., and Balachandar, P., 2002, "Effect of Free Rotation on the Motion of a Solid Sphere in Linear Shear Flow at Moderate Re," *Phys. Fluids*, **14**, pp. 2719–2737.
- [18] Naciri, M. A., 1992, "Contribution a l'etude des forces exercees por un liquide sur une bulle de gaz, masse ajoutee et interactions hydrodynamiques," Ph.D. Thesis, L'Ecole Central de Lyon, Lyon, France.
- [19] Loth, E., 2001, "An Eulerian Turbulent Diffusion Model for Particles and Bubbles," *Int. J. Multiphase Flow*, **27**, pp. 1051–1063.

Hiroiyuki Takahira*

Associate Professor
e-mail: takahira@energy.osakafu-u.ac.jp
Department of Energy Systems Engineering,
Osaka Prefecture University
1-1 Gakuen-cho, Sakai,
Osaka 599-8531, Japan

Tomonori Horiuchi

e-mail: horiuchi@fluid.energy.osakafu-u.ac.jp
Graduate School of Osaka Prefecture University
1-1 Gakuen-cho, Sakai,
Osaka 599-8531, Japan

Sanjoy Banerjee

Professor
e-mail: banerjee@engineering.ucsb.edu
Department of Chemical Engineering,
University of California
Santa Barbara, CA 93106, USA

An Improved Three-Dimensional Level Set Method for Gas-Liquid Two-Phase Flows

For the present study, we developed a three-dimensional numerical method based on the level set method that is applicable to two-phase systems with high-density ratio. The present solver for the Navier-Stokes equations was based on the projection method with a non-staggered grid. We improved the treatment of the convection terms and the interpolation method that was used to obtain the intermediate volume flux defined on the cell faces. We also improved the solver for the pressure Poisson equations and the reinitialization procedure of the level set function. It was shown that the present solver worked very well even for a density ratio of the two fluids of 1:1000. We simulated the coalescence of two rising bubbles under gravity, and a gas bubble bursting at a free surface to evaluate mass conservation for the present method. It was also shown that the volume conservation (i.e., mass conservation) of bubbles was very good even after bubble coalescence. [DOI: 10.1115/1.1777232]

Introduction

Direct numerical simulations of two-phase fluids are very useful for complementing difficult experiments on the interactions between turbulent flows and phase change at boundaries e.g., convective condensation, boiling and electrochemical gas generation. There are several numerical methods to treat the interface of two-phase fluids, such as the VOF method [1] and the Front Tracking method [2,3]. One useful method among these is the level set method. The level set method is based on an Eulerian formulation that describes the interface by the zero level of a Lipschitz-continuous function [4–11]. The interface is captured implicitly on an Eulerian grid by the zero level set. Recently, the level set method was used with the ghost fluid method [12] to capture sharp interfaces. There are many advantages to such a formulation. However, the level set method has been applied mainly to two-dimensional, and two-dimensional axisymmetric problems, and little work has been done on three-dimensional problems for two-phase flows with high-density ratio. In the three-dimensional level set method, it is difficult to analyze two-phase fluids with high-density ratio due to numerical instability near the interface. Mass conservation of two fluid systems is another difficulty [11]. The overall objectives of this study are to develop a three-dimensional numerical method based on the level set formulation for two-phase systems with high-density ratio in curvilinear coordinates, and improve mass conservation.

The present solver for the Navier-Stokes equations is based on the numerical scheme developed by Zang et al. [13]. They used a fractional step method (Projection Method) with a non-staggered grid in which the volume flux is defined on its corresponding face of the cell in addition to the Cartesian velocity components at the cell center. This non-staggered grid was used to calculate the flow field in curvilinear coordinates with high accuracy and a small amount of memory.

When we applied the above numerical method developed for single-phase incompressible flow to two-phase flow, serious numerical instability was found when the density ratio was high. The main reason for the instability was the interpolation method for

cell faces and the solver for the pressure Poisson equation. Therefore, to analyze two-phase systems, we improved the treatment of the convection terms and the interpolation method that was used to obtain the intermediate volume flux defined on the cell faces. We also improved the solver for the pressure Poisson equations. To achieve mass conservation in two fluid systems, we also improved the reinitialization procedure developed by Sussman et al. [8].

Numerical Method

Basic Equations. The Navier-Stokes equations are written to consider variable density and viscosity of the fluid, which allows consideration of multiphase systems, and gives rise to sharp changes in viscosity and density at interfaces. The governing equations in the present study are:

$$\frac{\partial u_j}{\partial x_j} = 0, \quad (1)$$

$$\rho(\varphi) \frac{\partial u_i}{\partial t} + \rho(\varphi) \frac{\partial}{\partial x_j} (u_j u_i) = - \frac{\partial p}{\partial x_i} + \frac{\partial \tau_{i,j}}{\partial x_j} - \left(\sigma \kappa(\varphi) \delta(\varphi) \frac{\partial \varphi}{\partial x_i} \right) - \rho(\varphi) g \delta_{i,3}, \quad (2)$$

where

$$\tau_{i,j} = \mu(\varphi) \left(\frac{\partial u_i}{\partial x_j} + \frac{\partial u_j}{\partial x_i} \right), \quad \kappa(\varphi) = \frac{\partial n_j}{\partial x_j}, \quad n_i = \frac{\partial \varphi}{|\nabla \varphi|}, \quad (3)$$

where u is the velocity component, ρ the density, p the pressure, σ the surface tension, μ the viscosity, g the gravitational acceleration, δ the delta function, and $\delta_{i,j}$ the Kronecker's delta. Gravity acts in the $-z$ direction. φ is the distance function from the interface and is called the level set function. Before developing the code for two-phase flows, we developed the code for single-phase incompressible flows using the conservative form in which the density was omitted. This was changed to the form of the left-hand side of Eq. (2) to extend the code to two-phase conditions.

Introducing the following dimensionless variables,

*Corresponding author.

Contributed by the Fluids Engineering Division for publication in the JOURNAL OF FLUIDS ENGINEERING. Manuscript received by the Fluids Engineering Division March 27, 2003; revised manuscript received November 8, 2003. Associate Editor: M. J. Andrews.

$$x_i = L_0 x'_i, \quad u_i = U_0 u'_i, \quad t = (L_0/U_0)t', \quad p = p' \rho_l U_0^2,$$

$$\rho = \rho_l \rho', \quad \mu = \mu_l \mu',$$

and substituting these variables into Eq. (2), and dropping the primes, we have

$$\begin{aligned} \rho(\varphi) \frac{\partial u_i}{\partial t} + \rho(\varphi) \frac{\partial}{\partial x_j} (u_j u_i) = & -\frac{\partial p}{\partial x_i} + \frac{1}{\text{Re}} \frac{\partial \tau_{i,j}}{\partial x_j} \\ & - \left(\frac{1}{\text{We}} \kappa(\varphi) \delta(\varphi) \frac{\partial \varphi}{\partial x_i} \right) - \rho(\varphi) \frac{\delta_{i,3}}{\text{Fr}}. \end{aligned} \quad (4)$$

The dimensionless groups used above are the Reynolds number, the Weber number and the Froude number. These are given, respectively, by

$$\text{Re} = \frac{\rho_l L_0 U_0}{\mu_l}, \quad \text{We} = \frac{\rho_l L_0 U_0^2}{\sigma}, \quad \text{Fr} = \frac{U_0^2}{gL_0},$$

where L_0 and U_0 are the characteristic length and velocity, respectively. The dimensionless density and viscosity are function of φ and are given, respectively, as

$$\rho(\varphi) = \{\lambda + (1-\lambda)H(\varphi)\}, \quad (5)$$

$$\mu(\varphi) = \{\eta + (1-\eta)H(\varphi)\}, \quad (6)$$

where $\lambda = \rho_g/\rho_l$ and $\eta = \mu_g/\mu_l$. H is a smoothed Heaviside function and is written as

$$H(\varphi) = \begin{cases} 0 & \text{if } \varphi < -\varepsilon \\ \frac{1}{2} \left\{ 1 + \frac{\varphi}{\varepsilon} + \frac{1}{\pi} \sin(\pi\varphi/\varepsilon) \right\} & \text{if } -\varepsilon \leq \varphi \leq \varepsilon \\ 1 & \text{if } \varphi > \varepsilon, \end{cases}$$

ε is the thickness of the interface and is taken to be $\alpha \times h$ where h is the grid spacing. α is taken to be 2 in the present calculation. The smoothed delta function $\delta(\varphi)$ is defined as $dH(\varphi)/d\varphi$. The viscous terms are separated into two terms as

$$\begin{aligned} \frac{1}{\rho(\varphi)} \frac{\partial \tau_{i,j}}{\partial x_j} &= \frac{1}{\rho(\varphi)} \frac{\partial}{\partial x_j} \left\{ \mu(\varphi) \left(\frac{\partial u_i}{\partial x_j} + \frac{\partial u_j}{\partial x_i} \right) \right\} \\ &= \frac{1}{\rho(\varphi)} \frac{\partial}{\partial x_j} \left\{ \mu(\varphi) \left(\frac{\partial u_i}{\partial x_j} \right) \right\} + \frac{1}{\rho(\varphi)} \frac{\partial}{\partial x_j} \left\{ \mu(\varphi) \left(\frac{\partial u_j}{\partial x_i} \right) \right\}. \end{aligned} \quad (7)$$

The second term on the right-hand side of Eq. (7) has non-zero values only near the interface because μ is constant far from the interface.

The level set function is obtained by solving the following equation:

$$\frac{\partial \varphi}{\partial t} + u_j \frac{\partial \varphi}{\partial x_j} = 0. \quad (8)$$

Discretization. The present solver for the Navier-Stokes equations is based on the numerical scheme developed by Zang et al. [13] and Zang and Street [14]. Their solution method was developed for the incompressible Navier-Stokes equations for single-phase flow in general curvilinear co-ordinates. The continuity equation is, for example, transformed into a general curvilinear co-ordinate system in "strong conservation law" form as,

$$\frac{\partial U_m}{\partial \xi_m} = 0, \quad (9)$$

where $m = 1, 2, 3$, the volume flux U_m and the Jacobian J are given by

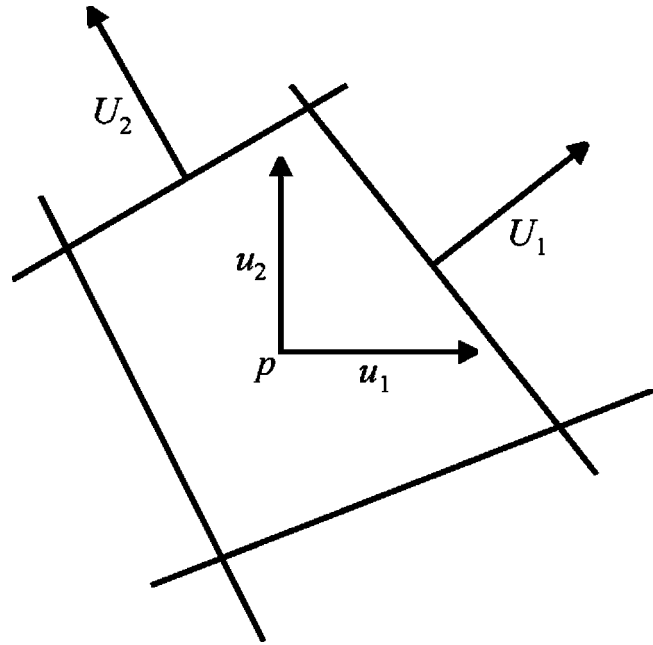


Fig. 1 Non-staggered grid.

$$U_m = J^{-1} \frac{\partial \xi_m}{\partial x_j} u_j, \quad J^{-1} = \det \left(\frac{\partial x_i}{\partial \xi_j} \right). \quad (10)$$

They used a non-staggered grid to discretize the governing equations. As is well known, solution methods for the incompressible N-S equations based on a traditional non-staggered grid, in which all the variables are defined only at the cell center, produce spurious oscillations in the pressure field, i.e., "checkerboard" patterns [15]. One of the fundamental causes is that, in a traditional non-staggered grid, a straightforward discretization of the continuity equation does not enforce mass conservation in the cell and causes decoupling of the pressure field. To prevent decoupling, in the non-staggered grid, the volume flux is defined on its corresponding face of the cell in addition to the Cartesian velocity components at the cell center as in Fig. 1. Therefore, both the momentum and the continuity equations are enforced in the same control volume. Also, this non-staggered grid is useful in analysis using curvilinear coordinates with high accuracy and a small amount of computer memory.

In the present two-phase code, we used the same non-staggered grid. Although our present solver is written for the Cartesian coordinate system with unequal spacing, to simplify the presentation of the discretized equation, the following formulation is restricted to the Cartesian co-ordinate system with equal spacing. We also use u_i as the Cartesian velocity components and U_i as the volume flux (the velocity on the cell face in the Cartesian coordinates) to distinguish both of them.

We use a semi-implicit time-advancement scheme with the Adams-Bashforth method for the explicit terms and the Crank-Nicolson scheme for the implicit terms. A fractional step method (Projection Method) is used to solve the N-S equations.

The discretized equations are written as:

$$\frac{\delta U_j}{\delta x_j} = 0, \quad (11)$$

$$\begin{aligned} \frac{u_i^{n+1} - u_i^n}{\Delta t} &= \frac{3}{2} (C_i^n + D_{Ei}^n) - \frac{1}{2} (C_i^{n-1} + D_{Ei}^{n-1}) + R_i(p^{n+1}) \\ &+ \frac{1}{2} (D_j(u_i^{n+1} + u_i^n)) + F_i^{n+1}, \end{aligned} \quad (12)$$

where $\delta/\delta x_j$ denotes the discrete finite difference operator, superscripts represent the time step, C_i is the convection term, R_i is the discrete operator for the pressure gradient terms and D_{Ei} is the explicitly treated viscous terms and D_I is the discrete operator representing the implicitly treated viscous terms, F_i is the sum of the surface tension term and the gravity term. C_i , R_i , D_I and D_{Ei} are given, respectively by

$$C_i = -\frac{\delta}{\delta x_j}(U_j u_i), \quad R_i = -\frac{1}{\rho(\varphi)}\left(\frac{\delta}{\delta x_j}\right),$$

$$D_I = \frac{1}{\rho(\varphi)\text{Re}} \frac{\delta}{\delta x_j} \left\{ \mu(\varphi) \left(\frac{\delta}{\delta x_j}\right) \right\},$$

$$D_{Ei} = \frac{1}{\rho(\varphi)\text{Re}} \frac{\delta}{\delta x_j} \left\{ \mu(\varphi) \left(\frac{\delta u_j}{\delta x_j}\right) \right\}.$$

Application of the fractional step method to Eq. (12) leads to the following predictor-corrector solution procedure.

1. Predictor

$$\left(I - \frac{\Delta t}{2} D_I\right)(u_i^* - u_i^n) = \Delta t \left[\frac{3}{2}(C_i^n + D_{Ei}^n) - \frac{1}{2}(C_i^{n-1} + D_{Ei}^{n-1}) + D_I(u_i^n) + F_i^{n+1} \right], \quad (13)$$

2. Corrector

$$u_i^{n+1} - u_i^* = \Delta t [R_i(\psi^{n+1})], \quad (14)$$

where I is the identity matrix and u_i^* is called the intermediate velocity. The variable ψ is related to the pressure p as

$$R_i(p) = \left(I - \frac{\Delta t}{2} D_I\right) R_i(\psi), \quad (15)$$

hereafter ψ is referred as the 'pressure.'

We discretize the convection terms C_i using the 2nd-order ENO scheme [8].

The first viscous term of the RHS of Eq. (7) is discretized implicitly using the Crank-Nicolson scheme as:

$$\frac{1}{\rho(\varphi)} \frac{\partial}{\partial x_j} \left\{ \mu(\varphi) \left(\frac{\partial u_i}{\partial x_j}\right) \right\} \cong \frac{1}{2} \left[\frac{1}{\rho^{n+1}} \frac{\delta}{\delta x_j} \left\{ \mu^{n+1} \left(\frac{\delta u_i^*}{\delta x_j}\right) \right\} + \frac{1}{\rho^n} \frac{\delta}{\delta x_j} \left\{ \mu^n \left(\frac{\delta u_i^n}{\delta x_j}\right) \right\} \right]. \quad (16)$$

On the other hand, the second term of the RHS of Eq. (7) is discretized explicitly. Second-order central differences are used to calculate viscous terms. It should be noted that we can obtain φ , ρ and μ at time $t = t^{n+1}$ by solving Eq. (8) before calculating the N-S equations.

The surface tension terms are discretized using φ at $t = t^{n+1}$ as:

$$\frac{1}{\rho(\varphi)} \left(\sigma \kappa(\varphi) \delta(\varphi) \frac{\partial \varphi}{\partial x_i} \right) \cong \frac{1}{\rho^{n+1}} \left(\sigma \kappa^{n+1} \delta^{n+1} \frac{\delta \varphi^{n+1}}{\delta x_i} \right). \quad (17)$$

Second-order central differences are used for the surface tension terms.

Equation (13) is solved with the approximate factorization technique in which the LHS of Eq. (13) is factorized into the tridiagonal matrices as

$$\left(I - \frac{\Delta t}{2} D_1\right) \left(I - \frac{\Delta t}{2} D_2\right) \left(I - \frac{\Delta t}{2} D_3\right) (u_i^* - u_i^n) = \text{RHS of (13)}, \quad (18)$$

where D_k ($k = 1, 2, 3$) is the discrete one-dimensional diagonal viscous operator and $D_I = D_1 + D_2 + D_3$.

To update the velocity components at the cell center, the pressure gradient in Eq. (14) is discretized as

$$R_i(\psi^{n+1}) \cong -\frac{1}{2} \left(\frac{1}{\rho_{i-1/2}^{n+1}} \frac{\psi_i^{n+1} - \psi_{i-1}^{n+1}}{\Delta x_i} + \frac{1}{\rho_{i+1/2}^{n+1}} \frac{\psi_{i+1}^{n+1} - \psi_i^{n+1}}{\Delta x_i} \right). \quad (19)$$

When we use the standard central difference:

$$R_i(\psi^{n+1}) \cong -\frac{1}{\rho_i^{n+1}} \frac{\psi_{i+1/2}^{n+1} - \psi_{i-1/2}^{n+1}}{\Delta x_i}, \quad (20)$$

numerical oscillations occur when the density ratio is high although the Eqs. (19) and (20) are identical with each other if the density is constant. After correcting step (14) the volume flux on the cell face ($= U_i^{n+1}$) is updated with

$$U_i^{n+1} = U_i^* - \Delta t \left(\frac{1}{\rho^{n+1}} \frac{\delta \psi^{n+1}}{\delta x_i} \right) \cong U_i^* - \frac{\Delta t}{\rho_{i+1/2}^{n+1}} \frac{\psi_{i+1}^{n+1} - \psi_i^{n+1}}{\Delta x_i}, \quad (21)$$

where U_i^* is the intermediate volume flux defined on the cell faces. The discretization with Eq. (21) is consistent with Eq. (19). To calculate U_i^* , the value of u_i^* which is defined at the cell center is interpolated onto cell faces with a third-order quadratic upwind interpolation scheme similar to that used in QUICK [13]. However, as shown in a later section, when we use U_i^n to determine the flow direction in the upwind interpolation, numerical oscillations occur when the density ratio of the two fluids is high and surface tension is considered. To avoid this problem, we use the following velocity to determine the flow direction on the cell faces inside the interface for the upwind interpolation scheme:

$$\Delta \tilde{U}_i = -\frac{\Delta t}{\rho^{n+1}} \left(\sigma \kappa^{n+1} \delta^{n+1} \frac{\delta \varphi^{n+1}}{\delta x_i} \right). \quad (22)$$

$\Delta \tilde{U}_i$ is regarded as the velocity increase induced by the pressure gradient due to the surface tension. The flow direction outside the interface is determined from the direction of the volume flux at $t = t^n$ on the cell faces.

Before u_i^{n+1} can be obtained from Eq. (14) or U_i^{n+1} from Eq. (21), we need to solve ψ^{n+1} from the following pressure Poisson equations:

$$\frac{\delta}{\delta x_j} \left(\frac{1}{\rho^{n+1}} \frac{\delta \psi^{n+1}}{\delta x_j} \right) = \frac{1}{\Delta t} \frac{\delta U_j^*}{\delta x_j}. \quad (23)$$

The LHS of Eq. (23) is discretized as

$$\frac{\delta}{\delta x_j} \left(\frac{1}{\rho^{n+1}} \frac{\delta \psi^{n+1}}{\delta x_j} \right) \cong \frac{1}{\Delta x} \left(\frac{1}{\rho_{i+1/2,j,k}^{n+1}} \frac{\psi_{i+1,j,k}^{n+1} - \psi_{i,j,k}^{n+1}}{\Delta x} - \frac{1}{\rho_{i-1/2,j,k}^{n+1}} \frac{\psi_{i,j,k}^{n+1} - \psi_{i-1,j,k}^{n+1}}{\Delta x} \right) + \frac{1}{\Delta y} \left(\frac{1}{\rho_{i,j+1/2,k}^{n+1}} \frac{\psi_{i,j+1,k}^{n+1} - \psi_{i,j,k}^{n+1}}{\Delta y} - \frac{1}{\rho_{i,j-1/2,k}^{n+1}} \frac{\psi_{i,j,k}^{n+1} - \psi_{i,j-1,k}^{n+1}}{\Delta y} \right) + \frac{1}{\Delta z} \left(\frac{1}{\rho_{i,j,k+1/2}^{n+1}} \frac{\psi_{i,j,k+1}^{n+1} - \psi_{i,j,k}^{n+1}}{\Delta z} - \frac{1}{\rho_{i,j,k-1/2}^{n+1}} \frac{\psi_{i,j,k}^{n+1} - \psi_{i,j,k-1}^{n+1}}{\Delta z} \right). \quad (24)$$

Equation (23) is solved using the preconditioned BiCGSTAB (Bi-Conjugate Gradient Stabilized) method [16,17]. We used ILU decompositions (L is lower triangular and U is upper triangular) for the preconditioning. This solver works well for the two fluids with high-density ratio even though the density ratio is 1:10000. When

we previously applied the multigrid method for the pressure Poisson solver, the iteration did not converge when the density ratio λ was less than about 0.05 [18].

The level set equation in Eq. (8) was also solved with the Adams-Bashforth method. The convection terms were discretized with the 2nd-order ENO scheme.

Reinitialization. When we solve the level set equation numerically, the value of φ may be diffused by numerical viscosity and distorted by the flow field. To avoid this problem, we have to construct a new distance function by solving a ‘‘reinitialization equation.’’ The reinitialization of the level set method is important in order to maintain φ as a true distance function, i.e. $|\nabla\varphi|=1$ near $\varphi=0$. This is necessary because of the way the density, viscosity and surface tension are incorporated near the interface. We have improved the reinitialization in order to apply a three-dimensional mesh with unequal spacing. We solve the following equation with constraints [8]

$$\frac{\partial d}{\partial \tau} = S(\varphi)(1 - |\nabla d|) + \Lambda_{i,j,k} f(\varphi) \equiv L(\varphi, d) + \Lambda_{i,j,k} f(\varphi), \quad (25)$$

with the initial conditions

$$d(\vec{x}, \tau=0) = \varphi(\vec{x}), \quad (26)$$

where $S(\varphi)$ is a sign function. $\Lambda_{i,j,k}$ is given as

$$\Lambda_{i,j,k} = - \frac{\int_{\Omega_{i,j,k}} H'(\varphi) L(\varphi, d) d\Omega_{i,j,k}}{\int_{\Omega_{i,j,k}} H'(\varphi) f(\varphi) d\Omega_{i,j,k}}, \quad (27)$$

$$H'(\varphi) = dH/d\varphi, \quad (28)$$

$$f(\varphi) = H'(\varphi) |\nabla\varphi|, \quad (29)$$

where $\Omega_{i,j,k}$ is the grid cell. The last term in Eq. (25) is used to keep the bubble volume constant during the reinitialization procedure. We used the same expression for f as that used in Sussman et al. [8]. Since $|\nabla\varphi|$ is nearly equal to 1 near the interface, the difference between the result obtained by using $f(\varphi) = H'(\varphi)$ and that obtained by using $f(\varphi) = H'(\varphi) |\nabla\varphi|$ may be small. As far as we checked, both expressions gave almost the same results. We solve Eq. (25) until the $|\nabla d|=1$ near the interface and then replace $\varphi(\vec{x})$ by the $d(\vec{x}, \tau^{steady})$ when Eq. (25) converges near the interface for the next time step of Eq. (8). In the present calculation, the convection term in Eq. (25) is discretized using a 2nd-order ENO scheme. The 2nd-order Runge-Kutta method is used in order to advance in τ .

d^{k+1} at $\tau^{k+1} = (k+1)\Delta\tau$ is obtained from the following algorithm [8]:

$$d^{k+1} = \tilde{d}^{k+1} + \tau^{k+1} \Lambda_{i,j,k}(\tilde{d}^{k+1}) f(\varphi), \quad (30)$$

$$\Lambda_{i,j,k}(\tilde{d}^{k+1}) \equiv - \frac{\int_{\Omega_{i,j,k}} H'(\varphi) L(\tilde{d}^{k+1}) d\Omega_{i,j,k}}{\int_{\Omega_{i,j,k}} H'(\varphi) f(\varphi) d\Omega_{i,j,k}}, \quad (31)$$

$$L(\tilde{d}^{k+1}) \equiv (\tilde{d}^{k+1} - \varphi) / \tau^{k+1}, \quad (32)$$

where φ denotes the initial value of d and \tilde{d}^{k+1} denotes the distance function d at $\tau = \tau^{k+1}$ in the Runge-Kutta procedure of Eq. (25) without the constraint term. We used the trapezoid method for the integral in Eq. (31). For the two-dimensional case with equal spacing, the integral in cell is given by

$$\int_{\Omega_{i,j}} Ad\Omega_{i,j} = \frac{h^2}{64} \{A_{i-1,j-1} + A_{i-1,j+1} + A_{i+1,j-1} + A_{i+1,j+1} + 6(A_{i-1,j} + A_{i+1,j} + A_{i,j-1} + A_{i,j+1}) + 36A_{i,j}\}. \quad (33)$$

When we applied this procedure for the bubble merger problem in a later section, about 7% mass was lost. To recover the mass, we add a multiplier of the order of one to the constraint term, and we solve the following equation:

$$d^{k+1} = \tilde{d}^{k+1} + c \tau^{k+1} \Lambda_{i,j,k}(\tilde{d}^{k+1}) f(\varphi), \quad (34)$$

where c is a multiplier of the order one. In the reinitialization procedure, whether the mass increases or decreases in a given cell depends on the interface behavior before modification by the constraint. In the present code, therefore, we check whether the mass increases or decreases due to the constraint in each time step. Since mass increase or decrease due to the reinitialization is dependent on the shape of the interface, and the constraint works to recover mass, a wrong multiplier may increase or decrease mass too much. In general, if mass is lost during the reinitialization without constraint, then the constraint acts so as to increase mass. On the other hand, if mass is gained during the reinitialization without constraint, then the constraint acts so as to decrease mass. Using this characteristic, we determine the multiplier. We let m_{wc} and m_{woc} to be the mass with constraint and without constraint, respectively. We define $\delta m_c = m_{wc} - m_{woc}$. We also define $\delta m_{ca} = m_{wc} - m_a$ where m_a is the actual mass. The multiplier c is obtained from

$$c = \begin{cases} c_1 & \text{if } \delta m_c \geq 0 \text{ and } \delta m_{ca} < 0 \text{ or if } \delta m_c < 0 \text{ and } \delta m_{ca} > 0 \\ c_0 & \text{if } \delta m_c \geq 0 \text{ and } \delta m_{ca} \geq 0 \text{ or if } \delta m_c < 0 \text{ and } \delta m_{ca} \leq 0, \end{cases} \quad (35)$$

where c_0 is taken to be 1.0 in the present calculation. c_1 is taken to be 1.05 and 1.08 for the bubble merger and bubble bursting problems, respectively. We need a larger value of c to recover larger mass. For the bubble bursting problem, we set $c_1 = 1.08$ to recover larger mass than that for the bubble merger problem. The value of c_1 is currently determined from experience, though an adaptive algorithm is under development.

We continue the above iteration until the following criterion is satisfied:

$$E = \frac{\sum_{|d^k| < \varepsilon} |d^{k+1} - d^k|}{M} < \beta \Delta\tau h^2, \quad (36)$$

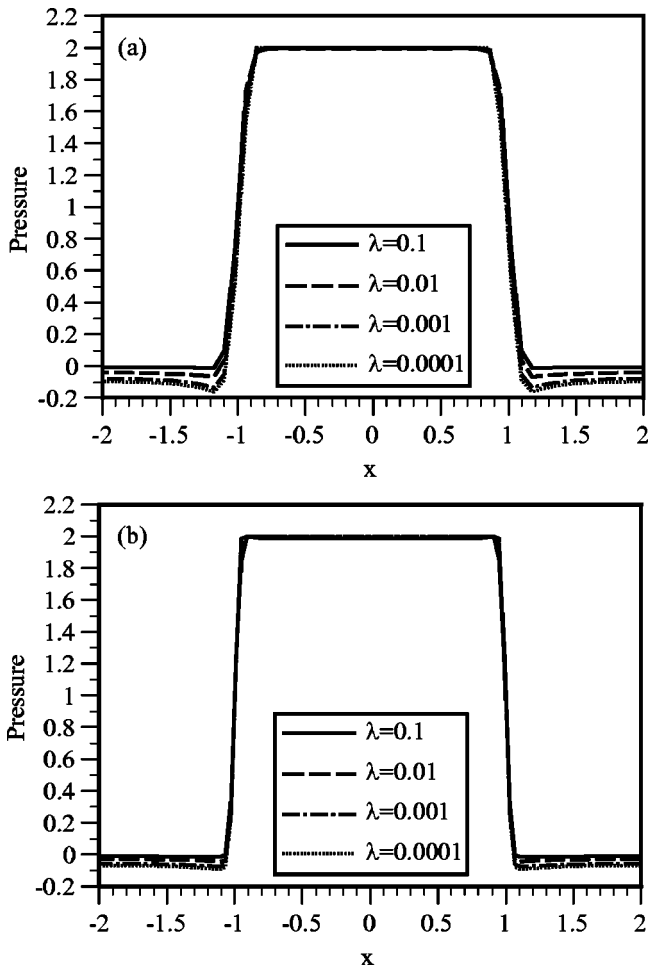


Fig. 2 Influence of density ratio on the pressure distribution: (a) $51 \times 51 \times 51$ mesh, (b) $102 \times 102 \times 102$ mesh.

where M is the number of grid points where $|d^k| < \varepsilon$ and h is the grid spacing. β and $\Delta\tau$ are taken to be 0.1 and $0.5h$ respectively.

Numerical Results and Discussion

Some Numerical Tests. We tested the present solver for some simple problems. Figure 2 shows the influence of the density ratio on the pressure Poisson equations. Test conditions follow. A spherical bubble with unit radius is at rest in the $4 \times 4 \times 4$ cubic box. No-slip boundary conditions are applied to every side of the cube. We set $Re=50$, $We=1$ and $Fr=0$. Therefore, the actual pressure jump at the interface is 2. The time interval Δt is taken to be 0.002. Figure 2 is the pressure distribution at $t=\Delta t$. Solid lines, dashed lines, dashed lines with one dot and dotted lines denote the results when the density ratio $\lambda = \rho_g / \rho_l = 0.1, 0.01, 0.001$ and 0.0001 , respectively. We used $51 \times 51 \times 51$ mesh with equal spacing in Fig. 2(a) and $102 \times 102 \times 102$ mesh with equal spacing in Fig. 2(b), respectively. As the density ratio becomes small in the coarse grid, an undershoot is found near the interface. However, even though the density ratio is 1:10000, the error of the pressure jump is less than about 8%. The finer the mesh becomes, the smaller the undershoot becomes. In Fig. 2(b), the error is less than 5% when the density ratio is 1:10000.

Figure 3 shows the influence of the interpolation method for the intermediate volume flux. Test conditions are the same as Fig. 2 except for $Fr=1$. The pressure contour at $t=0.2$ is shown in Fig. 3. We used 3rd-order upwind quadratic interpolation in every case. However, in Fig. 3(a) the flow direction on the cell faces inside the interface is evaluated with the velocity (volume flux) on

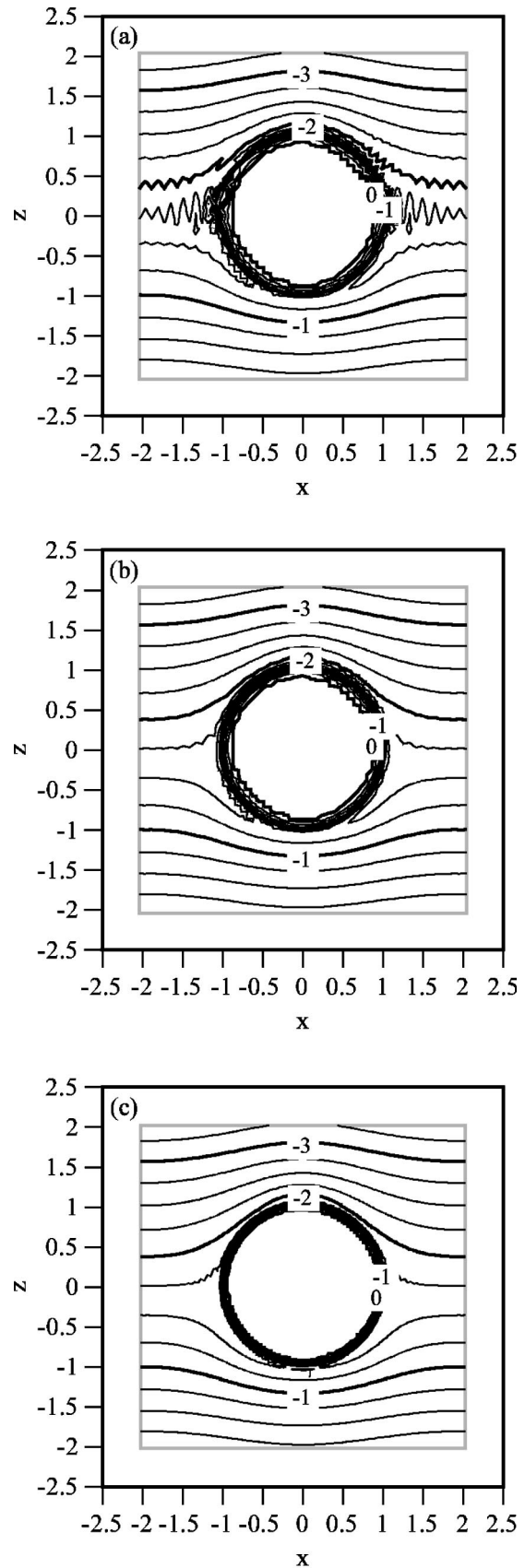


Fig. 3 Influence of interpolation for intermediate volume flux on pressure fields (pressure distribution: $Re=50$, $We=1$, $Fr=1$, $\lambda=0.001$): (a) use U_i^n with $51 \times 51 \times 51$ mesh, (b) use Eq. (22) with $51 \times 51 \times 51$ mesh, (c) use Eq. (22) with $102 \times 102 \times 102$ mesh.

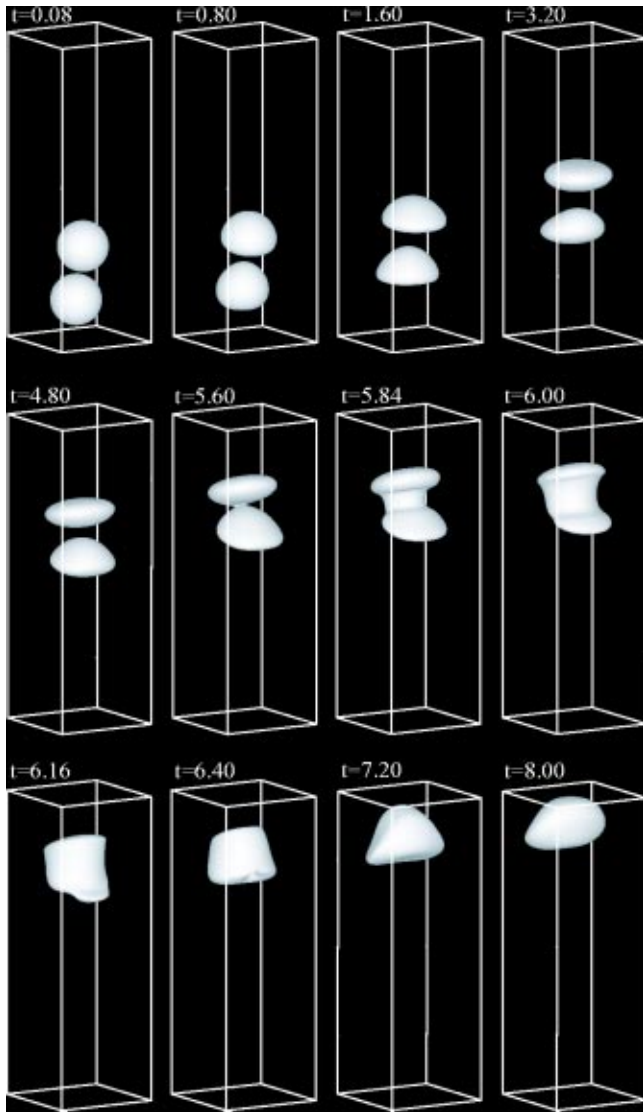


Fig. 4 Merger of two rising bubbles.

cell faces at the previous time step ($=U_i^n$). While in Fig. 3(b) and Fig. 3(c), the flow direction on the cell faces is evaluated with Eq. (22). As evident from Fig. 3(a), serious pressure oscillations appear when using the volume flux at the previous time step. On the other hand, the numerical oscillations diminish when we evaluate the flow direction with Eq. (22). This may be because that the flow direction of the intermediate volume flux is different from the previous time step because the intermediate volume flux is accelerated by the pressure gradient due to the surface tension. Using the finer mesh, the interface is captured more sharply, and the numerical oscillations do not appear.

Merger of Two Rising Bubbles. We simulated bubble coalescence when two bubbles rise in a liquid due to buoyancy. Test conditions are as follows: the computational domain is a $4 \times 4 \times 12$ ($-2 \leq x \leq 2$, $-2 \leq y \leq 2$, $-6 \leq z \leq 6$) rectangular box. Two spherical bubbles with unit radius are initially located at $(x, y, z) = (0.25, 0, -4.5)$ and $(x, y, z) = (-0.25, 0, -2.3)$, respectively. We use $51 \times 51 \times 153$ mesh with equal spacing. No-slip boundary conditions are used on the every side of the box. We set $Re=50$, $We=1.25$ and $Fr=1$. The density ratio, the viscosity ratio, and Δt are taken to be 0.001, 0.01816 and 0.001, respectively. The multiplier c_1 in Eq. (35) is taken to be 1.05.

As evident from Fig. 4, both bubbles assume a cap-like shape at

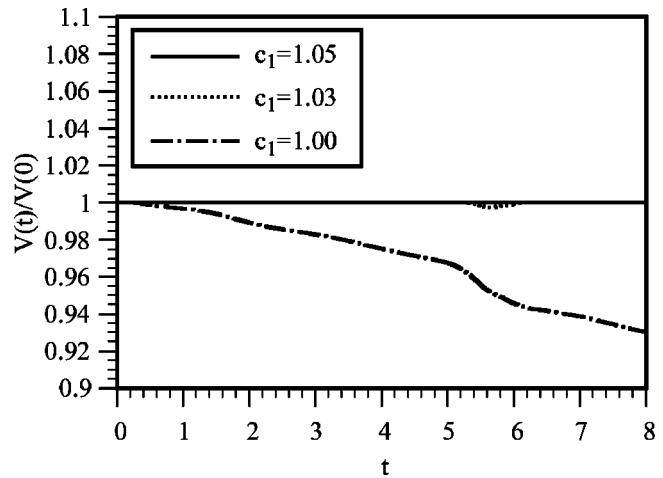


Fig. 5 Volume conservation for two rising bubbles.

about $t=1.6$ and then the upper bubble becomes saucer-shaped. At about $t=5.6$, they merge because the vortex flow created by the upper bubble accelerates the rise velocity of the lower bubble. After coalescence, a depression is found at the bottom surface of the merged bubble.

Time histories of the volume (or mass) of two bubbles are shown in Fig. 5. We compare the influence of the multiplier c in Eq. (34) for the reinitialization procedure, on mass conservation. The volume of bubbles are defined by

$$V(t) = \iiint (1-H) dx dy dz. \quad (37)$$

Solid lines, dotted lines and dashed line with one dot correspond to $c_1=1.05$, $c_1=1.03$ and $c_1=1$, respectively. When $c_1=1$, mass is lost gradually and the final mass becomes about 7% smaller than the initial mass. When $c_1=1.03$, mass conservation is better than when $c_1=1$. In this case, the mass is lost slightly when the distance between the two bubbles becomes short and they merge with each other. The maximum error at that time is about 0.25%. When $c_1=1.05$, mass conservation is very good.

Figures 6(a) and 6(b) show the relative error of bubble volume, $(V(t) - V(0))/V(0) \times 100$, when $c_1=1.05$ and $c_1=1.08$, respectively. Mass conservation is very good in both cases (the maximum error is less than about 0.013%). The result for $c_1=1.05$ is slightly better than that for $c_1=1.08$ although both results are acceptable.

Since the numerical diffusion of the advection terms in the level set equation may affect the mass conservation of bubbles, we compare the results obtained by using the 2nd-order ENO scheme when $c_1=1$ in Fig. 5 with those obtained by using the 3rd-order ENO scheme. As shown in Fig. 7, although the usage of 3rd-order ENO scheme improves mass conservation, the improvement is not enough. This suggests that our treatment for mass conservation is needed even though the higher order scheme is used.

Sussman and Smereka [6] simulated some experiments for rising bubbles by Hnat and Buckmaster [19] using the level set method and obtained different steady state solutions depending on the different initial conditions. Hnat and Buckmaster used a very large tank (150 cm in diameter \times 150 cm in height) to eliminate wall effects, while the typical bubble radius used in the experiments was about 1 cm. Although the influence of the initial conditions on bubble shape is an interesting problem, it is difficult to simulate their experiments correctly with the present code because the computational region becomes too wide. After implementing far-field boundary conditions in the present code, we will compare the numerical results with the experiments by Hnat and Buckmaster, and investigate the influence of initial conditions on the bubble shape in future work.

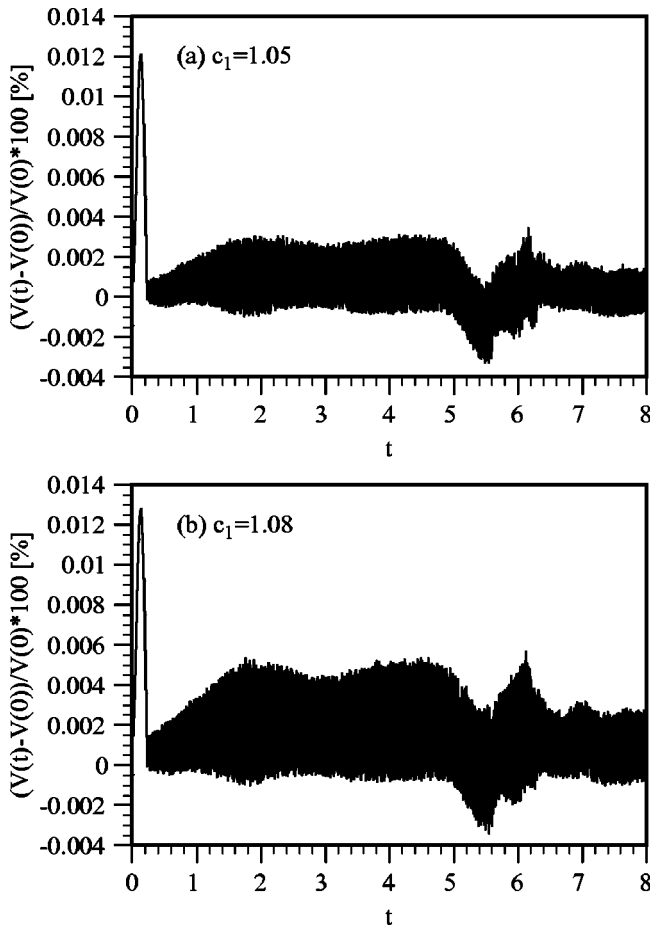


Fig. 6 Relative error of bubble volume for two rising bubbles.

Gas Bubble Bursting at a Free Surface. We also simulated the problem of a gas bubble rising to the free surface of a liquid. Figure 8 shows the evolution of a liquid jet resulting from the submerged gas bubble. The computational domain is a $6 \times 6 \times 12$ ($-3 \leq x \leq 3$, $-3 \leq y \leq 3$, $-6 \leq z \leq 6$) rectangular box. The mesh is $60 \times 60 \times 120$ with equal spacing. A spherical bubble with unit radius is released below the free surface. The initial bubble center is located at $(x, y, z) = (0, 0, -3.2)$. We used periodic

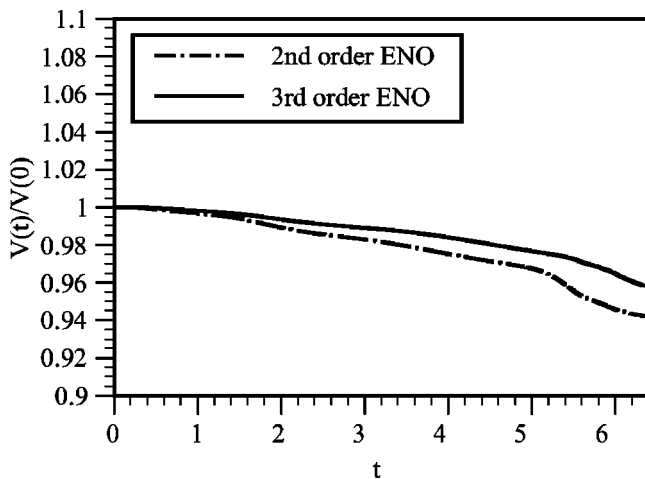


Fig. 7 Influence of numerical diffusion on the volume conservation for two rising bubbles.

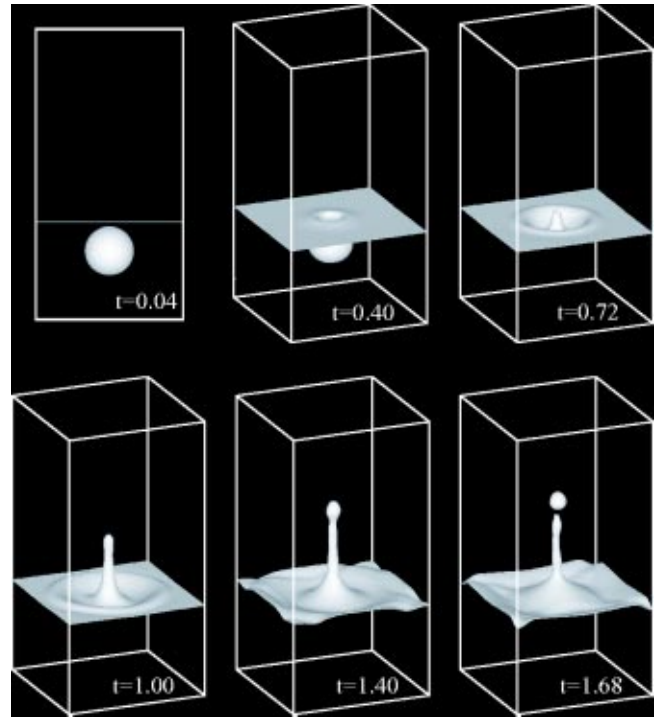


Fig. 8 Evolution of a liquid jet resulting from the submerged gas bubble.

boundary conditions in both the x and y directions. No-slip boundary conditions are used in the z direction. We set $Re = 474$, $We = 1$ and $Fr = 0.64$. The density ratio λ , the viscosity ratio η and the multiplier c_1 are taken to be 0.001, 0.01 and 1.08, respectively. As shown in Fig. 8, the liquid jet starts to break up into a drop at $t = 1.68$.

To check the volume conservation of the calculation, we define the following volume:

$$V_b(t) = V(t) - V_g, \quad (38)$$

where $V(t)$ is the volume of the gas phase in the whole computational region that is obtained from Eq. (37) and V_g is the initial volume of the gas over the free surface that is $6 \times 6 \times 8 = 288$ in the present calculation. Therefore, $V_b(t)$ denotes the volume of the submerged bubble. The time history of $V_b(t)/V_b(0)$ is shown in Fig. 9. As evident in Fig. 9, mass conservation is good. The

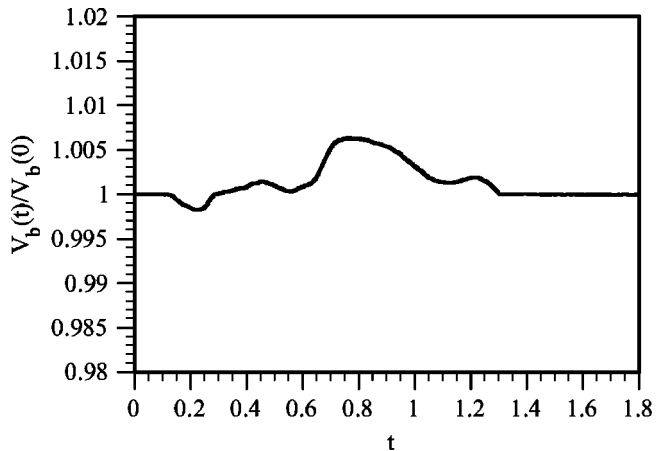


Fig. 9 Volume conservation for the gas bubble bursting at a free surface.

maximum error is about 0.6% in the present calculation. We may need to use a finer mesh to resolve the details of the drop.

Conclusions

We have developed a numerical method for the three-dimensional two-phase flows with unequal spacing based on the level set method. To analyze two-phase systems, we improved the treatment of the convection terms, and the interpolation method that was used to obtain the intermediate volume flux defined on the cell faces. We also improved the solver for the pressure Poisson equations. To achieve mass conservation for two fluid systems, we also improved the reinitialization procedure developed by Sussman et al. [8]. It was shown that the present solver worked very well even though the density ratio of the two fluids was 1:1000. We succeeded in simulating the merger of two rising bubble and the bursting of a submerged gas bubble with good mass conservation.

Nomenclature

C_i	= convection term
c, c_1, c_2	= multiplier for the constraint term
D_{Ei}	= explicitly treated viscous terms
D_I	= discrete operator for the implicitly treated viscous terms
d	= level set function (distance function)
E	= function defined in Eq. (36)
F_i	= sum of the surface tension term and the gravity term
Fr	= Froude number
f	= function defined in Eq. (29)
J	= Jacobian
g	= gravitational acceleration
H	= Heaviside function
h	= grid spacing
L	= $S(\varphi)(1 - \nabla d)$
L_0	= characteristics length
M	= number of grid points where $ d^k < \varepsilon$
m_a	= actual mass
m_{wc}	= mass with constraint
m_{woc}	= mass without constraint
δm_c	= $m_{wc} - m_{woc}$
δm_{ca}	= $m_{wc} - m_a$
n_i	= normal vector
p	= pressure
Re	= Reynolds number
R_i	= discrete operator for the pressure gradient term
S	= sign function
t	= time
U	= volume flux
U^*	= intermediate volume flux
U_0	= characteristics velocity
$\Delta \bar{U}_i$	= velocity increase defined in Eq. (22)
u	= velocity
u^*	= intermediate velocity
V	= volume
V_b	= volume of the submerged bubble
We	= Weber number
x, y, z	= Cartesian coordinates
α	= parameter for ε
β	= constant in Eq. (36)
δ	= delta function
$\delta_{i,j}$	= Kronecker's delta
ε	= thickness of interface ($= \alpha \times h$)
η	= μ_g / μ_l

κ	= curvature
Λ	= constraint
λ	= ρ_g / ρ_l
μ	= viscosity
ξ_1, ξ_2, ξ_3	= curvilinear coordinates
ρ	= density
σ	= surface tension
τ	= viscous stress or iteration time
φ	= level set function (distance function)
ψ	= pressure
Ω	= grid cell

Subscripts

b	= bubble
g	= gas
i, j, k	= grid locations in x, y, z directions
l	= liquid

Superscripts

k	= iteration level
n	= time level
*	= intermediate level
'	= dimensionless quantities

References

- Hirt, C. W., and Nichols, B. D., 1981, "Volume of Fluid (VOF) Method for the Dynamics of Free Boundaries," *J. Comput. Phys.*, **39**, pp. 201–225.
- Unverdi, S. O., and Tryggvason, G., 1992, "A Front-Tracking Method for Viscous, Incompressible, Multi-fluid Flows," *J. Comput. Phys.*, **100**, pp. 25–37.
- Juric, D., and Tryggvason, G., 1998, "Computations of Boiling Flows," *Int. J. Multiphase Flow*, **24**, pp. 387–410.
- Osher, S., and Sethian, J. A., 1988, "Fronts Propagating with Curvature-Dependent Speed: Algorithms Based on Hamilton-Jacobi Formulations," *J. Comput. Phys.*, **79**, pp. 12–49.
- Sussman, M., Smereka, P., and Osher, S., 1994, "A Level Set Approach for Computing Solutions to Incompressible Two-Phase Flow," *J. Comput. Phys.*, **114**, pp. 146–159.
- Sussman, M., and Smereka, P., 1997, "Axisymmetric Free Boundary Problems," *J. Fluid Mech.*, **341**, pp. 269–294.
- Son, G., and Dhir, V. K., 1998, "Numerical Simulation of Film Boiling Near Critical Pressures with a Level Set Method," *ASME J. Heat Transfer*, **120**, pp. 183–192.
- Sussman, M. et al., 1998, "An Improved Level Set Method for Incompressible Two-Phase Flows," *Comput. Fluids*, **27**, pp. 663–680.
- Sussman, M. et al., 1999, "An Adaptive Level Set Approach for Incompressible Two-Phase Flows," *J. Comput. Phys.*, **148**, pp. 81–124.
- Himeno, T., and Watanabe, N., 1999, "Numerical Analysis of Two-Phase Flow under Microgravity Condition," *Trans. Jpn. Soc. Mech. Eng., Ser. B*, **65**, pp. 2333–2340 (in Japanese).
- Sussman, M., and Puckett, E. G., 2000, "A Coupled Level Set and Volume-of-Fluid Method for Computing 3D and Axisymmetric Incompressible Two-Phase Flows," *J. Comput. Phys.*, **162**, pp. 301–337.
- Fedkiw, R. P. et al., 1999, "A Non-Oscillatory Eulerian Approach to Interfaces in Multimaterial Flows (The Ghost Fluid Method)," *J. Comput. Phys.*, **152**, pp. 457–492.
- Zang, Y. et al., 1994, "A Non-staggered Grid, Fractional Step Method for Time-Dependent Incompressible Navier-Stokes Equations in Curvilinear Coordinates," *J. Comput. Phys.*, **114**, pp. 18–33.
- Zang, Y., and Street, R. L., 1995, "A Composite Multigrid Method for Calculating Unsteady Incompressible Flows in Geometrically Complex Domains," *Int. J. Numer. Methods Fluids*, **20**, pp. 341–361.
- Patankar, S. V., 1980, "Numerical Heat Transfer and Fluid Flow," McGraw-Hill/Hemisphere.
- Van der Vorst, H. A., 1992, "Bi-CGSTAB: A Fast and Smoothly Converging Variant of Bi-CG for the Solution of Nonsymmetric Linear Systems," *SIAM (Soc. Ind. Appl. Math.) J. Sci. Stat. Comput.*, **13**, pp. 631–644.
- Fujino, S., and Zhang, S.-L., 1996, "Mathematics of Iterative Methods," Asakura Publishing Company, Tokyo (in Japanese).
- Takahira, H., and Banerjee, S., 2000, "Numerical Simulation of Three Dimensional Bubble Growth and Detachment in a Microgravity Shear Flow," *In Microgravity Fluid Physics and Heat Transfer*, V. Dhir, Ed., pp. 80–87, Begell House, New York, NY.
- Hnat, J. G., and Buckmaster, J. D., 1976, "Spherical cap bubbles and skirt formation," *Phys. Fluids*, **19**, pp. 182–194.

The Characteristics-Based Matching (CBM) Method for Compressible Flow With Moving Boundaries and Interfaces

R. R. Nourgaliev

Adjunct Assistant Professor
e-mail: robert@engineering.ucsb.edu

T. N. Dinh

Adjunct Associate Professor
e-mail: nam@engineering.ucsb.edu

T. G. Theofanous

Professor
e-mail: theo@engineering.ucsb.edu

Center for Risk Studies and Safety,
University of California, Santa Barbara,
6740 Cortona Drive, CA 93117, USA

Recently, Eulerian methods for capturing interfaces in multi-fluid problems become increasingly popular. While these methods can effectively handle significant deformations of interface, the treatment of the boundary conditions in certain classes of compressible flows are known to produce nonphysical oscillations due to the radical change in equation of state across the material interface. One promising recent development to overcome these problems is the Ghost Fluid Method (GFM). The present study initiates a new methodology for boundary condition capturing in multifluid compressible flows. The method, named Characteristics-Based Matching (CBM), capitalizes on recent developments of the level set method and related techniques, i.e., PDE-based re-initialization and extrapolation, and the Ghost Fluid Method (GFM). Specifically, the CBM utilizes the level set function to capture interface position and a GFM-like strategy to tag computational nodes. In difference to the GFM method, which employs a boundary condition capturing in primitive variables, the CBM method implements boundary conditions based on a characteristic decomposition in the direction normal to the boundary. In this way overspecification of boundary conditions is avoided and we believe so will be spurious oscillations. In this paper, we treat (moving or stationary) fluid-solid interfaces and present numerical results for a select set of test cases. Extension to fluid-fluid interfaces will be presented in a subsequent paper. [DOI: 10.1115/1.1778713]

1 Background and Motivation

One of the most popular and successful numerical methods for simulation of compressible fluid dynamics is due to Godunov [1]. The Godunov's method and its recent high-order-accurate extensions (see [2] for a review) incorporate a Riemann problem solution into the numerical procedure for integration of conservative equations of gas dynamics, allowing to construct accurate and robust weak solutions. Within this approach, all fluid discontinuities (i.e., shocks and contact lines) are numerically smeared over a few computational nodes, due to the numerical diffusion embedded naturally into the scheme. While capturing of shock waves is relatively simple, due to the natural self-sharpening mechanism attributed to the physics of shocks, description of *contact discontinuities* is more difficult. The problem is especially challenging in the case of contact discontinuity representing a *multi-material boundary (interface)*.

A common approach in the computation of two-material compressible flows is to define the concentration of one of the materials, say material one, to be Y , describing the fraction of the mass due to material one. Concentration of the material two is $(1 - Y)$, accordingly. Then, the advection equation for Y is constructed and solved, allowing to "capture" a local state of multi-material compressible flow. This approach is utilized in, e.g., [3] and [4]. The major problem with this approach is attributed to the numerical smearing of the concentration Y , which leads to the formation of the layer of the 'mixture fluid', for which the equation of state is unknown. A common treatment of the this layer is to specify a Y -weighted mixture equation of state. This leads to non-physical pressure oscillations near multi-material interfaces [3–6].

One possible remedy for this problem is to apply algorithms which prevent excessive numerical smearing. These include front tracking (e.g., [7]) and front capturing (e.g., the level set method [8]). Other methods for effective description of interface are developed in [9] (Immersed Boundary Method), [10,11] (Volume-of-Fluid, VOF) and [12]. All these methods can be grouped into the class of Eulerian methods for interface evolution description, originated from the pioneer Marker-and-Cell (MAC) method [13]. Using these methods, the interface is re-sharpened each time step, and special boundary treatment is applied near the interface (see [7] and [6]). However, the numerical errors of the Godunov-based discontinuity capturing schemes interfere with boundary condition treatment, generating over- or under-heating numerical errors. In the case of moving boundaries, these numerical errors tend to accumulate and grow to unacceptable level [14]. One recent promising development to "cure" the above-mentioned problems, is the Ghost-Fluid Method (GFM) [6].

The GFM method utilizes the level set method and related technology to capture interface position. Then, an heuristic coupling boundary treatment is applied. This boundary treatment capitalizes on the notion that fluid's normal velocity and pressure are continuous across the interface, while material properties (and, related to this, entropy, temperature etc.) are discontinuous. Specifically, the GFM simulation of two-material compressible flow involves two sets of flow variable fields—one for each material. Then, based of the sign of the level set function, all computational nodes for each field are tagged on Ghost and Real nodes. The task of the GFM boundary condition capturing is to properly populate "Ghost" nodes of each field. This is accomplished by copying normal velocity and pressure from the locally Real fluid, while all rest variables (i.e., entropy and tangential components of velocity) are extrapolated from the Real to Ghost zones. Moreover, in order to limit over-heating errors, the extrapolation of entropy is applied with some offset thickness, which allows to 'chop' a significant

Contributed by the Fluids Engineering Division for publication in the JOURNAL OF FLUIDS ENGINEERING. Manuscript received by the Fluids Engineering Division May 27, 2003; revised manuscript received November 8, 2003. Associate Editor: M. J. Andrews.

portion of numerical errors in profiles of density/temperature around the interface. This is called “isobaric fix” [14].

Effectively, the GFM applies boundary conditions in *primitive variables*, for each fluid. It is known, that primitive-variable boundary treatment allows to eliminate pressure oscillations in description of multi-material interfaces¹ (see [3–4]). In general, the GFM method produces excellent solutions for two-component γ -gas flows. In some cases, however, the GFM scheme fails to perform. For example, when it is applied for simulation of air-water flows, the “direct primitive-variable” GFM coupling described above does not produce stable solutions [15]. Since direct specification of pressure and normal velocity is prohibited by the characteristic properties of subsonic compressible flows (see [16]), the GFM treatment involves over-specification of boundary conditions and, related to this spurious pressure errors. While these pressure errors are insignificant for soft fluids (e.g., γ -gas), they are detrimental in the presence of stiff fluids (e.g., water).

We believe that in order to properly treat interfaces with stiff fluids, the boundary condition treatment (and coupling) must be applied in *characteristic variables*, as is a common practice in boundary treatment of single-phase compressible fluid dynamics (see for review [16]). This motivated us to pursue the development of a characteristics-based boundary treatment—the Characteristics-Based Matching (CBM) approach [17]. In this first step, we treated the case of a stationary solid-fluid boundary. In the present paper, we will focus on the CBM treatment of moving fluid-solid boundaries. The full CBM treatment for fluid-fluid interfaces is presented elsewhere.

The paper is organized as follows. First, we describe the numerical method utilized. In particular, we outline the basic idea of the CBM treatment at the immersed boundary, and describe details of the numerical implementation, i.e., the “Virtual Space Relaxation” (VSR) procedure and temporal and spatial characteristics-based conservative finite-difference discretization (CBCFD) schemes. Next, we show performance of the CBM method on several one-dimensional shock tube tests, with stationary and moving fluid-solid interfaces; multi-dimensional shock tube tests; multi-dimensional complex-geometry tests and, finally, multidimensional moving fluid-solid boundary test.

2 Governing Equations

We will consider a numerical solution of the following generic system of hyperbolic conservation laws with arbitrary source terms:

$$\mathbf{U}_t + [\vec{\mathcal{F}}(\mathbf{U})]_x + [\vec{\mathcal{G}}(\mathbf{U})]_y + [\vec{\mathcal{H}}(\mathbf{U})]_z = \mathbf{S}(t, \mathbf{x}, \mathbf{U}) \quad (1)$$

where t is time; $\mathbf{r} = (x, y, z)$ is a position-vector; $\mathbf{U} = (U_1, \dots, U_s)^\top$ and $(\vec{\mathcal{F}}, \vec{\mathcal{G}}, \vec{\mathcal{H}})$ are the vector of the conservation variables (CV) and the vector of physical fluxes in x , y and z directions respectively; s is a total number of the conservation variables. The Jacobian matrices $A^{(x)} = \partial \vec{\mathcal{F}} / \partial \mathbf{U}$, $A^{(y)} = \partial \vec{\mathcal{G}} / \partial \mathbf{U}$ and $A^{(z)} = \partial \vec{\mathcal{H}} / \partial \mathbf{U}$ must have m real eigenvalues and a complete set of eigenvectors. The vector of source terms $\mathbf{S}(t, \mathbf{x}, \mathbf{U})$ is a function of time, space and conservation variables, in the most general case.

As a particular example, we will operate with *Euler equations for compressible fluid dynamics* (extension to Navier-Stokes equations is straightforward, see [17]). In this case, $\mathbf{S}(t, \mathbf{x}, \mathbf{U}) = 0$; and the vectors of the conservation variables and fluxes are:

$$\mathbf{U} = \begin{pmatrix} \rho \\ \rho u \\ \rho v \\ \rho w \\ \rho e \end{pmatrix}, \quad \vec{\mathcal{F}} = \begin{pmatrix} \rho u \\ P + \rho u^2 \\ \rho uv \\ \rho uw \\ u(P + \rho e) \end{pmatrix} \quad (2)$$

$$\vec{\mathcal{G}} = \begin{pmatrix} \rho v \\ \rho vu \\ P + \rho v^2 \\ \rho vw \\ v(P + \rho e) \end{pmatrix}, \quad \vec{\mathcal{H}} = \begin{pmatrix} \rho w \\ \rho wu \\ \rho wv \\ P + \rho w^2 \\ w(P + \rho e) \end{pmatrix}$$

Here, ρ , P , (u, v, w) and e are the fluid density, static pressure, velocity vector and total specific energy, respectively. We will consider γ -law gas, with equation of state $P = (\gamma - 1)\rho i$, where i is a specific internal energy.

3 Numerical Approach

3.1 Immersed Boundary and Types of Nodes.

Consider a “level set” function [8] and [18]), defined in all computational nodes as a signed distance to the boundary, $\varphi_{(m,i,j,k)}^{(n)}$, where indices $[n, m, i, j, k]$ denote points of finite-difference discretization in virtual space (see below). For simplicity, we will consider uniform grids. Extension to adaptively refined grid will be presented elsewhere. Zero-level of the distance function represents an interface. We will consider it as a *one-sided boundary* [17]; i.e., zero-level separates boundary and fictitious nodes (GHOST region, $\varphi_{(m,i,j,k)}^{(n)} < 0$) from the fluid nodes (REAL region, $\varphi_{(m,i,j,k)}^{(n)} > 0$), Fig. 1. The level set function is either fixed (stationary one-sided boundary) or evolves in time (‘moving one-sided boundary’).

Based on the current value of the level set function, all computational nodes are “tagged” in four different groups:

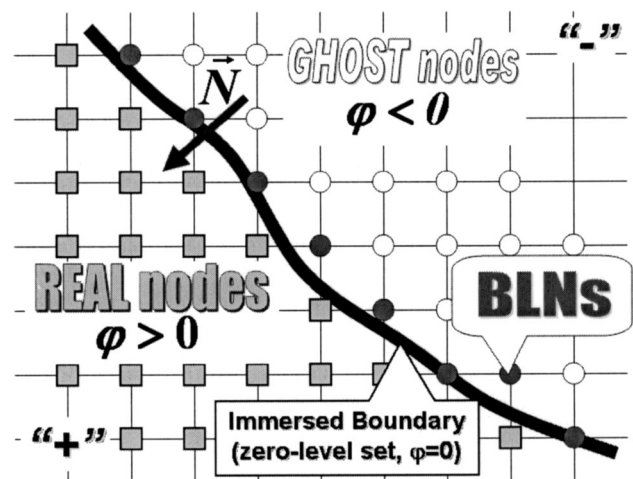


Fig. 1 On the formulation of the one-sided boundary of the CBM treatment

¹It is also known that the theory of weak solutions for non-conservative formulation is not well-established. Therefore, the best strategy would be to combine a conservative method for computational nodes located away from the interface with non-conservative method near interface (e.g., [5]), simultaneously reducing thus both pressure oscillations and conservation errors.

1. REAL nodes (RNs). These are nodes in which $\varphi_{(m,i,j,k)}^{(n)} > 0$, Fig. 1. Numerical solution at RNs is obtained using the *Characteristics-Based Conservative Finite Difference (CBCFD)* method (see below).

2. BOUNDARY LAYER nodes (BLNs). These nodes are located at zero-level ($\varphi_{(m,i,j,k)}^{(n)} = 0$) or in the GHOST region, in the vicinity of the zero-level

$$\left(\varphi_{(m,i,j,k)}^{(n)} < 0 \quad \text{and} \quad \begin{cases} \varphi_{(m,i \pm 1,j,k)}^{(n)} \geq 0 \text{ or} \\ \varphi_{(m,i,j \pm 1,k)}^{(n)} \geq 0 \text{ or} \\ \varphi_{(m,i,j,k \pm 1)}^{(n)} \geq 0 \end{cases} \right),$$

Fig. 1. A solution in BLNs is obtained/imposed using a *Characteristics-Based Matching (CBM)* approach (see below), which utilizes the level set function, the solution from the RNs (“one-sided”-“from-inside” treatment) and boundary conditions to be imposed. Each BLN is tagged to indicate what kind of boundary it represents (e.g., “slip,” “pressure,” “non-reflection,” etc.).

3. GHOST LAYER nodes (GLNs). These nodes are located in the GHOST region and they are within the stencil-range of the RNs and BLNs: $[-\Delta h \cdot (st+2) < \varphi_{(m,i,j,k)}^{(n)} < 0]$, where $\Delta h = \text{MAX}(\Delta x, \Delta y, \Delta z)$ is a grid scale, and st is a stencil of the numerical scheme utilized ($st=1$ for the 1st-order scheme and $st=3$ for ENO₃ and WENO₅). The GLNs are populated in a way, which would create a minimum effect on the solution in RNs and BLNs.

4. UNUSED nodes. These are all other nodes in the GHOST region.

Each time the level set function changes, as in the case of a moving boundary, all computational nodes are re-tagged.

3.2 Virtual Space Relaxation (VSR). In the present paper, we will utilize an implicit time discretization strategy, which is based on relaxation in virtual space defined as follows.

A new dimension is added, transforming the original set of equations (1) in physical four-dimensional space $\{t;x;y;z\}$ into the system of equations in “virtual” five-dimensional space $\{\tau;t;x;y;z\}$, where τ is an additional relaxation dimension. Written in a discrete form, we will consider the following system of PDE equations:

$$\mathbf{U}_\tau + \mathbf{U}_t + [\vec{\mathcal{F}}(\mathbf{U})]_x + [\vec{\mathcal{G}}(\mathbf{U})]_y + [\vec{\mathcal{H}}(\mathbf{U})]_z = 0 \quad (3)$$

This modification does not change the type of equations, i.e., the system (3) is τ -hyperbolic, since the original system Eq. (1) is t -hyperbolic.

Next, Eq. (3) can be written in the following discrete finite-difference form:

$$\mathbf{U}_{(m,i,j,k)}^{(n+1)} - \mathbf{U}_{(m,i,j,k)}^{(n)} = -\Delta\tau \begin{pmatrix} [\mathbf{U}_{(m,i,j,k)}^{(n)}]_t \\ + [\vec{\mathcal{F}}_{(m,i,j,k)}^{(n)}]_x \\ + [\vec{\mathcal{G}}_{(m,i,j,k)}^{(n)}]_y \\ + [\vec{\mathcal{H}}_{(m,i,j,k)}^{(n)}]_z \end{pmatrix} \quad (4)$$

where $[\mathbf{U}_{(m,i,j,k)}^{(n)}]_t$, $[\vec{\mathcal{F}}_{(m,i,j,k)}^{(n)}]_x$, $[\vec{\mathcal{G}}_{(m,i,j,k)}^{(n)}]_y$ and $[\vec{\mathcal{H}}_{(m,i,j,k)}^{(n)}]_z$ are point values of the backward-difference approximation of the time derivative and numerical flux functions in three spatial dimensions, correspondingly (see below).

At each physical time step $[m \rightarrow m+1]$, we would seek the steady-state solution in virtual space $\{\tau;t;x;y;z\}$. Projection of this solution into the space $\{t;x;y;z\}$ is our physical solution. After each round of relaxation in virtual time, all relevant discrete physical values Ψ are shifted as $\Psi_{l-1,i,j,k} = \Psi_{l,i,j,k}$, $l = n - st, \dots, n$, where st is

a stencil of the backward difference formula for physical time discretization (see below). Note, that we choose the first-order-accurate Euler scheme for virtual time τ discretization, since we are interested in a τ -steady-state. In this respect, it is instructive to note similarity between the VSR and the method of artificial compressibility (AC), widely used for simulation of incompressible fluid flows [19]—in both methods, the “dual time stepping” is used.

During each round of the VS-relaxation, the pseudo-time step is dynamically chosen based on the CFL limit in virtual space as $\Delta\tau = \sigma_\tau \min[\Delta t; \Delta h/\lambda_{\max}]$, where Δt and $\Delta h = \max[\Delta x, \Delta y, \Delta z]$ are the physical time and space steps, while λ_{\max} is the maximum characteristic speed (eigenvalue) corresponding to the Jacobian matrices of the flux terms $[\vec{\mathcal{F}}]_x$, $[\vec{\mathcal{G}}]_y$ and $[\vec{\mathcal{H}}]_z$. In all calculations presented here, we utilized τ -CFL number $\sigma_\tau = 0.4$.

Each round of the VS-relaxation is terminated when the following convergence criterium is achieved² [20]:

$$\left| \frac{\Delta \mathbf{U}}{\mathbf{U}_{\text{norm}}} \right| \leq \bar{\mathcal{E}} \quad (5)$$

where $\Delta \mathbf{U} = \max[\mathbf{U}_{(m,i,j,k)}^{(n)} - \mathbf{U}_{(m,i,j,k)}^{(n-1)}]_{\mathcal{D}}$; \mathcal{D} is the whole discrete $[\mathbf{U}_{(m,i,j,k)}]$ domain; \mathbf{U}_{norm} is a vector of the normalization conservative variables. For normalization of density and total energy, we utilized $[\mathbf{U}_{\text{norm}}]_1 = \min[\rho]_{\mathcal{D}}$ and $[\mathbf{U}_{\text{norm}}]_5 = \min[\rho e]_{\mathcal{D}}$; while the normalization parameter for momentum was set to 1. A tolerance vector $\bar{\mathcal{E}}$ was typically set to $[10^{-7}, 10^{-7}, 10^{-7}, 10^{-7}, 10^{-7}]^T$. With this level of tolerance, the procedure typically converged in 25–30 virtual time steps. Setting tolerance to the level of 10^{-2} , the convergence can be achieved in 5–7 steps. Moreover, even with this low level of tolerance, the VSR-based solution is found to be comparable with the RK-TVD-based scheme.

The VSR is found to be always convergent to τ -steady-state, because this state is t -hyperbolic. This is different from similar methods of artificial compressibility (AC), widely utilized in the case of incompressible fluids, for which τ -steady-state is elliptic—and there is no complete convergence, since there are always leftovers—“artificial compressibility” pressure waves, the level of which corresponds to the chosen numerical Mach number [19]. While the above argument is rather intuitive and, at the moment, it can be backed-up only by our practical experience with the VSR—we hope to prove it rigorously in future.

Apparent disadvantage of the VSR time discretization relatively to the explicit schemes is that each physical time step is more computationally expensive, which is a common feature for all implicit schemes. The major advantage of the VSR coupled with CBM—is that it allows to eliminate “small cell” problems, which otherwise would dwindle simulation time step due to the restrictive CFL condition on physical time. Note, that in VSR we utilize CFL restriction in τ but not in physical time t . We will discuss other *pros* of the VSR-based scheme later throughout the text. More about advantages of the VSR are presented in [20].

3.3 Physical Space Discretization. To discretize the conservative flux terms of the system of governing equations (3) at the computational node $[\mathbf{U}_{(m,i,j,k)}]$, we employ a “*Characteristics-Based Conservative Finite-Difference*” CBCFD approach [21]. Following Shu and Osher [22], the numerical flux functions can be defined as

$$\begin{aligned} [\vec{\mathcal{F}}_{(m,i,j,k)}^{(n)}]_x &= \frac{\mathbb{F}_{(m,i+1/2,j,k)}^{(n)} - \mathbb{F}_{(m,i-1/2,j,k)}^{(n)}}{x_{(m,i+1/2,j,k)} - x_{(m,i-1/2,j,k)}} + O(\Delta x^a) \\ [\vec{\mathcal{G}}_{(m,i,j,k)}^{(n)}]_y &= \frac{\mathbb{G}_{(m,i,j+1/2,k)}^{(n)} - \mathbb{G}_{(m,i,j-1/2,k)}^{(n)}}{y_{(m,i,j+1/2,k)} - y_{(m,i,j-1/2,k)}} + O(\Delta y^a) \\ [\vec{\mathcal{H}}_{(m,i,j,k)}^{(n)}]_z &= \frac{\mathbb{H}_{(m,i,j,k+1/2)}^{(n)} - \mathbb{H}_{(m,i,j,k-1/2)}^{(n)}}{z_{(m,i,j,k+1/2)} - z_{(m,i,j,k-1/2)}} + O(\Delta z^a) \end{aligned} \quad (6)$$

²More rigorous convergence criteria, based on L_1 - and L_2 -norms of errors, are developed in [21].

where a is a “target” accuracy of the scheme; while $F_{(m,i\pm 1/2,j,k)}$, $G_{(m,i,j\pm 1/2,k)}$ and $H_{(m,i,j,k\pm 1/2)}$, are the numerical fluxes at the edges of the computational cell, evaluated by the high-order-accurate characteristics-based upwind-differencing. Detail discussions of the characteristic decomposition and upwinding can be found in [17,21,23].

In the present study, we will utilize *a*) the WENO₅ scheme for extrapolation of point values of flow variables to the cell edges, (e.g., $[U_{m,i+s,j,k}^{(n)} \rightarrow U_{m,i+1/2,j,k}^{(n)}]_{s=-2,\dots,2}$); *b*) use Roe-Average (RA) approach for construction of the characteristic-decomposition-matrix; and *c*) Local-Lax-Friedrichs (LLF) and WENO₅ scheme for evaluation of fluxes in characteristic space. Correspondingly, the scheme will be denoted as VSR_♣/WENO₅/LLF_{RA}, where “♣” is the order of scheme for physical time discretization (see below).

3.4 Physical Time Discretization. In the frame of the VSR-based strategy, physical time can be treated in a similar fashion as physical space dimensions, i.e., the numerical time flux function can be defined as

$$[U_{(m,i,j,k)}^{(n)}]_t = \frac{U_{(m+1/2,i,j,k)}^{(n)} - U_{(m-1/2,i,j,k)}^{(n)}}{t_{(m+1/2,i,j,k)} - t_{(m-1/2,i,j,k)}} + O(\Delta t^a) \quad (7)$$

The characteristic speed is 1, which means that we need to utilize backward difference scheme for extrapolation to the cell edges. We will use the following three time discretization schemes:

$$\begin{array}{l} \text{The 1st-order} \\ \text{Piecewise-} \\ \text{Constant} \end{array} \rightarrow U_{(m+1/2,i,j,k)}^{(n)} = U_{(m,i,j,k)}^{(n)} + O(\Delta t)$$

$$\begin{array}{l} \text{The 2nd-order} \\ \text{Piecewise-} \\ \text{Linear} \end{array} \rightarrow U_{(m+1/2,i,j,k)}^{(n)} = \frac{3U_{(m,i,j,k)}^{(n)} - U_{(m-1,i,j,k)}^{(n)}}{2} + O(\Delta t^2) \quad (8)$$

$$\begin{array}{l} \text{The 3rd-order} \\ \text{Piecewise-} \\ \text{Parabolic} \end{array} \rightarrow U_{(m+1/2,i,j,k)}^{(n)} = \frac{15U_{(m,i,j,k)}^{(n)} - 10U_{(m-1,i,j,k)}^{(n)} + 3U_{(m-2,i,j,k)}^{(n)}}{8} + O(\Delta t^3)$$

In order to prevent Gibbs-phenomenon attributed to the high-order-schemes, we will apply geometrical limiter, implemented as follows. The high-order-accurate “correction vector” can be written as:

$$\delta U = U_{(m+1/2,i,j,k)}^{(n)} - U_{(m,i,j,k)}^{(n)} \quad (9)$$

Next, each component of the correction vector is limited as

$$\delta U^L = S \cdot \max \left[0, \min \left\{ |\delta U|, S \cdot \frac{\chi}{2} (U_{(m,i,j,k)}^{(n)} - U_{(m-1,i,j,k)}^{(n)}) \right\} \right] \quad (10)$$

for the 2nd-order scheme; and as

$$\delta U^L = S \cdot \max \left[0, \min \left\{ |\delta U|, S \cdot \frac{\chi}{2} (U_{(m,i,j,k)}^{(n)} - U_{(m-1,i,j,k)}^{(n)}), S \cdot \frac{\chi}{4} (U_{(m,i,j,k)}^{(n)} - U_{(m-2,i,j,k)}^{(n)}), S \cdot \frac{\chi}{2} (U_{(m-1,i,j,k)}^{(n)} - U_{(m-2,i,j,k)}^{(n)}) \right\} \right] \quad (11)$$

for the 3rd-order scheme. In Eqs. (10) and (11) above, $S = \text{Sign}(\delta U)$ and χ is a limiting parameter, which was set to 1/2 in the present study.

Finally, the ‘limited time-cell-edge high-order-accurate terms’ can be expressed as

$$U_{(m+1/2,i,j,k)}^{(n,L)} = U_{(m,i,j,k)}^{(n)} + \delta U^L \quad (12)$$

3.5 Characteristics-Based Matching (CBM). The purpose of the characteristics-based matching (CBM) is to “infuse” the desirable set of boundary conditions at the BLNs, see Figs. 1 and 2. The approach is based on the well-known one-dimensional

characteristic-decomposition-based boundary treatment of compressible fluid (see, e.g., [16]); and make use of the level set function to extend it to multiple dimensions.

3.5.1 “Normal” Coordinate System. Within the level set formulation, it is straightforward to define a normal vector as:

$$\vec{N} = \frac{\nabla \varphi}{|\nabla \varphi|} = (\xi_x, \xi_y, \xi_z) \quad (13)$$

It is instructive to note that the level set function is defined in such a way, so the unit normal \vec{N} is pointing from the GHOST to the REAL zones, Fig. 1.

Next, we define two tangential planes as follows:

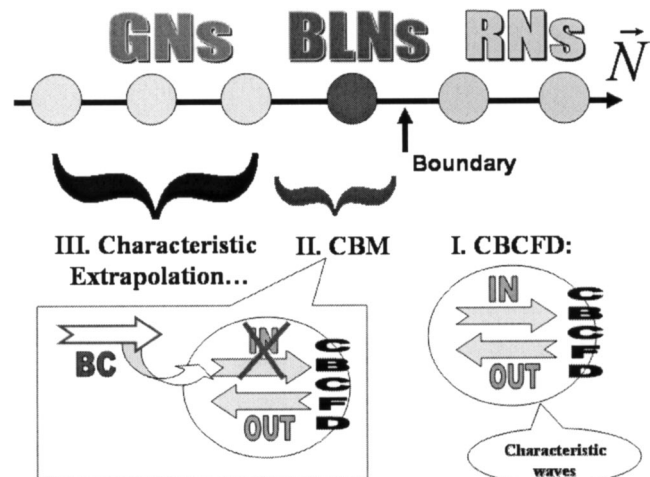


Fig. 2 On treatment of the RNs, BLNs and GNs

$$\underbrace{\begin{pmatrix} \eta_x \\ \eta_y \\ \eta_z \end{pmatrix}}_{\vec{T}'} = \begin{cases} \frac{\vec{N} \times (1,0,0)}{|\vec{N} \times (1,0,0)|} = \frac{(0, \xi_z, -\xi_y)}{\sqrt{\xi_z^2 + \xi_y^2}} & \text{if } \xi_x < \xi_y, \xi_z \\ \frac{\vec{N} \times (0,1,0)}{|\vec{N} \times (0,1,0)|} = \frac{(-\xi_z, 0, \xi_x)}{\sqrt{\xi_z^2 + \xi_x^2}} & \text{if } \xi_y < \xi_x, \xi_z \\ \frac{\vec{N} \times (0,0,1)}{|\vec{N} \times (0,0,1)|} = \frac{(\xi_y, -\xi_x, 0)}{\sqrt{\xi_x^2 + \xi_y^2}} & \text{if } \xi_z < \xi_y, \xi_x \end{cases} \quad (14)$$

and

$$\begin{aligned} \vec{T}'' &= (\zeta_x, \zeta_y, \zeta_z) = \vec{N} \times \vec{T}' \\ &= (\xi_y \eta_z - \xi_z \eta_y, \xi_z \eta_x - \xi_x \eta_z, \xi_x \eta_y - \xi_y \eta_x) \end{aligned} \quad (15)$$

Thus, knowing a signed distance function (a level set) at each computational node, we can transform our Cartesian coordinate system into a new local coordinate system (we will call it “normal”), which “fits” the shape of the boundary. Note, that this transformation is a simple rotation, which has the following Jacobian matrix and its inverse:

$$\bar{J} = \begin{bmatrix} \xi_x & \xi_y & \xi_z \\ \eta_x & \eta_y & \eta_z \\ \zeta_x & \zeta_y & \zeta_z \end{bmatrix}; \quad \bar{J}^{-1} = \begin{bmatrix} x_\xi & x_\eta & x_\zeta \\ y_\xi & y_\eta & y_\zeta \\ z_\xi & z_\eta & z_\zeta \end{bmatrix} \quad (16)$$

Importantly, the Jacobian of the rotation is

$$\bar{J} \equiv \det(\bar{J}^{-1}) = 1 \quad (17)$$

Transformation of the gradients of a scalar function ϕ can be accomplished using the following expressions:

$$\nabla \phi = \bar{J}^T \cdot \nabla' \phi \quad \text{and} \quad \nabla' \phi = [\bar{J}^{-1}]^T \cdot \nabla \phi \quad (18)$$

where the gradients in the “Cartesian” and “Normal” coordinate systems are

$$\nabla \phi = \begin{bmatrix} \partial_x \phi \\ \partial_y \phi \\ \partial_z \phi \end{bmatrix} \quad \text{and} \quad \nabla' \phi = \begin{bmatrix} \partial_\xi \phi \\ \partial_\eta \phi \\ \partial_\zeta \phi \end{bmatrix} \quad (19)$$

respectively.

Contravariant velocities are defined by

$$\mathbf{V}_c = \begin{bmatrix} V_\xi \\ V_\eta \\ V_\zeta \end{bmatrix} = \bar{J} \cdot \begin{bmatrix} u \\ v \\ w \end{bmatrix} \quad (20)$$

3.5.2 Governing Equations in the “Normal” Coordinate System. Using the transformation to a “normal” coordinate system, introduced in the previous section, the governing equations Eq. (3) can be re-formulated in the following “strong conservation form” (see, e.g., [24]):

$$\mathbf{U}_\tau + \mathbf{U}_\eta + [\tilde{F}(\mathbf{U})]_\xi + [\tilde{G}(\mathbf{U})]_\eta + [\tilde{H}(\mathbf{U})]_\zeta = \tilde{S}(\mathbf{U}) \quad (21)$$

where we utilized equation (17) for the Jacobian. The flux terms of this “Normal-Conservation Formulation (NCF)” are

$$\begin{aligned} \tilde{F}(\mathbf{U}) &\equiv \xi_x \vec{F} + \xi_y \vec{G} + \xi_z \vec{H} \\ \tilde{G}(\mathbf{U}) &\equiv \eta_x \vec{F} + \eta_y \vec{G} + \eta_z \vec{H} \quad \text{or} \quad \begin{pmatrix} \tilde{F} \\ \tilde{G} \\ \tilde{H} \end{pmatrix} = \bar{J} \cdot \begin{pmatrix} \vec{F} \\ \vec{G} \\ \vec{H} \end{pmatrix} \\ \tilde{H}(\mathbf{U}) &\equiv \zeta_x \vec{F} + \zeta_y \vec{G} + \zeta_z \vec{H} \end{aligned} \quad (22)$$

When dealing with boundary conditions, it is more convenient to operate with “primitive” variables. We define “normal-primitive variables (NPV)” as

$$\mathbf{U}^* = [\rho, P, V_\xi, V_\eta, V_\zeta]^T \quad (23)$$

The governing equations for NPVs \mathbf{U}^* can be expressed as

$$\underbrace{[\mathbf{U}^*]_\tau}_{P^{-1}[\mathbf{U}]_\tau} + \underbrace{\tilde{D}}_{\text{Normal flux: } P^{-1}[\tilde{F}(\mathbf{U})]_\xi} + \underbrace{\tilde{C}}_{\text{Transverse fluxes and sources: } P^{-1}([\mathbf{U}]_\eta + [\tilde{G}(\mathbf{U})]_\eta + [\tilde{H}(\mathbf{U})]_\zeta - S)} = 0 \quad (24)$$

The Jacobian of transformation from the conservative CV to the normal primitive NPV variables,

$$\mathbf{U} = \begin{pmatrix} \rho \\ \rho e \\ \rho u \\ \rho v \\ \rho w \end{pmatrix} \rightarrow \mathbf{U}^* = \begin{pmatrix} \rho \\ P \\ V_\xi \\ V_\eta \\ V_\zeta \end{pmatrix}$$

is defined by the following matrix:

$$P = \begin{bmatrix} 1 & 0 & 0 & 0 & 0 \\ e + \rho i_\rho & \rho i_\rho & \rho \begin{pmatrix} ux_\xi \\ +vy_\xi \\ +wz_\xi \end{pmatrix} & \rho \begin{pmatrix} ux_\eta \\ +vy_\eta \\ +wz_\eta \end{pmatrix} & \rho \begin{pmatrix} ux_\zeta \\ +vy_\zeta \\ +wz_\zeta \end{pmatrix} \\ u & 0 & \rho x_\xi & \rho x_\eta & \rho x_\zeta \\ v & 0 & \rho y_\xi & \rho y_\eta & \rho y_\zeta \\ w & 0 & \rho z_\xi & \rho z_\eta & \rho z_\zeta \end{bmatrix} \quad (25)$$

3.5.3 Characteristic Decomposition of the Normal Flux. The normal flux vector \tilde{D} can be linearized as

$$\tilde{D} = A^* \cdot [\mathbf{U}^*]_\xi \quad (26)$$

where the Jacobian matrix A^* is defined as

$$A^* \equiv P^{-1} \tilde{Q}; \quad \tilde{Q} \rightarrow q_{sr} \equiv \frac{\partial \tilde{F}_s}{\partial U_r^*} \quad (27)$$

The Jacobian matrix of the flux-transformation Q is given by

$$Q = \begin{bmatrix} V_\xi & 0 & \rho & 0 & 0 \\ Q_{21} & Q_{22} & Q_{23} & Q_{24} & Q_{25} \\ uV_\xi & \xi_x & \rho(u + V_\xi x_\xi) & \rho V_\xi x_\eta & \rho V_\xi x_\zeta \\ vV_\xi & \xi_y & \rho(v + V_\xi y_\xi) & \rho V_\xi y_\eta & \rho V_\xi y_\zeta \\ wV_\xi & \xi_z & \rho(w + V_\xi z_\xi) & \rho V_\xi z_\eta & \rho V_\xi z_\zeta \end{bmatrix} \quad (28)$$

where

$$Q_{21} = V_\xi (e + \rho i_\rho)$$

$$Q_{22} = V_\xi (1 + \rho i_\rho)$$

$$Q_{23} = P + \rho [e + V_\xi (ux_\xi + vy_\xi + wz_\xi)]$$

$$Q_{24} = \rho V_\xi (ux_\eta + vy_\eta + wz_\eta)$$

$$Q_{25} = \rho V_\xi (ux_\zeta + vy_\zeta + wz_\zeta)$$

With this, the Jacobian matrix A^* can be written as:

$$A^* = P^{-1} \cdot Q = \begin{bmatrix} V_\xi & 0 & \rho & 0 & 0 \\ 0 & V_\xi & \frac{\rho c^2}{\chi_\xi} & 0 & 0 \\ 0 & \frac{\chi_\xi}{\rho} & V_\xi & 0 & 0 \\ 0 & \frac{\chi_\eta}{\rho} & 0 & V_\xi & 0 \\ 0 & \frac{\chi_\zeta}{\rho} & 0 & 0 & V_\xi \end{bmatrix} \quad (29)$$

where the metrics coefficients for a rotation are:

$$\begin{cases} \chi_\xi = \xi_x^2 + \xi_y^2 + \xi_z^2 = |\vec{N}| \equiv 1 \\ \chi_\eta = \xi_x \eta_x + \xi_y \eta_y + \xi_z \eta_z = \vec{N} \cdot \vec{T}' \equiv 0 \\ \chi_\zeta = \xi_x \zeta_x + \xi_y \zeta_y + \xi_z \zeta_z = \vec{N} \cdot \vec{T}'' \equiv 0 \end{cases} \quad (30)$$

and the sound speed c is defined as

$$c \equiv \sqrt{\chi_\xi \frac{P - \rho^2 i_p}{\rho^2 i_p}} \quad (31)$$

The eigenvalues of the Jacobian matrix A^* are

$$\vec{\Lambda}^* = \begin{bmatrix} \lambda_1^* = V_\xi - c \\ \lambda_2^* = V_\xi \\ \lambda_3^* = V_\xi \\ \lambda_4^* = V_\xi \\ \lambda_5^* = V_\xi + c \end{bmatrix} \quad (32)$$

The left and right eigenvector matrices of the Jacobian matrix A^* are

$$L^* = \begin{bmatrix} 0 & 1 & -c\rho & 0 & 0 \\ 0 & 0 & 0 & 1 & 0 \\ c^2 & -1 & 0 & 0 & 0 \\ 0 & 0 & 0 & 0 & 1 \\ 0 & 1 & c\rho & 0 & 0 \end{bmatrix} \quad \text{and} \quad R^* = [L^*]^{-1} \quad (33)$$

respectively.

Decoupling of the governing equations in the NPF formulation Eq. (24) can be achieved by “putting” them into the “characteristic space” as:

$$L^* [U^*]_\tau + \vec{\mathcal{L}} + L^* \vec{C} = 0 \quad (34)$$

where

$$\mathcal{L}_i \equiv \lambda_i^* [L^*]_i [U^*]_\xi; \quad i = 1, \dots, m; \quad \begin{array}{l} m \text{ is a total} \\ \text{number of} \\ \text{equations} \end{array} \quad (35)$$

can be interpreted as the amplitude variations of the characteristic waves (AVCW) moving in the “normal”- (ξ) -direction (see, e.g., [25]). Eq. (34) can also be written in a component form as

$$\underbrace{[L^*]_s [U^*]_\tau}_{\mathcal{A}_s} + \mathcal{L}_s + [L^*]_s \vec{C} = 0 \quad (36)$$

where \mathcal{A}_s represents the time derivative of the amplitude of the s th characteristic wave (see study by Thompson [16]). Equation (36) will serve as a platform for incorporation of the desired set of BCs into the solution at the BLNs.

3.5.4 *The CBM Correction Term.* Let us re-formulate Eq. (36) by adding the correction term $\delta \mathcal{L}_{sBC}$:

$$\underbrace{[L^*]_s [U^*]_\tau}_{\mathcal{A}_s} + \delta \mathcal{L}_{sBC} + \underbrace{\mathcal{L}_s + [L^*]_s \vec{C}}_{[L^*]_s \vec{S}^*} = 0 \quad (37)$$

where

$$\vec{S}^* = P^{-1} \left(\underbrace{[U]_t + [\vec{\mathcal{F}}(U)]_x + [\vec{\mathcal{G}}(U)]_y + [\vec{\mathcal{H}}(U)]_z}_{\text{Evaluated using a CBCFD method}} - \mathbf{S} \right) \quad (38)$$

For the case of Euler equations, the correction term $\delta \mathcal{L}_{sBC}$ is set to zero, if the s th characteristic wave is leaving the computational domain—thus, a virtual-time-advancement of this wave would be consistent with the basic scheme utilized in RNs. If the s th characteristic wave is entering the REAL region, $\delta \mathcal{L}_{sBC}$ allows us to “blend-in” one boundary condition. For this purpose, let us put the system of Eq. (37) back into the physical space by multiplying it on the matrix R^* :

$$[U^*]_\tau + R^* \delta \vec{\mathcal{L}}_{BC} + \vec{S}^* = 0 \quad (39)$$

which for the case of the equations of gas dynamics can be expressed as:

$$\begin{bmatrix} \rho \\ P \\ V_\xi \\ V_\eta \\ V_\zeta \end{bmatrix}_\tau + \begin{bmatrix} \delta \mathcal{L}_{1BC} + 2\delta \mathcal{L}_{3BC} + \delta \mathcal{L}_{5BC} \\ \frac{2c^2}{\delta \mathcal{L}_{1BC} + \delta \mathcal{L}_{5BC}} \\ \frac{\delta \mathcal{L}_{5BC} - \delta \mathcal{L}_{1BC}}{2c\rho} \\ \delta \mathcal{L}_{2BC} \\ \delta \mathcal{L}_{4BC} \end{bmatrix} + \vec{S}^* = 0 \quad (40)$$

Now, using Eq. (40), we can calculate the correction terms $\delta \mathcal{L}_{sBC}$ allowing us to “infuse” the desired set of BCs in primitive variables.

Recipes for different types of boundary conditions for Euler and Navier-Stokes equations are given in [17]. Here, we will present the CBM correction terms for slip adiabatic stationary/moving wall and non-reflection (see below).

Once all CBM correction terms are computed, the vector of NPVs is advanced in virtual time, according to Eq. (40), and, then, all conservative variables are recovered.

3.5.5 *Slip Adiabatic (Moving/Stationary) Wall.* For this case, the following set of boundary conditions must be satisfied:

<p>I. Subsonic Inflow ($\lambda_2^* \geq 0$ $\lambda_1^* \leq 0$)</p> $\begin{pmatrix} V_\xi = \text{given} \\ \partial_\xi V_\eta = 0 \\ \partial_\xi V_\zeta = 0 \\ \partial_\xi T = 0 \end{pmatrix}$ <p style="text-align: center;">4 BCs</p>	<p>II. Subsonic Outflow ($\lambda_2^* < 0$, $\lambda_5^* \geq 0$)</p> <p style="text-align: center;">($V_\xi = \text{given}$)</p> <p style="text-align: center;">1 BC</p>	<p>III. Overspecified Subsonic Outflow ($\lambda_2^* < 0, \lambda_5^* \geq 0$)</p> $\begin{pmatrix} V_\xi = \text{given} \\ \partial_\xi T = 0 \end{pmatrix}$ <p style="text-align: center;">2 BCs</p>
--	---	--

$$(41)$$

Here, for simplicity, we will describe only subsonic case. Overspecified Subsonic Outflow boundary condition is considered in the context of over/under-heating in moving boundaries “in a rarefaction mode” (see below).

In details, the above set of BCs is implemented as follows. After all REAL nodes are updated, the following procedure is applied at each BLN:

1. Compute temperature and tangential components of the contravariant velocity using the “inverse” of the finite-difference representation of $\partial_\xi \Psi$ by Eq. (18), i.e.:

$$\Psi_{(m,i,j,k)}^{(BC)} = \frac{Q - \left[\begin{array}{l} (C_x^- \Psi_{(m,i-1,j,k)} + C_x^+ \Psi_{(m,i+1,j,k)}) x_{\xi}|_{(m,i,j,k)} \\ + (C_y^- \Psi_{(m,i,j-1,k)} + C_y^+ \Psi_{(m,i,j+1,k)}) y_{\xi}|_{(m,i,j,k)} \\ + (C_z^- \Psi_{(m,i,j,k-1)} + C_z^+ \Psi_{(m,i,j,k+1)}) z_{\xi}|_{(m,i,j,k)} \end{array} \right]}{C_x^L x_{\xi}|_{(m,i,j,k)} + C_y^L y_{\xi}|_{(m,i,j,k)} + C_z^L z_{\xi}|_{(m,i,j,k)}} \quad (42)$$

where $\Psi = T, V_\eta$ or V_ζ ; Q is a value of the gradient to be imposed (Q=0 in this particular case); while $C_s^{-,+L}$ ($s=x,y,z$) are the coefficients of the “normal-vector-based” finite-difference formulas for gradients $\partial_x \Psi, \partial_y \Psi$ and $\partial_z \Psi$, i.e.

$$\xi_s|_{(m,i,j,k)} > 0 \begin{cases} C_s^- = 0 \\ C_s^L = -1/\Delta s \\ C_s^+ = 1/\Delta s \end{cases}$$

$$\xi_s|_{(m,i,j,k)} < 0 \begin{cases} C_s^- = -1/\Delta s \\ C_s^L = 1/\Delta s \\ C_s^+ = 0 \end{cases} \quad (43)$$

$$\xi_s|_{(m,i,j,k)} = 0 \begin{cases} C_s^- = -1/(2\Delta s) \\ C_s^L = 0 \\ C_s^+ = 1/(2\Delta s) \end{cases}$$

2. Based on the currently available values, compute characteristic velocities at BLN, and determine the state of characteristic waves, see Eq. (41).

3. Perform the following iterative procedure, in order to compute $\delta \tilde{\mathcal{L}}_{BC}$:

- a. Using the equation of state, from the currently available local pressure $P_{(m,i,j,k)}^{(iter)}$ and temperature $T_{(m,i,j,k)}^{(BC)}$, calculate density $\rho_{(m,i,j,k)}^{(BC,iter)}$.
- b. Calculate CBM corrections as

$$\delta \mathcal{L}_{1BC} = 0$$

$$\delta \mathcal{L}_{2BC} = - \left[\frac{V_{\eta(m,i,j,k)}^{(BC)} - V_{\eta(m,i,j,k)}^{(n)}}{\Delta \tau} + \tilde{S}_4^* \right] \begin{array}{l} \text{I.} \\ \rightarrow \text{Subsonic} \\ \text{Inflow} \\ \rightarrow \text{Otherwise} \end{array}$$

$$= 0$$

$$\delta \mathcal{L}_{4BC} = - \left[\frac{V_{\zeta(m,i,j,k)}^{(BC)} - V_{\zeta(m,i,j,k)}^{(n)}}{\Delta \tau} + \tilde{S}_5^* \right] \begin{array}{l} \text{I.} \\ \rightarrow \text{Subsonic} \\ \text{Inflow} \\ \rightarrow \text{Otherwise} \end{array}$$

$$= 0$$

$$\delta \mathcal{L}_{5BC} = \delta \mathcal{L}_{1BC} - 2\rho_{(m,i,j,k)}^{(n)} c_{(m,i,j,k)}^{(n)} \left[\frac{V_{\xi(m,i,j,k)}^{(BC)} - V_{\xi(m,i,j,k)}^{(n)}}{\Delta \tau} + \tilde{S}_3^* \right]$$

$$\delta \mathcal{L}_{3BC} = - \frac{\delta \mathcal{L}_{1BC} + \delta \mathcal{L}_{5BC} + 2c_{(m,i,j,k)}^{(n^2)} \left[\frac{\rho_{(m,i,j,k)}^{(BC,iter)} - \rho_{(m,i,j,k)}^{(n)}}{\Delta \tau} + \tilde{S}_1^* \right]}{2} \begin{array}{l} \text{Subsonic} \\ \text{Inflow} \\ \text{(I) and} \\ \text{Over-} \\ \text{specified} \\ \text{Outflow} \\ \text{(III)} \end{array}$$

- c. Update NPVs, using a finite-difference discretization of Eq. (40).

- d. Iterate until convergence in $P_{(m,i,j,k)}^{(iter)}$ and $\rho_{(m,i,j,k)}^{(BC,iter)}$ is obtained. Typically, the convergence is achieved in three iterations.

4. Recover conservative variables.

It is instructive to note that during the calculation of the temperature and tangential components of the contravariant velocity by Eqs. (42) and (43), the right-hand side of Eq. (42) might contain both already updated values, $^{(n+1)}$ —from the neighbor RNs, and “old” values, $^{(n)}$ —from the neighbor BLNs and GNs. This

inconsistency is eliminated at the VSR-relaxed state, which is an important advantage of the VSR-based strategy. Furthermore, with the VSR, there is no need for a “locally refined matching (LRM)” procedure, utilized in [17] to alleviate “small cell” problem and make the scheme to be able of handling strong shocks.

3.5.6 Non-Reflection. This BC is one of the most common approaches for free-boundary treatment [16]. Nonreflection boundary condition requires the amplitudes of incoming characteristic waves to be constant in virtual time τ ($A_s=0$, see Eq. (36)). This condition is equivalent to stating that there are no incoming waves, as it is the variation in amplitude which constitutes the wave motion. With this, using Eq. (36), the CBM corrections for the s th incoming AVCWs are computed as

$$\delta \mathcal{L}_{s_{BC}} = -[L^*]_s \tilde{S}^* \quad (44)$$

or, more specifically:

$$\begin{aligned} \delta \mathcal{L}_{1_{BC}} &= -[\tilde{S}_2^* - c\rho\tilde{S}_3^*] \rightarrow \begin{array}{l} \text{Supersonic} \\ \text{Inflow, } \lambda_1^* > 0 \end{array} \\ \delta \mathcal{L}_{5_{BC}} &= -[\tilde{S}_2^* + c\rho\tilde{S}_3^*] \rightarrow \begin{array}{l} \text{Subsonic/Supersonic} \\ \text{Inflow and} \\ \text{Subsonic} \\ \text{Outflow} \\ \lambda_5^* > 0 \end{array} \\ \delta \mathcal{L}_{2_{BC}} &= -\tilde{S}_4^* \rightarrow \begin{array}{l} \text{Subsonic/Supersonic} \\ \text{Inflow } \lambda_2^* > 0 \end{array} \\ \delta \mathcal{L}_{4_{BC}} &= -\tilde{S}_5^* \rightarrow \begin{array}{l} \text{Subsonic/Supersonic} \\ \text{Inflow } \lambda_4^* > 0 \end{array} \\ \delta \mathcal{L}_{3_{BC}} &= -[c^2\tilde{S}_1^* - \tilde{S}_2^*] \rightarrow \begin{array}{l} \text{Subsonic/Supersonic} \\ \text{Inflow } \lambda_3^* > 0 \end{array} \end{aligned} \quad (45)$$

At this point, we would like to emphasize another advantage of the VSR-based strategy, in a frame of the nonreflection boundary treatment. While explicit-scheme-based non-reflection *freezes incoming characteristic waves in physical time* (see [17]), the VSR-based non-reflection freezes incoming characteristic wave in *virtual (relaxation) time*, which allows to take into account local time derivatives (incorporated into the source term \tilde{S}^* , see Eq. (38)).

3.6 Treatment of the Domain Boundaries (Patches). Population of GNs. Special treatment is required for computational nodes at the boundaries of the computational domain, see Fig. 3a. We have explored two options for setting normal vector at these nodes: a) Normal vector is re-set to be *normal to the boundary*, Fig. 3b; and b) Normal vector is re-set to be *tangential to zero-level*. In this case, the level-set-based normal is “switched” with one of the tangential vectors, Eqs. (14) and (15), choosing the one which forms the smallest angle with the normal to the boundary, Fig. 3c. As it is shown in our numerical tests, the second option is preferable. We will demonstrate the distorting effects of the first option later (see Test 5).

After all RNs and BLNs (both internal and at the boundary, Fig. 3a) nodes are updated, all GHOST nodes (GNs) are populated using the first-order-accurate PDE-based extension technique [26]. Note, that, during extrapolation, at the domain boundary, one can use both the normal to the boundary and tangential to zero level approach, according to the choice of boundary treatment of BLNs (see above).

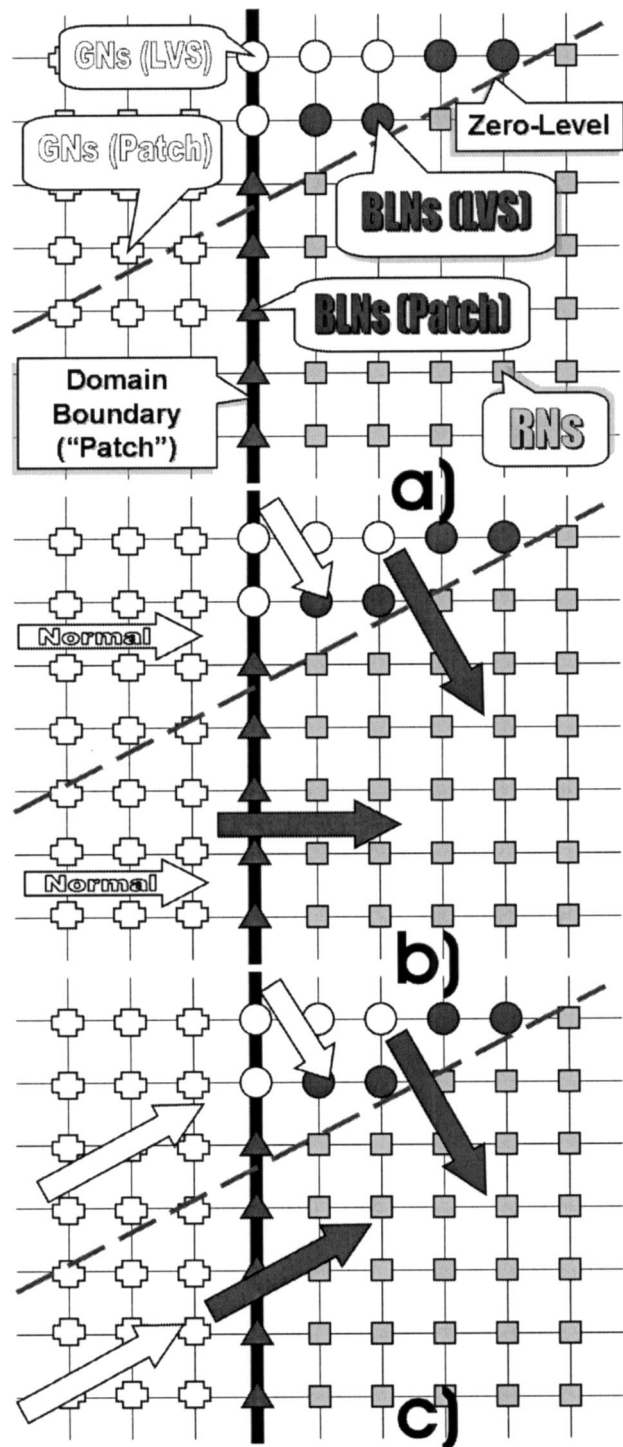


Fig. 3 On the treatment of “patch” boundaries of the computational domain

3.7 Note on Conservation. Our method utilizes conservative numerical scheme inside of fluid, but turns into non-conservative at the interface. Therefore, near the interface, there is formally a lack of discrete conservation on a set of measure zero.

The incentive to operate in conservative formulation originates from well-established theory to construct *weak solutions*, using the conservation properties of the system; while weak solutions to non-conservative formulations has yet to be defined. Both formulations are equivalent in smooth regions of the flow, but they are generally not equivalent if shocks waves are formed.

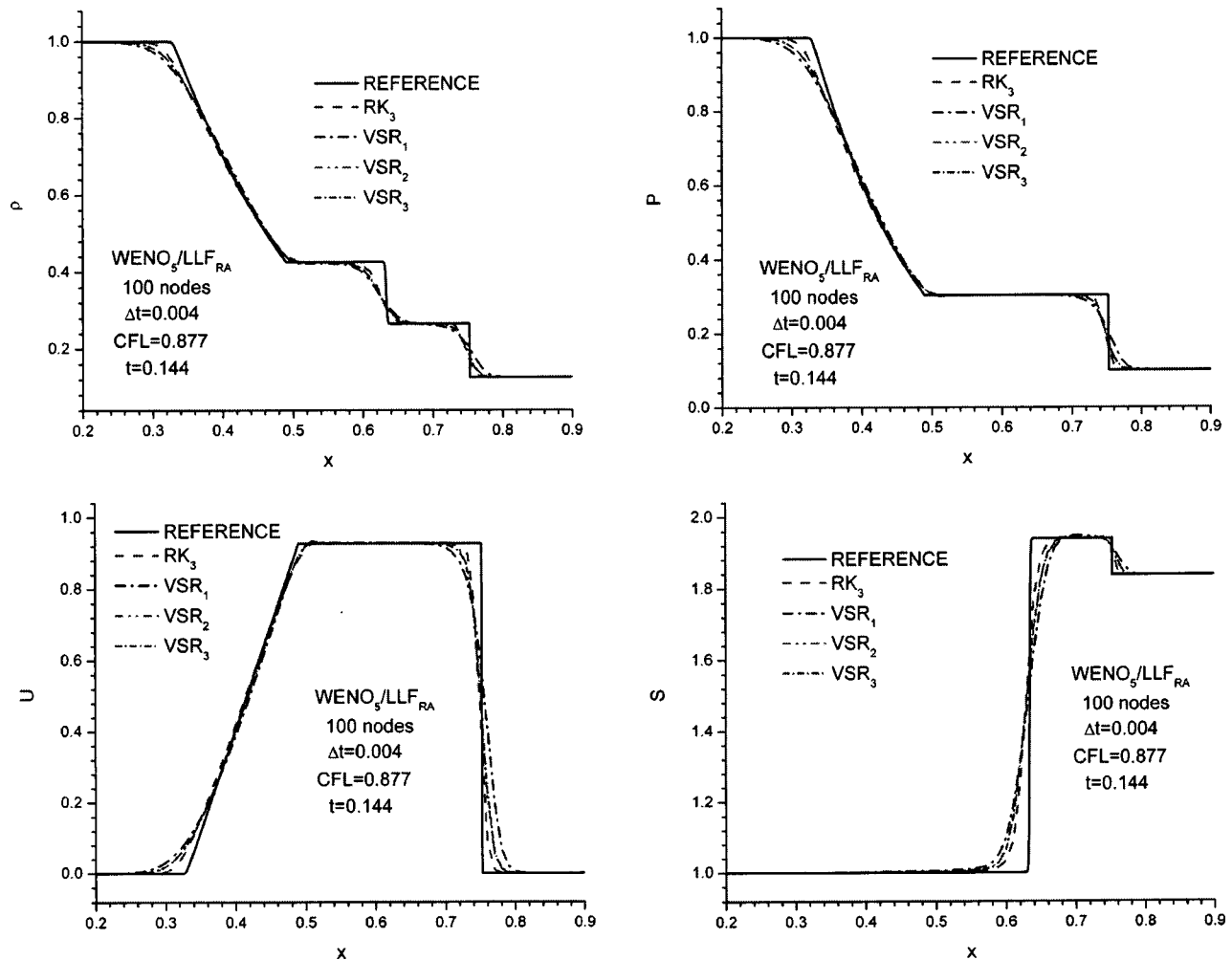


Fig. 4 Test 1: Comparison of the VSR-based time discretization strategy to the Runge-Kutta TVD scheme

On the other hand, when modelling multi-material contact discontinuities, switching to primitive (non-conservative) formulation is a common practice. This is because the non-conservative formulation allows to eliminate non-physical pressure oscillations at the interface [4,3,14] and [6]. Since the CBM non-conservative treatment is applied only at the boundary nodes, the conservation errors seem to be insignificant, even for strong shocks (see results of numerical examples below).

4 Numerical Examples

In the present section, we will test the CBM treatment on a number of numerical tests, with stationary and moving boundaries. We will start testing the VSR scheme, comparing it to the explicit RK-TVD scheme, see Test 1. Then we will move to the evaluation of the VSR-CBM scheme in one and multiple dimensions, for stationary and moving boundaries.

4.1 One-Dimensional Tests

4.1.1 Test 1: Sod's Test. As a first test-case, we take the following 1D Riemann problem, proposed by Sod [27]. Consider γ -gas ($\gamma=1.4$). At the center of the shock tube, there is a jump of flow variables. Initial conditions on the right R and left L of the jump are:

$$(\rho_L, U_L, P_L) = (1, 0, 1) \quad (46)$$

$$(\rho_R, U_R, P_R) = (0.125, 0, 0.1)$$

Calculations, performed using both the RK-TVD and the VSR-based approach, are shown in Fig. 4. The results of the third-order-accurate RK-TVD and VSR are nearly identical. The lower-order VSR schemes tend to smear-out both contact discontinuity and shock. For this test, the explicit RK-TVD scheme is more computationally efficient, because it requires less (3) iterations per time step. Setting tolerance of the VSR scheme to the level of 10^{-7} , the convergence is achieved in 20–30 iterations. If the tolerance is set to 10^{-2} , the convergence is achieved in 5–7 steps, which is quite close to the performance of the RK-TVD approach. Also, we numerically verified that even with this low tolerance level, the difference in computational results between the RK-TVD and the VSR scheme are insignificant.

In difference to the RK-TVD scheme, the VSR scheme permits calculations with CFL number (defined in $\{t;x;y;z\}$ space, σ_t) significantly more than 1. Figure 5 shows the results of calculations for σ_t varying from 0.88 to 3.52. Even with coarse physical

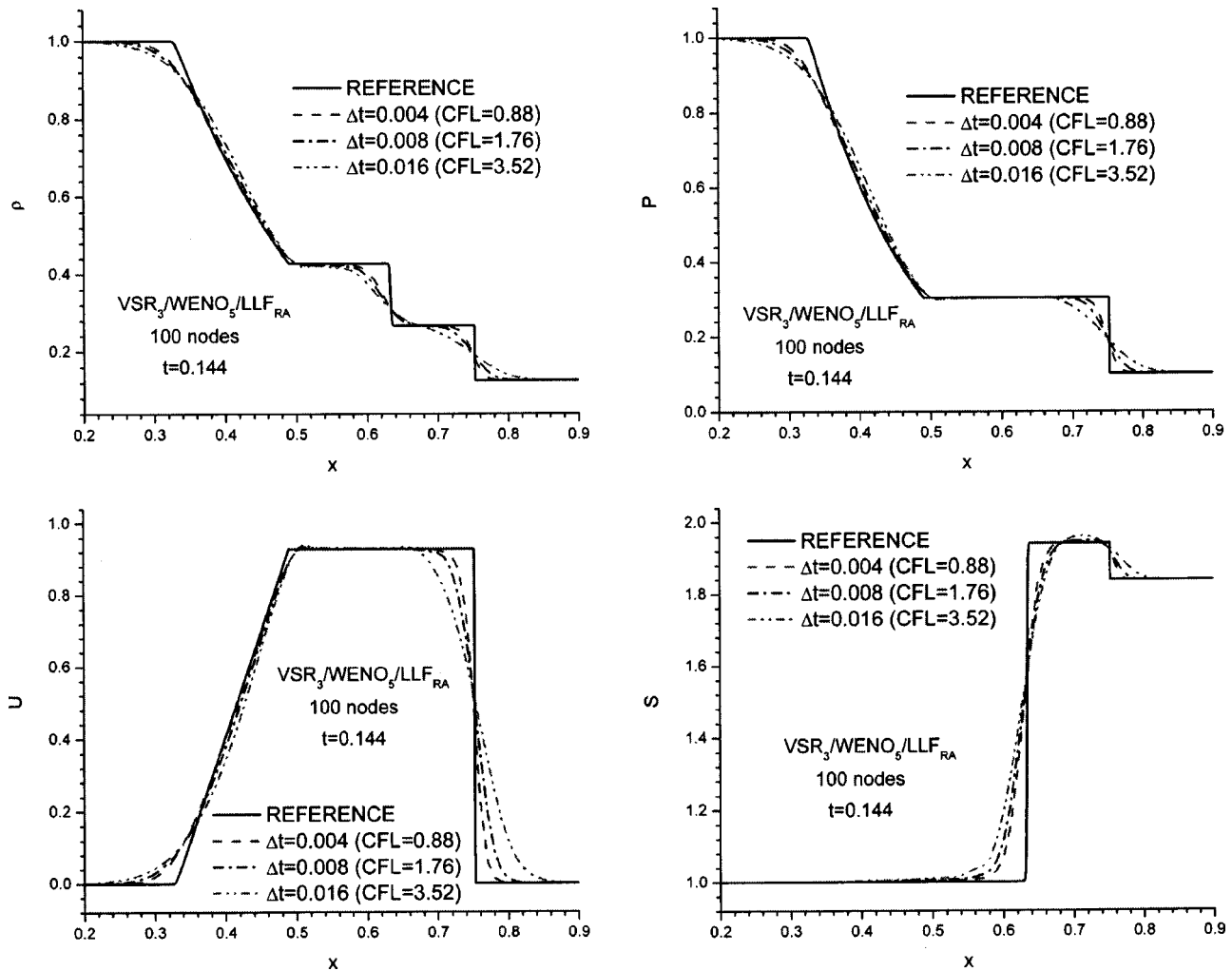


Fig. 5 Test 1: Effect of the physical time discretization on resolution of discontinuities

time resolution, the position of the contact discontinuity and shock are captured correctly. Though, one can observe significant smearing due to the physical time under-resolution. As such, the VSR scheme can be seen as an effective approach for modelling of stationary or slow-moving compressible fluid flows.

4.1.2 Note on the Origin of Over- or Under-Heating. The well-known overheating effect occurs when a shock reflects from a stationary wall boundary, leading to over- or undershoots in temperature and density distributions, while the pressure and velocity profiles remain unaffected.

Typical treatment of the solid wall boundary is to apply a reflection condition, i.e., the GHOST nodes are set in such a way, so that a shock impinging on a wall is met by a reflected shock of equal strength travelling in opposite direction.

There is a number of interpretations for overheating effects. Recently, Menikoff [28] suggested that the overheating errors are caused by smearing of the numerical shock profiles and that the spatial width of these errors tends to shrink to zero, as the effective numerical viscosity reduced to zero. The results of his calculations, however, show that the maximum overshoot at the wall does not shrink as the numerical dissipation goes to zero. The pressure and velocity profiles equilibrate quickly, while errors in

temperature and density remain. According to Menikoff, the overheating error is a symptom of the numerical scheme's unsuccessful attempt to simulate a physical phenomenon which occurs in reality.

Similar discussion of the overheating effects are presented by Noh [29]. Noh also stated that heat conduction at the wall would dissipate the overheating effect and that the failure of numerical schemes is partly due to the absence of heat conduction mechanism at the wall.

Some numerical schemes (e.g., Marquina's scheme, [30]) seem to possess a built-in heat conduction mechanism, which allows to generate lower level of overheating. In [14], it is argued that when Marquina's scheme is build on the WENO₅ low-viscosity flux splitting scheme, the errors due to the scheme viscosity are minimized and the intrinsic heat conduction property of the scheme helps to dissipate the remaining entropy errors, allowing a convergence in both L^2 and L^∞ sense. There are few examples when the 'heat conduction property' of the scheme operates on a much slower time scale than the accumulation of the overheating errors, which leads to a lack of convergence and significant distortion of the numerical results. The problem is especially acute for moving solid boundaries.

In [14], Fedkiw et al. introduced one possible solution to the overheating errors. In a procedure, called "isobaric fix," the overheating effects are removed by smearing thermodynamical param-

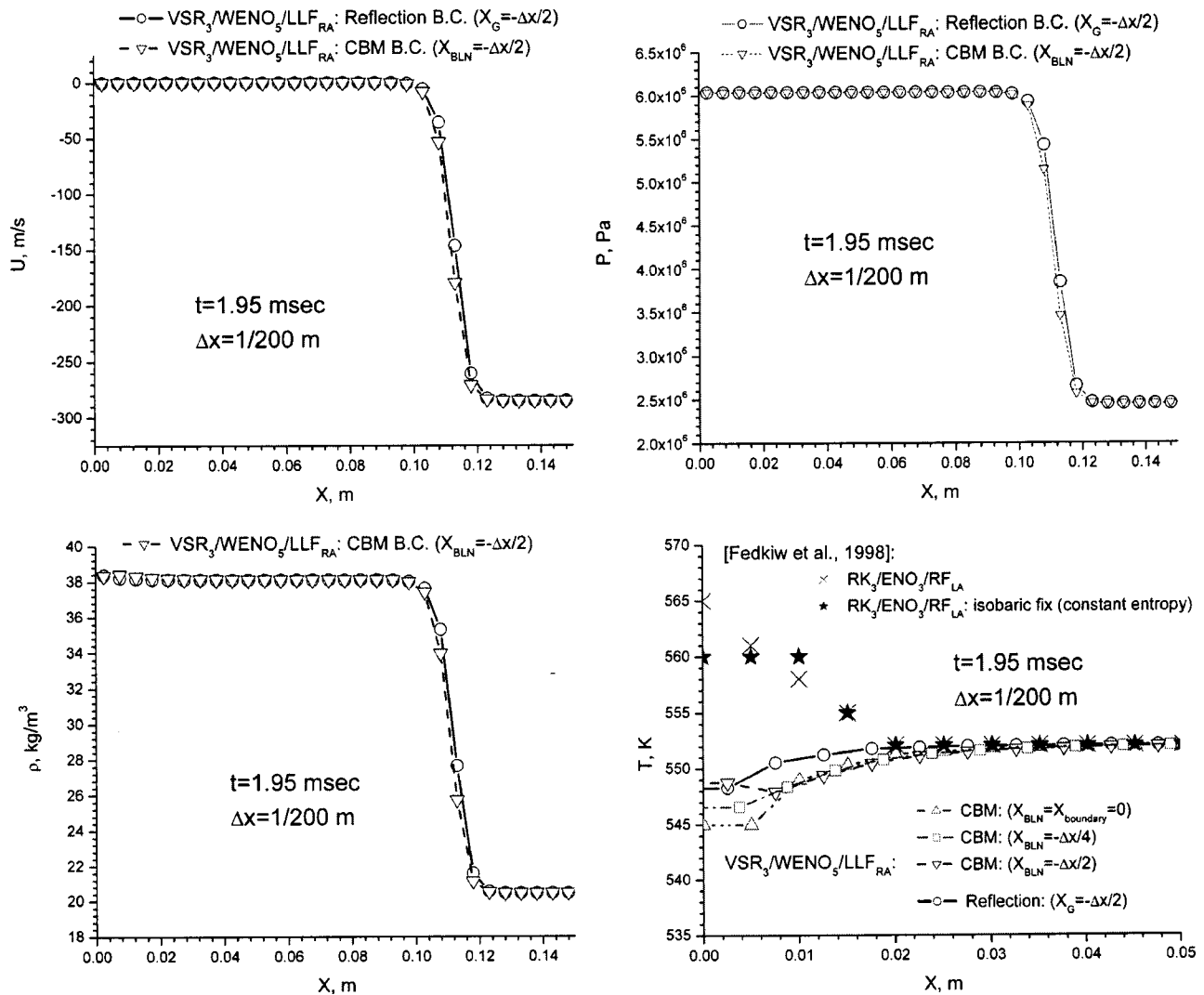


Fig. 6 Test 2: Study of the over/under-heating for a shock reflection from a stationary solid boundary

eters near the fluid-solid boundary. In the most successful isobaric fix strategy, the fluid's entropy is extrapolated normally to the boundary, from the layer of fluid located $\Delta h_{i.f.}$ inside of the domain. The thickness of the isobaric fix, $\Delta h_{i.f.}$, corresponds to the thickness of the smearing effect of the numerical scheme, for capturing contact lines, typically—1 or 2 computational nodes. While this approach does not eliminate overheating completely, it allows to limit overheating errors to some acceptable level.

In what follows (Test 2, 3, and 4), we will demonstrate that the CBM-based treatment of the stationary/moving boundaries does not generate, naturally, significant overheating.

4.1.3 Test 2: Shock Reflection at the Stationary Boundary. The purpose of this example is to demonstrate how the CBM scheme works for a standard shock reflection problem. The test problem we are considering was introduced in [14]. In the computational domain of size 1m, the following discontinuity is initially generated at $x=0.9$ m:

$$(\rho_L, U_L, T_L) = (10 \text{ kg/m}^3, 0 \text{ m/s}, 300 \text{ K})$$

$$(\rho_R, U_R, T_R) = (100 \text{ kg/m}^3, 0 \text{ m/s}, 300 \text{ K})$$

On the left, the solid wall boundary condition is applied (reflection or CBM-based). On the right, the domain is open (CBM-based non-reflection). The shock propagates to the left and reflects from the wall. The results of the calculations are compared for time $t = 1.95$ msec, Fig. 6, i.e. before the reflected shock interacts with the moving to the left contact line.

As it can be seen from Fig. 6, the pressure and velocity are continuous at the solid boundary. However, there exists small under-heating (from 5 to 7 K), when the VSR-based scheme is applied with both reflection and CBM treatment. This is lower than the result reported in [14], where the RK-TVD based scheme is applied with reflection boundary treatment (≈ 13 K). Note, that the scheme of [14] produced overheating. Also, the underheating errors of our scheme are lower than the errors of the isobaric fix treatment, which produced $\approx 8-9$ K overheating [14].

Next, we investigated the effect of the wall position, by shifting zero-level on some fraction of grid size, see Fig. 6. The underheating effects are found to be slightly higher (within 3 K), when the boundary of the domain is located close to the grid node. Probably, this effect can be attributed to the loss of the accuracy of the temperature gradient calculation by Eqs. (42) and (43), when the BLN is located close to the grid node.

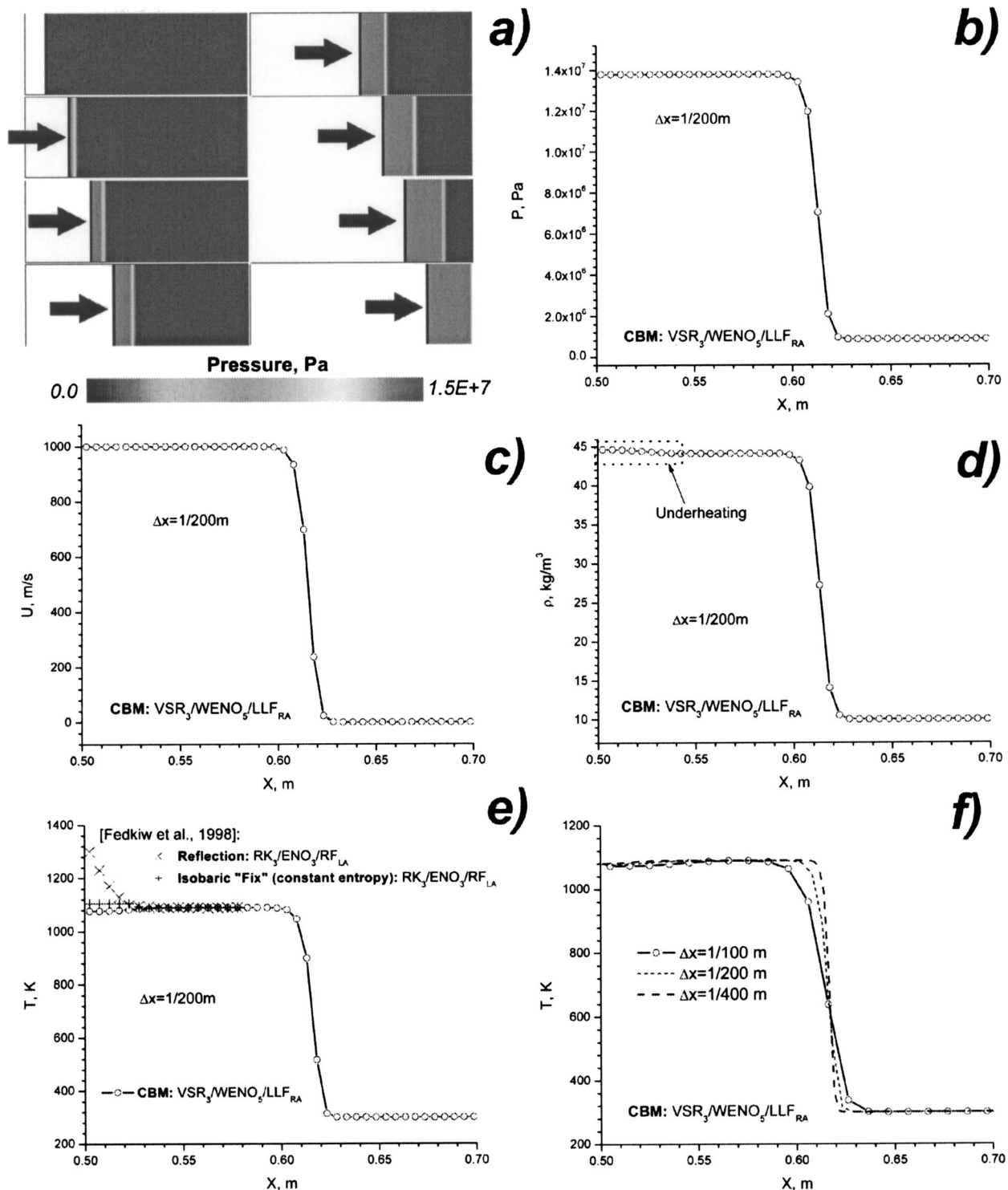


Fig. 7 Test 3: Study of the over/under-heating for a moving solid boundary (compression mode)

4.1.4 Test 3: Moving Piston: Compression. In this test, we will examine the CBM treatment of the moving boundary. Test conditions are the same as in example 2 of the paper [14], i.e., initially motionless air ($\gamma=1.4$) with parameters $\rho_{\text{init}}=10 \text{ kg/m}^3$ and $T_{\text{init}}=300 \text{ K}$ is suddenly compressed by a piston, see Fig. 7a. We consider a computational domain of size 1m, with open right boundary (CBM non-reflection boundary treatment). Initial position of the piston is 0.1 m. The piston is instantaneously accelerated to a velocity of 1000 m/s.

The results of the calculations are shown in Figs. 7b–f and

compared with both the reflection treatment of the moving boundary and the isobaric fix treatment, [14]. Similarly to the stationary boundary, both the RK-TVD-based reflection and isobaric fix generate over-heating, while the VSR-CBM scheme produces slight under-heating. The level of entropy errors of the CBM scheme is comparable to those of the isobaric fix treatment, in the range of 3 to 5 K. The reflection-based treatment resulted in significant over-heating errors, up to 200 K. Calculations with different resolutions demonstrate that the under-heating errors do not essentially depend on grid size, see Fig. 7f.

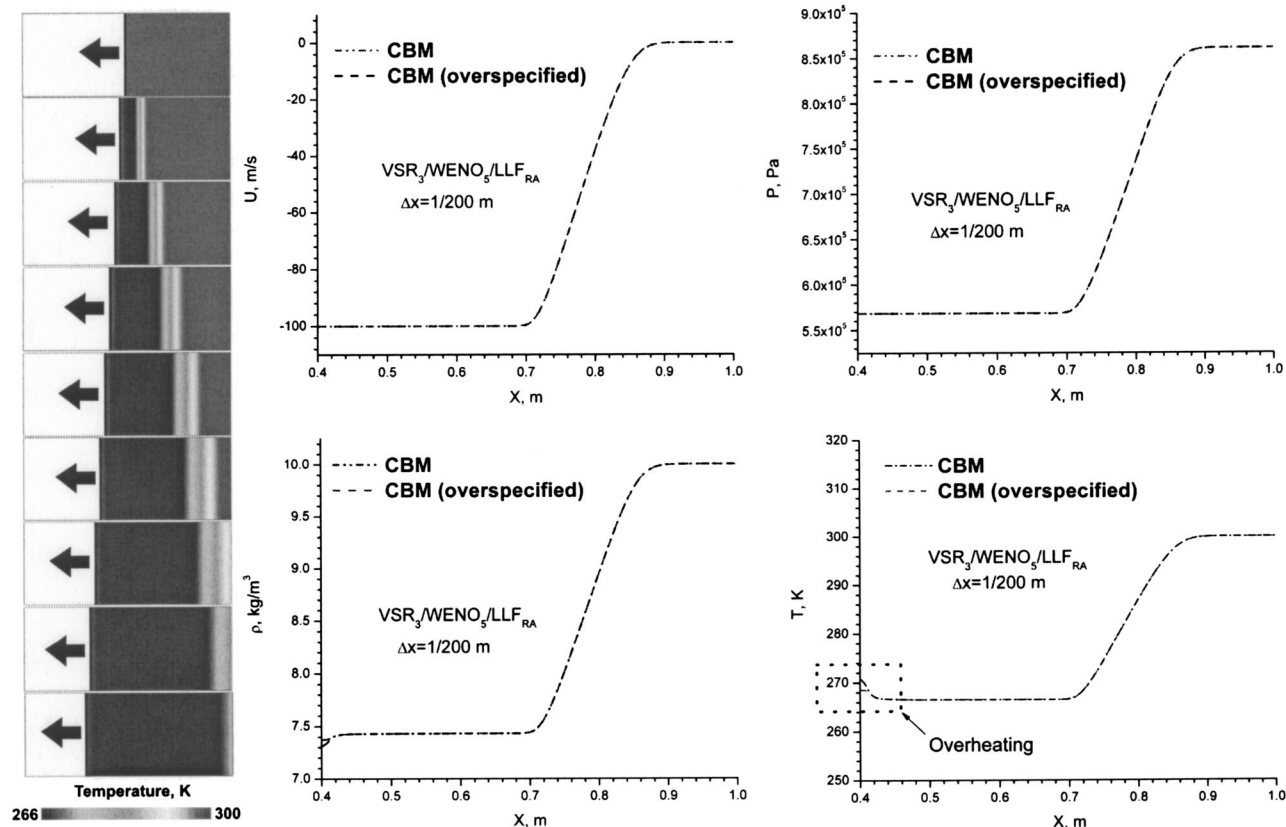


Fig. 8 Test 4: Study of the over/under-heating for a moving solid boundary (rarefaction mode)

4.1.5 Test 4: Moving Piston: Rarefaction. In this test, a piston, initially located at the position 0.5 m, is suddenly accelerated to a velocity of -100 m/s, i.e., gas is subjected to rarefaction. In this case, the CBM boundary treatment results in slight overheating, see Fig. 8. Importantly, from the point of view of the gas, the moving boundary is outlet, therefore, the standard CBM treatment would infuse only one boundary condition, i.e. fluid velocity, see Eq. (41). One can also force additional boundary condition on temperature gradient (overspecification), Eq. (41). In either case, the overheating errors are considerably smaller than those of the reflection boundary treatment, and at the same level as those of the isobaric fix, see Fig. 9a. Overheating effects of the reflection boundary treatment are dramatic—up to 80 K, for the present test problem.

As it can be seen in Fig. 9b, which shows temperature profiles in a coordinate system located at the fluid-solid boundary, the overheating errors do not grow in time. The maximum of the overheating tends to decrease, while the thickness of the overheated layer of fluid increases, probably due to numerical diffusion. Furthermore, with a better grid resolution, the overheating errors tend to decrease, Fig. 9c, which is consistent with the origin of these errors, discussed in Refs. [14], [28] and [29]. Also, Fig. 9d demonstrates the sensitivity to the time resolution, i.e., with smaller physical time step, the overheating errors seem to be smaller.

4.2 Test 5: Two-Dimensional Sod's Test. As a next example, we will consider a shock-tube test in two spatial dimensions. We shall demonstrate that the CBM boundary condition capturing strategy is able to maintain one-dimensionality of the flow. The level set function is generated, representing parallel-wall-boundaries of the shock tube. In the center of the shock tube, the jump conditions corresponding to the Sod's test Eq. (46) are initiated. Grid resolution was $\Delta x = \Delta y = 1/50$ and $1/200$. Five cases of the shock tube orientation relatively to the grid lines are

considered: a) aligned ($\alpha_{\text{rot}} = 0$ deg); b) $\alpha_{\text{rot}} = 15$ deg; c) $\alpha_{\text{rot}} = 20$ deg; d) $\alpha_{\text{rot}} = 30$ deg and e) $\alpha_{\text{rot}} = 45$ deg. To eliminate grid effect in initial conditions, the initial discontinuities are numerically smeared out over 2–3 grid nodes, using sinusoidal functions.

The results of the calculations are shown in Figs. 10, 11 and 12. First, the density distribution at the centerline of the shock tube is independent of the angle of the shock tube orientation, see Fig. 10. Notably, the results of the simulation demonstrate that the one-dimensionality of the flow is well preserved, see Fig. 12. Furthermore, due to the VSR-based strategy, this is achieved without 'locally-refined matching' (LRM) procedure, introduced in our previous study [17] to eliminate spurious normal streams generated at zero-level. At the boundary of the computational domain, the VSR-based non-reflection treatment has been applied. When the "tangential to zero-level" treatment is employed, see Figs. 3c, 11b and 12, a perfect "non-reflection" is achieved. In the case of the "normal to boundary" approach, as time progresses, the flow field is distorted at the junctions of zero-level and boundaries of the computational domain, Fig. 11a. This distortion generates reflected waves, which propagate along the shock tube walls, polluting the computational results.

4.3 Test 6: Three-Dimensional Shock Tube Test. Strong Shock. As a next example, we will consider a three-dimensional shock tube. The following discontinuity is generated at the center of 16 cm-long tube with radius of 5 cm:

$$(P_L, U_L, \rho_L) = (2 \cdot 10^5 \text{ Pa}, 0 \text{ m/s}, 2.32 \text{ kg/m}^3)$$

$$(P_R, U_R, \rho_R) = (4 \cdot 10^3 \text{ Pa}, 0 \text{ m/s}, 0.046 \text{ kg/m}^3)$$

which corresponds to a generated shock Mach number $M_{sh} = 2.13$.

Non-reflection and constant-pressure boundary conditions are applied at the right and left boundaries of the computational domain, respectively. Calculation is performed using 3D computa-

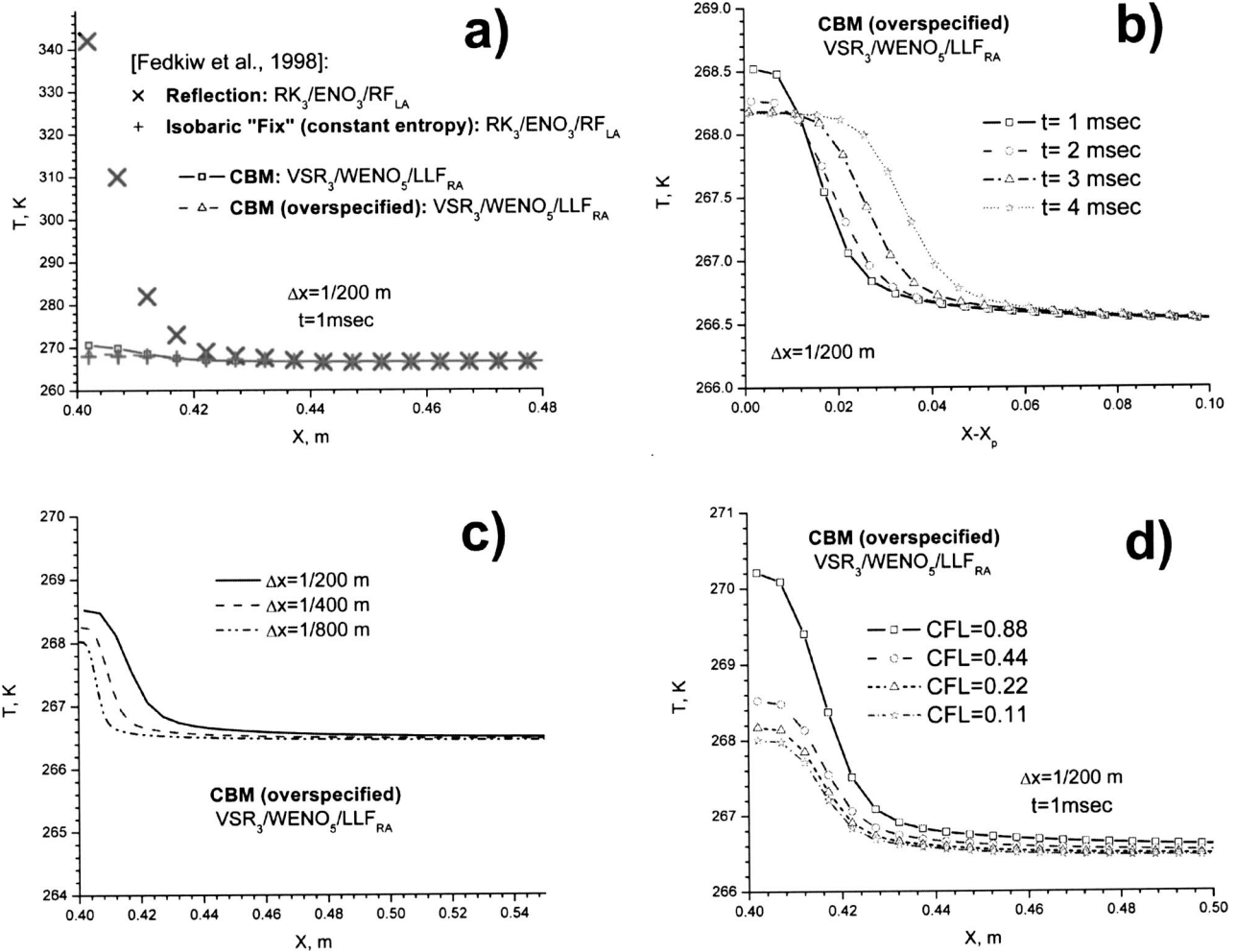


Fig. 9 Test 4: Study of the over/under-heating for a moving solid boundary (rarefaction mode), contd

tional grid of size $41 \times 21 \times 21$. Only quarter of the tube was modelled, with the CBM inviscid wall boundary treatment applied to represent symmetry BC conditions at the domain's LOW-J and LOW-K patch boundaries.

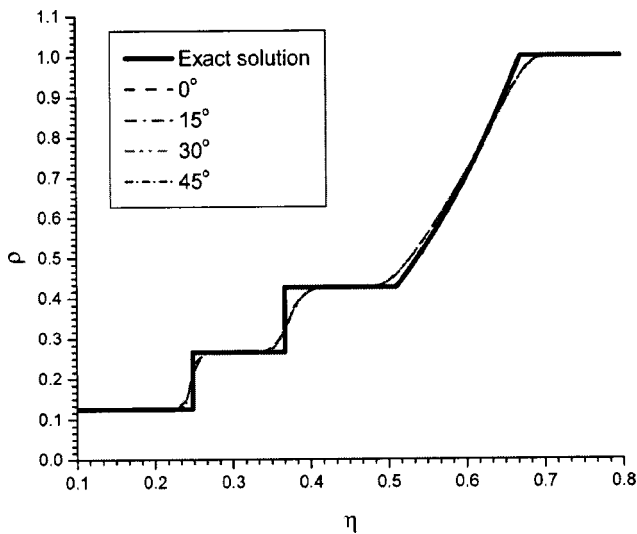


Fig. 10 Test 5: Density profile at the centerline of the shock tube

The dynamics of the density field is shown in Fig. 13. First, the one-dimensionality of the flow is perfectly preserved. Next, the CBM-based non-reflection boundary treatment produced a perfect non-reflecting solution. Finally, the solution procedure is robust, even for these quite strong shock conditions.

4.4 Test 7: Interaction of the $M=2.1$ Incident Shock With a Curved Channel. From now on, we will consider two-dimensional flows with complex geometry. The next test was described by Fursenko et al. in [31], where an interaction of the $M_{sh}=2.1$ incident shock waves with a curved two-dimensional channel were investigated. Experimental data were obtained by N. P. Mende [32].

The channel geometry utilized in the present study is described in Fig. 14. Parameters of the curved channel are $R_1=0.008$ and $R_2=0.028$ (in dimensionless units). The incident shock with $M_{sh}=2.1$ was generated by setting the following discontinuity at the inlet to the channel:

$$(P_D, V_{\eta,D}, \rho_D) = (1, 1.203) \quad (47)$$

$$(P_U, V_{\eta,U}, \rho_U) = (0.20087, 0, 0.3556)$$

where η denotes a direction of the channel axis. Non-reflection boundary conditions are specified at the inlet and outlet of the channel. Simulations were performed on a sequence of computa-

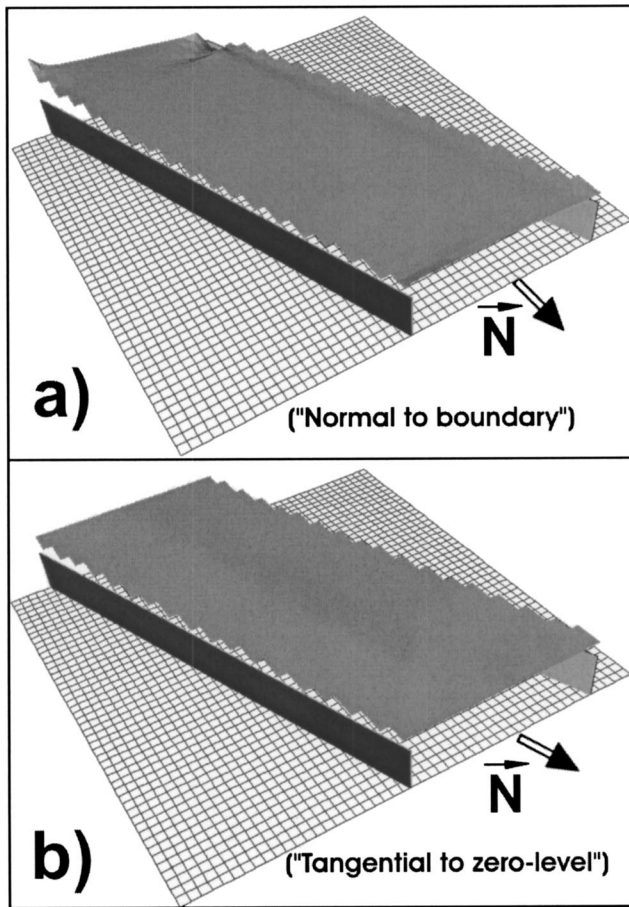


Fig. 11 Test 5: Effect of the patch boundary treatment on the steady-state density field

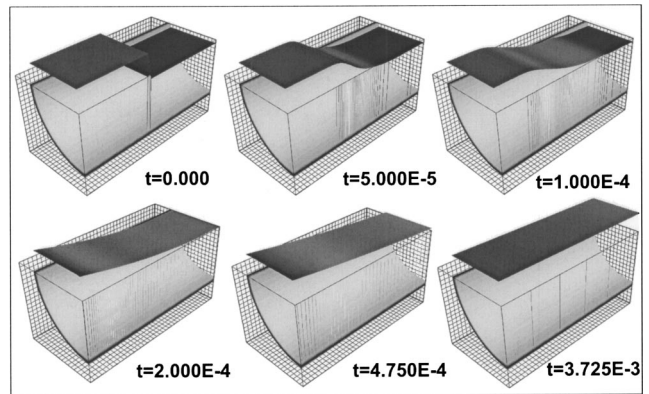


Fig. 13 Test 6: Dynamics of the density field. Density is colored and extruded, in accordance to its value. The boundary ("zero-level") is also shown.

tional grids with grid size $\Delta h = (R_2 - R_1)/20$, $(R_2 - R_1)/40$, $(R_2 - R_1)/80$ and $(R_2 - R_1)/160$, using the 'physical time CFL number' $\sigma_t \approx 1$.

Density distributions for different moments of the numerical simulation with grid size $\Delta h = (R_2 - R_1)/160$ are presented in Fig. 15. Due to the interaction of the incident shock with the curved wall of the channel, the λ -structure has been formed (Figs. 15b, c and d). Figure 16 shows comparison of the VSR-CBM-based simulation to the experimental interferogram, which represents lines of the constant density. Description of the experimental facility and measurement technique is given in [33]. As one can see, all major flow structures are captured well. These include the position of the incident shock, formation of λ -structure, "outer near-wall contact line," and "inner-wall rarefaction zone."

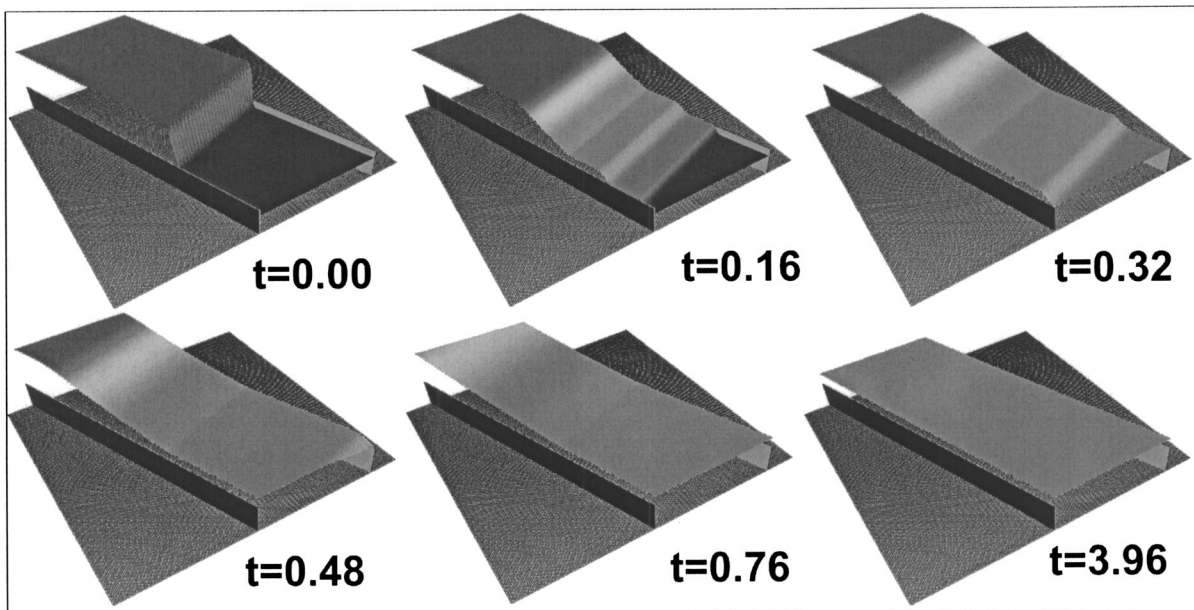


Fig. 12 Test 5: Dynamics of the density distribution for a Sod's test in two spatial dimensions. Shock tube orientation relatively to the grid lines is 20 deg. Density is colored and extruded normally to the computational plane, in accordance to its value. The boundary ("zero-level") is also shown. Grid size is 200^2 and $\sigma_t = 1.0$. Normal vector at the boundary of the domain is set to be 'tangential to zero-level'.

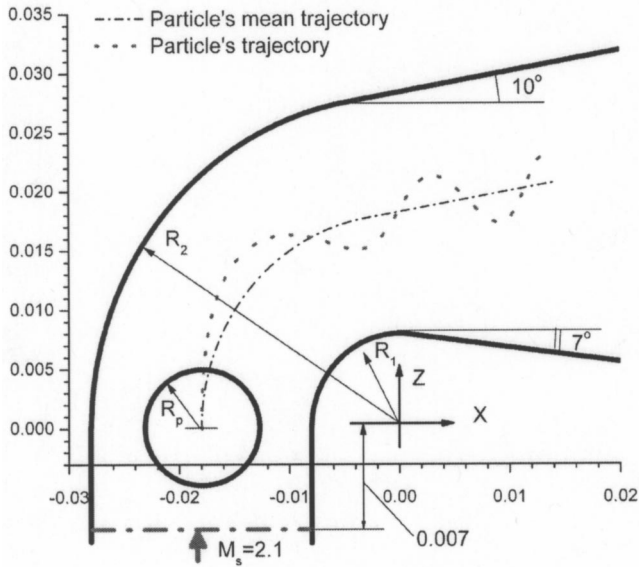


Fig. 14 Test 7, 8, 9: On the formulation of the curved channel geometry (tests 7, 8, and 9) and cylindrical particle's trajectory (test 9)

Figure 17 presents a comparison of the λ structure obtained by a) the VSR-CBM-based scheme; b) the second-order Godunov (SOG) scheme on a body-fitted structured grid [31]; and c) the SOG scheme on unstructured grid [31]. The presented results of the VSR-CBM scheme are computed on a grid resolution $(R_2 - R_1)/160$.

4.5 Test 8: Interaction of the $M=2.1$ Incident Shock With Obstacles. In the next test, we will include two cylindrical obstacles in the channel. The first one is located in the curved part, with a center positioned at 45 deg relatively to the center of coordinate system. The second obstacle is located at the expanding part, positioned 0.002 length units downstream from the beginning of the expansion. The radii of both obstacles are $R_0 = 0.005$. Importantly, a generation of the body-fitted structured grid for this geometry is challenging. Our grid is structured, and,

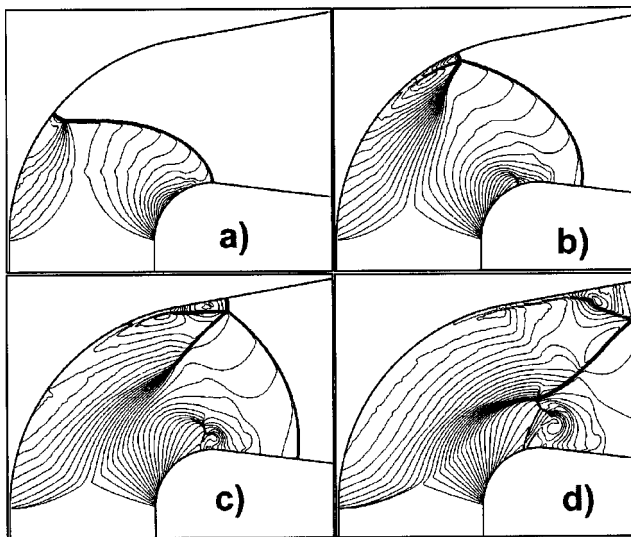


Fig. 15 Test 7: Dynamics of the density field. a) $t = 1.05 \cdot 10^{-2}$; b) $t = 1.55 \cdot 10^{-2}$; c) $t = 2.05 \cdot 10^{-2}$; d) $t = 2.55 \cdot 10^{-2}$.

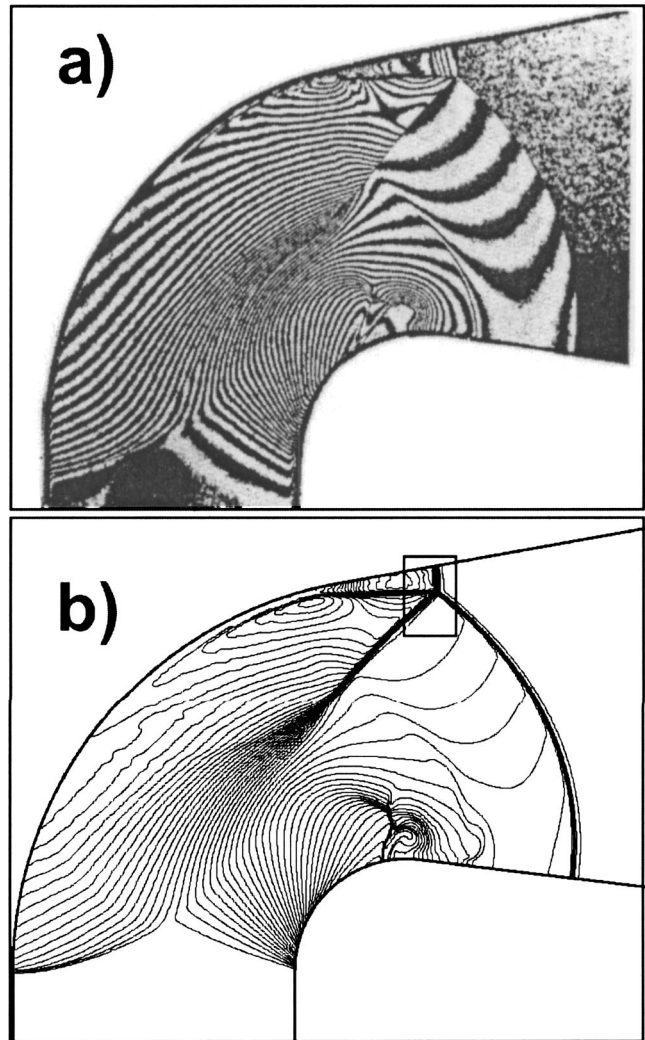


Fig. 16 Test 7: Propagation of the initially planar shock wave ($M_{sh}=2.1$) through the curved channel. a) interferogram from the experiment; b) computed density field, using the CBM-based approach.

at the same time, there are no difficulties to construct the level set function representing this complex solid-fluid boundary.

Dynamics of the density field is presented in Figs. 18a–f, for different moments of the simulation. In Figs. 19a and b, the results of the VSR-CBM-based calculation are compared to those using

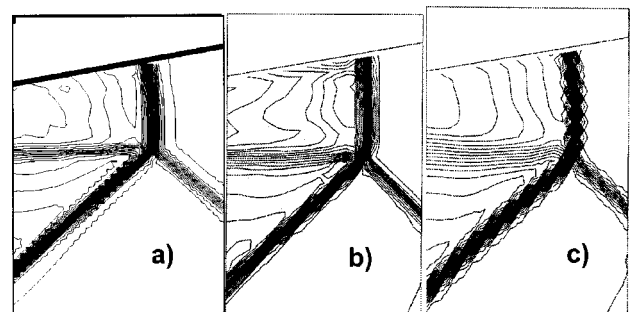


Fig. 17 Test 7: Resolution of the λ -structure by a) the CBM-based approach (VSR₃/WENO₅/LLF_{RA} scheme); b) the second-order Godunov (SOG) scheme on a body-fitted structured grid [31]; and c) the SOG scheme on unstructured grid [33]

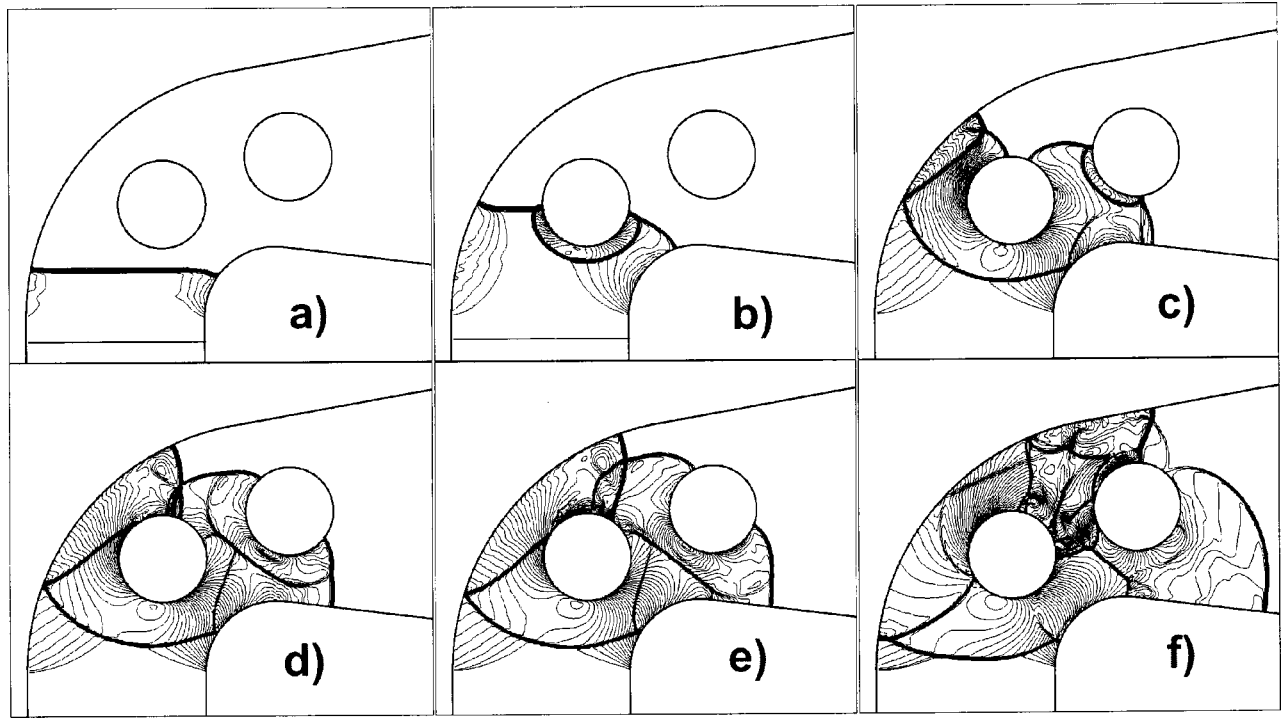


Fig. 18 Test 8: Dynamics of the density field. a) $t=4.5 \cdot 10^{-3}$; b) $t=8.1 \cdot 10^{-3}$; c) $t=1.32 \cdot 10^{-2}$; d) $t=1.56 \cdot 10^{-2}$; e) $t=1.68 \cdot 10^{-2}$; f) $t=2.22 \cdot 10^{-2}$.

the SOG on unstructured grid [31], obtained for similar geometry and approximately the same time moment. Both calculations reveal similar structures of the flow.

4.6 Test 9: Moving Particle in Supersonic Flow. In our last numerical test, we will model a moving cylindrical particle in supersonic flow. Initial conditions for a simulation and initial position of the particle in a curved channel are shown in Fig. 14. Incident shock $M_{sh}=2.1$ conditions Eq. (47) are specified at the position of 0.007 length units below the particle's initial position. Particle's radius was 0.005 units of length. The motion of particle starts at the time $t_0=0.00282$. Its trajectory and velocity are described by the following set of equations:

$$V_x = \begin{cases} V_x^{(0)} = 0.75 & t \geq t_0 \\ 0 & t < t_0 \end{cases}$$

$$\chi(t) = \begin{cases} V_x^{(0)}(t-t_0) & t \geq t_0 \\ 0 & t < t_0 \end{cases}$$

$$\Psi(t) = \Psi_0 \sin \left[\left(\frac{t-t_0}{T} \right)^2 \right]$$

where $T=0.015$ and $\Psi_0=0.0025$. Next, if $\chi \leq \chi_0$:

$$x_p(t) = -(R_m + \Psi) \cos \frac{\chi}{R_m}$$

$$y_p(t) = (R_m + \Psi) \sin \frac{\chi}{R_m}$$

$$u_p(t) = V_x \left[1 + \frac{\Psi}{R_m} \right] \sin \frac{\chi}{R_m} - V_\Psi \cos \frac{\chi}{R_m}$$

$$v_p(t) = V_x \left[1 + \frac{\Psi}{R_m} \right] \cos \frac{\chi}{R_m} + V_\Psi \sin \frac{\chi}{R_m}$$

Otherwise:

$$x_p(t) = -(R_m + \Psi) \sin \alpha_0 + (\chi - \chi_0) \cos \alpha_0$$

$$y_p(t) = (R_m + \Psi) \cos \alpha_0 + (\chi - \chi_0) \sin \alpha_0$$

$$u_p(t) = V_x \cos \alpha_0 - V_\Psi \sin \alpha_0$$

$$v_p(t) = V_x \sin \alpha_0 + V_\Psi \cos \alpha_0$$

where $\chi_0 = R_m[\pi/2 - \alpha_0]$; $R_m = (R_1 + R_2)/2$; $\alpha_0 = \pi/18$ and

$$V_\Psi(t) = \frac{2\Psi_0}{T^2} (t-t_0) \cos \left[\left(\frac{t-t_0}{T} \right)^2 \right]$$

The trajectory of the particle is shown in Fig. 14. The particle's motion is transonic, based on both pre- and post-incident-shock parameters of the flow, see Fig. 20.

Simulation was performed on a computational grid of size $\Delta h = (R_2 - R_1)/160$, with $\sigma_r \approx 1$.

The results of the calculation are shown in Fig. 21, which presents the dynamics of the density field and position of the cylindrical particle for different moments of the numerical simulation.

5 Concluding Remarks

A new method (Characteristic-Based Matching (CBM)) for modelling of immersed stationary/moving boundaries in a compressible fluid is developed. The method is based on the level-set technology and characteristic decomposition at boundary nodes, which enable an efficient, robust and accurate treatment of complex moving fluid-solid boundaries.

The method has been extensively tested on a number of compressible fluid dynamics problems, which include shock tube tests, complex-geometry strong shock tests and moving piston and particle tests. The entropy (overheating) errors of the approach have been examined. These errors, typically present in other boundary treatment techniques, are found to be insignificant.

Current development of the CBM method is focussed on multi-fluid interfaces.

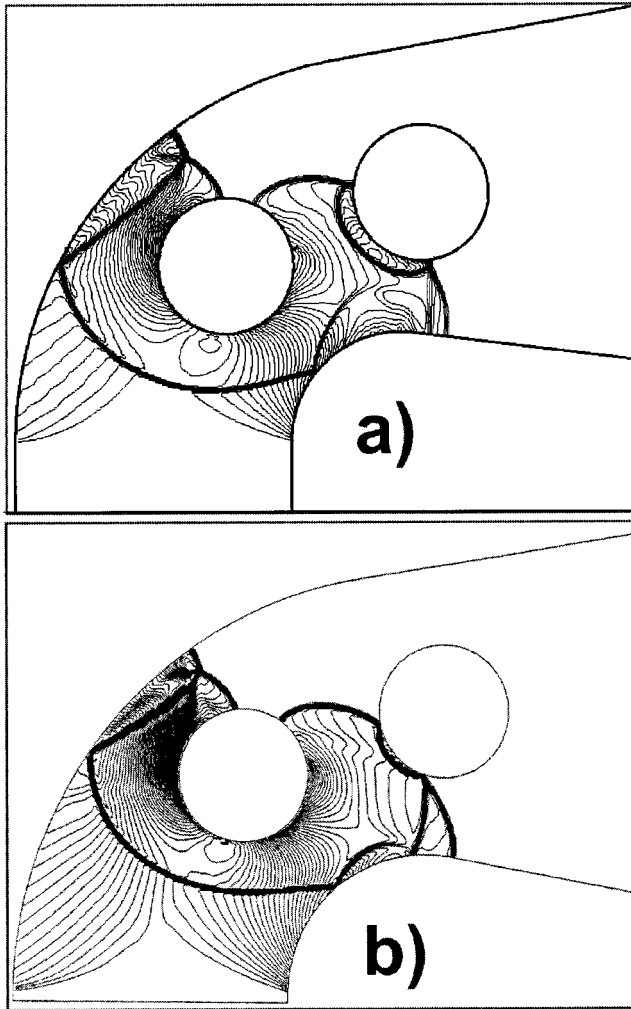


Fig. 19 Test 8: Density field computed by a) the CBM-based approach (VSR₃/WENO₅/LLF_{RA} scheme); and b) the SOG on unstructured grid [33]

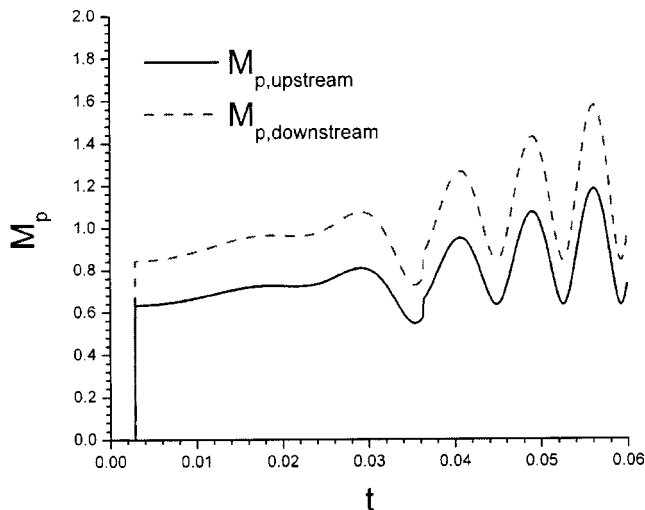


Fig. 20 Test 9: Dynamics of the moving particle's Mach number, based on the initial upstream and downstream flow conditions in a laboratory frame

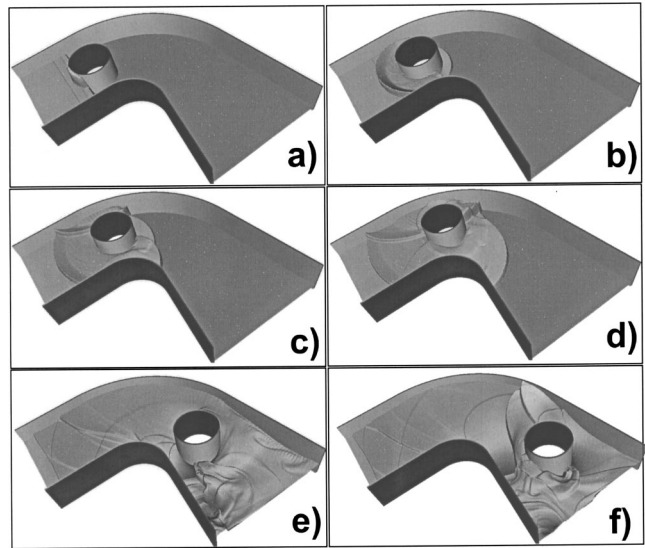


Fig. 21 Test 9: Dynamics of the density field. Density is colored and extruded normally to the computational plane, in accordance to its value. The boundary ("zero-level") is also shown. a) $t=2 \cdot 10^{-3}$; b) $t=6 \cdot 10^{-3}$; c) $t=1 \cdot 10^{-2}$; d) $t=1.4 \cdot 10^{-2}$; e) $t=3.9 \cdot 10^{-2}$; and f) $t=4.9 \cdot 10^{-2}$.

Acknowledgment

This work is performed under support of the US Nuclear Regulatory Commission's (NRC) Office of Regulatory Research and Lawrence Livermore National Laboratory. Support of Dr. Glen Nakafuji are gratefully acknowledged.

References

- [1] Godunov, S. K., 1959, "A Difference Method for Numerical Calculation of Discontinuous Solutions of Hydrodynamics," *Mat. Sb.*, **47**(3), pp. 271–306.
- [2] LeVeque, R. J., 1992, *Numerical Methods for Conservation Laws, Lectures in Mathematics, ETH Zürich*, Birkhäuser Verlag, Basel-Boston-Berlin.
- [3] Karni, S., 1996, "Multicomponent Flow Calculations by a Consistent Primitive Algorithm," *J. Comput. Phys.*, **112**, pp. 31–43.
- [4] Abgrall, R., 1996, "How to Prevent Pressure Oscillations in Multicomponent Flow Calculations: A Quasi Conservative Approach," *J. Comput. Phys.*, **125**, pp. 150–160.
- [5] Karni, S., 1996, "Hybrid Multifluid Algorithms," *SIAM J. Sci. Comput. (USA)*, **17**(5), pp. 1019–1039.
- [6] Fedkiw, R. P., Aslam, T., Merriman, B., and Osher, S., 1999, "A Non-oscillatory Eulerian Approach to Interfaces in Multimaterial Flows (the Ghost Fluid Method)," *J. Comput. Phys.*, **152**, 457–492.
- [7] Chern, I.-L., Glimm, J., McBryan, O., Plohr, B., and Yaniv, S., 1986, "Front Tracking for Gas Dynamics," *J. Comput. Phys.*, **62**, pp. 83–110.
- [8] Osher, S., and Sethian, J. A., 1988, "Fronts Propagating with Curvature-Dependent Speed: Algorithms Based on Hamilton-Jacobi Formulations," *J. Comput. Phys.*, **79**, 12–49.
- [9] Peskin, C. S., 1977, "Numerical Analysis of Blood Flow in the Heart," *J. Comput. Phys.*, **25**, pp. 220–252.
- [10] Hirt, C. W., and Nichols, B. D., 1981, "Volume of Fluid (VOF) Method for the Dynamics of Free Boundaries," *J. Comput. Phys.*, **39**, pp. 201–225.
- [11] Rider, W. J., and Kothe, D. B., 1998, "Reconstructing Volume Tracking," *J. Comput. Phys.*, **141**(2), pp. 112–152.
- [12] Unverdi, S. O., and Tryggvason, G., 1992, "A Front-Tracking Method for Viscous, Incompressible, Multi-Fluid Flows," *J. Comput. Phys.*, **100**, pp. 25–37.
- [13] Harlow, F. H., and Welch, J. E., 1965, "Numerical Calculation of Time-Dependent Viscous Incompressible Flow of Fluid With Free Surface," *Phys. Fluids*, **8**, pp. 2182–2189.
- [14] Fedkiw, R. P., Marquina, A., and Merriman, B., 1999, "An Isobaric Fix for the Overheating Problem in Multimaterial Compressible Flows," *J. Comput. Phys.*, **148**, 545–578.
- [15] Fedkiw, R. P., 2002, "Coupling an Eulerian Fluid Calculation to a Lagrangian Solid Calculation With the Ghost Fluid Method," *J. Comput. Phys.*, **175**, 200–224.
- [16] Thompson, K. W., 1990, "Time-Dependent Boundary Conditions for Hyperbolic Systems, II," *J. Comput. Phys.*, **89**, pp. 439–461.
- [17] Nourgaliev, R. R., Dinh, T. N., Suschikh, S. Yu., Yuen, W. W., and Theofanous, T. G., 2003, "The Characteristics-Based Matching Method for Compressible

Flow in Complex Geometries," *AIAA 2003-0247, 41st AIAA Aerospace Sciences Meeting and Exhibit*, January 6–9, 2003, Reno, NV, USA.

- [18] Sethian, J. A., 1999, *Level Set Methods and Fast Marching Methods*, Cambridge University Press.
- [19] Nourgaliev, R. R., Dinh, T. N., and Theofanous, T. G., 2004, "A Pseudocompressibility Method for the Simulation of Single- and Multiphase Incompressible Flows," *Int. J. Multiphase Flow*, (in press).
- [20] Nourgaliev, R. R., Dinh, T. N., and Theofanous, T. G., 2003, "On Capturing of Interfaces in Multimaterial Compressible Flows Using a Level-Set-Based Cartesian Grid Method. Multiphase Compressible Fluid-Solid (Particulate) Flows," *CRSS Research Report 05/03-1*, 53p., May 23, 2003.
- [21] Fedkiw, R., Merriman, B., Donat, R., and Osher, S., 1998, "The Penultimate Scheme for Systems of Conservation Laws: Finite Difference ENO with Marquina's Flux Splitting," *Progress in Numerical Solutions of Partial Differential Equations*, Arcachon, France, edited by M. Hafez, July 1998.
- [22] Shu, C.-W., and Osher, S., 1989, "Efficient Implementation of Essentially Non-Oscillatory Shock-Capturing Schemes II (Two)," *J. Comput. Phys.*, **83**, 32–78.
- [23] Shu, C.-W., 1997, "Essentially Non-Oscillatory and Weighted Essentially Non-Oscillatory Schemes for Hyperbolic Conservation Laws," *NASA/CR-97-206253, ICASE Report No. 97-65*.
- [24] Anderson, J. D., 1995, *Computational Fluid Dynamics, The Basics With Applications*, McGraw-Hill, Inc.
- [25] Poinso, T. J., and Lele, S. K., 1992, "Boundary Conditions for Direct Simulations of Compressible Viscous Flows," *J. Comput. Phys.*, **101**, pp. 104–129.
- [26] Peng, D. P., Merriman, B., Osher, S., Zhao, H., and Kang, M., 1999, "A PDE-Based Fast Local Level Set Method," *J. Comput. Phys.*, **155**, pp. 410–438.
- [27] Sod, G. A., 1978, "A Survey of Several Finite Difference Methods for Systems of Nonlinear Hyperbolic Conservation Laws," *J. Comput. Phys.*, **27**, 1–31.
- [28] Menikoff, R., 1994, "Errors When Shocks Waves Interact due to Numerical Shock Width," *SIAM J. Sci. Comput. (USA)*, **15**(5), p. 1227.
- [29] Noh, W., 1978, "Errors for Calculations of Strong Shocks Using an Artificial Viscosity and an Artificial Heat Flux," *J. Comput. Phys.*, **72**, p. 78.
- [30] Donat, R., and Marquina, A., 1996, "Capturing Shock Reflections: An Improved Flux Formula," *J. Comput. Phys.*, **125**, 42–58.
- [31] Fursenko, A. A., Sharov, D. M., Timofeev, E. V., and Voinovich, P. A., 1992, "Numerical Simulation of Shock Wave Interaction With Channel Beds and Gas Nonuniformities," *Comput. Fluids*, **21**(3), pp. 377–396.
- [32] Goloviznin, V. P., Zhmakin, A. I., Komissaruk, B. A., Mende, H. P., and Fursenko, A. A., 1981, "On Propagation of Shock Waves in Planar and Axisymmetric Channels," *Preprint of FTI-709*, Leningrad, 49 p. (In Russian).
- [33] Dukhovski, I. A., Komissaruk, B. A., Kovalev, P. I., and Mende, H. P., 1985, "High-Speed Photography of the Interaction of a Water Drop With a Supersonic Sphere," *Opt. Laser Technol.*, **17**(3), pp. 148–150.

Byeong Rog Shin

Associate Professor
Department of Mechanical Engineering,
Changwon National University,
Changwon 641-773, Korea
e-mail: brshin@changwon.ac.kr

Satoru Yamamoto

Associate Professor
Department of Aeronautic
and Space Engineering,
Tohoku University,
Sendai 980-8579, Japan

Xin Yuan

Professor
Department of Thermal Engineering,
Tsinghua University,
Beijing 100084, P.R. China

Application of Preconditioning Method to Gas-Liquid Two-Phase Flow Computations

A preconditioned numerical method for gas-liquid two-phase flows is applied to solve cavitating flow. The present method employs a finite-difference method of the dual time-stepping integration procedure and Roe's flux difference splitting approximation with the MUSCL-TVD scheme. A homogeneous equilibrium cavitation model is used. The present density-based numerical method permits simple treatment of the whole gas-liquid two-phase flow field, including wave propagation, large density changes and incompressible flow characteristics at low Mach number. Two-dimensional internal flows through a backward-facing step duct, convergent-divergent nozzles and decelerating cascades are computed using this method. Comparisons of predicted and experimental results are provided and discussed. [DOI: 10.1115/1.1777230]

Introduction

Cavitation is a phase change phenomenon accompanying the appearance of vapor bubbles inside a homogeneous liquid medium that occurs in the domain below vapor pressure according to the decrease in local pressure when fluid devices move at high speed in a working fluid in the liquid state. Cavitation takes various forms according to the flow conditions, and causes noise, vibration and damage, as well as reduced performance in hydraulic machine systems when cavitation bubbles unexpectedly attach and collapse on body surfaces. Therefore, in order to reduce these unfavorable effects, technology for accurate prediction and estimation of cavitation are very important in the development of high-speed fluid devices.

In order to clarify and understand the behavior of cavity flow, cavity flow models and analytical methods for numerical simulations have been proposed [1,2], among which, gas-liquid two-phase flow approaches that consider homogeneous equilibrium [3–6] are more advantageous. However, because originally cavity flows have strong unsteady flow phenomena, including phase changes, fluid transients, vortex shedding and turbulence, a numerical method by which to solve these flows has not yet been established. In general, there are few comprehensive applications to the transient flow range from the subcavitation state to the supercavitation state. Recently, we have proposed a mathematical cavity flow model [7,8] based on a homogeneous equilibrium model taking into account the compressibility of the gas-liquid two-phase media. With this model and TVD-MacCormack scheme [9] or a high-order MUSCL-TVD solution method [10], the mechanism of developing cavitation has been investigated through application to cavitating flows around a hydrofoil [11–13].

The purpose of this paper is to verify the applicability of the preconditioning solution method by the author [13] and to extend to a method for unsteady flow by using a dual time-stepping procedure to treat both compressibility and incompressibility effects associated with a very large range of mixture sound speeds which can arise in cavity flows with multi-rates of void fraction. As numerical examples, two-dimensional (2-D) internal flows

through a backward-facing step duct, convergent-divergent nozzles and decelerating cascades are simulated. The detailed cavity flow behavior, including the growing and shedding of the cavity for the above flow fields, are investigated. Velocity and pressure distributions obtained by the present preconditioned and non-preconditioned solution method are compared with experimental data.

Homogeneous Cavitation Model

Cavity flow of gas-liquid two-phase flow can be modeled as an apparent single-phase flow using the concept of the homogeneous equilibrium model [7,8,13]. Under the this model concept, the pressure for gas-liquid two-phase media is determined using a combination of two equations of state for gas phase and liquid phase, which is written as follows:

$$\rho = \frac{p(p+p_c)}{K(1-Y)p(T+T_c) + RY(p+p_c)T} \quad (1)$$

where ρ , p , Y , and T are the mixture density, pressure, quality (dryness) and the temperature, respectively. R is the gas constant and K , p_c and T_c represent the liquid constant, pressure constant and the temperature constant for water, respectively. This equation is derived from the local equilibrium assumption, and corresponds to the following equations of state for a pure liquid ($Y=0$), by Tammann [14], and an ideal gas ($Y=1$), respectively.

$$\begin{aligned} p+p_c &= \rho_\ell K(T+T_c); \quad \text{for } Y=0, \\ p &= \rho_g RT; \quad \text{for } Y=1 \end{aligned} \quad (2)$$

where the subscripts ℓ and g indicate liquid phase and gas phase, respectively. Therefore, the apparent compressibility is considered, and the sound speed c becomes

$$\frac{1}{c^2} = \frac{\partial \rho}{\partial T} (\rho C_p)^{-1} + \frac{\partial \rho}{\partial p} \quad (3)$$

C_p is the specific heat capacity at constant pressure of $C_p = Y C_{p_g} + (1-Y) C_{p_\ell}$. The relationship between the local void fraction α and the quality Y is given as $\rho(1-Y) = (1-\alpha)\rho_\ell$ and $\rho Y = \alpha\rho_g$, where

$$\alpha = \frac{RY(p+p_c)T}{K(1-Y)p(T+T_c) + RY(p+p_c)T} \quad (4)$$

The constants p_c , K and T_c for water (p in the above equations

Contributed by the Fluids Engineering Division for publication in the JOURNAL OF FLUIDS ENGINEERING. Manuscript received by the Fluids Engineering Division May 27, 2003; revised manuscript received February 18, 2004. Associate Editor: M. J. Andrews.

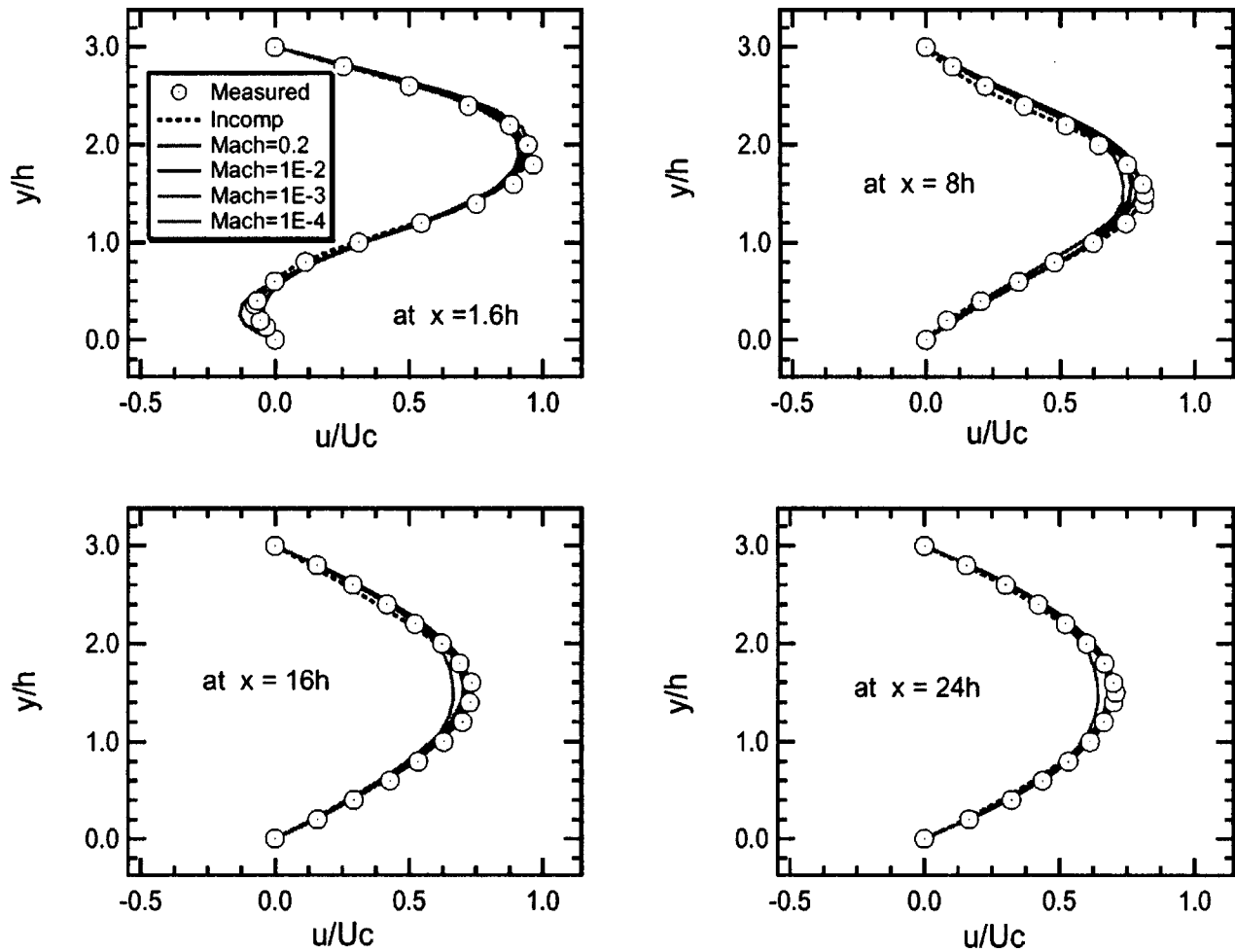


Fig. 1 Comparison of measured and predicted velocity profiles for a backward-facing step at several mach numbers

were estimated as 1944.61 MPa, 472.27 J/Kg K and 3837 K, respectively.

Fundamental Equations

Based on the cavitation model concept mentioned above and neglecting the surface tension for simplicity, the 2-D governing equations for the mixture mass, momentum, energy and the gas-phase mass conservation can be written in the curvilinear coordinates (ξ, η) as follows:

$$\frac{\partial \mathbf{Q}}{\partial t} + \frac{\partial \mathbf{E}}{\partial \xi} + \frac{\partial \mathbf{F}}{\partial \eta} = \frac{\partial \mathbf{E}_v}{\partial \xi} + \frac{\partial \mathbf{F}_v}{\partial \eta} + \mathbf{S} \quad (5)$$

where \mathbf{Q} is an unknown variable vector, \mathbf{E} , \mathbf{F} are flux vectors and \mathbf{E}_v , \mathbf{F}_v are viscous terms, and \mathbf{S} is the source term.

$$\mathbf{Q} = J \begin{pmatrix} \rho \\ \rho u \\ \rho v \\ e \\ \rho Y \end{pmatrix}, \quad \mathbf{S} = J \begin{pmatrix} 0 \\ 0 \\ 0 \\ 0 \\ S_e - S_c \end{pmatrix},$$

$$\mathbf{E} = J \begin{pmatrix} \rho U \\ \rho u U + \xi_x p \\ \rho v U + \xi_y p \\ \rho U H \\ \rho U Y \end{pmatrix}, \quad \mathbf{F} = J \begin{pmatrix} \rho V \\ \rho u V + \eta_x p \\ \rho v V + \eta_y p \\ \rho V H \\ \rho V Y \end{pmatrix},$$

$$\mathbf{E}_v = J \begin{pmatrix} 0 \\ \xi_x \tau_{xx} + \xi_y \tau_{xy} \\ \xi_x \tau_{yx} + \xi_y \tau_{yy} \\ \xi_x T_{11} + \xi_y T_{22} \\ \xi_x \mathfrak{R} Y_x + \xi_y \mathfrak{R} Y_y \end{pmatrix}, \quad \mathbf{F}_v = J \begin{pmatrix} 0 \\ \eta_x \tau_{xx} + \eta_y \tau_{xy} \\ \eta_x \tau_{yx} + \eta_y \tau_{yy} \\ \eta_x T_{11} + \eta_y T_{22} \\ \eta_x \mathfrak{R} Y_x + \eta_y \mathfrak{R} Y_y \end{pmatrix},$$

where the Jacobian J of the transformation from Cartesian coordinates x_i to general curvilinear coordinates ξ_i is defined as $J \equiv \partial(x, y) / \partial(\xi, \eta) = x_{\xi} y_{\eta} - x_{\eta} y_{\xi}$. The relationships between the physical velocity u_i in x_i space and the contravariant velocity U_i in ξ_i space are $U_i = (\partial \xi_i / \partial x_j) u_j$ and $u_i = (\partial x_i / \partial \xi_j) U_j$ respectively, using the summation convention. $T_{11} = u \tau_{xx} + v \tau_{xy} + \kappa \partial T / \partial x$, $T_{22} = u \tau_{yx} + v \tau_{yy} + \kappa \partial T / \partial y$ and κ is the coefficient of thermal conductivity. Also, \mathfrak{R} is the effective exchange coefficient, S_e is the rate of evaporation and S_c is the rate of condensation.

The stress tensor τ , the mixture density ρ and the mixture viscosity μ [15] can be expressed as

$$\tau_{xx} = \frac{2}{3} \mu \left(2 \frac{\partial u}{\partial x} - \frac{\partial v}{\partial y} \right), \quad \tau_{yy} = \frac{2}{3} \mu \left(2 \frac{\partial v}{\partial y} - \frac{\partial u}{\partial x} \right),$$

$$\tau_{xy} = \tau_{yx} = \mu \left(\frac{\partial u}{\partial y} + \frac{\partial v}{\partial x} \right), \quad \rho = (1 - \alpha) \rho_{\ell} + \alpha \rho_g,$$

$$\mu = (1 - \alpha)(1 + 2.5\alpha) \mu_{\ell} + \alpha \mu_g.$$

H in Eq. (5) is the enthalpy defined by total energy $e = \rho H - p$.

Preconditioning Formulation

The hydraulic flow including cavitations can be characterized as fully three-dimensional, non-linear, viscous flow with laminar and turbulent regions. In addition, this flow with hydraulic transients and hydroacoustics has compressible flow characteristic at low Mach number. For such a flow, a compressible flow model that includes a preconditioning method [16,17] is advantageous. Preconditioning is a way to extend the functionality of existing codes for fully compressible flows to almost incompressible flows.

Applying the preconditioning method to Eq. (5), we obtain 2-D preconditioned governing equations with unknown variable vectors $\mathbf{W}=[p,u,v,T,Y]^T$ written in curvilinear coordinates as follows [13]:

$$\Gamma^{-1} \frac{\partial \mathbf{W}}{\partial \tau} + \Gamma_w^{-1} \frac{\partial \mathbf{W}}{\partial t} + \frac{\partial(\mathbf{E}-\mathbf{E}_v)}{\partial \xi} + \frac{\partial(\mathbf{F}-\mathbf{F}_v)}{\partial \eta} = \mathbf{S} \quad (6)$$

In this study, τ is pseudo-time and Γ_w^{-1} is a transform matrix of the Jacobian matrix $\partial \mathbf{Q} / \partial \mathbf{W}$. The preconditioning matrix Γ^{-1} is formed by the addition of the vector $\theta[1,u,v,H,Y]^T$ to the first column of the $\partial \mathbf{Q} / \partial \mathbf{W}$. Parameter θ is chosen by Weiss & Smith [18],

$$\theta = \frac{1}{a^2} - \frac{1}{c^2}, \quad (7)$$

$$a^2 = \min[c^2, \max(|\mathbf{u}|^2, \beta |U_0|^2)]$$

where, U_0 is a fixed reference velocity such as average incoming freestream velocity, β is a constant that will be determined empirically for the appropriate precondition. In general, the value of β will be chosen so that θ becomes small because, if there is no problem with stability, small θ gives better solution for governing equation (5). In addition, time accuracy of the solution of Eq. (6) is independent of the pseudo-time term because when the pseudo-time integration converge, next physical time step is marched.

Source Term

The source terms of the rate of evaporation and condensation in Eq. (5) can be assumed as functions of pressure and other selected parameters. For example, S_e for transformation of liquid to vapor and S_c for vapor to liquid are modeled as being proportional to the vapor mass fraction and pressure difference between the local pressure and vapor pressure (p_v) as,

$$S_e = C_e (1 - Y) \max(0, p_v - p) \quad (8)$$

$$S_c = C_c Y \max(0, p - p_v) \quad (9)$$

where, $C_e = C_1 \rho_l / (0.5 \rho_\infty u_\infty^2 t_\infty)$, $C_c = C_e C_2 / C_1$, $t_\infty = l / u_\infty$, and C_1 and C_2 are empirical constants. l is the characteristic length and a_∞ is the inlet valve of a . These terms are similar to those used by Singhal et al. [5] and Kunz et al. [19] for both evaporation and condensation under the conditions that heat conduction and thermal effects on phase change are neglected.

Numerical Method

In this paper, the preconditioned governing equations (6) are numerically integrated using the three-point backward finite-difference method of the dual time-stepping integration procedure. Then, Roe's flux difference splitting (FDS) method [20] with the MUSCL-TVD scheme [10] is applied to enhance the numerical stability, especially for steep gradients in density and pressure near the gas-liquid interface. Therefore, the derivative of the flux

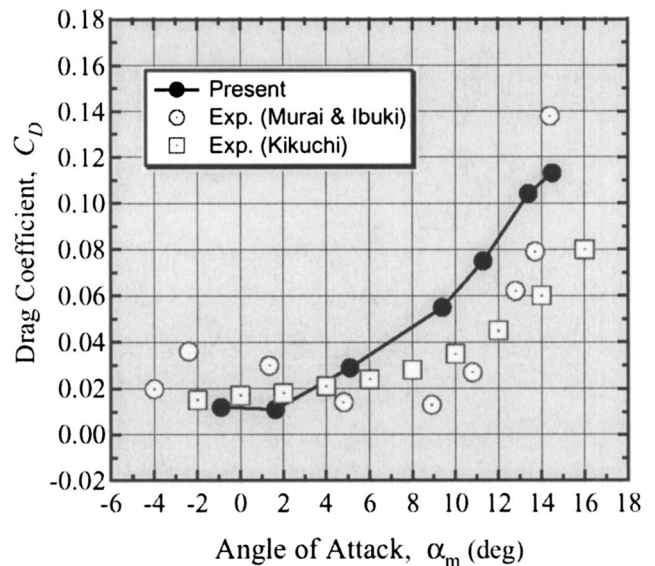
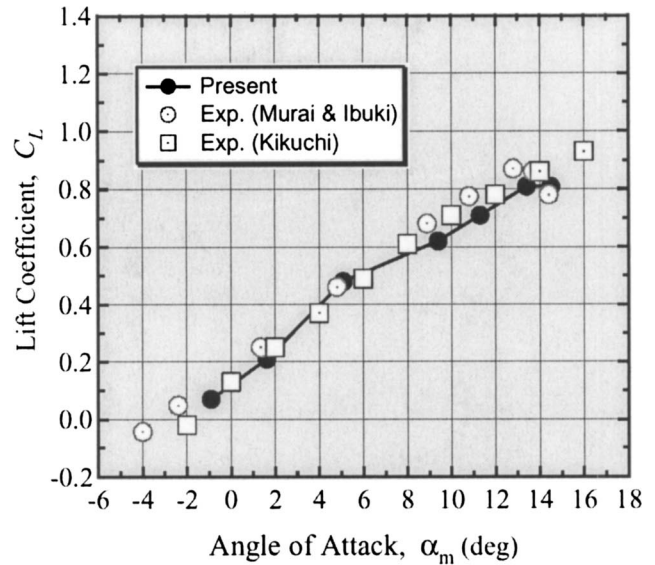


Fig. 2 Comparison of lift and drag coefficients

vector, for instance, \mathbf{E} with respect to ξ at point i can be written with the numerical flux as $(\partial \mathbf{E} / \partial \xi) = (\mathbf{E}_{i+1/2} - \mathbf{E}_{i-1/2}) / \Delta \xi$ and then, the approximate Riemann solver based on the Roe's FDS is applied. Hence, the numerical flux $\mathbf{E}_{i+1/2}$ is written as

$$\mathbf{E}_{i+1/2} = \frac{1}{2} \{ \mathbf{E}(\mathbf{Q}_{i+1/2}^L) + \mathbf{E}(\mathbf{Q}_{i+1/2}^R) - Z_{i+1/2}^{-1} (\mathbf{L}_p^{-1} |\Lambda| \mathbf{L}_p)_{i+1/2} (\mathbf{W}_{i+1/2}^R - \mathbf{W}_{i+1/2}^L) \} \quad (10)$$

where, $\Lambda = (U/\alpha, \tilde{U} + \tilde{c}, U/\alpha, \tilde{U} - \tilde{c}, U/\alpha)^D$ is the diagonal matrix of eigenvalues and \mathbf{L}_p and \mathbf{L}_p^{-1} are the left eigenvectors of $Z \partial \mathbf{E} / \partial \mathbf{W}$. $Z^{-1} = \Gamma^{-1} + \Gamma_w^{-1} \delta / 2$, $\delta = \Delta \tau / \Delta t$, $\tilde{U} \pm \tilde{c} = U/\alpha - (EV)^\mp / 2$, and

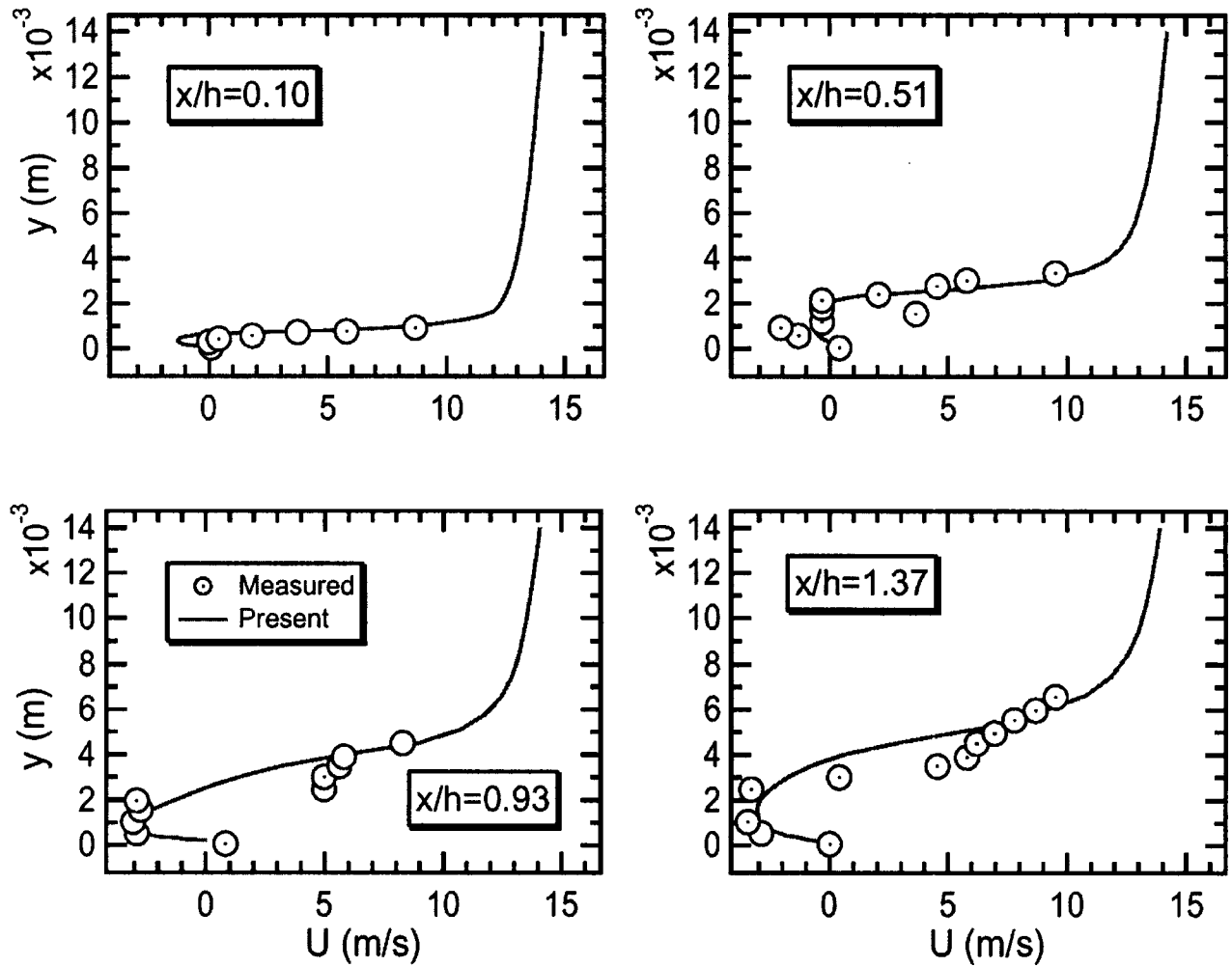


Fig. 3 Comparison of velocity profiles for 4-deg divergent nozzle

$$L_p = \begin{pmatrix} 1 & 0 & 0 & -\rho C_p & 0 \\ 1 & \xi_x \ell^- & \xi_y \ell^- & 0 & 0 \\ 0 & \xi_y & -\xi_x & 0 & 0 \\ 1 & \xi_x \ell^+ & \xi_y \ell^+ & 0 & 0 \\ 0 & -\xi_y & \xi_x & 0 & 1 \end{pmatrix}$$

$$\ell^\pm = \frac{-2}{(EV)^\pm} \rho c^2 A$$

$$(EV)^\pm = B \pm \sqrt{B^2 + 4A^2 c^2 g_{11} / \alpha}$$

$$A = \frac{\rho_T + \rho C_p \rho_p}{\rho_T \alpha + \rho C_p (\theta + \rho_p \alpha)}, \quad B = \frac{U / \alpha \rho C_p \theta}{\rho_T \alpha + \rho C_p (\theta + \rho_p \alpha)}$$

where $\alpha = 1 + \delta 3/2$, $\rho_p = \partial \rho / \partial p$, $\rho_T = \partial \rho / \partial T$, $g_{11} = \xi_x^2 + \xi_y^2$, and the eigenvectors are estimated by introducing Roe's averaging. $W_{i+1/2}^{L,R}$ is obtained by applying the third-order MUSCL-TVD scheme as

$$W_{i+1/2}^L = W_i + (\phi/4) \{ (1 - \kappa) D^+ W_{i-1/2} + (1 + \kappa) D^- W_{i+1/2} \} \quad (11)$$

$$W_{i+1/2}^R = W_{i+1} - (\phi/4) \{ (1 - \kappa) D^- W_{i+3/2} + (1 + \kappa) D^+ W_{i+1/2} \}$$

Here, the flux-limited values of DW and the minmod function are determined by

$$D^+ W_{i-1/2} = \min\text{mod}(\delta W_{i-1/2}, b \delta W_{i+1/2}),$$

$$D^- W_{i+1/2} = \min\text{mod}(\delta W_{i+1/2}, b \delta W_{i-1/2}), \quad (12)$$

$$\delta W_{i+1/2} = W_{i+1} - W_i,$$

$$\min\text{mod}(x, y) = \text{sign}(x) \max[0, \min\{|x|, |y \text{ sign}(x)|\}]$$

The linear combination parameter κ is determined by the range of $-1 \leq \kappa \leq 1$ and has an effect on the accuracy. That is, Eq. (11) has 3rd-order accuracy at $\kappa = 1/3$ and $\phi = 1$. At $\phi = 0$, this equation has first-order accuracy [21]. Typically, flows with cavitation contain regions with sharp interfaces between liquid and gas phases. However, application of the 3rd-order upwind bias scheme to these regions gives over- or undershoots for the solution at these interfaces, which can be a cause of the instability in the computation, particularly for the mass fraction equations. In order to improve this difficulty, the flux evaluation is made locally first-order in the presence of sharp gradients in the mixture quality Y . This is achieved through the application of an artificial dissipation such as a second-order dissipation by Jameson et al. [22]. Specifically, a dissipation is expressed for each coordinate direction as $\phi_i = 1 - d_i$ in Eq. (11).

$$d_i = \frac{|Y_{i+1} - 2Y_i + Y_{i-1}|}{Y_{i+1} + 2Y_i + Y_{i-1}} \quad (13)$$

The term of artificial dissipation d_i is very small except in the immediate vicinity of gas-liquid interfaces. On the other hand, the

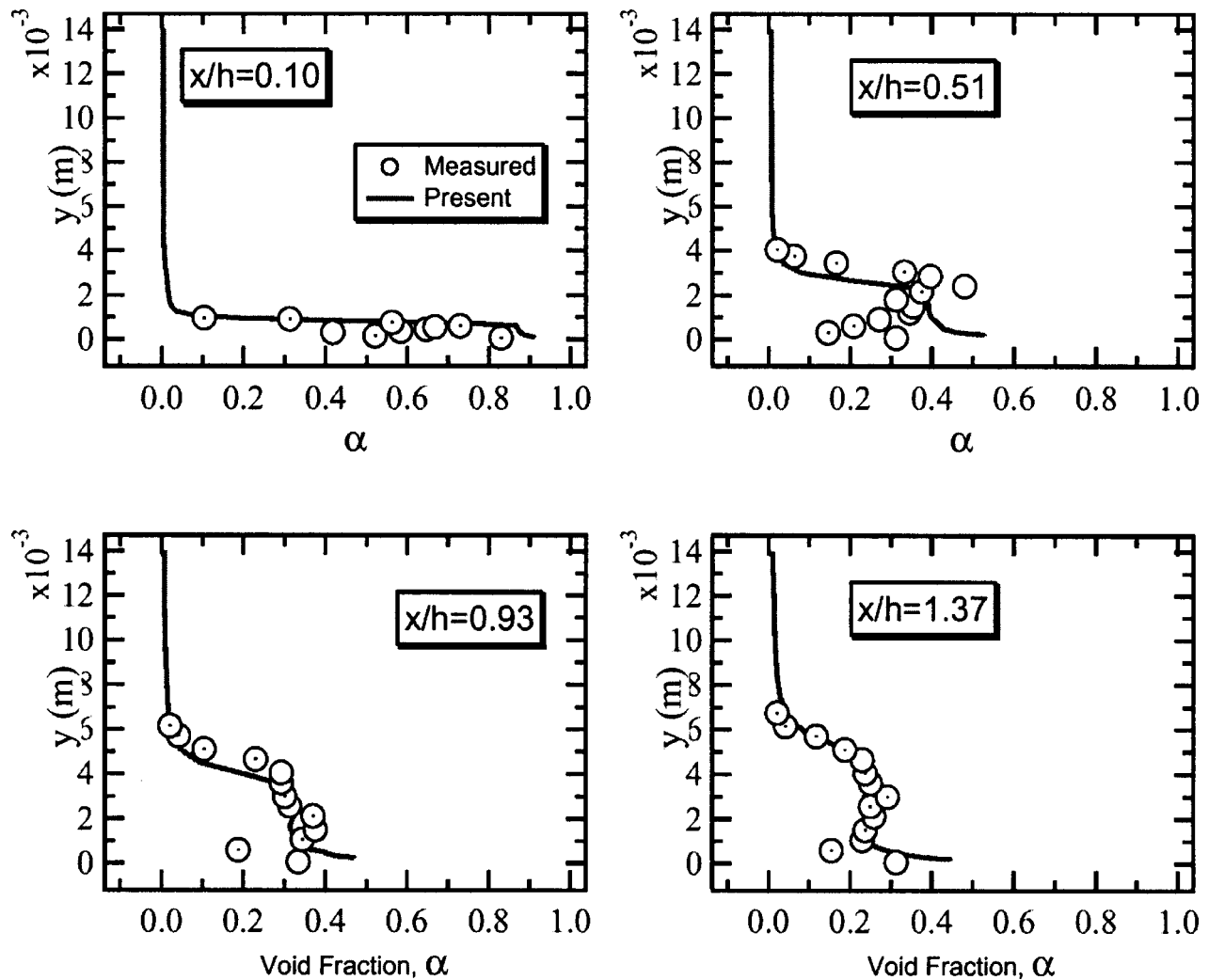


Fig. 4 Comparison of void fraction distributions for 4-deg divergent nozzle

slope of the flux in the minmod function is controlled by the limiter b . The range of b , $1 \leq b \leq (3 - \kappa)/(1 - \kappa)$, is determined by the condition of TVD stability. In this computation, a b of 4 and a κ of 1/3 are used. Numerical damping arisen from TVD upwinding scheme probably affects the accuracy. In the previous investigation [21], however, it was confirmed that the effect of the damping was limited and there was no sharp drop in accuracy.

Numerical Results

Validation. At first, the present computational method has been validated for the noncavity laminar duct flow over a backward-facing step. The expansion ratio of the duct is 1.5 [23]. The Reynolds number Re is 150 based on the step height h and inlet maximum velocity U_c . A curvilinear coordinates grid with 90×21 grid points is used. An ordinary compressible flow boundary condition is imposed.

Figure 1 shows comparisons of streamwise velocities at several downstream locations $x/h = 1.6, 8, 16$ and 24 behind the step with experimental data. In the computation for steady state laminar single-phase flow at several inlet Mach number, β of 0.1 in Eq. (7) was used except the case of inlet Mach number of $M_{in} = 0.2$ computed without preconditioning. The results obtained by present preconditioning method are fairly well predicted. It seems that differences between experimental data are increased with decrement of the Mach number, because of increment of θ in Eq. (7) for constant β of 0.1. The difference can be controlled by choosing

appropriate β . It is confirmed that at nearly incompressible flow condition with inlet Mach number of 1×10^{-4} , the present method still maintains and shows a reasonable solution. In addition, we know that the flow at $M_{in} = 0.2$ is solved by the present compressible flow formulation of Eq. (5) without θ and predicted well. For reference, results by the incompressible Navier-Stokes solver [24] are also shown in this figure.

Next, the present cavitation code with preconditioning method was applied to a two-phase flow with very small void fraction approximated by the single-phase. The cavitation number was adjusted so that no cavitation took place. The flow field is a single-passage of decelerating cascade with a pitch-chord ratio of 0.9 and a stagger angle of 30 deg. The blade profile is a Clark Y 11.7% hydrofoil. The Reynolds number Re based on the inlet mean velocity is approximately 2×10^5 and $M_{in} \approx 0.002$. The upstream and downstream boundaries of the computational domain are located at distances of 2 and 5 times chord length C from the leading and trailing edges of the hydrofoil, respectively. A body fitted H-type computational grid having 211×81 grid points is used. The flow is probably turbulent flow, however, as a first step, computation was performed without turbulent model but with relatively fine grid, because it was worried that conventional single-phase flow turbulent models gave rather uncertainties in the confirmation of inherent feature of the present numerical method as inconsistencies with each other.

Figure 2 shows a comparison of lift (C_L) and drag (C_D) coef-

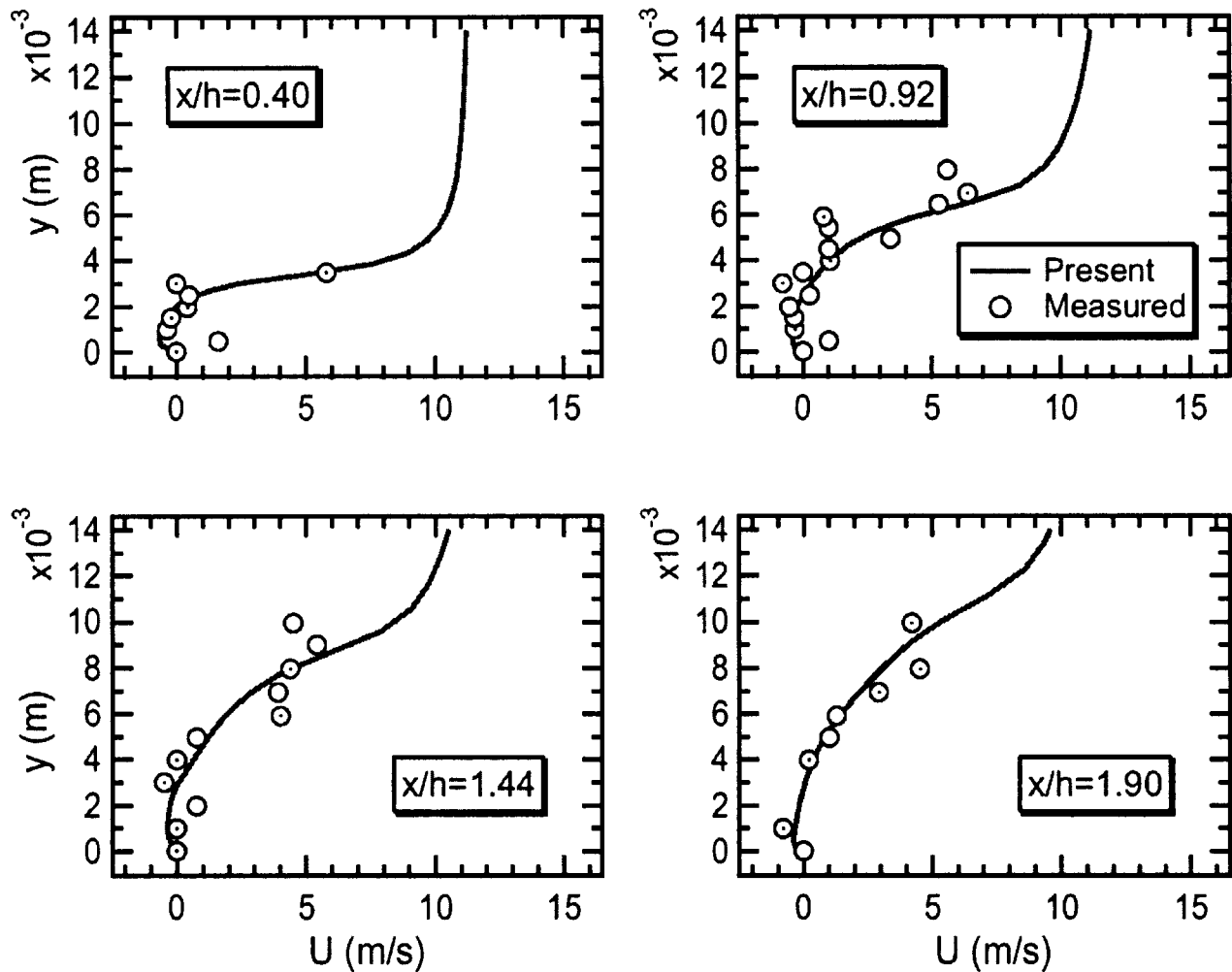


Fig. 5 Comparison of velocity profiles for 8-deg divergent nozzle

ficients at several angles of attack by preconditioning. C_L , C_D values estimated with mean properties (by subscript m) between one chord of upstream and downstream boundaries are very reasonable compared with the experimental data [25,26]. However, in the range of 6~15-deg angles of attack, C_D shows some differences from experiments. Experimental data are also scattered in this region. From this, the discrepancy is considered that it is due to measurement of originally small value of drag coefficients with uncertainty. Examined flows are considered as a reason, that is, the present results are obtained from a two-phase flow approximated by single-phase while experimental data are results of exact single-phase flow.

Cavitating Flow. Based on the validity of the present preconditioning method, the present preconditioning method was applied to cavitating flow through two convergent-divergent nozzles [3,27,28]. The height (h) of the throat sections are 43.7 mm and 34.3 mm. Angles of the convergent and the divergent parts of the lower wall are 4.3 deg and 4 deg, respectively for the large throat height. The other one has 18 deg and 8 deg. This flow field is very similar to the cascade with a large stagger angle such as turbopump inducer in liquid rocket engine. In the present computation, 351×85 points of a body-fitted grid generated by applying the boundary layer theory are used. The computational conditions of the isothermal temperature of 293 K and the Reynolds number of approximately 3.2×10^5 with inlet values are applied. An inlet void fraction of 0.1% and a β of 50~100 in Eq. (7) were imposed.

As a first step, the effective exchange coefficient was neglected and the empirical constants in Eqs. (8) and (9) $C_1 = 0.01$ and $C_2 = 2C_1$ at constant time increment.

Figure 3 shows a comparison of predicted time-averaged velocity distribution with optical probes measurement [3] focused inside the cavity in the small divergent nozzle (4.3-4 deg). In this figure, y represents the normal distance from the lower wall. Overall, u -velocity profiles agree well with each other. However, the separation region is somewhat under predicted especially at section of $0.51h$ downstream from the throat. This region is gradually extended toward downstream. In this case, distributions of void fraction were predicted as shown in Fig. 4. A thin sheet cavitation exists in vicinity of the throat and maximum void fraction is approximately 90%. At x/h of 0.51 and near bottom wall, a significant discrepancy between present and experimental results is observed, however, the profile of void ratio is very similar. As a hole, the shape of cavitation is well simulated in the all regions. In Figs. 3 and 4, it is easy to understand a typical cavitating flow pattern, a two-phase flow structure and void fraction distributions of inside the cavity.

Figure 5 shows another comparison of predicted velocity distribution in the 8-deg divergent nozzle streamwise velocity profiles agree well with each other. In particular, the thickness of the boundary layer existing cavitation is very well captured along the lower wall behind the throat. The cavity thickness is larger than that in the previous configuration of Fig. 3. The reverse flow ap-

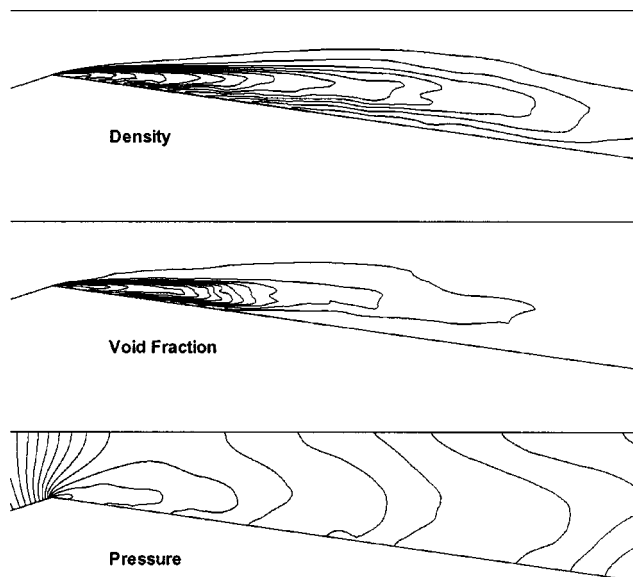


Fig. 6 Time-averaged density, void fraction and pressure contours for 8-deg divergent nozzle

proaches the throat. The mean cavity length evaluated by 10% void fraction on the wall was approximately 8 cm. Under the similar flow condition, Reboud et al. [3] obtained a length of 5 cm by experimental investigation; however, the value of the void fraction used in the evaluation is uncertain. Time-averaged void fraction, density and pressure distributions are shown in Fig. 6. We can see the typical cavity shape and its internal structure. The maximum void fraction was approximately 90% near the throat.

Figure 7 shows the time evolution of cavity shape (void fraction) appearing nearly one periodic cycle. Sheet cavitation occurring near the throat develops and flows downstream with nearly periodic behavior. When a kind of previously formed cloud cavitation is sufficiently far downstream, an attached cavity grows from the throat. A re-entrant jet develops along the wall (Fig. 7(c,d)), and then its interaction with the main flow in the near throat breaks off the attached cavity (Fig. 7(e)), and the cavitation cloud is regenerated (Fig. 7(f)). At this time, some of tiny cavitation scattered by the instability are merged together. As described in Figs. 7(a)–(d), regenerated cavitation cloud is convected again by the main stream. Very thin and short sheet cavitation is observed on the upper wall. The shape of the cavity is somewhat irregular but the formation and development of the cloud cavitation were simulated well in this figure.

Conclusions

Using the preconditioned numerical method for gas-liquid two-phase flows previously proposed by the author, cavitating and noncavitating flows through a 2-D backward-facing step duct, convergent-divergent nozzles and a decelerating cascade were computed. In the present method, a finite-difference method of a dual time-stepping integration procedure combined with the MUSCL-TVD scheme is employed, and a homogeneous equilibrium model of cavitating flow is applied.

Through the numerical examination, it was confirmed that the present preconditioning method yielded good computational performance and reliability, even at low Mach number. In addition, application to cavitating convergent-divergent nozzles flows was successful, and good prediction of velocity and void fraction distributions in comparison with experimental data was obtained. From the unsteady results of the void fraction and velocity field in the cavity, the complex cavity flow behaviors of the cavitation occurrence and its growing and shedding were clarified.

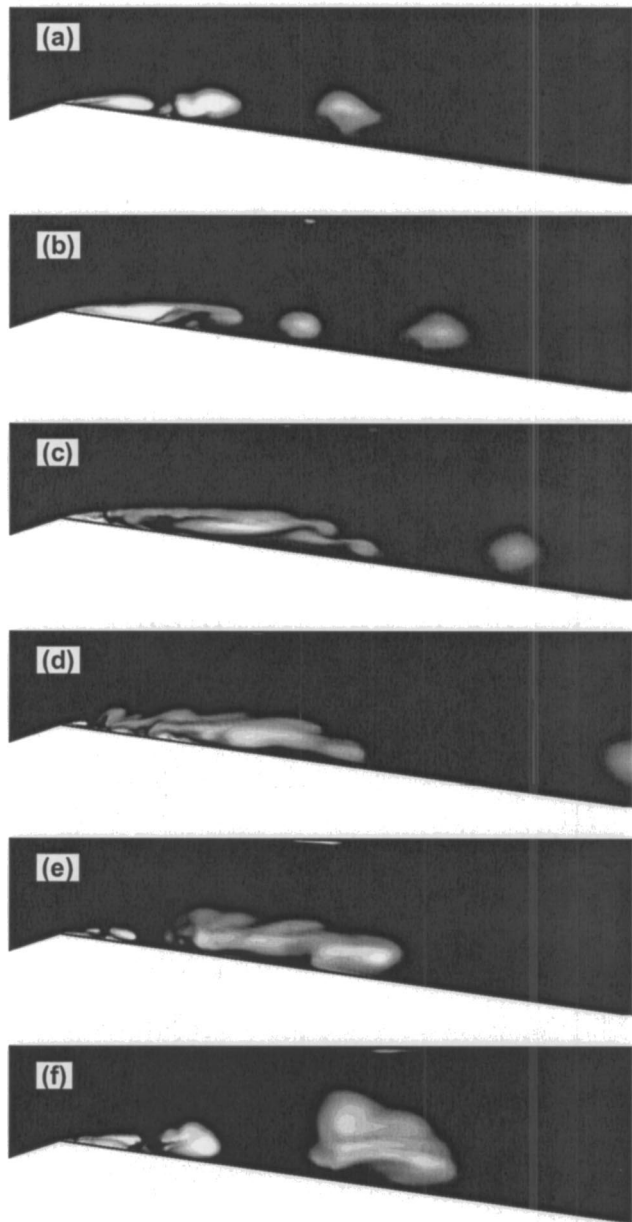


Fig. 7 Time evolution of cavity flow (void fraction) for 8-deg divergent nozzle

Acknowledgment

The authors thank Prof. Jean-Luc Reboud at University of Grenoble for his useful discussion and cooperation related to the geometry of the convergent-divergent nozzles studied at Laboratoire LEGI-INPG (Grenoble-France).

References

- [1] Matsumoto, Y., Kanbara, T., Sugiyama, K., and Tamura, Y., 1998, "Numerical Study of Cavitating Flow on a Hydrofoil," Proc. ASME PVP Conf. ASME PVP-Vol. 377-2, pp. 243–248.
- [2] Deshpande, M. et al., 1997, "Numerical Modeling of the Thermodynamic Effects of Cavitation," J. Fluids Eng., **119**, pp. 420–427.
- [3] Reboud, J. L. et al., 1998, "Two-Phase Flow Structure of Cavitation: Experimental and Modeling of Unsteady Effects," Proc. 3rd Int. Symp. on Cavitation, **1**, pp. 203–208.
- [4] Chen, Y., and Heister, S. D., 1995, "Two-Phase Modeling of Cavitated Flows," Comput. Fluids, **24**, pp. 799–809.
- [5] Singhal, A. K. et al., 1997, "Multi-Dimensional Simulation of Cavitating Flows Using a PDF Model for Phase Change," ASME Paper FEDSM97-3272.
- [6] Merkle, C. L. et al., 1998, "Computational Modeling of the Dynamics of Sheet Cavitation," Proc. 3rd Int. Symp. on Cavitation, **2**, pp. 307–311.

- [7] Shin, B. R., Iwata, Y., and Ikohagi, T., 2003, "Numerical Simulation of Unsteady Cavitating Flows Using a Homogeneous Equilibrium Model," *Comp. Mech.*, **30**, pp. 388–395.
- [8] Iga, Y., Shin, B. R., and Ikohagi, T., 2003, "Numerical Study of Sheet Cavitation Breakoff Phenomenon on a Cascade Hydrofoil," *ASME J. Fluids Eng.*, **125**, pp. 643–651.
- [9] Yee, H. C., 1987, "Upwind and Symmetric Shock-Capturing Scheme," NASA TM-89464, 1987.
- [10] van Leer, B., 1979, "Towards the Ultimate Conservative Difference Scheme V. A Second-Order Sequel to Godunov's Method," *J. Comput. Phys.*, **32**, pp. 101–136.
- [11] Shin, B. R., and Ikohagi, T., 1999, "Numerical Analysis of Unsteady Cavity Flows Around a Hydrofoil," ASME Paper FEDSM99-7215.
- [12] Shin, B. R. et al., 2001, "Numerical Analysis of Cavitating Flow Through a 2-D Decelerating Cascade," *Proc. 1st Int. Conf. on Comput. Fluid Dyn. ICCFD, Computational Fluid Dynamics 2000*, (ed., N. Satofuka), Springer-Verlag, Berlin, pp. 651–656.
- [13] Shin, B. R., 2001, "Numerical Analysis of Unsteady Cavitating Flow by a Homogeneous Equilibrium Model," AIAA Paper 2001-2909.
- [14] Chen, H. T., and Collins, R., 1971, "Shock Wave Propagation Past on Ocean Surface," *J. Comput. Phys.*, **7**, pp. 89–101.
- [15] Beattie, D. R. H., and Whally, P. B., 1982, "A Simple Two-Phase Frictional Pressure Drop Calculation Method," *Int. J. Multiphase Flow*, **8**, pp. 83–87.
- [16] Choi, Y. H., and Merkle, C. L., 1993, "The Application of Preconditioning in Viscous Flows," *J. Comput. Phys.*, **105**, pp. 207–233.
- [17] Edwards, J. R. et al., 2000, "Low-Diffusion Flux-Splitting Methods for Real Fluid Flows With Phase Transitions," *AIAA J.*, **38**, pp. 1624–1633.
- [18] Weiss, J. M., and Smith, W. A., 1995, "Preconditioning Applied to Variable and Constant Density Flows," *AIAA J.*, **33**, pp. 2050–2057.
- [19] Kunz, R. F. et al., 2000, "A Preconditioned Navier-Stokes Method for Two-Phase Flows With Application to Cavitation Prediction," *Comput. Fluids*, **29**, pp. 849–875.
- [20] Roe, P. L., 1981, "Approximate Riemann Solvers, Parameter Vectors and Difference Scheme," *J. Comp. Phys.*, **43**, pp. 357–372.
- [21] Shin, B. R., 2003, "A Stable Numerical Method Applying a TVD Scheme for Incompressible Flow," *AIAA J.*, **41**(1), pp. 49–55.
- [22] Jameson, A. et al., 1981, "Numerical Solutions of the Euler Equations by Finite Volume Methods Using Runge-Kutta Time-Stepping Schemes," AIAA Paper 81-1259.
- [23] Kueny, J. L., and Binder, G., 1984, "Viscous Flow Over Backward Facing Steps, An Experimental Investigation," *Note on Numerical Fluid Mechanics*, **9**, pp. 32–47, Vieweg.
- [24] Shin, B. R. et al., 1993, "An Unsteady Implicit SMAC Scheme for Two-Dimensional Incompressible Navier-Stokes Equations," *JSME Int. J.*, **36-B**, pp. 598–606.
- [25] Murai, H., and Ibuki, S., 1981, "Research on Axial-Flow Turbomachinery With Swept-Back or Swept-Forward Blades (Report 1, Experimental Research on Cascade of Swept-Back Blades)," *Mem. Inst. High Speed Mech., Tohoku Univ.*, **47**, pp. 117–142.
- [26] Kikuchi, H., 1959, "An Experimental Study on Stall Characteristics in Decelerating Cascade (Report 1)," *Mem. Inst. High Speed Mech., Tohoku Univ.*, **14**(139), pp. 193–219.
- [27] Stutz, B., and Reboud, J. L., "Measurements Within Unsteady Cavitation," *Exp. Fluids*, **29**, pp. 545–552.
- [28] Stutz, B., and Reboud, J. L., 1997, "Two Phase Flow Structure of Sheet Cavitation," *Phys. Fluids* **9**(12), pp. 3678–3686.

The Influence of Small Particles on the Structure of a Turbulent Shear Flow

David I. Graham

Principal Lecturer
School of Mathematics and Statistics,
University of Plymouth,
Drake Circus, Plymouth,
Devon PL4 8AA, U.K.
e-mail: dgraham@plymouth.ac.uk

In this paper, an analytical solution is found for the Reynolds equations describing a simple turbulent shear flow carrying small, wake-less particles. An algebraic stress model is used as the basis of the model, the particles leading to source terms in the equations for the turbulent stresses in the flow. The sources are proportional to the mass loading of the particles and depend on the temporal correlations of the fluid velocities seen by particles, $R_{ij}(\tau)$. The resulting set of equations is a system of nonlinear algebraic equations for the Reynolds stresses and the dissipation. The system is solved exactly and the influence of the particles can be quantified. The predictions are compared with DNS results and are shown to predict trends quite well. Different scenarios are investigated, including the effects of isotropic, anisotropic and non-equilibrium time scales and negative loops in $R_{ij}(\tau)$. The general trend is to increase anisotropy and attenuate turbulence with higher mass loadings. The occurrence of turbulence enhancement is investigated and shown to be theoretically possible, but physically unlikely. [DOI: 10.1115/1.1779662]

1 Introduction

It is well known that the turbulence characteristics of particle-laden carrier flows are influenced by the presence of the particles if particle concentrations are high enough. The surveys by Gore and Crowe [1] and Hetsroni [2], for example, show that turbulence levels can be enhanced for large particles, apparently due to the formation of turbulent wakes behind such particles. The effect of small particles, however, is usually to suppress the turbulence by extracting energy from the primary flow turbulence. This conclusion has been reinforced recently by the experiments of Savolainen et al. [3] and Varaksin et al. [4]. The present paper is concerned with the case of small, wake-less particles.

In the last two decades, there have been several attempts to formulate models to describe the turbulence modulation effect. A discussion of some of the available models is given in Crowe [5]. A common approach is to investigate the extra dissipation due to the presence of particles, which appears as a source (or sink) term in the equation for the Reynolds stresses or turbulence kinetic energy. The approach used here, following several authors including Berlemont et al. [6], Eaton [7] and Varaksin et al. [4] is exactly that described (and criticized) by Crowe [5]. First, the momentum equation for the carrier phase is augmented by a source term due to the presence of a point particle. This equation is then multiplied by the fluid velocity. The fluid velocity is expressed as an average value plus a fluctuating part. Subtracting away the mean part of the resulting equation from the full expression gives a relation for the Reynolds stress source terms. Crowe's [5] objection to this method is that it is not possible to treat the influence of the particle as if it acts at a point. This will be true for relatively large particles, but it is felt here that the method should be reasonable if the particle size is considered to be small compared with the smallest length scales of the turbulence.

The DNS results of Squires and Eaton [8] have shown that correlations between fluid velocities and concentrations can be very important in turbulence modulation. This is particularly true for particles with (Kolmogorov) Stokes numbers St_K (defined as the ratio of the particle relaxation time and the Kolmogorov time scale) of the order of unity. In practice, the range over which this

effect is important is quite small and it appears safe to assume that the particle concentration fluctuations are negligible. Here, we are mainly interested in the behavior for particles for which St_K is large. In these cases, the concentrations are independent of the fluid and particle velocities (Squires and Eaton, [8]). This leads to a considerable simplification in the expression for particle sources, compared with that developed by Eaton [7].

In the present paper, the source terms are derived for a simple turbulent shear flow in which the Reynolds stresses are constant throughout the flow, but the mean flow is sheared. This paper complements the analysis in Graham [9]. There, the effect of the presence of particles on turbulence kinetic energy levels in the simple shear flow was examined. Given that we are again concerned with wake-less particles, we expect to find that turbulence is again attenuated. In the current paper, the changes in the structure of the flow are also investigated. The basis of the model presented is an algebraic stress model, which provides a good description of the this flow in the unladen case (see Libby [10]). Source terms due to particles are used to modify the algebraic stress equations describing this flow. Expressions for the source terms are taken from the analysis presented by the author in Graham [11].

There have been several experimental studies of such flows (see Tavoularies and Karnik [12] for a review) and there have recently been some numerical studies using LES (Simonin et al. [13]) or DNS (Taulbee et al. [14]). Tavoularies and Karnik [12] considered that there were two distinct classes of flows corresponding to these conditions. The first class was one in which the Reynolds stresses reach equilibrium values. This corresponds to the shear flows studied experimentally by Champagne et al. [15], Rose [16], as well as some of the flows studied by Tavoularies and Karnik [12]. The other class was one in which the Reynolds stresses grew exponentially in time. In this paper, we are mainly concerned with the first class in which the Reynolds stresses approach equilibrium values when the production of turbulence kinetic energy exactly balances its dissipation. Even for these equilibrium flows, however, it appears that the integral length scales (and therefore presumably the corresponding integral time scales) grow in time (Tavoularies and Karnik, [12]). Here, we assume that the length and time scales have attained finite longtime values. Equivalently, the period over which the system is studied must be

Contributed by the Fluids Engineering Division for publication in the JOURNAL OF FLUIDS ENGINEERING. Manuscript received by the Fluids Engineering Division August 15, 2002; revised manuscript received January 1, 2004. Associate Editor: T. B. Gatski.

small compared with the development time for the integral scales. A brief discussion on the non-equilibrium case is, however, included.

The layout of the paper is as follows. In Section 2, the algebraic stress equations governing the fluid flow are modified to include the influence of particles. The solutions to the algebraic stress equations under various different scenarios are investigated in Section 3. Conclusions from the study are presented in Section 4.

2 Algebraic Stress Equations

The flow to be considered is one in which the Reynolds stresses are constant throughout the flow, but in which the mean velocity U_i is sheared:

$$\overline{u_i} = U_i = \delta_{i1} \frac{\partial U_1}{\partial x_2} x_2 = \delta_{i1} s x_2,$$

where x_i is the ordinate in the i -direction, δ_{ij} is the Kronecker delta, s is the shear gradient and the overbar indicates an ensemble-averaged quantity. In the absence of particles, the equations for the Reynolds stresses $\overline{u_i u_j}$ are (see Libby [10]):

$$\begin{aligned} \overline{u_1 u_2} \frac{dU_1}{dx_2} &= \frac{p}{\rho_f} \frac{\partial u_1}{\partial x_1} - \varepsilon_{11}, \\ 0 &= \frac{p}{\rho_f} \frac{\partial u_2}{\partial x_2} - \varepsilon_{22}, \\ 0 &= \frac{p}{\rho_f} \frac{\partial u_3}{\partial x_3} - \varepsilon_{33}, \\ \overline{u_1^2} \frac{dU_1}{dx_2} &= \frac{p}{\rho_f} \frac{\partial u_1}{\partial x_2} + \frac{p}{\rho_f} \frac{\partial u_2}{\partial x_1} - \varepsilon_{12}, \end{aligned} \quad (2.1)$$

where p is the pressure, ε_{ij} is the dissipation tensor and ρ_f , μ_f are the fluid density and viscosity. Using second-order algebraic stress modelling of the pressure-strain terms (Libby [10]), and adding the extra source terms S_{ij} due to the presence of particles gives the following system:

$$\begin{aligned} \overline{su_1 u_2} &= -c_1 \frac{\varepsilon}{\kappa} \left(\overline{u_1^2} - \frac{2}{3} \kappa \right) + \left(\frac{4}{3} c_2 - 1 \right) \overline{su_1 u_2} - \frac{2}{3} \varepsilon + S_{11}, \\ 0 &= -c_1 \frac{\varepsilon}{\kappa} \left(\overline{u_2^2} - \frac{2}{3} \kappa \right) - \frac{2}{3} c_2 \overline{su_1 u_2} - \frac{2}{3} \varepsilon + S_{22}, \\ 0 &= -c_1 \frac{\varepsilon}{\kappa} \left(\overline{u_3^2} - \frac{2}{3} \kappa \right) - \frac{2}{3} c_2 \overline{su_1 u_2} - \frac{2}{3} \varepsilon + S_{33}, \\ \overline{su_1^2} &= -c_1 \frac{\varepsilon}{\kappa} \overline{u_1 u_2} + c_2 \overline{su_2^2} + S_{12}, \end{aligned} \quad (2.2)$$

where κ is the turbulence kinetic energy and ε is its rate of dissipation. The coefficients c_1 and c_2 are constants, normally given numerical values of 1.5 and 0.625, respectively.

Using the expressions for the Reynolds stress source terms given in the Appendix and noting that the only non-zero turbulent shear stress is $\overline{u_1 u_2} = \overline{u_2 u_1}$, the sources can be listed as:

$$\begin{aligned} S_{11} &= -\frac{\overline{u_1^2}}{\tau_{11}} a_{11} + 2 \overline{su_1 u_2} b_{12}, & S_{22} &= -\frac{\overline{u_2^2}}{\tau_{22}} a_{22}, \\ S_{33} &= -\frac{\overline{u_3^2}}{\tau_{33}} a_{33}, & S_{12} = S_{21} &= -\frac{\overline{u_1 u_2}}{\tau_{12}} a_{12} + \overline{su_2^2} b_{22}, \end{aligned} \quad (2.3)$$

where

$$a_{ij} = 2M\beta \left(1 - \beta \int_0^\infty e^{-\beta\tau} R_{ij}(\tau) d\tau \right), \quad (2.4)$$

$$b_{ij} = M\beta^2 \int_0^\infty \tau e^{-\beta\tau} R_{ij}(\tau) d\tau.$$

In the above expression, M is the mass loading, $\beta = 1/\tau_p$ is the reciprocal of the Stokesian particle relaxation time τ_p and $R_{ij}(\tau)$ is the correlation of the fluid velocities seen by particles, with associated integral time scale τ_{ij} .

Full details of the derivation of the source terms are given in the appendix. The method used is identical to that used in Graham [11]. We should point out that the analysis leading to the source terms is strictly valid only in the case of Stokesian drag i.e. for low particle Reynolds number. Furthermore, we are interested in the long-time limiting forms only. Several other assumptions have been required to simplify the analysis. The reader is referred to the appendix for full details.

Following the practice commonly employed in Lagrangian particle dispersion models (see Gosman and Ioannides [17], Berlemont et al. [6]), the integral time scales are expressed as

$$\tau_{ij} = C_{ij} \frac{\kappa}{\varepsilon}, \quad (2.5)$$

where C_{ij} is constant. We note that this assumption is supported by Squires and Eaton's [18] DNS study of isotropic turbulence, although a more recent study by Boivin et al. [19] casts doubt on the validity of the assumption. The latter results indicate that the constant C_{ij} is not independent of the mass loading. However, taking C_{ij} as a scalar constant should be a reasonable first guess, and this is done here. Writing $A_{ij} = a_{ij}/C_{ij}$ and $B_{ij} = b_{ij}$, and using dimensionless variables,

$$\begin{aligned} G_{11} &= \rho_f \overline{u_1^2} / \kappa; & G_{22} &= \rho_f \overline{u_2^2} / \kappa; & G_{33} &= \rho_f \overline{u_3^2} / \kappa; \\ G_{12} &= \rho_f \overline{u_1 u_2} / \kappa; & E &= \varepsilon / (s\kappa), \end{aligned}$$

the final system of equations becomes:

$$\begin{aligned} G_{12} &= -c_1 E \left(G_{11} - \frac{2}{3} \right) + \left(\frac{4}{3} c_2 - 1 \right) G_{12} - \frac{2}{3} E - A_{11} G_{11} E \\ &\quad + 2B_{12} G_{12}, \\ 0 &= -c_1 E \left(G_{22} - \frac{2}{3} \right) - \frac{2}{3} c_2 G_{12} - \frac{2}{3} E - A_{22} G_{22} E, \\ 0 &= -c_1 E \left(G_{33} - \frac{2}{3} \right) - \frac{2}{3} c_2 G_{12} - \frac{2}{3} E - A_{33} G_{33} E, \\ G_{22} &= -c_1 G_{12} E + c_2 G_{22} - A_{12} G_{12} E + B_{22} G_{22}. \end{aligned} \quad (2.6)$$

System (2.6) is a set of nonlinear algebraic equations whose solution can be found once the source terms are known. The source terms are determined by the correlation functions $R_{ij}(\tau)$, the associated Stokes numbers $St_{ij} = \tau_p / \tau_{ij}$ and the mass loading.

3 Influence of Particles

3.1 Isotropic Correlations

3.1.2 Flow Solution. In the following, it is assumed that the $R_{ij}(\tau)$ are identical to the Lagrangian correlation $R_L(\tau)$, and that the values of C_{ij} are also identical. The value $C_{ij} = 0.4$ is fairly consistent with the DNS results of Boivin [20] and is used to produce the results discussed in this section. We note that this value is slightly higher than the value of around 0.2 normally used in particle models based κ - ε (see Berlemont et al. [6] for example). In the first instance, it is assumed that the correlations $R_{ij}(\tau)$ are negative exponential in form, $R_{ij}(\tau) = e^{-|\tau|/\tau_L}$, with common integral time scale τ_L . It then follows that the A_{ij} are identical for all i, j and that

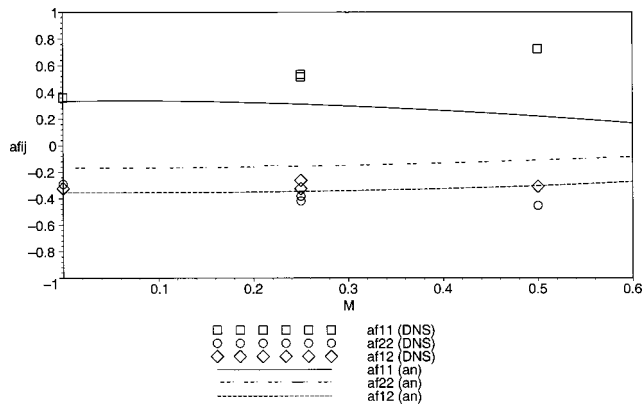


Fig. 1 Anisotropy Tensor: Comparison between DNS and Analytical model—Isotropic Correlations

$$A_{ij} \equiv A = 5M/(1 + St),$$

$$B_{ij} \equiv B = M/(1 + St)^2,$$

where $St = \tau_p/\tau_L = 1/\beta\tau_L$. For this simple case, the second and third of Eq. (2.6) are also identical and imply that $u_2^2 = u_3^2$. Thus $\kappa = \rho_f(1/2u_1^2 + u_2^2)$.

The solution to the final system of equations is:

$$G_{11} = \frac{\left(\frac{4}{3} + \frac{2c_1}{3} + 2A\right)(1-B) - \frac{4c_2}{3}(1+A)}{(c_1+A)(1-B)},$$

$$G_{22} = \frac{\frac{2}{3}\{(c_1-1)(1-B) + c_2(1+A)\}}{(c_1+A)(1-B)},$$

$$E = \sqrt{\frac{(1-B)G_{22}(1-c_2-B)}{(1+A)(c_1+A)}},$$

$$G_{12} = -\frac{(1+A)}{(1-B)}E. \quad (3.1)$$

The amount of data with which to compare our solution is fairly limited. Here, we compare with results from the DNS computations of Taulbee et al. [14]. We note that the DNS results were computed for a fixed shear of 62.8 s^{-1} . In Fig. 1, we compare the DNS and analytical values of the components of the fluid anisotropy tensor

$$a_{ij}^f = G_{ij} - \frac{2}{3}\delta_{ij}.$$

Although the off-diagonal term a_{12}^f is predicted reasonably well, the trend of increasing anisotropy with increased mass loading is not demonstrated by the model. Indeed, the model in this case predicts that particles tend to reduce anisotropy and with high enough mass loading would lead to isotropic turbulence (i.e., all elements of the anisotropy tensor tend to zero). This feature is fairly insensitive to the choice of C_{ij} discussed above. We should note that there are differences between DNS and analytical results even when the particle mass loading is zero. These are due to the deficiencies in the underlying algebraic stress model of the turbulence.

The experimental evidence on the influence of particles on flow anisotropy is some-what mixed. The pipe flow experimental results of Savolainen and Karvinen [3], show that anisotropy increases with mass loading, whilst anisotropy is slightly decreased in the pipe flow results of Varaksin et al. [4].

Table 1 Comparison production/dissipation

		$\tau_p = .016$		$\tau_p = .032$
Mass Loading	0	.25	.5	.25
Prod/diss (DNS)	1.56	1.91	1.95	1.56
Prod/diss (An)	1	2.14	3.75	1.81

We now investigate the turbulence modulation effect. We first note that

$$\frac{-E}{G_{12}} = \frac{\varepsilon/(s\kappa)}{-\rho_f u_1 u_2 / \kappa} = \frac{\varepsilon}{-s\rho_f u_1 u_2} = \frac{1-B}{1+A} \quad (3.2)$$

is the ratio of dissipation of turbulence kinetic energy to its production. Generally, the ratio of production to dissipation increases with particle loading from an initial value of unity. As shown in the Table 1, this trend is in general agreement with the DNS results of Taulbee et al. [14], though the production always exceeds the dissipation even at zero mass-loading for the non-equilibrium flow considered by these authors and the influence of particles is greater in the analytical model than the simulations.

We now follow Graham [9] and investigate turbulence modulation by assuming that the production is unchanged by the presence of particles and that the ratio κ/ε is similarly fixed. This leads to the conclusion that the ratio $-E/G_{12}$ is also equal to κ/κ_0 . Here the subscript 0 indicates the value in the unladen flow and the ratio thus provides a measure of the attenuation of the turbulence by the presence of particles. Graham [9] showed that the turbulence attenuation predicted by the above expression was in good agreement with the pipe flow results of Varaksin et al. [4].

Before proceeding, we should investigate the second of these assumptions to make sure that it is consistent with the DNS results. From the definitions, we see that

$$\frac{E}{E_0} = \frac{\varepsilon/s\kappa}{\varepsilon_0/s_0\kappa_0} = \frac{\varepsilon}{\varepsilon_0} \times \frac{\kappa_0}{\kappa} \times \frac{s}{s_0}. \quad (3.3)$$

If we assume that s is fixed (as in the DNS of Taulbee et al. [14]), then E/E_0 gives the relative change in the ratio κ/ε . Although Table 2 (extracted from Fig. 1 of Taulbee et al. [14]) shows that this ratio is not fixed, the range of variation between $t=4/s$ and $t=12/s$ is small enough for the assumption of constancy to be reasonable.

Figure 2 compares predictions of $\varepsilon/\varepsilon_0 \times \kappa_0/\kappa$ and the turbulence modulation κ/κ_0 with the DNS results. Since the turbulence modulation is changing in time in the DNS, we compare with the results at $t=12/s$ in the DNS. Although the same trends are evident from predicted and DNS results, the analytical model generally predicts significantly more turbulence modulation than the DNS results indicate. It should be noted that it is possible to tweak the multiplier C_{ij} to provide closer comparisons between analytical and DNS results for turbulence modulation. For example, a value of C_{ij} of 2 provides much improved predictions. Even for this value, the enhanced anisotropy evident from the DNS results is not modeled so this is not pursued here.

In passing, we should note that an alternative interpretation of [3.3] is to assume that $\varepsilon/\varepsilon_0 \times \kappa_0/\kappa$ is fixed. Under this assumption, the shear gradient s must increase in the presence of particles.

3.2 Anisotropic Correlations. The results above show that the use of isotropic correlations in the analytical model (i.e., identical integral time-scales τ_{ij} in all directions) leads to a tendency

Table 2 Comparison: ratio time scales
[[$(\varepsilon/\varepsilon_0)/(\kappa/\kappa_0)$]($t=12/s$)]/[$(\varepsilon/\varepsilon_0)/(\kappa/\kappa_0)$]($t=4/s$)]

		$\tau_p = .016$		$\tau_p = .032$
Mass Loading	0	.25	.5	.25
E/E_0 DNS	1	1.04	0.88	1.27

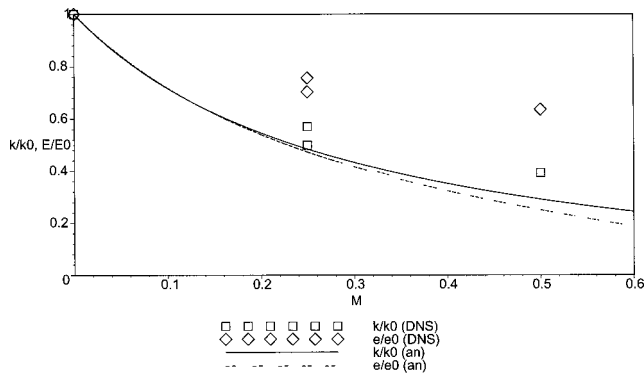


Fig. 2 Turbulence modulation: Comparison between DNS and Analytical model—Isotropic Correlations

for particles to decrease flow anisotropy. As we have seen, this is contrary to observations in the DNS simulations. In this section, we attempt to remedy this. Thus, we allow τ_{11} , the integral time scale in the streamwise direction, to be greater than the other time scales and investigate the results from the model. Again, the correlations $R_{ij}(\tau)$ are assumed to be negative exponential in form. For simplicity, we set $\tau_{11} = 2\tau_{12} = 2\tau_{22} = 2\tau_{33} = \tau_L$. Again, we assume that $\tau_L = 0.4\kappa/\varepsilon$. The results are again dependent on the mass loading and the Stokes number $St = \tau_p/\tau_L$. These assumptions again imply that $G_{22} = G_{33}$. The source terms can easily be evaluated by integrating Eq. (2.4). The solution of the resulting system of equations is

$$G_{11} = \frac{(1-B_{12})\left(\frac{4}{3} + \frac{2c_1}{3} + 2A_{22}\right) - \frac{4}{3}c_2(1+A_{22})}{(c_1+A_{11})(1-B_{12}) - \frac{2}{3}c_2(A_{11}-A_{22})},$$

$$G_{22} = \frac{2}{3} \frac{(c_1-1)(1-B_{12}) + c_2(1+A_{11})}{(c_1+A_{11})(1-B_{12}) - \frac{2}{3}c_2(A_{11}-A_{22})},$$

$$E = \sqrt{\frac{(1-B_{12})G_{22}(1-c_2+B_{22})}{(1+G_{22}(A_{22}-A_{11})+A_{11})(c_1+A_{12})}},$$

$$G_{12} = -\frac{1+A_{22}+G_{11}(A_{11}-A_{22})}{(1-B_{12})}E. \quad (3.4)$$

Figure 3 shows that in this case, adding particles does give the correct trends of increasing a_{11}^f and making a_{22}^f more negative, i.e.

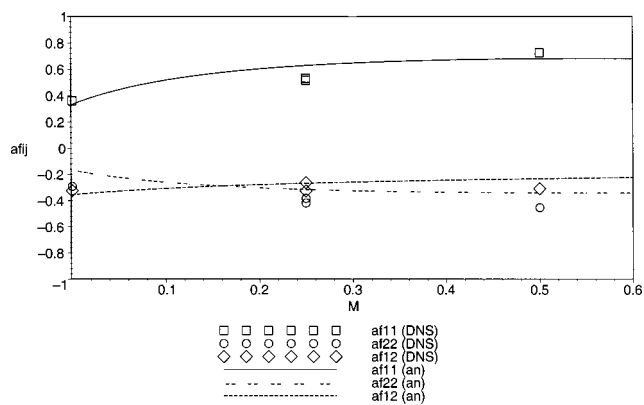


Fig. 3 Anisotropy Tensor: Comparison between DNS and Analytical model—Anisotropic Correlations

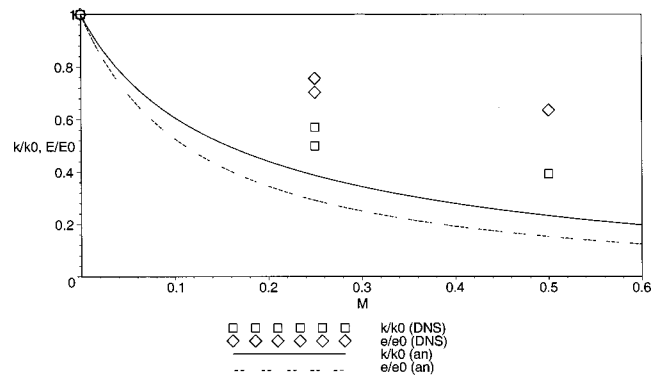


Fig. 4 Turbulence modulation: Comparison between DNS and Analytical model—Anisotropic Correlations

increasing anisotropy. We also note from Fig. 3 that, although the off-diagonal component changes more dramatically in the analytical model than in the DNS, the trend of a_{12}^f decreasing with increased mass loading is predicted correctly. It is generally clear that the use of anisotropic time-scales markedly improves the predictive capability of the model.

Figure 4 plots the ratios E/E_0 and $-E/G_{12}$ and again compares with the DNS results. Again, the general trend is for particles to attenuate the turbulence, with the level of attenuation increasing with mass loading and decreasing with Stokes number. Similar to Fig. 2, however, turbulence modulation κ/κ_0 is modelled more successfully than the time-scale ratio $\varepsilon/\varepsilon_0 \times \kappa_0/\kappa$. Again, predictions of both of these quantities can be significantly improved by changing the parameters C_{ij} . However, it is difficult to pick a combination of these parameters that enables the model to predict experimentally measured trends in all of a_{11}^f , a_{22}^f , a_{12}^f , κ/κ_0 and $\varepsilon/\varepsilon_0 \times \kappa_0/\kappa$ simultaneously. The three free parameters in our solution are the constants C_{11} and the ratios C_{22}/C_{11} and C_{12}/C_{11} . A parameter study has indicated the constraints on these quantities as follows:

1. C_{11} should be large in order to increase predicted values of κ/κ_0 and $\varepsilon/\varepsilon_0 \times \kappa_0/\kappa$. Values exceeding 5 provide reasonable predictions of these quantities.
2. C_{22}/C_{11} must decrease as C_{11} increases so that the anisotropy tensor values remain in line with DNS results. For $C_{11}=5$, the value of C_{22}/C_{11} should be around 0.2.
3. C_{12}/C_{11} should be less than 1 so that anisotropy increases with mass loading, as in the DNS results. The ratio should be close to 1 so that $\varepsilon/\varepsilon_0 \times \kappa_0/\kappa$ exceeds κ/κ_0 . For $C_{11}=5$, values of C_{12}/C_{11} around 0.9 are effective.

Thus, after much experimentation with the analytical result, the combination $C_{11}=5$, $C_{22}=1$, $C_{12}=4.5$ proved to be quite successful (see Figs. 5 and 6). It must be pointed out that there is no direct experimental evidence to support this choice, since techniques for measuring the correlations $R_{ij}(\tau)$ are not yet available. Here, we rely on indirect evidence and choose a set of parameters that give the best overall comparison with the DNS results. We should note that the values of C_{11} and C_{12} are much higher than the conventional values of around 0.2 used in many computational methods utilizing $\kappa-\varepsilon$ as the base flow model.

Overall, the combination of parameters chosen leads to the model predicting trends very reasonably when compared with DNS results. We now investigate the analytical solution further and investigate a possible scenario whereby turbulence can be enhanced by particles.

3.3 Negative Loops and Turbulence Enhancement. It was noted in Graham [11] that the source term B_{ij} could change sign if the correlation $R_{ij}(\tau)$ contained negative loops. It was then thought that this might possibly lead to

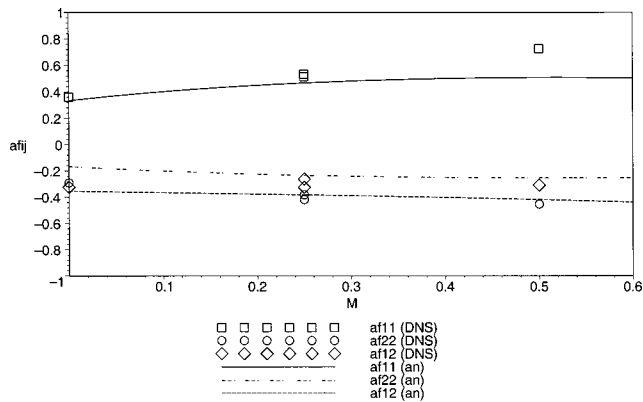


Fig. 5 Anisotropy Tensor: Comparison between DNS and Analytical model—Anisotropic Correlations with high C_{ij}

turbulence enhancement, even by small, wake-less particles. This aspect is considered in the following section. We first assume that the correlations are represented by the Frenkiel functions: $R_{ij}(\tau) = e^{-|\tau|/[(m^2+1)\tau_{ij}]} \cos(m\tau[(m^2+1)\tau_{ij}])$. The reason for this choice is simply to provide a correlation with negative loops and to investigate the consequences. Evidence suggests that the existence of negative loops occurs only for low-inertia particles, whereas we shall see that it is for high-inertia particles that the greatest changes in behavior are observed. Nevertheless, we proceed with caution with what can be thought of as a numerical experiment. The source terms are again bound by substituting the above expression for $R_{ij}(\tau)$ into equation (2.4).

Before we begin our investigation, we first note that κ/κ_0 is given by

$$\frac{-E}{G_{12}} = \frac{(1 - B_{12})}{\left(1 + A_{11} + \frac{1}{2} G_{22}(A_{22} - A_{11})\right)}. \quad (3.5)$$

Inspecting Eq. (3.5), we can see that the only way that $-E/G_{12}$ can increase is if $1 - B_{12}$ is larger than $1 + A_{11} + 1/2 G_{22}(A_{22} - A_{11})$. This can happen if the integral time scales τ_{11} and τ_{22} are large multiples of the ratio κ/ε i.e. that the multipliers C_{ii} in the expression $\tau_{ii} = C_{ii}\kappa/\varepsilon$ are larger than unity. Figure 7 shows a plot of relative turbulence level κ/κ_0 as a function of mass loading, for the case $C_{11} = C_{22} = C_{12} = 10$, for $m = 3$ and for Stokes numbers $1/(\beta\tau_L)$ of 5, 10, and 15. For extremely high mass loadings, and for Stokes numbers above about 5, turbulence is enhanced. For less inertial particles, turbulence is again attenuated. Given that turbulence enhancement is possible only

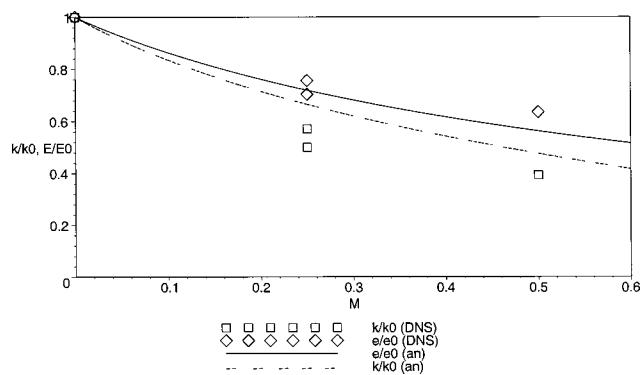


Fig. 6 Turbulence modulation: Comparison between DNS and Analytical model—Anisotropic Correlations with high C_{ij}

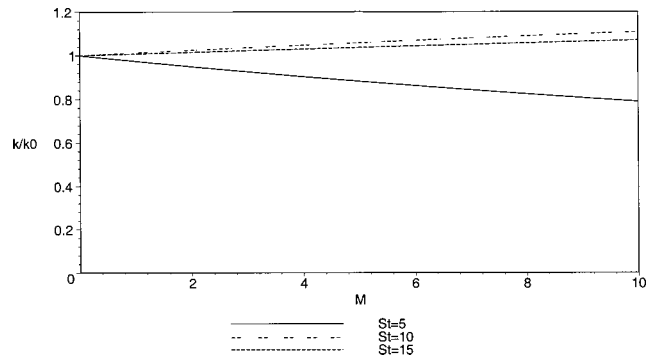


Fig. 7 Turbulence Enhancement: κ/κ_0 for $R_{ij}(\tau)$ with negative loops

with a somewhat unlikely combination of circumstances and parameters, we must conclude that, physically, this combination of circumstances is unlikely to occur in practice.

3.4 Non-Equilibrium Length and Time Scales. In the preceding analysis, we have assumed that the Reynolds stresses $u_i u_j$ are homogeneous in space and time. We also assume that the correlations $R_{ij}(\tau)$ and the associated time scales τ_{ij} are similarly homogeneous. We noted in the introduction that experimental and DNS evidence indicates that the time scales grow in time. If this growth continues in time, then the Stokes number $St_{ij} = \tau_p / \tau_{ij}$ becomes small, so that the influence of particles in the longtime limit is independent of the particle inertia and depends only upon the limiting values of the functions A_{ij} and B_{ij} as $St \rightarrow 0$.

For the related time microscales to be finite, the correlations $R_{ij}(\tau)$ should be flat at $\tau = 0$. In this case, the analyses of Graham [11,21] show that, in the limit of vanishing Stokes number, $A_{ij} \rightarrow 0$, $B_{ij} \rightarrow M$. In this case, the structure of the turbulence depends only on the mass loading. Here, the presence of particles always leads to attenuation, since $\kappa/\kappa_0 = 1 - M$. Clearly, this analysis is valid only when the mass loading is less than unity.

4 Conclusions

Modification of the primary flow by the presence of small, wake-less particles in a homogeneous turbulent shear flow has been investigated analytically. The equations resulting from second-order algebraic stress modeling of the turbulence have been solved. The effects of the presence of particles on the turbulence structure have been investigated and the results have been compared with those from the DNS study of Taulbee et al. [14]. The following general conclusions can be drawn:

1. the structure of the resulting flow is strongly dependent on the correlations $R_{ij}(\tau)$ and the associated integral time scales $t_{ij} = C_{ij}\kappa/\varepsilon$;
2. the use of isotropic time scales (i.e. $C_{11} = C_{22} = C_{12}$) wrongly predicts decreased anisotropy with increased mass loading;
3. anisotropy can be well modeled with moderate values of C_{ij} namely $C_{11} = 0.4$, $C_{22} = 0.1$ and $C_{12} = 0.1$ though turbulence modulation is thereby over-predicted;
4. all aspects of the DNS results including turbulence modulation can be modeled by using $C_{11} = 3$, $C_{22} = 0.6$ and $C_{12} = 2.7$ though these values are significantly higher than those used in existing $\kappa - \varepsilon$ models;
5. while turbulence is generally attenuated by particles, the model caters for turbulence enhancement although the conditions necessary for this to happen appear to be physically unlikely.
6. in the case of non-equilibrium time scales, turbulence is attenuated by the presence of particles.

Appendix: Reynolds Stress Source Term

We restrict our attention to small, high-density particles for which the equation of motion is given by

$$\frac{du_i^p}{dt} = \beta(u_i^f - u_i^p), \quad (A1)$$

where u_i^p is the instantaneous particle velocity (in the x_i -direction), u_i^f is the instantaneous fluid velocity 'seen' by the particle and ρ_p is the particle density. The parameter β is the reciprocal relaxation time scale of the particle. Accelerations due to gravity and other body forces are omitted here, but can easily be included in the analysis. We assume that the viscous drag follows Stokes' law, so that β is a constant, given by

$$\beta = \frac{18\mu_f}{\rho_p d_p^2}, \quad (A2)$$

where d_p is the particle diameter and μ_f is the fluid laminar viscosity.

We aim to find an expression for the particle source term

$$S_{ij} = C\beta[\langle u_i'^f(u_j'^f - u_j'^p) \rangle + \langle u_j'^f(u_i'^f - u_i'^p) \rangle], \quad (A3)$$

where C is the concentration of particles and the primes refer to velocity fluctuations. We proceed as follows: the solution to equation [A1] is given by:

$$u_i^p(t) = e^{-\beta t} u_i^p(0) + \beta e^{-\beta t} \int_0^t e^{\beta t'} u_i^f(t') dt'. \quad (A4)$$

Following Riley and Corrsin [22], the fluid velocity (evaluated here along a particle path) is given by

$$u_i^f(t) = s \delta_{i1} x_2^p(t) + u_i'^f(t) = s \delta_{i1} \left[x_2^p(0) + \int_0^t u_2^p(t'') dt'' \right] + u_i'^f(t), \quad (A5)$$

where $x_i^p(t)$ is the particle position at time t , so that

$$u_i^p(t) = e^{-\beta t} u_i^p(0) + \beta e^{-\beta t} \int_0^t e^{\beta t'} \left\{ s \delta_{i1} \left[x_2^p(0) + \int_0^{t'} u_2^p(t'') dt'' \right] + u_i'^f(t') \right\} dt'. \quad (A6)$$

We can simplify the analysis by assuming without loss of information that $u_i^p(0)$ and $x_i(0)$ are all zero (i.e. the particles are released from a static source at the origin), so that

$$u_i^p(t) = \beta e^{-\beta t} \int_0^t e^{\beta t'} \left[s \delta_{i1} \int_0^{t'} u_2^p(t'') dt'' + u_i'^f(t') \right] dt'. \quad (A7)$$

Now the fluctuating part of the particle velocity is given by

$$u_j'^p(t) = u_j^p(t) - s \delta_{j1} x_2^p(t), \quad (A8)$$

where $x_2^p(t)$ is the x_2 coordinate of the particle at time t :

$$x_2^p(t) = \int_0^t u_2^p(t'') dt''. \quad (A9)$$

[Note that this assumes that the mean particle velocity at some point in the flow is exactly equal to the mean fluid velocity there. This will be true in the long-time limit, and it is this case in which we are interested here.]

The source term due to the presence of particles is determined by the quantity

$$u_i'^f(t)[u_j'^f(t) - u_j'^p(t)] = u_i'^f(t) \left[u_j'^f(t) - \left(u_j^p(t) - s \delta_{j1} \int_0^t u_2^p(t'') dt'' \right) \right]. \quad (A10)$$

From equation [A7], the solution for $u_2^p(t)$ is

$$u_2^p(t) = \beta e^{-\beta t} \int_0^t e^{\beta t'} u_2'^f(t') dt', \quad (A11)$$

so that

$$\begin{aligned} \langle u_i'^f(t) u_j'^p(t) \rangle &= \delta_{j1} \beta^2 s \int_0^t \int_0^{t'} \int_0^{t''} e^{\beta(-t+t'+t''+t''')} \\ &\quad \times \langle u_i'^f(t) u_2'^f(t'') \rangle dt'' dt' + \beta \int_0^t e^{\beta(-t+t')} \\ &\quad \times \langle u_i'^f(t) u_j'^f(t') \rangle dt'. \end{aligned} \quad (A12)$$

Substituting $t''' = t + \tau$ in the first integral, and $t' = t + \tau$ in the second integral, exploiting the symmetry of the fluid velocity correlations and simplifying the resulting integral gives

$$\begin{aligned} \langle u_i'^f(t) u_j'^p(t) \rangle &= s \delta_{j1} \langle u_i' u_2' \rangle \int_0^t R_{i2}(\tau) [1 - e^{-\beta\tau}(1-\tau)] d\tau \\ &\quad + \beta \langle u_i' u_j' \rangle \int_0^t e^{-\beta\tau} R_{ij}(\tau) d\tau, \end{aligned} \quad (A13)$$

where

$$R_{ij}(\tau) = \frac{\langle u_i'^f(t) u_j'^f(t+\tau) \rangle}{\langle u_i'^f u_j'^f \rangle} \quad (A14)$$

is the fluid velocity correlation function following a particle (we are assuming that the correlations are stationary i.e. independent of the 'starting time' t). Similarly,

$$\left\langle u_i'^f(t) s \delta_{j1} \int_0^t u_2^p(t'') dt'' \right\rangle \quad (A15)$$

can be evaluated to give

$$s \delta_{j1} \langle u_i' u_2' \rangle \int_0^t R_{i2}(\tau) [1 - e^{-\beta\tau}] d\tau. \quad (A16)$$

Combining equations [A13] and [A16] gives

$$\begin{aligned} \langle u_i'^f(t) u_j'^p(t) \rangle &= s \delta_{j1} \langle u_i' u_2' \rangle \int_0^t \tau e^{-\beta\tau} R_{i2}(\tau) d\tau \\ &\quad + \beta \langle u_i' u_j' \rangle \int_0^t e^{-\beta\tau} R_{ij}(\tau) d\tau \end{aligned} \quad (A17)$$

As a result, the Reynolds Stress source term

$$S_{ij} = C\beta[\langle u_i'^f(u_j'^f - u_j'^p) \rangle + \langle u_j'^f(u_i'^f - u_i'^p) \rangle] \quad (A18)$$

is given by substituting equation (A17) into the above expression and taking the limit as $t \rightarrow \infty$:

$$\begin{aligned} S_{ij} &= -2C\beta \langle u_i' u_j' \rangle \left(1 - \beta \int_0^\infty e^{-\beta\tau} R_{ij}(\tau) d\tau \right) \\ &\quad + Cs\beta^2 \delta_{j1} \langle u_i' u_2' \rangle \int_0^\infty \tau e^{-\beta\tau} R_{i2}(\tau) d\tau Cs\beta^2 \delta_{i1} \langle u_j' u_2' \rangle \\ &\quad \times \int_0^\infty \tau e^{-\beta\tau} R_{j2}(\tau) d\tau. \end{aligned} \quad (A19)$$

$R_{ij}(0)$ is, of course, the fluid Reynolds stress $\langle u_i^f u_j^f \rangle$ (evaluated along the particle path, in fact, but it is assumed here that it is identical to the usual Eulerian expression). [Note that in the body of the main text, we use the notation $\overline{u_i u_j} = \langle u_i^f u_j^f \rangle$ for brevity.]

References

- [1] Gore, R. A., and Crowe, C., 1989, "Effect of Particle Size on Modulating Turbulent Intensity," *Int. J. Multiphase Flow*, **15**(2), 279–285.
- [2] Hetsroni, G., 1989, "Particle-Turbulence Interaction," *Int. J. Multiphase Flow*, **15**(5), 735–746.
- [3] Savolainen, K., and Karvinen, R., 1998, "The effect of Particles on Gas Turbulence in a Vertical Upward Pipe Flow," Third International Conference on Multiphase Flow, ICMF'98, Lyon, France.
- [4] Varaksin, A. Y., Kurosaki, Y., Satoh, I., Polezhaev, Y. V., and Polyakov, A. F., 1998, "Experimental Study of the Direct Influence of the Small Particles on the Carrier Air Turbulence Intensity for Pipe Flow," Third International Conference on Multiphase Flow, ICMF'98, Lyon, France.
- [5] Crowe, C. T., 1999, "On Models for Turbulence Modulation in Fluid-Particle Flows," *Int. J. Multiphase Flow*, **26**(5), 719–727.
- [6] Berlemont, A., Desjonqueres, P., and Gouesbet, G., 1990, "Particle Lagrangian Simulation in Turbulent Flows," *Int. J. Multiphase Flow*, **16**(1), 19–34.
- [7] Eaton, J. K., 1995, "Turbulence Modification by Particles in Shear Flows," paper presented at the Symposium on Gas/Particle Flows, ASME FED Summer Meeting, Hilton Head, SC, USA.
- [8] Squires, K. D., and Eaton, J. K., 1990, "Particle Response and Turbulence Modification in Isotropic Turbulence," *Phys. Fluids A*, **2**, 1191–1203.
- [9] Graham, D. I., 2000, "Turbulence Attenuation by Small Particles in Simple Shear Flows," *ASME J. Fluids Eng.*, **122**(1), 134–137.
- [10] Libby, P. A., 1996, "Introduction to Turbulence," Taylor and Francis, New York, USA.
- [11] Graham, D. I., 1998, "Turbulence Modulation by Particles in Homogeneous Shear," paper 5008, ASME FED Summer Meeting, Washington DC.
- [12] Tavoulari, S., and Karnik, U., 1989, "Further Experiments on the Evolution of Turbulent Stresses and Scales in Uniformly Sheared Turbulence," *J. Fluid Mech.*, **204**, 457–478.
- [13] Simonin, O., Deutsch, E., and Boivin, M., 1995, "Large Eddy Simulation and Second-Moment Closure Model of Particle Fluctuating Motion in Two-Phase Turbulent Shear Flows," in *Selected Papers from the Ninth Symposium on Turbulent Shear Flows*, eds F. Durst, N. Kasagi, B. E. Launder, F. W. Schmidt, and J. H. Whitelaw, Springer-Verlag, Germany.
- [14] Taulbee, D. B., Mashayek, F., and Barre, C., 1999, "Simulation and Reynolds Stress Modelling of Particle-Laden Turbulent Shear Flows," *Int. J. Heat Mass Transfer*, **20**, 368–373.
- [15] Champagne, F. H., Harris, V. G., and Corrsin, S., 1970, "Experiments on Nearly Homogeneous Shear Flow," *J. Fluid Mech.*, **41**, 247.
- [16] Rose, W. G., 1970, "Interaction of Grid Turbulence With a Uniform Mean Shear," *J. Fluid Mech.*, **44**, 767.
- [17] Grosman, A. D., and Ioannides, E., 1981, "Aspects of Computer Simulation of Liquid-Fueled Combustors," AIAA paper 81-0323, 19th Aerospace Science meeting, St. Louis, USA.
- [18] Squires, K. D., and Eaton, J. K., 1994, "Effect of Selective Modification of Turbulence on Two-Equation Models for Particle-Laden Turbulent Flows," *ASME J. Fluids Eng.*, **116**, 778–784.
- [19] Boivin, M., Simonin, O., and Squires, K. D., 1998, "Direct Numerical Simulation of Turbulence Modulation by Particles in Isotropic Turbulence," *J. Fluid Mech.*, **375**, 235–263.
- [20] Boivin, M., 1996, "Etude de l'Influence des Particules sur la Turbulence a partir de Simulations Directes et de Simulations des Grand Echelles d'Ecoulements Diphasiques Gaz-Solides Homogenes Isotropes Stationnaires," Report HE-44/96/010/A, Departement Laboratoire National d'Hydraulique, Electricite de France, France.
- [21] Graham, D. I., 1997, "Turbulence Modification in the Limiting Cases of Heavy- and Tracer-Particles," *ASME J. Fluids Eng.*, **119**(2), 458–460.
- [22] Riley, J. J., and Corrsin, S., 1974, "The Relation of Turbulent Diffusivity to Lagrangian Velocity Statistics for the Simplest Shear Flow," *J. Geophys. Res.*, **79**(2), 1768–1771.

A Stochastic Model for Gravity Effects in Particle-Laden Turbulent Flows

Z. Gao

F. Mashayek*

Department of Mechanical and Industrial Engineering,
University of Illinois at Chicago,
842 West Taylor Street,
Chicago, IL 60607

A stochastic model is presented for the prediction of the gravity effects on velocity and temperature fluctuations in turbulent flows laden with solid particles. Both temporal and spatial correlations as well as the anisotropy of turbulence are included in the model. It is found that the inclusion of the spatial correlation is imperative for capturing the gravity effects. The performance of the stochastic model is assessed by comparisons of the results with direct numerical simulation data for isotropic and homogeneous shear turbulent flows. The comparisons are also used to investigate the effect of the empirical constant that appears in the expression used for the spatial correlation. [DOI: 10.1115/1.1778714]

Introduction

In a recent paper [1], we presented a stochastic model for the prediction of velocity and temperature fluctuations in non-isothermal turbulent flows laden with solid particles. The model accounted for anisotropy of turbulence and included the effects of the temporal correlations. In the present paper, we introduce an improved form of this model which can be used for accurate prediction of gravity effects. More importantly, we show that in order to capture the gravity effects the turbulence spatial correlation must be incorporated into the stochastic model.

The gravitational force acting on a particle moving in a turbulent flow results in a drift velocity which could have significant effects on various particle statistics such as the variance of the velocity fluctuations and the particle turbulence diffusivity. From a physical point of view, a heavy particle moving in a gravity field changes its neighboring fluid particle more rapidly as compared to a particle moving in the absence of gravity. This leads to the well-known “crossing-trajectories effect” which was first introduced by Yudine [2]. Later, Csanady [3] pointed out an associated phenomena known as “continuity effect” that could explain the presence of negative loops in the particle velocity autocorrelation. These effects have been further investigated and quantified by various investigators in recent years (see e.g. [4,5] and references therein).

The important role of temporal and spatial correlations of turbulence in the construction of stochastic models has come under a close scrutiny in recent years. Mashayek and Pandya [6] provided a review of various stochastic models by dividing them into two groups. The first group are the models that provide a representation of turbulence temporal correlation in only an implicit manner [7–11]. This group includes the popular and widely-utilized eddy-interaction models in which the interaction of particles with random-velocity fluid eddies are considered. A particle is assumed to interact with the same eddy for a time interval that is the minimum of two characteristic times, i.e. the eddy life time and the eddy crossing time. Various models differ in their approach of implementing these characteristic times and may consider only one or both. Wang and Stock [12] have shown that the temporal velocity correlation for these stochastic processes may be obtained by transforming the ensemble average into time average for a stationary random process and employing physical reasoning to find the contribution of individual velocity pairs to the velocity

autocorrelation function. The form of the ‘implicit’ temporal correlation depends on whether a constant or a random time step size is used for sampling the random fluid velocity at the particle location.

The second group of models considered in [6] are characterized as models that allow for ‘explicit’ incorporation of turbulence correlations. These models are more sophisticated and can provide a more accurate prediction of the statistics of the dispersed phase [13–17]. They can be rigorously developed using the method of time series analysis and can allow for incorporation of various forms of the correlation functions. Among these studies, only [17] considers the case of a non-isothermal flow, but without explicitly accounting for temporal or spatial correlations. In this paper, we present a new stochastic model that incorporates both temporal and spatial correlations. The performance of the model is assessed by comparison with direct numerical simulation (DNS) results and the effect of the empirical constant appearing in the specified form of the spatial correlation function is discussed.

Problem Formulation and Model Development

We consider a two-phase system composed of a large number of solid particles dispersed in a non-isothermal carrier phase. The mass loading of the particles is small so that particle-particle interactions can be neglected. However, the effects of the particles on turbulence, i.e. the two-way coupling, can be considered within this framework. This requires a modification of the carrier-phase equations by introducing proper source/sink terms, as discussed elsewhere in the literature [6]. The ratio of the particle and fluid densities is large so that only inertia, drag and gravitational forces are significant to the particle dynamics, and each particle is assumed to have a uniform temperature. With these assumptions, the Lagrangian equations for individual particles are described as

$$\frac{d\tilde{x}_p}{dt} = \tilde{u}_p, \quad (1)$$

$$\frac{d\tilde{u}_p}{dt} = \frac{f_1}{\tau_p} (\tilde{u} - \tilde{u}_p) + \frac{\tilde{u}_{dr}}{\tau_p}, \quad (2)$$

$$\frac{d\tilde{T}_p}{dt} = \frac{f_2}{\tau_p} (\tilde{T} - \tilde{T}_p), \quad (3)$$

where \tilde{x}_p , \tilde{u}_p and \tilde{T}_p are the instantaneous position, velocity and temperature of the particles, respectively, and \tilde{u} and \tilde{T} are the instantaneous carrier fluid velocity vector and temperature at the particle location, respectively. The effect of gravity is included through the drift velocity $\tilde{u}_{dr} \equiv (u_{dr}, v_{dr}, w_{dr})$ with the magnitude

*Corresponding author. E-mail: mashayek@uic.edu.

Contributed by the Fluids Engineering Division for publication in the JOURNAL OF FLUIDS ENGINEERING. Manuscript received by the Fluids Engineering Division April 5, 2003; revised February 13, 2004. Associate Editor: K. D. Squires.

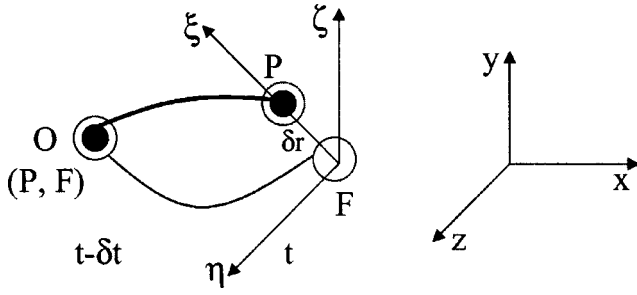


Fig. 1 Schematic of fluid particle (F) and heavy particle (P) trajectories along with global (xyz) and local ($\xi\eta\zeta$) coordinate systems

$g\tau_p$ where g is the gravity constant. All of the variables are normalized by reference length (L_f), density (ρ_f), velocity (U_f), and temperature (T_f) scales. Consequently, reference Reynolds and Prandtl numbers are defined as $Re_f = \rho_f U_f L_f / \mu$ and $Pr = C_p \mu / \kappa$, respectively, where μ , κ and C_p are the viscosity, the thermal conductivity and the specific heat of the fluid, respectively.

In (2) and (3), the non-dimensional particle time constant is $\tau_p = Re_f \rho_p d_p^2 / 18$, where d_p and ρ_p are the particle diameter and density, respectively. The function $f_1 = 1 + 0.15 Re_p^{0.687}$ in (2) represents an empirical correction to the Stokes drag due to particle Reynolds numbers of order unity and larger and is valid for particle Reynolds numbers $Re_p = Re_f \rho d_p |\tilde{u} - \tilde{u}_p| \leq 1000$, where ρ is the fluid density at the particle position. The factor $f_2 = Nu/3Pr\sigma$ represents a correlation for the convective heat transfer coefficient based on an empirically corrected Nusselt number, $Nu = 2 + 0.6 Re_p^{0.5} Pr^{0.33}$, where σ is the ratio of the particle specific heat and the fluid specific heat.

To update the particle properties, Eqs. (1)–(3) must be integrated in time using the instantaneous velocity and temperature of the carrier fluid at the particle location. We decompose these fluid variables into mean, $\bar{U} \equiv (U_1, U_2, U_3)$ and T , and fluctuation, $\tilde{u} \equiv (u_1, u_2, u_3) \equiv (u, v, w)$ and θ , respectively. The mean variables can be found using various single-point statistical models, such as Reynolds averaged Navier-Stokes (RANS) models and their determination is not the subject of this paper. Here, we focus on the fluctuating components and derive a stochastic model for their calculation. In doing so, we note that single-point models can also provide information regarding second-moment statistical properties of the fluid, i.e. Reynolds stresses, temperature fluctuation variance, and velocity-temperature cross-correlations. This information will be used in the process of stochastic model derivation below.

To explain the main features of the stochastic model, we consider the schematic in Fig. 1. Assume that the heavy particle and its corresponding fluid particle are initially at the same position O at a time $t - \delta t$. After a time step δt , the heavy particle moves to P and the fluid particle moves to F. Depending on the inertia of the heavy particle and the flow structure, these points may depart

from each other by a distance δr . In our previous study [1], we assumed that the departure distance δr was negligible and considered the temporal correlation between points O and F only. In this work, we relax this assumption and derive a model for finite δr by considering the spatial correlation between points F and P, in addition to the above temporal correlation. This extension is necessary in order to account for the effects of gravity.

The stochastic model derivation is based on the method of time series analysis [18] in which the fluctuating velocity components and temperature at different times or locations are used to define autoregressive processes. First, we consider the temporal processes that relate the values at the current time t (at point F) to those at a previous time $t - \delta t$ (at point O)

$$\vec{A}_{F,t} = \beta \cdot \vec{A}_{F,t-\delta t} + \vec{d}_t, \quad (4)$$

where boldface shows a tensor, and

$$\vec{A}_{F,t} = \begin{pmatrix} u_{F,t} \\ v_{F,t} \\ w_{F,t} \\ \theta_{F,t} \end{pmatrix}, \quad \beta = \begin{pmatrix} \beta_{uu} & \beta_{uv} & \beta_{uw} & \beta_{u\theta} \\ \beta_{vu} & \beta_{vv} & \beta_{vw} & \beta_{v\theta} \\ \beta_{wu} & \beta_{wv} & \beta_{ww} & \beta_{w\theta} \\ \beta_{\theta u} & \beta_{\theta v} & \beta_{\theta w} & \beta_{\theta\theta} \end{pmatrix}, \quad \vec{d}_t = \begin{pmatrix} d_{tu} \\ d_{tv} \\ d_{tw} \\ d_{t\theta} \end{pmatrix}. \quad (5)$$

Then, we define similar autoregressive processes in space to relate statistics at points F and P at the same time t

$$\vec{A}_{P,t} = \gamma \cdot \vec{A}_{F,t} + \vec{e}_t, \quad (6)$$

where

$$\vec{A}_{P,t} = \begin{pmatrix} u_{P,t} \\ v_{P,t} \\ w_{P,t} \\ \theta_{P,t} \end{pmatrix}, \quad \gamma = \begin{pmatrix} \gamma_{uu} & \gamma_{uv} & \gamma_{uw} & \gamma_{u\theta} \\ \gamma_{vu} & \gamma_{vv} & \gamma_{vw} & \gamma_{v\theta} \\ \gamma_{wu} & \gamma_{wv} & \gamma_{ww} & \gamma_{w\theta} \\ \gamma_{\theta u} & \gamma_{\theta v} & \gamma_{\theta w} & \gamma_{\theta\theta} \end{pmatrix}, \quad \vec{e}_t = \begin{pmatrix} e_{tu} \\ e_{tv} \\ e_{tw} \\ e_{t\theta} \end{pmatrix}. \quad (7)$$

The combination of processes (4) and (6) provides a means for calculation of the fluid properties at the new particle location P in terms of the known fluid properties at the previous location O.

The calculation of $\vec{A}_{F,t}$ using (4) is described in [1], here we focus on expressions for γ and \vec{e}_t which are needed for calculation of $\vec{A}_{P,t}$. The procedure to obtain γ and \vec{e}_t is similar to that used for β and \vec{d}_t in [1] and we only present the final results for brevity. The expression for γ reads

$$\gamma = \mathbf{D} \cdot \mathbf{cov}^{-1}(\vec{A}_{F,t}, \vec{A}_{F,t}^T). \quad (8)$$

where

$$\mathbf{D} = \begin{pmatrix} R_{uu}(\delta r) \sqrt{u_{P,t}^2} \sqrt{u_{F,t}^2} & R_{uv}(\delta r) \sqrt{u_{P,t}^2} \sqrt{v_{F,t}^2} & R_{uw}(\delta r) \sqrt{u_{P,t}^2} \sqrt{w_{F,t}^2} & R_{u\theta}(\delta r) \sqrt{u_{P,t}^2} \sqrt{\theta_{F,t}^2} \\ R_{vu}(\delta r) \sqrt{v_{P,t}^2} \sqrt{u_{F,t}^2} & R_{vv}(\delta r) \sqrt{v_{P,t}^2} \sqrt{v_{F,t}^2} & R_{vw}(\delta r) \sqrt{v_{P,t}^2} \sqrt{w_{F,t}^2} & R_{v\theta}(\delta r) \sqrt{v_{P,t}^2} \sqrt{\theta_{F,t}^2} \\ R_{wu}(\delta r) \sqrt{w_{P,t}^2} \sqrt{u_{F,t}^2} & R_{wv}(\delta r) \sqrt{w_{P,t}^2} \sqrt{v_{F,t}^2} & R_{ww}(\delta r) \sqrt{w_{P,t}^2} \sqrt{w_{F,t}^2} & R_{w\theta}(\delta r) \sqrt{w_{P,t}^2} \sqrt{\theta_{F,t}^2} \\ R_{\theta u}(\delta r) \sqrt{\theta_{P,t}^2} \sqrt{u_{F,t}^2} & R_{\theta v}(\delta r) \sqrt{\theta_{P,t}^2} \sqrt{v_{F,t}^2} & R_{\theta w}(\delta r) \sqrt{\theta_{P,t}^2} \sqrt{w_{F,t}^2} & R_{\theta\theta}(\delta r) \sqrt{\theta_{P,t}^2} \sqrt{\theta_{F,t}^2} \end{pmatrix}. \quad (9)$$

and

$$\mathbf{cov}(\vec{A}_{F,t}, \vec{A}_{F,t}^T) = \begin{pmatrix} \overline{uu} & \overline{uv} & \overline{uw} & \overline{u\theta} \\ \overline{vu} & \overline{vv} & \overline{vw} & \overline{v\theta} \\ \overline{wu} & \overline{wv} & \overline{ww} & \overline{w\theta} \\ \overline{\theta u} & \overline{\theta v} & \overline{\theta w} & \overline{\theta\theta} \end{pmatrix}_{F,t}. \quad (10)$$

To determine \vec{e}_t , first it can be shown that

$$\mathbf{cov}(\vec{e}_t, \vec{e}_t^T) = \mathbf{cov}(\vec{A}_{P,t}, \vec{A}_{P,t}^T) - \gamma \cdot \mathbf{D}^T. \quad (11)$$

Then, we write

$$\vec{e}_t = \mathbf{S} \cdot \vec{Z}, \quad (12)$$

where \mathbf{S} is a matrix, which needs to be determined, and \vec{Z} is a random vector, each component of which sampled from a standard normal distribution with a mean of zero and a variance of unity. After some algebraic manipulations, we obtain

$$\mathbf{S} \cdot \mathbf{S}^T = \mathbf{cov}(\vec{e}_t, \vec{e}_t^T), \quad (13)$$

from which \mathbf{S} can be determined by using Cholesky factorization of matrix $\mathbf{cov}(\vec{e}_t, \vec{e}_t^T)$. This completes the determination of γ and \vec{e}_t . By combining the solution for Eqs. (4) and (6), the fluctuations at time t and at the particle location P can be determined from fluctuations at time $t - \delta t$.

To implement the model, spatial correlation functions $R_{\alpha\beta}(\delta r)$ in (9) must be specified in advance. In principal, the modeling approach here allows for implementation of any form for these correlations. To proceed, we consider the widely-utilized exponential form,

$$R_{\alpha\beta}(\delta r) = \frac{\overline{\alpha_{P,t}\beta_{F,t}}}{\sqrt{\alpha_{P,t}^2}\sqrt{\beta_{F,t}^2}} \exp\left(\frac{-\delta r}{L_{E\alpha\beta}}\right), \quad (14)$$

where α and β represent u, v, w or θ , and $L_{E\alpha\beta}$ includes a total of sixteen Eulerian length scales. Due to symmetry, only ten length scales are needed to be specified, but lack of experimental data makes the task of specification of these length scales difficult and could affect the overall accuracy of the model. Therefore, to further reduce the number of length scales, we follow the approach suggested by Lu et al. [19]. In this approach, the fluctuations $\vec{A}_{F,t}$ and $\vec{A}_{P,t}$ are normalized by the square roots of their respective local variances, e.g. $u_{F,t}^* = u_{F,t} / \sqrt{\overline{u_{F,t}^2}}$ where the superscript* shows the normalized variable and $\sqrt{\overline{u_{F,t}^2}}$ is known from the solution of single-point turbulence models. With this normalization, Eq. (6) becomes

$$\vec{A}_{P,t}^* = \gamma^* \cdot \vec{A}_{F,t}^* + \vec{e}_t^*. \quad (15)$$

It can be argued that the normalized fluctuations are nearly isotropic so that the off-diagonal components of the Reynolds stress tensor and turbulence fluxes of temperature fluctuations can be neglected. With this assumption, the time series expression can be simplified as in the following:

$$a_{\alpha(P,t)}^* = \gamma_{\alpha}^* a_{\alpha(F,t)}^* + e_{\alpha,t}^*, \quad (16)$$

with no summation over the repeated Greek indices. Here, $\alpha = 1, 2, 3, 4$ such that a_{α} corresponds to u, v, w, θ , respectively,

$$\gamma_{\alpha}^* = \exp\left(\frac{-\delta r}{L_{E\alpha}}\right), \quad (17)$$

and $e_{\alpha,t}^*$ are Gaussian random variables with means of zero. The variance of $e_{\alpha,t}^*$ can be obtained by squaring both sides of (16), and then taking the expectations. This leads to

$$\overline{e_{\alpha,t}^{*2}} = 1 - \gamma_{\alpha}^{*2}. \quad (18)$$

With the above procedure, only four Eulerian length scales need to be specified. This is best accomplished by selecting a local coordinate system $\xi\eta\zeta$ such that the ξ coordinate is always aligned with δr as shown in Fig. 1. In this manner, one can use the well-established spatial correlations of isotropic turbulence in longitudinal (ξ) and transversal (η and ζ) directions. Here, we use

$$L_{E\xi} = 2L_{E\eta} = 2L_{E\zeta} = C_1 \tau_L u' \quad (19)$$

as previously used by Lu [16] and Mashayek [20]. In (19), $u' = \sqrt{2k/3}$ where k is the turbulence kinetic energy of the fluid phase. A similar expression is also used for temperature fluctuations. The coordinate transformation from xyz to $\xi\eta\zeta$ and its inverse transformation are performed once for each particle during each time step.

Model Assessment and Results

To assess the stochastic model performance, we consider the DNS data for two different flow configurations, i.e. the isotropic flow of Mashayek et al. [5] and the homogeneous shear flow of Shotorban et al. [21]. The details of these simulations are explained elsewhere, and will not be repeated here. The carrier phase is incompressible in both cases and the particle concentration is low enough to neglect the effects of particles on turbulence, i.e. one-way coupling. Our stochastic simulations are conducted using similar initial conditions as those used in DNS studies. All the fluid related statistics are also taken directly from the DNS. This provides a framework for assessing the performance of the stochastic model by comparison of the particle related statistics with DNS data. These statistics are calculated by averaging the velocity and temperature fluctuations obtained by tracking a total number of 20,000 particles using a fourth-order Runge-Kutta scheme to integrate particle equations in time. For temporal correlations, that are embedded in the process defined by (4), we also use an exponential form

$$R_{\alpha\beta}(\delta t) = \frac{\overline{\alpha_{F,t}\beta_{F,t-\delta t}}}{\sqrt{\alpha_{F,t}^2}\sqrt{\beta_{F,t-\delta t}^2}} \exp\left(\frac{-\delta t}{T_{L\alpha\beta}}\right), \quad (20)$$

where α and β again represent u, v, w or θ and $T_{L\alpha\beta}$ is the Lagrangian integral time scale. Similarly to our previous study [1], for convenience, we assume $T_{L\alpha\beta} = \tau_L$ for all components.

Some previous studies [22,20] have proposed that various time scales to be adjusted for a more reasonable comparison between the model predictions and DNS results. This is due to the fact that the model is based on parameters which are defined for high Reynolds number flows whereas DNS is conducted at low Reynolds numbers. Here, we adjust the particle time constant, τ_p , and the drift time scale, $\tau_g = d_p / v_{dr}$, using the following relations [20]:

$$\left(\frac{\tau_p}{\tau_E}\right)_{\text{DNS}} = \left(\frac{\tau_p}{\tau_E}\right)_{\text{STH}}, \quad \left(\frac{\tau_g}{\tau_E}\right)_{\text{DNS}} = \left(\frac{\tau_g}{\tau_E}\right)_{\text{STH}}, \quad (21)$$

where STH refers to the stochastic model and $\tau_E = \tau_L / C_2$ is the Eulerian integral time scale with $C_2 = 0.73$. This scaling assumes that the particle dynamics is primarily affected by the large scales of the flow.

We first discuss the results of the isotropic flow for which we use $\tau_L = C_3(u')^2/\epsilon$ with $C_3 = 0.212$. This choice is consistent with previous studies in isotropic flows [16,20]. Here, ϵ is the rate of dissipation of the carrier phase turbulence kinetic energy and is also taken directly from DNS. The importance of the inclusion of the spatial correlation in the stochastic model for capturing the gravity effects is clearly demonstrated in Fig. 2. This figure shows comparisons of the predictions of the stochastic model without the spatial correlation with the DNS data for the variance of the particle velocity fluctuations as normalized by that of the fluid in the isotropic flow. The results are provided for different values of the particle time constant at three different drift velocities $v_{dr} = 0, v_k$ and $5v_k$ where v_k is the Kolmogorov velocity in DNS. Also, in

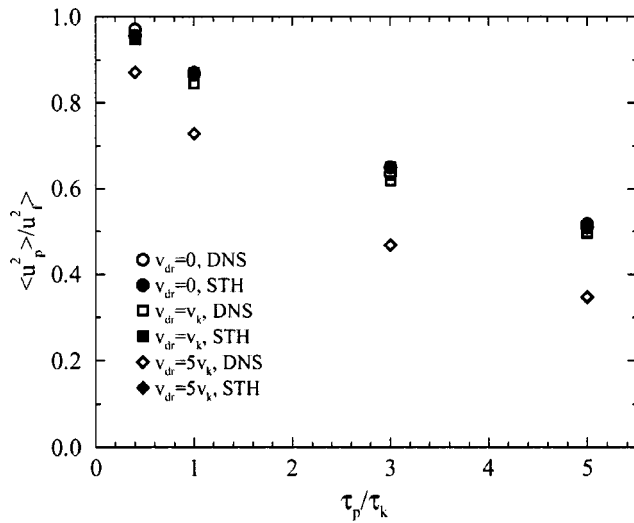


Fig. 2 Results from the stochastic model without implementing the spatial correlation in isotropic flow. DNS results for corresponding cases are also shown for comparison.

the figure, τ_k is the Kolmogorov time scale from DNS and $\langle \rangle$ denotes the ensemble average over the number of particles. It is noted that, the absence of the spatial correlation in the stochastic model leads to identical results for all values of the drift velocity. This is clearly in disagreement with the DNS data which shows a decrease of the variance of the particle velocity fluctuations with the increase of the drift velocity.

Similar results for the particle velocity variance are shown in Fig. 3a while incorporating the spatial correlation into the stochastic model. For this comparison, we have used $C_1 = 2.778$ which is again the value suggested in [16,20]. It is clear that the trends are correctly captured for changes in both particle time constant and drift velocity. The quantitative agreement is very good for smaller drift velocity but some deviations are noted at higher drift velocity. The results in Fig. 3b show that quantitative agreement can be improved by changing the value of the constant C_1 to 4.1, i.e. an increase of 50%. The comparison of the results in Figs. 2 and 3 shows that the inclusion of the spatial correlation is imperative for capturing the gravity effects.

Next, we consider simulations of a homogeneous shear turbulent flow laden with solid particles. This flow is characterized by a mean velocity gradient imposed in the cross-stream direction. The magnitude of the mean velocity gradient, dU_1/dx_2 , is constant in time, where indices 1 and 2 denote the streamwise and cross-stream directions, respectively. In addition, to assess the statistics related to the temperature field, a constant mean temperature gradient, dT/dx_2 , is also imposed on the flow. The scaling (21) for particle time constant has been applied by incorporating the values of τ_E from DNS as a function of time. We did not apply the scaling for τ_g as there was no DNS data available for gravity cases and thus no need for a direct comparison.

For comparison, we consider a case with one-way coupling and particle time constant $\tau_p = 0.3$ from the DNS study [21]. The particles are injected and tracked in stochastic simulations following exactly the same procedure as that described in our previous study [1]. For these comparisons we have used $\tau_L = 0.482k/\epsilon$ and $C_1 = 4.1$. Figure 4 shows the model predictions and the DNS data for temporal variations of $\langle v_1 v_1 \rangle$, $\langle v_1 v_2 \rangle$, $\langle v_1 \theta_p \rangle$, $\langle v_2 \theta_p \rangle$ and $\langle \theta_p \theta_p \rangle$. In this figure, the time axis has been normalized using the mean velocity gradient magnitude $\alpha = dU_1/dx_2$. All the variables used in these simulations are nondimensionalized using the same reference scales as those implemented in the DNS formulation. In

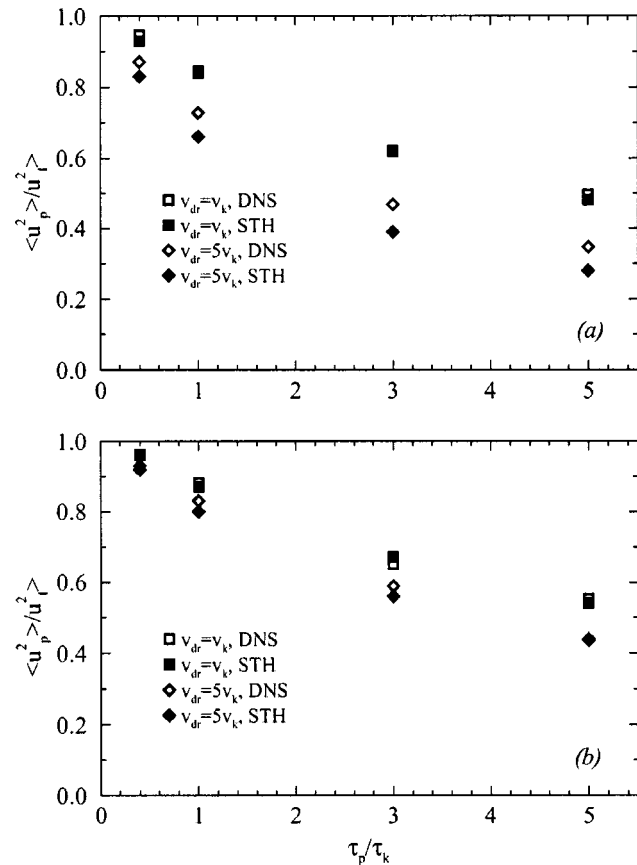


Fig. 3 Comparison of stochastic model predictions with DNS results in isotropic flow for (a) $C_1 = 2.73$, (b) $C_1 = 4.1$

this nondimensional form the magnitudes of mean velocity and mean temperature gradients are the same, i.e. $dU_1/dx_2 = dT/dx_2 = 2$.

The stochastic simulations are conducted with different gravity levels and directions—in each case only one gravity direction is considered. The DNS data are available for homogeneous flow without gravity only and are used here for validation. Cases with non-zero drift velocities are presented to show the gravity effects on the particle statistics in homogeneous shear flow. For these cases, the fluid statistics are also taken from the DNS case without gravity. Therefore, the results shown in Fig. 4 for cases with gravity are to be treated as qualitative rather than quantitative. These results are useful to show the trend of variation for various statistics as the magnitude and direction of the drift velocity are changed. Although not shown here, our simulations indicated that, similarly to the isotropic flow, the stochastic model without the spatial correlation does not capture any of the gravity effects.

The comparison with DNS for the case without gravity shows encouraging agreements. It should be added here that the DNS cases were started from a random field as initial condition, therefore, turbulence correlations were not well established during the very early stages of DNS. This may have contributed in part to deviations between the model prediction and DNS data. The presence of gravity decreases the magnitudes of all of the particle statistics as shown in Fig. 4. This is in agreement with the results of the isotropic flow in Fig. 3 and can be directly attributed to the “crossing trajectories effect.” For the parameter values considered in this study, it appears that gravity exerts a minimal effect on the particle fluctuating temperature variance. This, however, may not be the case for other values of the Prandtl number. The choice of the integral length scale in stochastic model may also have contributed to this behavior. For these simulations, we assumed the

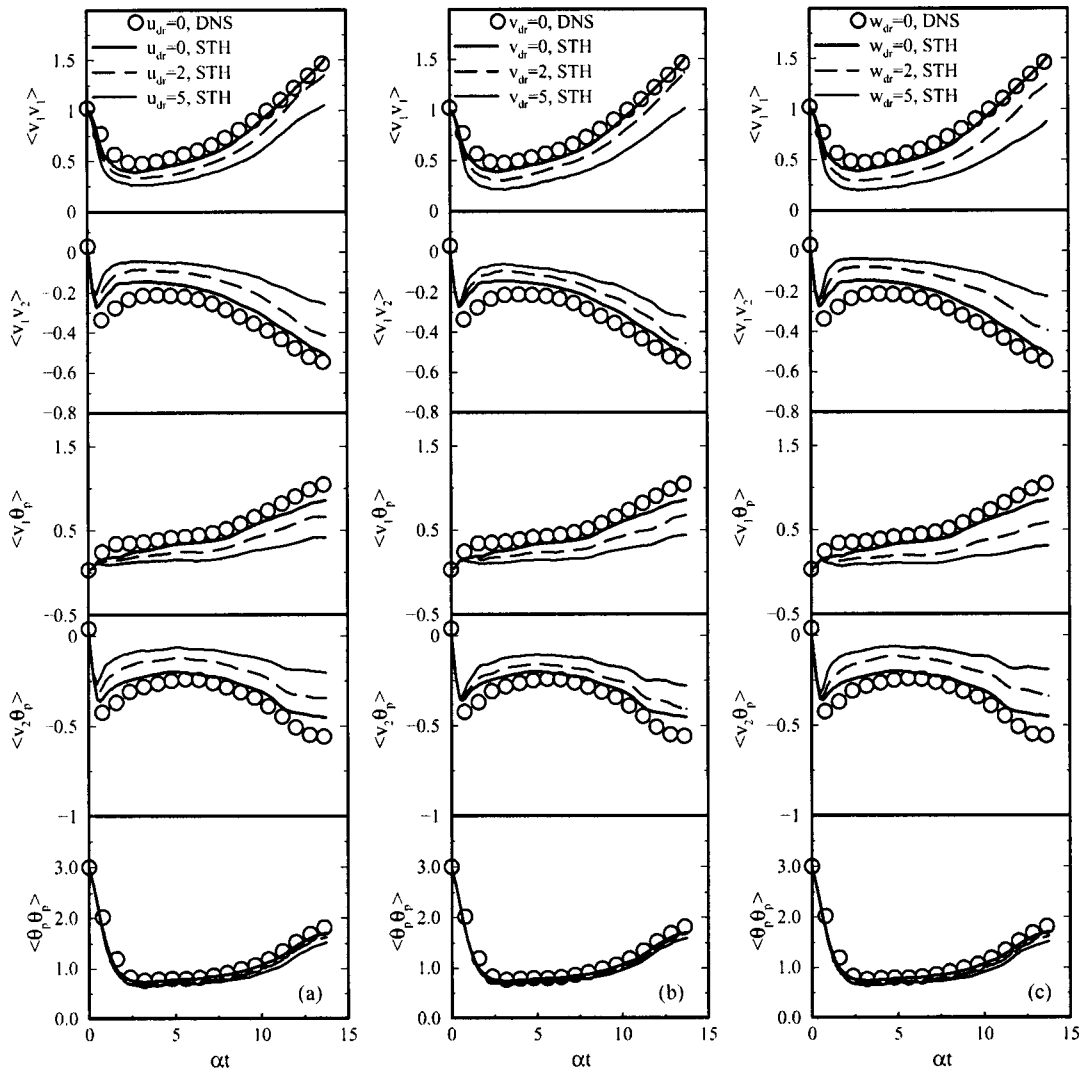


Fig. 4 Stochastic model predictions in homogeneous shear flow for various magnitudes of the gravitational force in (a) streamwise, (b) cross-stream and (c) spanwise directions. The figure also shows a comparison with DNS data in zero gravity.

same length scale for temperature as that for velocity. The issue of specifying accurate length scales remains as one of the main future tasks for researchers in this area.

Conclusion

An improved stochastic model has been proposed for the prediction of gravity effects on velocity and temperature fluctuations in turbulent flows laden with solid particles. The model is based on a first-order time-series analysis and addresses the anisotropy of turbulence, temporal correlation and spatial correlation. It has been found that the lack of the spatial correlation results in the failure of the model to capture the gravity effects.

Direct numerical simulation (DNS) data in two different flow configurations have been used for a preliminary assessment of the model performance. The comparisons in isotropic flow are conducted for various drift velocities and indicate good agreements for different values of particle time constant. These comparisons have also been used to investigate the effect of the empirical constant that specifies the spatial correlation. The comparisons in homogeneous shear flow are conducted for zero gravity only, due to the lack of DNS data in the presence of gravity. This comparison shows encouraging agreements. Additional stochastic simulations are conducted in this flow with different gravity levels and direc-

tions. These results are used qualitatively to discuss the trends of the variations in particle statistics with changes in the drift velocity and gravity direction.

Whereas by implementing turbulence correlations the stochastic model is inherently more robust, it should be noted that the success of the model is closely linked to the level of accuracy by which these correlations can be specified. This important issue remains open for future research and relies heavily on the availability of experimental data in various flows.

Acknowledgments

The support for this work was in part provided by the U.S. Office of Naval Research and the National Science Foundation.

References

- [1] Gao, Z., and Mashayek, F., 2003, "A Stochastic Model for Non-Isothermal Droplet-Laden Turbulent Flows," *AIAA J.*, **42**(2), pp. 255–260.
- [2] Yudine, M. I., 1959, "Physical Considerations on Heavy-Particle Diffusion," *Adv. Geophys.*, **6**, pp. 185–191.
- [3] Csanady, G. T., 1963, "Turbulent Diffusion of Heavy Particles in the Atmosphere," *J. Atmos. Sci.*, **20**, pp. 201–208.
- [4] Wang, L.-P., and Maxey, M. R., 1993, "Settling Velocity and Concentration Distribution of Heavy Particles in Isotropic Turbulence," *J. Fluid Mech.*, **256**, pp. 27–68.

- [5] Mashayek, F., Jaber, F. A., Miller, R. S., and Givi, P., 1997, "Dispersion and Polydispersity of Droplets in Stationary Isotropic Turbulence," *Int. J. Multiphase Flow*, **23**(2), pp. 337–355.
- [6] Mashayek, F., and Pandya, R. V. R., 2003, "Analytical Description of Particle/Droplet-Laden Turbulent Flows," *Progress in Energy and Combustion Science*, **29**(4), pp. 329–378.
- [7] Gosman, A. D., and Ioannides, E., "Aspects of Computer Simulation of Liquid-Fuelled Combustors," AIAA Paper 81-0323, 1981.
- [8] Etasse, E., Meneveau, C., and Poinso, T., 1998, "Simple Stochastic Model for Particle Dispersion Including Inertia, Trajectory-Crossing, and Continuity Effects," *ASME J. Fluids Eng.*, **120**, pp. 186–192.
- [9] Graham, D., and James, P., 1996, "Turbulent Dispersion of Particles Using Eddy Interaction Models," *Int. J. Multiphase Flow*, **22**(1), pp. 157–175.
- [10] Graham, D. I., 1996, "On the Inertia Effect in Eddy Interaction Models," *Int. J. Multiphase Flow*, **22**(1), pp. 177–184.
- [11] Graham, D. I., 2001, "Spectral Characteristics of Eddy Interaction Models," *Int. J. Multiphase Flow*, **27**(6), pp. 1065–1077.
- [12] Wang, L.-P., and Stock, D. E., 1992, "Stochastic Trajectory Models for Turbulent Diffusion: Monte Carlo Process Versus Markov Chains," *Atmos. Environ., Part A*, **26**(9), pp. 1599–1607.
- [13] Parthasarathy, R. N., and Faeth, G. M., 1990, "Turbulent Dispersion of Particles in Self-Generated Homogeneous Turbulence," *J. Fluid Mech.*, **220**, pp. 515–537.
- [14] Berlemont, A., Desjonqueres, P., and Gouesbet, G., 1990, "Particle Lagrangian Simulation in Turbulent Flows," *Int. J. Multiphase Flow*, **16**(1), pp. 19–34.
- [15] Zhou, Q., and Leschziner, M. A., "A Time-Correlated Stochastic Model for Particle Dispersion in Anisotropic Turbulence," *8th Turbulent Shear Flows Symp.*, Munich, 1991.
- [16] Lu, Q. Q., 1995, "An Approach to Modeling Particle Motion in Turbulent Flows-I. Homogeneous, Isotropic Turbulence," *Atmos. Environ.* **29**(3), pp. 423–436.
- [17] Moissette, S., Oesterle, B., and Boulet, P., 2001, "Temperature Fluctuations of Discrete Particles in a Homogeneous Turbulent Flow: A Lagrangian Model," *Int. J. Heat Fluid Flow*, **22**(3), pp. 220–226.
- [18] Box, G. E. P., and Jenkins, G. M., *Time Series Analysis*, Holden-Day, Oakland, CA, 1976.
- [19] Lu, Q. Q., Fontaine, J. R., and Aubertin, G., 1993, "Particle Dispersion in Shear Turbulent Flows," *Aerosol Sci. Technol.*, **18**, pp. 85–99.
- [20] Mashayek, F., 1999, "Stochastic Simulations of Particle-Laden Isotropic Turbulent Flow," *Int. J. Multiphase Flow*, **25**(8), pp. 1575–1599.
- [21] Shotorban, B., Mashayek, F., and Pandya, R. V. R., 2003, "Temperature Statistics in Particle-Laden Turbulent Homogeneous Shear Flow," *Int. J. Multiphase Flow*, **29**, No. 8, pp. 1333–1353.
- [22] Elghobashi, S., and Truesdell, G. C., 1992, "Direct Simulation of Particle Dispersion in a Decaying Isotropic Turbulence," *J. Fluid Mech.*, **242**, pp. 655–700.

On the Criterion for the Determination Transition Onset and Breakdown to Turbulence in Wall-Bounded Flows¹

J. Jovanović

Senior Research Scientist

M. Pashtrapanska

Ph.D. Student

Lehrstuhl für Strömungsmechanik,
Universität Erlangen-Nürnberg,
Cauerstrasse 4, D-91058, Germany

Starting from the basic conservation laws of fluid flow, we investigated transition and breakdown to turbulence of a laminar flat plate boundary layer exposed to small, statistically stationary, two-component, three-dimensional disturbances. The derived equations for the statistical properties of the disturbances are closed using the two-point correlation technique and invariant theory. By considering the equilibrium solutions of the modeled equations, the transition criterion is formulated in terms of a Reynolds number based on the intensity and the length scale of the disturbances. The deduced transition criterion determines conditions that guarantee maintenance of the local equilibrium between the production and the viscous dissipation of the disturbances and therefore the laminar flow regime in the flat plate boundary layer. The experimental and numerical databases for fully developed turbulent channel and pipe flows at different Reynolds numbers were utilized to demonstrate the validity of the derived transition criterion for the estimation of the onset of turbulence in wall-bounded flows. [DOI: 10.1115/1.1779663]

1 Introduction

There have been many theoretical and experimental studies of the processes that cause laminar to turbulent transition in boundary layers and the phenomena occurring in the inner region of fully developed turbulent flows. These studies led to the conclusion that there is a strong similarity between the mechanisms responsible for transition and the continuous production of turbulence close to the solid boundaries. Hinze [[1], pp. 600–613] provided a brief review of the subject based on linear and nonlinear stability theory. Hinze also presented experimental results deduced from hot-wire measurements and flow visualizations which revealed interesting details of the sequence of the events during the transition process. Studies of the dynamics of coherent structures close to the wall by Kline et al. [2], Kim, Kline and Reynolds [3] and Falco [4] showed remarkable analogies to the sequence of events leading to the transition which led Laufer [5,6] to the conclusion that these processes are very closely interconnected and therefore should be treated theoretically using the same mathematical concepts. This issue was raised by J. Laufer, P. Klebanoff, R. Falco and M. Landahl during participation in the round-table discussion organized by Z. Zarić at the ICHMT Symposium on Structure of Turbulence in Heat and Mass Transfer (Dubrovnik, 1980). Although there has been an explosion of activity during last two decades, apparently no one has yet succeeded in providing a description of transition and breakdown to turbulence using statistical techniques.

The purpose of this paper is to fill the gaps in the theoretical treatment of the transition process using statistical techniques. An attempt is made to establish quantitative links between the transition process and fully developed turbulence using stochastic tools suitable for describing random, 3-D flow-fields. We shall provide rational approximations for the mechanisms involved in the tran-

sition process using the two-point correlation technique and invariant theory and finish with a closed set of transport equations from which it was possible to deduce the criterion for the determination transition onset and breakdown to turbulence in wall-bounded flows.

2 Basic Equations

Starting from the Navier-Stokes and continuity equations for a viscous incompressible fluid:

$$\frac{\partial u_i}{\partial t} + u_k \frac{\partial u_i}{\partial x_k} = -\frac{1}{\rho} \frac{\partial p}{\partial x_i} + \nu \frac{\partial^2 u_i}{\partial x_k \partial x_k}, \quad \frac{\partial u_k}{\partial x_k} = 0, \quad i, k = 1, 2, 3 \quad (1)$$

and introducing the conventional method of separating the instantaneous velocity u_i and the pressure p into the mean-laminar flow and disturbances u'_i and p' superimposed on it:

$$u_i = U_i + u'_i, \quad p = P + p' \quad (2)$$

one obtains the equations for the disturbances:

$$\frac{\partial u'_i}{\partial t} + U_k \frac{\partial u'_i}{\partial x_k} + u'_k \frac{\partial U_i}{\partial x_k} = -\frac{1}{\rho} \frac{\partial p'}{\partial x_i} + \nu \frac{\partial^2 u'_i}{\partial x_k \partial x_k}, \quad \frac{\partial u'_k}{\partial x_k} = 0. \quad (3)$$

In the derivation of the above equations, it is assumed that the disturbances are much smaller than the corresponding quantities of the mean flow:

$$u'_i \ll U_i, \quad p' \ll P \quad (4)$$

and that they satisfy the Navier-Stokes and continuity equations.

If we consider the disturbances to be random and statistically stationary then by systematic manipulation of (3) it is possible to obtain transport equations for the “apparent” stresses (see, for example, Hinze [[1], pp. 323–324]):

¹This paper was originally prepared to be communicated on the occasion of Professor Franz Durst 60th birthday held on February 16, 2001 at the Technical Faculty of the Friedrich-Alexander Universität Erlangen-Nürnberg. The authors are pleased to dedicate this article to him.

Contributed by the Fluids Engineering Division for publication in the JOURNAL OF FLUIDS ENGINEERING. Manuscript received by the Fluids Engineering Division March 12, 2003; revised manuscript received March 2, 2004. Associate Editor: T. B. Gatski.

$$\frac{\partial \overline{u'_i u'_j}}{\partial t} + U_k \frac{\partial \overline{u'_i u'_j}}{\partial x_k} = -\overline{u'_j u'_k} \frac{\partial U_i}{\partial x_k} - \overline{u'_i u'_k} \frac{\partial U_j}{\partial x_k} - \frac{1}{\rho} \underbrace{\left[\overline{u'_j \frac{\partial p'}{\partial x_i}} + \overline{u'_i \frac{\partial p'}{\partial x_j}} \right]}_{\Pi_{ij}} - 2\nu \underbrace{\frac{\partial \overline{u'_i}}{\partial x_k} \frac{\partial \overline{u'_j}}{\partial x_k}}_{\epsilon_{ij}} + \nu \frac{\partial^2 \overline{u'_i u'_j}}{\partial x_k \partial x_k} \quad (5)$$

In the above equations, one can identify two different types of unknown correlations: the velocity/pressure gradient correlations (Π_{ij}) and the dissipation correlations (ϵ_{ij}). These correlations must be expressed in terms of U_i and $\overline{u'_i u'_j}$ in order to close the resultant equations (5) for the stresses.

3 The Closure Problem for Small, Two-Component, Three-Dimensional Disturbances

Let small disturbances be statistically stationary, two-component and three-dimensional, consisting of longitudinal (u'_1) and transverse (u'_2) velocity pulsations, while the lateral component (u'_3) of the pulsations is assumed to be zero everywhere in time and space. Such disturbances can be produced by a small, 2-D roughness element placed at the wall in a laminar boundary layer as shown in Fig. 1. Measurements of the anisotropy invariants Π_a and III_a , discussed below, of the disturbances clearly demonstrate that these are almost two-component for different free stream velocities and low Reynolds numbers [7,8]. The laminar to turbulence transition process initialized by the two-component disturbances is characterized by abrupt and explosive breakdown to the fully developed turbulent state at a fixed value of the Reynolds number which is very close those met in engineering practice. This is indicated in Fig. 2(c), from which it appears that approaching the breakdown point from the laminar, two-component state and from the fully developed turbulent state results in the same estimate of the critical Reynolds number. We shall exploit this experimental evidence in order to provide the quantitative link between results of the theoretical considerations of the transition process with those of fully developed turbulence which are available from numerous experiments and also from direct numerical simulations.

A few remarks follow with respect to the role of the natural disturbances in the transition process. Figure 2(b) shows that for such disturbances laminar to turbulence transition is weaker than transition induced by the two-component disturbances shown in Fig. 2(c). Natural disturbances, which originate in technical practice, can be considered in a statistical sense of Fig. 3 as nearly axisymmetric. For this type of disturbances, theoretical considerations, following the same analytical path as used in this study, show that the critical Reynolds number for breakdown to turbulence depends strongly on the anisotropy of the disturbances. If the intensity of the streamwise velocity component is lower than the intensities of the normal and lateral components, $\text{III}_a < 0$, the transition process is promoted and occurs at low Reynolds numbers. For the reverse situation when the intensity of the streamwise velocity component is higher than the intensities of the normal and lateral components, $\text{III}_a > 0$, the transition process is delayed and occurs at high Reynolds number. Since the continuity equation near the wall dictates that $\text{III}_a > 0$, the results in Fig. 2(b) are logical and not surprising.

For small, statistically stationary, two-component, 3-D disturbances it is possible to attack the closure of (5) using the two-point correlation technique developed by Chou [9] and invariant theory introduced by Lumley and Newman [10]. Application of the two-point correlation technique permits the separation of the

inhomogeneous effects in the treatment of the unknown terms involved in (5) and recasting of the inhomogeneous problem into the corresponding problem of a statistically homogeneous flow-field. Then, using invariant theory, it is possible to isolate the effects of the anisotropy in the “apparent” stresses from all other flow properties, which allows rational construction of the closure approximations that include all physically realistic states of the disturbances.

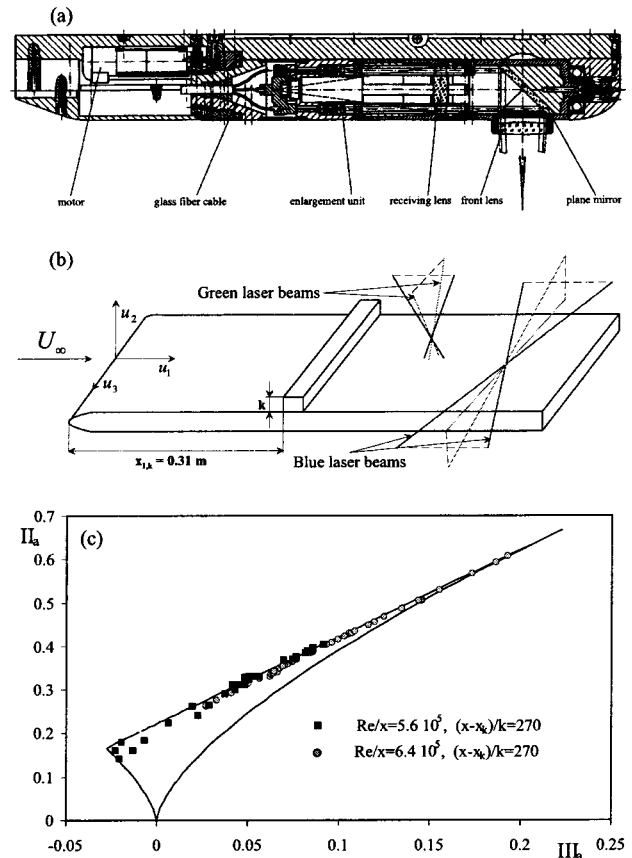


Fig. 1 Anisotropy-invariant mapping of the disturbances generated by small, two-dimensional roughness element in an initially laminar flat plate boundary layer from Fischer, Jovanović and Durst [7]: (a) specially designed two-component laser-Doppler system for near-wall measurements; (b) schematic of flat plate arrangement in the wind tunnel with layout of two different beam configurations which allowed measurements of all components of the “apparent” stresses of the disturbances; (c) traces of the joint variations of invariants Π_a and III_a across the anisotropy invariant map confirm the two-component nature of the disturbances

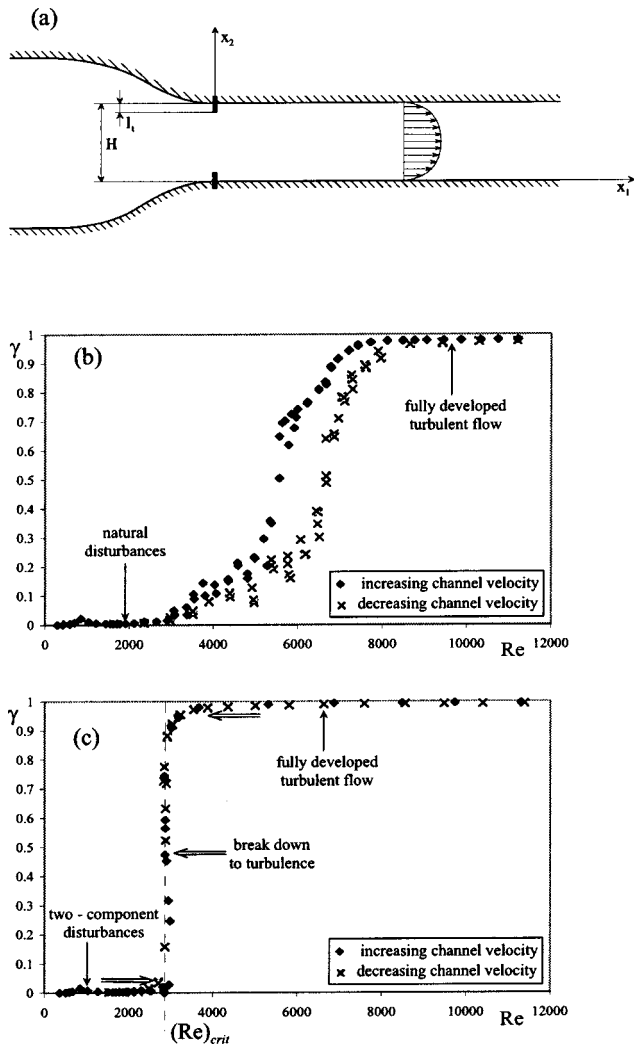


Fig. 2 Intermittency (γ) measurements of the transition process from laminar to turbulent states at the channel centerline from Fischer [8]: (a) channel flow test section; (b) transition due to the natural disturbances is accompanied by large hysteresis in the experimental data; (c) transition due to the two-component disturbances implies that for such disturbances the critical Reynolds number may be found by extrapolation data of a fully developed turbulent flow if the transition criterion is known

3.1 Application of the Two-Point Correlation Technique for Interpretation of ϵ_{ij} . Let us first consider closure for the terms which are related to the dissipation process:

$$\epsilon_{ij} = \nu \frac{\partial u'_i}{\partial x_k} \frac{\partial u'_j}{\partial x_k} \quad (6)$$

that appear in (5). The most efficient procedure to treat these correlations is based on the two-point correlation technique that was originally developed by Chou [9] and subsequently refined by Kolovandin and Vatutin [11] and Jovanović, Ye and Durst [12]. However, application of this technique to the study of the dynamics of the disturbances is complicated, tedious and very demanding for the reader. Here we shall provide only a brief account of the parts of the subject which are relevant for the present study.

In order to separate the effect of local character from global, large-scale fluid motion, we must first express the dissipation correlations ϵ_{ij} in a coordinate system relative to two closely separated points A and B in space as follows:

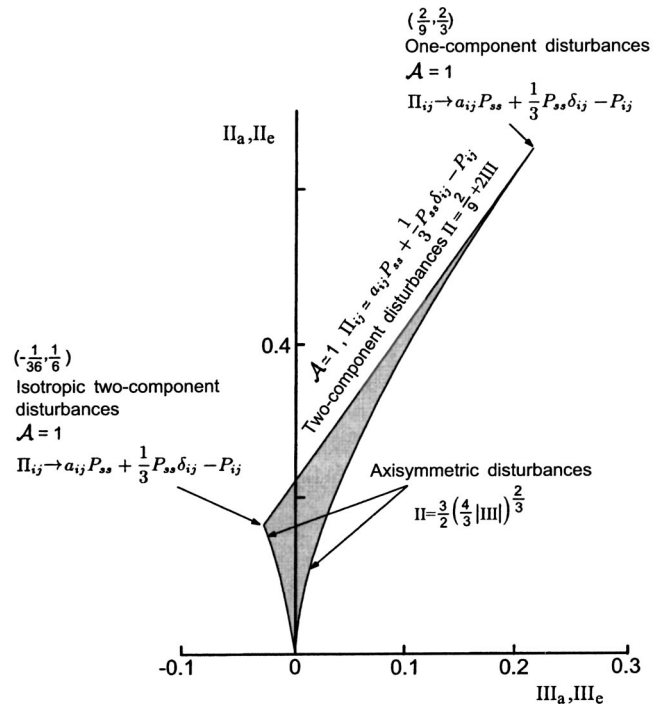


Fig. 3 Anisotropy invariant map and the asymptotic forms for the unknown correlations involved in the equations for the “apparent” stresses

$$\begin{aligned} \epsilon_{ij} &= \nu \frac{\partial u'_i}{\partial x_k} \frac{\partial u'_j}{\partial x_k} = \nu \lim_{A \rightarrow B} \left(\frac{\partial u'_i}{\partial x_k} \right)_A \left(\frac{\partial u'_j}{\partial x_k} \right)_B \\ &= \nu \lim_{A \rightarrow B} \left(\frac{\partial}{\partial x_k} \right)_A \left(\frac{\partial}{\partial x_k} \right)_B \overline{(u'_i)_A (u'_j)_B} \end{aligned} \quad (7)$$

Expressing the partial differential operators in (7) at points A and B as functions of the position in space and the relative coordinates between these two points:

$$\xi_k = (x_k)_B - (x_k)_A, \quad (8)$$

and taking the limit $A \rightarrow B$ yields (Jovanović et al. [12])

$$\epsilon_{ij} = \nu \frac{\partial u'_i}{\partial x_k} \frac{\partial u'_j}{\partial x_k} = \underbrace{\frac{1}{4} \nu \Delta_x \overline{u'_i u'_j}}_{\text{inhomogeneous}} - \underbrace{\nu (\Delta_\xi \overline{u'_i u'_j})_0}_{\text{homogeneous}}, \quad (9)$$

where the double prime “” indicates a value of the two-point correlation function at point B, $\overline{(u'_i)_A (u'_j)_B} \equiv \overline{u'_i u'_j}$, the subscript 0 represents zero relative separation in space, $\xi=0$, and Δ corresponds to the Laplace operator ($\Delta_x \equiv \partial^2 / \partial x_k \partial x_k$, $\Delta_\xi \equiv \partial^2 / \partial \xi_k \partial \xi_k$).

Equation (9) shows that ϵ_{ij} is composed of an inhomogeneous part $1/4 \nu \Delta_x \overline{u'_i u'_j}$ and a homogeneous part $\epsilon_{ij}^h = -\nu (\Delta_\xi \overline{u'_i u'_j})_0$. Since the tensor ϵ_{ij} is symmetrical, from (9) it follows that

$$(\Delta_\xi \overline{u'_i u'_j})_0 = (\Delta_\xi \overline{u'_j u'_i})_0, \quad (10)$$

the two-point velocity correlation of second rank in the limit when $\xi \rightarrow 0$ satisfies the same relationship as in a statistically homogeneous flow field. This peculiarity of the two-point velocity correlation, deduced only from kinematic considerations, permits us to

introduce the concept of local homogeneity for the disturbances, which leads to radical simplifications of the dynamic equations for the dissipation correlations.

Since the inhomogeneous part of ϵ_{ij} can be directly related to $\overline{u'_i u'_j}$, we need to consider only the homogeneous part of (9). Using the two-point correlation technique, kinematic constraints and the continuity equation, it can be shown ([9,11,13]) that the components of the homogeneous part of (9) can be interpreted analytically in terms of its trace $\epsilon_h = -\nu(\Delta_\xi \overline{u'_s u''_s})_0$ and the “apparent” stresses $u'_i u'_j$. Therefore, only the equation for ϵ_h needs to be considered. This equation is obtained by operating the dynamic equation for the two-point velocity correlation in a relative coordinate system with respect to $-\nu\Delta_\xi$ and setting $\vec{\xi} \rightarrow 0$ to obtain (Jovanović et al. [12])

$$\begin{aligned} & -\nu \frac{\partial}{\partial t} (\Delta_\xi \overline{u'_s u''_s})_0 - \nu U_k \frac{\partial}{\partial x_k} (\Delta_\xi \overline{u'_s u''_s})_0 \\ & \approx 2\nu (\Delta_\xi \overline{u'_k u''_s})_0 \frac{\partial U_s}{\partial x_k} + 2\nu \left(\frac{\partial^2}{\partial \xi_l \partial \xi_k} \overline{u'_s u''_s} \right)_0 \frac{\partial U_k}{\partial x_l} \\ & - 2\nu^2 (\Delta_\xi \Delta_\xi \overline{u'_s u''_s})_0 - \frac{1}{2} \nu^2 \Delta_x (\Delta_\xi \overline{u'_s u''_s})_0. \end{aligned} \quad (11)$$

The approximate equation for the homogeneous part of the dissipation rate involves only the derivatives of two-point velocity correlations. In the derivation of this equation, the concept of local homogeneity was utilized by applying the relationships for the derivatives of the two-point correlation functions for zero separation ($\vec{\xi}=0$) that are valid in a statistically homogeneous flow-field.

The first two terms on the right-hand side of (11) are the production terms that originate from the mean velocity gradient. A firm analytical closure for these terms can be formulated only for the case of axisymmetric disturbances. For such disturbances Jovanović, Otić and Bradshaw [14] showed that the above-mentioned terms are equal, and their sum is given by

$$\begin{aligned} & 2\nu (\Delta_\xi \overline{u'_k u''_s})_0 \frac{\partial U_s}{\partial x_k} + 2\nu \left(\frac{\partial^2}{\partial \xi_l \partial \xi_k} \overline{u'_s u''_s} \right)_0 \frac{\partial U_k}{\partial x_l} \\ & = -2\mathcal{A} \frac{\overline{\epsilon_h u'_i u'_k}}{k} \frac{\partial U_i}{\partial x_k}, \end{aligned} \quad (12)$$

where $k \equiv 1/2 \overline{u'_k u'_k} \equiv 1/2 q^2$ and the scalar function \mathcal{A} depends on the anisotropy in $u'_i u'_j$ and ϵ_{ij}^h , to be discussed later. Figure 3 shows that, for the limiting states of axisymmetric disturbances which lie at the two-component limit, $\mathcal{A}=1$ and therefore we may suggest closure for such a disturbance state in the following form:

$$2\nu (\Delta_\xi \overline{u'_k u''_s})_0 \frac{\partial U_s}{\partial x_k} + 2\nu \left(\frac{\partial^2}{\partial \xi_l \partial \xi_k} \overline{u'_s u''_s} \right)_0 \frac{\partial U_k}{\partial x_l} \approx -2 \frac{\overline{\epsilon_h u'_i u'_k}}{k} \frac{\partial U_i}{\partial x_k}. \quad (13)$$

The third term on the right-hand side of (11) represents the viscous destruction of ϵ_h and can be approximated using the scaling arguments based on the asymptotic balance of the dissipation rate equation (Tennekes and Lumley [[15], pp. 88–92]) in the form

$$-2\nu^2 (\Delta_\xi \Delta_\xi \overline{u'_s u''_s})_0 \approx -2\nu^2 \frac{q^2}{\lambda^2 \eta^2}, \quad (14)$$

where λ and η are the Taylor microscale and the Kolomogorov length scale, respectively. These scales can be interpreted in terms of the dissipation rate as

$$\lambda = \left(\frac{5\nu q^2}{\epsilon_h} \right)^{1/2}, \quad \eta = \left(\frac{\nu^3}{\epsilon_h} \right)^{1/4}. \quad (15)$$

Using the above relations, (14) can be written as

$$-2\nu^2 (\Delta_\xi \Delta_\xi \overline{u'_s u''_s})_0 \approx -\frac{\sqrt{5}}{25} R_\lambda \frac{\epsilon_h^2}{k}, \quad (16)$$

where $R_\lambda = q\lambda/\nu$ is the Reynolds number based on statistical properties of the disturbances. The above result also follows from the asymptotic balance of the dissipation rate equation (11) at the wall where the viscous destruction $-2\nu^2 (\Delta_\xi \Delta_\xi \overline{u'_s u''_s})_0$ is in balance with the viscous diffusion $1/2\nu^2 \Delta_x (\Delta_\xi \overline{u'_s u''_s})_0$ (Fischer, Jovanović and Durst [16]). It is therefore not surprising that both of the suggested proposals (13) and (16) for the closure of (11) agree closely with the available data from direct numerical simulations of wall-bounded flows in the region of the viscous sublayer (Jovanović [17]).

3.2 Construction of the Closure Approximations Using Invariant Theory. We shall now apply invariant theory developed by Lumley and Newman [10] to formulate the closures for partition of the homogeneous part of the dissipation tensor and also for the velocity/pressure gradient correlations. These authors introduced the tensor

$$a_{ij} = \frac{\overline{u'_i u'_j}}{q^2} - \frac{1}{3} \delta_{ij}, \quad (17)$$

and its scalar invariants

$$\text{II}_a = a_{ij} a_{ji}, \quad \text{III}_a = a_{ij} a_{jk} a_{ki}, \quad (18)$$

to quantify the anisotropy and define the limiting states of the disturbances. A cross plot of II_a versus III_a for axisymmetric disturbances ($\text{II}_a = 3/2[4/3|\text{III}_a|]^{2/3}$) and two-component disturbances ($\text{II}_a = 2/9 + 2\text{III}_a$) defines the anisotropy invariant map which, according to Lumley [18], bounds all physically realizable disturbances. This plot is shown in Fig. 3 and the asymptotic forms for the unknown correlations involved in (5) that can be derived for the two-component disturbances.

For the axisymmetric disturbances, Jovanović and Otić [19] showed that all second-rank correlation tensors involved in (5) are linearly aligned in terms of each other. For such disturbances we may write

$$e_{ij} = \mathcal{A} a_{ij}, \quad \mathcal{A} = \left(\frac{\text{II}_e}{\text{II}_a} \right)^{1/2}, \quad (19)$$

where e_{ij} is the anisotropy tensor of the homogeneous part of ϵ_{ij} :

$$e_{ij} = \frac{\epsilon_{ij}^h}{\epsilon_h} - \frac{1}{3} \delta_{ij}, \quad (20)$$

and

$$\text{II}_e = e_{ij} e_{ji}, \quad \text{III}_e = e_{ij} e_{jk} e_{ki}. \quad (21)$$

For the two-component isotropic state and also for the one-component state, $\text{II}_a = \text{II}_e$, so that $\mathcal{A}=1$, and for these extreme cases, which both lie on the two-component state, (19) satisfies

$$e_{ij} = a_{ij}. \quad (22)$$

We may assume, therefore, that this analytical relationship holds along the entire two-component state and suggest an expression for partition of the dissipation tensor ϵ_{ij} for such a state as follows:

$$\epsilon_{ij} \approx \frac{1}{4} \nu \Delta_x \overline{u'_i u'_j} + \frac{\overline{u'_i u'_j}}{q^2} \epsilon_h. \quad (23)$$

It can be shown (Jovanović et al. [13]), that a Taylor series expansion near the wall for the instantaneous disturbances leads to relations for the asymptotic behavior of the components of ϵ_{ij} in close agreement with those obtained from (23).

We may follow the same analytical path as outlined above for the treatment of the velocity/pressure gradient correlations, which can be split into the pressure-transport term and the pressure-strain term:

$$\Pi_{ij} = -\frac{1}{\rho} \left[\overline{u'_j \frac{\partial p'}{\partial x_i}} + u'_i \overline{\frac{\partial p'}{\partial x_j}} \right] = -\underbrace{\frac{1}{\rho} \frac{\partial}{\partial x_j} \overline{p' u'_i}}_{\text{pressure-transport}} - \underbrace{\frac{1}{\rho} \frac{\partial}{\partial x_i} \overline{p' u'_j}}_{\text{pressure-strain}} + \frac{p'}{\rho} \left(\frac{\partial u'_i}{\partial x_j} + \frac{\partial u'_j}{\partial x_i} \right). \quad (24)$$

In wall-bounded flows the pressure-transport contribution is usually small and we may seek closure for the pressure-strain part by considering the equation for the anisotropy of the stresses in a statistically homogeneous field:

$$\frac{\partial a_{ij}}{\partial t} = \frac{1}{q^2} \left[P_{ij} - \left(a_{ij} + \frac{1}{3} \delta_{ij} \right) P_{ss} \right] + \frac{\Pi_{ij}}{q^2} + \frac{2\epsilon_h}{q^2} (a_{ij} - e_{ij}), \quad (25)$$

where $P_{ij} = -\overline{u'_i u'_k \partial U_j / \partial x_k} - \overline{u'_j u'_k \partial U_i / \partial x_k}$. From this equation we deduce the asymptotic behavior of Π_{ij} as $\partial a_{ij} / \partial t \rightarrow 0$ and $e_{ij} \rightarrow a_{ij}$, which corresponds to the cases of the axisymmetric distortions when the “apparent” stresses approach the limiting states located at the two-component limit:

$$\left. \begin{aligned} (\Pi_{ij})_{2C\text{-iso}} &\rightarrow a_{ij} P_{ss} + \frac{1}{3} P_{ss} \delta_{ij} - P_{ij}, \\ (\Pi_{ij})_{1C} &\rightarrow a_{ij} P_{ss} + \frac{1}{3} P_{ss} \delta_{ij} - P_{ij}. \end{aligned} \right\} \quad (26)$$

This behavior suggests that the pressure-strain correlations for the two-component state may be approximated as follows:

$$\frac{p'}{\rho} \left(\frac{\partial u'_i}{\partial x_j} + \frac{\partial u'_j}{\partial x_i} \right) \approx \frac{\overline{u'_i u'_j}}{q^2} P_{ss} - P_{ij}. \quad (27)$$

The suggested closure approximations (23) and (27) satisfy the concept of realizability introduced by Schumann [20] and follow closely the data obtained from direct numerical simulations of turbulent wall-bounded flows in the region of the viscous sublayer.

4 Determination of the Transition Criterion

Using the suggested forms for the dissipation and the pressure-strain correlations and for the dissipation rate equation, the transport equations for the two-component disturbances can be written as

$$\begin{aligned} \frac{\partial \overline{u'_i u'_j}}{\partial t} + U_k \frac{\partial \overline{u'_i u'_j}}{\partial x_k} &\approx 2 \frac{\overline{u'_i u'_j}}{q^2} (P_k - \epsilon_h) + \frac{1}{2} \nu \frac{\partial^2 \overline{u'_i u'_j}}{\partial x_k \partial x_k}, \quad (28) \\ \frac{\partial \epsilon_h}{\partial t} + U_k \frac{\partial \epsilon_h}{\partial x_k} &\approx -2 \frac{\overline{\epsilon_h u'_i u'_k}}{k} \frac{\partial U_i}{\partial x_k} - \frac{\sqrt{5}}{25} R_\lambda \frac{\epsilon_h^2}{k} + \frac{1}{2} \nu \frac{\partial^2 \epsilon_h}{\partial x_k \partial x_k}, \quad (29) \end{aligned}$$

where $P_k = P_{ss}/2$.

If we consider transition of the flow in the flat plate boundary layer with intention to provide quantitative description of the interaction mechanism between the disturbances of the free stream and the boundary layer, in the way proposed by Taylor [21], then (28) immediately suggests stability towards small disturbances if the production is balanced by the dissipation:

$$P_k \approx \epsilon_h. \quad (30)$$

The equilibrium constraint leads to the equations for the stresses:

$$\frac{\partial \overline{u'_i u'_j}}{\partial t} + U_k \frac{\partial \overline{u'_i u'_j}}{\partial x_k} \approx \frac{1}{2} \nu \frac{\partial^2 \overline{u'_i u'_j}}{\partial x_k \partial x_k}, \quad (31)$$

which are of boundary layer character and do not allow amplification of disturbances in the boundary layer (Schlichting [[22], pp. 278–284]). In connection with this issue, it is interesting that the results of Becker [23] on laser-Doppler measurements in the transitional boundary layer developing in the presence of natural disturbances corroborate the findings mentioned above. Inserting (30) into the dissipation rate equation (29):

$$\frac{\partial \epsilon_h}{\partial t} + U_k \frac{\partial \epsilon_h}{\partial x_k} \approx \underbrace{\left(2 - \frac{\sqrt{5}}{25} R_\lambda \right)}_{\substack{\geq 0 \\ \text{to insure that } \epsilon_h \geq 0}} \frac{\epsilon_h^2}{k} + \frac{1}{2} \nu \frac{\partial^2 \epsilon_h}{\partial x_k \partial x_k}, \quad (32)$$

and specifying that the dissipation rate is always positive, $\epsilon_h \geq 0$, and at the critical point follows the energy k (as emerges from the work of Kolmogorov [24]), we deduce the transition criterion in terms of the Reynolds number based on the intensity and the length scale of the disturbances:

$$(R_\lambda)_{\text{crit}} \approx 10\sqrt{5}. \quad (33)$$

Thus, the derived transition criterion suggests the permissible magnitudes for the intensity and the length scale of disturbances $R_\lambda \leq (R_\lambda)_{\text{crit}}$ that guarantee (30) ($P_k \approx \epsilon_h$ with $\epsilon_h \geq 0$) and therefore maintenance of the laminar flow regime in the flat plate boundary layer.

The critical Reynolds number is determined from the requirement that the boundary layer should be neutrally stable to small, statistically stationary two-component disturbances, which is equivalent to the local (and therefore also global) equilibrium discussed above. As a consequence of this requirement, the stresses $\overline{u'_i u'_j}$ (and the energy k) cannot grow in the boundary layer above corresponding values of the free stream. However, this conclusion does not hold for the scale λ , which must follow increases in the shear layer thickness ($\lambda \sim \delta$) as it develops downstream. This behavior of q^2 and λ implies that the dissipation rate $\epsilon_h = 5\nu q^2/\lambda^2$ will decrease with increasing Reynolds number until it reaches some minimum value required by the dissipation rate equation to induce transition and breakdown to turbulence.

Examination of anisotropy invariant maps of turbulence utilizing the numerical databases of wall-bounded flows at low Reynolds numbers, shown in Fig. 4, suggests that invariants in the viscous sublayer which are lying along the two-component limit tend to move towards the right corner point of the map, which corresponds to the one-component state, as $\text{Re} \rightarrow (\text{Re})_{\text{crit}}$ [25–29]. For this special situation, which is the realistic state of the disturbances preceding breakdown to turbulence, theoretical considerations of Jovanović and Hillerbrand [30] and all numerical simu-

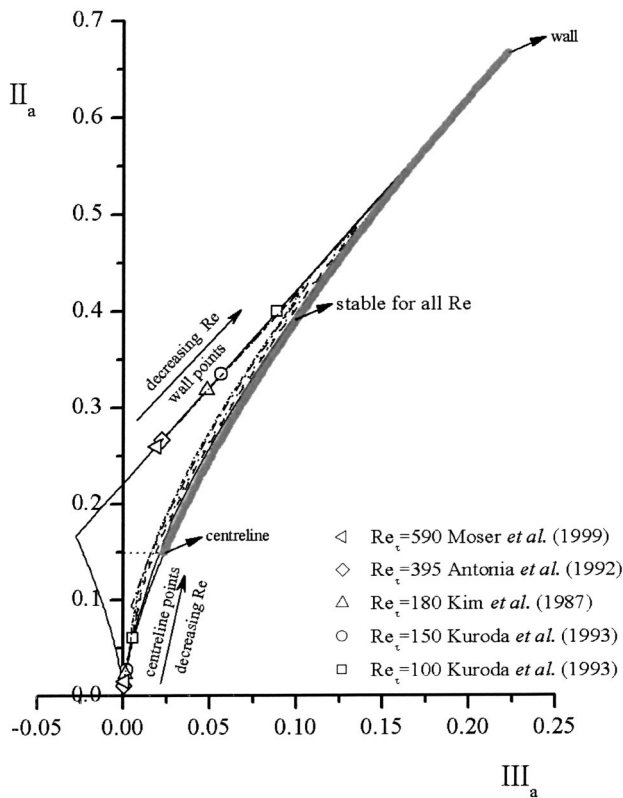


Fig. 4 Anisotropy invariant mapping of turbulence in a channel flow. Data, which correspond to low Reynolds numbers, show the trend as $Re \rightarrow (Re)_{crit}$ towards the theoretical solution valid for small, neutrally stable, statistically stationary, axisymmetric disturbances (Jovanović, Hillerbrand and Pashtropanska [29]). The shading indicates the area occupied by the stable disturbances: for such disturbances a laminar regime in the boundary layer will persist up to very high Reynolds numbers.

lations available displayed in Fig. 5 show that not only the energy but also the dissipation rate must vanish at the wall. Hence, the appearance of an indefinite term ϵ_h^2/k in the dissipation rate equation due to the imposed boundary conditions at the wall is not surprising and suggests that it is not suited for the numerical treatment when turbulence approaches a deterministic, one-component limit. However, the dissipation rate equation is of the boundary layer type and from it, it is possible to conclude that ϵ_h will remain positive as long as $(2 - \sqrt{5}/25R_\lambda)\epsilon_h^2/k$ is also positive. Thus, the conservative criterion (33) restricts the magnitude of R_λ and prevents negative values of ϵ_h from developing locally within the boundary layer.

In providing support for the above-discussed process which causes laminar-turbulent transition and breakdown to turbulence, the central role is played by numerical simulations which offer physical understanding relevant, however, for the dynamics of axisymmetric disturbances as already discussed in Sec. 3 ($III_a \geq 0$). By casting the flow development around the airfoil at a moderate angle of attack from the real space into the anisotropy invariant map, Jovićić [31] was able to animate visually all phases of the transition process and show that these remarkably coincide with the theoretical predictions of the transition process induced by small axisymmetric disturbances shown in Fig. 4 even over the details: disturbances appear in the anisotropy map first at the one-component limit and proceed to develop by decreasing the anisotropy until it reaches the level required by the dissipation rate equation to initialize transition and breakdown to turbulence.

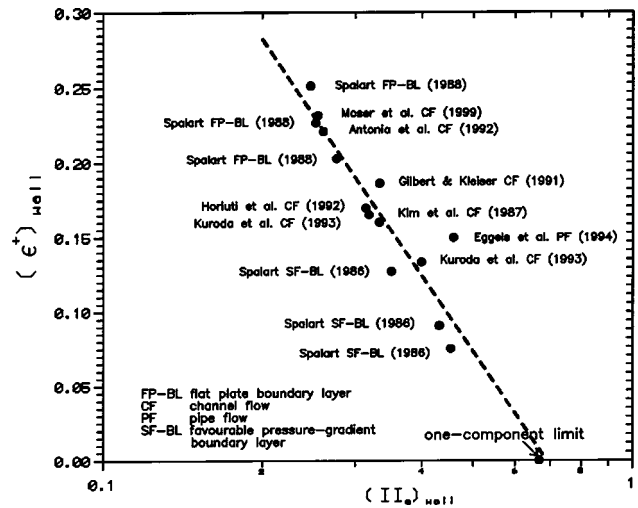


Fig. 5 Turbulent dissipation rate at the wall normalized with the wall shear velocity and the kinematic viscosity of the flow medium versus the anisotropy of turbulence II_a at the wall. A best-line fit through the numerical data extrapolates fairly well the expected trend $\epsilon \rightarrow 0$ as the one-component limit ($II_a = 2/3$) is approached.

Further convincing evidence supporting the above-discussed mechanism which causes laminar-turbulent transition and breakdown to turbulence is presented in the work of Seidl [32]. He simulated the flow past a sphere at low Reynolds numbers. Using very fine unstructured grids, he was able to resolve the development of a thin laminar boundary layer over the sphere and the near-wake region behind it which undergoes transition, leading to rapid development of turbulence. Contour plots of the turbulent kinetic energy, the dissipation rate and the anisotropy invariants reveal all the features of the transition process that can be predicted for small, statistically stationary, axisymmetric disturbances. Seidl [32] was able to show that within the shear layer which separates from the sphere, develops oscillations, then rolls up vortex pairs and finally breakdown to turbulence, the flow is initially very close to the one-component state.

5 Analysis of the Transition Process in Wall-Bounded Flows

The governing equations describing the behavior of the laminar to turbulence transition process, (28) and (29), are identical with those for fully developed turbulent flows in the region of the viscous sublayer close to the wall. We may attempt, therefore, to use the data for these flows to extract information about the functional dependence of R_λ in terms of the Reynolds number based on the global flow parameters in order to demonstrate the validity of the derived criterion (33) for the onset of turbulence in wall-bounded flows (see the caption of Fig. 2c).

Figure 6 shows the data for R_λ of fully developed turbulent channel flow, averaged over the cross-section, versus the Reynolds number, $Re_\tau = Hu_\tau/\nu$, based on the full height (H) of the channel and the friction velocity u_τ . These data were calculated from databases of direct numerical simulations (DNS) from Antonia et al. [26], Kim, Moin and Moser [27], Kuroda, Kasagi and Hirata [28] Gilbert and Kleiser [33] and Horiuti et al. [34]. The plotted data closely follow the expected behavior, proportional to $R_\lambda^{1/2}$, based on the evidence that, near the channel centerline, turbulence intensities scale with the wall variables [35]. The least-squares fit of the data from Fig. 6 yields

$$R_\lambda \approx 2.971 \left(\frac{Hu_\tau}{\nu} \right)^{1/2} - 6.618. \quad (34)$$

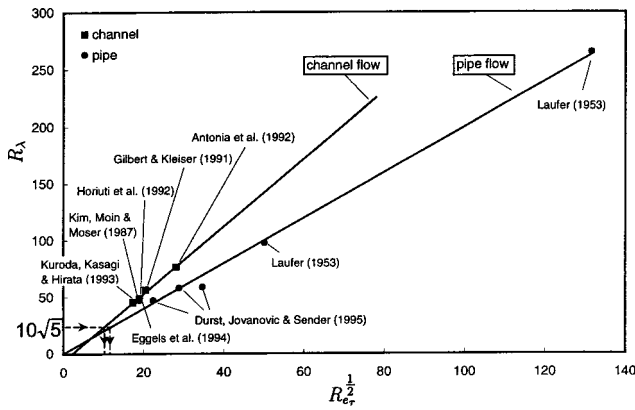


Fig. 6 Cross plot of R_λ versus $Re_\tau^{1/2}$ for fully developed turbulent pipe and channel flows at low Reynolds numbers

By extrapolating (34) towards the transition criterion (33) using the friction coefficient valid for laminar flow conditions, we obtain the critical Reynolds number based on the full channel height and the centerline velocity as

$$(Re)_{crit} \approx 2260. \quad (35)$$

This result is in close agreement with all accumulated observations available from either numerical simulations or flow visualization experiments (see, for example, Orszag and Kells [36]; Alavyoon, Henningson and Alfredsson [37]; Carlson, Widnall and Paeters [38]). We may consider, in an analogous way, transition in a pipe flow. For this flow there exists only one set of published data from full numerical simulations, reported by Eggels et al. [39]. An effort was made, therefore, to deduce the required information using the published experimental data on fully developed turbulent pipe flow from Laufer [40] and Durst, Jovanović and Sender [41]. These authors provided information for the mean flow and the intensities of all three fluctuating velocity components. To determine R_λ from these data, the mean energy dissipation rate was calculated from the mean energy production assuming flow equilibrium. The computed data for R_λ are displayed in Fig. 6 in the same form as for the channel flow with the exception that the Reynolds number $Re_\tau = Du_\tau/\nu$ is defined in terms of the pipe diameter (D). A least-squares fit through the pipe data gives

$$R_\lambda \approx 1.996 \left(\frac{Du_\tau}{\nu} \right)^{1/2} + 0.108. \quad (36)$$

If we extrapolate (36) in the same way as for the channel flow, the critical Reynolds number based on the pipe diameter and the bulk velocity emerges as

$$(Re)_{crit} \approx 1930. \quad (37)$$

The value obtained is in good agreement with the results deduced from flow visualization experiments by Reynolds [42], $1900 < (Re)_{crit} < 2000$, and many other experimental studies reviewed in the revised and updated book by Monin and Yaglom [[43], pp. 7–25].

It is also possible to examine applicability of (33) for the prediction the onset of transition in a laminar boundary layer using the databases of direct numerical simulations from Spalart [44,45]. Figure 7 shows the turbulent Reynolds number R_λ , averaged over the shear layer thickness, versus the Reynolds number, $Re_\tau = \delta u_\tau/\nu$, based on the boundary layer thickness and the friction velocity. The least-squares fit of these data yields

$$R_\lambda \approx 2.674 \left(\frac{\delta u_\tau}{\nu} \right)^{1/2} + 11.022. \quad (38)$$

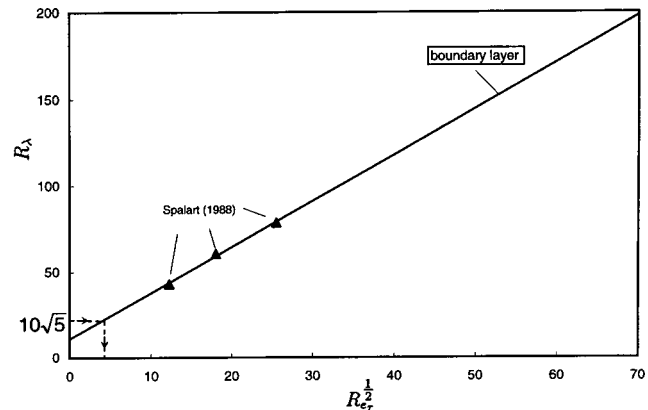


Fig. 7 Cross plot of R_λ versus $Re_\tau^{1/2}$ for turbulent boundary layer at low Reynolds numbers

By extrapolating (38) towards the established criterion (33) we obtain the critical Reynolds number:

$$(Re_\tau)_{crit} \approx 17. \quad (39)$$

This value is in good agreement with the experimental results of Tani and co-workers reported by Schlichting [22] for transition induced by a two-dimensional roughness element attached to the wall and placed perpendicular to the stream direction (see Fig. 1).

Acknowledgments

This research received financial support from the Deutsche Forschungsgemeinschaft (DFG) within the project Du 101/54-3. The authors gratefully acknowledge this support. We are grateful for enlightening discussions we have had with the Associate Editor Dr. Thomas Gatski from NASA-Langley Research Center.

References

- [1] Hinze, J. O., 1975, "Turbulence," 2nd ed., McGraw-Hill, New York.
- [2] Kline, S. J., Reynolds, W. C., Schraub, F. A., and Runstadler, P. W., 1967, "The Structure of Turbulent Boundary Layers," *J. Fluid Mech.*, **30**, pp. 741–773.
- [3] Kim, H. T., Kline, S. J., and Reynolds, W. C., 1971, "The Production of Turbulence Near Smooth Wall in a Turbulent Boundary Layer," *J. Fluid Mech.*, **50**, pp. 133–160.
- [4] Falco, R. E., 1978, "The Role of Outer Flow Coherent Motions in the Production of Turbulence Near a Wall," In *Coherent Structure of Turbulent Boundary Layer* (ed. by C. R. Smith and D. E. Abbott), AFOSR/Lehigh University, pp. 448–461.
- [5] Laufer, J., 1975, "New Trends in Experimental Turbulence Research," *Annu. Rev. Fluid Mech.*, **7**, pp. 307–326.
- [6] Laufer, J., 1982, "Flow Instability and Turbulence," In *Structure of Turbulence in Heat and Mass Transfer*, Ed. by Z. Zarić, Hemisphere.
- [7] Fischer, M., Jovanović, J., and Durst, F., 2000, "Near-Wall Behavior of Statistical Properties in Turbulent Flows," *Int. J. Heat Fluid Flow*, **21**, pp. 471–479.
- [8] Fischer, M., 1999, "Turbulente wandgebundene Strömungen bei kleinen Reynoldszahlen," Ph.D. Thesis, Universität Erlangen-Nürnberg, pp. 63–65.
- [9] Chou, P. Y., 1945, "On the Velocity Correlation and the Solution of the Equation of Turbulent Fluctuation," *Q. Appl. Math.*, **3**, pp. 38–54.
- [10] Lumley, J. L., and Newman, G., 1977, "The Return to Isotropy of Homogeneous Turbulence," *J. Fluid Mech.*, **82**, pp. 161–178.
- [11] Kolovandin, B. A., and Vatutin, I. A., 1972, "Statistical Transfer Theory in Nonhomogeneous Turbulence," *Int. J. Heat Mass Transfer*, **15**, pp. 2371–2383.
- [12] Jovanović, J., Ye, Q.-Y., and Durst, F., 1995, "Statistical Interpretation of the Turbulent Dissipation Rate in Wall-Bounded Flows," *J. Fluid Mech.*, **293**, pp. 321–347.
- [13] Jovanović, J., Ye, Q.-Y., and Durst, F., 1992, "Refinement of the Equation for the Determination of Turbulent Micro-Scale," Universität Erlangen-Nürnberg Rep., LSTM 349/T/92.
- [14] Jovanović, J., Otić, I., and Bradshaw, P., 2003, "On the Anisotropy of Axisymmetric Strained Turbulence in the Dissipation Range," *J. Fluids Eng.*, **125**, pp. 401–413.
- [15] Tennekes, H., and Lumley, J. L., 1972, "A First Course in Turbulence," MIT Press, Cambridge, MA.
- [16] Fischer, M., Jovanović, J., and Durst, F., 2001, "Reynolds Number Effects in

the Near-Wall Region of Turbulent Channel Flows,” *Phys. Fluids*, **13**, pp. 1755–1767.

- [17] Jovanović, J., 2004, “The Statistical Dynamics of Turbulence,” Springer-Verlag, Berlin.
- [18] Lumley, J. L., 1978, “Computational Modeling of Turbulent Flows,” *Adv. Appl. Mech.*, **18**, pp. 123–176.
- [19] Jovanović, J., and Otić, I., 2000, “On the Constitutive Relation for the Reynolds Stresses and the Prandtl-Kolmogorov Hypothesis of Effective Viscosity in Axisymmetric Strained Turbulence,” *J. Fluids Eng.*, **122**, pp. 48–50.
- [20] Schumann, U., 1977, “Realizability of Reynolds Stress Turbulence Models,” *Phys. Fluids*, **20**, pp. 721–725.
- [21] Taylor, G. I., 1936, “Statistical Theory of Turbulence. Part V. Effects of Turbulence on Boundary Layer. Theoretical Discussion of Relationship Between Scale of Turbulence and Critical Resistance of Spheres,” *Proc. R. Soc. London, Ser. A*, **156**, pp. 307–317.
- [22] Schlichting, H., 1968, *Boundary-Layer Theory*, 6th edn., McGraw-Hill, New York.
- [23] Becker, S., 1999, personal communication.
- [24] Kolmogorov, A. N., 1941, “On Degeneration of Isotropic Turbulence in an Incompressible Viscous Liquid,” *Dokl. Akad. Nauk SSSR*, **6**, pp. 538–540.
- [25] Moser, R. D., Kim, J., and Mansour, N. N., 1999, “Direct Numerical Simulation of Turbulent Channel Flow up to $Re_\tau=590$,” *Phys. Fluids*, **11**, pp. 943–945.
- [26] Antonia, R. A., Teitel, M., Kim, J., and Browne, L. W. B., 1992, “Low-Reynolds Number Effects in a Fully Developed Channel Flow,” *J. Fluid Mech.*, **236**, pp. 579–605.
- [27] Kim, J., Moin, P., and Moser, R. D., 1987, “Turbulence Statistics in a Fully Developed Channel Flow at Low Reynolds Numbers,” *J. Fluid Mech.*, **177**, pp. 133–166.
- [28] Kuroda, A., Kasagi, N., and Hirata, M., 1993, “Direct Numerical Simulation of the Turbulent Plane Couette-Poiseuille Flows: Effect of Mean Shear on the Near Wall Turbulence Structures,” *Proc. 9th Symp. on Turbulent Shear Flows*, Kyoto, pp. 8.4.1–8.4.6.
- [29] Jovanović, J., Hillerbrand, R., and Pashtropanska, M., 2001, “Mit statistischer DNS-Datenanalyse der Entstehung von Turbulenz auf der Spur,” *KONWIHR Quart.*, **31**, pp. 6–8.
- [30] Jovanović, J., and Hillerbrand, R., 2003, “On the Chief Peculiarity of the Velocity Fluctuations in Wall-Bounded Flows,” *J. Fluid Mech.*, submitted.
- [31] Jovičić, N., 2003, personal communication.
- [32] Seidl, V., 1997, “Entwicklung und Anwendung eines Parallelen Finite-Volume-Verfahrens zur Strömungssimulation auf unstrukturierten Gittern mit lokaler Verfeinerung,” Institut für Schiffbau, Universität Hamburg, Bericht Nr. 585.
- [33] Gilbert, N., and Kleiser, L., 1991, “Turbulence Model Testing With the Aid of Direct Numerical Simulation Results,” *Proc. Eighth Symp. on Turbulent Shear Flows, Munich*, pp. 26.1.1–26.1.6.
- [34] Horiuti, K., Miyake, Y., Miyauchi, T., Nagano, Y., and Kasagi, N., 1992, “Establishment of the DNS Database of Turbulent Transport Phenomena,” *Rep. Grants-in-aid for Scientific Research*, No. 02302043.
- [35] Durst, F., Fischer, M., Jovanović, J., and Kikura, H., 1998, “Methods to Set-up and Investigate Low Reynolds Number, Fully Developed Turbulent Plane Channel Flows,” *J. Fluids Eng.*, **120**, pp. 496–503.
- [36] Orszag, S. A., and Kells, C., 1980, “Transition to Turbulence in Plane Poiseuille and Plane Couette Flow,” *J. Fluid Mech.*, **96**, pp. 159–205.
- [37] Alavyoon, F., Henningson, D. S., and Alfredsson, P. H., 1986, “Turbulence Spots in Plane Poiseuille Flow-Flow Visualization,” *Phys. Fluids*, **29**, pp. 1328–1331.
- [38] Carlson, D. R., Widnall, S. E., and Paeters, M. F., 1982, “A Flow-Visualization Study of Transition in Plane Poiseuille Flow,” *J. Fluid Mech.*, **121**, pp. 487–505.
- [39] Eggels, J. G. M., Unger, F., Weiss, M. H., Westerweel, J., Adrian, R. J., Friedrich, R., and Nieuwstadt, F. T. M., 1994, “Fully Developed Turbulent Pipe Flow: a Comparison Between Direct Numerical Simulation and Experiment,” *J. Fluid Mech.*, **268**, pp. 175–209.
- [40] Laufer, J., 1953, “The Structure of Turbulence in Fully Developed Pipe Flow,” *NACA TN*, 2954.
- [41] Durst, F., Jovanović, J., and Sender, J., 1995, “LDA Measurements in the Near-Wall Region of a Turbulent Pipe Flow,” *J. Fluid Mech.*, **295**, pp. 305–355.
- [42] Reynolds, O., 1883, “An Experimental Investigation of the Circumstances Which Determine Whether the Motion of Water Shall be Direct or Sinuous, and the Law of Resistance in Parallel Channels,” *Philos. Trans. R. Soc. London*, **174**, pp. 935–982.
- [43] Monin, A. S., and Yaglom, A. M., 1997, *Statistical Fluid Mechanics—Mechanics of Turbulence*, Vol. I, Chapter 2, CTR Monograph, Stanford University, Stanford, CA, pp. 7–25.
- [44] Spalart, P. R., 1986, “Numerical Study of Sink-Flow Boundary Layers,” *J. Fluid Mech.*, **172**, pp. 307–328.
- [45] Spalart, P. R., 1988, “Direct Simulation of a Turbulent Boundary Layer up to $Re_\theta=1410$,” *J. Fluid Mech.*, **187**, pp. 61–98.

Modeling the Rapid Part of the Pressure-Diffusion Process in the Reynolds Stress Transport Equation

Kazuhiko Suga

Spray & Combustion Lab., Toyota Central R & D
Labs., Inc.,
Nagakute, Aichi, 480-1192, Japan
Phone: +81 561 63 4439
Fax: +81 561 63 6114
e-mail: k-suga@mosk.tytlabs.co.jp

Modeling the pressure-diffusion process is discussed to improve the prediction of turbulent recirculating flows by a second moment closure. Since the recent DNS research of a turbulent recirculating flow by Yao et al. [Theore. Comput. Fluid Dynamics 14 (2001) 337–358] suggested that the pressure-diffusion process of the turbulence energy was significant in the recirculating region, the present study focuses on the rapid part of the process consisting of the mean shear. This rapid pressure-diffusion model is developed for the Reynolds stress equation using the two-component-limit turbulence condition and added to a low Reynolds number two-component-limit full second moment closure for evaluation. Its effects are discussed through applications of turbulent recirculating flows such as a trailing-edge and a back-step flows. Encouraging results are obtained though some margins to be improved still remain. [DOI: 10.1115/1.1779660]

Introduction

Recently, the direct numerical simulation (DNS) by Yao et al. [1] pointed out that the effects of the “pressure-diffusion” process in the turbulence energy transport equation were significant in the recirculating flow region behind a rectangular trailing-edge. Surprisingly, its magnitude was even larger than that of the shear production term of the turbulence energy and much larger than that of the turbulent-diffusion. This fact requires further considerations on modeling the diffusion processes of the turbulence energy or the Reynolds stress transport equation.

The diffusion terms of the Reynolds stress equation have been modeled by the gradient diffusion concept. Daly and Harlow [2] proposed a rather simple model using the generalized gradient diffusion hypothesis (GGDH) for the triple moment: turbulent-diffusion process. Hanjalić and Launder [3] developed a model by simplification of the transport equation of the triple moment. Mellor and Herring [4] used effectively a simplified isotropic version of the Hanjalić-Launder model. Although these models do not include any model for the pressure-diffusion process explicitly, they say that its effects are considered to be modeled altogether with the turbulent-diffusion process. In fact, the models were usually calibrated empirically so that the pressure-diffusion may be effectively included. However, Lumley [5] proposed separate models for each process. His pressure-diffusion model was derived from considering realizability conditions to the part of the pressure-diffusion including the triple moment, namely the “slow part.” According to his discussion, the slow pressure-diffusion process can be modeled as a sub-process of the turbulent-diffusion. Note that the pressure-diffusion term includes another part consisting of mean strain, namely the “rapid part.”

Demuren and Sarkar [6], and Schwarz and Bradshaw [7] examined the performance of the above mentioned diffusion models using existing experimental data of simple flows with mean shear. In their discussions, they had to neglect the unmeasurable pressure-diffusion process, unfortunately. However, as Schwarz and Bradshaw commented, the pressure-diffusion is certainly small near the outer edge of a boundary layer so that the equation

balances plausibly without it. Note that this is only true in such a simple shear flow case though this might have been blinding us to considering the pressure-diffusion process. More recently, Straatman et al. [8] also evaluated the models for the diffusion process in zero-mean-shear turbulence. The absence of mean shear enabled them to discuss on the diffusive transport more directly. After examining Lumley’s [5] model, one of their conclusions was that the pressure-diffusion played a central role in establishing anisotropy in diffusive turbulence. This highlighted the importance of the pressure-diffusion, but the role of the rapid pressure-diffusion part was excluded due to its absence in the zero-mean-shear turbulence.

There were several other attempts to include the pressure-diffusion effects since the DNSs of turbulent wall shear flows [9,10] revealed that the pressure-diffusion balances the dissipation rate in the region very near a wall. Amongst those attempts, Kawamura and Kawashima [11] and Nagano and Shimada [12] employed a term consisting of the second derivative of the dissipation rate in their modeled turbulence energy equation to obtain a reasonable profile of the dissipation rate. The theoretical background of such a term came from the proposal of Yoshizawa [13] by the two-scale direct-interaction approximation (TSDIA). Craft and Launder [14] also devised a pressure-diffusion model for near-wall turbulence but using dependency on stress invariants. However, the effects of those model terms are limited into a near-wall region and the mean strain effects are not explicitly included.

Thus, the role of the rapid part of the pressure-diffusion term has not been well recognized. As mentioned above, the DNS of Yao et al. [1] showed that the turbulent-diffusion was rather small compared with the pressure-diffusion in the recirculating region. Since both the turbulent-diffusion and the slow pressure-diffusion part are composed of the triple moment, those facts revealed by the DNS imply that the rapid part is the main contributor to the profile of the pressure-diffusion there. Such a flow, thus, cannot be captured precisely without a proper model for the process. Note that turbulent-diffusion models or even aforementioned pressure-diffusion models do not include the mean strain effects at all. This is one of the reasons why many turbulence models perform poorly in turbulent wake flows behind a bluff body. In fact, it is well known that higher order models based on Reynolds averaged Navier-Stokes equation (RANS) such as nonlinear eddy viscosity

Contributed by the Fluids Engineering Division for publication in the JOURNAL OF FLUIDS ENGINEERING. Manuscript received by the Fluids Engineering Division December 3, 2003; revised manuscript received February 25, 2004. Associate Editor: T. B. Gatski.

models and second moment closures predict slower recovery of turbulence properties in the region downstream a recirculation [15].

Hence, modeling the rapid pressure-diffusion effects should be regarded as an important issue. Accordingly, Yoshizawa [16] recently discussed the effects of mean strain on the pressure-velocity correlation by the TSDIA and proposed a model form explicitly including mean shear for the turbulence energy equation. This paper, however, discusses another attempt for modeling the rapid part of the pressure-diffusion term by the same modeling strategy as that for constructing the two-component-limit (TCL) realizable second moment closure (SMC) of the UMIST group [14,17,18]. In order to confirm the effects of the presently developed model term, it is included in a low Reynolds number (LRN) full SMC which is called the TCL SMC [18]. The considered flow field applications are the turbulent wake flow behind a trailing-edge of Yao et al. [1] and the back-step flow of Kasagi and Matsunaga [19].

Modeling the Pressure-Diffusion

Derivation of the Basic Form. The transport equation of the Reynolds stress $u_i u_j$ may be written as

$$\frac{D \overline{u_i u_j}}{Dt} = d_{ij}^v + d_{ij}^t + P_{ij} + \Pi_{ij} - \varepsilon_{ij} \quad (1)$$

where d_{ij}^v , d_{ij}^t , P_{ij} , Π_{ij} and ε_{ij} are, respectively, the viscous-diffusion, turbulent diffusion, production, pressure correlation and dissipation terms. The pressure correlation term is usually split into the pressure-strain ϕ_{ij} and the pressure-diffusion d_{ij}^p term:

$$\begin{aligned} \Pi_{ij} = & -u_i \overline{\frac{\partial p}{\partial x_j}} - u_j \overline{\frac{\partial p}{\partial x_i}} = \underbrace{\frac{p}{\rho} \left(\frac{\partial u_i}{\partial x_j} + \frac{\partial u_j}{\partial x_i} \right)}_{\phi_{ij}} \\ & + \underbrace{\frac{\partial}{\partial x_m} \left(-\frac{\overline{u_j p}}{\rho} \delta_{im} - \frac{\overline{u_i p}}{\rho} \delta_{jm} \right)}_{d_{ij}^p} \end{aligned} \quad (2)$$

where u_i , p , ρ and $\overline{(\quad)}$ are the instantaneous velocity, pressure, fluid density and a Reynolds averaged value. The Poisson equation of the instantaneous pressure and its integration far away from a wall may be written as

$$\begin{aligned} \frac{1}{\rho} \frac{\partial^2 p}{\partial x_k^2} = & -\frac{\partial^2}{\partial x_k \partial x_l} (\overline{u_l u_k} - \overline{u_l u_k}) - 2 \frac{\partial \overline{u_k}}{\partial x_l} \frac{\partial u_l}{\partial x_k} \\ \frac{1}{\rho} p = & \frac{1}{4\pi} \int_{vol} \left(\frac{\partial^2 u'_k u'_l}{\partial x'_l \partial x'_k} - \frac{\partial^2 \overline{u'_k u'_l}}{\partial x'_l \partial x'_k} \right) \frac{dVol}{|r|} \\ & - \frac{1}{2\pi} \int_{vol} \frac{\partial \overline{u'_k}}{\partial x'_l} \frac{\partial u'_l}{\partial x'_k} \frac{dVol}{|r|} \end{aligned} \quad (3)$$

where r is a position vector and a prime denotes that the quantity is a function of the integration variable. Then, the pressure-

velocity correlation term may be written as

$$\begin{aligned} \frac{\overline{u_j p}}{\rho} = & -\frac{1}{4\pi} \int_{vol} \underbrace{\left(\frac{\partial^2 \overline{u'_k u'_l u'_j}}{\partial r_l \partial r_k} \right)}_{\phi_{j1}^p} \frac{dVol}{|r|} \\ & - \frac{1}{2\pi} \frac{\partial \overline{u'_k}}{\partial x'_l} \int_{vol} \underbrace{\frac{\partial u'_l u'_j}{\partial r_k}}_{\phi_{j2}^p} \frac{dVol}{|r|}. \end{aligned} \quad (4)$$

In the context of the single point closure methodology, a linear expression of the triple moments in ϕ_{j1}^p results in

$$\phi_{j1}^p = \frac{1}{5} \overline{u_k u_k u_j} \quad (5)$$

for satisfying realizability conditions as Lumley [5] discussed. This implies that the slow part is similar to turbulent diffusion: $d_{ij}^t = -\partial \overline{u_i u_j u_k} / \partial x_k$, and with a smaller magnitude. Thus, at the current stage, the slow part can be considered to be absorbed in the turbulent-diffusion model and it is not explicitly considered. (Note that we have to return to this point in the future study when the triple moment modeling is considered further.)

The rapid part ϕ_{j2}^p is presently modeled as a linear function of both the Reynolds stress and a length-scale vector: ℓ_k , as

$$\phi_{j2}^p = \frac{\partial \overline{u_k}}{\partial x_l} \gamma_k^{lj} (\overline{u_l u_j}, \ell_k) \quad (6)$$

There must be several options for determining the length-scale vector. For the third rank tensor γ_k^{lj} , the general form satisfying symmetry in the indexes l, j may be written as

$$\begin{aligned} \frac{\gamma_k^{lj}}{k} = & \beta_1 \ell_k \delta_{jl} + \beta_2 (\ell_l \delta_{jk} + \ell_j \delta_{kl}) + \beta_3 \ell_k a_{jl} + \beta_4 (\ell_l a_{jk} + \ell_j a_{kl}) \\ & + \beta_5 \ell_m a_{km} \delta_{jl} + \beta_6 \ell_m (a_{lm} \delta_{jk} + a_{jm} \delta_{kl}) \end{aligned} \quad (7)$$

where $a_{ij} = \overline{u_i u_j} / k - 2/3 \delta_{ij}$, $k = \overline{u_k u_k} / 2$ and β 's are model coefficients. In order to determine the coefficients, the continuity and the TCL turbulence conditions can be applied. The continuity condition: $\gamma_k^{kj} = 0$, leads to

$$\gamma_k^{kj} / k = (\beta_1 + 4\beta_2) \ell_j + (\beta_3 + \beta_4 + \beta_5 + 4\beta_6) \ell_k a_{kj} = 0. \quad (8)$$

The TCL condition: ($d_{22}^p = 0$, if $u_2 = 0$), on a plane boundary leads to

$$\begin{aligned} & \frac{\partial}{\partial x_2} \left(\frac{\partial \overline{u_k}}{\partial x_l} \gamma_k^{l2} \right) \\ = & \frac{\partial}{\partial x_2} \left[\frac{\partial \overline{u_1}}{\partial x_1} \left\{ \ell_2 \left(\beta_2 + \left(\delta + \frac{1}{3} \right) \beta_4 - \frac{2}{3} \beta_6 \right) \right\} k + \frac{\partial \overline{u_1}}{\partial x_2} \left\{ \ell_1 \left(\beta_1 \right. \right. \right. \\ & \left. \left. \left. - \frac{2}{3} \beta_3 + \left(\delta + \frac{1}{3} \right) \beta_5 \right) + \ell_3 a_{13} \beta_5 \right\} k + \frac{\partial \overline{u_1}}{\partial x_3} \left\{ \ell_2 a_{13} \beta_4 \right\} k \right. \\ & \left. + \frac{\partial \overline{u_2}}{\partial x_2} \left\{ \ell_2 \left(\beta_1 + 2\beta_2 - \frac{2}{3} \beta_3 - \frac{4}{3} \beta_4 - \frac{2}{3} \beta_5 - \frac{4}{3} \beta_6 \right) \right\} k \right. \\ & \left. + \frac{\partial \overline{u_3}}{\partial x_1} \left\{ \ell_2 a_{13} \beta_4 \right\} k + \frac{\partial \overline{u_3}}{\partial x_2} \left\{ \ell_3 \left(\beta_1 - \frac{2}{3} \beta_3 + \left(\delta + \frac{1}{3} \right) \beta_5 \right) \right. \right. \\ & \left. \left. + \ell_1 a_{13} \beta_5 \right\} k + \frac{\partial \overline{u_3}}{\partial x_3} \left\{ \ell_2 \left(\beta_2 + \left(-\delta + \frac{1}{3} \right) \beta_4 - \frac{2}{3} \beta_6 \right) \right\} k \right] \\ = & 0 \end{aligned} \quad (9)$$

since $\overline{\partial u_2 / \partial x_1} = \overline{\partial u_2 / \partial x_3} = 0$, $a_{12} = a_{23} = 0$, $a_{22} = -2/3$, $a_{11} = \delta + 1/3$, $a_{33} = -\delta + 1/3$, with δ as an unknown value. Note that a plane boundary condition leads to $\overline{\partial u_2 / \partial x_1} = \overline{\partial u_2 / \partial x_3} = 0$ while the general TCL condition does not necessarily lead to it. However, in the present study, we follow this condition for simplicity because the boundaries of the present test cases are composed of plane walls.

Although we can derive several equations for satisfying Eqs. (8) and (9), many of them are not linearly independent. The resultant linearly independent equation set is

$$\begin{aligned}\beta_1 + 4\beta_2 &= 0 \\ \beta_3 + 4\beta_6 &= 0 \\ \beta_1 - \frac{2}{3}\beta_3 &= 0 \\ \beta_4 &= 0 \\ \beta_5 &= 0.\end{aligned}\quad (10)$$

Solving the system of equations in terms of β_1 yields

$$\beta_2 = -1/4\beta_1, \quad \beta_3 = 3/2\beta_1, \quad \beta_4 = \beta_5 = 0, \quad \beta_6 = -3/8\beta_1. \quad (11)$$

Thus, β_1 is an undetermined coefficient to be optimized. (On the most general TCL condition, however, further equations such as $\beta_2 - 2\beta_4/3 = 0$ and $\beta_6 = 0$ need to be satisfied. These require that the optimized coefficient β_1 also vanish at the TCL boundary. To meet this, the coefficient needs to be a function of the stress flatness parameter: A , that also vanishes at the TCL boundary, say $\beta_1 = cA^\alpha$.) Consequently, the basic form of the present rapid pressure-diffusion model may be written as

$$\begin{aligned}d_{ij2}^p &= \frac{\partial}{\partial x_m} (\varphi_{j2}^p \delta_{im} + \varphi_{i2}^p \delta_{jm}) \\ &= \frac{\partial}{\partial x_m} \left[\frac{\partial u_k}{\partial x_l} \beta_1 k \left\{ \left(\ell_k \delta_{jl} - \frac{1}{4} (\ell_l \delta_{jk} + \ell_j \delta_{kl}) \right. \right. \right. \\ &\quad \left. \left. \left. + \frac{3}{2} \ell_k a_{jl} - \frac{3}{8} \ell_m (a_{lm} \delta_{jk} + a_{jm} \delta_{kl}) \right) \delta_{im} \right. \right. \\ &\quad \left. \left. + \left(\ell_k \delta_{il} - \frac{1}{4} (\ell_l \delta_{ik} + \ell_i \delta_{kl}) + \frac{3}{2} \ell_k a_{il} \right. \right. \right. \\ &\quad \left. \left. \left. - \frac{3}{8} \ell_m (a_{lm} \delta_{ik} + a_{im} \delta_{kl}) \right) \delta_{jm} \right\} \right].\end{aligned}\quad (12)$$

A Variant Form for Implementation. As Lumley [20] noted, there are several ways of splitting the pressure correlation term into the pressure-strain and pressure-diffusion terms. The form discussed by Mansour et al. [9] and used in Craft and Launder [14] may be written as

$$\Pi_{ij} = \phi_{ij}^* + \frac{\overline{u_i u_j} d_{kk}^p}{k \frac{2}{d_{ij}^*}} \quad (13)$$

where ϕ_{ij}^* and d_{ij}^{p*} are the redefined pressure-strain and pressure-diffusion terms, respectively. The model of d_{kk}^p by Eq. (12) vanishes in a fully developed turbulent flow parallel to a wall if ℓ_k is zero with the index k denoting the direction parallel to the wall. Consequently, the pressure-diffusion term of Eq. (13) does not affect the prediction of such a flow field. Usually, any established RANS model has been calibrated in such flows, and thus the form of Eq. (13) is a desirable option for implementation into a well calibrated model. Therefore, in the present study, the term:

$$d_{ij2}^{p*} = \frac{\overline{u_i u_j} d_{kk}^p}{k \frac{2}{d_{ij}^*}} \quad (14)$$

is simply added to a TCL LRN full SMC. Another benefit of this form is that we can include it in the diagonal element of the matrix of the discretized transport equation to stabilize the solution. Indeed, by doing so, the solution process experienced in this study has been stable and thus total computational time has been almost the same as that of the original TCL model. With the TCL model, the length scale vector ℓ_i is presently modeled as

$$\ell_i = \frac{k^{1.5}}{\varepsilon} d_i^A, \quad (15)$$

where ε is the dissipation rate of k and d_i^A is Craft and Launder's [14] inhomogeneity indicator defined as

$$d_i^A = \frac{N_i^A}{0.5 + (N_k^A N_k^A)^{0.5}}, \quad N_i^A = \frac{\partial(A^{0.5} k^{1.5} / \varepsilon)}{\partial x_i} \quad (16)$$

using Lumley's [5] stress flatness parameter: $A = 1 - (9/8)(a_{ij} a_{ji} - a_{ij} a_{jk} a_{ki})$. Note that in a fully developed wall flow, ℓ_i is zero if the index i denotes the direction parallel to a wall since N_i^A vanishes. In order to optimize the coefficient β_1 in Eq. (12) a priori testing might be useful, however, without the field data of the DNS of a recirculating flow in the literature, it has been optimized through the applications. It is currently set as a constant value: $\beta_1 = -0.05$.

TCL Second Moment Modeling

Craft and Launder [14] proposed a TCL SMC after a series of development for a full realizable SMC by the UMIST group. The employed pressure-strain model is the cubic quasi isotropic (QI) model of Fu [17]. The Craft-Launder model is the first LRN version of its series totally free from topographical parameters. Its re-distributive term was modeled as

$$\phi_{ij}^* = \phi_{ij1} + \phi_{ij2} + \phi_{ij1}^{inh} + \phi_{ij2}^{inh} \quad (17)$$

where ϕ_{ij1}^{inh} and ϕ_{ij2}^{inh} are the correction terms for inhomogeneity effects. The cubic QI pressure-strain model employs the most general forms for ϕ_{ij1} and ϕ_{ij2} as:

$$\begin{aligned}\phi_{ij1} &= -c_1 \varepsilon \left\{ a_{ij} + c_1' \left(a_{ik} a_{jk} - \frac{1}{3} A_2 \delta_{ij} \right) \right\} - c_1'' \varepsilon a_{ij} \\ \phi_{ij2} &= -0.6 \left(P_{ij} - \frac{1}{3} P_{kk} \delta_{ij} \right) + 0.3 a_{ij} P_{kk} - 0.2 \left\{ \frac{\overline{u_j u_k} \overline{u_i u_l}}{k} S_{kl} \right. \\ &\quad \left. - \frac{\overline{u_k u_l}}{k} \left(\frac{\overline{\partial u_j}}{\partial x_l} + \frac{\overline{\partial u_i}}{\partial x_l} \right) \right\} - c_2 \{ A_2 (P_{ij} - D_{ij}) \\ &\quad + 3 a_{mi} a_{nj} (P_{mn} - D_{mn}) \} + c_2' \left\{ \left(\frac{7}{15} - \frac{A_2}{4} \right) \left(P_{ij} - \frac{1}{3} \delta_{ij} P_{kk} \right) \right. \\ &\quad \left. + 0.1 \left\{ a_{ij} - \frac{1}{2} \left(a_{ik} a_{kj} - \frac{1}{3} \delta_{ij} A_2 \right) \right\} P_{kk} - 0.05 a_{ij} a_{kl} P_{kl} \right. \\ &\quad \left. + 0.1 \left\{ \left(\frac{\overline{u_i u_m}}{k} P_{jm} + \frac{\overline{u_j u_m}}{k} P_{im} \right) - \frac{2}{3} \delta_{ij} \frac{\overline{u_i u_m}}{k} P_{lm} \right\} \right. \\ &\quad \left. + 0.1 \left(\frac{\overline{u_j u_k} \overline{u_i u_l}}{k^2} - \frac{1}{3} \delta_{ij} \frac{\overline{u_i u_m} \overline{u_k u_m}}{k^2} \right) (6 D_{kl} + 13 k S_{kl}) \right. \\ &\quad \left. + 0.2 (D_{kl} - P_{kl}) \frac{\overline{u_j u_k} \overline{u_i u_l}}{k^2} \right\}\end{aligned}\quad (18)$$

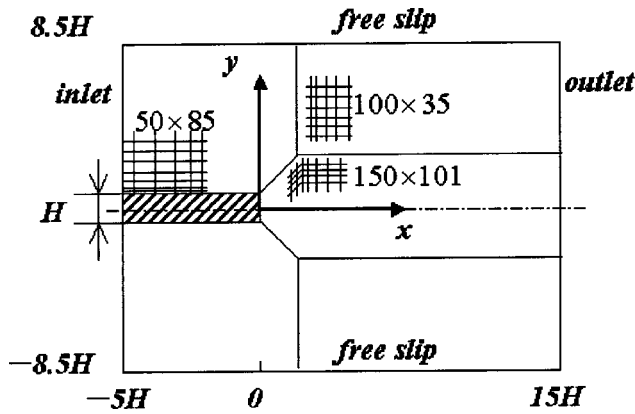


Fig. 1 Computational domain and grid for flow behind a rectangular trailing-edge.

where $A_2 = a_{ij}a_{ij}$, $P_{ij} = -(\overline{u_i u_k} \partial \overline{u_j} / \partial x_k + \overline{u_j u_k} \partial \overline{u_i} / \partial x_k)$, $D_{ij} = -(\overline{u_i u_k} \partial \overline{u_k} / \partial x_j + \overline{u_j u_k} \partial \overline{u_k} / \partial x_i)$, and $S_{ij} = \partial \overline{u_i} / \partial x_j + \partial \overline{u_j} / \partial x_i$. The inhomogeneity correction terms, ϕ_{ij1}^{inh} and ϕ_{ij2}^{inh} , effectively replace the traditional wall-reflection terms using inhomogeneity indicators which are basically the gradients of turbulent length scales. This model is realizable and validated in the TCL turbulence boundaries. Even though the model equations look complicated, it is thought to be rather economical because the realizability contributes to rapid convergence of the solution.

Later, Batten et al. [18] of the UMIST group modified the Craft-Launder model and extended its applicability to compressible flows. The present study thus follows this modified version. Note that although the original Craft-Launder model employs the Hanjalić-Launder [3] model for the turbulent-diffusion, Batten et al. returned to the usual GGDH of Daly and Harlow [2]:

$$d_{ij}^t = \frac{\partial}{\partial x_k} \left(\frac{-k}{c_s u_k u_l \varepsilon} \frac{\partial u_i u_j}{\partial x_l} \right) \quad (19)$$

with $c_s = 0.22$. See Appendix for further equations and coefficients of the TCL model.

Results and Discussions

All numerical computations have been performed by a general unstructured grid code of Suga et al. [21] using the PISO scheme (Issa [22]) with the Rhie-Chow [23] type interpolation and the third-order MUSCL type scheme (van Albada [24]) for the convection terms.

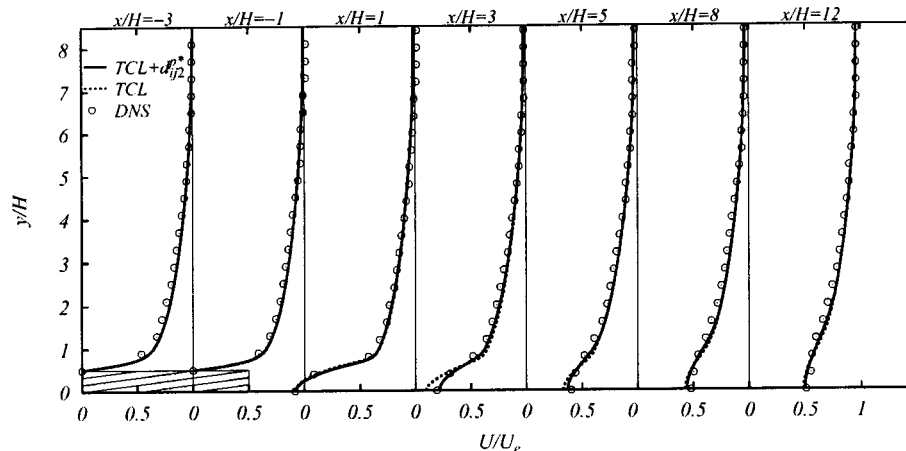


Fig. 2 Mean velocity distribution in the trailing-edge flow.

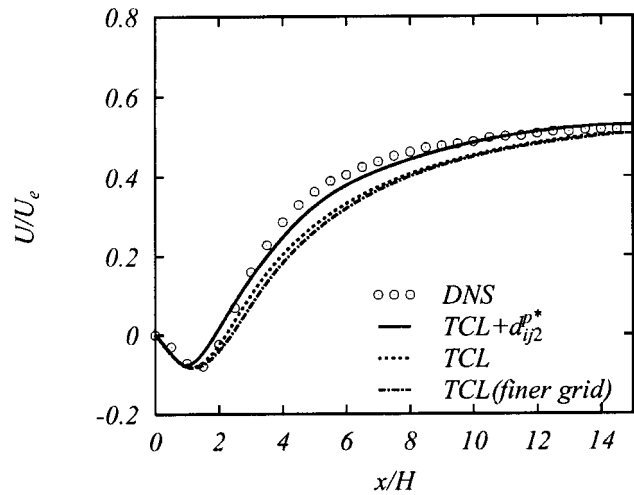


Fig. 3 Streamwise velocity along the centerline.

Rectangular Trailing-Edge Flow. Figure 1 illustrates the geometry of the wake flow behind a rectangular trailing-edge of Yao et al. [1]. A developed boundary layer flow comes in from the inlet boundary at the Reynolds number of 1000, based on the free-stream inlet velocity U_e and the trailing edge height H . The present 2-D computational grid consists of five blocks and 30,650 rectangular cells in total. The grid points are distributed nonuniformly to set the first grid points from the walls in the distance under unity of the wall unit. A grid-refinement test with a finer grid having twice node points in each direction has indicated that numerical errors are unimportant with the present grid (see the comparison in Fig. 3).

Figure 2 compares the mean velocity distribution with that of the DNS of Yao et al. [1]. Although both of the TCL models with and without d_{ij}^{p*} term perform equally well, discrepancies can be seen on the centerline $y/H = 0$. (The TCL model means the TCL model without d_{ij}^{p*} hereafter.) In order to confirm this, Fig. 3 compares the predicted streamwise mean velocity along the centerline behind the trailing-edge. It is obvious that including the d_{ij}^{p*} term reasonably improves recovery in the wake region though it leads to a slightly shorter recirculation.

Figure 4 compares the Reynolds stress distribution. Although the agreement is not perfect, the d_{ij}^{p*} term generally improves the predictive performance of the TCL model. There can be also found clear discrepancies between the models. In the recirculation

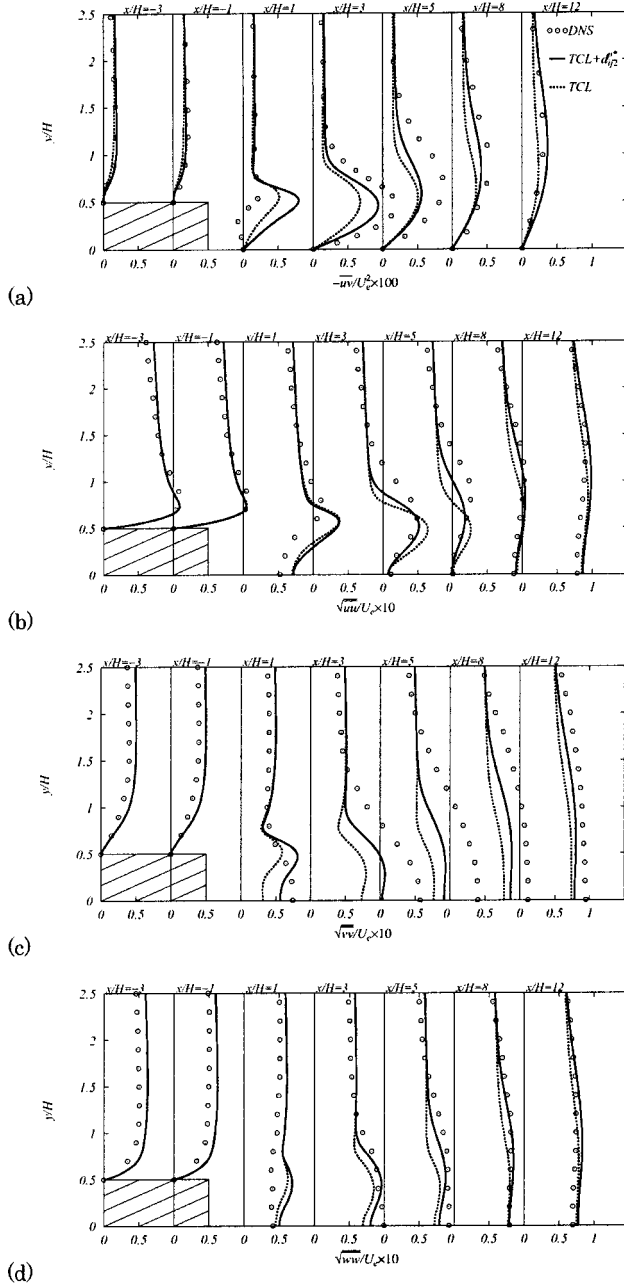


Fig. 4 Reynolds stress distribution in the trailing-edge flow.

region at $x/H=1$, the TCL model overpredicts the shear stress $-\overline{uv}$ (Fig. 4(a)) resulting in a little high level of streamwise normal stress \overline{uu} (Fig. 4(b)). Although including the d_{ij2}^{p*} term tends to enhance the overprediction of the shear stress there, it does not affect the \overline{uu} distribution and does improve the \overline{vv} distribution near the centerline (Fig. 4(c)). In the sections downstream of the recirculation ($x/H \geq 3$), all the profiles of the development of the Reynolds stresses are obviously improved by the d_{ij2}^{p*} term though \overline{vv} is still smaller near the centerline. This encourages the present modeling strategy though further considerations may be needed for the recirculating region.

The DNS data show that the pressure-diffusion of $k: d_k^p$, has a great positive value in the shear layer at the section of $x/H=1$ (the related discussion will be made in the later section with Fig. 7). Thus, the present pressure-diffusion term of each Reynolds stress component modeled as $\overline{u_i u_j} d_k^p / k$ has the same sign as the

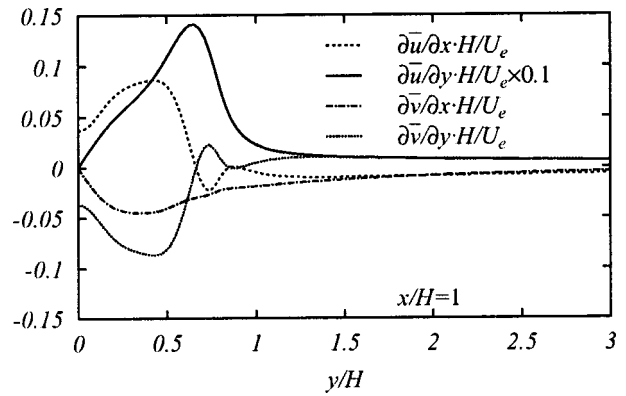


Fig. 5 Mean velocity gradients in the recirculating region of the trailing-edge flow.

stress component and acts as a source term. Due to the other transport processes, the value at the centerline also tends to increase except for \overline{uv} . As shown in Fig. 5, although $\partial \overline{u}/\partial y$ and $\partial \overline{v}/\partial x$ vanish at the centerline, $\partial \overline{u}/\partial x$ and $\partial \overline{v}/\partial y$ respectively have positive and negative non zero values. Consequently, the production terms there become $P_{11} = -2\overline{u^2} \partial \overline{u}/\partial x < 0$ and $P_{22} = -2\overline{v^2} \partial \overline{v}/\partial y > 0$. Then, the amplification effects around the centerline tend to be canceled for $\overline{u^2}$ but further amplified for $\overline{v^2}$. This is one of the reasons of the different tendencies of the normal stress components with the present pressure-diffusion term around the centerline. Due to the increase of the sum of the normal components, the recovery of the mean velocity profile along the centerline is improved.

Back-Step Flow. Another evaluation of the effects of the d_{ij2}^{p*} term has been performed in the back-step flow of Kasagi and Matsunaga [19]. Its Reynolds number is 5500 based on the step height H and the inlet centerline velocity U_c . The computational grid used has a structure similar to that for the trailing-edge wake flow and consists of 19,000 rectangular cells in the domain of $-5H \leq x \leq 30H$. The grid resolution has been confirmed to be fine enough since a finer grid with twice node points in each direction has produced less than 2% longer reattachment length than that by the present grid. The predicted reattachment length is $6.3H$ for both the cases with and without the d_{ij2}^{p*} term though the experimentally measured one is $6.5H$.

Figure 6(a) shows the distribution of the mean velocity. It is obvious that the d_{ij2}^{p*} term does not affect the mean velocity distribution and both the model predictions are well agree with the experiments. In the distribution of the Reynolds shear and normal stresses (Fig. 6(b)–(e)), although both the model predictions agree well with the experiments, there can be slight discrepancies between the predictions in the bottom half region behind the step. It seems to be difficult to judge which model performs better from the comparison with the experiments. However, slight improvement of the \overline{vv} distribution by the d_{ij2}^{p*} term can be recognized.

Budget Terms. For assessing the effects of the modeled rapid pressure-diffusion term in the recirculating flow regions more directly, the behavior of budget terms in the transport equation is discussed. Fig. 7(a) compares the turbulence energy budgets by the DNS [1] and the TCL model with d_{ij2}^{p*} at $x/H=1$ of the trailing-edge flow. Since the length of the recirculating bubble is roughly $2H$ (see Fig. 3), the section is in middle of the recirculating flow region. Clearly no predicted process accords well with the DNS data. (Note that due to the elliptic nature of the flow, the section integral of the pressure-diffusion term indicated by the DNS is not zero.) Apart from the pressure-diffusion d_k^p , the dis-

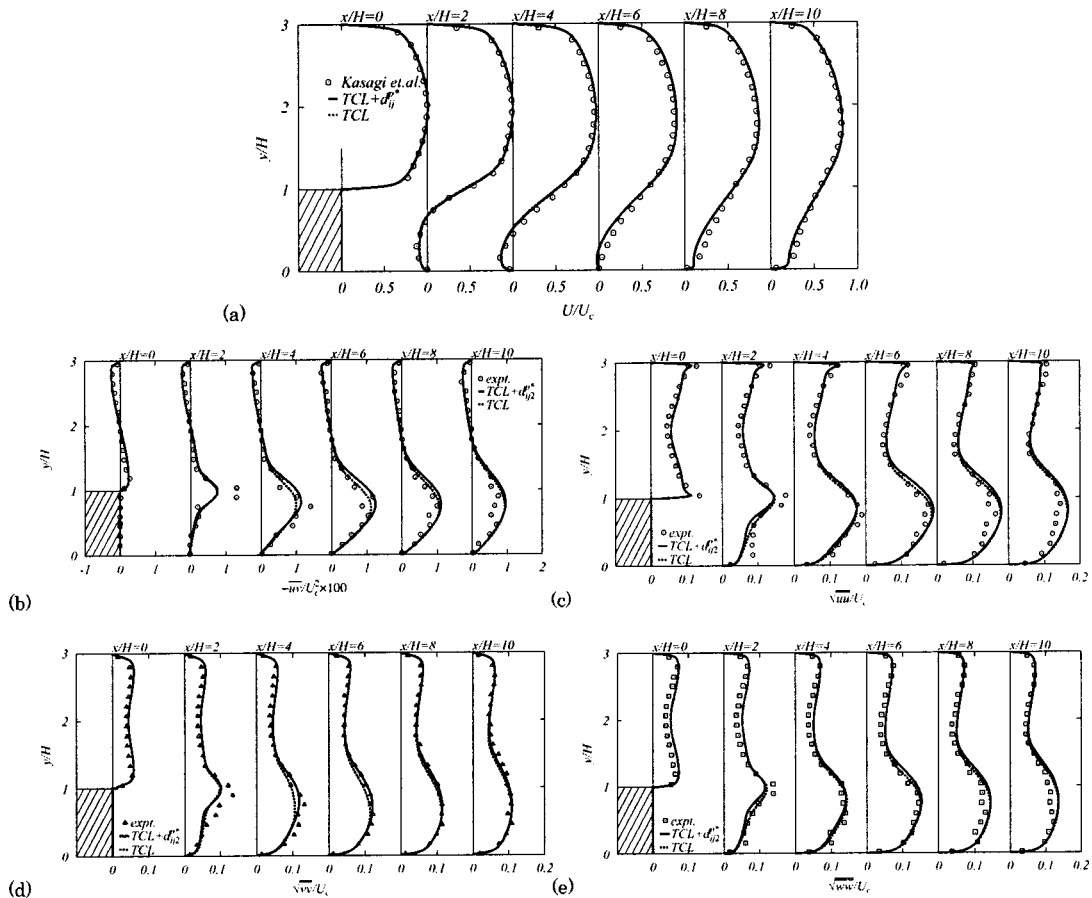
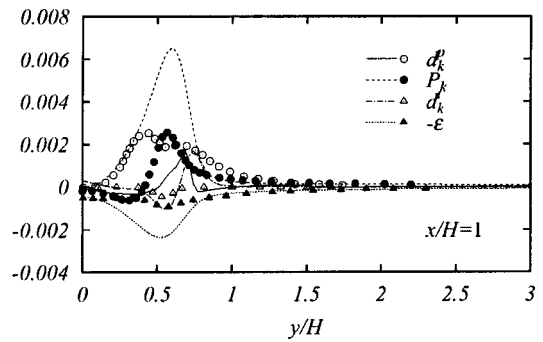


Fig. 6 Mean velocity and Reynolds stress distribution in the back-step flow.

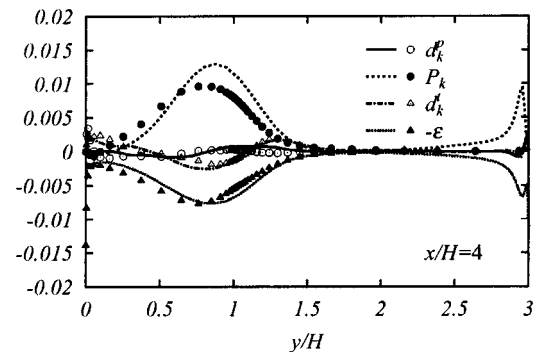
sipation ε and the turbulent diffusion d_k^t need to be improved. Due to the overprediction of $-\overline{uv}$ at this position as shown in Fig. 4(a), the production P_k is overpredicted though P_k itself does not need any modeling. However, the predicted d_k^p keeps a certain level and distributes quite differently from the turbulent-diffusion term. Thus it can be said that the d_{ij2}^{p*} term leads the solution to the right direction though its effect is still unsatisfactory.

Figure 7(b) shows the comparison of the budget terms of the k equation at $x/H=4$ in the recirculating region of the back-step flow. The section is also around the middle of the recirculation because the reattachment position is $6.5H$. The DNS data of Le et al. [25] are used for comparison. (They performed the DNS of a back-step flow whose Reynolds number was 5100. Although the flow boundary conditions are different from the experiments, Kasagi and Matsunaga [19] confirmed that the experimentally measured budget terms well accorded with the DNS of Le et al. near the bottom wall.) Unlike in the Fig. 7(a), each of the presently predicted profiles generally well agrees with that by the DNS near the bottom wall. It is also noticeable that the tendency of each process is very different from that in the trailing-edge flow though both the sections discussed are thought to be in comparable position of the recirculating flow. In the back-step flow, the pressure-diffusion process is not so dominant as in the trailing-edge flow. (Due to this nature, even without the pressure-diffusion term, computations can be performed reasonably well.) The present pressure-diffusion term captures the general tendency well.

The existence of the wall at $y/H=0$ causes the aforementioned differences between the two flow cases. Without a wall, the flow is not damped at the centerline of the trailing-edge flow, and thus the reverse flow is stronger than in the back-step flow leading to the



(a)



(b)

Fig. 7 Budget of the k equation in the recirculating regions; (a) trailing-edge flow, (b) back-step flow; symbols: DNS, lines: $TCL + d_{ij2}^{p*}$, normalized by $U_2^3/H, U_c^3/H$.

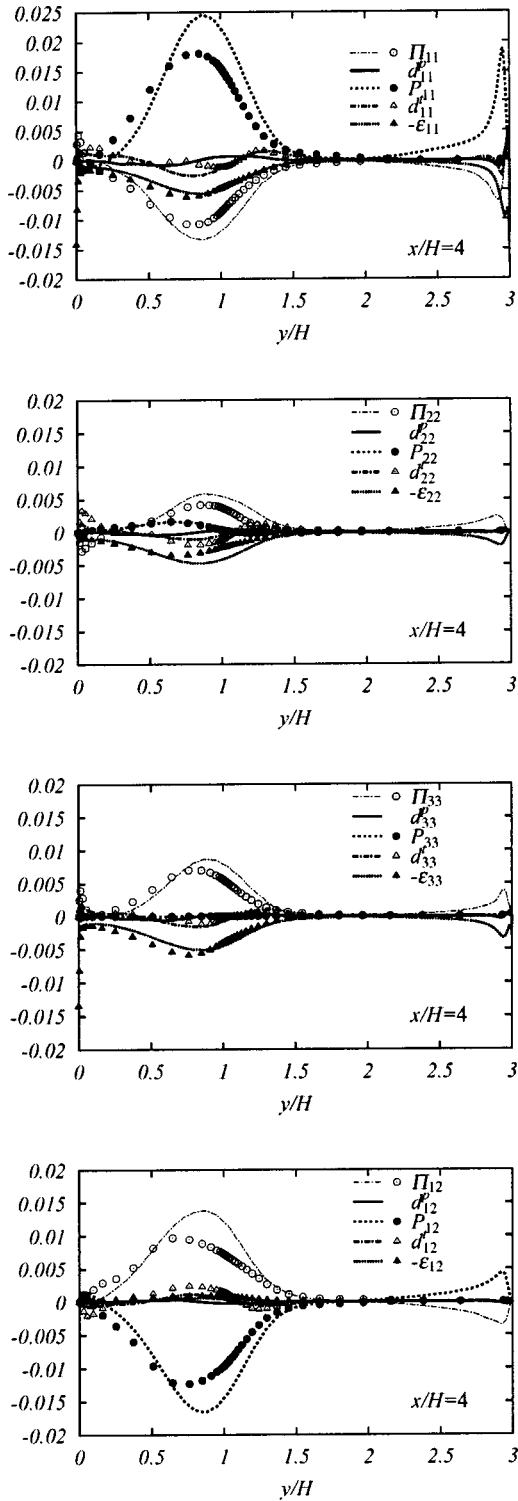


Fig. 8 Budget of the Reynolds stresses in the back-step flow; symbols: DNS, lines: TCL+ d_{ij}^{p*} , normalized by U_0^2/H .

shorter recirculation bubble whose normalized recirculation length by the half of the edge height (which is equivalent to the step height) is about 4. This results in a stronger shear layer and streamline curvature. Accordingly, the mean velocity gradients (particularly, $\partial \bar{u} / \partial y$ as shown in Fig. 5) have steeper profiles there and thus lead to a larger rapid pressure-diffusion process since the process consists of the second gradients of the mean velocity components.

Figure 8 shows the distribution of the budget terms of the Reynolds stress equations. (In the DNS data set, the pressure-diffusion is not split from the pressure correlation process Π_{ij} , and thus only present pressure-diffusion profiles are plotted.) Although it is not perfect, generally reasonable agreement can be seen in each process between the DNS and the present computation. This implies that each of the presently used model terms is reasonable at least for the back-step flow.

Concluding Remarks

In the present study, the pressure-diffusion process of the Reynolds stress equation is modeled. The effects of the proposed term in the two-component-limit second moment closure are discussed through the applications to turbulent recirculating flows. The following remarks are concluded:

1. Applying the two-component-limit turbulence condition, the rapid part of the pressure-diffusion process is systematically modeled. Mathematical discussion determines most of the coefficients leaving one undetermined coefficient. The undetermined coefficient is optimized empirically through the applications.
2. The presently proposed rapid pressure-diffusion model gives generally reasonable improvement in the prediction of the turbulent recirculating flows.
3. The magnitude of the pressure-diffusion is significant in the recirculating flow region behind the trailing-edge while it is small in the back-step flow. The present model reasonably captures this tendency.
4. Although obvious improvement in the recovery of the Reynolds stress distribution can be found downstream the recirculation zone, still further consideration to the model equations (not only the pressure-diffusion but also the other processes such as the dissipation and the turbulent-diffusion) may be needed, particularly, for the region just behind the bluff body.

Appendix: Model Equations of the TCL SMC

The model equations not described in the main part are summarized below.

In the Craft-Launder [14] model, to balance the near wall variation of the dissipation rate of k , the term

$$-\frac{1}{\rho} \frac{\partial}{\partial x_k} [-\rho c_{pd} (0.5 d_k + 1.1 d_k^A) (\nu \varepsilon k A A_2)^{1/2}] \quad (20)$$

is used for d_{kk}^p , where d_i is another inhomogeneity indicator:

$$d_i = \frac{N_i}{0.5 + (N_k N_k)^{1/2}}, \quad N_i = \frac{\partial (k^{1.5} / \varepsilon)}{\partial x_i} \quad (21)$$

Thus, in the present study, the sum of Eq. (20) and the rapid part model: Eq. (12) forms d_{kk}^p in Eq. (13). The presently used coefficient is

$$c_{pd} = 1.5(1 - A^2) [\{ 1 + 2 \exp(-R_t/40) \} A_2 + 0.4 R_t^{-1/4} \exp(-R_t/40)] \quad (22)$$

where the turbulent Reynolds number is $R_t = k^2 / (\nu \varepsilon)$. The inhomogeneity correction terms which were simplified by Batten et al. [18] are

$$\begin{aligned} \phi_{ij1}^{inh} = & f_{w1} \frac{\varepsilon}{k} \left(\overline{u_i u_k d_i^A d_k^A} \delta_{ij} - \frac{3}{2} \overline{u_i u_k d_j^A d_k^A} - \frac{3}{2} \overline{u_j u_k d_i^A d_k^A} \right) \\ & + f_{w2} \frac{\varepsilon}{k^2} \left(\overline{u_m u_n} \overline{u_m u_i d_n^A d_i^A} \delta_{ij} - \frac{3}{2} \overline{u_i u_m} \overline{u_m u_i d_j^A d_i^A} \right. \\ & \left. - \frac{3}{2} \overline{u_j u_m} \overline{u_m u_i d_i^A d_j^A} \right) \quad (23) \end{aligned}$$

Table 1 Model coefficients and functions in the TCL second moment closure.

$c_1 = 3.2 f_A A_2^{1/2} f_{Rt}$	$c_2 = \min \left[0.55 \left\{ 1 - \exp \left(\frac{-A^{1.5} R_t}{100} \right) \right\}, \frac{3.2A}{1+S} \right]$	$c'_1 = 1.1$	$c'_2 = \min(0.6A^{1/2}) + f_S$
$f_{w1} = 3(1 - A^{1/2}) f'_{Rt}$	$f_{w2} = 0.6A_2(1 - A^{1/2}) f''_{Rt} + 0.1$	$c''_1 = A^{1/2}$	$f_{Rt} = \min\{(R_t/200)^2, 1\}$
$f_A = (A/14)^{1/2}, A \leq 0.05$	$f'_{Rt} = \min[1, \max\{0, 1 - (R_t - 55)/70\}]$	$f_I = 3f_A$	$f''_{Rt} = \min \left\{ 1, \max \left(0, 1 - \frac{R_t - 50}{200} \right) \right\}$
$f_A = A/0.7^{1/2}, 0.05 < A < 0.7$	$f_R = (1 - A) \min\{(R_t/80)^2, 1\}$	$S = (k/\varepsilon) \sqrt{S_{ij} S_{ij}/2}$	$f_\varepsilon = 20A^{1.5}, A \leq 0.05$
$f_A = A^{1/2}, A \geq 0.7$	$f_S = \frac{3.5(S - \Omega)}{3 + S + \Omega} - 4\sqrt{6} \min[S_{ij} S_{jk} S_{kj} / (S_{ij} S_{ij})^{1.5}, 0]$	$\Omega = (k/\varepsilon) \sqrt{\Omega_{ij} \Omega_{ij}/2}$	$f_\varepsilon = A^{1/2}, A > 0.05$

$$\phi_{ij2}^{inh} = f_I k \frac{\partial \bar{u}_l}{\partial x_n} d_l d_n \left(d_i d_j - \frac{1}{3} d_k d_k \delta_{ij} \right). \quad (24)$$

The dissipation tensor is modeled as

$$\varepsilon_{ij} = (1 - f_\varepsilon) (\varepsilon'_{ij} + \varepsilon''_{ij}) / D + \frac{2}{3} \delta_{ij} f_\varepsilon \varepsilon \quad (25)$$

with

$$\varepsilon'_{ij} = 2\nu \frac{\partial k^{1/2}}{\partial x_m} \left(\frac{\partial k^{1/2}}{\partial x_i} \frac{\overline{u_j u_m}}{k} + \frac{\partial k^{1/2}}{\partial x_j} \frac{\overline{u_i u_m}}{k} \right) + 2\nu \frac{\partial k^{1/2}}{\partial x_k} \frac{\partial k^{1/2}}{\partial x_m} \frac{\overline{u_k u_m}}{k} \delta_{ij} + \frac{\overline{u_i u_j}}{k} \varepsilon \quad (26)$$

$$\varepsilon''_{ij} = f_R \varepsilon \left(2 \frac{\overline{u_i u_k}}{k} d_k^A d_i^A \delta_{ij} - \frac{\overline{u_i u_l}}{k} d_l^A d_j^A - \frac{\overline{u_j u_l}}{k} d_l^A d_i^A \right) \quad (27)$$

where $D = (\varepsilon'_{kk} + \varepsilon''_{kk}) / (2\varepsilon)$. The transport equation for the isotropic dissipation rate: $\tilde{\varepsilon} = \varepsilon - 2\nu(\partial k^{1/2}/\partial x_k)(\partial k^{1/2}/\partial x_k)$ is modeled as

$$\frac{D\tilde{\varepsilon}}{Dt} = \frac{\partial}{\partial x_k} \left\{ \left(\nu \delta_{kl} + 0.18 \frac{\overline{u_k u_l}}{\varepsilon} \right) \frac{\partial \tilde{\varepsilon}}{\partial x_l} \right\} + c_{\varepsilon 1} \frac{P_{kk}}{2} \frac{\tilde{\varepsilon}}{k} - c_{\varepsilon 2} \frac{\tilde{\varepsilon}^2}{k} - \frac{(\varepsilon - \tilde{\varepsilon})\tilde{\varepsilon}}{k} + P_{\varepsilon 3} + Y_E \quad (28)$$

where $c_{\varepsilon 1} = 1.44$, $c_{\varepsilon 2} = 1.92$ and $P_{\varepsilon 3} = 0.4 \nu \overline{u_j u_k} / \varepsilon \partial^2 \bar{u}_k / \partial x_i \partial x_j \partial^2 \bar{u}_k / \partial x_j \partial x_l$.

The length-scale correction term of Iacovides and Raisee [26]:

$$Y_E = 0.83 \frac{\tilde{\varepsilon}^2}{k} \max\{F(F+1)^2, 0\} \quad (29)$$

is employed with $F = 1/c_I (\partial(k^{1.5}/\varepsilon)/\partial x_k \partial(k^{1.5}/\varepsilon)/\partial x_k)^{1/2} - \{1 - \exp(-B_\varepsilon R_t) + B_\varepsilon R_t \exp(-B_\varepsilon R_t)\}$, $c_I = 2.55$ and $B_\varepsilon = 0.1069$.

All other model coefficients and functions are listed in Table 1. (In Table 1, the vorticity tensor is defined as $\Omega_{ij} = \partial \bar{u}_i / \partial x_j - \partial \bar{u}_j / \partial x_i$.)

References

[1] Yao, Y. F., Thomas, T. G., Sandham, N. D., and Williams, J. J. R., 2001, "Direct numerical simulation of turbulent flow over a rectangular trailing edge," *Theoret. Comput. Fluid Dynamics*, **14**, pp. 337–358.
 [2] Daly, B. J., and Harlow, F. H., 1970, "Transport equation in turbulence," *Phys. Fluids*, **13**, pp. 2634–2649.
 [3] Hanjalić, K., and Launder, B. E., 1972, "A Reynolds stress model of turbu-

lence and its application to thin shear flows," *J. Fluid Mech.*, **52**(4), pp. 609–638.

[4] Mellor, G. L., and Herring, H. J., 1973, "A survey of mean turbulent field closure," *AIAA J.*, **11**, pp. 590–599.
 [5] Lumley, J. L., 1978, "Computational modeling of turbulent flows," *Adv. Appl. Mech.*, **18**, pp. 123–176.
 [6] Demuren, A. O., and Sarkar, S., 1993, "Perspective: Systematic study of Reynolds stress closure models in the computations of plane channel flows," *ASME J. Fluids Eng.*, **115**, pp. 5–12.
 [7] Schwarz, W. R., and Bradshaw, P., 1994, "Term-by-term tests of stress-transport turbulence models in a three-dimensional boundary layer," *Phys. Fluids*, **6**(2), pp. 986–998.
 [8] Straatman, A. G., Stubble, G. D., and Raithby, G. D., 1998, "Examination of diffusion modeling using zero-mean-shear turbulence," *AIAA J.*, **36**(6), pp. 929–935.
 [9] Mansour, N. N., Kim, J., and Moin, P., 1988, "Reynolds-stress and dissipation-rate budgets in a turbulent channel flow," *J. Fluid Mech.*, **194**, pp. 15–44.
 [10] Spalart, P. R., 1988, "Direct simulation of a turbulent boundary layer up to $R_\theta = 1410$," *J. Fluid Mech.*, **187**, pp. 61–98.
 [11] Kawamura, H., and Kawashima, N., 1994, "A proposal of k-ε model with relevance to the near-wall turbulence," *Proc. Int. Symp. on Turbulence, Heat and Mass Transfer*, Lisbon, Vol. 2, P.I.1.1-P.I.1.4.
 [12] Nagano, Y., and Shimada, M., 1995, "Rigorous modeling of dissipation-rate equation using direct simulations," *JSME Int. J., Ser. B*, **38**, pp. 51–59.
 [13] Yoshizawa, A., 1987, "Statistical modeling of a transport equation for the kinetic energy dissipation rate," *Phys. Fluids*, **30**, pp. 628–631.
 [14] Craft, T. J., and Launder, B. E., 1996, "A Reynolds-stress closure designed for complex geometries," *Int. J. Heat Fluid Flow*, **17**, pp. 245–254.
 [15] Hanjalić, K., and Obi, S. (editors), 1997, "Case 6.3 Flow around surface-mounted cubical obstacle," *Proc. The sixth ERCOFTAC/AHR/COST Workshop on Refined Flow Modeling*, TU Delft, The Netherlands.
 [16] Yoshizawa, A., 2002, "Statistical analysis of mean-flow effects on the pressure-velocity correlation," *Phys. Fluids*, **14**, pp. 1736–1744.
 [17] Fu, S., 1988, "Computational modeling of turbulent swirling flows with second-moment closures," Ph.D. Thesis, UMIST, Manchester.
 [18] Batten, P., Craft, T. J., Leschziner, M. A., and Loyau, H., 1999, "Reynolds-stress-transport modeling for compressible aerodynamics applications," *AIAA J.*, **37**, pp. 785–797.
 [19] Kasagi, N., and Matsunaga, A., 1995, "Three-dimensional particle-tracking velocimetry measurement of turbulence statistics and energy budget in a backward-facing step flow," *Int. J. Heat Fluid Flow*, **16**, pp. 477–485.
 [20] Lumley, J. L., 1975, "Pressure strain correlation," *Phys. Fluids*, **19**, p. 750.
 [21] Suga, K., Nagaoka, M., Horinouchi, N., Abe, K., and Kondo, Y., 2001, "Application of a three equation cubic eddy viscosity model to 3-D turbulent flows by the unstructured grid method," *Int. J. Heat Fluid Flow*, **22**(3), pp. 259–271.
 [22] Issa, R., 1985, "Solution of implicitly discretized fluid flow equations by operator splitting," *J. Comput. Phys.*, **62**, pp. 40–65.
 [23] Rhie, C. M., and Chow, W. L., 1983, "Numerical study of the turbulent flow past an airfoil with trailing edge separation," *AIAA J.*, **21**, pp. 1525–1532.
 [24] van Albada, G. D., van Leer, B., and Roberts, W. W., 1991, "A comparative study of computational methods in cosmic gas dynamics," *Astron. Astrophys.*, **29**(7), pp. 1092–1110.
 [25] Le, H., Moin, P., and Kim, J., 1997, "Direct numerical simulation of turbulent flow over a backward-facing step," *J. Fluid Mech.*, **330**, pp. 349–374.
 [26] Iacovides, H., and Raisee, M., 1999, "Recent progress in the computation of flow and heat transfer in internal cooling passages of turbine blades," *Int. J. Heat Fluid Flow*, **20**, pp. 320–328.

Loss Reduction Using Riblets on a Supersonic Through-Flow Fan Blade Cascade

Todd Ninnemann

Wing F. Ng

Mechanical Engineering Department,
Virginia Tech, MC 0238,
Blacksburg, VA 24061

An experimental and computational study to determine the effects of riblets on the performance of the Supersonic Throughflow Fan (STF) cascade blades was performed. The cascade was tested in the Virginia Tech intermittent wind tunnel facility, where the Mach and Reynolds (based on chord) numbers were 2.36 and 4.8×10^6 , respectively. The riblet sheets were symmetric v-grooved type and were applied onto the blade surfaces. Three different riblet heights were tested: 0.023, 0.033, and 0.051 mm. Riblet testing was conducted at design incidence as well as at off-design conditions (incidence angles: +5, -10 deg). Loss coefficients were measured and compared with a control test case where an equivalent thickness of smooth material was applied to the blade. Results show that at the design incidence, the riblet sheet with a height of 0.033 mm provides the optimal benefit, with a reduction of 8.5% in loss coefficient compared to the control case. Smaller effects were measured at the off-design conditions. In addition to the experimental study, a numerical investigation of the riblet effect on the STF cascade was conducted at design incidence. A simple method was developed to model riblet effects due to decrease in turbulent viscous drag and the delay of turbulent transition on the blades. Conclusions from numerical study indicate the 2/3 of the total decrease in losses are the result of delaying the transition location. The final 1/3 decrease in loss coefficient comes from the decrease in turbulent viscous losses. [DOI: 10.1115/1.1667883]

Introduction

Renewed interest in supersonic transport creates a need for a markedly new propulsion system to deliver a competitive and economically viable commercial aircraft for the future. One approach to meet these demands is the new turbofan concept referred to as the supersonic throughflow fan (STF). The distinction of the STF from a conventional turbofan is that the axial flow entering the fan is supersonic. Potential advantages of the STF compared to a conventional turbofan engine include a 25% reduction in the propulsion system weight and a 12% reduction in fuel consumption, which combined would provide a 25% increase in range Francis [1].

Until recently, experimental studies to determine the feasibility of a fan accepting supersonic axial flow were limited, with Boxer, Savage, and Breugelmanns [2-4] providing only preliminary data. As a result, the NASA Lewis Research Center initiated the STF program to design, build, and test a fan rotor that operates with supersonic axial velocity from inlet to exit. In conjunction with the STF development work at NASA Lewis Research Center, Virginia Tech constructed a linear supersonic throughflow cascade to study in more detail the flow physics of the STF fan rotor. Previous research at Virginia Tech with the STF cascade extensively tested the original prototype blading design Bowersox, Chesnakas, and Andrew [5-7]. The emphasis of this research is to improve the performance of the STF cascade by modifying the blade surface with riblets.

For more than a decade, evidence showed modifications to the geometry of a wall in turbulent flow can passively reduce viscous losses. This achievement resulted from the modifications of the surface of the wall with micro-grooves, known as riblets, and aligning these grooves longitudinally with the mean flow direc-

tion. Although riblets increased the wetted surface area, the net result was a significant reduction in viscous drag when compared to a smooth surface.

Most of the riblet research concentrated on subsonic and transonic external flow with simple wall geometries such as a flat plate. One of the first researchers to investigate riblet performance was Walsh [8]. Through an extensive parametric study, Walsh found up to 8% drag reduction could be obtained with triangular riblets of height and span about twice the sublayer thickness. This result was later confirmed by a number of other researchers Bandyopadhyay, Sundaram [9,10].

Similar results to those of the flat plate studies were documented for internal flow studies. Most of this research was centered on pipe flow experiments. Rohr, Liu, [11,12]. In cascade flow, there was only one successful riblet study reported. Feng [13] studied a cascade of NACA-65-0100 compressor blades at low speed. A decrease in losses of more than 10% was reported with the performance insensitive to small changes in incidence flow angle.

For supersonic flows, the amount of riblet research was limited to a few studies in external flows. Robinson [14] analyzed the effects of riblets on turbulence structure at a Mach number of 2.97. Although no attempt was made to measure the change in drag with riblets, Robinson believed that riblets could be effective in supersonic speeds. Gaudet [15] studied the riblet effects of a flat plate. At a Mach number of 1.25, he measured a maximum reduction of 7% of drag reduction. A preliminary study by Coustols [16] on a flat plate at a Mach number of 1.9, measured a maximum drag reduction close to 10%. Another experimental study conducted on a cylindrical centerbody with Mach numbers varying between 1.6 and 2.5 measured a reduction in drag of up to 4.5% Coustols [17].

Even though riblets were successfully tested in a wide variety of different flow environments, they were never tested in a flow similar to that provided by an STF cascade. The flow physics is one of supersonic internal flow where shock-boundary layer interaction prevails. Also present in the STF cascade is an overall favorable pressure gradient which accelerates the flow as it pro-

Contributed by the Fluids Engineering Division for publication in the JOURNAL OF FLUIDS ENGINEERING. Manuscript received by the Fluids Engineering Division March 12, 2002; revised manuscript received October 30, 2003. Associate Editor: W. W. Copenhaver.

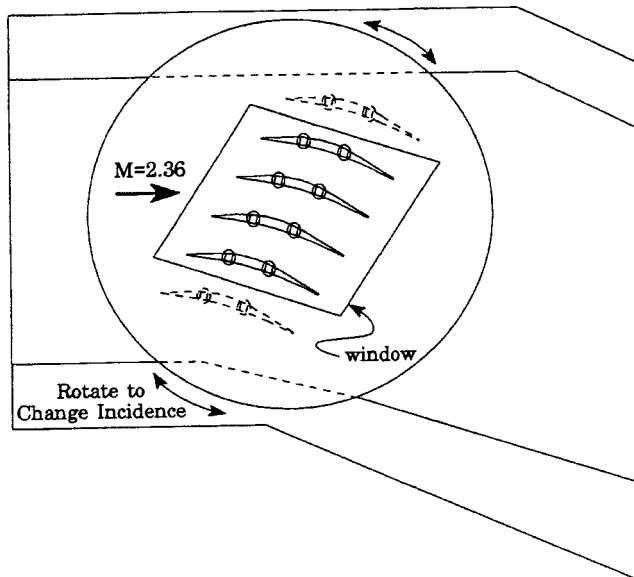


Fig. 1 STF Test Section

ceeds through the blade passage, thereby minimizing boundary layer growth. More detail of the unique flow field of the STF cascade is provided later in this paper.

At this time, the mechanism for the riblet's ability to reduce viscous losses is poorly understood. In this study, the size of the riblets precludes any detailed measurement in the riblet vicinity. The purpose of this research is to study the effects of riblets on the supersonic through-flow cascade blades by measuring differences in the wake profile downstream of the cascade. Experimental results of riblet effects on the STF blades for varied riblet heights and different inflow incidence angles are presented in this paper. This is followed by a numerical study as an attempt to explain the riblet effects on the loss reduction.

Experimental Setup

The riblet study was conducted at the Virginia Tech 2-D supersonic cascade wind tunnel. The tunnel is a blowdown facility that has an operating time of approximately 20 seconds at Mach 2.36. The test section, 15.2×22.9 cm, consists of six blades. As seen in Fig. 1, the circular test section doors are designed to rotate for facilitating the testing of the blades at different inflow incidence angles. Riblet tests in this study were done at design incidence, $+5$ deg and -10 deg incidence. The cascade wind tunnel was typically operated at a Reynolds number of approximately 4.4×10^5 per cm. The freestream turbulence intensity is approximately 1%, and the inflow Mach number is uniform to ± 0.05 . Characteristics of the tunnel flow are more fully documented in Chesnakas [18].

The cascade blade shapes were derived from the NASA Lewis baseline STF rotor at mid-span. The chord length, C , was 100.3 mm, spacing, S , was 30.2 mm, and span was 152 mm. The solidity, σ , of the blades was 3.32 and the maximum blade thickness was 5.8 mm.

Measurements were made with a Pitot-static probe at a traverse location approximately $1/3$ chord length downstream of the trailing edge of the blades. The probe traversed in the direction parallel to the trailing edge of the blades for at least one complete pitch. The measured Pitot and static pressures were used to calculate the total pressure. The total pressure was integrated across the pitch to calculate a mass-averaged loss coefficient. This loss coefficient was used to evaluate the overall performance of the riblets. A description of the probe and the calculation for the loss coefficient can be found in Chesnakas [18].

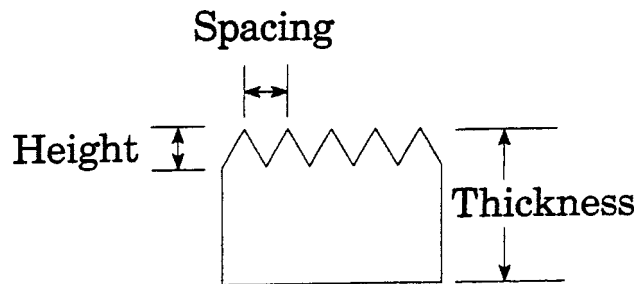


Fig. 2 Riblet Material

Three different size riblets were tested at design conditions. The riblet material was manufactured by 3M and consists of vinyl sheeting with machined v -grooves and a self adhesive backing. The height of the riblets were 0.023 mm, 0.033 mm, and 0.051 mm. With a blade chord of 100.3 mm, these heights of the riblets were equivalent to 0.023%, 0.033%, and 0.051% of the blade chord respectively. Figure 2 provides a description of the height, spacing, and thickness of the riblet material. The spacing and height for this riblet material are equal. Table 1 shows a list of the thicknesses of the three different sizes of riblet materials used in the experiment. Riblet material was applied to the surfaces of the blades by starting at the pressure side trailing edge and wrapping the material around the leading edge. The application was completed at the trailing edge of the suction side. This procedure provided a smooth continuous ribletted surface for the STF blades.

The leading edge radius of the bare blade is 0.18 mm. The application of the riblets produces an increase in the radius of the leading edge. Due to the supersonic nature of the STF cascade, any increase in the leading edge radius results in a significant increase in the losses from the leading edge shock. As a result, the riblet performance was not compared to that of a smooth bare blade; rather, an "equivalent" control test case needs to be established for a valid comparison with the ribletted blade. The ideal control test case would have been to apply a layer of smooth material with the exact same thickness as that of the riblet sheets tested in Table 1, and then measured the losses in the cascade with this layer of smooth material and compared the results with the losses obtained with the ribletted blade. However, after an extensive search, smooth materials of the exact same thicknesses as that shown in Table 1 were not available. Instead, a sheet of smooth material with a thickness of 0.081 mm was used. By applying two layers, a thickness of 0.162 mm ($0.081 \text{ mm} \times 2$) of smooth material was created. The performance of the ribletted blade was compared to that from a blade with an "equivalent" thickness of smooth material. The performance of the blade with this "equivalent" thickness of smooth material was obtained by linearly interpreting the downstream total pressure profiles from the testing using one layer of smooth material (0.081 mm thick) on the blade, as well as the testing based on two layers of smooth material (0.162 mm thick) on the blade. In the following, this interpreted result is referred to as an "equivalent" layer of smooth material.

Since the riblet material thickness is not uniform, an appropriate thickness must be determined for the riblet material on the leading edge of the STF blades. In an attempt to answer which appropriate thickness should be used for the riblet material, the

Table 1 Thickness of Riblet Test Material

Material	Thickness (mm)
0.023 mm height riblet	0.099
0.033 mm height riblet	0.135
0.051 mm height riblet	0.137

Design Incidence

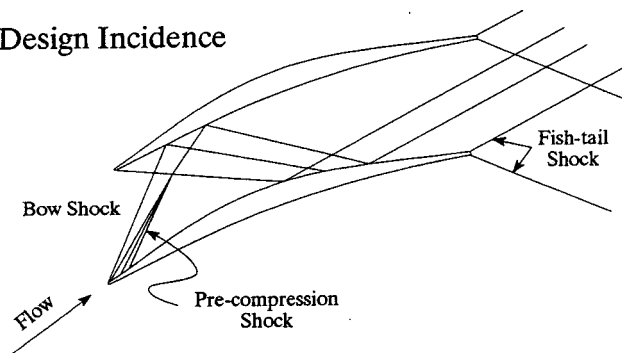


Fig. 3 Flow Field Description, Design Incidence

0.033 mm height riblet material is applied only to the leading edge of the STF blades, and compared to results obtained by applying one layer as well as two layers of smooth material to the leading edge of the STF cascade. (In this case, the smooth material covered 5% chord near the leading edge of the blade on both the pressure and suction sides.) Based on this comparison, it's determined that the appropriate leading edge thickness should be measured up to the riblet peak (as shown in Fig. 2). Thus all results of the riblet study presented in this paper are based on the thickness measured from the peak of the riblet. Details of this leading edge study are available in Ninnemann [19].

Experimental Results

The goal of this study is to measure small differences from riblet effects in the wake profile behind the STF cascade blades. This is accomplished by comparing the mass-averaged loss coefficient and total pressure profiles of the ribletted blades to an equivalent layer of smooth material. Presented first is a description of the major features of the flow field for design and off-design conditions in the STF cascade that provides a unique test for a riblet study. Results from the riblet height study, in which three different heights of riblets were tested, are then presented. Finally, the influences of incidence angle, off-design conditions, on the performance of the riblets are described.

Flow Field Description. The major characteristics of the flow field in the STF cascade for design, -10 deg incidence, and $+5$ deg incidence are briefly described. The flow physics differ for all three incidence angles and each provides a unique environment for the riblet study. The description of the flow field is based on a combination of techniques: surface oil flow visualization, surface pressure measurements, and shadowgraph photography. Additional details on the STF cascade flow field can be found in Andrew and Ng [20], Chesnakas and Ng [6].

A schematic of the major flow field features of the STF cascade at design incidence is displayed in Fig. 3. A favorable pressure gradient exists through the blade passage that limits boundary layer growth and helps prevent massive flow separation. Bow shocks originate at the leading edge of the blade and move downstream into the blade passage where they reflect on corresponding blade surfaces. At design incidence, the blades are designed to prevent boundary layer separation from the shock-boundary layer interaction. A pre-compression wave forms due to a coalescence of Mach lines above the concave curvature at the leading edge suction surface. This shock reflects at the adjoining pressure surface and back to the suction surface near $3/4$ chord. At the trailing edge, weak "fishtail" shocks adjust flow conditions.

At -10 deg, incidence, the bow shock from the leading edge of the suction side is strong enough to cause the flow to separate when it impinges on the boundary layer on the pressure surface of the adjacent blade. The shock-separated region is located at about 10% chord from the leading edge. The separated flow reattaches

Table 2

	Freestream	Wake	Mass averaged
M	$\pm 3.7\%$	$\pm 2.0\%$	—
P_t	$\pm 7.4\%$	$\pm 2.3\%$	$\pm 7.1\%$
ϖ	—	—	± 0.068

to the blade pressure surface at about 20% chord from the leading edge, forming a bubble. This separation bubble is followed by a localized adverse pressure gradient on the blade surface. As a result of the shock-boundary layer interaction, a separation shock and a reattachment shock are formed and impinge on the opposing suction side blade surface.

At $+5$ deg incidence, the bow shock from the leading edge of the pressure side is strong enough to cause the flow to separate when it impinges on the boundary layer on the suction surface of the adjacent blade. This separation starts at about 40% from the leading edge. The separated flow reattaches on the suction surface at about 60%, forming a separation bubble. The resultant separation and reattachment shocks propagate downstream striking the adjoining pressure surface.

Riblet Height Study. Three different riblet heights were tested at design incidence: 0.023 mm, 0.033 mm, and 0.051 mm. These sizes were chosen because they showed in previous research in supersonic flows to provide a reduction in viscous losses. For the three sizes tested in the STF cascade, the 0.033 mm height riblet material provided the optimum benefit, with a reduction in mass-averaged loss coefficient, $\Delta\varpi$, of 8.5%. The reduction in mass-averaged loss coefficient was defined as

$$\Delta\varpi = \frac{\varpi_{\text{riblet}} - \varpi_{\text{smooth}}}{\varpi_{\text{smooth}}}$$

The measurement uncertainty for the Pitot/Static probe is detailed in Chesnakas [18], and is summarized in Table 2. Uncertainties listed include both bias and precision errors. Bias errors in general, predominate.

Previous researchers' findings Walsh [8], Gaudet, [15] demonstrate that a wide range of riblet heights, defined in terms of the h^+ parameter, provide a decrease in viscous losses. The h^+ parameter is defined as

$$h^+ = \frac{u_\tau h}{\gamma_w}$$

where u_τ is the friction velocity, h is the riblet height, and γ_w is the kinematic viscosity at the wall. An optimum reduction is achieved at approximately an h^+ of 13. The trend for riblet heights shows the benefit diminishes as the height digresses from the optimum riblet height. The results from the STF riblet height study, along with their uncertainty band, are presented in Fig. 4. The maximum benefit of 8.5% occurs at the intermediate height tested of 0.033 mm. Smaller benefits of 1.8% and 5.1% result from the 0.023 mm and 0.051 mm height riblets, respectively. Coinciding with the STF cascade results in Fig. 4 is the trend for riblet heights which from previous studies Walsh [21] appears as a shaded region. The STF riblet height results demonstrate a similar trend when compared to previous research.

The comparison of the mass-averaged loss coefficient provides an assessment of the overall performance of the ribletted STF cascade, however it does not indicate where the benefit occurs. To better understand the riblet effect on the STF cascade blades, total pressure profiles of the riblet and equivalent layer of smooth material are compared. Calculation of the equivalent layer total pressure profile requires interpolation between the profiles of one (0.081 mm thick) and two layers (0.162 mm thick) of smooth material, to the riblet thickness of 0.135 mm (0.033 mm height riblet).

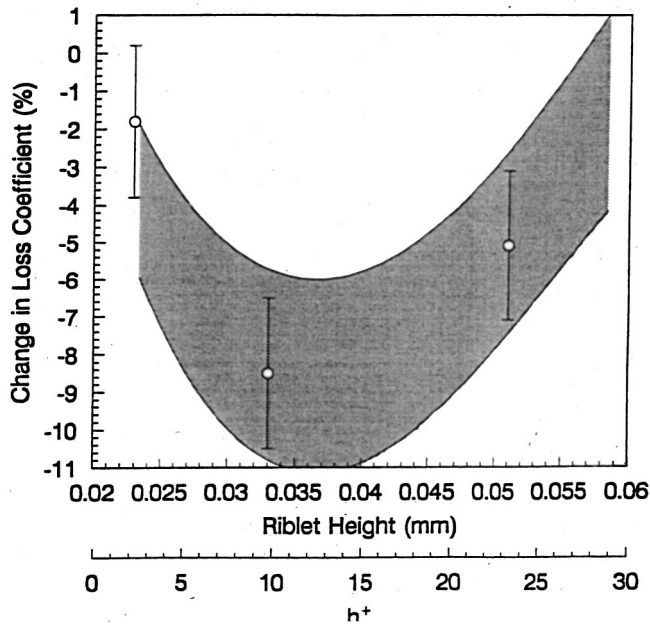


Fig. 4 Riblet Height Study (Shaded band is the trend based on previous studies)

Total pressure profiles for the optimum riblet height of 0.033 mm and the equivalent layer of smooth material profile are shown in Fig. 5. The total pressure profiles are nondimensionalized by the total pressure measured upstream of the STF cascade. The traverse location, y , is nondimensionalized by inter-blade spacing S . The profiles consist of a pitch-wise traverse approximately 1/3 chord length downstream of the blades. The profile starts at a location of $y/S = -0.5$ in the core flow and moves toward the pressure surface side of the wake. At $y/S = -0.28$ in the profile the location of the "fishtail" shocks are indicated by the small spike in the total pressure profile. (Note that due to probe resolution problem and the uncertainty in the data, the measured total

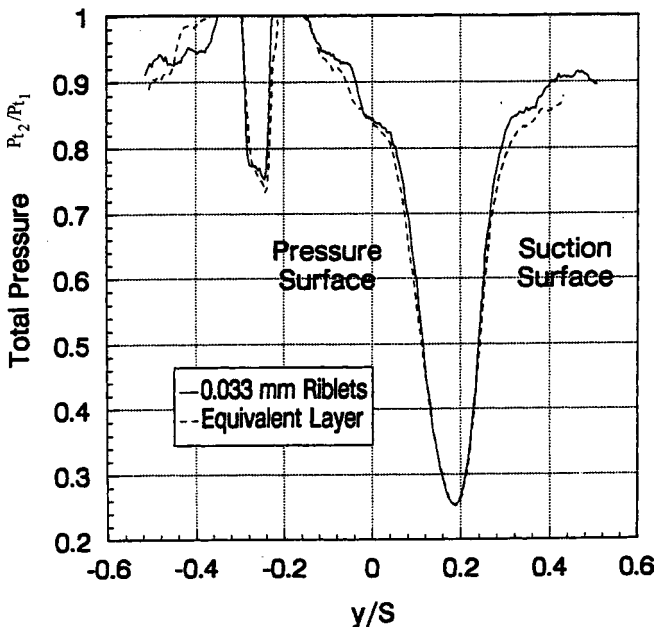


Fig. 5 Measured Total Pressure Profiles Normalized by Upstream Total Pressure, Design Incidence

Table 3 Off-Design Results

Incidence	% change in ω
-10 deg	3.0
Design	-8.5
+5 deg	-2.5

pressure ratio is greater than 1.0 at this location). Finally, the profile passes through the blade wake and ends in the core flow region above the suction surface of the wake at $y/S = 0.5$.

The total pressure profile comparison indicates the riblets provide a reduction in mass-averaged loss coefficient. The higher values of total pressure in the riblet profile are indicative of lower losses. The only location where the riblet profile is lower than the smooth layer is at $y/S = -0.4$ which is also the location of the reflected bow shock in the survey. Small changes in the total pressure are present throughout the profile; both in the wake and core flow regions. Through the integration of the profiles, the total amount of 8.5% change in loss coefficient is determined. Another approach to view the effect of the riblets is to divide the profiles into two regions; core and wake, and calculate the loss coefficients for each region (e.g., wake region in Fig. 5 is $y/S = 0.0$ to 0.3). This technique reveals that out of the 8.5% change in mass-averaged loss coefficient, 70% of the net benefit in the profile occurs in the wake region, with the rest found in the core flow.

Off-Design Study. The off-design cases of +5 deg and -10 deg incidence are tested with the optimum riblet height for design conditions of 0.033 mm. As described earlier, the flow physics inside the STF cascade changes with the incidence angles. The amount of benefit the riblets provide also varies. The performance of the riblets on the STF cascade blades for the off-design study are presented in Table 3. A small benefit of 2.5% is provided by the riblets at +5 deg incidence. A penalty of 3.0% is seen for the -10° incidence. Compared to the benefit provided by the riblets at design incidence, the riblet effect for off-design conditions is small. To better understand why the performance of the riblets has changed for the off-design cases, total pressure profiles of the riblet and equivalent layer of smooth material are compared.

For the +5 deg incidence, a 2.5% reduction in mass-averaged loss coefficient is determined for this off-design case. Recall from the flow field description, the impingement of the bow shock on the suction surface results in the separation of the boundary layer. As a result, only a small difference in the total pressure between riblet and smooth layer occurs in the suction side of the blade wake as compared to the pressure side. The separation of the boundary layer appears to diminish the riblet benefit on the suction surface of the blade.

Unlike the case of +5 deg incidence, the -10 deg incidence condition shows an increase in losses when riblets are applied to the STF blades. In the -10 deg incidence case, the boundary layer separates and reattaches on the pressure surface of the blade. Following the reattachment, the boundary layer encounters a significant localized adverse pressure gradient on the blade surface. As a result, the total pressure from the riblet profile is considerably lower than the smooth layer profile in the pressure side of the wake. Thus the overall mass-averaged loss coefficient is increased by 3% with the use of the riblets, when compared to the equivalent smooth layer.

Numerical Simulation

The losses in the STF cascade are the result of both shock and viscous effects. The viscous losses in the cascade at design incidence are no more than 1/2 of the total losses Chesnakas and Ng [6]. Therefore, the maximum 8.5% decrease in loss coefficient at design incidence represents a significantly greater reduction in the viscous losses. Taking into account the increase in losses due to the enlarged leading edge radius of the blades from the riblet

material, the 8.5% decrease in the total loss coefficient corresponds to approximately a 25% decrease in the viscous losses. This is much greater than the 10% decrease in turbulent viscous losses that has been reported by other researchers and suggests that the riblets are decreasing the viscous losses in another manner. As a result, a numerical study was performed to investigate two different riblet effects: a reduction in turbulent viscous losses and a delayed transition location of the turbulent boundary layer on the surface of the blade.

In the numerical simulation, the two riblet effects were studied separately in order to determine the contribution from each riblet effect on the total decrease in losses. The delayed transition effect was established by initiating the turbulent boundary layer further downstream on the blade's suction surface in the simulation. Modeling for the decrease in turbulent viscous losses due to riblet required modifying the existing turbulent model. The numerical simulation focused on the flow field for design incidence only, with an emphasis for modeling the situation where there is an optimum riblet benefit (i.e., riblet height of 0.033 mm).

Numerical Model. The code used in this simulation was ANSERS (Algorithm for the Navier-Stokes Equations using the Reimann Solver) developed by Thomas and Walters [22]. Significant improvements to the original code have been developed by Taylor, Brock [23,24], and Andrew [7]. In ANSERS, the compressible, 2-D, full Reynolds-averaged Navier-Stokes equations are solved by a time marching method. The integral conservation law form of the governing equations are solved with a cell-centered finite-volume formulation. The upwind scheme of Roe [25] was used to evaluate the inviscid flux terms. In this paper, spatial discretization for the inviscid flux terms is third-order accurate upwind-biased. The viscous fluxes were determined by a second-order accurate central differencing method.

A periodic *C*-mesh was used to model the STF cascade blade. The mesh was generated with an elliptic grid generator. The grid contains 481 cells in the stream-wise direction and 61 cells in the pitch-wise direction. Grid points are closely packed to the blade surface with additional points concentrated near the leading and trailing edges to ensure proper resolution of the flow physics. Adequate clustering was verified to resolve the viscous layers and the shock layer sufficiently. Only limited study on grid resolution was performed in this research. Solutions were grid independence in most part of the flow field, except at location of shock/boundary layer interaction.

In general, the number of required iterations for convergence was typically 12,000, and were carried out at a CFL number of 6. The applied convergence iteration was the consistency of the skin friction over an interval of 1,500 iterations; the completed pressure distributions converged more quickly.

Supersonic flow at the upstream, inflow boundary dictates that four boundary conditions be specified there in an explicit manner. These are density, two components of velocity, and pressure. At the out flow boundary, supersonic exit flow requires that for boundary conditions are extrapolated from the computational domain. Density, two components of velocity, and boundary segments are specified as periodic over the cascade pitch. Two types of boundary conditions are appropriate at the inner boundary: a no-slip, adiabatic condition at the wall, and periodicity along the wake centerline.

All calculations were performed with an inflow Mach number of 2.36 and at design incidence. Four different simulations were performed to investigate the riblet effects. In the first simulation, the flow field was calculated for the smooth blades. This simulation served as the baseline test and was compared to the simulated riblet results. In the next two simulations, the two riblet effects, turbulent viscous reduction and delayed transition, were calculated separately. Finally, in the last simulation, the combination of the two riblet effects was computed to determine the total decrease in viscous losses.

Turbulent Model. The Baldwin-Lomax [26] turbulent model was used to provide closure for the ANSERS code. This model was chosen for its robustness and ease of implementation. The Baldwin-Lomax model is an algebraic eddy viscosity model which handles the turbulent boundary layer as a composite of two layers; an inner and outer region. To model for a reduction in turbulent viscous losses, one parameter in the turbulent model, A^+ (Van Driest damping coefficient), was modified.

Riblet Turbulent Model. A method to simulate the riblet effects on the STF cascade blades was developed for the Baldwin-Lomax turbulent model. Rather than physically model the riblets themselves, the turbulent model was modified to simulate for a decrease in turbulent viscous losses by adjusting the A^+ parameter in the Van Driest damping factor equation. This idea for modeling the riblet effect is based on the work conducted by Schetz and Nerney [27], who successfully modeled surface roughness effects with the Reichardt turbulent model.

The riblets' effects in a turbulent boundary layer are a reduction in viscous losses and a corresponding upward shift in the law of the wall profile. Based on classical surface effects on the wall of the law plot of u^+ versus y^+ Schetz [28], riblets act like "negative roughness" with a shift upward and to the left from the smooth surface profile in the logarithmic region. On the other hand, an increase in drag, from roughness effects, produces a shift downward and to the right. The slope of the lines for both roughness and riblets effects, however, remains the same as the smooth surface line Sawyer and Winter [29] and Schetz [27].

From the literature, in the Van Driest damping factor equation, the A^+ value of 26 was chosen because it provided the best agreement with the experimental, smooth surface law of the wall profiles Baldwin-Lomax [26]. For the same reason, different values of A^+ can be used to describe the micro-surface effects on a turbulent boundary layer profile. When comparing with smooth surface results, higher values of A^+ would represent a reduction in viscous drag (upward shift in the law of the wall profile) and lower values would represent an increase viscous drag (downward shift in the law of the wall profile).

Relating A^+ to Change in Drag (ΔD). To determine the influence of different A^+ values on a turbulent boundary layer profile, a numerical flat plate simulation, with zero pressure gradient was conducted. The inflow conditions for the flat plate simulation were the same as the supersonic through-flow cascade. For the flat plate study, the range of A^+ values varied between 24 and 37. Starting with an A^+ of 24 in the Van driest damping equation, the flat plate simulation was computed. The calculated viscous drag was compared to the smooth surface result ($A^+=26$). Next, the A^+ value was incremented by one and the simulation was repeated. This procedure continued until the change in viscous drag, ΔD , was determined for the complete range of A^+ values from 24 to 37. Here ΔD is defined as

$$\Delta D = \frac{\text{Drag}_{\text{riblet}} - \text{Drag}_{\text{smooth}}}{\text{Drag}_{\text{smooth}}}$$

Based on the flat plate simulation results, a relationship between A^+ and ΔD is established. Compared to the smooth surface result, the A^+ value of 24 produces a 2.4% increase in viscous losses. On the other hand, the A^+ value of 37 decreases the viscous losses by 10.9%. The range of A^+ values and their corresponding changes in drag are used to simulate the varied riblet effect on the blade surface.

Relating h^+ to A^+ . Unlike the flat plate study, the STF cascade simulation will not have a constant riblet effect—constant A^+ value—over the blade surface. Due to the flow conditions in the STF cascade, the local riblet effect will vary along the blade surface. In the STF simulation, an estimated h^+ profile on the smooth blade surface is calculated to help determine the localized

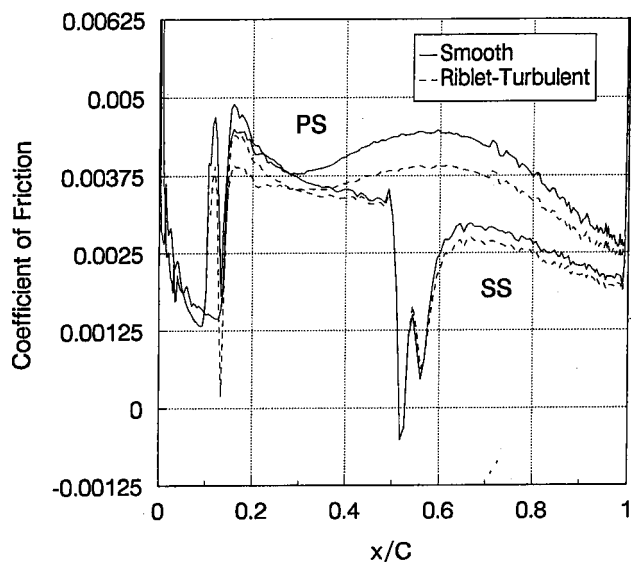


Fig. 6 Comparison of calculated skin friction coefficients, smooth blade versus simulated riblet effect (with no delayed transition)

riblet effect. The procedure to relate values of h^+ to A^+ requires matching the change in viscous drag, ΔD , (from the h^+ trend similar to that shown in Fig. 4) and the flat plate simulation which relates the A^+ parameter to change in drag, ΔD , as described above. More detail of this entire procedure can be found in Ninemann [19].

To summarize, the process for simulating the riblet effect for a decrease in viscous losses involves a number of steps. First, the flow field for smooth blades, $A^+ = 26$, is simulated. With the smooth blade results, an estimated h^+ profile of the blade surface is computed. A corresponding A^+ profile is generated from the above established relationship of A^+ versus h^+ and then placed into the CFD code. The flow field for the local riblet effect is then calculated.

Using the above method, the modification to the A^+ parameter in the Baldwin-Lomax model can reproduce the riblet effects on a turbulent boundary layer.

Delayed Transition Due to Riblet. In the numerical simulation, the transition from laminar to turbulent boundary layer was delayed by moving the location where the turbulent boundary layer begins on the blade surface. Based on shadowgraphs obtained from the experiment, for smooth blades, the transition appears to occur at approximately 15% chord on the suction side and 10% on the pressure side. For the simulation of the riblet covered blades, the inception of the turbulent boundary layer was moved to the 50% chord location on the suction side, where the shock impingement occurred. In this numerical study, the transition process was not modeled. The boundary layer was simulated to be either completely laminar before transition and then completely turbulent after transition.

Numerical Results

The varying riblet effect in the simulation of the STF cascade is observed by comparing skin friction values. A comparison of the calculated skin friction between the riblet and smooth surface is presented in Fig. 6. Near the leading edge, there is no difference in the coefficient of friction as the boundary layer is laminar. As expected, the riblet effect produced lower values of skin friction. The greatest decrease in skin friction is seen on the pressure surface side of the blade. In the region following the shock impingement at $x/C = 0.15$ to $x/C = 0.8$, the riblet effect produced a local-

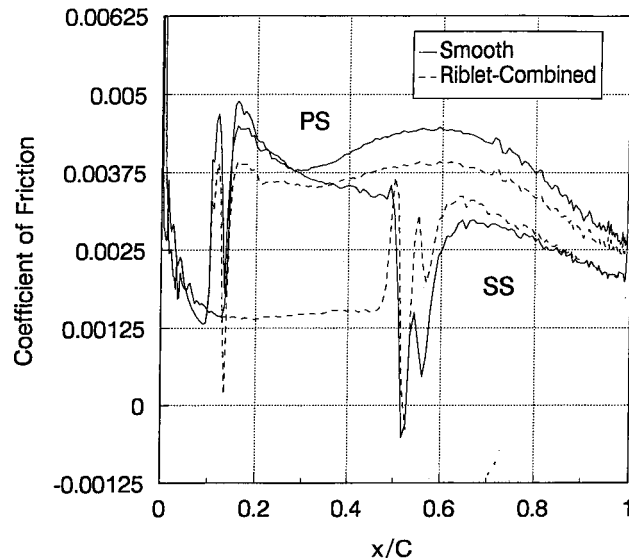


Fig. 7 Comparison of calculated skin friction coefficients, smooth blade versus combined effect of riblet and delayed transition

ized decrease coefficient of friction of approximately 10%. On the suction side, the modeled riblet effect resulted in a small change in the coefficient of friction.

The overall effect from the localized reduction in viscous losses on the blade surfaces is determined by the change in mass-averaged loss coefficient. This riblet effect, modeling only for a decrease in the turbulent viscous losses, produced a 2.5% change in loss coefficient. This change in loss coefficient is much smaller than the experimental optimum riblet results. However, the reduction in turbulent viscous losses is only one part of the riblet effect on the STF cascade blades.

In the final numerical simulation, the flow field for the combined riblet effects was computed. In the numerical study, the combined riblet effect simulates for a delayed transition and a decrease in turbulent viscous losses. The comparison of the calculated skin friction between the combined riblet effect and the smooth surface is presented in Fig. 7. On the pressure side, a near optimum decrease in the turbulent viscous losses is seen. For the suction surface, the delayed transition is responsible for most of the decrease in viscous losses.

The change in loss coefficient for a combined riblet effect was 6%. This numerical result is comparable to the measured experimental result and supports the hypothesis that transition was delayed on the STF blades.

To investigate the simulated results in more detail, the total pressure profiles for the smooth and combined riblet effect were compared. Presented in Fig. 8 are the total pressure profiles for the combined riblet effect and smooth case, along with a plot showing the difference between the two profiles. For Fig. 8(a), the riblet profile shows higher total pressure values through out the blade pitch. For the total pressure profile downstream of the cascade, the combined riblet effect produces a wake that is thinner and less deep.

In Fig. 8(b), the difference between the profiles, ΔP_t , illustrates that the riblet benefit occurs on both sides of the blade's surface, but not by the same amount. The suction side, where transition was delayed, shows a peak difference between the profiles occurs in mid portion of the suction side wake. For the pressure side wake, the riblet effect produces a smaller difference between the two profiles. At the wake minimum point, a slightly smaller change in total pressure profiles exist compared to changes on either the suction or pressure side wake.

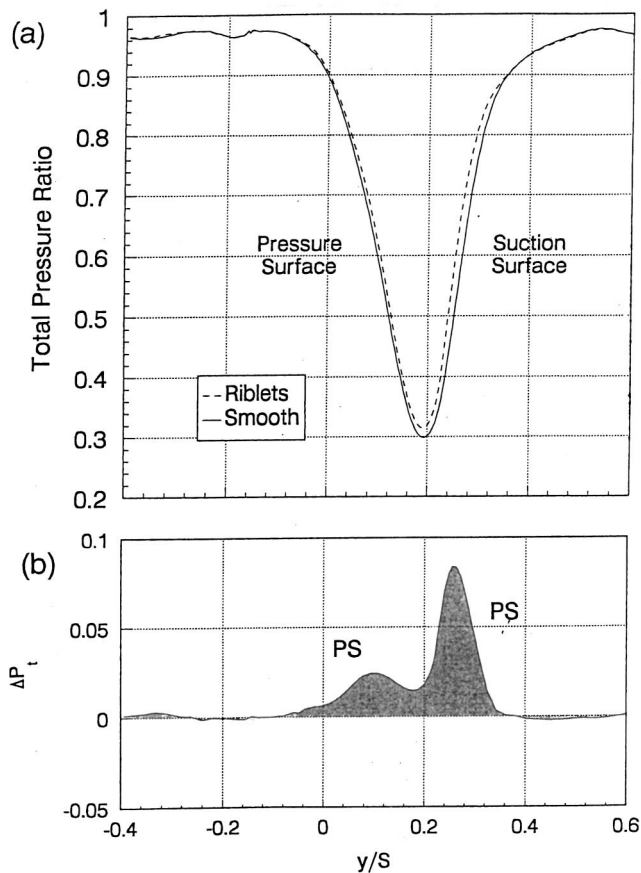


Fig. 8 Comparison of calculated total pressure profiles, smooth blade versus combined effect of riblet and delayed transition

As seen in the numerical investigation, a significant local decrease in viscous losses on the blades surface produces a much smaller change in the mass-averaged loss coefficient. As mentioned earlier, shock losses in the cascade account for a good portion of the total losses. Therefore, this suggests that only a combined riblet effect—delayed transition and decrease in turbulent viscous losses—is able to produce the significant decrease in losses that were measured experimentally.

Discussion and Conclusions

An experiment was undertaken with emphasis on improving the aerodynamic performance of the supersonic throughflow cascade blades by applying riblets to the blade surface. The STF cascade presented a unique flow environment for the riblet study. The performance of the blades was evaluated by comparing the mass-averaged loss coefficient of the riblets to an equivalent layer of smooth material. For details on how the riblets affect the performance of the STF blades, total pressure profiles were compared. In this riblet study, three different heights of riblets were tested at design conditions. The optimum riblet height for design incidence was tested at off-design conditions of +5 deg incidence and -10 deg incidence.

In the riblet study, an optimum riblet height was found to provide an 8.5% decrease in the mass-averaged loss coefficient. Smaller benefits were seen for a larger and a smaller riblet height. The results of this riblet study are consistent with results from previous researchers. Within the 8.5% decrease in loss coefficient at design condition, 70% of the benefit was seen in the wake region of the total pressure profile, with the rest in the core region.

It is interesting to note, riblets affected the core flow region that is not associated with viscous effects. The riblets possibly altered the structure of the shock-boundary layer interaction and weakened the strength of the reflected shock.

Compared to the design incidence results the riblets produce smaller overall effects on the mass-averaged loss coefficient for the STF cascade blades at off-design conditions. The change in performance is attributed to the difference in flow physics at off-design conditions where separation of the boundary layer is a prevalent feature. As noted in the comparison of total pressure profiles, the riblets provide no benefit and even increase the losses on the side of the wake where separation occurs. The result of this boundary layer separation for +5 deg incidence is the small benefit from the riblets of 2.5%. In the -10 deg incidence case, the combination of boundary layer separation and adverse pressure gradient with the riblets increases the losses by 3%.

The findings from the total pressure profile comparison for off-design conditions indicate the riblets can perform two contradicting functions. The riblets can increase the performance on one side of the blade and decrease it on the other. As a positive effect, the riblets appear to suppress the momentum exchange near the surface of the blade, resulting in lower viscous losses. On the negative side, lower momentum exchange near the blade surface increases the possibility of extreme separation of the boundary layer. Flow fields that include adverse pressure gradients and shock impingement may limit the performance of the riblets.

The CFD simulation presented here is a plausible explanation of the effects of the riblet on losses. It is hypothesized that riblets are able to dampen the original disturbances that lead to transition in the STF cascade blades. Possibly, the slow moving fluid inside the riblet grooves is sustaining the laminar boundary layer. At design incidence, the pressure gradient on the blades' suction surface becomes favorable around 20% chord and continues until the shock impingement location at 50% chord. Perhaps, the combination of the riblets and the favorable pressure gradient on the blade surface is responsible for the laminar boundary layer existing up to the shock impingement location. For the smooth blade surface, the boundary layer is already turbulent at 20% chord and the mild pressure gradient would affect the turbulent boundary layer by only minimizing its growth.

This experiment represents a successful application of riblets to the original prototype design of the STF blades. The choice of riblet height and type of flow field determines the success of the riblets. The potential for the riblets to reduce aerodynamic losses in more conventional high speed turbine and compressor fields should be explored further.

Nomenclature

A^+	= Van Driest damping coefficient
C	= chord
C_f	= coefficient of friction
D	= drag
h	= riblet height
h^+	= nondimensional riblet height
i	= cascade incidence angle
M	= Mach number
p	= local static pressure
p_p	= pitot pressure
P_t	= local total pressure
s	= spacing between riblet peaks
S	= blade spacing or pitch
u	= velocity component in pitch-wise direction
u_τ	= wall-friction velocity
u^+	= u/u_τ
x	= stream-wise direction
y	= transverse or pitch-wise direction
y_n	= distance from the wall
y^+	= $u_\tau y_n / \gamma_w$

Greek Letters

- σ = solidity
 α = yaw angle
 γ = ratio of specific heats
 γ_w = kinematic viscosity
 Δ = difference between riblets and equivalent smooth layer
 ν = turbulent viscosity
 ρ = local density
 $\bar{\omega}$ = mass-averaged loss coefficient

Superscripts

- = averaged

Subscripts

- 1 = conditions upstream of cascade
2 = conditions downstream of cascade
s = smooth surface
w = wall conditions

References

- [1] Franciscus, L. C., 1987, "The Supersonic Through-Flow Turbofan for Mach Propulsion," NASA-TM-100114.
- [2] Boxer, E., 1967, "The Variable-Pitch Supersonic Inflow Compressor and Its Application in a Hypersonic Engine," Proceedings from a Conference on Hypersonic Aircraft Technology, NASA SP-148, pp. 401–416.
- [3] Savage, M., Boxer, E., and Erwin, J. R., 1961, "Resume of Compressor Research at the NACA Langley Laboratory," J. Eng. Power, **83**(3), pp. 269–285.
- [4] Breugelmanns, F. A. E., 1975, "The Supersonic Axial Inlet Component in a Compressor," ASME Paper No. 75-GT-26.
- [5] Bowersox, R. D. W., 1990, "Meanflow and Turbulence Measurements in the Wake of a Supersonic Through-Flow Fan," Master of Science Thesis, Department of Aerospace and Ocean Engineering, Virginia Tech, Blacksburg VA.
- [6] Chesnakas, C. J., and Ng, W. F., 2003, "Supersonic Through-Flow Fan Blade Cascade Studies," ASME J. Fluids Eng., **125**(5), pp. 796–805.
- [7] Andrew, P. L., 1992, "Experimental and Numerical Investigations of the Off-Design Flow Physics in a Supersonic Through-Flow Fan Cascade," Ph.D. Dissertation, Virginia Tech, Blacksburg, VA.
- [8] Walsh, M. J., 1982, "Turbulent Boundary Layer Drag Reduction Using Riblets," AIAA Paper No. 82-0169.
- [9] Bandyopadhyay, P. R., 1986, "Review-Mean Flow in Turbulent Boundary Layers Disturbed to Alter Skin Friction," J. Fluids Eng., **108**, pp. 127–140.
- [10] Sundaram, S., Viswanath, P. R., and Subaschandar, N., 1999, "Viscous Drag Reduction Using Riblets on a Swept Wing," AIAA J., **37**(7), pp. 851–856.
- [11] Rohr, J., Anderson, G. W., and Reidy, L. W., 1989, "An Experimental Investigation of the Drag Reducing Effects of Riblets in Pipes," In *Drag Reduction in Fluid Flows* (Eds. R. H. J. Sellin and R. T. Moses, Ellis Horwood Publishers), pp. 43–52.
- [12] Liu, K. N., Christodoulou, G., Riccius, O., and Fulachier, L., 1990, "Drag Reduction in Pipe Lined with Riblets," AIAA J., **28**(10), pp. 1697–1698.
- [13] Feng, C., Yan-Ping, T., and Mao-Zhang, C., 1990, "An Experimental Investigation of Loss Reduction with Riblets on Cascade Blade Surfaces and Isolated Airfoils," ASME Paper No. 90-GT-207.
- [14] Robinson, S. K., 1988, "Effects of Riblets on Turbulence in a Supersonic Boundary Layer," AIAA Paper No. 88-2526.
- [15] Gaudet, L., 1989, "Properties of Riblets at Supersonic Speed," Appl. Sci. Res., **46**(3), pp. 245–254.
- [16] Coustols, E., and de Zotti, A., 1990, Proceedings of the 5th European Drag Reduction Working Meeting, Teddington.
- [17] Coustols, E., 1991, Proceedings of the 6th European Drag Reduction Working Meeting, Eindhoven.
- [18] Chesnakas, C. J., 1991, "Experimental Studies in a Supersonic Through-Flow Fan Blade Cascade," Ph.D. Dissertation, Virginia Tech, Blacksburg, VA.
- [19] Ninnemann, T. A., 1994, "Effects of Riblets on the Performance of the Supersonic Through-Flow Fan Cascade Blades," Ph.D. Dissertation, Mechanical Engineering Department, Virginia Tech, Blacksburg, VA.
- [20] Andrew, P. L., and Ng, W. F., 1994, "Turbulence Characteristics in a Supersonic Cascade Wake Flow," ASME J. Turbomach., **116**(4), pp. 586–596.
- [21] Walsh, M. J., and Anders, J. B., 1989, "Riblet/LEBU Research at NASA Langley," Appl. Sci. Res., **46**(3), pp. 255–262.
- [22] Thomas, J. L., and Walters, R. W., April 1987, "Upwind Relaxation Algorithms for the Navier Stokes Equations," AIAA J., **25**(4), pp. 527–534.
- [23] Taylor, A. C., III, "Convergence Acceleration of Upwind Relaxation Methods for the Navier-Stokes Equations," Ph.D. Dissertation, Department of Mechanical Engineering, Virginia Polytechnic Institute and State University, Blacksburg, VA, July 1989.
- [24] Brock, J. S., "A Modified Baldwin-Lomax Turbulence Model for Turbomachinery Wakes," Masters of Science Thesis, Department of Mechanical Engineering, Virginia Polytechnic Institute and State University, Blacksburg, VA, January 1991.
- [25] Roe, P. L., 1981, "Approximate Riemann solvers, Parameter Vectors, and Difference Schemes," J. Comput. Phys., **43**, pp. 357–372.
- [26] Baldwin, B. S., and Lomas, H., "Thin Layer Approximation and Algebraic Model for Separated Turbulent Flows," AIAA Paper No. 78–257.
- [27] Schetz, J. A., and Nerney, B., September 1977, "The Turbulent Boundary Layer with Injection and Surface Roughness," AIAA J., **20**(9), pp. 1268–1294.
- [28] Schetz, J. A., Foundations of Boundary Layer Theory for Momentum, Heat, and Mass Transfer, Prentice-Hall, Inc., Englewood Cliffs, New Jersey, 1984.
- [29] Sawyer, W. G., and Winter, K. G., "An Investigation of the Effect on Turbulent Skin Friction of Surfaces with Streamwise Grooves," *Proceedings of Turbulent Drag Reduction by Passive Means Conference*, Royal Aeronautical Society, London 15–17 September 1987.

Secondary Flow Control Using Vortex Generator Jets

R. K. Sullerey

Professor

Department of Aerospace Engineering,
Indian Institute of Technology,
Kanpur-208 016, India
Ph: +91-512-2597863
Fax: +91-512-2590007
e-mail: suller@iitk.ac.in

A. M. Pradeep

Research Scholar

Department of Aerospace Engineering,
Indian Institute of Technology,
Kanpur-208 016, India

In this paper, results are presented of an experimental investigation into the effectiveness of vortex generator jets in controlling secondary flows in two-dimensional S-duct diffusers. The experiments were performed in uniform and distorted inflow conditions and the performance evaluation of the diffuser was carried out in terms of static pressure recovery and quality of the exit flow. In the case with inflow distortion, tapered fin vortex generators were employed in addition to vortex generator jets to control flow separation that was detected on the wall with inflow distortion. Detailed measurements including total pressure, velocity distribution, surface static pressure, skin friction, and boundary layer measurements were taken at a Reynolds number of 7.8×10^5 . These results are presented in terms of static pressure rise, distortion coefficient, and total pressure loss coefficient at the duct exit. For uniform inflow, the use of vortex generator jets resulted in more than a 30 percent decrease in total pressure loss and flow distortion coefficients. In combination with passive device (tapered fin vortex generators), the vortex generator jets reduce total pressure losses by about 25 percent for distorted inflow conditions. A potential application of this method may include control of secondary flows in turbo machinery.

[DOI: 10.1115/1.1779661]

Introduction

Air intakes are vital components of any air-breathing engine. Combat aircraft have one or two engines, which are generally integrated with the fuselage. Supplying them with the necessary quantity of air for generating thrust takes place by means of specially designed inlets, through which air is taken from the external flow and supplied to the engines. The use of geometrically complex ducts becomes inevitable and hence has been a subject of interest to several researchers. As is expected of an aircraft intake, the flow must be decelerated in such a way that there is a uniform flow at the compressor face with minimum stagnation pressure loss.

S-duct diffusers used in air intakes generally have high degrees of centerline curvature due to their short length that results from severe space constraints. Due to centerline curvature, there are cross-stream pressure gradients resulting in migration of boundary layer fluid in the direction of the pressure gradient giving rise to secondary flows (The term "secondary flows" in this paper refers to the flow that has an orientation perpendicular to the main or primary flow). Within the boundary layer this imparts cross-flow velocities creating non-uniform total pressure profiles. In addition, there is a stream-wise pressure gradient resulting from increasing cross-sectional area. The combined effect may result in increased total pressure nonuniformity (i.e., distortion) and total pressure loss at the duct exit. The engine response to the flow delivered by the intake depends not only on the total pressure provided but also, more significantly, on the quality of the flow (flow uniformity) at the compressor face. The objective of this research was to study the effectiveness of vortex generator jets in reducing inlet flow distortion and improve pressure recovery by effective secondary flow control in a diffusing S-duct.

Control of secondary flows and separation by passive means has been explored by a number of investigators. Guo and Seddon [1] studied the swirl in an S-shaped duct of typical aircraft intake proportions at different incidences and through flow ratios. In order to reduce the magnitude of swirl at high angles of incidences, two methods were studied. One, to change the distortion of the

pressure by means of a spoiler and two, to re-energize the separated flow and inflow of freestream air through auxiliary inlets. Of the anti-swirl devices, the spoiler was found to be more powerful and could be sized to either reverse the swirl direction or to eliminate the swirl completely. Wendt and Reichert [2] have experimentally studied the effect of nonuniform upstream flow arising due to vortex ingestion in a diffusing S-duct inlet with and without an array of surface mounted vortex generators. The ingested vortex was observed to have a strong influence on duct flow field, but only when the vortex trajectory was near the region of separation that existed in the baseline S-duct.

Sullerey and Mishra [3] have studied the effectiveness of boundary layer fences in improving the performance of S-duct diffusers of rectangular cross-section in a uniform inlet flow. Significant improvement in performance of the diffusers was observed with top and bottom wall fences. Various fence heights were tried to achieve optimum performance of the duct.

Reichert and Wendt [4] could improve the total pressure distortion and recovery performance of a diffusing S-duct using low-profile vortex generators (so-called wishbone types). Reichert and Wendt [5] also presented a compilation of the previous study with additional data on the effectiveness of various vortex generator configurations in reducing exit flow distortion of circular S-ducts.

In a further study, Reichert and Wendt [6] used tapered-fin type vortex generators with an objective of controlling the development of secondary flows. The application of vortex generators here differed from conventional point of view of vortex generators as devices that re-energize the boundary layer by mixing free stream and boundary layer fluids, rather the objective was to control the development of secondary flows.

The above papers (Refs. [4–6]) give a clear description on the flow physics involved in an S-duct diffuser and how secondary flows affect diffuser performance in terms of outflow quality and pressure recovery. The studies also show how vortex generators improve diffuser performance by effectively controlling secondary flows. Lakshminaraya [7] also describes the development of secondary flows in curved passages and the theory of secondary flows in detail.

Foster et al. [8] conducted measurements in flow through a rectangular-to-semi annular transition duct to demonstrate the effectiveness of vortex generators to reduce the circumferential total pressure distortion. Sullerey et al. [9] studied the effectiveness of

Contributed by the Fluids Engineering Division for publication in the JOURNAL OF FLUIDS ENGINEERING. Manuscript received by the Fluids Engineering Division July 17, 2003; revised manuscript received February 13, 2004. Associate Editor: H. Johari.

boundary layer fences and tapered fin vortex generators in controlling secondary flows. The study revealed that significant improvement in performance could be achieved by judicious use of the passive control devices. Sullerey and Pradeep [10,11] also studied the effect of inflow distortion on *S*-duct diffuser performance and the performance enhancement by the use of tapered-fin vortex generators.

Shih and Lin [12] carried out computations based on ensemble-averaged compressible Navier-Stokes equations to investigate the effects of a leading edge airfoil fillet and inlet swirl angle on the secondary flow structure and hence to reduce aerodynamic loss and surface heat transfer. It was observed that since the intensity and size of the cross flow were found to increase instead of decrease by inlet swirl and the type of fillet geometries, the mechanisms responsible for aerodynamic loss and surface heat transfer are more complex than just the intensity and magnitude of secondary flows.

Ball [13] studied the effect of centerline offset, wall suction and blowing on diffuser performance. The effectiveness of wall suction and blowing in separation control was investigated. The centerline offset, hole area and blowing slot height were varied to attain optimum performance. It was observed that good performance could be achieved by using small amounts of wall suction and blowing upstream of the separation point.

Active boundary layer control using steady blowing in diffusers was investigated by Kwong and Dowling [14]. The new jet geometries used were compared with conventional blowing methods. Active feedback control was employed to control separation that occurred in the wide angled rectangular diffuser used. It was concluded that a combination of steady and unsteady blowing could give better diffuser performance in terms of pressure recovery and reduced pressure oscillations.

Johnston and Nishi [15] proposed an active method of separation control termed "Vortex Generator Jets." Their low speed experiments demonstrated that the cross-stream mixing associated with the vortices generated by the VGJ is effective in separation control.

Earlier Innes et al. [16] reported a set of experiments designed to show the effectiveness of VGJs for the control of separation on a complex airfoil. A three-element airfoil in a configuration typical of landing and take-off was studied. The study revealed a substantial improvement in the normal force coefficient and the stall angle of attack.

Khan and Johnston [17] have described in detail the vortex development from VGJ. Johnston [18] in his review article describes the application of VGJ for separation control. The paper also reviews the use of pulsed vortex generator jets. The addition of pulsing was observed to provide a more efficient use of the jet fluid. It was also observed that it might be possible to gain better control by using pulsed vortex generator jets than that with steady VGJ.

Sullerey and Pradeep [19] recently reported secondary flow control using VGJ in *S*-duct diffusers where in a significant improvement in diffuser performance was obtained. To the best of the author's knowledge, this was the first application of VGJ for secondary flow control. Presently the results of this study as well as those obtained by a combination of both active and passive methods are presented. The *S*-duct diffuser has a curvature and divergence angle of typical combat aircraft inlet geometry. The study was carried out both with and without the presence of inflow distortion. Detection of flow separation was carried out using an LVDT displacement based shear stress sensor. The VGJs were positioned in such a manner that the vortices generated by their interaction with the main flow have an orientation opposing the secondary flows. The VGJ skew angles and jet-to-freestream velocity ratios were varied to optimize diffuser performance.

For flow with distorted inflow, VGJs continued to be used for secondary flow control but additionally tapered-fin vortex generators were used to control flow separation on the wall of the dif-

fuser where flow separation was observed as a result of distorted inflow. The performance improvement resulting from this configuration was much better than that obtained by employing VGJs alone.

Experimental Setup and Procedure

The measurements were carried out in an open-circuit wind tunnel. A blower discharged air through a diffuser into a large settling chamber with a honeycomb and three sets of wire mesh screens. A contraction section of an area ratio of 17 accelerated the flow into the test section entrance of cross-section area of 380 mm (width) \times 305 mm (height). A large contraction ratio ensured a uniform flow at the inlet. The measured free stream turbulence level of the inlet flow was less than 0.5 percent. Between the contraction and the *S*-duct diffuser, a straight duct of 300 mm length was provided to obtain fully developed, zero pressure gradient turbulent boundary layer at the diffuser inlet. Detailed velocity measurements were carried out across the diffuser inlet (free-stream) and in the inlet boundary layers. The diffuser inlet flow was kept uniform (in the absence of inflow distortion grid) with an average wall boundary layer momentum thickness equal to 0.2 percent of the inlet width. The tests were carried out at a Reynolds number of 7.8×10^5 based on the diffuser inlet width (free stream velocity = 31 m/s and Mach number = 0.1). A constant area duct extension of 300 mm length was also placed at the diffuser exit to provide smooth, continuous flow exiting the duct.

S-Duct Diffuser. The diffuser on which the experiments were carried out had a rectangular cross-section with an aspect ratio of 0.8 at inlet. The area ratio and semi-divergence angle of the diffuser was 1.39 and 8 degrees respectively (Fig. 1). The radius ratio of the diffuser was chosen based on typical combat aircraft intake geometry. The semi-divergence angle corresponds to an equivalent straight diffuser of same area ratio. To increase the area, the diffuser width was varied linearly along the duct centerline while keeping the height constant. The width was equally distributed normal to the centerline. The radius ratio of the diffuser was fixed as 4. Two planar circular arcs with identical radii defined the duct centerline. The plane at which the centerline curvature changes from concave to convex is known as the inflection plane.

Vortex Generator Jet. The VGJ arrangement used in the present study (Fig. 2a) was designed based on the jets used by Johnston and Nishi [15]. In previous studies carried out (Refs. [8–10]) using tapered fin vortex generators, a set of three vortex generators at locations of maximum secondary flow strength was observed to be optimum. Hence, it was decided to use the same number of VGJs in the present study, too.

Figure 2a gives the vortex generator jet flow arrangement, and the VGJ defining angles with reference to the secondary flow are shown in Fig. 2b. In the present investigation, the pitch angle was kept fixed at 45 deg (based on Johnston and Nishi [15]) and the skew angle was varied (in the range 0 to 140 deg) to obtain optimum performance. The set of three VGJs at the two locations were oriented in such a manner that the vortices generated from interaction of the VGJs with the freestream would tend to nullify the secondary flows, i.e., the VGJs were directed towards the high pressure side (as secondary flows occur from the high pressure side to the low pressure side). The optimum condition was obtained by varying the skew angle of the VGJ. The air supply to the VGJs was provided from a separate centrifugal blower. At each station, the three VGJs were supplied air through a compartment consisting of a settling chamber, three wire mesh screens and a nozzle (refer Fig. 2a). This was done to ensure uniform air supply to all the VGJs. The velocity of each VGJ was measured using a fine Pitot tube of 0.8 mm diameter simultaneously to ensure that all the jets had equal velocity.

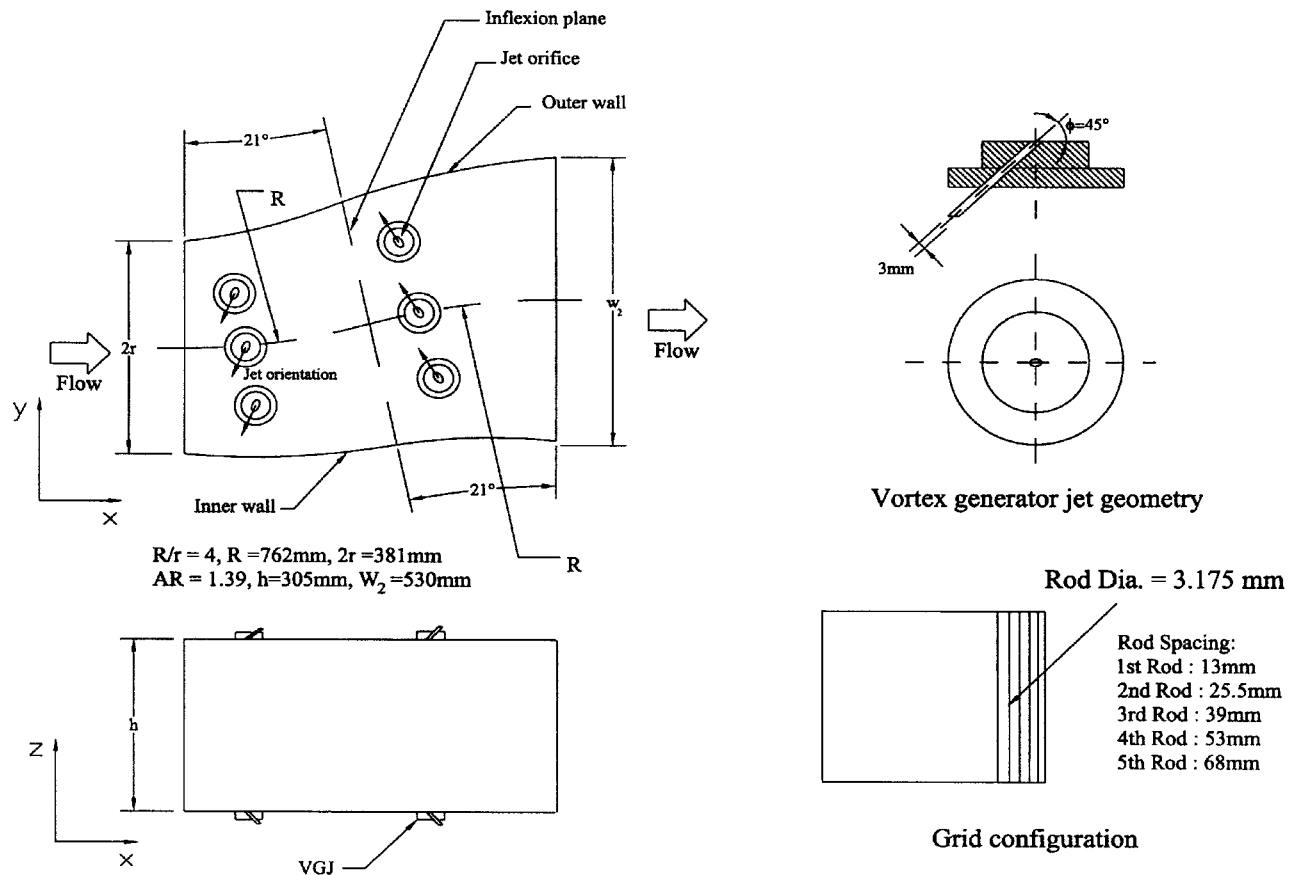


Fig. 1 S-duct diffuser, vortex generator jet (VGJ) and VGJ flow arrangement

Grid for Inflow Distortion. In order to explore the effect of distorted inflow on diffuser performance and to study the effectiveness of vortex generators in such a situation, a grid was designed to thicken the boundary layer at the diffuser inlet. The grid used in the previous studies (Refs. [10, 11]) was used in the present investigation too and is shown in Fig. 1. Since the outer wall (refer Fig. 1) of the diffuser was more prone to adverse pressure gradients, it was considered appropriate to use the grid on the outer wall of the diffuser. The introduction of a thickened boundary layer on the outer wall was expected to induce flow separation on the wall. The effectiveness of vortex generator jets in situations with flow separation could thus be studied. The boundary layer momentum thickness at the diffuser inlet (on the outer wall) increased from 0.17 percent of the inlet width to 0.22 percent with the introduction of the grid. The corresponding increase in the displacement thickness was from 0.185 percent to 0.234 percent of the inlet width.

Experimental Procedure. The experiments were carried out in two stages. In the first stage, the inflow to the diffuser was uniform. Flow in this case was separation free in the diffuser. Span wise (y-direction) array of three vortex generator jets (both on top and bottom walls) were employed, one before the inflexion plane and one after it with the objective of control of secondary flow in the diffuser. In the second stage of experiments, distorted inflow was introduced at the diffuser inlet. The distortion in the inflow was such as to thicken the inlet boundary layer on the side of the outer wall causing flow separation (as detected using the floating element wall shear stress sensor, Preston tubes and sublayer fences) on it at downstream locations close to diffuser outlet. The active flow control strategy employed for secondary flow control was again vortex generator jets (VGJs). The measurements were taken with distorted inflow with and without vortex genera-

tor jets. The performance improvement with VGJs was less in the second stage of the experiments compared to the first. As this is likely to be a result of separation of flow on the outer wall, tapered fin vortex generators were employed on the outer wall as a passive device for separation control in combination with VGJs for secondary flow control (as used in Sullerey and Pradeep [10,11]). The results for the various configurations i.e., diffuser with uniform inflow, diffuser with distorted inflow and diffuser with tapered-fin vortex generators are presented below.

Instrumentation and Measurement Techniques

The measurements included diffuser wall static pressure distributions, mean velocities, boundary layer and skin friction measurements and flow angularity. A Furness (FCO510 model) digital multi-channel micro-manometer was used for all pressure measurements. The static pressure measurements were taken with wall pressure taps at nine axial stations on each diffuser side wall. In addition, each station had nine circumferential pressure taps of 0.8 mm diameter (three on each curved walls and three on the top wall). There were fifteen pressure taps at the inflexion plane, diffuser inlet and exit (refer Sullerey et al. [9] for details on location of pressure taps). The C_p values were expected to be within one percent accuracy with a standard deviation of 0.49 percent of the mean value (on the basis of 30 measurements at a given station).

The skin friction measurements were made using wall mounted Preston tubes of 0.8 mm diameter and sublayer fences of fence height 0.1 mm. The design and calibration details of Preston tubes and sublayer fences can be obtained from Patel [20] and Vagt and Fernholtz [21], respectively. These were fitted along the centerline of inner and outer walls at nine stations. Sublayer fences were used in regions of adverse pressure gradients, as its accuracy is

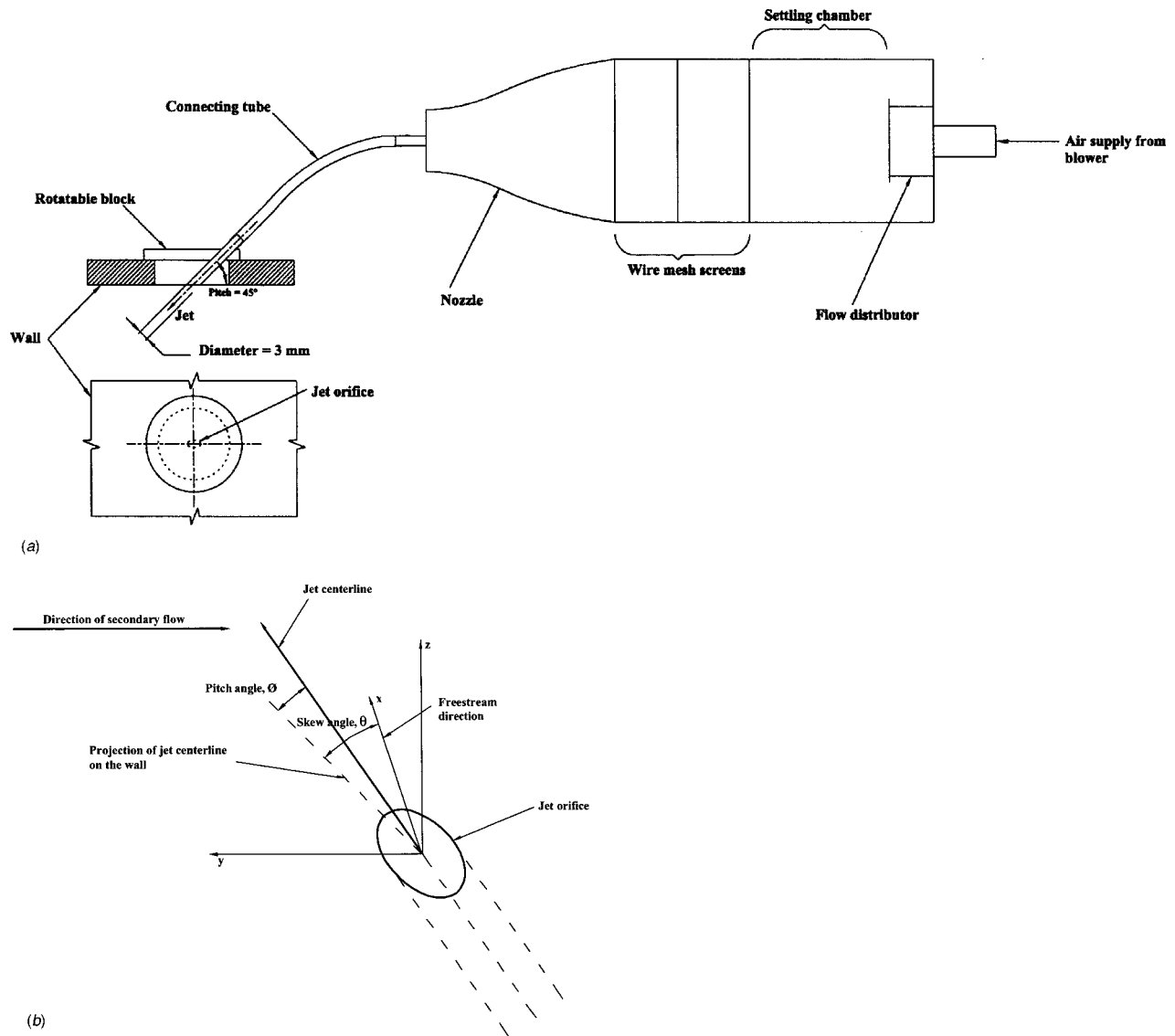


Fig. 2 (a) Vortex generator jet flow arrangement, (b) definition of coordinate system and vortex generator jet angles

higher in such situations compared to Preston tubes. The Preston tubes and sublayer fences were calibrated using a floating element shear stress sensor that was based on a linear voltage differential transformer (LVDT) displacement sensor. This device consisted of a floating element that would remain flush with the wall where the skin friction was to be measured. The central part of the sensor was an LVDT that could detect displacements up to 0.127 mm. The sensor was calibrated for shear force using fractional weights attached to the floating element. The skin friction measurements were expected to be within 2 percent accuracy. More than for the skin friction measurements, the basic purpose of using Preston tubes and sublayer fences in the present experiments was to detect regions of flow separation. The sublayer fences were also successfully used to detect secondary flows. With the fence aligned to the free stream, the sign of the pressure difference indicates the direction of secondary flows. Frei and Thomann [22] have discussed floating element sensors for shear stress measurement. The paper also discusses their calibration and use in adverse pressure gradients.

The boundary layer measurements were made on all four walls at inlet, inflection and the exit planes of the *S*-duct diffuser. A 0.8 mm diameter pitot probe was used for this purpose. The boundary layer measurements were taken by traversing the probe in inter-

vals of 0.5 mm. The total pressure and velocity measurements (including flow angularity) were made using a five-hole conical probe of diameter 6.4 mm based on the design details provided by Ohman and Nguyen [23]. The probe was calibrated using a calibration rig similar to Nowak [24]. For probe traverse, an accurate three-dimensional traverse system (least count 0.5 mm) was used. The five-hole probe was calibrated with one-degree interval and hence the accuracy in flow angularity was expected to be within one degree. Detailed flow measurements using the five-hole probe were made at the inflection and the diffuser exit plane for the various configurations tested. The total pressure measurements were expected to be within one percent accuracy.

The uncertainties in the above measurements are expected to be within ± 5 percent (estimated based on Abernathy et al. [25], Moffat [26], and Kline [27]).

Results and Discussions

Diffuser With Uniform Inflow. The VGJs were placed in regions of highest pressure differentials to neutralize the secondary flow (from high pressure to low pressure wall). Two such regions (one before the inflection plane and other after it) can be seen from wall pressure distributions shown in Fig. 3. The C_p

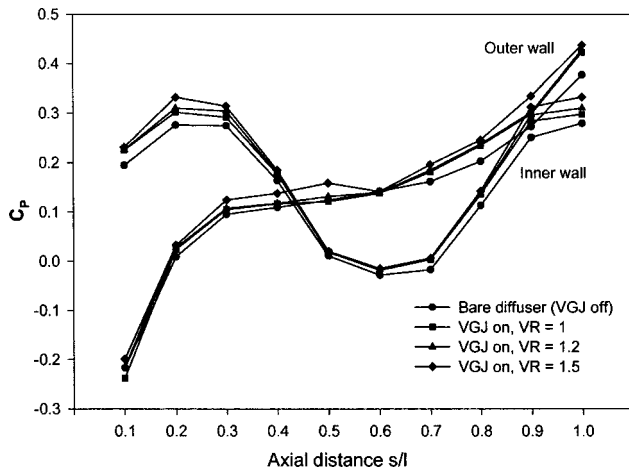


Fig. 3 Variation of wall static pressure distribution with velocity ratio (skew angle=135 deg)

distributions are shown in terms of non-dimensional axial distance from the diffuser inlet that refers to the locations where the static pressure taps were fixed. The plus and minus angles are with reference to the radial line at the inflection plane (refer to Fig. 1). The optimum combination of skew angle and velocity ratio was arrived at by detailed investigations for a range of skew angle (where the vortex created by jet flow interacting with free stream would be opposing the secondary flow present in the flow field) and velocity ratio. Some of the results of the effect of variation of skew angle are given below. In all cases the pitch angle was kept at 45 degrees in line with Johnston and Nishi [15].

Since external energy is added to the diffuser, the definition of C_p from Kwong and Dowling [14] (as defined in the nomenclature) was used to account for the VGJ energy addition.

Mass averaged quantities are defined in the following manner (refer Stevens et al. [28]):

$$\bar{p} = 1/m \int_0^A p dm, \quad (1)$$

Where, \bar{p} is any mass averaged quantity, p is a measured quantity to be mass averaged and m is the mass flow rate through the area A .

Table 1 gives the variation of static pressure recovery at the diffuser exit for different skew angles at a velocity ratio of 1.0. A VGJ skew angle of 135 deg (refer Fig. 1 for VGJ orientation) in both the planes resulted in optimum performance. Another parameter that was varied was the jet to freestream velocity ratio. The velocity ratio was varied with the skew angle fixed at 135 deg. It was observed that the optimum performance was achieved at a velocity ratio of 1.5. The VGJ Reynolds number based on jet diameter at a velocity ratio of 1.5 was 9212 (jet velocity = 46.5 m/s, Mach number=0.15).

The C_p distributions along the inner and outer walls of the diffuser with and without VGJs are given in Fig. 3 for several jet-to-freestream velocity ratios. The static pressure distributions in the figure for velocity ratios above 1.5 have not been presented for the sake of clarity. Moreover, the performance improvement with a velocity ratio of 1.6 was observed to be less than that at a velocity ratio of 1.5. The inner and outer wall pressures at a par-

Table 1 Effect of skew angle on diffuser static pressure recovery (VR=1.0)

Skew angle in deg	90	110	130	135	140
Mass averaged C_p	0.336	0.342	0.348	0.350	0.346

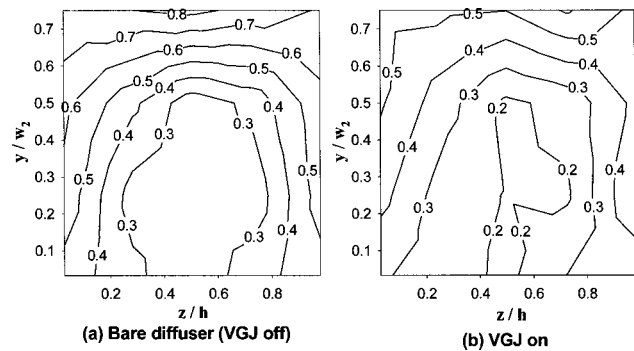


Fig. 4 Total pressure loss coefficient contours without and with VGJ

ticular station can be seen to differ considerably. The wall pressure differentials between the inner and outer wall creates secondary flows by causing slow moving boundary layer fluid to move from high- to low-pressure regions. The secondary flow in the plane upstream of the inflection plane has a direction from the inner wall to the outer wall. Since the wall curvature changes after the inflection plane, the direction of secondary flow at the plane downstream of the inflection plane of the diffuser is opposite (i.e. from outer wall to the inner wall) to that at the former plane. The VGJ skew angle was therefore measured and varied in a clockwise sense (i.e. pointing towards the inner wall) in the plane upstream of the inflection plane while that at the second plane in the counter-clockwise direction (pointing towards the outer wall).

As is evident from the Fig. 3 and Table 1, jet to freestream velocity ratio of 1.5 and a skew angle of 135 deg respectively yielded the best static pressure recovery. Therefore the results discussed below will be for this case.

The effectiveness of the VGJs in improving the flow quality can be assessed by looking at the total pressure loss coefficient contours. Figures 4a and 4b give the total pressure loss coefficient contours without and with VGJs respectively. The losses are higher towards the outer wall due to the increased curvature along that wall. The deployment of VGJs resulted in significant reduction in the losses. The mass averaged total pressure loss coefficient has reduced from 0.387 to 0.254 with the deployment of VGJ. The range of loss coefficient reduced from 0.3–0.8 to 0.2–0.5. Thus, the extent of high loss region has been significantly reduced by employing VGJs.

Table 2 gives the summary of results for the diffuser with and without VGJs. The effectiveness of VGJs in secondary flow control can be observed from the distortion coefficient, D_c (the total pressure nonuniformity as defined by Reichert and Wendt [4]) that reduced from a value of 0.832 to 0.687 with the VGJs on. The VGJs have been found to be much more effective than tapered fin vortex generators that were used in earlier studies [10,11]. Tapered fin vortex generators (owing to their physical presence in the flow field) produce drag losses and there is little control over these devices other than changing their geometry. VGJs on the other hand can be controlled in terms of skew angle and velocity ratio and moreover VGJs do not result in any drag losses when not in operation.

Table 2 Summary of results with uniform inflow

Exit flow property	Diffuser with tapered fin vortex generators		
	Bare diffuser	[10,11]	Diffuser with VGJ
Mass averaged C_p	0.312	0.340	0.362
D_c	0.832	0.743	0.687
ϖ	0.387	0.281	0.254

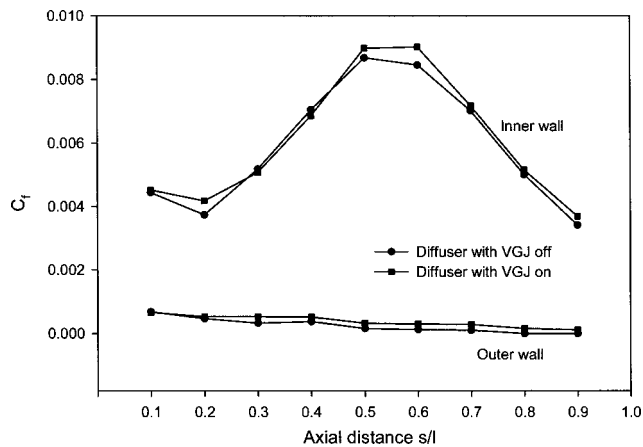


Fig. 5 Skin friction distribution along the inner and outer walls of the diffuser

Diffuser With Distorted Inflow. From previous studies [10,11] it was concluded that distorted inflow severely affects the diffuser performance. Moreover, the introduction of inflow distortion resulted in flow separation towards the exit on the outer wall of the diffuser [28]. It was therefore considered appropriate to study the efficacy of VGJs in such flow situation.

The sublayer fence and Preston tube measurements indicated flow separation at centerline arc angles of 8.4 and 4.2, respectively. The presence of separation was confirmed by using the LVDT based floating element shear stress sensor. The sensor showed a negative reading at these locations indicating flow reversal. Figure 5 shows the skin friction distribution along the walls of the diffuser. As is evident from the plot, the skin friction towards the exit of the diffuser on the outer wall attains a value of zero indicating flow separation.

The total pressure loss coefficient contours are plotted in Figs. 6a and 6b. The effectiveness of VGJ in improving flow quality can be clearly seen from the figure. The range of total pressure loss coefficient has been brought down from 0.3–0.8 to 0.2–0.6 with the use of VGJ. Moreover, the extent of high loss regions has considerably reduced.

The summary of results of the diffuser with distorted inflow is given in Table 3 below. The distortion coefficient reduced from a value of 0.851 to 0.809. A similar improvement in mass averaged total pressure loss coefficient was observed, too. The VGJs were again found to be more effective in improving the diffuser performance compared to tapered fin vortex generators [10,11].

Diffuser With Tapered-fin Vortex Generator. As is evident from the above results for the diffuser with a distorted inflow, the effectiveness of the VGJs has reduced drastically. This is due to the presence of flow separation resulting from the distorted inflow

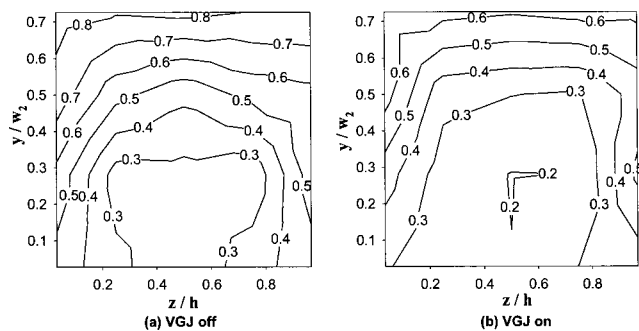


Fig. 6 Total pressure loss coefficient contours without and with VGJ in distorted inflow

Table 3 Summary of results with distorted inflow

Exit flow property	Diffuser with distorted inflow	Diffuser with tapered fin vortex generators (Ref. [10], [11])	Diffuser with VGJ
Mass averaged C_p	0.297	0.309	0.311
D_C	0.851	0.812	0.809
$\bar{\omega}$	0.395	0.375	0.363

that adds to the already deteriorated performance of the diffuser due to secondary flows. It was therefore decided to use tapered-fin vortex generators to control flow separation in addition to VGJs that were used for secondary flow control. The tapered-fin vortex generator configuration was similar to the one used in Sullerey and Pradeep [11].

The skin friction distribution along the inner and outer walls of the diffuser is shown in Fig. 7. The elimination of flow separation is clear from the figure indicated by the positive value of skin friction at locations where it was previously zero. The skin friction values were verified using the LVDT shear stress sensor.

The total pressure loss coefficient contours at the diffuser exit with distorted inflow and with VGJs alone is shown in Fig. 8a. The total pressure loss coefficient contours with VGJ and tapered-fin vortex generators on the outer wall is given in Fig. 8b. The range of total pressure loss coefficient has reduced from 0.3–0.8 to 0.2–0.6 with the use of VGJ in addition to tapered fin vortex generators. The extent of high loss regions has also considerably reduced. The improvement in flow quality due to flow separation control is hence evident from the figures.

Table 4 gives the summary of the results with tapered-fin vortex generators in addition to VGJs. A significant improvement in distortion coefficient and total pressure loss coefficient compared to the case with VGJ alone can be observed from the results. This is due to the efficient control of secondary flows by VGJs and flow separation by tapered-fin vortex generators.

Table 5 gives the boundary layer momentum thickness (as percentage of diffuser inlet width) for the three cases discussed above. Boundary layer momentum thickness is direct indication of the total pressure losses and hence increase in momentum thickness implies increased losses. The effectiveness of the flow control devices can be observed from the reduction in boundary layer momentum thickness as compared to the situations devoid of the devices.

Conclusions

Active flow control using vortex generator jets was employed to study its effect on a wide angled S-duct diffuser subjected to

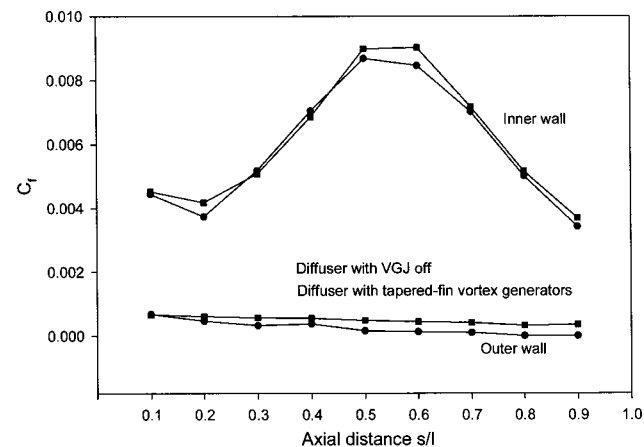


Fig. 7 Skin friction distribution along the inner and outer walls of the diffuser

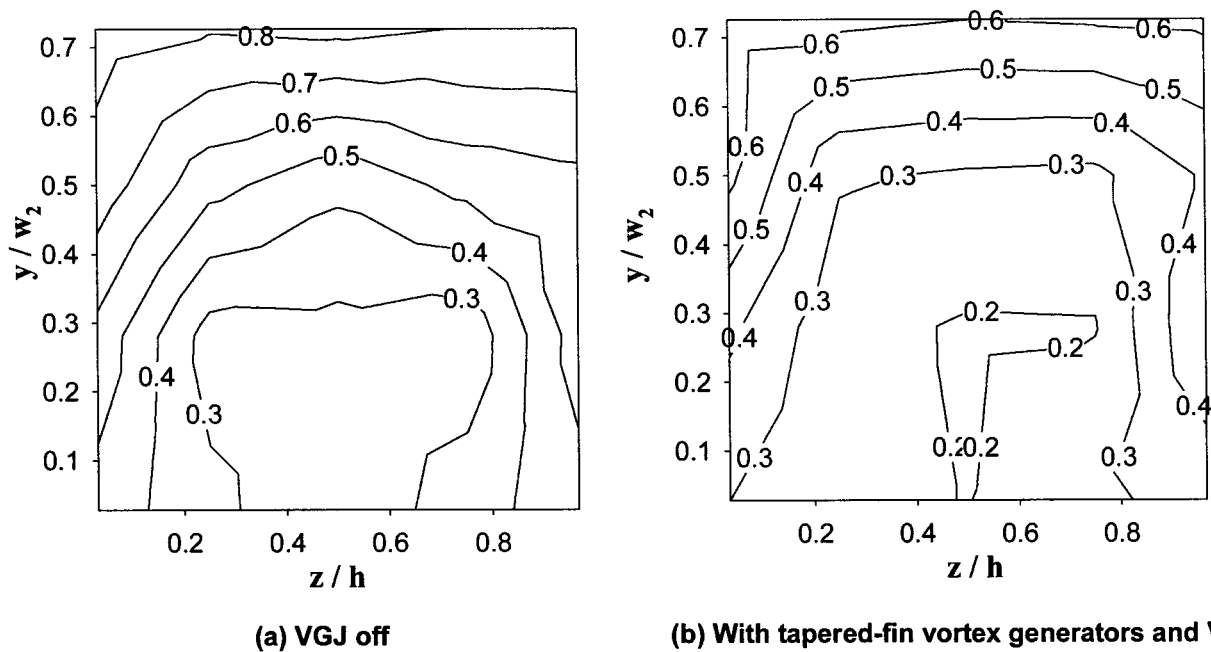


Fig. 8 Total pressure loss coefficient contours without and with tapered-fin vortex generators in distorted inflow

uniform and distorted inflow. Substantial improvement in performance was achieved by the use of VGJs. The method can also have potential applications in secondary flow control in turbo machinery. For uniform inflow in *S*-duct diffusers, use of vortex generator jets results in more than a 30 percent decrease in total pressure loss and flow distortion coefficients. Similar improvement in mass averaged static pressure recovery was observed. The performance improvement achieved using VGJs were higher than that when tapered fin vortex generators were used alone.

The effectiveness of the VGJs was observed to be reduced when used in a distorted inflow situation due to the presence of flow separation. The mass averaged total pressure loss coefficient was reduced marginally by around 8 percent and the reduction in distortion coefficient by around 5 percent. However, the VGJs gave a slightly better performance compared to tapered fin vortex generators. The improvement in performance of the diffuser in both uniform and distorted inflow situation was due to the effective reduction in secondary flows by VGJs.

Table 4 Summary of results with tapered-fin vortex generators

Exit flow property	Diffuser with distorted inflow	Diffuser with VGJ	Diffuser with tapered fin vortex generators on outer wall
Mass averaged C_p	0.297	0.311	0.344
D_c	0.851	0.809	0.742
$\bar{\omega}$	0.395	0.363	0.278

Table 5 Boundary layer momentum thickness at diffuser exit

Boundary layer momentum thickness (as percentage of diffuser inlet width)	Diffuser with uniform flow		Diffuser with distorted inflow		Diffuser with VGJ and tapered fin vortex generators
	Diffuser with uniform flow	Diffuser with VGJ	Diffuser with distorted inflow	Diffuser with VGJ	
Inner wall	2.81	2.41	3.10	2.71	2.54
Outer wall	1.37	0.72	1.47	0.79	0.70

In combination with passive device (tapered fin vortex generators), the vortex generator jets reduce total pressure losses by about 25 percent for distorted inflow conditions. The application of tapered-fin vortex generators for separation control along with VGJs for secondary flow control thus results in substantially higher performance than that obtained with the use of tapered-fin vortex generators alone.

Nomenclature

- AR = area ratio of the diffuser
- C_p = pressure coefficient = $(p - p_{ref})(\dot{m}_d + \dot{m}_j) / (1/2 \rho V_d^2 \dot{m}_d + 1/2 \rho V_j^2 \dot{m}_j)$
- C_f = skin friction coefficient
- D_c = distortion coefficient = $(p_{oav} - p_{omin}) / q_{av2}$
- R = duct centerline radius of curvature
- Re = Reynolds number based on inlet diffuser width
- V = fluid velocity
- VR = jet to freestream velocity ratio
- \dot{m} = mass flow rate
- ϕ = pitch angle of the vortex generator jet
- θ = skew angle of the vortex generator jet
- $\bar{\omega}$ = average total pressure loss coefficient = $(p_{o1} - p_{o2av}) / (1/2 \rho V_\infty^2)$
- ρ = fluid density
- h = diffuser height (constant)
- l = duct centerline length
- p = static pressure
- p_o = total pressure
- q = dynamic head
- r = inlet half width
- s = distance along the duct centerline from diffuser inlet
- w = diffuser width
- y = distance along duct centerline radius from inner wall of the diffuser
- z = distance along diffuser height from the bottom of the diffuser
- R/r = diffuser radius ratio

Subscripts

- av = average value
 d = diffuser
 j = jet
max = maximum value
min = minimum value
ref = inlet plane (reference)
1,2 = notations for inlet and exit planes
 ∞ = free stream value at inlet plane
 o = total pressure

References

- [1] Guo, R. W., and Seddon, J., 1983, "The Swirl in an S-duct of Typical Intake Proportions," *Aeronaut. Q.*, **34**, pp. 99–129.
- [2] Wendt, B. J., and Reichert, B. A., 1996, "Vortex Ingestion in a Diffusing S-duct Inlet," *J. Aircr.*, **33**, pp. 149–154.
- [3] Sullerey, R. K., and Mishra, S., 2000, "Performance Improvement of S-duct Diffusers with Boundary Layer Fences," FEDSM2000-11240, Proceedings of 2000 ASME Fluids Engineering Conference, Boston, USA.
- [4] Reichert, B. A., and Wendt, B. J., 1993, "Experimental Investigation of S-duct Flow Control using Arrays of Low Profile Vortex Generator," AIAA Paper 93-0018.
- [5] Reichert, B. A., and Wendt, B. J., 1994, "Improving Diffusing S-duct Performance by Secondary Flow Control," NASA Technical Memorandum 106492.
- [6] Reichert, B. A., and Wendt, B. J., 1996, "Improving Curved Subsonic Diffuser Performance with Vortex Generators," *AIAA J.*, **34**, pp. 65–72.
- [7] Lakshminarayana, B., 1996, *Fluid Dynamics and Heat Transfer of Turbomachinery*, John Wiley and Sons Inc., New York, 1st edition, pp. 322–328, Chap. 4.
- [8] Foster, J., Wendt, B. J., Reichert, B. A., and Okiishi, T. H., 1997, "Flow Through a Rectangular-to-Semi-Annular Diffusing Transition Duct," *Journal of Propulsion and Power*, **13**, pp. 312–317.
- [9] Sullerey, R. K., Mishra, S., and Pradeep, A. M., 2002, "Application of Boundary Layer Fences and Vortex Generators in Improving the Performance of S-duct Diffusers," *ASME J. Fluids Eng.*, **124**, pp. 136–142.
- [10] Sullerey, R. K., and Pradeep, A. M., 2001, "Effect of Flow Distortion on S-duct Diffuser Performance," FEDSM2001-18152, Proceedings of 2001 ASME Fluids Engineering Conference, New Orleans, Louisiana, U.S.A.
- [11] Sullerey, R. K., and Pradeep, A. M., 2002, "Effectiveness of Flow Control Devices on S-duct Diffuser Performance in the Presence of Inflow Distortion," *ASME J. Turbomach.*, **19**, pp. 259–270.
- [12] Shih, T. I.-P., and Lin, Y.-L., 2003, "Controlling Secondary-Flow Structure by Leading-Edge Airfoil Fillet and Inlet Swirl to Reduce Aerodynamic Loss and Surface Heat Transfer," *ASME J. Turbomach.*, **125**, pp. 48–56.
- [13] Ball, W. H., 1985, "Tests of Wall Suction and Blowing in Highly Offset Diffusers," *J. Aircr.*, **22**, pp. 161–167.
- [14] Kwong, A. H. M., and Dowling, A. P., 1994, "Active Boundary-Layer Control in Diffusers," *AIAA J.*, **32**, pp. 2409–2414.
- [15] Johnston, J. P., and Nishi, M., 1990, "Vortex Generator Jets—Means for Flow Separation Control," *AIAA J.*, **28**, pp. 989–994.
- [16] Innes, F., Pearcey, H. H., and Sykes, D. M., 1995, "Improvements in the Performance of a Three Element High Lift System by the Application of AirJet Vortex Generators," *Aeronaut. J.*, **99**, pp. 265–274.
- [17] Khan, Z. U., and Johnston, J. P., 2000, "On Vortex Generating Jets," *Int. J. Heat Fluid Flow*, **21**, 506–511.
- [18] Johnston, J. P., 1999, "Pitched and Skewed Vortex Generator Jets for Control of Turbulent Boundary Layer Separation: A Review," FEDSM99-6917, Proceedings of 3rd ASME/JSME Joint Fluids Engineering Conference, San Francisco, California, USA.
- [19] Sullerey, R. K., and Pradeep, A. M., 2003, "Secondary Flows and Separation in S-duct Diffusers—Their Detection and Control," FEDSM2003-45109, Proceedings of the 4th ASME/JSME Joint Fluids Engineering Conference, Honolulu, Hawaii, USA.
- [20] Patel, V. C., 1965, "Calibration of the Preston Tube and Limitations on its Use in Pressure Gradients," *J. Fluid Mech.*, **23**, pp. 185–208.
- [21] Vagt, J. D., and Fernholz, H., 1973, "Use of Surface Fences to Measure Wall Shear Stress in Three-Dimensional Boundary Layers," *Aeronaut. Q.*, **24**, pp. 87–91.
- [22] Frei, D., and Thomann, H., 1980, "Direct measurements of skin friction in a turbulent boundary layer with a strong adverse pressure gradient," *J. Fluid Mech.*, **101**, pp. 79–95.
- [23] Ohman, L. H., and Nguyen, V. D., 1993, "Applications of the Five Hole Probe Technique for Flow Field Surveys at the Institute for Aerospace Research," Proceedings of the AGARD Meeting on Wall Interference, Support Interference and Flow Field Measurements.
- [24] Nowak, C. F. R., 1970, "Improved Calibration Method for a Five-Hole Spherical Pitot Probe," *Journal of Physics*, Sec. E3, No. 1–2, p. 21.
- [25] Abernethy, R. B., Benedict, R. P., and Dowell, R. B., 1985, "ASME Measurement Uncertainty," *ASME J. Fluids Eng.*, **107**, pp. 161–164.
- [26] Moffat, R. J., 1985, "Using Uncertainty Analysis in the Planning of an Experiment," *ASME J. Fluids Eng.*, **107**, pp. 173–180.
- [27] Kline, S. J., 1985, "The Purposes of Uncertainty Analysis," *ASME J. Fluids Eng.*, **107**, pp. 153–160.
- [28] Steves, S. J., Nayak, U. S. L., Preston, J. F., Robinson, P. J., and Scrivener, C. T. J., 1978, "Influence of Compressor Exit Conditions on Diffuser Performance," *J. Aircr.*, **15**, pp. 482–488.

The Design of a New Flow Meter for Pipes Based on the Drag Force Exerted on a Cylinder in Cross Flow (Drag Force Flow Meter: DFFM)

C. Ruppel

e-mail: ruppel@lstm.ruhr-uni-bochum.de

T. Funke

F. Peters*

e-mail: peters@lstm.ruhr-uni-bochum.de

Fluid Mechanics, Ruhr-University Bochum,
44780 Bochum, Germany

It is shown how to design a new method (DFFM) of flow metering in pipes from basic principles. The method relies on the well known drag force on a cylindrical body and the force measurement by a load cell. The drag force is exclusively measured in the axial flow direction, the only one that contributes to the flow rate. That way disturbing tangential swirl components which do not contribute remain unconsidered. By means of an upstream screen the meter is desensitized to disturbing axial velocity profile distortions. Testing with various installations demonstrates the main features and the error bar to be expected. [DOI: 10.1115/1.1779665]

1 Introduction

Commonly engineering faces either of two situations. In the first one a mechanism, an instrument, a design or else has come into existence one way or another and needs to be analyzed and understood before changes or improvements can be made. In the second one, typically when engineering capacity and theoretical knowledge is affluent, the procedure can be turned around in order to design something from scratch to the requirement of the user and the satisfaction of the engineer.

In pipe flow metering the first situation is likely to be encountered. A large number of instruments exists the underlying fluid mechanics of which are hardly understood. Most often much effort is made in calibration and signal processing while the analysis of flow characteristics is neglected. For example, the orifice has been in use for many decades on basis of a compilation of calibration data laid down in DIN 1952 while the understanding of the flow is poor and often done away with Bernoulli's equation. Other examples are the vortex meter or the rotameter (Baker [1]). With an increasing demand for more meter accuracy in the gas and petroleum industry research has become necessary to improve existing instruments for non-ideal installation situations. It has become a widely held view that substantial progress can be achieved through a better understanding of the interaction of the upstream flow and the meter. There is more potential in eliminating the ambiguity of this interaction than in the refinement of the meter itself. The vanishing point of this development is the "intelligent meter" (Wildemann et al. [2]) which would recognize the upstream flow situation and correct for it.

In this paper we do not want to struggle with the fluid mechanics of an existing instrument, we would rather like to go the other way showing how to design a meter from scratch including the upstream installation problem from the beginning. Looking for a measuring principle (Ruppel and Peters [3]) we observed that the force is hardly used among the numerous measured quantities like length (rotameter), time (ultrasound), frequency (vortex meter), pressure (orifice, Venturi) or electrical potential (electromagnetic

flow meters). At the same time force measurement is not at all unusual in fluid mechanics, especially aerodynamics, although forces can be small e.g. in the Newton range.

We choose a thin bar (a cylinder in this investigation) mounted radially from wall to wall in a pipe's cross section and record its drag force which is a measure for the velocity. Normal flow past a cylinder is one of the most fundamental flow cases quoted as the drag coefficient vs Reynolds number plot in most fluid mechanics text books (Schlichting [4]). We have to take into account though that the cylinder collects a velocity profile along the radius rather than a uniform velocity. We also have to consider that in real situations the profile may not be rotationally symmetric and that the flow may be disturbed in the way of swirl. These problems are successfully solved by an upstream screen that flattens the profile and by the way the cylinder is mounted which excludes swirl from entering the measurement.

Due to expense of time and material the experimental part of the following could only be a case study for gas in a 150 mm i.d. pipe featuring an 8 mm cylinder. Yet, similarity is based on Reynolds number and Dean number which lie in a realistic range. In principle the extension to liquids should be feasible and worthwhile.

2 Measuring Principle

We divide the description of the measuring principle into two parts. The first part deals with the problem how the flow exerts a force onto the cylinder and how this force relates to the flow rate. The second part shows how this force is properly measured.

2.1 Flow Rate and Drag Force. A body in a uniform stream of velocity u and fluid density ρ experiences a drag force which is proportional to ρ , the projection area A in flow direction and the square of the velocity. The proportionality coefficient, called drag coefficient c_D , depends on the Reynolds number Re

$$c_D = c_D(Re) \quad (1)$$

$$Re = \frac{u \cdot d_{cyl}}{\nu} \quad (2)$$

based on the dynamic viscosity ν and a characteristic length of the body which is the cylinder diameter d_{cyl} in our case. The most frequently quoted data on $c_D(Re)$ of a cylinder are those by Wieselsberger [5,6] reproduced in Fig. 1.

*Corresponding author.

Contributed by the Fluids Engineering Division for publication in the JOURNAL OF FLUIDS ENGINEERING. Manuscript received by the Fluids Engineering Division June 3, 2003; revised manuscript received February 17, 2004. Associate Editor: J. Lee.

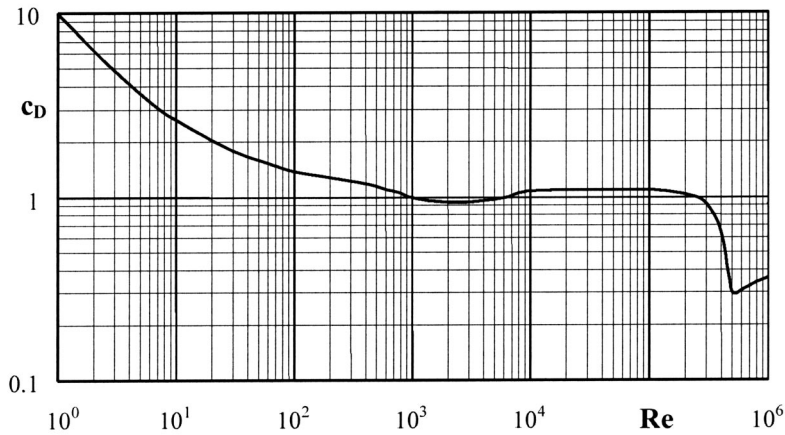


Fig. 1 Drag coefficient of a cylinder as function of Reynolds number from Wieselsberger [5,6]

When the cylinder is mounted radially across the pipe as shown in Fig. 2 flow direction and magnitude at the cylinder will in general depend on the radius r and the angle φ . In well defined cases such as developed laminar flow, developed turbulent flow and uniform flow (square profile) the flow remains normal to the cylinder in pipe direction and the velocity is merely a function of the radius. In general, reality differs considerably from these flow patterns, yet they lend themselves for reference purposes. In reality the profiles show distorted shapes and swirl occurs superposed to the main flow not to speak of large scale turbulence which may add time dependence. A key benefit of our design is that we do not need to worry about the swirl component from the beginning. The way the beam is mounted (see below) only the force in pipe direction is measured meaning that only flow in pipe direction is recorded which is exactly the one that contributes to the flow rate.

Velocity and Reynolds number along the cylinder at a fixed angle φ are now functions of the radius

$$Re(r) = \frac{u(r) \cdot d_{cyl}}{\nu} \quad (3)$$

so that the drag coefficient has to be written in the form

$$c_D = c_D(Re(r)) \quad (4)$$

yielding the total force F on the cylinder in flow direction ($D=2R$)

$$F = \frac{1}{2} \cdot \rho \cdot d_{cyl} \cdot \int_{-R}^R c_D(Re(r)) \cdot u^2(r) dr. \quad (5)$$

In the simple reference case of the square profile with uniform velocity u_m the force reduces to

$$F_{sq} = \rho \cdot c_D(Re_m) \cdot d_{cyl} \cdot R \cdot u_m^2. \quad (6)$$

Using this reference force F_{sq} for scaling the general force of Eq. (5) we have

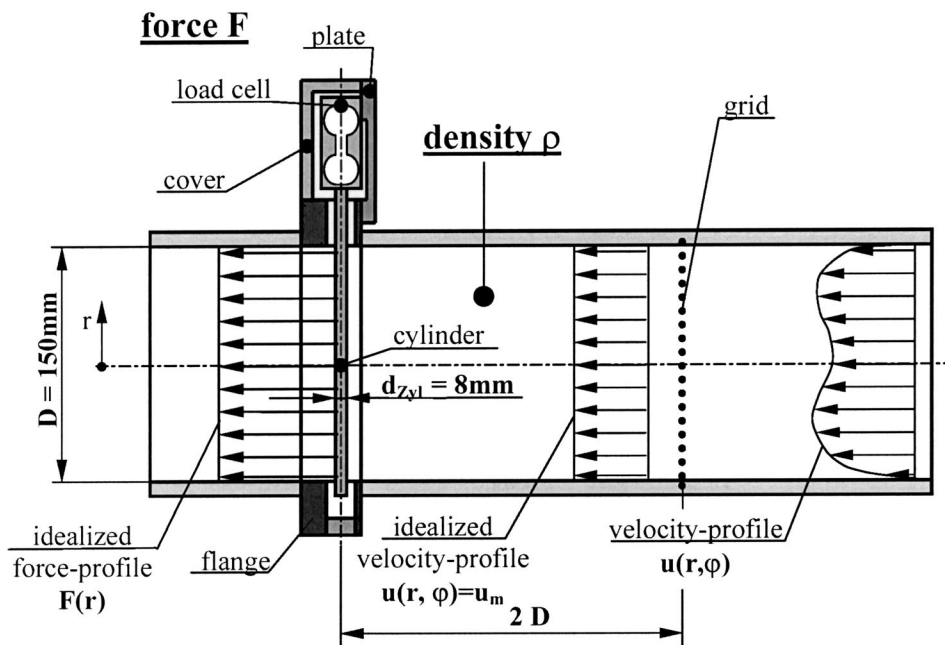


Fig. 2 Working principle of the Drag Force Flow Meter (DFFM)

$$\frac{F}{F_{sq}} = \frac{1}{2} \int_{-1}^1 \frac{c_D(\text{Re}(r)) \cdot u^2(r)}{c_D(\text{Re}_m) \cdot u_m^2} d\frac{r}{R}. \quad (7)$$

We now interpret the integral as a shape factor f

$$f = \frac{1}{2} \int_{-1}^1 \frac{c_D(\text{Re}(r)) \cdot u^2(r)}{c_D(\text{Re}_m) \cdot u_m^2} d\frac{r}{R}. \quad (8)$$

The shape factor is a measure for the deviation of the real profile with respect to the reference square profile including the influence of a variable drag coefficient along the cylinder.

Figure 1 teaches that the drag coefficient is approximately constant over a wide range of Reynolds numbers which is limited by very small ($\text{Re} < 500$) and very large Reynolds numbers ($\text{Re} > 2 \cdot 10^5$). Reynolds numbers $> 2 \cdot 10^5$ are not envisaged in our design. Reynolds numbers down to zero are present in the wall boundary layer, yet the contribution of this range is very small anyhow. Therefore we approximate

$$c_D(\text{Re}(r)) \approx c_D(\text{Re}_m). \quad (9)$$

With this approximation the shape factor can readily be calculated for known profiles. For the parabolic laminar profile we find $f = 2.13$ independent of Reynolds number, which means that the laminar profile more than doubles the force as compared to the square one. This shows the dominant influence of the squared velocity in a peaked profile.

The shape factor of the developed turbulent profile exhibits a slight dependence on pipe Reynolds number Re_D as Table 1 shows. For the calculation the profile given by Gersten and Herwig [7] was used.

Table 1 Shape factor f for developed turbulent profiles for various pipe flow Reynolds numbers Re_D

$\text{Re}_D = u_m \cdot D / \nu$	shape factor f turbulent profile
50,000	1.170
100,000	1.158
150,000	1.151
200,000	1.146
250,000	1.142

In order to express the mass flux \dot{m} as function of the force F we eliminate u_m from Eq. (6) and in the resulting equation replace F_{sq} by means of (F/f) from Eqs. (7,8). Then multiplication with the density ρ and the pipe area $R^2 \pi$ yields

$$\dot{m} = \frac{1}{\sqrt{c_D(\text{Re}_m)} \cdot f} \cdot \sqrt{\frac{R^3 \cdot \pi^2}{d_{cyl}}} \cdot \sqrt{F \cdot \rho}. \quad (10)$$

Here the force is the measured quantity. The density is either known or measured through temperature and pressure for a gas. Pipe and cylinder diameter are given. The drag coefficient is close to 1 (Fig. 1). The crucial parameter is the form factor f . It is only known when the profile is ideal (Table 1) or measured which, of course, would save the flow meter. Our answer to the real, distorted profile is a wire screen placed upstream of the cylinder. Such a screen produces relatively small pressure losses and needs little space. It has a smoothing and equilibrating effect on upstream profile distortions such that the downstream profile ap-

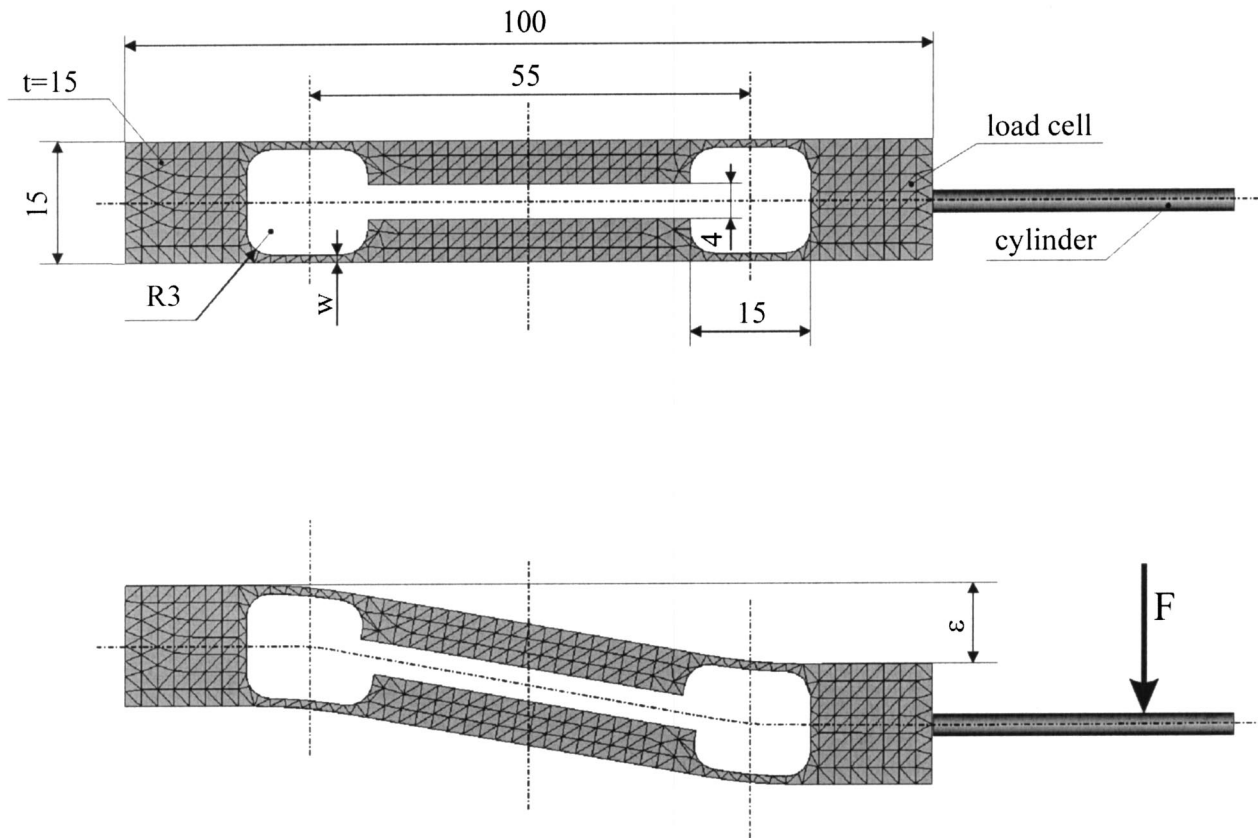


Fig. 3 FEM-designed load cell with (bottom) and without load (top)

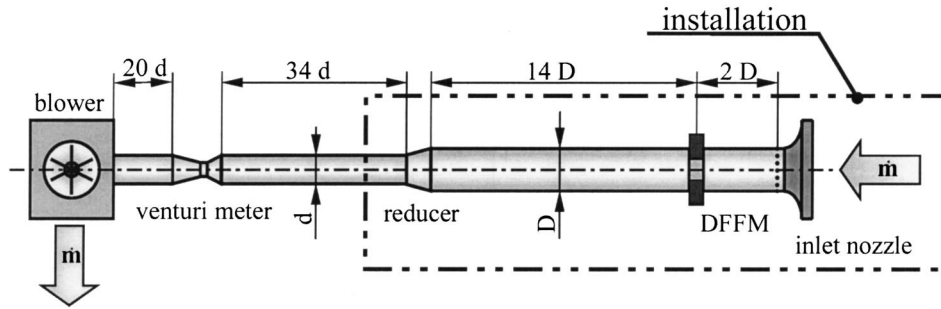


Fig. 4 Calibration set-up indicating installation range

proaches the square shape. In contrast to the flow straightener it has little impact on the swirl which we are not concerned about anyhow. Squaring the profile the screen pushes the shape factor f closer to one without reaching it, of course. It gets close enough though, so that Eq. (10) is suitable for the design process of the meter which will normally start with the range of \dot{m} required by the user for a given pipe of radius R . The cylinder ought to be much smaller than the pipe, $d_{cyl} \ll D$. With the product of c_D and f close to one the force F on the cylinder follows for known density. F then determines the design of the load cell.

After the design has been completed and the load cell has been made calibration of \dot{m} vs $F \cdot \rho$ according to Eq. (10) in a reference situation becomes inevitable to accomplish high accuracy. We'll go through these steps further down concluding with an investigation on the sensitivity to installations.

2.2 Drag Force and Load Cell. The fluid force on the cylinder is an integrated load with varying load distribution. To measure this load independent of the distribution a load cell as shown in Fig. 3 is suitable. Kinematically the four thin portions of the cell constitute the joints of a parallelogram. The front part with the attached cylinder moves under load parallel to the rear part fixed to a rigid base such that the attached cylinder remains in radial direction in the pipe. At the same time the thin portions flex like

leaf springs transforming the acting force into deformation. The deformation can be measured by strain gauges or optical displacement sensors (or others).

Our goal is the design of the entire meter. Therefore, as an example, we selected material (aluminum 7075 T7351) and shape of a particular load cell as given in Fig. 3. All measures but the wall thickness w of the flexible joints were fixed. This given configuration was fed into a FEM program to calculate the displacement of the cylinder as function of the load for various wall thicknesses. The calculated results were checked versus a simple measurement in which the load was simulated by weights and the displacement was measured by an optical gauge (optoNCDT by Micro-Epsilon). Excellent agreement within $\pm 2.5\%$ was found. The outcome of this investigation is the following formula

$$\varepsilon w^{2.7935} = 0.0982 F. \quad (11)$$

It relates the wall thickness w in mm, the displacement ε in mm and the force F in Newton. Most importantly, a linear relationship between force and displacement is achieved. In the design process the maximum force will be known from the flow rate as described above. A corresponding maximum displacement has to be chosen according to the type of length measurement available (strain gauges, optical devices or others). Then Eq. (11) delivers the

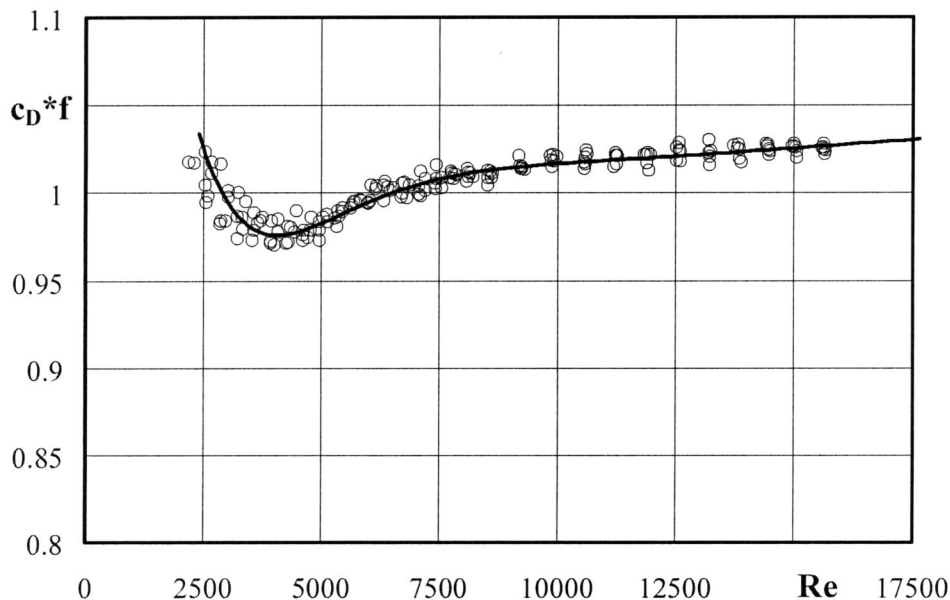


Fig. 5 Calibration curve

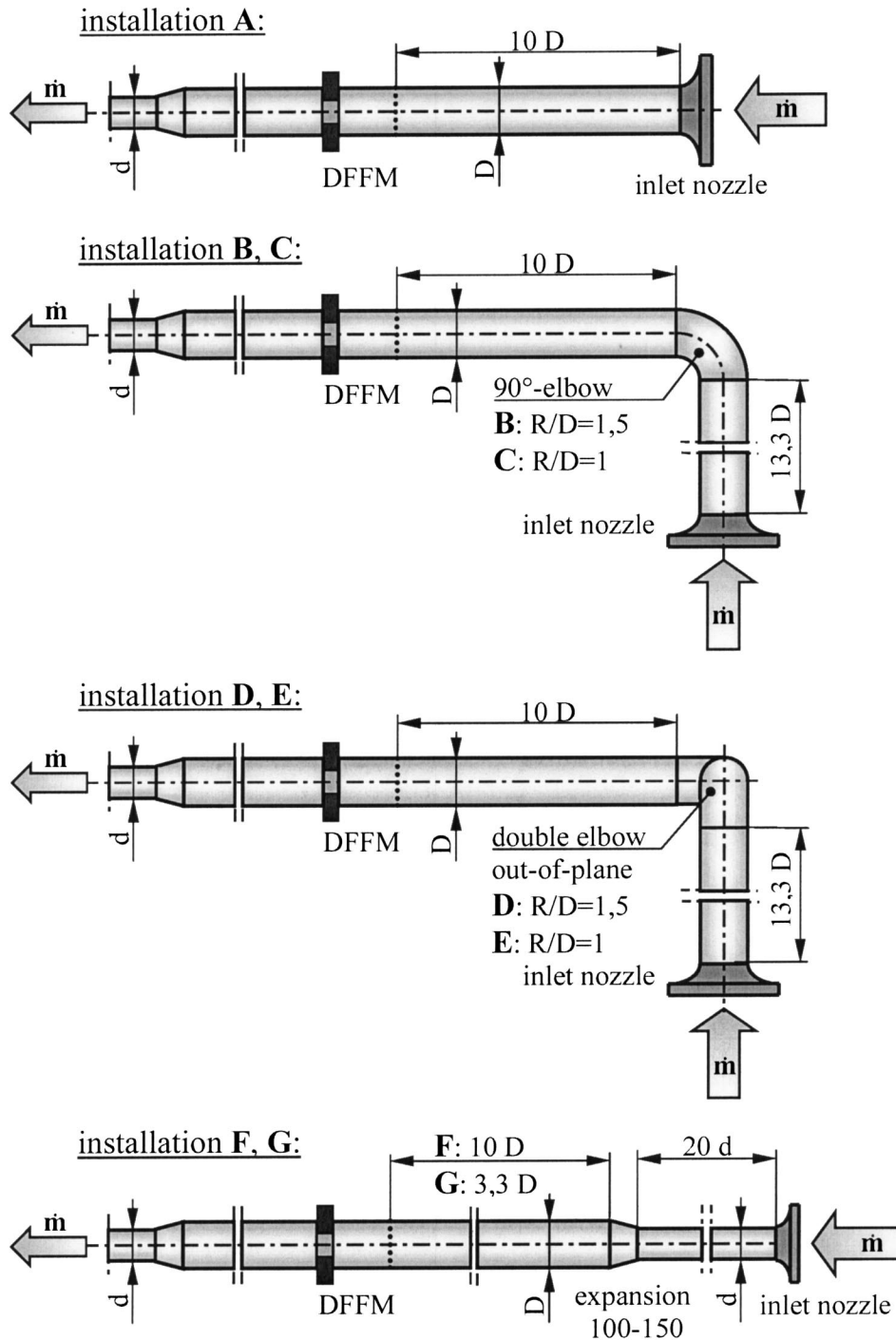


Fig. 6 The investigated installations

thickness w , which of course is bound by upper and lower limits. The lower limit is set by machining and the upper limit by the condition that the flexible joint needs to be thin relative to the side-pieces of the cell. The range $0,5 \text{ mm} < w < 1,5 \text{ mm}$ was found reasonable for the test design.

Please note that this test design was just to show the designability of the load cell. The ranges of measures and forces have to be tuned to the application.

3 Set-Up and Calibration

Figure 4 illustrates the basic set-up in the calibration mode. An air blower driven by a frequency controlled AC motor circulates

room air through a pipe system (precision pipes DIN 2391). Air enters the test pipe of $D=150 \text{ mm}$ i.d. through a nozzle and a wire screen of 1 mm wire and 3 mm mesh size. The pipe is segmented and assembled by flanges (not shown) to allow variable configurations of pipe and installations including the DFFM and the screen which are integrated into flanges themselves. The big pipe reduces to a smaller one of $d=100 \text{ mm}$ i.d. which incorporates a Venturi meter $20 d$ upstream of the blower. The Venturi provides the mass flux reference after careful calibration against another reference placed downstream of the blower described elsewhere [8]. The DFFM is fitted with a 8 mm cylinder of carbon fibre laminate for best stiffness to mass ratio. The displacement was to

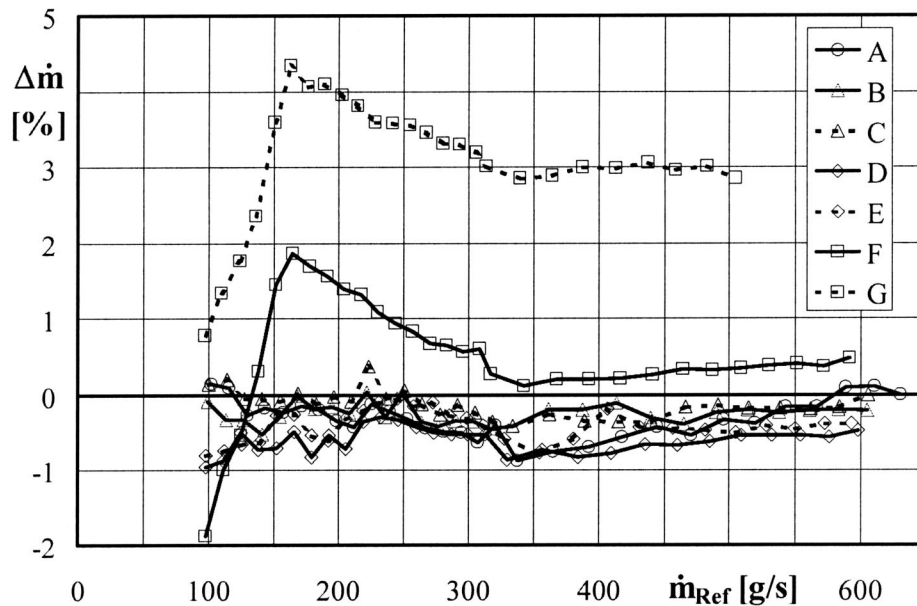


Fig. 7 Relative deviation of the mass flux measured by the DFFM versus the reference mass flux for the installations of Fig. 6

be measured by an integrated strain gauge because we were not able to integrate the optical device mentioned earlier into the flange. A commercial load cell (PW4FC3 by HBM) of the type tested in Section 2 was purchased in one piece with the strain gauge and an appropriate amplifier (BA 651 by BLH).

Data acquisition is by a National Instruments A/D card “PCI-6024E” in combination with the LabView 6i software. Besides the force temperature and pressure in the pipe are recorded at the sampling rate of 10^4 s^{-1} . Due to an eigen vibration of the bar/cell arrangement of the order of 200 Hz a mean value of the force has to be taken. In order to do so the integration time should not drop below 0.1 s. The LabView program views the recorded data including the reference mass flux from the Venturi.

The calibration procedure is as follows. Starting from $u_m = 3.5 \text{ m/s}$ mean velocity in the big pipe the blower motor frequency is risen stepwise up to the mean pipe velocity of about 32 m/s. For each step ρ is determined from p and T (including relative humidity) and F is measured. The reference mass flux \dot{m} is obtained from the Venturi. This information together with Eq. (10) yields the calibration diagram Fig. 5 displaying $c_D \cdot f$ versus Re . As c_D is close to one (see Fig. 1 and discussion) the message drawn from this plot is that f in fact comes close to one too meaning that the screen provides an approximately square profile at least in this calibration arrangement right downstream of a rounded inlet nozzle. Of course, the residual Reynolds number dependence must be taken into account. The relationship

$$c_D f = 0.64 \exp(-64 \cdot 10^{-5} Re) \cos(-535 \cdot 10^{-6} Re - 0.05) + 1.91 \cdot 10^{-6} Re + 0.997 \quad (12)$$

fits the data quite well constituting the analytical calibration curve of this particular DFFM. With the help of Eq. (10) it transforms into the mass flux vs force relationship.

With respect to accuracy it is important to distinguish between the accuracy of \dot{m} obtained from Eq. (10) and the accuracy achievable in disturbed flow. After calibration the first one depends only on the measurement accuracy of force and density. For example, when either force and density are uncertain to $\pm 1\%$ the mass flux is uncertain to only $\pm 0.7\%$. This is a result of the law of error propagation. The actual uncertainties depend strongly on the

effort spent. We were sure to get the density by temperature and pressure measurements to within $\pm 0.5\%$ and the force to within $\pm 0.2\%$.

The second one concerns the performance of the meter when exposed to (disturbed) installation flows different from the calibration situation. This is the subject of the next section.

4 Results for Installations

A calibrated DFFM exposed to any square velocity profile in the adequate range will be accurate within a small margin of reproducibility. Obviously, it is not possible to predict the efficiency of the screen for any installed upstream disturbance. As a consequence typical installation situations have to be tested before a reliable error prediction can be made.

Figure 6 compiles seven variants covering quite common installations and an extreme one. The common ones are the inlet nozzle with 10D of straight pipe (A), two regular elbow bends (B,C) and two double bends (D,E). A pipe expansion (F,G) opening from 100 to 150 mm i.d. on a short distance of 3.3 D introduces flow separation, an undoubtedly extreme disturbance bound to lead to substantial indication errors of most any meter placed close to it.

Results are compiled in Fig. 7. The relative deviation of the DFFM in terms of

$$\Delta \dot{m} = \frac{\dot{m}_{\text{DFFM}} - \dot{m}_{\text{ref}}}{\dot{m}_{\text{ref}}} 100 \quad (13)$$

is plotted versus the reference mass flux. The covered range of mass fluxes corresponds to mean velocities in the big pipe from 5 to 28 m/s.

When $\Delta \dot{m} > 0$ the DFFM overpredicts the flow rate and the other way round for $\Delta \dot{m} < 0$. The first five installations show consistent negative deviations with some scatter. In view of the shape factor discussion the consistency suggests that in all these cases the profile tends to be somewhat “flatter” than in the calibration case.

Elbow and double elbow produce strong disturbances which are described by Hilgenstock and Ernst [9]. Generally, the main problem of the disturbance is swirl which is known to decay slowly (Schlüter and Merzkirch [10]). Here the DFFM is in the advanta-

geous position that it is not affected by radial and tangential velocity components as already explained in Section 2.2. What remains is a moderate dent in the profile which is dealt with by the screen and, to some extent, by the 10D of pipe length. In sum, the installations lead to deviations from the calibration arrangement, yet, it must be emphasized that the deviation stays within a percent! Furthermore the deviation exhibits a systematic character which could be corrected for.

The pipe expansion of installation F, G produces substantial positive deviations. Certainly, it is not recommendable to place a DFFM (or any other instrument) into such a position. We have included these installations just to show how well the deviations of a DFFM can be interpreted. The diffusor angle of the expansion enforces flow separation with high velocities on the center of the pipe and low ones in the separated region (or even negative). The profile will be extremely peaked entailing large positive deviation up to 4% in case G. In the other case F with the DFFM moved downstream the flow seems to be reattached with a broader profile and correspondingly smaller deviations down to half a percent for the higher flow rates.

5 Conclusions

We have shown how to design a flow meter for the mass flux in pipes from scratch. The design is based on fundamental fluid mechanics (flow past a cylinder) and a well understood type of load cell. The load cell determines the force on the cylinder which is an accurate measure of the flow rate when the velocity profile is known. As the profile is normally not known the DFFM generates its own profile by means of an upstream screen. This profile approximates the square one used for calibration. The deviation of the screen profile from the calibration profile causes the uncertainty of the measurement. Tangential and radial disturbances in the velocity distribution are eliminated by the meter from the beginning saving further consideration.

In a number of real installation situations different from the calibration situation we have demonstrated that the DFFM works very well. It shows an error bar of less than a percent with a consistent shift that can be rationalized so that accuracy could be even improved by corrections.

The elements of the meter allow refinements which should be looked at in further developments. Especially, the selection of the screen parameters has some potential. Worth mentioning is that two screens, upstream and downstream, would allow to reverse the flow direction.

In conclusion, the philosophy of the DFFM is to prevent flow disturbances from even entering the signal generation which then can be based on known mechanics.

Acknowledgment

This work was done in the research group "Fluid Mechanics of Flow Metering" funded by Deutsche Forschungsgemeinschaft.

References

- [1] Baker, R. C., 2000, "Flow Measurement Handbook," Cambridge University Press.
- [2] Wildemann, C., Merzkirch, W., and Gersten, K., 2002, "A Universal, Nonintrusive Method for Correcting the Reading of a Flow Meter in Pipe Flow Disturbed by Installation Effects," *J. Fluids Eng.*, **124**, pp. 650–656.
- [3] Ruppel, C., and Peters, F., 2001, "Messung des Massenstroms in Rohrleitungen durch die Widerstandskraft eines quer angeströmten Zylinders (DFFM-Methode)," *tm-Technisches Messen*, **68**, pp. 465–472.
- [4] Schlichting, H., 1960, "Boundary Layer Theory," 4th ed. McGraw-Hill New York.
- [5] Wieselsberger, C., 1921, "Neuere Feststellungen über die Gesetze des Flüssigkeits- und Luftwiderstandes," *Physikalische Zeitschrift*, **22**, pp. 321–328.
- [6] Wieselsberger, C., 1922, "Weitere Feststellungen über die Gesetze des Flüssigkeits- und Luftwiderstandes," *Physikalische Zeitschrift*, **23**, pp. 219–224.
- [7] Gersten, K., and Herwig, H., 1992, "Strömungsmechanik," Vieweg-Verlag Wiesbaden.
- [8] Wildemann, C., 2000, "Ein System zur Automatischen Korrektur der Messabweichungen von Durchflussmessgeräten bei gestörter Anströmung," Dissertation, Universität Essen.
- [9] Hilgenstock, A., and Ernst, R., 1996, "Analysis of Installation Effects by Means of Computational Fluid Dynamics-CFD vs Experiments?" *Flow Meas. Instrum.*, **7**, pp. 161–171.
- [10] Schlüter, Th., and Merzkirch, W., 1996, "PIV Measurements of the Time-Averaged Flow Velocity Downstream of Flow Conditioners in a Pipeline," *Flow Meas. Instrum.*, **7**, pp. 173–179.

Momentum Flux in Plane, Parallel Jets

Robert E. Spall*

e-mail: spall@engineering.usu.edu

Elgin A. Anderson**

Jeffrey Allen***

Department of Mechanical and Aerospace
Engineering,
UMC 4130,
Utah State University,
Logan, UT 84322-4130

The evolution of the streamwise momentum flux for two turbulent, plane, parallel jets discharging through slots in a direction normal to a wall was studied both numerically and experimentally. The numerical results, obtained by solving the Reynolds-averaged Navier-Stokes equations employing a standard $k-\epsilon$ turbulence model, predicted to within experimental error measured integrals of the momentum flux downstream of the merge point for jet spacing $S/d=5$. Integration of the streamwise component of the Reynolds-averaged Navier-Stokes equations over a control volume results in an integral constant that was evaluated numerically for jet spacings $S/d=3, 5, 7, 9, \text{ and } 11$, and for different levels of turbulence kinetic energy and dissipation rate at the jet inlet boundaries. Results revealed that the integral constant is decreased as the jet spacing increases, and is also decreased as jet entrainment rates are increased due to higher levels of inlet turbulence kinetic energy, or alternatively, decreased levels of dissipation rate. Streamwise distance to the merge point was also found to decrease for increased levels of turbulence kinetic energy or decreased levels of dissipation rate at the jet inlet. [DOI: 10.1115/1.1778717]

Introduction

Single turbulent plane and offset wall jets have been studied extensively. This is due, in part, to the many practical applications of wall jets, including burners, boilers, film-cooling, fuel-injection, and heating and air conditioning systems, [1–3]. However, relatively few investigations into the properties of multiple plane, parallel jets appear in the literature. In addition to the applications mentioned above, the study of multiple jets may also be important in the design of pollutant exhaust stacks. Specifically, relative to a single exhaust stack, the close grouping of stacks to form parallel jets may be employed as a means to increase the exhaust plume trajectory and consequently decrease the impact of exhaust pollutants [4].

The earliest experimental studies of two plane, parallel wall jets were those of Tanaka [5,6] in which the basic flow patterns and entrainment mechanisms of parallel jets were described in terms of three distinct regions. The first was termed the converging region, which begins at the nozzle exit and extends to the point where the inside shear layers of the jets merge, which is termed the merge point. By definition, the velocity on the symmetry plane is zero at the merge point. The merging is due to the asymmetric nature of the entrainment rates of the individual jets, which leads to a region of low pressure between the jets. Downstream of the merge point an intermediate, or merging region, exists. This region extends to the combined point, which is defined as the point along the symmetry plane at which the velocity is a maximum. Finally, the combined region occurs downstream of the combined point. In this region the two jets begin to resemble a self-similar single jet. Tanaka's experimental results also showed that an integral constant, discussed further in the Results section, was nearly constant at any streamwise location [6].

The mixing between two parallel jets was investigated experimentally by Elbanna et al. [7]. Their results showed that the mean velocity profile of the parallel jets agreed well with the single jet in the region downstream of the combined point. Also, in that region the mean velocity decay matched that of a single jet. While

self-preservation for the mean flow was attained a short distance downstream from the combined point, the turbulent velocity fluctuation only became self-preserving much further downstream.

Lin and Sheu [8,9] used hot-wire anemometry to show that the mean velocity approaches self-preservation in both the merging and combined regions, while the Reynolds shear stresses approach self-preservation in the combined region only. Measurements also indicated that the entrainment and spreading rates in the combined region were greater than those in a single jet flow. This was attributed to significant increases in the values of lateral turbulence intensity and the Reynolds shear stress relative to a single jet.

Nasr and Lai [10] provide an experimental comparison between parallel, plane jets and an offset jet (where a wall replaces the symmetry plane). The interaction of the two shear layers on both sides of the symmetry plane resulted in a much more turbulent near-field for the parallel jet, relative to the offset jet. In addition, the recirculation zone was significantly smaller for the two jets than for the offset jet. In a later work Nasr and Lai [11] also performed an experimental investigation into the effect of jet spacing on the mean streamwise momentum flux measured at the combine point. They reported that the mean momentum flux decreases linearly with increased jet spacing.

Anderson and Spall [12] recently presented experimental and numerical results for isothermal, plane parallel jets at spacings $S/d=9, 13, \text{ and } 18.25$ (where S is the spacing between jet centerlines and d is the jet width, see Fig. 1). Values of the merge and combined points computed using both the standard $k-\epsilon$ and a differential Reynolds stress model were compared with experimentally measured values. Good agreement between numerical and experimental results was obtained. Furthermore, relatively small differences between the results of the two turbulence models were observed. Spall [13] extended the numerical work in Anderson and Spall [12] to include buoyant jets. The results indicated that, for heated jets, buoyancy effects and associated increases in entrainment resulted in a significant decrease in the streamwise distance to the merge point.

In the present work, the streamwise momentum flux of isothermal, parallel jet configurations is investigated both numerically and experimentally. Numerical and experimental results for components of an integral constant are compared for jet spacing $S/d=5$. Additional numerical results, in terms of merge points and the integral constant, are presented at higher Reynolds numbers for jet spacings ranging from 3 to 11. We also investigate the sensitivity of the numerical solutions, in terms of computed merge points and

*Member, ASME.

**Present Address: Lockheed Martin Missiles and Fire Control-Orlando 5600 Sand Lake Road, MP-605 Orlando, FL 32819-8907.

***Graduate Research Assistant.

Contributed by the Fluids Engineering Division for publication in the JOURNAL OF FLUIDS ENGINEERING. Manuscript received by the Fluids Engineering Division April 4, 2003; revised manuscript received February 13, 2004. Associate Editor: W. W. Copenhaver.

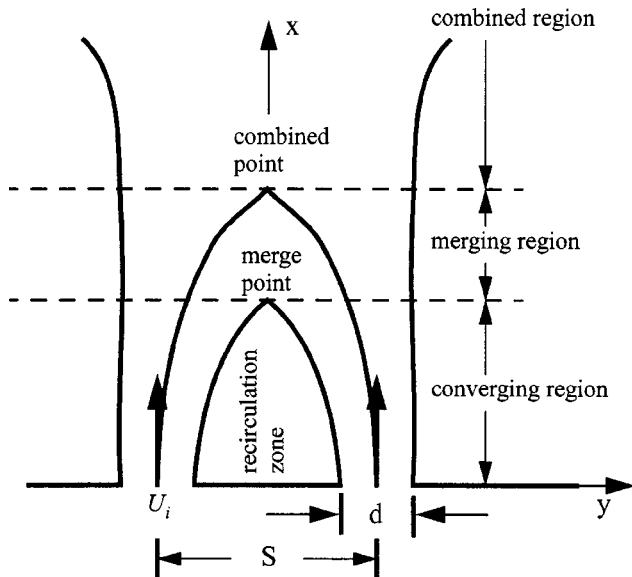


Fig. 1 Description of parallel jet flow field parameters and coordinate system

values of the integral constant, to the inlet jet boundary conditions on turbulence kinetic energy and dissipation rate when using a $k-\varepsilon$ model.

Numerical Procedure

The governing equations consist of the unsteady, incompressible Reynolds-averaged Navier-Stokes equations, and equations for turbulence closure. The equations were solved using the pressure-based, structured-grid, finite-volume code CFD-ACE (Version 4, CFD Research Corp., Huntsville, AL).

In the experimental work of Anderson et al. [14] it was shown, for sufficiently small jet spacings ($S/d < 2$), that unsteady flows may develop. Consequently, an unsteady numerical formulation was employed. However, over the range of S/d considered herein, integration of the governing equations in time, using a dimensionless time step ($U_i/d \Delta t = 1.0$ (where U_i is the jet inlet velocity), resulted in steady, time independent solutions.

Results presented in Anderson and Spall [12] revealed only small differences in the predicted merge point locations and mean profiles obtained using either $k-\varepsilon$ or differential Reynolds stress turbulence models. Consequently, for this study a $k-\varepsilon$ model was employed for turbulence closure. The empirical constants in the model were taken as $C_{\varepsilon 1} = 1.44$, $C_{\varepsilon 2} = 1.92$, $C_{\varepsilon 3} = 1.0$, $C_{\mu} = 0.09$, $\sigma_k = 1.0$, and $\sigma_{\varepsilon} = 1.3$.

Interpolation to cell faces for the convective terms was performed using a third-order Osher-Chakravarthy scheme (c.f., Yang and Przekwas [15]); second-order central differencing was used for the viscous terms; a first-order implicit Euler scheme was used for the temporal discretization. Pressure-velocity coupling was based on the SIMPLEX procedure. Calculations were carried out in time until a steady state was achieved.

Geometry and Boundary Conditions

The computational domain was defined by a rectangular region discretized using a cartesian grid covering the entire flow field. Symmetry boundary conditions along the plane midway between the jets were not employed in order to accommodate the possibility of unsteady, asymmetric oscillations in the jet flow patterns. The domain was bounded on the $x=0$ plane by a wall along which equilibrium wall functions were specified. Openings of width d in the wall defined the locations of the jet inlets over

which uniform velocity profiles were set. The inlets were placed to provide jet spacings $S/d = 3, 5, 7, 9$, and 11 , where S represents the spacing between jet centerlines.

Constant pressure conditions were specified on the lateral boundaries defined at $y/d = \pm 30$, while an outflow (zero normal derivative) boundary condition was specified at $x_{\max}/d = 80$. The authors also applied constant modified pressure boundary conditions at the outflow boundary, where the modified pressure is defined as $\bar{p} = p + 2/3 \rho k$. This condition can be justified by recognizing that beyond the combine point (where the flow is nearly a parallel shear flow) a higher-order version of the boundary-layer approximation to the transverse momentum equation may be written as $\partial/\partial y(p + \rho \overline{v'v'}) = 0$ (Ref. [16]). Far from the jet centerline, the turbulence quantities are negligible, and thus the modified pressure may be set to zero along the entire boundary at $x_{\max}/d = 80$. Results from the two approaches are essentially indistinguishable.

Finally, we note that results of numerical tests performed by doubling the extent of the domain in each direction for the $S/d = 9$ case are presented in the Results section. In essence, these results will confirm that the extent of the domain as described above is sufficient.

The relevant Reynolds number for the problem was defined as $Re = (\rho U_i d) / \mu$ (where ρ is the density, U_i the uniform jet inlet velocity, and μ is the dynamic viscosity). We note that results from previous studies indicates that the location of the merge and combine points are nearly independent of the Reynolds number (c.f., Ref. [17]).

Given the turbulence intensities (T_i) at the inlet, a uniform turbulence kinetic energy distribution was specified from the relation:

$$k = 1.5(U_i T_i)^2 \quad (1)$$

The dissipation rate inlet boundary condition was then specified as:

$$\varepsilon = C_{\mu}^{0.75} k^{1.5} / L \quad (2)$$

The turbulence length scale L was taken as $0.07d$, where the factor 0.07 is based on the maximum mixing length in a turbulent pipe flow. Of course, the dissipation rate as computed by Eq. (2) is no more than an estimate. Consequently, an examination of the sensitivity of the results to the specified values of inlet kinetic energy and dissipation rates is presented in the Results section.

By scaling k with U_i^2 and ε with U_i^3/d the dimensionless forms of Eqs. (1) and (2) are written as:

$$k = 1.5 T_i^2 \quad (3)$$

and

$$\varepsilon = C(k)^{3/2} \quad (4)$$

respectively, where $C = C_{\mu}^{0.75} / 0.07$ is a constant. Beginning with Eqs. (3) and (4), all variables presented are to be considered dimensionless except when units are included, or when referring to streamwise distances and jet spacings, where x/d and S/d , respectively, are used.

Five different grid resolutions were employed for the dual jet $S/d = 9$ case to assess grid convergence. These grids contained 149×200 , 229×300 , 299×400 , 299×600 , and 399×600 points, respectively. The number of grid points across each jet at the inlet ranged from 10 to 30. In all cases, cells were clustered laterally toward the jets, and toward the wall at $x/d = 0$. The results, which are presented in detail in a subsequent section, indicated that acceptable grid convergence was obtained using a 299×400 grid. Consequently, all other cases were computed on a 299×400 grid. The 299×400 grid used for the $S/d = 9$ case is shown in Fig. 2 where, for purposes of clarity, we have limited the plotting to every fourth grid line in each direction. To provide further per-

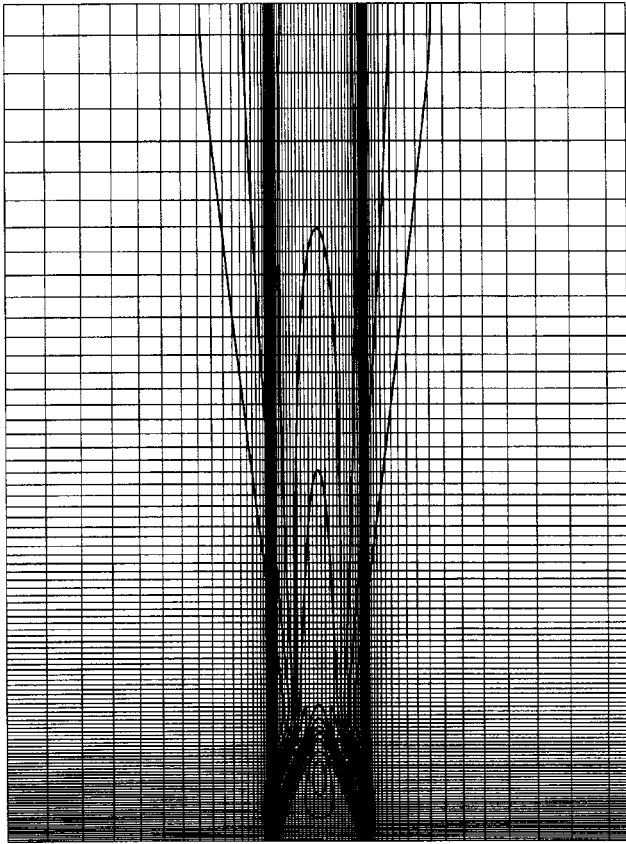


Fig. 2 Representative computational grid (299×400) with contours of velocity magnitude superimposed for the $S/d=9$ configuration at $Re=50,000$. For purposes of clarity, every fourth grid line is plotted in each direction.

spective on the grid clustering, contours of constant velocity magnitude for the $Re=50,000$ case presented in the Results section are also superimposed on the grid.

Experimental Procedure and Uncertainties

The schematic shown in Fig. 1 defines the relevant parameters for the parallel jet configuration. The origin of the two-dimensional coordinate system was oriented with the vertical axis intersecting the center of the nozzle plate. The jet nozzles had a width $d=0.318$ cm and a spanwise length of 20.32 cm giving a jet aspect ratio of 64. The spacing S was kept constant for all configurations at a value of 1.588 cm for a non-dimensional spacing parameter, $S/d=5$.

Flow was produced by a 1 HP blower controlled by a variable frequency drive. Jet nozzle slots were machined into 1.27 cm thick aluminum plate. Vertical end plates were positioned at the spanwise termination of each nozzle to enhance the two-dimensionality of the mean flow, and to minimize spanwise entrainment of ambient fluid. Two-dimensionality was confirmed by velocity surveys at the spanwise coordinates of $z=0.00$, and ± 1.27 cm that indicated negligible changes in the velocity statistics. An exit velocity of 18.4 m/s was selected giving a Reynolds number based on the jet nozzle width of approximately $Re=3600$. The streamwise turbulence intensity at the nozzle exit was approximately 1.0%.

A constant temperature anemometer system was incorporated with TSI ThermalPro software to acquire the velocity measurements. A single axis hot film probe was applied at the jet exit plane to obtain an estimate of the jet exit profile. A single axis probe was used here to maximize the transverse spatial resolution of the measurement. The design of two axis probes results in a

smearing of the velocity profile near the shear layers, and would produce a significant error in the momentum flux calculation in this region. The portions of the flow field downstream of the merge point were surveyed utilizing a two-axis (x -wire) probe. The probe was positioned by a computer controlled two-degree-of-freedom traverse with positioning accuracy of ± 0.01 mm.

The mean velocity and turbulent normal stress results presented in this study are based on an average of 2^{14} samples per data point acquired at a sample rate of 4000 Hz for a total sample period of 8.19 s. The sample rate was defined by the minimum sample rate beyond which the statistical quantities remain constant and repeatable. Calibration of the hot-wire probe was accomplished using a TSI Model 1129 automatic air velocity calibrator. The mean standard errors of the velocity calibration are as follows; <3% for velocities between 0–1 m/s, <1.5% for velocities between 1–8 m/s, and <0.5% for velocities greater than 9 m/s.

The exit momentum flux was calculated from the mean velocity profile measured a distance of 1 mm above the nozzle exits. The downstream values of the mean and turbulent momentum flux were calculated by integrating a theoretical curve fit of the experimental data at three streamwise positions, $x/d=32, 40$, and 48. The curve fit was required to remove the error introduced by the hot-film probe near the tails of the mean profiles. This error is caused by the presence of a transverse entrainment flow which produces a cooling velocity perpendicular to the axis of the probe which dominates near the tails of the mean profile. The consequence of this error is a streamwise mean velocity profile that does not decay to zero near the jet boundaries but instead maintains a constant plateau value. This effect is only of consequence near the jet boundaries. Therefore, a curve fit was produced based on the theoretically justified hyperbolic secant squared mean profile (Ref. [16]). A best fit was calculated to match the width and magnitude of the experimental profile. The theoretical profile decays to zero near the jet boundaries and therefore significantly reduces the error introduced by the hot film probe in that region. The resulting profile was integrated to determine the mean momentum flux. The accuracy of this method was confirmed by applying it to experimental data for the single jet case. As desired, the integration of the best fit theoretical profile at various downstream locations matched the momentum flux at the exit. The turbulent momentum flux was determined by direct integration of the streamwise normal Reynolds stress.

Momentum flux is an integrated quantity and therefore represented by a finite sum from experimental results. Each component of the sum has an uncertainty associated with it. We assume that the uncertainty in a particular component $U(i)$ is unrelated to the uncertainty in another component $U(i+1)$, i.e. independent, a typical and reasonable assumption. For such situations it is appropriate to sum the uncertainties in quadrature, i.e. root-sum-square method (Ref. [18]). It is not adequate to simply assume that the total uncertainty in a summation is the summation of the component uncertainties as this approach gives a unrealistically high uncertainty which approaches infinity as the number of components of the sum approaches infinity. The momentum flux uncertainty calculations were performed for each configuration. Each component of the summation has a specific uncertainty in length measurement, velocity measurement, and density measurement. Only the velocity measurement uncertainty varies from component to component since the length uncertainty is constant and, since we assume incompressible flow, the density uncertainty is constant. Using the root-sum-square method, the uncertainty in the experimental values of the total momentum flux was computed as 1.5%.

Results

In his experimental investigation of two-dimensional parallel jets, Tanaka [6] found that the spanwise integral of mean momentum, pressure and turbulence fluctuations was constant for all streamwise locations x/d . To derive an appropriate integral rela-

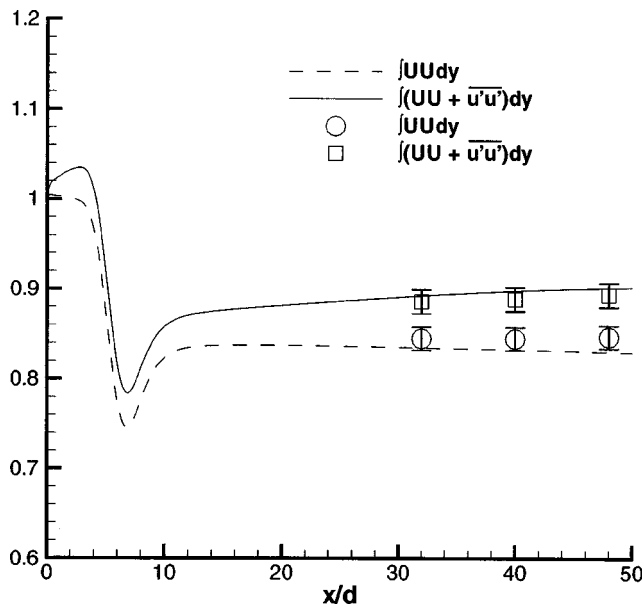


Fig. 3 Comparison between numerical and experimental results for the time-averaged streamwise momentum flux, $UU + \overline{u'u'}$, integrated over planes of constant x/d at $S/d=5$ (experimental data represented by symbols)

tion that may be applied to our numerical results, we first write the streamwise (x -direction) component of the incompressible, Reynolds-averaged Navier-Stokes equations, employing the Boussinesq approximation for the turbulent stresses, in dimensionless form as:

$$\frac{\partial}{\partial x}(UU) + \frac{\partial}{\partial y}(VU) = -\frac{\partial}{\partial x}\left(P + \frac{2}{3}k\right) + \frac{\partial}{\partial x}\left(\frac{2}{\text{Re}_t} \frac{\partial U}{\partial x}\right) + \frac{\partial}{\partial y}\left[\frac{1}{\text{Re}_t}\left(\frac{\partial U}{\partial y} + \frac{\partial V}{\partial x}\right)\right] \quad (5)$$

Integrating Eq. (5) over a control volume that defines the computational domain results in the integral constraint:

$$\int_{y_{\min}}^{y_{\max}} \left(UU + P + \frac{2}{3}k - \frac{2}{\text{Re}_t} \frac{\partial U}{\partial x} \right) dy = \text{constant} \quad (6)$$

for high Reynolds number flows evaluated along planes of constant x/d . We note that the computational and experimental domains extend sufficiently far in the lateral directions so that the entrainment is perpendicular to the boundaries at $y/d = \pm 30$ (i.e., $U \approx 0$).

To validate the numerical work, in Fig. 3 we present a comparison of numerical and experimental results for the integral (evaluated across the domain, for constant x/d) of the time-averaged streamwise momentum flux, $\int(UU + \overline{u'u'})dy$, at jet spacing $S/d=5$. We note that the measured inlet turbulence intensity was 1% which was used to specify the value of the turbulence kinetic energy at the inlet for the numerical calculations using Eq. (1). The dissipation rate was then specified using Eq. (2). The Reynolds number for both the experimental and numerical work was 3600. For the numerical results, the Reynolds stress term was computed using the Boussinesq approximation, $\overline{u'u'} = 2/3k - (2/\text{Re}_t)(\partial U/\partial x)$. Relative to the experimentally determined values the numerical results under predict by approximately 1.5% the integral of the mean velocity squared, and over predict by approximately 1% the integral of the total momentum flux. (Note that the difference between the two sets of data represents the contributions due to the integral of the $\overline{u'u'}$ stress term.) We may also compare the results for the mean momentum flux with ex-

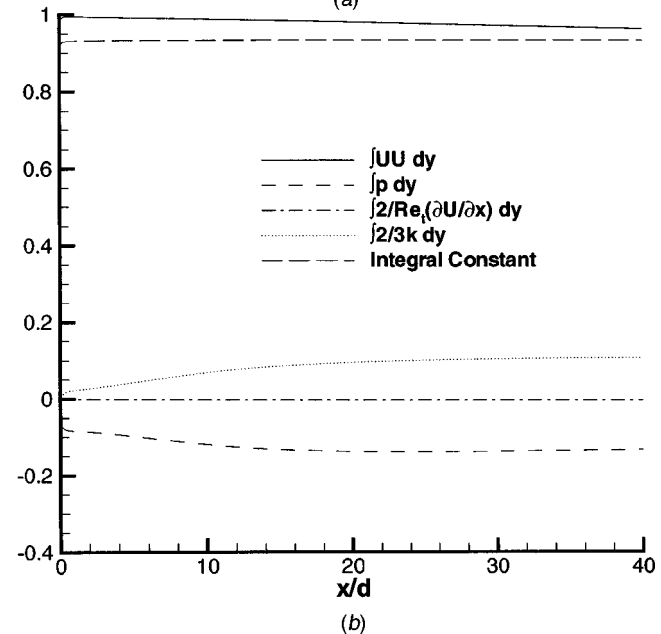
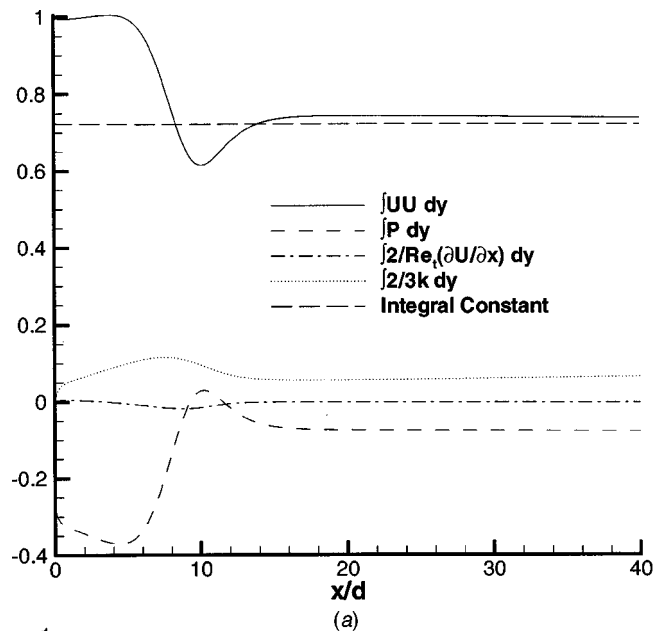


Fig. 4 Numerical results of term-by-term evaluation of integral equation, Eq. (6). (a) $S/d=9$ configuration. (b) Single jet configuration.

perimental results presented in Ref. [11]. One may extrapolate between the results in Ref. [11] for jet spacings of 4.25 and 7.5 (measured at the combine point) to estimate a mean momentum flux of approximately 0.80. This is slightly below the nearly constant value (approximately 0.84) revealed in Fig. 3 in the region well downstream of the merge point (located at $x/d = 6.02$). However, no information concerning the inlet turbulence quantities was presented in Ref. [11]. As will be shown at a later point, the integral constants are dependent on the inlet boundary conditions on k and ε ; consequently closer comparison with the results in Ref. [11] are not warranted. Based on the above results, we conclude that the $k-\varepsilon$ model performs reasonably well in predicting the integral of the momentum flux in the region downstream of the merge point. Since the flow direction cannot be determined based on hot-wire results, no experimental data is available near or upstream of the merge point.

The remainder of the results to be presented represent numeri-



Fig. 5 Sensitivity of streamwise momentum flux to variations in the jet inlet turbulence kinetic energy and dissipation rate boundary conditions

cal solutions. For these cases, the inlet turbulence intensity was, unless otherwise specified, fixed at 5% from which the turbulence kinetic energy and dissipation rate were then derived using Eqs. (1) and (2). The Reynolds number was set to 50,000. These values, larger than available from the experiments, were used to better model higher Reynolds number flows typical of industrial applications. (However, as previously mentioned, merge point locations are not strongly dependent on the Reynolds number.) Based on these conditions, the results for each individual term within Eq. (6) have been plotted in Fig. 4(a) for jet spacing $S/d = 9$. The sum of these terms, representing the integral constant of Eq. (6), is also shown in the figure. The dominant terms in the balance over the converging region are those representing the mean momentum and the pressure, with contributions from the normal Reynolds stress term, computed as $(2/3k - (2/Re_c) \times (\partial U/\partial x))$, of lesser significance. Downstream of the combine point each of the terms become nearly constant with $\int p dy \approx -(2/3) \int k dy$ as dictated by a higher-order boundary layer approximation applied to a single jet. Results for the spacings $S/d = 3, 5, \text{ and } 7$ are qualitatively similar to the $S/d = 9$ results, hence for purposes of brevity are not shown. The integral constants for jet spacings $S/d = 3, 5, 7, 9, \text{ and } 11$ were found to decrease, and were computed as 0.828, 0.776, 0.747, 0.721, and 0.701, respectively. (Note that the sensitivity of the solutions, in terms of grid resolution, is discussed at a later point.) These results may be compared with single jet results shown in Fig. 4(b), for which the integral constant was computed as 0.933. We also note that the streamwise locations of the merge points were computed as $x/d = 2.97, 5.30, 7.42, 9.26$ and 10.93 for jet spacings $S/d = 3, 5, 7, 9$ and 11 , respectively.

Calculations were also performed to assess the sensitivity of the solutions to the inlet boundary conditions on k and ε . These results, in terms of integral constants and merge point locations, are shown in Fig. 5 for the dual jet $S/d = 9$ case with four different combinations of k and ε . The dissipation rate inlet boundary conditions are presented according to Eq. (4) with the value of the constant C adjusted to provide varying levels of ε . In particular, the proportionality constant for the cases (k, ε) defined by $(0.00375, 0.00054)$ and $(0.015, 0.00431)$ is equal, and given as 2.347. As indicated in Fig. 5, the results for these two cases, expressed in terms of the momentum flux, are very similar downstream of the merge point, which occurs near $x/d = 9$. We also

Table 1 Value of integral constant and merge point as a function of inlet k and ε boundary conditions for the $S/d = 9$ case

k	ε	ν_t/ν	constant	merge point
0.00375	0.00216	29	0.743	9.60
0.00375	0.00054	117	0.721	9.25
0.015	0.00431	235	0.717	9.00
0.015	0.00054	1875	0.692	8.60

present in Table 1 the computed values of the integral constants as a function of inlet k and ε . The corresponding value of the inlet turbulent viscosity ratio is also given. The results reveal that the integral constant (see Eq. (6)) for these two cases is, to within two decimal places, equal. Two additional cases are also shown on the figure. In one case the dissipation rate was increased by a factor of four, from 0.00054 to 0.00216, with k held constant at 0.00375. This resulted in an increase in momentum flux downstream of the merge point, along with an increase in the integral constant from 0.72 to 0.74. Conversely, when the dissipation rate was held constant at 0.00054 and the turbulence kinetic energy was increased by a factor of four, from 0.00375 to 0.015, the momentum flux downstream of the merge point, relative to the other cases, decreased. Consistent with that result, the integral constant decreased to 0.69. The inlet turbulence viscosity ratios are also shown in Table 1. As expected, an increase in the viscosity ratio is accompanied by a decrease in the streamwise distance to the merge point and a decrease in the integral constant.

These results can be explained in terms of entrainment rates and associated pressures between the jets in the converging region. For instance, a relative increase in the turbulence kinetic energy of the jets (with ε held constant) is associated with an increase in entrainment rates, which, in turn, decreases the distance to the merge point, and decreases the pressure along the wall between the jets. Since the value of the integral constant at $x/d = 0$ (along the wall) is dictated primarily by the pressure and mean momentum terms, the value of the integral constant is thus decreased for increased rates of entrainment associated with the increase in turbulence kinetic energy of the inlet jets. Of course, the converse is true for an increase in the inlet dissipation rate (with k held constant). We also note that this demonstrated sensitivity of the merge point location to inlet flow conditions, which is on the order of

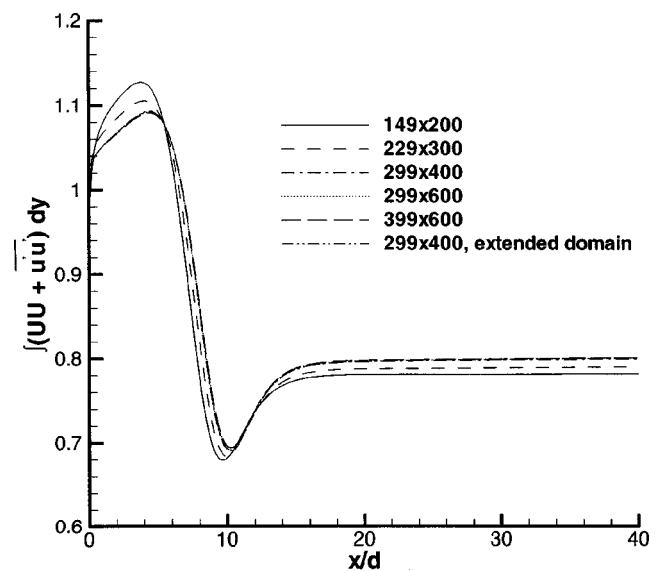


Fig. 6 Sensitivity of the numerical solutions to grid resolution and the size of the computational domain for spacing $S/d = 9$

10%, may account for some of the differences in experimentally measured merge point locations (c.f., a summary of published experimental results tabulated in Ref. [10].)

Finally, the sensitivity of the numerical solutions to grid resolution, and to the size of the computational domain, is examined for the dual jet case defined by $S/d=9$. Results are shown in Fig. 6 in terms of the integrated momentum flux for grid resolutions consisting of 149×200 , 229×300 , 299×400 , 299×600 , and 399×600 grid points in the spanwise and streamwise directions, respectively. The results indicate that a grid converged solution has been achieved on the 299×400 grid. Also shown in the figure are results for a (larger) domain that extends over the range $-60 \leq y/d \leq 60$, $0 \leq x/d \leq 160$ which was computed on a 229×300 grid. Here, the clustering parameters were set such that the grid spacings in the near wall and jet regions were nearly the same as those on the smaller domain discretized using 229×300 grid points. (This was done to ensure nearly equal grid resolution in the regions of high gradients, and thus minimize differences in the solution due to truncation errors.) The results reveal essentially no difference between the solutions for the two domains, indicating that the domain bounded by $-30 \leq y/d \leq 30$ and $0 \leq x/d \leq 80$ is sufficiently large. We also note that the integral constants, to three decimals, were computed as 0.721, 0.722, and 0.722, using grid resolutions of 299×400 , 299×600 , 399×600 , respectively. Consequently, in terms of truncation error the results of the integral constant on the 299×400 grid are accurate to within ± 0.001 .

Summary

The results presented herein indicate that a two-equation $k-\varepsilon$ model is able to predict quite well experimentally measured integrals of total and mean momentum fluxes downstream of the merge point for jet spacing $S/d=5$. An integral constraint was also defined and evaluated numerically for jet spacings $S/d=3, 5, 7, 9$, and 11 , and for different levels of turbulence kinetic energy and dissipation rate defining the jet inlet boundary conditions. Consistent with what has been reported in previous experimental work, the results showed that the integral constant decreases as the jet spacing increases. In addition, the constant is decreased as jet entrainment rates are increased as a result of higher levels of inlet turbulence kinetic energy, or alternatively, as a result of de-

creased levels of dissipation rate. Streamwise distance to the merge point also decreased as inlet turbulence kinetic energy levels were increased, or as levels in dissipation rate were decreased. These results were explained in terms of the effect of entrainment rates and associated pressure distributions in the wall region between the jets.

References

- [1] Thomas, F. O., 1991, "Structure of Mixing Layers and Jets," *Appl. Mech. Rev.*, **44**, pp. 119–153.
- [2] Everitt, K. W., and Robins, A. G., 1978, "The Development and Structure of Turbulent Plane Jets," *J. Fluid Mech.*, **88**, pp. 563–568.
- [3] Gutmark, E., and Wagnanski, I., 1976, "The Planar Turbulent Jet," *J. Fluid Mech.*, **73**, pp. 465–495.
- [4] *ASHRAE Handbook of Fundamentals*, 1997, Ch. 15, p. 10, American Society of Heating, Refrigerating and Air Conditioning Engineers, Atlanta, GA.
- [5] Tanaka, E., 1970, "The Interference of Two-Dimensional Parallel Jets (1st Report, Experiments on Dual Jet)," *Bull. JSME*, **13**(56), pp. 272–280.
- [6] Tanaka, E., 1974, "The Interference of Two-Dimensional Parallel Jets (2nd Report, Experiments on the Combined Flow of Dual Jet)," *Bull. JSME*, **17**(109), pp. 920–927.
- [7] Elbanna, H., Gahin, S., and Rashed, M. I. I., 1983, "Investigation of Two Plane Parallel Jets," *AIAA J.*, **21**, pp. 986–990.
- [8] Lin, Y. F., and Sheu, M. J., 1990, "Investigation of Two Plane Parallel Unventilated Jets," *Exp. Fluids*, **10**, pp. 17–22.
- [9] Lin, Y. F., and Sheu, M. J., 1991, "Interaction of Parallel Turbulent Plane Jets," *AIAA J.*, **29**, pp. 1372–1373.
- [10] Nasr, A., and Lai, J. C. S., "Comparison of Flow Characteristics in the Near Field of Two Parallel Plane Jets and an Offset Plane Jet," *Phys. Fluids*, **9**, pp. 2919–2931.
- [11] Nasr, A., and Lai, J. C. S., "Effects of Nozzle Spacing on the Development of Two Parallel Plane Jets," *International Journal of Transport Phenomena*, **2**, pp. 43–56.
- [12] Anderson, E. A., and Spall, R. E., 2001, "Experimental and Numerical Investigation of Two-Dimensional Parallel Jets," *J. Fluids Eng.*, **123**, pp. 401–406.
- [13] Spall, R. E., 2002, "A Numerical Study of Buoyant, Plane Parallel Jets," *J. Heat Transfer*, **124**, pp. 1210–1213.
- [14] Anderson, E. A., Snyder, D. O., and Christensen, J., 2003, "Periodic Flow Between Low Aspect Ratio Parallel Jets," *J. Fluids Eng.*, **125**, pp. 389–392.
- [15] Yang, H. Q., and Przekwas, A. J., "Pressure-based High-Order TVD Methodology for Dynamic Stall Simulation," *AIAA-93-0680*.
- [16] Mathieu, J., and Scott, J., 2000, *An Introduction to Turbulent Flow*, Cambridge University Press, pp. 164–168.
- [17] Nasr, A., and Lai, J. C. S., "Two Parallel Plane Jets: Mean Flow and Effects of Excitation," *Exp. Fluids*, **22**, pp. 251–260.
- [18] Taylor, J. R., 1997, *An Introduction to Error Analysis*, 2nd edition, University Science Books.

Measurement and Modeling of Propeller Cavitation in Uniform Inflow

Francisco Pereira

e-mail: f.pereira@insean.it

Phone: +39 06 50299281

Francesco Salvatore

Fabio Di Felice

Istituto Nazionale per Studi ed Esperienze di
Architettura Navale,
Via di Vallerano, 139-00128 Rome, Italy

An experimental and theoretical investigation on a cavitating propeller in uniform inflow is presented. Flow field investigations by advanced imaging techniques are used to extract quantitative information on the cavity extension. A refined map of the propeller cavitating behavior is established. Measurements are compared to numerical results obtained using an inviscid flow boundary element method for the analysis of blade partial sheet cavitation and supercavitation. The effect of the trailing wake vorticity on the prediction of the cavitation pattern is analyzed via a wake alignment technique.

[DOI: 10.1115/1.1778716]

Introduction

Visual observations and photographic recordings have been and are in many practical situations the common means to provide a "measure" of the cavitation pattern. With regard to the research in the field, various methods are reported in the literature that allow more accurate estimates of both the extension and volume of the cavity shape. For instance, Dupont and Avellan [1] and Pereira [2] report precise measurements of the cavity length and thickness on isolated two-dimensional and three-dimensional hydrofoils, using charge coupled devices (CCD's) and laser light structured into a plane sheet. Pereira et al. [3] describe a fully three-dimensional method to measure the volume of the vapor structures as they are generated by leading edge cavitation. In the case of cavitating propellers, the pin gauge method is the simplest and most immediate approach, but highly intrusive as the pins also cavitate [4]. Lehman [5] seems to be the first to present nonintrusive quantitative measurements, using multiple orthographic views to build an estimate of the cavity volume on a model propeller. Using stereophotography, Sontvedt and Frivold [6] report volume measurements on model and full-scale propeller-hull configurations. They find large discrepancies, with an inaccuracy ranging from 30% to 100%. Working on model configurations, Ukon and Kurobe [7] devise a method where the spot of a laser beam scattered by the cavity surface is detected and used to measure the thickness and extension of the cavity. Implementing laser beam scanning and CCD technology, the same group [8] further develop this laser scattering technique, and perform the mapping of unsteady cavity surface on propellers behind complete ship models. Kodama et al. [9], and later Tanibayashi et al. [10], extend the principle using two laser beams, applying it to full scale cavity thickness measurements. Another variant of this double-laser beam approach is proposed by Stinzing [11], with application to model scale tests in nonuniform flow.

In the present work, new developments are introduced into the observation and quantification of the cavitation pattern and are applied to a skewed four-blade model propeller in uniform inflow. Using a novel cavitation analysis approach suitable for field applications, the area of the leading edge cavitation is accurately quantified throughout an exhaustive range of working conditions.

A modified Wageningen type model propeller (INSEAN E779A) was selected for the present research project, for it has been thoroughly studied in non-cavitating flow conditions with pressure and noise measurements and state-of-the-art visualization

techniques, such as laser Doppler velocimetry [12] and particle image velocimetry [13]. The present work extends the existing database to cavitating flow conditions. In addition, the E779A geometry is very close to that of many existing twin-screw ship propellers, thus enhancing the interest of the study. Finally, the E779A propeller provides a complete and challenging test case for the validation of numerical codes.

The data collected in the present work covers a large number of flow conditions. A rich cavitating flow database is being constructed, representing a powerful tool to investigate in detail the range of applicability of new theoretical models and to assess the accuracy of predictions. As a matter of fact, the validation of numerical predictions against experimental flow data is generally not possible, even though the numerical field is very active and eager for such information [14,15]. The lack of quantitative data, accurate and covering a useful spectrum of flow conditions, explains the situation. Moreover, inadequate data formats have been used that are not suitable for a convenient exchange of information.

Here, cavitating propeller measurements are used to perform a thorough assessment of a computational prediction tool that is valid for sheet cavitation analysis of isolated propellers in uniform inviscid flows. The theoretical formulation is based on a boundary integral methodology for the velocity potential, derived from Morino et al. [16]. The trailing wake vorticity path is accurately described through a wake alignment technique. The cavitation model considered here is derived using standard procedures of boundary element methods [17,18]. The model is based on a non-linear free cavity length approach and is valid to study leading-edge attached cavities and supercavitating flow conditions. Both the wake alignment technique and the cavitation model are integrated into the boundary integral methodology through iterative procedures.

The paper describes, in a first part, the experimental methodologies that are introduced to characterize the cavitation development on a rotating propeller. In a second part, an outline of the numerical approach is given. Finally, the results of the experimental investigation are used to assess the validity of the numerical method.

Experimental Analysis

Setup. The experiments are carried out at the Italian Navy cavitation tunnel facility (C.E.I.M.M.). The tunnel is a closed water circuit with a 0.6 m×0.6 m×2.6 m square test section. Optical access to the section is possible through large Perspex windows. The nozzle contraction ratio is 5.96:1 and the maximum water

Contributed by the Fluids Engineering Division for publication in the JOURNAL OF FLUIDS ENGINEERING. Manuscript received by the Fluids Engineering Division July 4, 2003; revised manuscript received February 20, 2004. Associate Editor: Y. Tsujimoto.

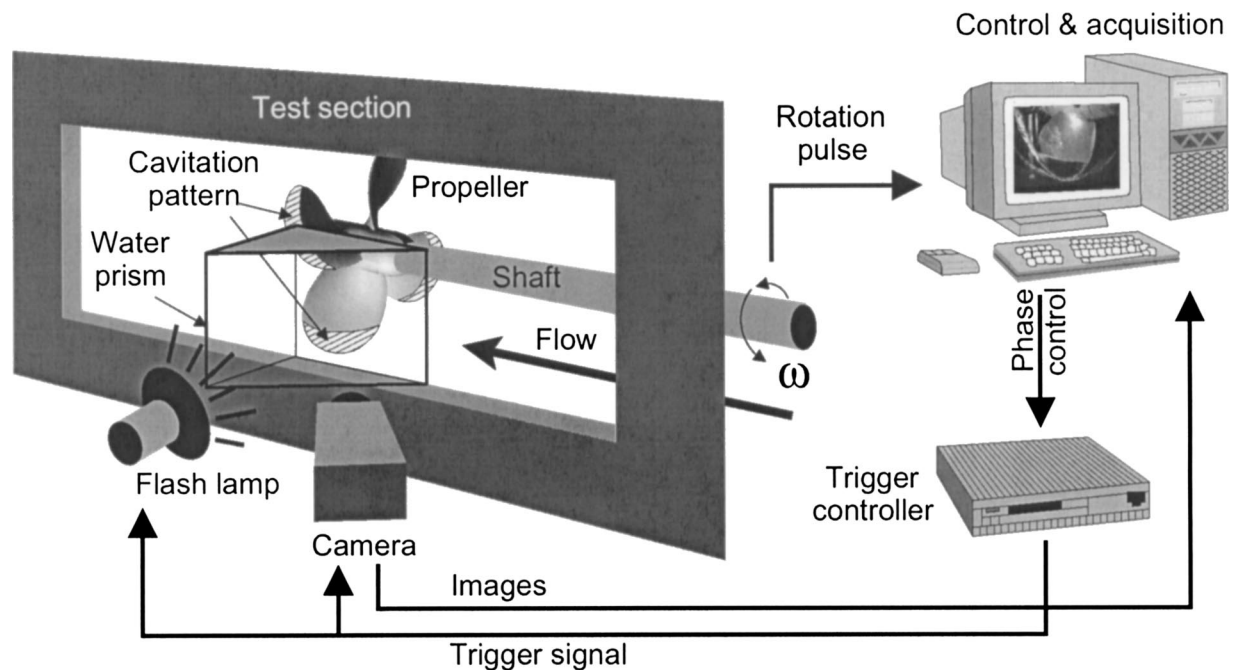


Fig. 1 Experimental setup

speed is $12 \text{ m} \cdot \text{s}^{-1}$. The maximum free stream turbulence intensity in the test section is 2%. The flow uniformity is within 1% for the axial component and 3% for the vertical one.

The skewed four-blade model propeller has a radius $R = D/2 = 0.117 \text{ m}$, a pitch-to-diameter ratio of 1.1 and a forward rake angle of 4.05 deg. The blockage ratio in the test section is about 10%.

In the following sections, J , K_Q and K_T are the advance, the torque and the thrust coefficients, respectively. σ_0 is the cavitation number related to the reference pressure p_0 measured at the propeller axis, and σ_n is the cavitation number related to the propeller rotational speed n . The measurements described here have been performed across an extensive range of working conditions, with σ_0 and J being the control parameters.

The measurement configuration is pictured in Fig. 1. The blade angular position is adjusted to allow a full view of the blade face. A CCD camera is dedicated to the measurement of the pattern area and is oriented at an angle with respect to the test section window. Looking at an angle through the thick window introduces strong aberrations, which are almost fully cancelled using a water-filled glass tank in the form of a wedge, and placed so that the camera optical axis is normal to the wedge face. The propeller shaft is equipped with a rotary encoder that supplies an electrical trigger signal, used to pilot a pulse delay generator, which in turn controls the phase between the propeller and the image capture and synchronizes the camera with the illumination system. A single high intensity flash lamp, with a $10 \mu\text{s}$ light pulse, is used to observe the cavitation pattern. For every flow condition, 128 images are recorded, simultaneously with the corresponding flow parameters.

Cavitation Extension Measurement. We introduce a novel methodology to determine the cavity area, designed to be highly robust and accurate. The common method of analyzing cavitation images consists of enhancing the contrast between the cavitation pattern and the rest of the image. This is usually done by thresholding the image [19]. However, it is well known that this approach is very sensitive to variations in the illumination. The region of interest needs also to be easily distinguishable from the background. In a complex environment such as a rotating propeller, this approach is not reliable enough: tip vortex, scattering of

the blade, fluctuations of the illumination intensity, objects in the field of view, are among many other causes that make the task difficult and unreliable, especially if done automatically.

The approach used here, and depicted in Fig. 2, is based on the cross-correlation between a template image (Fig. 2a), i.e., the blade viewed in non-cavitating conditions, and the image being analyzed (Fig. 2b). The cross-correlation is a robust tool to make the comparison between images: a high correlation would indicate that the template and the image are similar, while a slight difference would result in a lower correlation coefficient. In order to localize the transition regions between the cavitating and the non-cavitating situations, the cross-correlation is performed on small image regions, represented in Figs. 2a and 2b. Figure 2c shows the result. The convolution operation is performed across the whole image to produce a correlation image, see Fig. 2d, where the

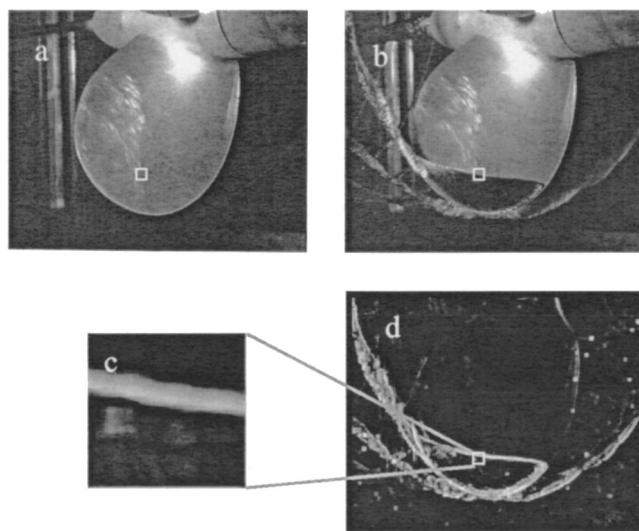


Fig. 2 Image cross-correlation procedure: (a) template image; (b) cavitation pattern image; (c) local cross-correlation; (d) correlation image

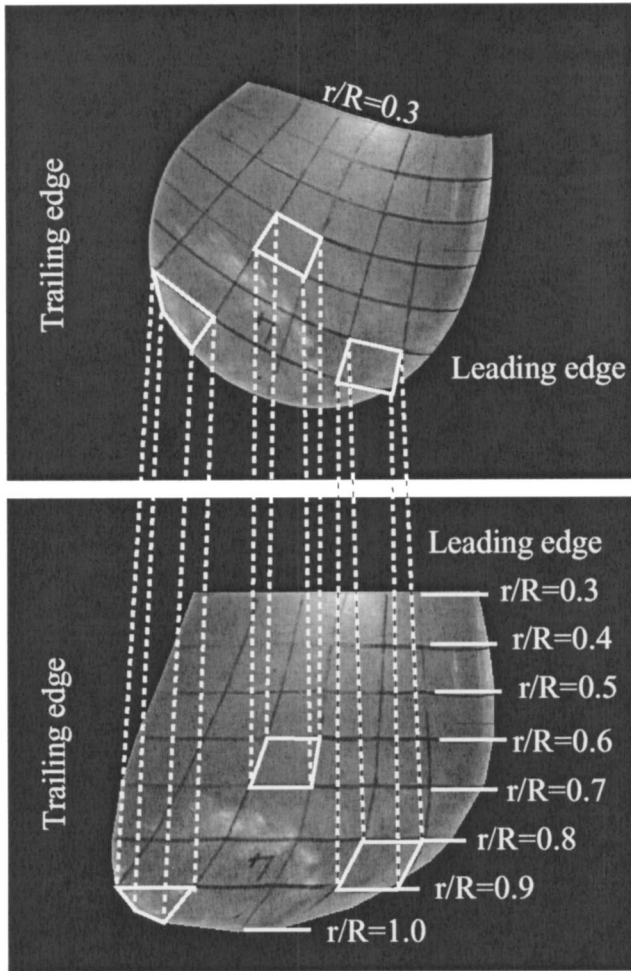


Fig. 3 Warping procedure: original (top) and warped (bottom) images

differences between the template and the image being analyzed are clearly identified as cavitation features: cavitating vortices from the blade tips, contour of the attached cavity.

The correct quantitative evaluation of the cavitation area A_c is only possible if done in a known coordinate system. The registered image is a perspective projection of the three-dimensional

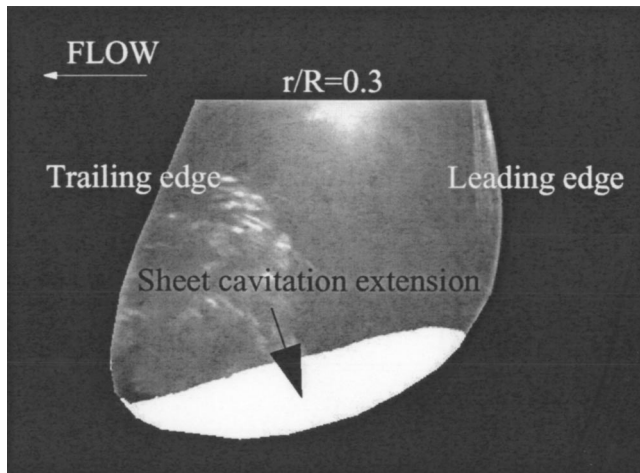


Fig. 4 Cavitation extension

blade surface and pattern. A back projection using basic geometric optics would report this image information into a plan view, and this would correct for the variable magnification. However, this is only valid if the system is free of optical aberrations and requires exact knowledge of the optical parameters and of the blade geometry. In fact, the complex lens system composed of the camera objective, the prism, the test section window and the water medium, introduces focusing aberrations and optical distortions, which are the source of nonlinear magnification. The image distortions can be corrected by calibration procedures. To do so, we apply here a technique known in the image processing field as the warping transformation [20], with a second-order perspective operator to account for the nonlinear effects. If x_i ($i=1,2$) are the original image coordinates of a point, the warped image coordinates x'_i are then defined by

$$x'_i = \frac{a_{i,0}x_1 + a_{i,1}x_2 + a_{i,2} + a_{i,3}x_1^2 + a_{i,4}x_2^2 + a_{i,5}x_1x_2}{b_{i,0}x_1 + b_{i,1}x_2 + b_{i,2} + b_{i,3}x_1^2 + b_{i,4}x_2^2 + b_{i,5}x_1x_2} \quad (1)$$

where $a_{i,j}$ and $b_{i,j}$ are the coefficients of the transform. $a_{i,j}$ and $b_{i,j}$ are unknowns that are determined by a Nelder-Mead least-square minimization method, using reference points on the distorted image.

To make this correspondence, a grid is printed on a blade, with lines drawn spanwise at various r/R , and radial lines regularly spaced chordwise, see Fig. 3. Instead of determining one unique transformation for the whole image, as commonly done, Eq. (1) is calculated for each polygon defined by the intersection of the two sets of lines. This approach refines the transformation and avoids the side-effects inherent to the use of nonlinear polynomials in regions where calibration points are not available. Three sample distorted polygons are shown in the top image of Fig. 3 with the corresponding locally warped image displayed in the picture below. For clarity, we show only four vertices for each polygon.

The warping procedure is applied to the correlation image (Fig. 2d), followed by standard threshold techniques to track the cavitation pattern, now possible without the drawbacks outlined previously. Morphological operators may then be used to filter the main cavitation pattern from undesired features, such as traveling bubbles. This sequence of operations results in a pattern image (Fig. 4), where the cavitation region over the blade is clearly outlined, measurable and suitable for comparison with the computations described in the next sections. The cavitation area A_c is expressed in percentage of the blade face area A_0 obtained for $r/R \geq 0.3$.

The error that arises from the warping transformation is estimated by comparing the calculated and the actual areas of the surface polygonal elements on the calibration blade (Fig. 3). A mean error of 0.64% is found, which could be improved using a finer calibration grid.

Theoretical Model

The theoretical hydrodynamic model considered here is based on a boundary integral formulation for the analysis of incompressible inviscid flows around lifting bodies. Propeller load-induced vorticity shedding is described by means of a trailing wake alignment model, whereas cavity pattern predictions are obtained by using a nonlinear sheet cavity model that is valid for both partial and supercavitation. The theoretical formulation is briefly outlined here. A detailed derivation is given by Salvatore and Testa [21].

Governing Equations and BEM. Assuming that the unperturbed flow is inviscid and irrotational, a scalar potential φ is introduced to express the propeller-induced perturbation velocity as $\mathbf{v} = \nabla\varphi$. In a frame of reference ($Oxyz$) fixed to the propeller with the x -axis parallel to the propeller axis and pointing downstream, the incoming flow velocity reads $\mathbf{v}_i = \mathbf{v}_A + \bar{\Omega} \times \mathbf{x}$, where $\mathbf{v}_A = (v_0, 0, 0)$ is the axial inflow to the propeller, $\bar{\Omega} = (2\pi n, 0, 0)$ is the angular velocity of the propeller, and $\mathbf{x} = (x, y, z)$. The present

derivation is valid for unsteady flow analysis of an isolated propeller in which the inflow v_0 is uniform whereas both v_0 and n may be time-dependent. The velocity field in the propeller frame of reference is $\mathbf{q} = \mathbf{v}_i + \nabla\varphi$. Under incompressible flow assumptions, the continuity equation reduces to the Laplace equation $\nabla^2\varphi = 0$.

The pressure p is given by Bernoulli's theorem that, in the frame of reference fixed to the propeller, reads

$$\frac{\partial\varphi}{\partial t} + \frac{1}{2}q^2 + \frac{p}{\rho} + gz_0 = \frac{1}{2}v_i^2 + \frac{p_0}{\rho}, \quad (2)$$

where $q = \|\mathbf{q}\|$, $v_i = \|\mathbf{v}_i\|$, g is the gravity acceleration and z_0 denotes depth.

Flowfield predictions are obtained by solving the Laplace equation for φ with suitable boundary conditions. The potential-flow domain \mathcal{V}_p is delimited by the propeller surface \mathcal{S}_B , the trailing wake surface \mathcal{S}_W and the cavity surface \mathcal{S}_C .

On the cavitation-free portion of the propeller surface \mathcal{S}_{WB} , the impermeability condition yields $\mathbf{q} \cdot \mathbf{n} = 0$. Recalling $\mathbf{q} = \mathbf{v}_i + \nabla\varphi$, this condition reads

$$\frac{\partial\varphi}{\partial n} = -\mathbf{v}_i \cdot \mathbf{n} \quad \text{on } \mathcal{S}_{WB}, \quad (3)$$

where \mathbf{n} is the outward unit normal to the surface.

The trailing wake surface \mathcal{S}_W represents a zero-thickness layer over which the vorticity generated on the body is shed downstream. In the potential field theory, \mathcal{S}_W denotes a discontinuity surface for the velocity potential. Applying the mass and momentum conservation laws under non-cavitating flow conditions, and letting $\Delta(\cdot)$ be the discontinuity across the two sides of the wake surface, we have $\Delta(\partial\varphi/\partial n) = 0$ and $\Delta p = 0$. Thus, from the Bernoulli equation (2), $\Delta\varphi$ is found to be constant as one follows the wake particles, i.e.

$$\Delta\varphi(\mathbf{x}, t) = \Delta\varphi(\mathbf{x}_{TE}, t - \tau) \quad \text{on } \mathcal{S}_W, \quad (4)$$

where \mathbf{x}_{TE} is a wake point at the blade trailing edge and τ is the convection time between wake points \mathbf{x} and \mathbf{x}_{TE} . A further condition on φ is required in order to assure that no finite pressure jump may exist at the body trailing edge (Kutta condition). Following Morino et al. [16], this is equivalent to impose $\Delta\varphi(\mathbf{x}_{TE}) = \varphi_{TE}^u - \varphi_{TE}^l$, where φ_{TE}^u and φ_{TE}^l are evaluated, respectively, at the body trailing edge suction and pressure sides.

The boundary conditions on the cavity surface \mathcal{S}_C are imposed assuming that the cavity is a fluid region where the pressure is constant and equal to the vapor pressure p_v . Thus, requiring that $p = p_v$ on \mathcal{S}_C , and using the Bernoulli equation (2), it follows

$$q = \left[(nD)^2 \sigma_n - 2 \left(\frac{\partial\varphi}{\partial t} + gz_0 \right) + v_i^2 \right]^{1/2} \quad \text{on } \mathcal{S}_C, \quad (5)$$

where $\sigma_n = (p_0 - p_v) / 0.5 \rho_0 (nD)^2$ is the cavitation number referred to the propeller rotational speed n and diameter D . Equation (5) is used to obtain a Dirichlet-type condition for φ on \mathcal{S}_C in terms of σ_n . Introducing on \mathcal{S}_C a curvilinear coordinate system with s and u being the arclengths in the chordwise and spanwise directions, respectively, and recalling $\mathbf{q} = \mathbf{v}_i + \nabla\varphi$, one obtains a nonlinear condition for φ of the type

$$\varphi(s, u) = \varphi(s_{CLE}, u) + \int_{s_{CLE}}^s \mathcal{F} \left(q, \frac{\partial\varphi}{\partial u}, \frac{\partial\varphi}{\partial n}, \mathbf{v}_i \right) d\bar{s} \quad \text{on } \mathcal{S}_C, \quad (6)$$

where s_{CLE} is the cavity leading edge abscissa. A detailed derivation of Eq. (6) and the expression of the function \mathcal{F} is given by Salvatore and Testa [21].

At the cavity trailing edge, the Dirichlet-type condition given by Eq. (6) and the Neumann-type condition Eq. (3) should be both imposed. However, this causes a non-physical discontinuity in both the velocity and pressure fields. To overcome the singularity,

we create a small transitional region across the cavity trailing edge and apply a cavity closure condition: the pressure is forced to smoothly vary from p_v to the wetted flow values downstream the cavity. Inside the transitional region, the quantity σ_n in Eq. (5) is replaced by

$$\sigma_n^* = \sigma_n H_1(\xi) - (C_p)^{TD} H_2(\xi) - (C_p')^{TD} H_4(\xi), \quad (7)$$

where ξ spans between -1 and $+1$, and $H_i(\xi)$ are Hermite polynomials. $(C_p)^{TD}$ and $(C_p')^{TD}$ denote respectively the pressure coefficient and its s -wise derivative at the downstream boundary (TD) of the transitional region. This pressure-based condition is closely related to the velocity-based condition proposed by Lemonnier and Rowe [22]. However, the present approach does not require the introduction of any arbitrary parameters, once the extension of the transitional region is set (10% of the cavity length in our case).

An expression of the cavity thickness h_c is obtained with a non-penetration condition on \mathcal{S}_C . By combining the constant-pressure and the non-penetration conditions, it follows that \mathcal{S}_C is a material surface. If \mathcal{S}_{CB} and \mathcal{S}_{CW} are the cavitating areas on the body and on the wake surfaces, respectively, and if ∇_s is the surface gradient acting on those surfaces, then it follows

$$\frac{\partial h_c}{\partial t} + \nabla_s h_c \cdot \mathbf{q} = \chi_c \quad \text{on } \mathcal{S}_{CB} \cup \mathcal{S}_{CW}, \quad (8)$$

where $\chi_c = \partial\varphi/\partial n + \mathbf{v}_i \cdot \mathbf{n}$ on \mathcal{S}_{CB} and $\chi_c = \Delta(\partial\varphi/\partial n)$ on \mathcal{S}_{CW} .

The Laplace equation for the velocity potential is solved by means of a boundary integral formulation. Assuming that the perturbation vanishes at infinity, the third Green identity yields

$$\begin{aligned} \varphi(\mathbf{x}) = & \oint_{\mathcal{S}_{B+C}} \left(\frac{\partial\varphi}{\partial n} G - \varphi \frac{\partial G}{\partial n} \right) dS(\mathbf{y}) \\ & - \int_{\mathcal{S}_W} \Delta\varphi \frac{\partial G}{\partial n} dS(\mathbf{y}) \quad \mathbf{x} \in \nu_p \setminus \partial\nu_p, \end{aligned} \quad (9)$$

where $\mathcal{S}_{B+C} = \mathcal{S}_{WB} \cup \mathcal{S}_C$ delimits both the body and the cavity, and $G = -1/4\pi\|\mathbf{x} - \mathbf{y}\|$ is the unit source.

Equation (9) is solved using a boundary element approach in the limit as the distance of \mathbf{x} from \mathcal{S}_{B+C} tends to zero. The boundary surfaces are divided into hyperboloidal quadrilateral elements, and the flow quantities are assumed to be constant on each element. Equation (9), in discretized form, is enforced at the element centroids and is solved with the boundary conditions expressed by Eqs. (3) to (6). The source G and the dipole $\partial G/\partial n$ influence terms are integrated using an analytical approach [16]. Inviscid-flow hydrodynamic loads are computed after integration of the pressure on \mathcal{S}_B from Eq. (2). The viscosity contribution to the propeller torque is estimated using flat plate friction line formulae.

Numerical Solution Procedure. The cavity surface \mathcal{S}_C and the wake surface \mathcal{S}_W used in Eq. (9) are not known a priori. In order to limit the computational effort and to avoid numerical instabilities from the regridding of the cavity surface during the cavitation model iterative procedure, Eq. (9) is numerically solved with singularities distributed on the surface $\mathcal{S}_{CB} \cup \mathcal{S}_{CW}$ rather than on the cavity edge \mathcal{S}_C . This simplification is consistent with the present sheet cavitation model that is limited to analyze thin vapor-filled regions attached to body and wake surfaces.

The wake surface may be either prescribed (prescribed wake approach) or determined as a part of the flowfield solution (free wake approach). In the prescribed wake approach, \mathcal{S}_W is approximated by a helical surface with a prescribed pitch distribution. At the trailing edge, the wake surface is assumed to be tangent to the blade suction side, whereas an average between the hydrodynamic pitch of the unperturbed inflow and the blade pitch angle is used downstream the propeller.

In the free wake approach, a physically consistent shape of \mathcal{S}_W is determined upon requirement that the wake points move ac-

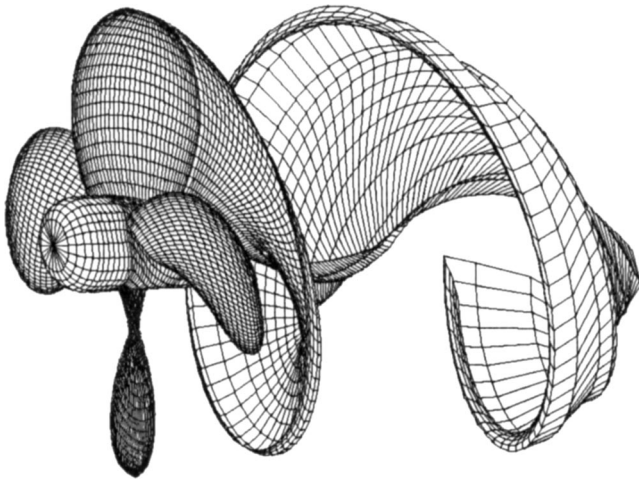


Fig. 5 Computational grid used for flowfield analysis of the E779A propeller, and wake surface evaluated by the flow-alignment technique ($M_B=36$, $M_B/N_B=2$, $M_W/N_B=5$, $N_H^{tot}=252$)

According to the local velocity field. A boundary integral representation of the perturbation velocity field $\nabla\varphi$ is obtained taking the gradient from both sides of Eq. (9). Starting with an initial prescribed-pitch guess for S_W , the computed velocity field is used to update the location of each wake node. Once S_W has been modified, the potential field is re-computed through Eq. (9). The process is repeated until convergence of the aligned wake shape. Details of this technique are given by Giordani et al. [23].

In the proposed methodology, the cavitation model and the wake alignment technique are combined under the assumption that the trailing wake location is not affected by the cavity-induced flowfield perturbation [24]. Within this context, the wake alignment procedure is performed under non-cavitating flow conditions. Once the actual shape of the trailing wake is determined, an initial guess $S_{CB}^{(0)}$ for the cavity planform is imposed, Eq. (9) is solved under cavitating flow conditions, and the cavity thickness is evaluated by Eq. (8). The leading edge cavity detachment is also set, this being supported by experimental observations. The cavity trailing edge is determined by imposing $h_c=0$ at each surface strip in the chordwise direction. If this condition is not veri-

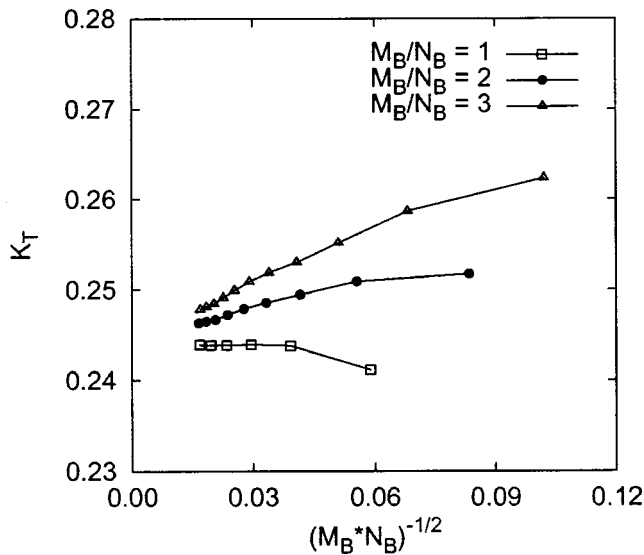


Fig. 6 Effect of grid refinement on the non cavitating thrust coefficient K_T at $J=0.71$

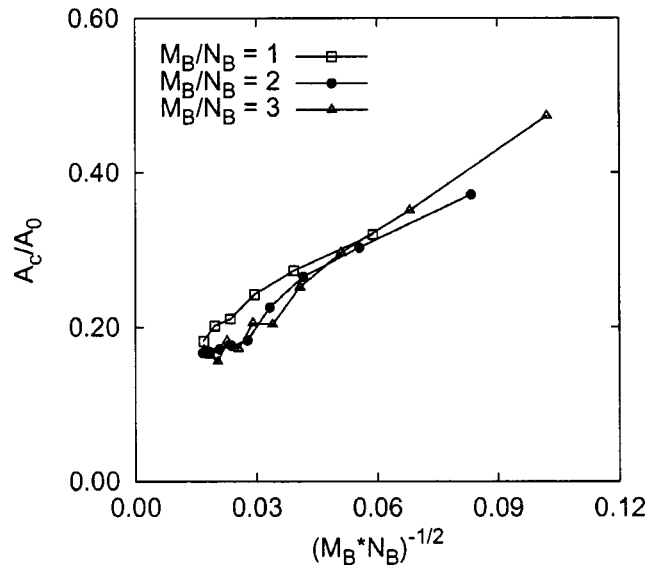


Fig. 7 Effect of grid refinement on the cavity area fraction A_c/A_0 at $J=0.71$, $\sigma_n=1.515$

fied within $S_{CB}^{(0)}$, it is assumed that the guessed planform is too small and a cavity planform extrapolation procedure is used. Hence, an updated cavity planform is obtained and the procedure is repeated until convergence of the cavity shape and of the potential field.

A representative computational grid on the propeller surface and on the wake is depicted in Fig. 5. On each blade side, $M_B=36$ and $N_B=18$ elements are used in chordwise and spanwise directions, respectively. $M_W=90$ elements are used on each wake turn in streamwise direction, and $N_H^{tot}=252$ elements are used on each hub surface sector. For the sake of clarity, the wake emanating from only one blade is depicted in Fig. 5 (free-wake calculation result).

The numerical solution sensitivity to the computational grid refinement is addressed in Fig. 6. Specifically, the top picture shows the effect of grid refinement on the calculated propeller thrust coefficient K_T under non-cavitating flow conditions at $J=0.71$. In particular, numerical results using grids with $M_B=[12,18,\dots,60]$, $M_B/N_B=[1,2,3]$, $M_W/N_B=5$, and N_H^{tot}

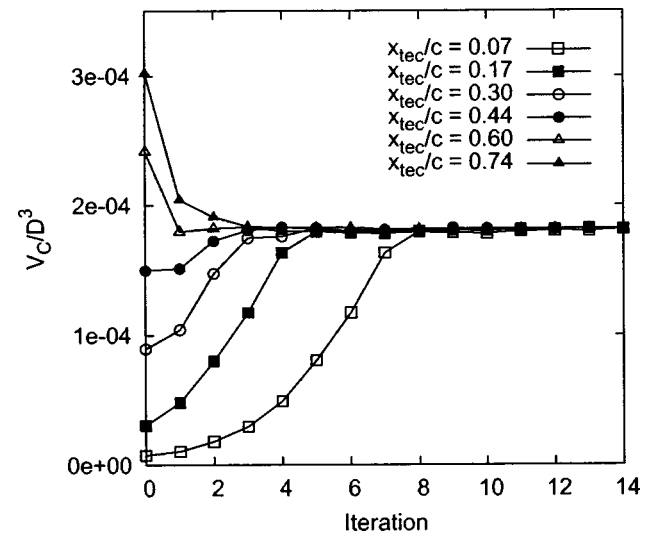


Fig. 8 Cavity volume histories using different initial guesses of the cavity extension ($J=0.71$, $\sigma_n=1.515$)

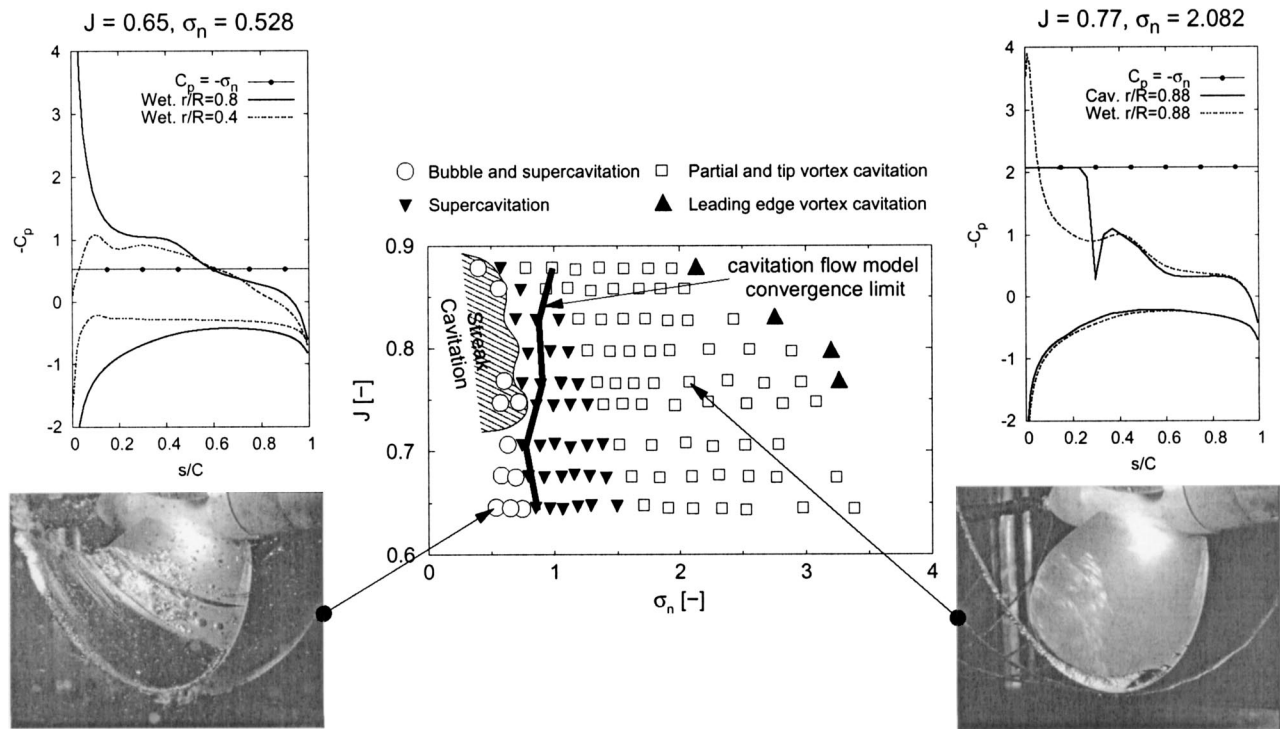


Fig. 9 E779A model propeller cavitation chart; pressure coefficient distributions on the blade suction and pressure sides and associated images, at two characteristic conditions: $J=0.65$, $\sigma_n=0.528$; $J=0.77$, $\sigma_n=2.082$

$=[132, \dots, 372]$ are compared. The following observations are also applicable to the propeller torque coefficient K_Q calculations (not shown here).

The ratio between the blade discretization elements in chordwise and spanwise directions does affect the rate of convergence. However, the extrapolated values as the grid refinement parameter $1/(M_B \times N_B)$ tends to zero are barely influenced by this grid parameter. Indeed, we find a converged K_T value of 0.246, while the measured one is 0.255, hence the discrepancy is 3.5% circa. This error can be seen as global, i.e., the combined result of the uncertainties that originate from the numerical simulation, from the measurement of the experimental flow parameters, from the propeller actual geometry and from the experimental setup and data analysis.

The effect of grid refinement on the computed cavity area is shown in Fig. 7 for cavitating flow conditions ($J=0.71$, $\sigma_n=1.515$). The discretization errors on the cavity area predictions tend to decrease as $1/(M_B \times N_B)$ approaches zero.

The results above indicate that discretization errors are reasonably small if computational grids having $M_B \geq 36$ are used. In particular, all the numerical results presented hereafter have been obtained using the computational grid depicted in Fig. 5.

The convergence of the iterative procedure used to solve the nonlinear algorithms (cavitation model and wake alignment, in the present methodology) is also a fundamental aspect of numerical scheme verification. With regard to the cavitation model, a representative result is provided in Fig. 8, which shows different cavity volume histories for the case $J=0.71$, $\sigma_n=1.515$, obtained using different initial guesses of the cavity planform. Specifically, the chordwise location x_{tec} of the cavity trailing edge ranges from 7% to 74% of the local chord, the leading edge cavity detachment being preset. As one would expect, the converged value of the cavity volume is not affected by the choice of the initial guess.

Flow Field Investigations

Analyzing the individual cavitation images across the complete measurement chart, the E779A model propeller can be described

in terms of distinct cavitation patterns. Figure 9 represents a map of the cavitating behavior of the propeller, also known as a bucket diagram, where the main figures of cavitation have been identified. The propeller presents five main patterns: bubble cavitation/traveling cavitation, supercavitation, sheet cavitation, leading edge (LE) and tip vortex cavitation. A curve $\sigma_n^{\min}(J)$ is also plotted to delimit flow conditions characterized by $\sigma_n < \sigma_n^{\min}(J)$, where the cavity pattern predictions by the present theoretical model are not reliable (we recall that the current cavitation model is not intended for bubble cavitation). In such cases, the iterative cavitating flow procedure usually fails to converge.

Two cases of interest are displayed on this figure, with the associated C_p distributions (both suction and pressure sides) and pattern image: $J=0.65$, $\sigma_n=0.528$; $J=0.77$, $\sigma_n=2.082$. These two cavitating situations are discussed hereafter.

Bubble cavitation is present at low values of the cavitation number σ_n and is coexisting in most of the cases with supercavitation. This situation can be observed on the left photograph taken at $J=0.65$, $\sigma_n=0.528$, at mid-span of the profile, and is fully consistent with the numerical predictions of the pressure coefficient C_p using a non-cavitating flow model (this flow case is beyond the convergence limit $\sigma_n^{\min}(J)$). At $r/R=0.4$, the calculated C_p on the suction side has a very smooth evolution in the chordwise direction, which favors the explosion of nuclei into bubbles. Closer to the blade tip (e.g., at $r/R=0.8$), the presence of a strong pressure gradient next to the leading edge starts a fully developed sheet cavitation extending past the trailing edge.

The second case (right part of Fig. 9) corresponds to $J=0.77$, $\sigma_n=2.082$. Close to the tip (here at $r/R=0.88$), the C_p distribution on the suction side, calculated using the cavitating model, clearly shows the region at $C_p = -\sigma_n$ and the recompression zone in the closure of the cavity. The C_p then recovers back to the wet (non-cavitating) C_p levels, which are also represented to show the consistency between the non-cavitating and the cavitating calculations. The attached sheet cavitation observed in these conditions mixes with the tip vortex structure and, for the highest values of σ_n , transforms into the so-called leading edge cavitating vortex.

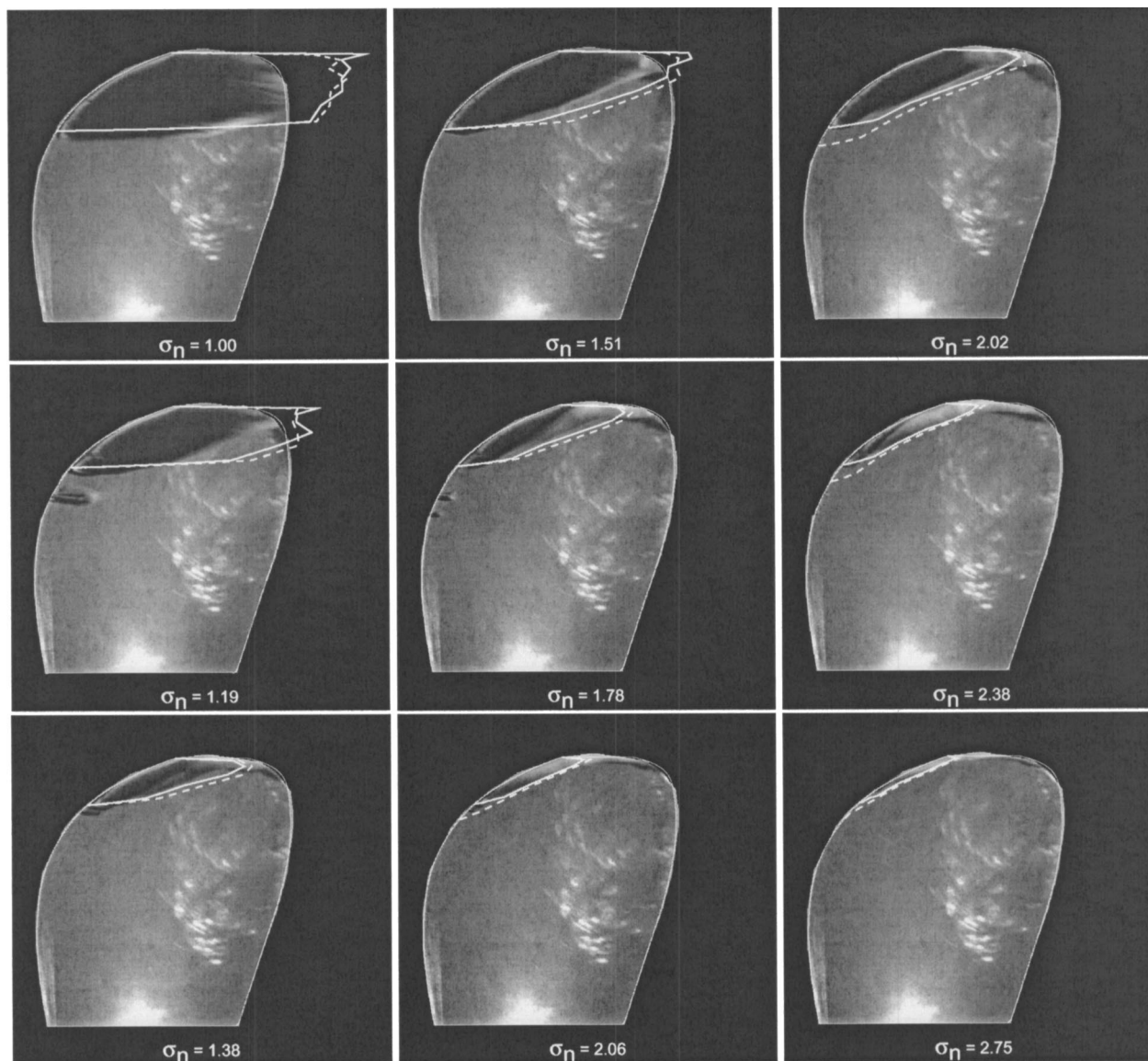


Fig. 10 Planform view of the cavitating blade and predicted cavitation area at $J=0.71$ (top row), 0.77 (center) and 0.83 (bottom): free wake model (solid line), prescribed wake model (dashed line)

The propeller also presents a form of streak cavitation, moderately present for $J=0.65$, $\sigma_n=0.528$. This pattern is characterized by two or three vapor streaks detaching at precise locations along the leading edge. This situation is thought to be caused by surface irregularities of the model blade geometry (i.e., local roughness) that, combined with the flat C_p distribution, become the place of early and very localized cavitation spots.

Images of the cavitation pattern for nine selected flow conditions are shown in Fig. 10. These images have been obtained using the warp procedure described earlier. The cavity areas calculated using both the free wake model (solid line) and the prescribed wake model (dashed line) are also shown for comparison. The predicted extension of the cavitating area is clearly affected by the shape of the trailing wake used in the calculations. In particular, if a correct location of the trailing vorticity is provided via the wake alignment technique (free wake model), the numerical results (solid curves) are in closer agreement with the experiments as compared to those obtained using a prescribed wake model (dashed curves).

A quantitative comparison between the observed and the calculated cavity extensions is made possible using the area measure-

ment technique described in this work. Results are shown in Fig. 11, where the data referred to five values of the advance coefficient are shown. The area is expressed as the ratio between the measured cavitation area A_c and the blade planform area A_0 for $r/R \geq 0.3$. The experimental mean values are represented with the corresponding standard deviation. We recall that the image analysis error was estimated to be less than 1%.

The cavitation area fluctuations are in general very small, in the range of 1% to 3%, except for the cases at the lowest values of the cavitation number σ_n , where the occurrence of bubble cavitation is the source of important variations of the pattern figure. The agreement between numerical predictions and experimental data is generally very good. Some discrepancies are observed when σ_n approaches the model convergence limit displayed in Fig. 9, and when low J values are considered (e.g., curves at $J=0.65$ and $J=0.71$). We observe that the numerical simulations tend to systematically overpredict the measurements, and differences range from 1%–2% at high σ_n and high J , to 10%–15% at low σ_n and low J .

The tendency of the present theoretical model to overpredict the extension of the cavitating flow region may be due, at least in part,

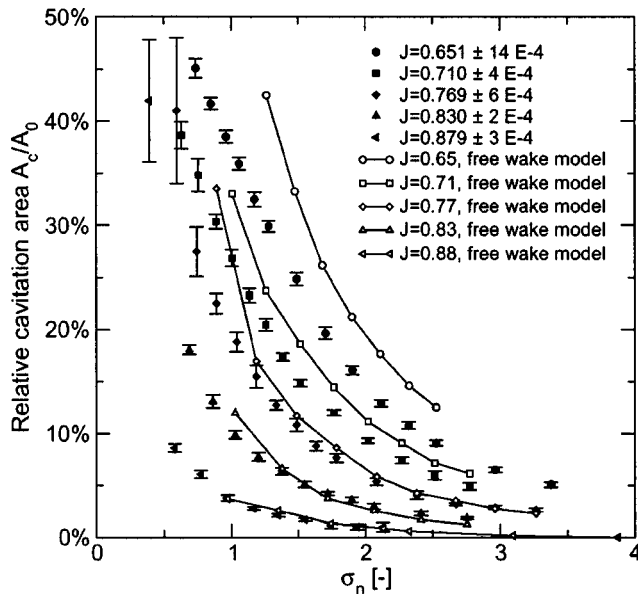


Fig. 11 Effect of parameters J and σ_n on the cavity area A_c . Comparison between measurements and numerical results (free wake model).

to both the numerical discretization errors and the inviscid flow assumptions. For instance, the case $J=0.71$, $\sigma_n=1.515$ shown in Fig. 11 reports a discrepancy between the measured and predicted values of about 26%, half of which are due to discretization errors, as also visible in Fig. 6. With regard to the inviscid flow assumptions, Salvatore and Esposito [25] show that the inclusion of viscous flow effects induces a non-negligible reduction of both the cavity extension and thickness as compared to inviscid flow calculations.

The propeller thrust and torque coefficients for three values of the advance coefficient are shown in Figs. 12 and 13. A common feature is that both K_T and K_Q increase as the cavitation number is increased. At low σ_n , this trend is more evident and is associated with the presence of extensive cavitation on the blades. Numerical calculations are also given for comparison. A satisfactory agreement between numerical predictions and measurements is ob-

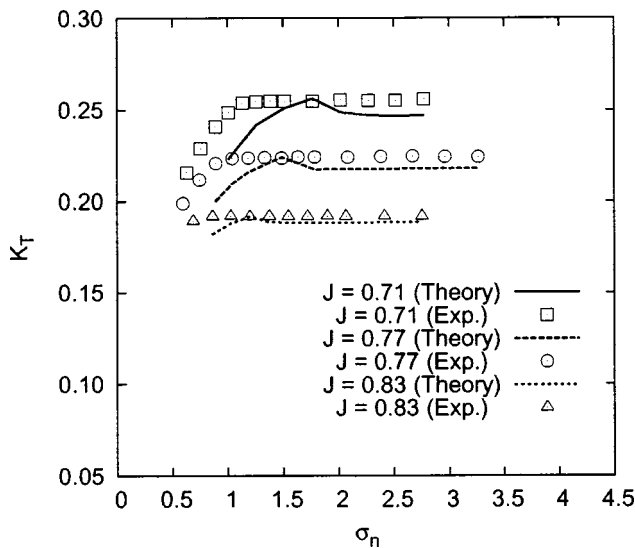


Fig. 12 Effect of cavitation number σ_n on the propeller thrust coefficient

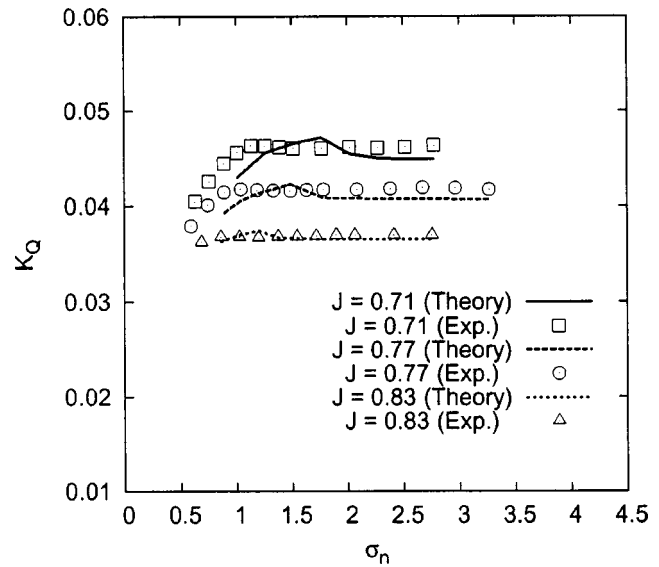


Fig. 13 Effect of cavitation number σ_n on the propeller torque coefficient

tained, except for flow conditions at low σ_n where both K_T and K_Q calculations are biased by the convergence limit and by the overestimation of the cavitation pattern.

Concluding Remarks

An experimental investigation on a cavitating propeller in a uniform inflow has been presented. The cavitation figures have been analyzed through novel, accurate and robust analysis methods. A complete map of the propeller hydrodynamic characteristics has been established and the cavitating behavior quantified in terms of cavitation extension.

We used the measurements to assess an inviscid flow boundary element method for the analysis of blade partial sheet and supercavitation. The methodology included a refined evaluation of the trailing wake vorticity path by means of a wake alignment technique.

Comparison with the experimental measurements showed that the present theoretical methodology was able to accurately predict the sheet cavitation area across a wide range of advance ratios and of cavitation number values. The importance of having a good description of the trailing wake vorticity has been highlighted and the range of applicability of the present prediction model clearly identified.

The present work constitutes the first phase of a joint experimental and theoretical research project. Phase two of the project extends the current results to the hydrodynamic/hydroacoustic analysis of propellers in non-uniform inflow conditions. Experimental effort is also ongoing to extend the cavity area measurement principle to the volume measurement. From a theoretical viewpoint, the inclusion of viscous flow modeling and the analysis of tip-vortex cavitation are being addressed.

A database accessible to the public (<http://crm.insean.it/E779A>) is being regularly updated with the latest results and developments, complementing the already existing propeller geometry, pressure, noise, PIV, and LDV data.

Acknowledgments

The authors are grateful to the CEIMM personnel. The work was performed in the construct of the INSEAN 2000-2002 Research Program supported by the Italian *Ministero dei Trasporti e della Navigazione*.

Nomenclature

- \mathbf{n} = Boundary surface outward unit normal
 \mathbf{q} = Total velocity: $\mathbf{q} = \mathbf{v}_i + \nabla\varphi$
 \mathbf{v} = Perturbation velocity
 \mathbf{v}_i = Inflow velocity
 S_B = Body surface
 S_{CB} = Cavitating area on body surface
 S_{CW} = Cavitating area on wake surface
 S_C = Cavity surface
 S_{WB} = Non-cavitating body surface
 S_W = Trailing wake surface
 \mathcal{V}_P = Potential flow domain
 A_0 = Blade face area for $r/R \geq 0.3$
 A_c = Cavity area
 C_p = Pressure coefficient, $(p - p_0)/0.5\rho(nD)^2$
 D = Propeller diameter, $2R$
 h_c = Cavity thickness
 J = Advance coefficient, v_0/nD
 K_Q = Torque coefficient, $Q/\rho n^2 D^5$
 K_T = Thrust coefficient, $T/\rho n^2 D^4$
 M_B = Chordwise number of blade face elements
 M_W = Streamwise number of wake-turn elements
 n = Propeller angular velocity (rps), normal
 N_B = Spanwise number of blade face elements
 N_H^{tot} = Number of hub sector elements
 p = Pressure
 p_0 = Pressure at propeller axis
 p_v = Vapor pressure
 Q = Torque
 R = Propeller radius
 s = Surface arclength in chordwise direction
 T = Thrust
 u = Surface arclength in spanwise direction
 v_0 = Upstream axial inflow velocity
 V_c = Cavity volume
 ρ = Fluid density
 σ_0 = Cavitation number referred to v_0 , $(p_0 - p_v)/0.5\rho v_0^2$
 σ_n = Cavitation number referred to n , $(p_0 - p_v)/0.5\rho(nD)^2$
 φ = Perturbation velocity potential

References

- [1] Dupont, P., and Avellan, F., 1991, "Numerical Computation of a Leading Edge Cavity," *Proc. of Int. Symposium on Cavitation and Multiphase Flow*, vol. FED-116, ASME-JSME, Portland, Oregon (USA), pp. 47–54.
- [2] Pereira, F., 1997, "Prédiction de l'Érosion de Cavitation: Approche Énergétique," Ph.D. thesis, Ecole Polytechnique Fédérale de Lausanne, Institut de Machines Hydrauliques et de Mécanique des Fluides (IMHEF-LMH), no 1592.
- [3] Pereira, F., Avellan, F., and Dupont, P., 1998, "Prediction of Cavitation Erosion: An Energy Approach," *J. Fluids Eng.*, **120**(4), pp. 719–727.
- [4] Chiba, N., Sasajima, T., and Hoshino, T., 1980, "Prediction of Propeller-Induced Fluctuating Pressures and Correlation With Full Scale Data," *Proc. of the 13th Symposium on Naval Hydrodynamics*, ONR, Tokyo, pp. 89–103.
- [5] Lehman, A. F., 1966, "Determination of Cavity Volumes Forming on a Rotating Blade," *11th International Towing Tank Conference*, ITTC, Tokyo (Japan), pp. 250–253.
- [6] Sontvedt, T., and Frivold, H., 1976, "Low Frequency Variation of the Surface Shape of Tip Region Cavitation of Marine Propeller Blades and Corresponding Disturbances on Nearby Solid Boundaries," *Proc. of the 11th Symposium on Naval Hydrodynamics*, ONR, London, pp. 717–729.
- [7] Ukon, Y., and Kurobe, Y., 1981, "Measurement of Cavity Thickness Distribution on Marine Propellers by Laser Scattering Technique," *Proc. of the 16th ITTC*, vol. 2, Leningrad (USSR), pp. 241–245.
- [8] Ukon, Y., Kudo, T., and Kurobe, Y., 1991, "Measurement of Cavity Thickness Distribution on the Blade of Propeller Models by Laser-CCD Method," *Proc. of the 1st ASME-JSME Fluids Engineering Conference*, vol. FED-116, Portland, Oregon (USA), pp. 99–104.
- [9] Kodama, Y., Takei, Y., and Kakugawa, A., 1983, "Measurement of Cavity Thickness on a Full Scale Ship Using Lasers and a TV Camera," *Papers of Ship Research Institute*, **73**, pp. 1–42.
- [10] Tanibayashi, H., Saito, Y., and Fujino, R., 1991, "Full-Scale Measurement of Cavity Over the Blades of Marine Propellers," *Proc. of Int. Cavitation and Multiphase Flow Forum*, vol. FED-109, 1st ASME/JJSE Fluids Engineering Conference, Portland, Oregon (USA), pp. 107–110.
- [11] Stünzing, H. D., 1990, "Cavity Thickness on Rotating Propeller Blades," *Proc. of the 18th Symposium on Naval Hydrodynamics*, ONR, Ann Arbor, Michigan, pp. 75–85.
- [12] Stella, A., Guj, G., Di Felice, F., and Elefante, M., 2000, "Experimental Investigation of Propeller Wake Evolution by Means of LDV and Flow Visualizations," *Journal of Ship Research*, **44**(3), pp. 155–169.
- [13] Di Felice, F., Romano, G. P., and Elefante, M., 2000, "Propeller Wake Evolution by Means of PIV," *Proc. 23rd Symposium on Naval Hydrodynamics*, ONR, Val de Reuil (France), pp. 62–76.
- [14] Kim, Y. G., and Lee, C. S., 1997, "Prediction of Unsteady Performance of Marine Propellers with Cavitation Using Surface-Panel Method," *Proc. of the 21st Symposium on Naval Hydrodynamics*, Trondheim (Norway), pp. 913–929.
- [15] Mueller, A. C., and Kinnas, S. A., 1997, "Cavitation Predictions Using a Panel Method," *Proc. of the ASME Symposium on Marine Hydrodynamics and Ocean Engineering*, Dallas (USA).
- [16] Morino, L., Chen, L. T., and Suci, E. O., 1975, "Steady and Oscillatory Subsonic and Supersonic Aerodynamics Around Complex Configurations," *AIAA J.*, **13**, pp. 368–374.
- [17] Lee, J. T., 1987, *A Potential Based Panel Method for the Analysis of Marine Propellers in Steady Flow*, Tech. Rep. 87-13, Dept. Ocean Engineering, MIT, Cambridge, Massachusetts (USA).
- [18] Kinnas, S. A., and Fine, N. E., 1992, "A Nonlinear Boundary Element Method for the Analysis of Propeller Sheet Cavitation," *Proc. of the 19th Symposium on Naval Hydrodynamics*, ONR, Seoul (Korea), pp. 1–17.
- [19] Pham, T. M., Larrarte, F., and Fruman, D. H., 1998, "Investigation of Unstable Cloud Cavitation," *Proc. of the 3rd Int. Symp. on Cavitation*, vol. 1, pp. 215–220.
- [20] Wolberg, G., 1996, *Digital Image Warping*, IEEE Computer Society Press, Los Alamitos, CA (USA).
- [21] Salvatore, F., and Testa, C., 2002, *Theoretical Modelling of Marine Propeller Cavitation in Unsteady High-Reynolds Number Flows*, Tech. Rep. 2002-077, INSEAN, Rome (Italy).
- [22] Lemonnier, H., and Rowe, A., 1988, "Another Approach in Modelling Cavitating Flows," *J. Fluid Mech.*, **195**, pp. 557–580.
- [23] Giordani, A., Salvatore, F., and Esposito, P., 1999, "Free Wake Analysis of a Marine Propeller in Uniform Flow," *Proc. of the XXI Int. Conference on Boundary Element Methods*, Oxford (U.K.).
- [24] Arndt, R. E. A., Arakeri, V. H., and Higuchi, H., 1991, "Some Observations of Tip-Vortex Cavitation," *J. Fluid Mech.*, **229**, pp. 269–289.
- [25] Salvatore, F., and Esposito, P., 2001, "An Improved Boundary Element Analysis of Cavitating Three-Dimensional Hydrofoils," *Proc. of the 4th International Symposium on Cavitation*, B1.006, Pasadena, CA (USA).

An Experimental Study on the Influence of Flow Maldistribution on the Pressure Drop Across a Plate Heat Exchanger

B. Prabhakara Rao

Sarit K. Das*

Heat Transfer and Thermal Power Laboratory,
Department of Mechanical Engineering,
Indian Institute of Technology Madras,
Chennai-600 036 (INDIA)

A detailed experimental study on flow maldistribution from port to channel of a plate heat exchanger is presented. In general, flow maldistribution brings about an increase in pressure drop across the heat exchanger. This increase is found to depend on flow rate, number of channels and port size. Experiments show that analytical predictions of pressure drop including maldistribution effect are quite accurate for practical purposes. The results indicate that under identical conditions, maldistribution is more severe in Z-type plate heat exchanger compared to U type. Experiments are also carried out under non-isothermal realistic operating conditions, which show increased flow maldistribution at elevated temperature. Finally predictions are made for industrial plate heat exchangers, which show the limitation of adding additional plates beyond a certain limit. An insight to the physical aspects of maldistribution and its possible reduction through proper design strategy is also indicated. [DOI: 10.1115/1.1779664]

Introduction

In recent years there has been an increasing usage of Plate Heat Exchangers (PHE) in industries around the world. PHEs were originally invented for hygienic industries such as brewery, dairy and food processing due to its ease of cleaning and maintenance. Later on they have been found to possess other advantages such as compactness, ability to recover heat with very small temperature difference, flexibility, lesser tendency to fouling and less susceptibility to flow induced vibration. Also, the advancement of material technology brought about new temperature and pressure resistant materials for gasket, which enhanced the temperature and pressure range of its application. This has made it possible to use these heat exchangers in power and chemical process industry. In a plate heat exchanger corrugated channels are used to enhance heat transfer by promoting turbulence. However this also brings about higher-pressure drop. Hence the trade off between heat transfer and pressure drop is a major concern in a plate heat exchanger making the accurate prediction of overall pressure drop across the apparatus a task of prime importance.

In plate heat exchangers the pressure drop as well as thermal performance depends critically on distribution of fluid. Flow maldistribution can increase pressure drop and deteriorate thermal performance significantly nullifying its prime advantage. A good review of the work devoted to the problem associated with maldistribution has been compiled by Mueller and Chiou [1]. They explained that flow maldistribution can be induced by heat exchanger geometry, operating conditions (such as viscosity or density-induced maldistribution), multiphase flow, fouling phenomena, etc. Geometry-induced flow maldistribution can be classified into gross flow maldistribution, passage-to-passage flow maldistribution and manifold-induced flow maldistribution. The flow arrangement in plate heat exchangers can be mainly classified into two categories, U-type and Z-type configurations as

shown in Fig. 1. For PHE, the ports acting as manifolds induce maldistribution of flow into the channels which is dependent on flow configuration (U or Z type) and pass arrangement. The analytical model for flow distribution in manifolds had been described and presented as closed form equations using the general flow channelling and unification concept by Bajura and Jones [2,3]. Their result was used in developing the flow distribution model for PHE by Bassiouny and Martin [4,5]. Analytical flow distribution and pressure drop models have been developed by them under the assumption of variable flow rates in channels. The model was compared to experiments with simple tubular manifolds and tubular channels but not validated with flow through a real plate heat exchangers. Using numerical technique Datta and Majumdar [6] analyzed the effect of flow maldistribution of the fluid inside the channels of a single pass PHE. The influence of flow maldistribution on heat transfer equipment performance was clearly mentioned by Kitto and Robertson [7]. With different plate channel groups, Huang [8] stated that HTRI has developed an equation to predict port pressure distributions and channel flow rate distributions in a single pass plate heat exchanger based on its port maldistribution data. However, due to commercial interest they gave no indication about those data. Guidelines were presented by them to minimize port flow maldistribution. Muley and Manglik [9] has presented experimental investigation of isothermal friction factor and heat transfer data for chevron plates with angle of 60 deg but they didn't considered flow maldistribution from port to channels. Rao et al. [10] presented an analytical model for thermal response of single pass PHE incorporating the flow maldistribution model of Bassiouny and Martin [4,5].

Thus, majority of the investigators have reported results with uniform flow distribution from port to channels neglecting flow maldistribution in a plate heat exchanger, which limits its performance. The few studies available on flow maldistribution are theoretical in nature validated by only simple configurations such as manifold to tube channelling. In literature no experimental studies have been reported considering the influence of port to the channel flow distribution on the hydraulic performance of a real plate heat exchanger with respect to total pressure drop. The present experimental study brings out a clear picture about how the pressure drop is affected by maldistribution in a PHE and identifies the parameters affecting this distribution. The emphasis of the study is

*Corresponding author: Heat Transfer and Thermal Power Laboratory Department of Mechanical Engineering IIT Madras, Chennai-600 036 (INDIA) Fax: (+91)-44-22570545; Ph: (+91)-44-22578550; E-mail: skdas@iitm.ac.in sarit_das@hotmail.com

Contributed by the Fluids Engineering Division for publication in the JOURNAL OF FLUIDS ENGINEERING. Manuscript received by the Fluids Engineering Division February 21, 2003; revised manuscript received March 4, 2004. Associate Editor: M. V. Ötügen.

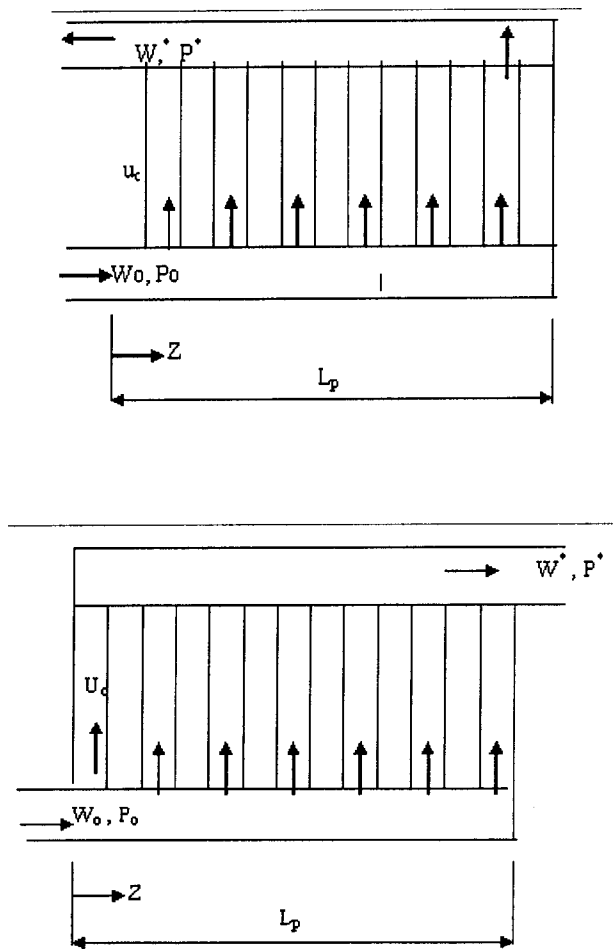


Fig. 1 Flow arrangement for U and Z type Plate Heat Exchangers

the application of simplified flow channeling theory to the engineering of PHEs for practical applications. This brings out the main physical features of a maldistributed flow and the design strategy to deal with it.

Experimental Setup and Procedure

A schematic of the closed loop experimental set-up layout is shown in Fig. 2. The test plate heat exchanger consists of 40 corrugated stainless steel plates. Geometrical features of these chevron plates are given below. The details of the plate are shown in Fig. 3 and its dimensions are tabulated in Table 1.

The working fluid used for the test is demineralized water stored in a tank. It has been pumped with the help of circulating pump of 3 HP rating and flow rates are controlled by the control valve. Using flow meter, the flow rates are measured. The pressure taps are located near inlet and exit of PHE as shown in Fig. 2. Both U and Z type flow arrangement can be measured with the same setting by using stop valves and. Closure of valve (10) makes it operate as a U type PHE while closure of valve (9) makes it a Z-type PHE. For this purpose, the end plate used in the heat exchanger must be a special plate with only one out of four ports are open. The pressure drop data have been measured with help of U tube type differential mercury manometer and cross-checked by digital manometer. To investigate the effect of port dimension a mandrel was inserted inside the port in few experimental cases to reduce the effective port diameter. The mandrel dimension was so chosen that the effective port diameter reduce from 70 mm to 35 mm as shown in Fig. 4. In order to evaluate hysteresis effects, the experiments were conducted with both in-

creasing and decreasing flow rates and the mean of the two readings were taken. The flow rate was measured by an ASME standard orifice meter with a differential mercury manometer connected across. The orifice was calibrated and an average C_d was measured to be 0.5942. The port inlet velocity, W_o is calculated from this flow rate. In order to evaluate the hydraulic parameters under non-isothermal condition under which a real PHE operates a thermal test loop as shown in Fig. 2 was built. The working fluid has been pumped with the help of circulating pump of 3 HP rating and flow rates are controlled by the control valve. Using orifice flow meter, for both hot and cold fluids the flow rates are measured. The pressure taps are located near inlet and exit of PHE as shown in Fig. 5. Both hot and cold fluids have been pumped through the plate heat exchanger. Cold process fluid is pumped out of the cooling tower well into the plate heat exchanger where heat is transferred from the hot fluid to the cold fluid. The cold fluid then enters a cooling tower where it is cooled to feed back to the plate heat exchanger. The hot fluid is also pumped with the help of a 3 HP pump into the plate heat exchanger where it transfers heat to the cold fluid prior to flowing back into the feed water heating storage tank. Data were obtained by holding the process fluid flow rate constant with constant amount of heat input from the submerged heating element with maximum capacity of 42 kW. The temperature limits were determined by the limitations of the cooling tower outlet water maximum temperature. The flow rate limits were determined by the maximum allowable heat transfer to the cooling tower, and by the system's ability to achieve steady state within a reasonable time.

The experiments were conducted with both increasing and decreasing flow rates and the mean of the two readings were taken. The four T-type thermocouples used to measure the temperature of both hot and cold fluid in the present study were calibrated over the range of interest, using a precision thermometer and a constant temperature bath.

Data Reduction and Error Estimates

All the experimental data were obtained under steady state conditions and the range of operating flow rates were taken to have Reynolds number from 700 to 7000 for both U and Z type PHE. For evaluating the friction factor, the experimental data for a single channel pressure drop has been obtained. Figure 6 shows this general behavior of the hydraulic resistance in a channel with increasing Reynolds number. The correlation between friction factor and Reynolds number has been found to be

$$f = 21.41 \text{Re}^{-0.301} \quad \text{for } 1000 < \text{Re} < 7000 \quad (1)$$

It must be mentioned here that the Reynolds number for PHE is defined on the basis of twice the plate spacing b , as

$$\text{Re} = \frac{U_c(2b)}{\nu}$$

Usually in PHE, the transition from laminar to turbulent flow takes place between Re values of 400 to 500. Hence the range of Re chosen is in the turbulent regime.

This flow friction data was used in the following channel pressure drop equation to obtain the channel friction coefficient, ζ_c ,

$$\zeta_c = \frac{2(\Delta P)_{ch}}{\rho U_c^2} \quad (2)$$

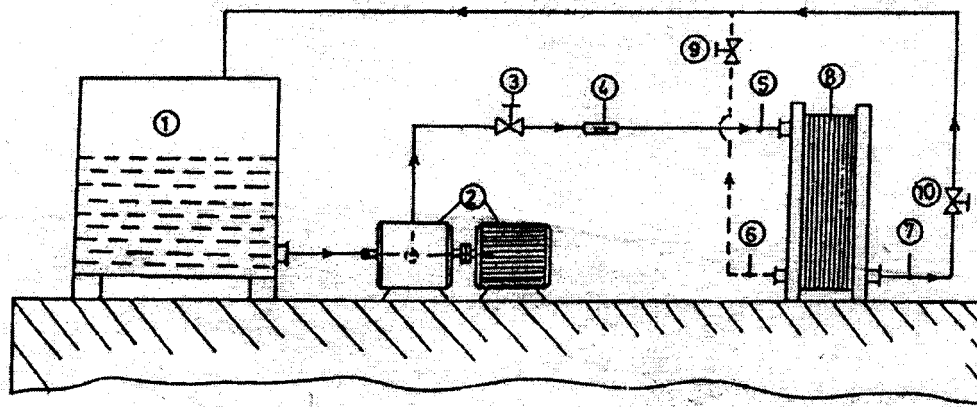
where $\zeta_c = fl/d_e + \text{other minor losses including turning}$

The non-dimensional pressure drop can be written as

$$\Delta p^* = \frac{P - P^*}{\rho W_o^2}$$

where, W_o = velocity of flow in the port at the entry

The pressure drop measured with the help of the U tube differential mercury manometer across the PHE has been non-



- 1 Storage tank
- 2 Pump with 3 HP motor
- 3 Flow control valve
- 4 Flow meter
- 5 Pressure tap inlet
- 6 & 7 Pressure tap outlet
- 8 Plate heat exchanger
- 9 & 10 Stop valve

Fig. 2 Schematic view of experimental test facility

dimensionalized and this value is compared with the theoretical pressure drop. A wide range of experiments was carried out for U and Z type plate heat exchanger with different combinations of fluid (water) flow rate ranging from 0.13 to 3.6 liters/s.

The uncertainty of the pressure drop measurement was found to be 4.5% (maximum) for mercury manometer used across the orifice flow meter. The uncertainty of measurement of orifice diameter was 3%. From the calibration curve of discharge coefficient of the orifice was found to be 2%. From these parameters, the following procedure outlined by Moffat [11] the uncertainty in the flow measurement was calculated to be 3.1%. Also pressure drop across the PHE is required to be measured. The uncertainty in the measurement of pressure drop across the PHE was found to be 4.5% maximum. The uncertainty in temperature measurement was within $\pm 0.21^\circ\text{C}$, which is 4% of the minimum temperature difference.

Pressure Drop and Maldistribution Parameters in PHE

The pressure profiles in both the intake and exhaust conduits of the plate heat exchangers are due to momentum change as a result of flow branching to the channels, while the effect of friction losses in the port are considered to be negligibly small. In a Z-type plate heat exchanger, the flow enters one side of the bottom and leaves other side of the top as shown in Fig. 1. In case of U type plate heat exchanger, both entry and exit of fluid will be on same side.

To calculate the total pressure drop of a plate heat exchanger and flow distribution from port to channel, equations have been developed by Bassouiny and Martin [4,5] for U and Z-type flow arrangement considering momentum balance on elemental fluid volume inside inlet and exit port. The continuity and momentum equations are applied to the conduit sections for both dividing and combining flow conduits. The final form of these equations can be written for negligible port friction as

For U-type

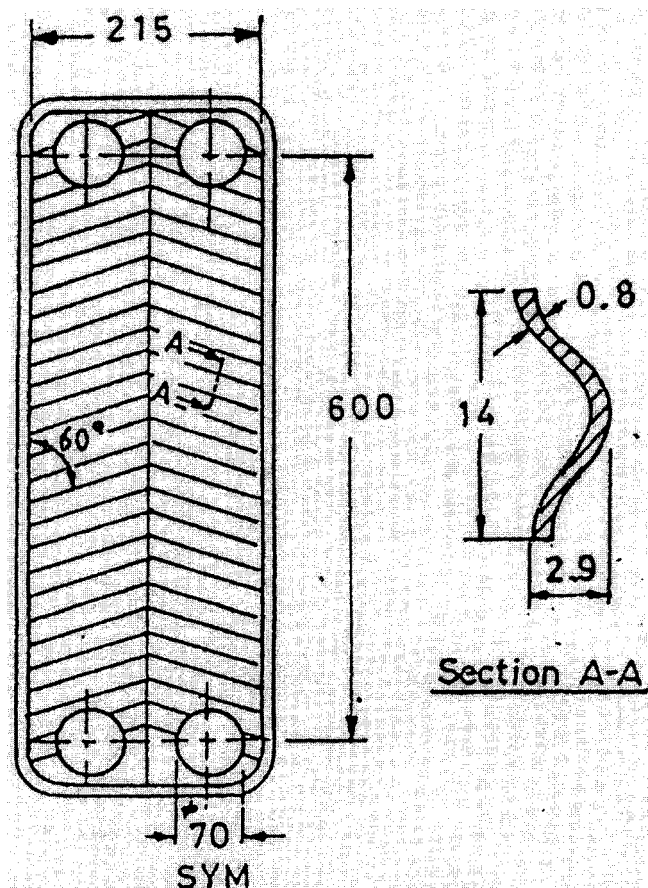


Fig. 3 Geometrical attributes of the chevron plate

Table 1 Geometric characteristics of a plate

S. No	Particulars	Dimensions
1	Port diameter, D_p	70 mm
2	Equivalent diameter of the channel, d_c	5.8 mm
3	The vertical distance between ports, L_p	600 mm
4	Plate width (gasket to gasket), w	215 mm
5	Chevron angle, β	60 deg
6	Corrugation pitch, δ	14 mm
7	Amplitude of corrugation, b	2.9 mm
8	The plate material	SS
9	The gasket material	Nitrile Rubber

$$\frac{d(p-p^*)}{dz} + \left[(2-\beta^*) \left(\frac{A}{A^*} \right)^2 - (2-w) \right] \frac{dw}{dz} = 0 \quad (3)$$

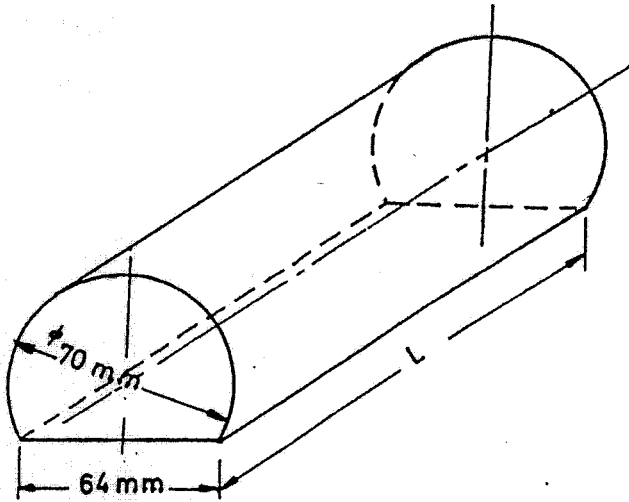


Fig. 4 Schematic view of the mandrel

For Z-type

$$\frac{d(p-p^*)}{dz} - \left[(2-\beta^*) \left(\frac{A}{A^*} \right)^2 - (2-w) \right] \frac{dw}{dz} = 0 \quad (4)$$

$$p-p^* = \frac{1}{2} \left(\frac{A}{A_c n} \right)^2 \left(\frac{dw}{dz} \right)^2 \quad (5)$$

From equation (3) and (4), we can obtain two ordinary differential equations for the velocity in the intake conduit.

For U-type

$$\frac{d^2(w)}{dz^2} - m^2(w) = 0 \quad (6)$$

For Z-type

$$\frac{d^2(1-w)}{dz^2} - m^2(1-w) = \varepsilon \quad (7)$$

and

$$\frac{dw}{dz} = 0 \quad (8)$$

where

$$m^2 = \left\{ \left[\left(\frac{2-\beta^*}{2-\beta} \right) \left(\frac{A}{A^*} \right) \right]^2 - 1 \right\} \varepsilon$$

and

$$\varepsilon = \frac{2-\beta}{\zeta_c \left(\frac{A}{A_c n} \right)^2}$$

where

$$w = \frac{W}{W_o}, \quad \beta = \frac{W_c}{W}$$

- 2 & 6 Flow control valve
- 1 Plate heat exchanger
- 3 Hot water tank with temperature controller
- 4 & 5 Circulating pump
- 7 Cooling tower

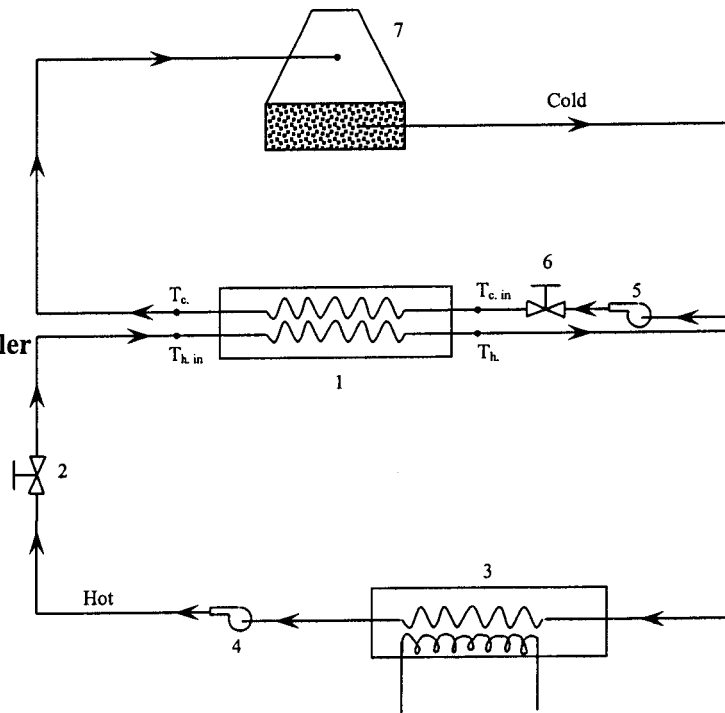


Fig. 5 A schematic view of the thermal test circuit of the PHE

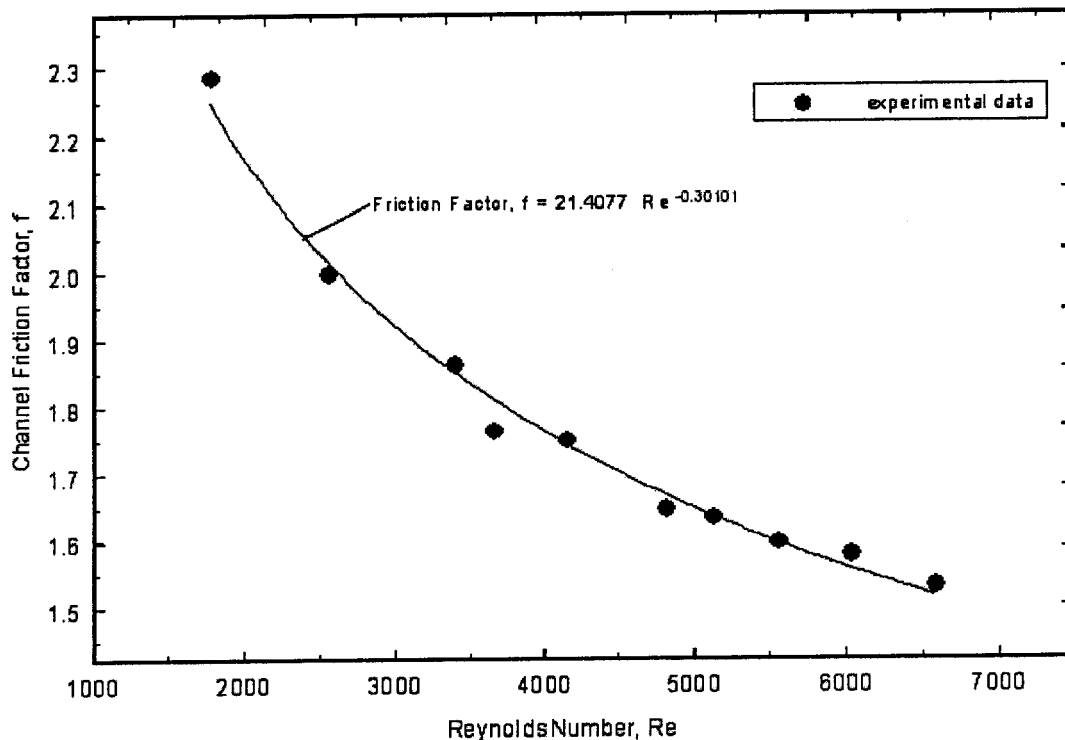


Fig. 6 Flow friction characteristics of a single channel

For identical inlet and exit port $\beta \approx 0$ and $\beta^* \approx 1$
 Giving

$$m^2 = \left(\frac{nA_c}{A} \right)^2 \frac{1}{\zeta_c} \quad (9)$$

Here ζ_c is the total frictional resistance of the channel defined by Eq. (2). In these equations m^2 is the parameter which is a measure of flow maldistribution. The value of m^2 approaches zero when flow is uniformly distributed amongst channels. More the flow maldistribution, the larger the value of m^2 . The theoretical values of m^2 for the present PHE is shown in Table 2.

Applying the boundary conditions one obtains the following final equation for port to channel flow distribution as given by Bassiouny and Martin [4,5]

U-type

$$u_c = \left(\frac{A}{nA_c} \right) m \frac{\cosh m(1-z)}{\sinh m} \quad (10a)$$

Z-type

$$u_c = \left(\frac{A}{nA_c} \right) m \frac{\cosh mz}{\sinh m} \quad (10b)$$

The total dimensionless pressure drop of the Plate Heat Exchanger is

Table 2 The parameter m^2 for the flow distribution in test PHE

Re	N=10	N=33	N=100	N=400
500	0.0078	0.0852	0.7825	12.520
1000	0.0096	0.1050	0.9640	15.425
2000	0.0118	0.1293	1.1878	19.000
3000	0.0134	0.1461	1.3419	21.470
5000	0.1560	0.1704	1.5649	25.039
10000	0.1920	0.2099	1.9280	30.848

U-type

$$p_0 - p_0^* = \left(\frac{m^2}{\tanh^2 m} \right) \left(\frac{A}{nA_c} \right)^2 \frac{\zeta_c}{2} \quad (11a)$$

Z-type

$$p_0 - p_0^* = \left[\left(\frac{m^2}{\tanh^2 m} \right) + \varepsilon \left(1 + \frac{\varepsilon}{m^2} \right) \frac{(1 - \sec hm)^2}{\tanh^2 m} \right] \times \left(\frac{A}{nA_c} \right)^2 \frac{\zeta_c}{2} \rho W_o^2 \quad (11b)$$

Using Eqs. (1) and (2) ζ_c has been calculated and the value of the maldistribution parameter, m^2 has been computed from Eq. (9). These values have been incorporated in Eq. (11) to calculate the theoretical non-dimensional pressure drop across the plate heat exchanger.

Results and Discussion

A number of experiments were conducted for the range of Reynolds number from 700 to 7000 for U and Z-type flow arrangement. The main operating parameters are the flow rate, number of channels, port size and flow configuration (U and Z type). The port size has been changed with the help of the mandrel. The mandrel has been inserted into actual port to reduce the cross section to one fourth. This helps to create the flow maldistribution from port to channel while varying the ratio of the channel cross section to port cross section area and thus increase the value of m^2 by a factor of 16.

In Figs. 7 and 8 the comparison of experimental values of non-dimensional pressure drop with the theoretical data for different channels of U and Z-type PHE is presented. The number of channels taken is 10, 15 and 18 for Z type and 10 and 15 for U-type. The lines indicate the theoretical prediction. Both the theoretical and experimental data are found to be in good agreement. The

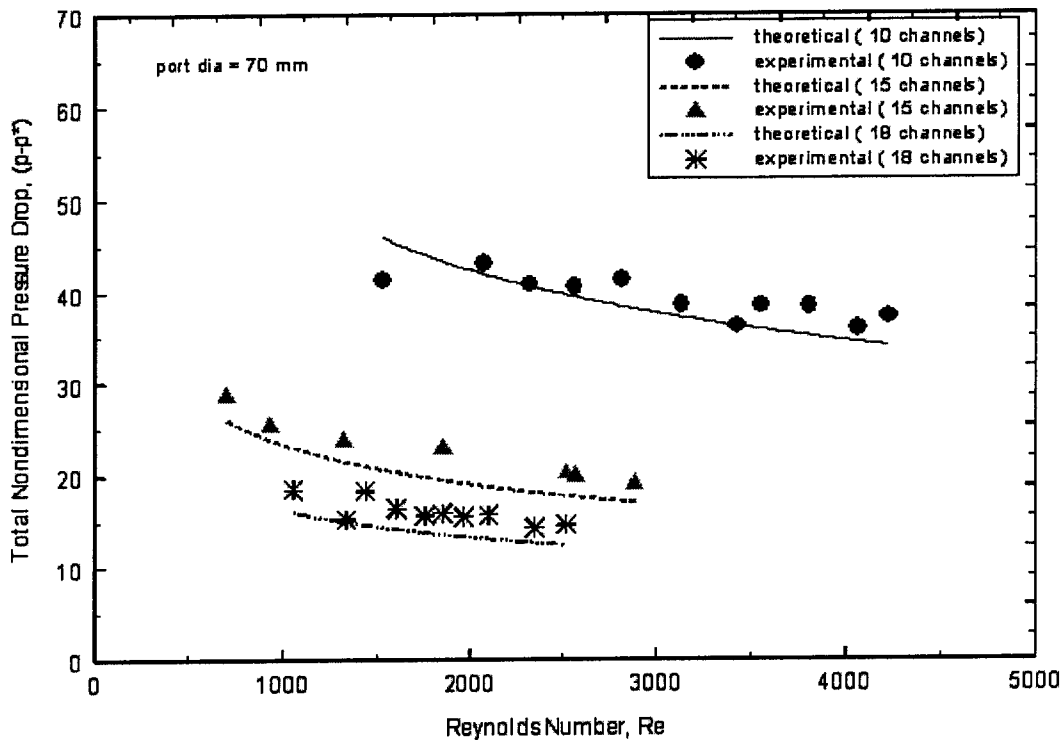


Fig. 7 Comparison of experimental pressure drop with theoretical prediction for a Z-type PHE

deviation of the experimental data from theoretical predictions is within 10% as can be seen from the parity plot given in Fig. 9. From these plots (Figs. 7 and 8) it can be observed that the non-dimensional pressure drop decreases with increasing channel Reynolds number because the non-dimensionalizing velocity, W_0 itself increases for a fixed number of channels. Obviously for a

given number of channels the total dimensional pressure drop increases with channel flow rate as shown in Fig. 11. Figure 10 shows the variation of the flow maldistribution parameter, m^2 with Reynolds number for 10 and 15 channel Z-type PHE of different effective port sizes of 70 mm and 35 mm. This gives an idea of how the flow maldistribution parameter changes with the change

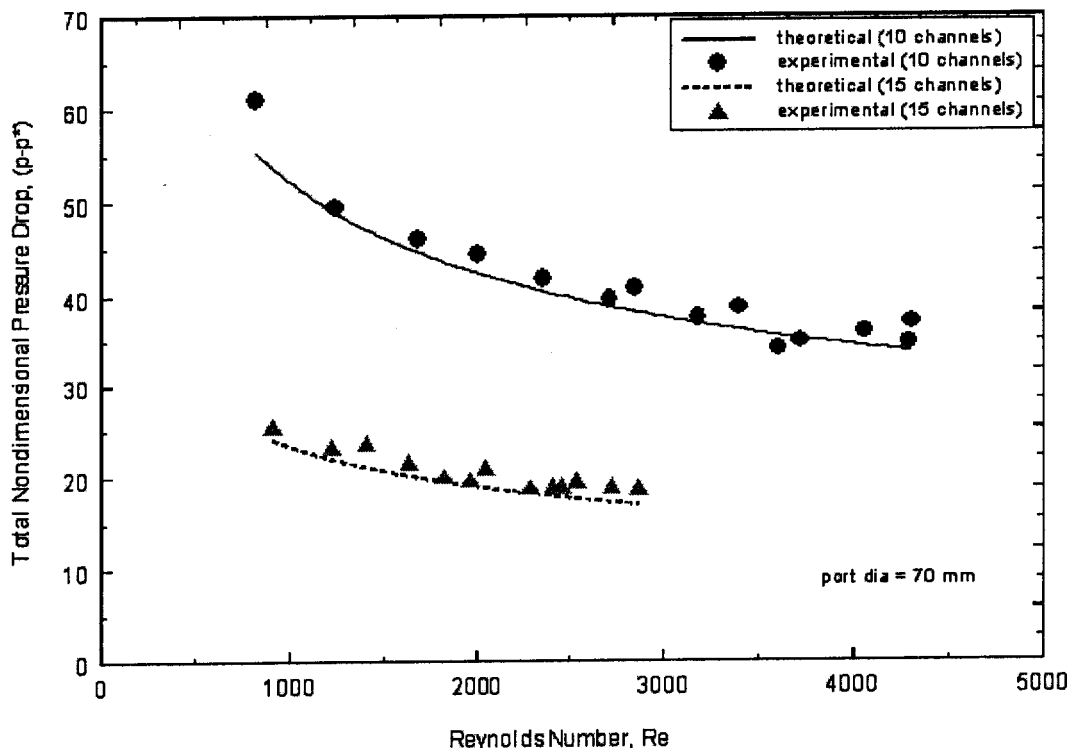


Fig. 8 Comparison of experimental pressure drop with theoretical prediction for a U-type PHE

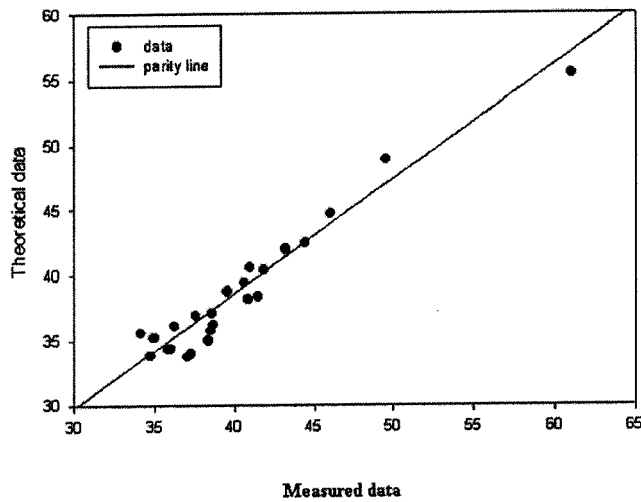


Fig. 9 Parity plot between theoretical and experimental pressure drop in PHE

of the port sizes. At normal values of port size, the m^2 value does not change with the flow rates appreciably and the values are close to zero indicating a good flow distribution. But when the effective port diameter is reduced to half its normal value, it changes considerably with the flow rate. At higher flow rates, it changes rapidly with change of flow rate. These values of maldistribution parameters bring out the dimensional pressure drop in the heat exchanger depicted in Fig. 11. It can be seen that as the port size decreases, the pressure drop increases due to maldistribution. The increase in pressure drop is more for larger number of channels because maldistribution is a strong function of number of channels. Figure 12 show this effect of port diameter on the distribution of channel velocities (and hence channel flow distribution) for Z-type PHE which follows from the increase in pressure drop. The flow distribution is uniform at actual port diameter

of 70 mm over the entire flow rate range but when port sizes reduces, flow maldistribution is created which is higher at higher flow rates. These results indicate that the flow from the first channel to last channel varies from lower to higher value in case of Z-type PHE. Figure 13 predicts the effect of flow and change of port size on maldistribution parameter, m^2 for U-type PHE and Fig. 14 channel velocity for the same. In case of U-type PHE the flow varies from higher to lower value from the first to the last channel. Here also, the role of port size and flow velocity is found to be crucial. Figure 15 shows that the comparison of m^2 for U and Z-type PHE for the same conditions of port sizes and flow rates. It clearly indicates that the flow maldistribution is more severe in case of Z-type than U-type PHE for smaller port sizes. Figure 16 shows the prediction of flow distribution when higher number of channels is considered as in the case of practical applications (from 100 to 400 channels) with the present plates. This will be the case in typical industrial heat exchangers. For the range of 100 channels, the m^2 will be of smaller value if the port diameter is kept 70 mm but in case of higher number of channels (400) its value is much higher even with such large port diameter.

It can be seen from Fig. 16 that for 100 channels PHE the maximum channel velocity can be 50% higher than mean velocity. For 200, 300 and 400 plates this maximum values can be as high as 2.5, 3.5 and 5 times the mean value respectively. On the other hand the plates at remote end of this U type heat exchanger may hardly receive any flow. With 400 plates more than last 100 plates receive almost no flow. This gives an idea about how addition of plates instead of increasing the plate heat exchanger performance can only add to the flow maldistribution resulting in higher pressure drop and lower heat transfer. The point to be noted here is the fact that this severe flow maldistribution has been achieved with even 70 mm of port diameter which with 15 and 18 channels gave no flow maldistribution at all. Figure 17 shows the prediction of m^2 values at different higher number of channels for the same range of 100 to 400 plates. It is clearly evident that when number of channels are higher and port sizes are reduced, the m^2 values increases substantially so that the flow distribution will be even worse. The maldistribution parameter for different port sizes with

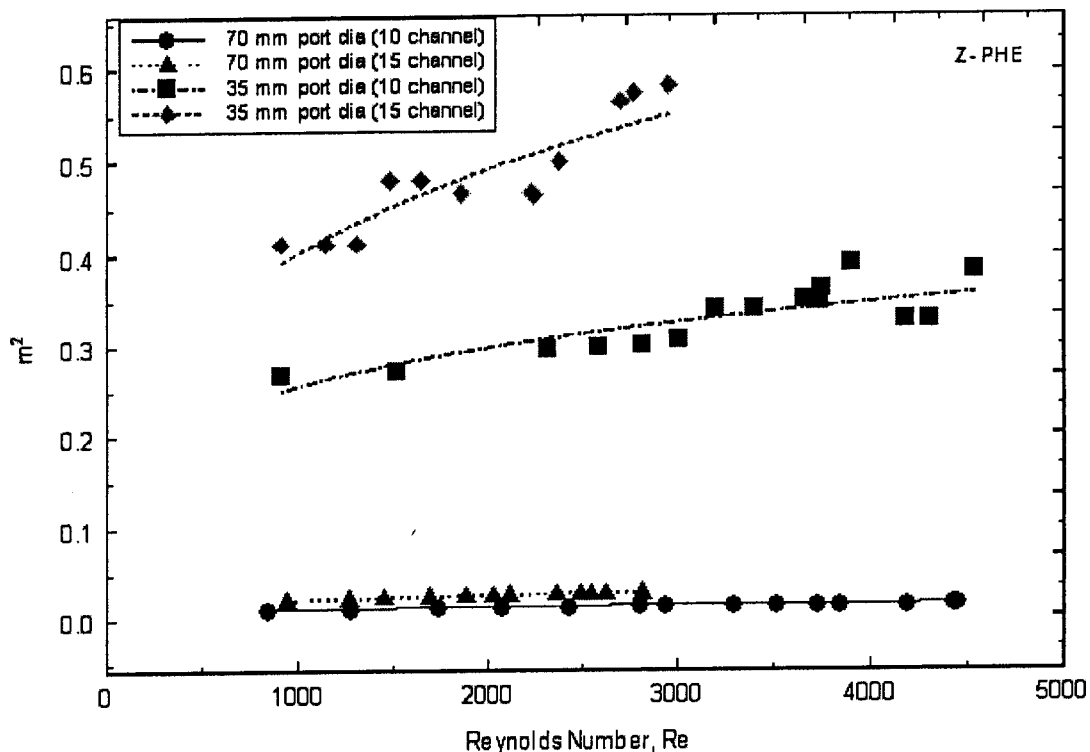


Fig. 10 Variation of m^2 with port size and number of channels for Z-type PHE

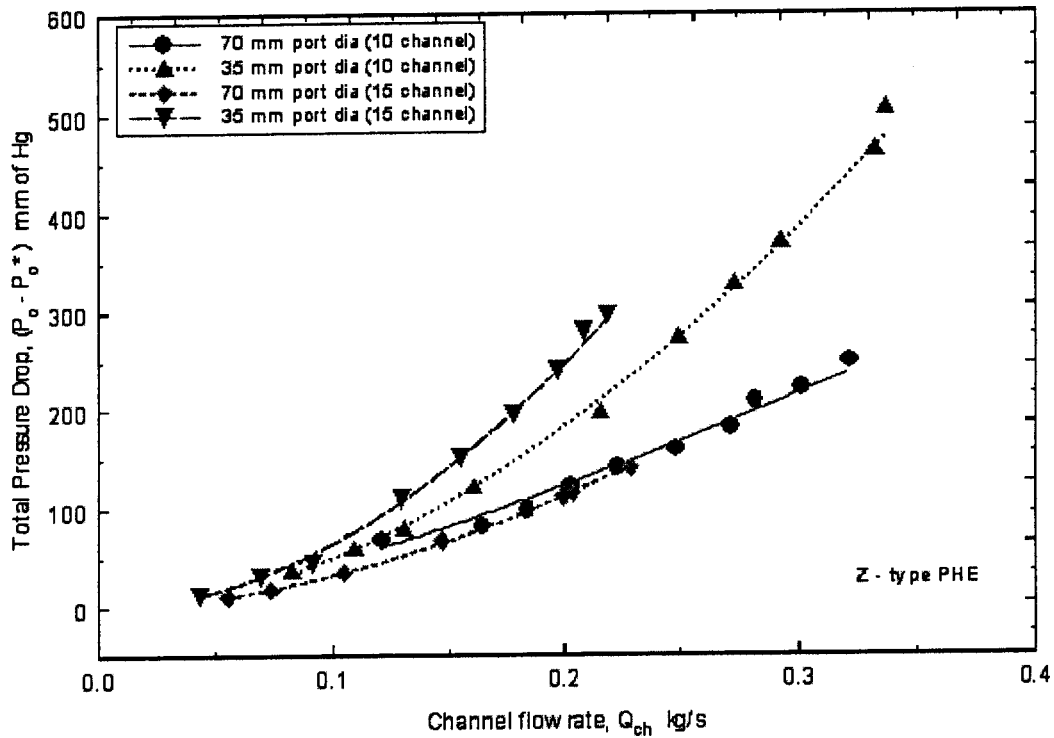


Fig. 11 Variation of total pressure drop with port size and number of channels for Z-type PHE

increase of number of channels is also presented in Fig. 17. It can be seen that the parameter increases exponentially with number of channels at smaller port diameters. Hence the flow maldistributions in the channel with small port diameters are likely to be even more severe than the one given in Fig. 16.

All the above discussions pertain to the flow distribution inside the plate heat exchanger under isothermal conditions. In reality both hot and cold fluid flow inside the heat exchanger under non-isothermal conditions. To account for this realistic condition, experiments are carried out while the heat transfer is taking place

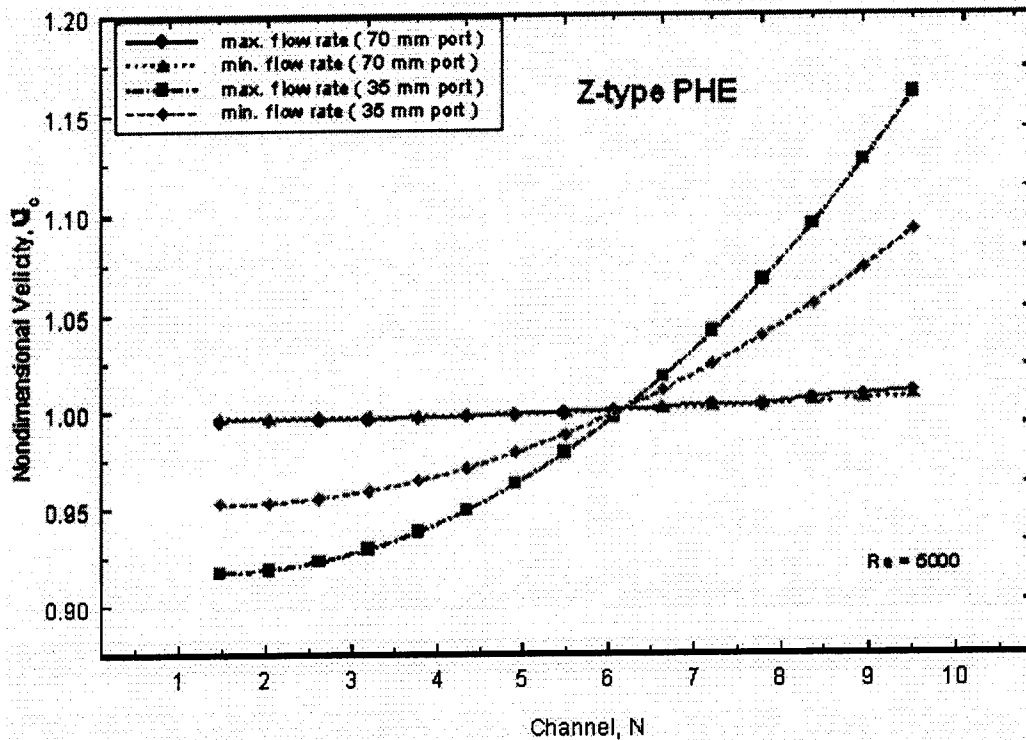


Fig. 12 Flow distribution to the channels for maximum and minimum flow rates for a 15 channel Z-type PHE

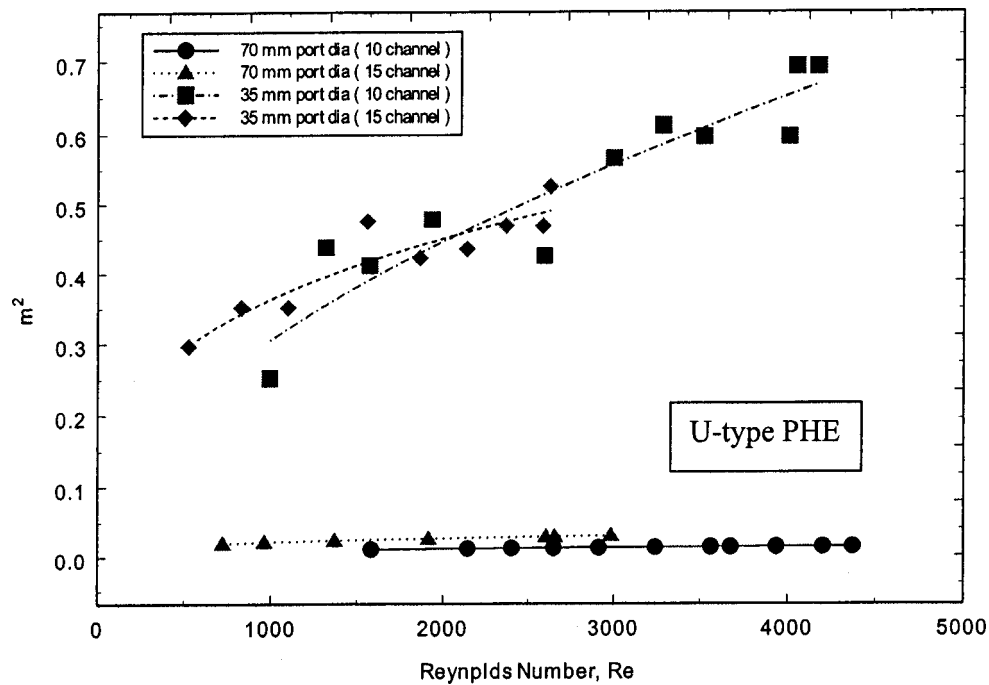


Fig. 13 Variation of m^2 with port size and number of channels for U-type PHE

between hot and cold fluids using the thermal circuit is shown in Fig. 5. The typical results of these non-isothermal hydraulic experiments are plotted in Fig. 18. This figure clearly indicates that thermal conditions affect the pressure drop in heat exchanger considerably. It is interesting to note that while the isothermal experiments brings out the least pressure drop, the pressure drop increases with the increase of mean temperature giving the highest pressure drop for the hot fluid side. This can be explained by the fact that the increase in temperature of the fluid decreases the viscosity which in turn increases the Reynolds number and de-

creases friction coefficient. As decrease of the friction coefficient increases the maldistribution parameter m^2 (Eq. (9)), the maldistribution increases and as a result pressure drop also increases. This feature further emphasizes the importance of the present work indicating on even higher level of maldistribution at elevated temperature.

The above results clearly indicate the effect of flow maldistribution on hydraulic performance of PHE. The main cause of port to channel flow maldistribution in PHE is in difference in pres-

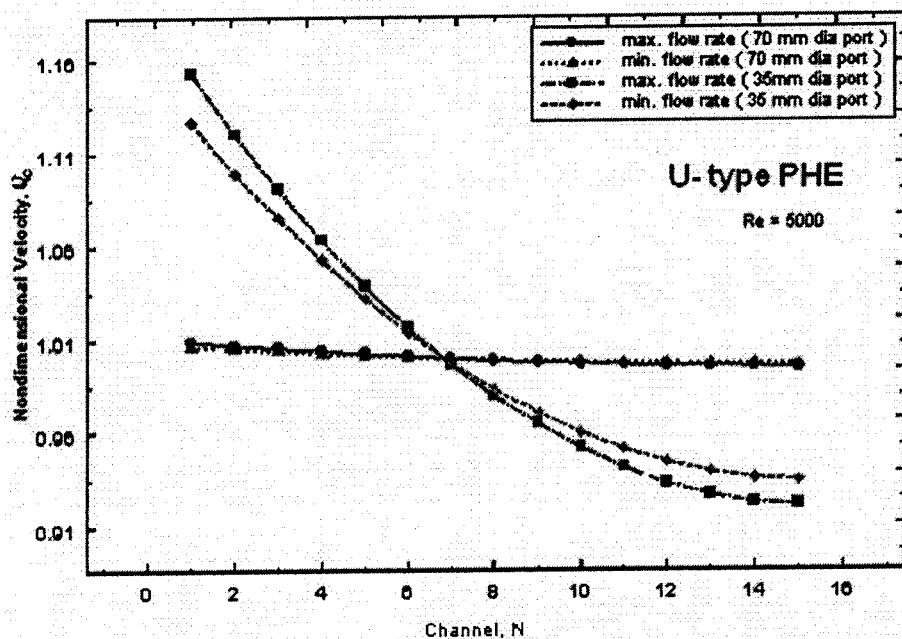


Fig. 14 Flow distribution to the channels for maximum and minimum flow rates for a 15 channel U-type PHE

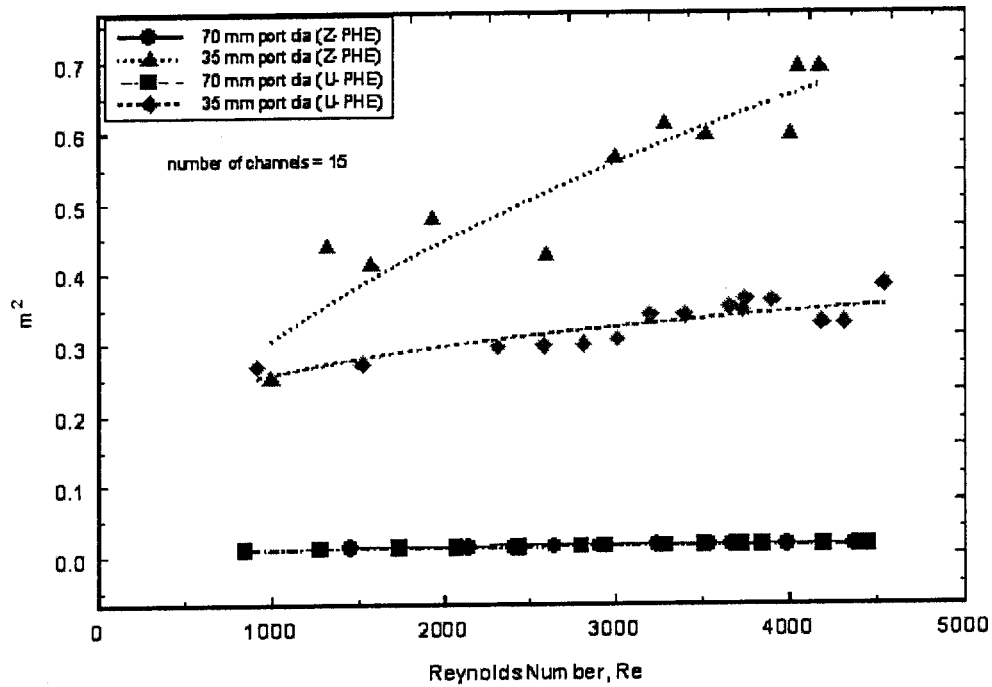


Fig. 15 Comparison of m^2 values for U and Z-type PHE

sure profile of inlet and outlet port of the PHE. It is well known that while the pressure in the combining port (exit port) drops sharply in the flow direction that in the dividing port (inlet port) increases at a rate depending on port friction. In case of plate heat exchangers since the resistance to flow within the corrugated

channel is much higher, the influence of the port pressure drop due to friction is not significant. However insertion of the mandrel brings out an increase in the port pressure drop which is the reason for getting higher values of measured pressure drop compared to prediction (Fig. 7 and Fig. 8). This port pressure distribution

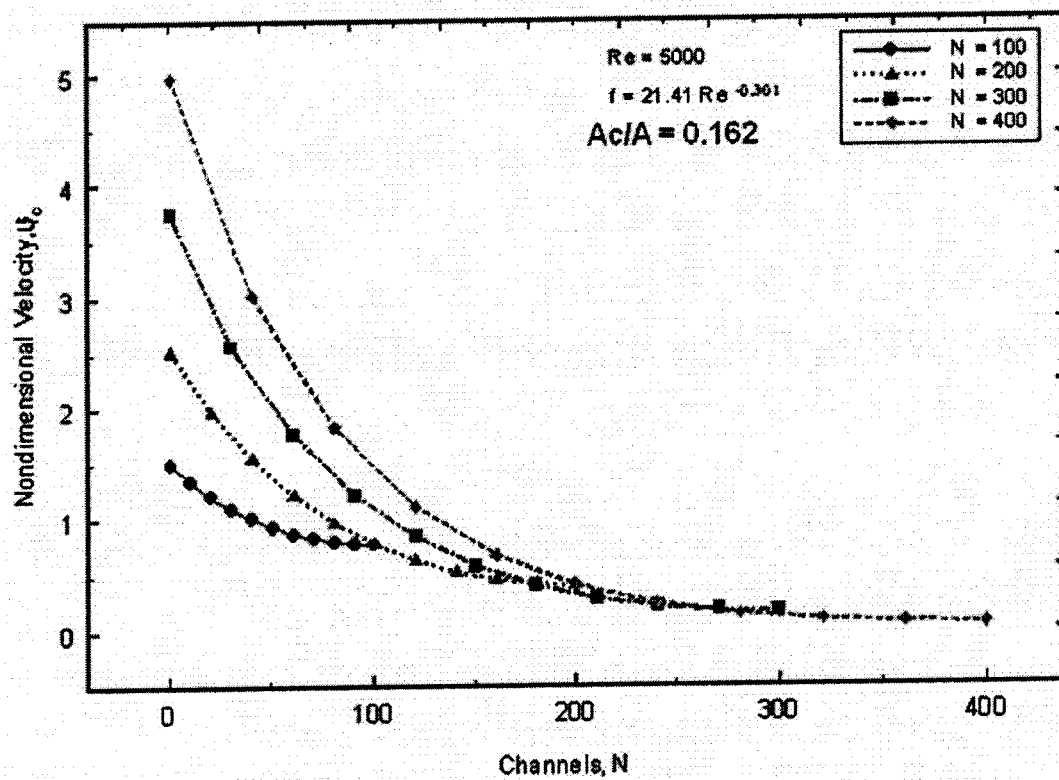


Fig. 16 Flow distribution prediction for an industrial PHE with large number of plates

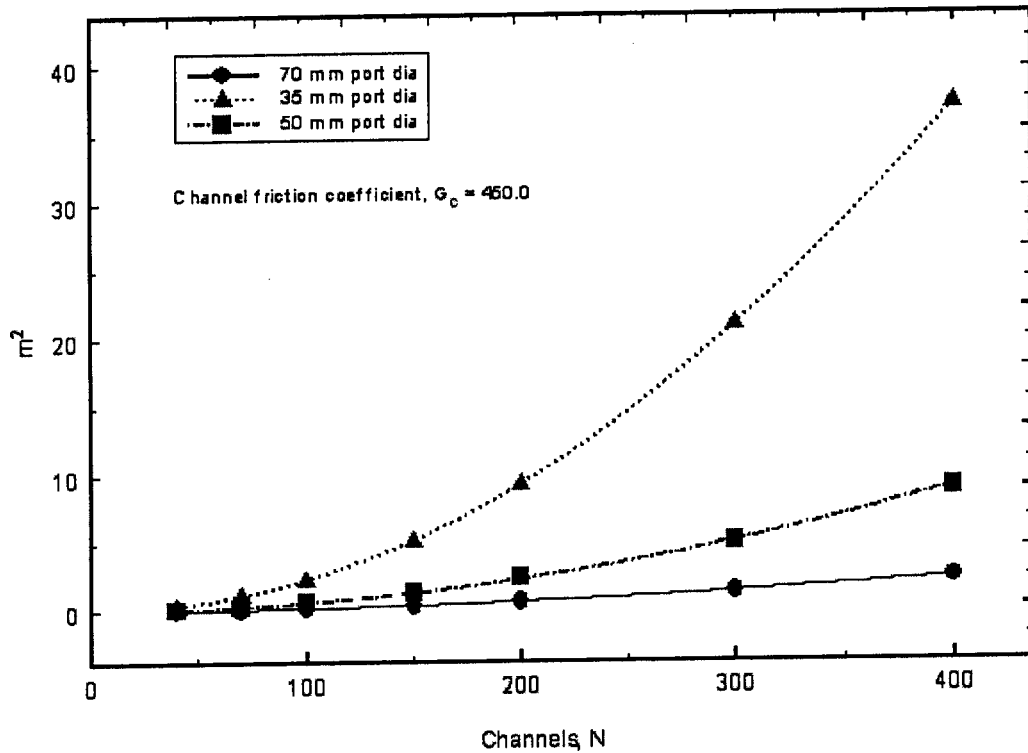


Fig. 17 m² values for an industrial PHE with different port sizes

and consequently the flow maldistribution depend largely on the port cross-sectional area available for the fluid relative to the channel cross-sectional area. From practical design aspect this essentially means that larger the port area less is the flow maldistribution. Therefore, it is suggested that the largest acceptable port

diameter be used for a given plate area. However this is limited by manufacturing considerations as well as consideration of loss of heat transfer area due to increase in port size. The results also indicate that the pressure drop during an non-isothermal actual operation of PHE is also affected by the viscosity clearly indicat-

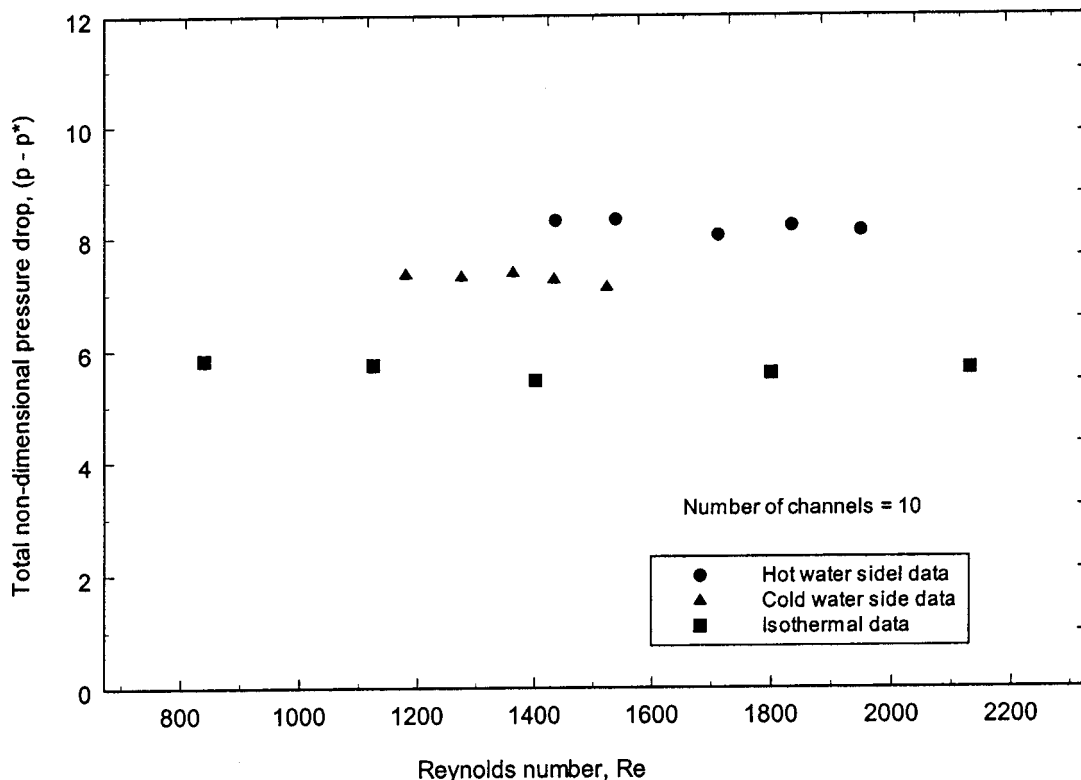


Fig. 18 The comparison of pressure drops under isothermal and non-isothermal conditions

ing that this is not due to a simple property variation (which should decrease with the decrease of viscosity) but due to an increased maldistribution brought about by changes in viscosity at elevated temperature.

Conclusions

A detailed experimental study has been presented to investigate the effect of port to channel flow maldistribution on the pressure drop across a plate heat exchanger. The study confirms the applicability of manifold flow dividing and combining theory to real plate heat exchangers. The results show that the major factor in the physics of maldistributed flow is the channel resistance. The flow inside port is important from the branching and recombining point of view rather than the flow characteristics inside the port. Frictional characteristics in both the ports being similar their effect on pressure drops across the channel and hence flow maldistribution will be minimum. The experimental results indicate the importance of port size on maldistribution suggesting that this should be kept at maximum permitted by manufacturing and heat transfer considerations to keep the flow maldistribution at its minimum. The total pressure drop across the heat exchanger is found to be critically dependent on flow rate as well as port size. The other important parameter is the number of channels. It is important to note that increase in pressure drop due to flow maldistribution may be inevitable in industrial PHEs containing hundreds of plates because a proportional increase of port size is not possible. Hence the computation of pressure drop and flow distribution is required to determine the maximum number of plates acceptable for a given plate size beyond which further addition of plates does not effectively increase heat transfer area. The study also indicates that lowering the channel resistance of both the cold and hot side of the heat exchanger due to increase in temperature creates an additional flow maldistribution under the actual non-isothermal conditions in plate heat exchangers.

Nomenclature

A = cross-sectional area of the port, m²
 A_c = cross-sectional area of a channel, m²
 b = plate spacing, m
 C_d = discharge coefficient of the orifice meter
 d_e = equivalent diameter of port, 2b, m
 l = vertical distance between two ports, m
 L_p = length of port, m
 f = friction factor, from Eq. (1)
 m² = maldistribution parameter
 n = number of channels per fluid
 N = number of channels per fluid
 p = dimensionless pressure in the port, P/ρW_o²
 P = pressure in the port, N/m²
 ΔP = dimensional pressure drop across a PHE, N/m²

Δp = dimensionless pressure drop across a plate heat exchanger
 Re = Reynolds number, Re = u_c(2b)/ν
 u_c = dimensionless channel velocity, U_c/U_m
 U_c = channel velocity, m/s
 U_m = mean channel velocity, m/s
 w = dimensionless velocity in the port, W/W_o
 W = velocity of port, m/s
 W_c = axial component of the inlet flow velocity of channel, m/s
 X = axial coordinate along the port, m
 z = dimensionless axial coordinate, Z/L_p
 Z = axial coordinate in the port, m
 β = average velocity ratio in the port, W_c/W
 ε = 2 - β/ζ_c(A/A_cn)²
 ζ_c = Channel frictional coefficient, from Eq. (2)
 ρ = density of fluid, kg/m³
 ν = kinematic viscosity of fluid, m²/s

Subscript

without
 subscript = intake port
 o = at inlet
 * = exhaust port
 ch = channel

References

- [1] Mueller, A. C., and Chiou, J. P., 1988, "Review of Various Types of Flow Maldistribution in Heat Exchangers," *Heat Transfer Eng.*, **9**(2), pp. 36–50.
- [2] Bajura, R. A., 1971, "A Model for Flow Distribution in Manifolds," *ASME J. Eng. Power*, pp. 7–12, January.
- [3] Bajura, R. A., and Jones, Jr., E. H., 1976, "Flow Distribution Manifolds," *ASME J. Fluids Eng.*, **98**, pp. 654–666.
- [4] Bassiouny, M. K., and Martin, H., 1984, "Flow Distribution and Pressure Drop in Plate Heat Exchangers-I, U-Type Arrangement," *Chem. Eng. Sci.*, **39**(4), pp. 693–700.
- [5] Bassiouny, M. K., and Martin, H., 1984, "Flow Distribution and Pressure Drop in Plate Heat Exchangers-II, Z-Type Arrangement," *Chem. Eng. Sci.*, **39**(4), pp. 701–704.
- [6] Datta, A. B., and Majumdar, A. K., 1980, "Flow Distribution in Parallel and Reverse Flow Manifolds," *Int. J. Heat Fluid Flow*, **2**(4), pp. 253–262.
- [7] Kitto, Jr., J. B., and Robertson, J. M., 1989, "Effects of Maldistribution of Flow on Heat Transfer Equipment Performance," *Heat Transfer Eng.*, **10**(1), pp. 18–25.
- [8] Huang, L., 2001, "Port Flow Distribution in Plate Heat Exchangers," Proceedings of the Third International Conference on Compact Heat Exchangers and Enhancement Technology for the Process Industries, Davos, Switzerland, pp. 259–264, July.
- [9] Muley, Arun., and Manglik, R. M., 1995, "Experimental Investigation of Heat Transfer Enhancement in a PHE With β=60° Chevron Plates," Proceedings of the Second ISHMT-ASME Heat and Mass Transfer Conference and Thirteenth National Heat and Mass Transfer Conference, Dec 28–30.
- [10] Rao, Prabhakara, B., Krishna, Kumar, P., and Sarit, K., Das., 2002, "Effect of Flow Distribution to the Channels on the Thermal Performance of a Plate Heat Exchanger," *Dokl. Akad. Nauk UzSSR*, **41**, pp. 49–58.
- [11] Moffat, R. J., 1988, "Describing the Uncertainties in Experimental Results," *Exp. Therm. Fluid Sci.*, **1**, pp. 3–17.

Effects of Inclination Angle of Ribs on the Flow Behavior in Rectangular Ducts

Xiufang Gao¹

Bengt Sundén*

e-mail: Bengt.Sunden@vok.lth.se

Division of Heat Transfer,
Lund Institute of Technology,
Box 118, 221 00 Lund, Sweden

The flow behavior in rib-roughened ducts is influenced by the inclination of ribs and the effect is investigated in the present study by Particle Image Velocimetry (PIV). The local flow structures between two adjacent ribs were measured. The Reynolds number was fixed at 5800. The flow field description was based on the PIV results in planes both parallel and perpendicular to the ribbed walls at various locations. The rib angle to the main flow direction was varied as 30 deg, 45 deg, 60 deg and 90 deg. The ribs induce three dimensional flow fields. The flow separation and reattachment between adjacent ribs are clearly observed. In addition, the inclined ribs are found to alter the spanwise distribution of the streamwise velocity component. The streamwise velocity component has its highest values at the upstream end of the ribs, and decreases continuously to its lowest values at the downstream end. Strong secondary flow motion occurs over the entire duct cross section for the inclined ribs. The flow structures between two consecutive ribs show that the fluid flows along the ribs from one end of the ribs to the other end, and then turns back at the transverse center. Downwash and upwash flows are observed at the upstream end and downstream end of the ribs, respectively. [DOI: 10.1115/1.1778715]

Introduction

Useful publications exist concerning the heat transfer and flow characteristics in rib-roughened passages with different rib arrangements, aiming for the enhanced heat transfer in heat exchangers such as car radiators and gas turbine applications [1–7]. The effects of the Reynolds number and the rib geometry on the heat transfer and pressure drop were obtained in some cases [8–10]. Further results were presented to show the detailed heat transfer results for the perpendicular, parallel, broken and V-shaped rib-roughened ducts [11–14]. The combined effects of aspect ratio of the rectangular ducts and the rib angle of attack were investigated in references [15,16]. All the studies showed that angled ribs provide better heat transfer enhancement than perpendicular ribs, but there is very little work on the flow characteristics comparison. On the other hand, detailed heat transfer measurement technologies such as liquid crystal thermography and holographic interferometry map the whole surface temperature, making the detailed temperature distribution visible. Therefore, detailed flow structures in rib-roughened ducts are helpful in understanding the complicated heat transfer distributions. In addition knowledge about the flow mechanisms is beneficial as further improvement of the heat transfer process is desired.

Although there are a number of references dealing with the effects of angle of attack of ribs on the heat transfer field, only few reported the essential flow field which caused the differences in heat transfer. Perpendicular ribs are mostly investigated cases but most data available were obtained with Laser Doppler Velocimetry (LDV) or hot wire anemometry, which were also limited to square ducts or high aspect ratio rectangular ducts at high Reynolds numbers, such as references [17–19]. However, because LDV usually makes measurements at a single point, it has the limitation that it cannot capture the spatial structure of a flow

field. Flow visualization has been used to show different secondary flow structures for ribs with different attack angles, but detailed characteristics were not available [20].

Whole field measurements are preferred to show how the ribs alter the flow field, and how different attack angles affect the flow structures. PIV is a non-intrusive optical method, which enables one to obtain instantaneous velocity profiles in a flow plane of interest. The average velocity maps, instantaneous or average vorticity maps, turbulence intensity maps and spatial correlation maps could be calculated using proper post processing [21–23]. This measurement technique hence gives access to quantitative information that is very useful for the characterization of flows.

PIV has recently been successfully used to investigate the flow characteristics within square coolant ducts in references [24–27], where details of the flow structures were studied in a smooth duct and the ones with 90 and 45 deg ribs over a sharp 180 deg bend region. Detailed flow structures by different authors are reported in references [24–27].

The Reynolds number range less than 10,000 occurs often in compact heat exchangers such as car and truck radiators, and circular ribs are used in this work to simulate the rounded shape of the surface modifications in those cases. The macroscopic flow characteristics such as the secondary flow scheme, the flow reattachment and redevelopment, are expected to be similar to those caused by ribs of other shape. The purpose of this study is to implement the PIV measurement to investigate the air flow through a 1:8 rectangular duct with 90, 60, 45 and 30 deg ribs. The detailed flow structures in several planes at a fixed Reynolds number of 5800 are obtained for all rib configurations. This Reynolds number was chosen because the measured flow pattern was used to correlate the previous heat transfer results at such Reynolds number. The results are used to analyze and improve the understanding of the characteristics of the flow field introduced by different rib configurations.

Description of Experimental Equipment and Procedure

A sketch of the experimental set-up is shown in Fig. 1. The Plexiglas rectangular duct consisted of two 700 mm length parts, with an internal cross section of 14.5×112.5 mm. The second part of the duct was roughened by 1.5 mm circular plastic ribs arranged in a staggered manner on two opposite wide walls. The

¹Now with Siemens Industrial Turbines, 61282 Finspång, Sweden.

*Corresponding author.

Contributed by the Fluids Engineering Division for publication in the JOURNAL OF FLUIDS ENGINEERING. Manuscript received by the Fluids Engineering Division November 18, 2003; revised manuscript received February 12, 2004. Associate Editor: S. L. Ceccio.

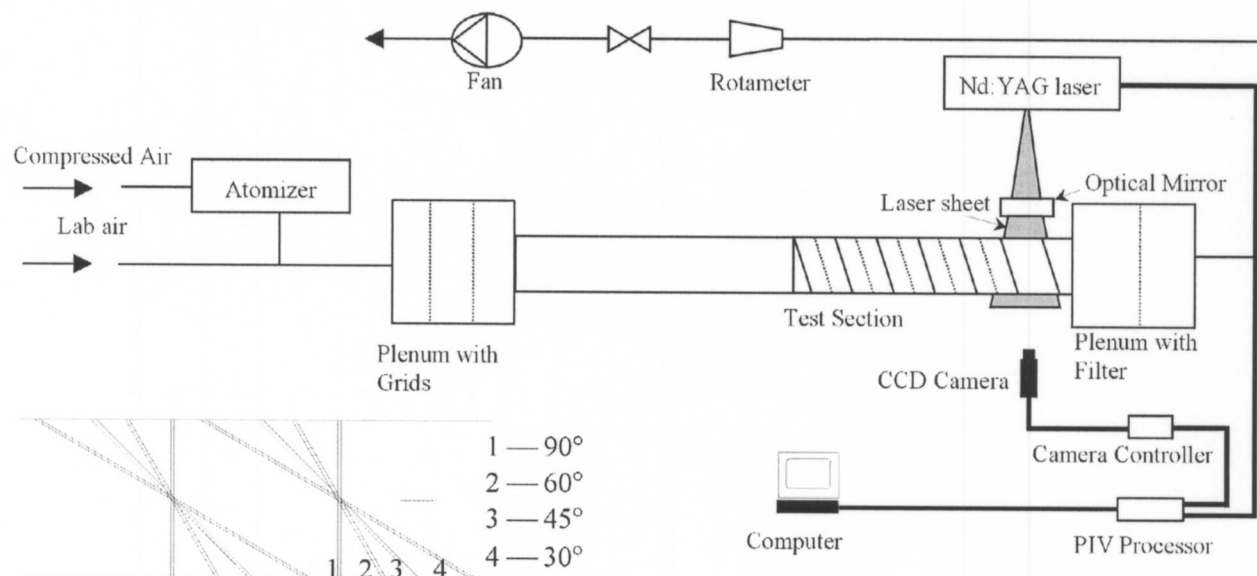


Fig. 1 Sketch of the experimental setup

measurement location was at approximately $50 < x/D_h < 52$ from the inlet of the rectangular duct. The rib height-to-hydraulic diameter was about 0.06. The pitch-to-rib height ratio was kept as 10 for all the rib arrangements. Only the inclination angle of the ribs to the mainflow direction was changed to be 90, 60, 45 and 30 deg, as illustrated in Fig. 1.

Laboratory air enters the first plenum via a 100 mm tube. The plenum is equipped with two grids to evenly distribute the seeding particles. Glycerol is used as seeding particles, which are generated by a TSI model 9306 six-jet atomizer supplied by compressed air. The density of the seeding particles of 5–10 particles in each interrogation area is controlled by the compressed air pressure and the number of open jets. In PIV measurement, velocities of the particles are measured. Thus the Stokes number of the particles must be sufficiently small. The Stokes number is the ratio between the particle response time and the flow time scale. The particles must, however, be so large that sufficient light is scattered for detection by the CCD camera. There are particles available offering good scattering efficiency and sufficiently small velocity lag. In gas flow PIV measurement aluminum, magnesium and glycerol particles have been employed. In this investigation, every effort was taken to satisfy these conditions.

The four walls of the duct were designated to be ribbed wall A, ribbed wall B, top wall and bottom wall hereafter as illustrated in Fig. 2. The end of the inclined V-ribs that is close to the flow inlet is called the upstream end of the ribs hereafter, and the other end is called the downstream end as illustrated. The ribs were painted black to eliminate scattering light and thus decrease the noise level. Two coordinate systems are defined in Fig. 3. Because the flow field is fully developed, and also in order to simplify later presentation of the results at different locations, where the flow obtained is between different physical rib pairs, the coordinates x and ξ do not originate from a fixed physical point, instead they start at the center of the first rib on wall B at each measured location in all presented figures.

Typically, PIV measurements were carried out in three planes, A, B, and C in order to investigate the three-dimensional flow feature. The test facility was designed in such a way that it allowed turning the test section by an angle of 90 deg without changing the flow condition. The horizontal laser sheet was turned to go through the test section from top to bottom vertically. In plane A, the x - y plane velocity field can be obtained. In plane B, the inclined ribs themselves blocked part of the camera view,

therefore in the area which is less than one rib height from the ribbed walls, no valid velocity vectors were obtained. The measurements carried out in plane C for inclined rib configurations complement plane B measurements to show the vortices behind the ribs. The laser sheet could be adjusted to the desired position for all the measurement arrangements using a traversing system.

A Quantel Q-Switched Nd:Yag double cavity pulsed laser provides pulsed light sheets at a wavelength of 532 nm with a maximum output energy of 120 mJ. Each pulse duration is 10 ns. The time interval between two pulses can be adjusted according to the velocity range and for different test planes. The laser was kept horizontal with an optical mirror to turn the laser sheet 90 deg to enter the window on the top of the duct vertically.

A Dantec 80C60 HiSense PIV camera with a high performance progressive scan interlines CCD chip having 1024×1280 pixels, together with a Nikon AF Micro 60 f/2.8D lens was used to record the seeding images on double frames. An optical filter of 532 nm was used in front of the camera to allow only the signal illumination wavelength to pass.

For the 90 and 60 deg ribs, the camera view field was first set approximately to be 115×144 mm for plane A measurements, to obtain an overview of the whole flow field between two consecutive ribs. The camera was then adjusted to focus on a small area of

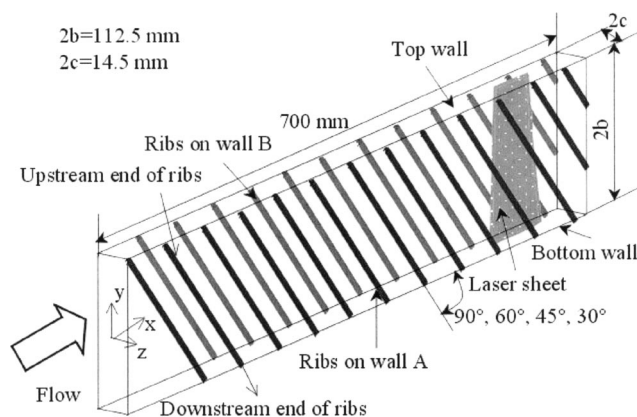


Fig. 2 Definition of the coordinate system

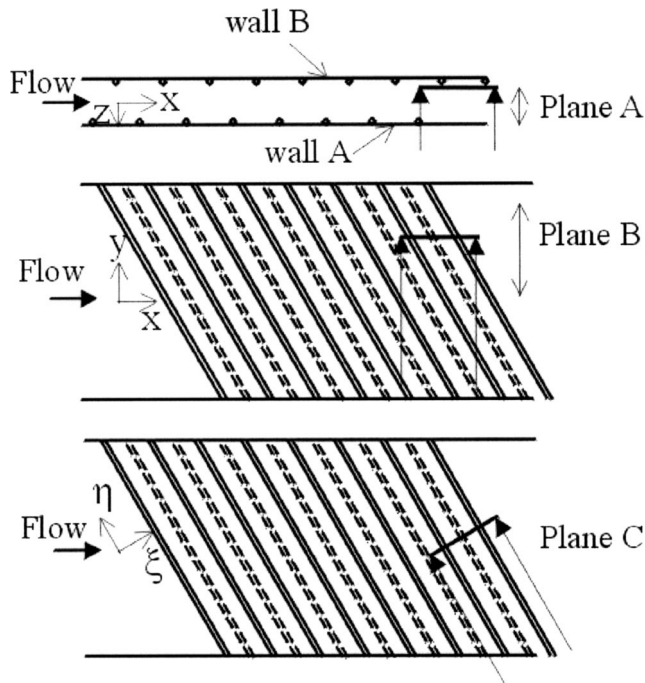


Fig. 3 Laser sheet locations for PIV measurements

plane A, approximately 30×35 mm, either close to the top wall or in the middle of the duct, to reveal the detailed flow structure with a higher spatial resolution. For 45 and 30 deg ribs, the long streamwise distance for a complete rib made the whole field measurement with one image unrealistic, because it would cause a too low spatial resolution. Therefore, two or three measurements were carried out to capture the flow field over a certain height of the duct, and then these were carefully combined together. For planes B and C, the view field was about 15×19 mm for all ribs.

The PIV recordings from the CCD camera were processed with the Dantec software Flow Manager. A cross-correlation analysis method was used with an interrogation area size of 32×32 pixels with 50% overlap between the interrogation areas. The vector field was then evaluated in relation to a predefined velocity magnitude and the invalid ones were replaced by the moving average method. Instantaneous velocity field were obtained and a series of 250 of instantaneous measurements were statistically averaged to get the mean velocity profile.

The uncertainty is dependent on the imperfections of the apparatus, the measurement plane location, the particular PIV acquisition parameters, the flow nature, etc. The dimensions of the Plexiglas duct are accurate within ± 0.1 mm and the rib height within ± 0.05 mm. The position of the ribs on the wall is estimated to be within ± 0.5 mm. The laser sheet position was controlled by an accurate traversing system and is accurate to ± 0.01 mm. The software interpolation accuracy is expected to be 0.1 pixel. The existence of an out-of-plane velocity in the three-dimensional flow field influences the accuracy of the in-plane velocities in the two-dimensional measurement, and the effect is different at different locations.

The sample size is another error source for the mean velocity calculation by statistics for both smooth and ribbed ducts. A detailed analysis for the mean velocities, the turbulence intensities was discussed in [28]. The results of the smooth duct were compared with LDV measurements presented in [29] and good agreement was observed. A statistical investigation of the V-shaped rib-roughened duct, which had highest turbulence level among all rib configurations tested, was included in [28] to study the effect of the sample number on the obtained flow parameters and it was found that 250 instantaneous velocity field samples could provide

a reasonable accuracy as a compromise between acquisition time, disk space and accuracy. The uncertainty of the time-average velocities was estimated to be between $\pm 0.02U_m$ to $\pm 0.08U_m$ for all three velocity components, where the worst cases occurred for the streamwise velocity component U when the whole plane A measurement was carried out close to the ribbed walls. This implies that the relative error involved in the measurements of the velocity components V and W is higher due to their small magnitudes, and because both are measured in planes A or B together with the U component.

Results and Discussion

90 deg Ribs. The time-averaged velocity vectors in the whole plane A at $z/c = +0.9$ are shown in Fig. 4(a). The x coordinate is doubled in size, to avoid a very narrow and unclear figure. The main flow direction is from left to right. It is observed that close to the top and bottom walls, there is a small area having a local maximum of the streamwise velocity, which is even higher than in the symmetry plane. Additional measurements at other transverse locations confirm that this velocity displacement persists until $z/c = +0.8$, but disappears further away from the ribbed wall at $z/c = +0.5$. In the transverse center, the U velocity component shows a very even distribution over a large spanwise distance of $-0.9 < y/b < +0.9$, and then decreases quickly close to the walls. This spanwise profile of the streamwise velocity component U is similar to that in a smooth duct. The flow right in front of the downstream rib shows either an upflow or downflow impinging on the smooth walls.

A closer examination was made in the same plane but observing a smaller area adjacent to the top wall to obtain the flow structures with a higher spatial resolution and the velocity vectors are displayed in Fig. 4(b). The time-averaged velocity shows the upflow to the smooth top wall in front of the second rib on wall A more clearly. This characteristic feature was also detected by LDV in reference [30].

The isolines of the normalized streamwise velocity component U/U_m shown in Fig. 4(b) are illustrated in Fig. 4(c). The negative velocities behind the ribs represent the separation zone. The area close to the top wall ($y/b \cong +0.97$) shows local maximum values. The phenomenon is in accordance with the results for a square duct in reference [29]. But the relative position to the symmetry plane is different. The smaller distance behind the first rib where U/U_m changes sign in the region close to the top smooth wall also implies that the flow reattachments occur earlier there. Efforts were made to capture the velocity vectors in plane B at the location of $y/b = +0.97$, but these were not successful because of the strong reflection from the top wall. The normalized spanwise velocity component V/U_m is very small (about 2% of the mean velocity) in most of the area except immediately right in front of the downstream rib, where a slightly higher V/U_m is observed showing impingement flow on the smooth wall.

Vector plots of the normalized streamwise and transverse velocities U/U_m and W/U_m in planes B at different spanwise locations generally follow a similar style. Therefore, only the results in the symmetry plane ($y/b = 0$) are given in Fig. 4(d). The flow caused by staggered ribs is symmetric relative to the ribs, as suggested by the velocity results across the entire $x-z$ plane. The scale-up figure of the vortex is shown in Fig. 4(e). The results verify the existence of the separation zone behind ribs. The separated flow reattaches to the wall at about 4 to 4.5 rib heights from the upstream rib center. This is consistent with the conclusion of between 4 and 4.25 rib heights measured in [30] by LDV. The acceleration of the core flow by the geometric contraction can be more easily seen from the contour map of the normalized streamwise and transverse velocity components, U/U_m and W/U_m , which are shown in Figs. 4(f) and (g). The vertical shadow created by the ribs on wall A in the original particle images of plane B

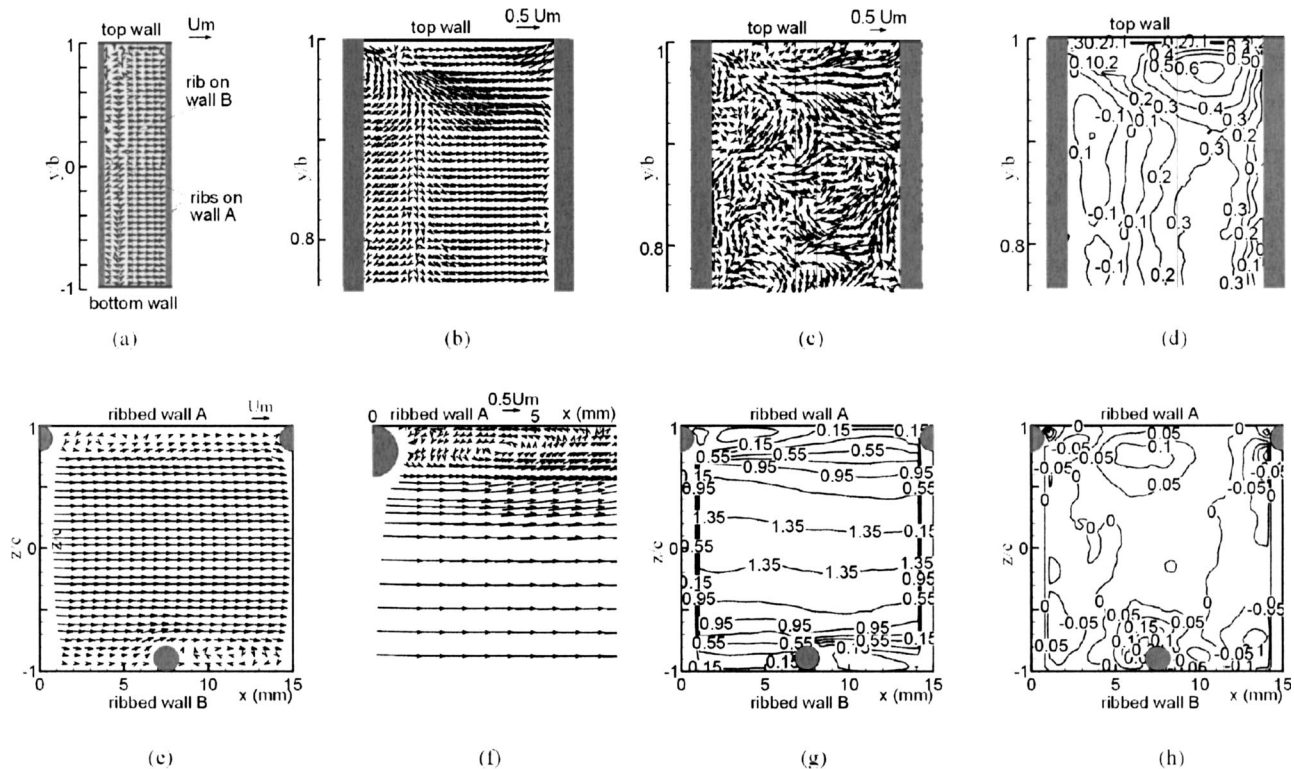


Fig. 4 Velocity vectors and component isolines in planes A and B of 90 deg ribs: (a) time-averaged velocity vectors in plane A near wall A ($z/c = +0.9$); (b) instantaneous velocity vectors in plane A close to the top wall ($z/c = +0.9$); (c) time-averaged velocity vectors ($z/c = +0.9$); (d) normalized U velocity component U/U_m of (c); (e) time-averaged vectors in symmetry plane in plane B ($y/b = 0$); (f) scale-up of the vortex in plane (e); (g) normalized U velocity component U/U_m of (e); (h) normalized W velocity component W/U_m of (e)

measurements leads to invalid velocity vectors in these areas and are simply ruled out. These “zero” velocity areas causes vertical lines in the contour maps.

The direct measurement of the secondary flow in the cross section $y-z$ was unfortunately impossible to carry out because the high streamwise velocity would act as a large out-of-plane velocity, which would cause significant error in the measurements. Nevertheless, from the aforementioned measurements and as suggested by measurements in reference [30] and numerical simulation in references [31–33], it might be imagined that there is very weak secondary flow over the cross section. However, the strength of the secondary flow is expected to be low, as implied by the very low V and W velocities detected.

60 deg Ribs. Figure 5 shows the results between two consecutive ribs in plane A in the 60 deg rib-roughened duct. The x coordinate is again doubled in the $x-y$ velocity vector fields in Figs. 5(a) and (b). The vectors at two transverse locations, namely $z/c = 0$ and $z/c = +0.9$ are illustrated. The main flow stream flows from the upstream end of the ribs down along the ribs toward the downstream end at $z/c = 0$ in (a). It is again observed that the streamwise velocity at the upstream end of the ribs in the areas close to the top wall, where y/b is close to 1, is high. However, unlike the symmetric distribution for 90 deg ribs, there is a continuous spanwise decrease of U/U_m , and it reaches the lowest value close to the bottom wall ($y/b \sim -1$) at the downstream end of the ribs. The U contours in a cross section obtained by LDV presented in [1] also showed this main flow velocity displacement. This strong spanwise variation of the streamwise velocity component is conjectured to be particularly exaggerated in the narrow duct having an aspect ratio of 1:8. In a square duct, the smooth walls would act as barriers and the spanwise variation is expected to be weaker.

Figure 5(c) shows V/U_m at the three intersection lines between planes A at $z/c = +0.9, 0, -0.9$ and the $\eta-\zeta$ plane which is two rib width behind the center of the first rib on wall A. It shows clearly that close to the rib-roughened wall ($z/c = \pm 0.9$), the flow is coming down from the top wall to the bottom wall, having a negative V . The flow is upward in the transverse center of the duct ($z/c = 0$). The spanwise distribution of this velocity component at the transverse locations of $z/c = \pm 0.9$ follow each other closely.

A closer examination of a smaller part of plane A was made to capture the detailed spatial structure at $z/c = +0.9$, and the time-averaged velocity vectors in the region $-0.2 < y/b < +0.2$ are shown in Fig. 5(d). Figures 5(e) and (f) show the isolines of the normalized velocity components U/U_m and V/U_m . The relatively constant distance of the U/U_m isoline downstream the first rib suggests that the reattachment length is the same in this region.

In the measurement over the upper part of plane A, $+0.6 < y/b < +1$, U/U_m is higher. Close to the top wall, U/U_m changes sign after a shorter distance behind the rib, which implies a relatively shorter reattachment length. On the contrary, the reattachment point was found to move downstream in the lower part of plane A at the downstream end of the ribs where $y/b \sim -1$.

The angled ribs blocked part of the camera visual field in plane B measurements, and these areas are marked as rib blockage in the figures. The velocity fields were thus only obtained in the region of $-0.8 < z/c < +0.8$ for most of the runs.

The distributions of U/U_m in three $x-z$ planes at $y/b = +0.9, 0$ and -0.9 are shown in Figs. 6(a–c). The velocity profile at $y/b = \pm 0.9$ shows altered behavior. The acceleration over the ribs caused U/U_m to be higher above or under them, and the isolines are distorted. This effect attenuates along the streamwise direction until the rib on the other wall acts in the same way and draws the isoline to that wall. In addition, the magnitude of U/U_m is even

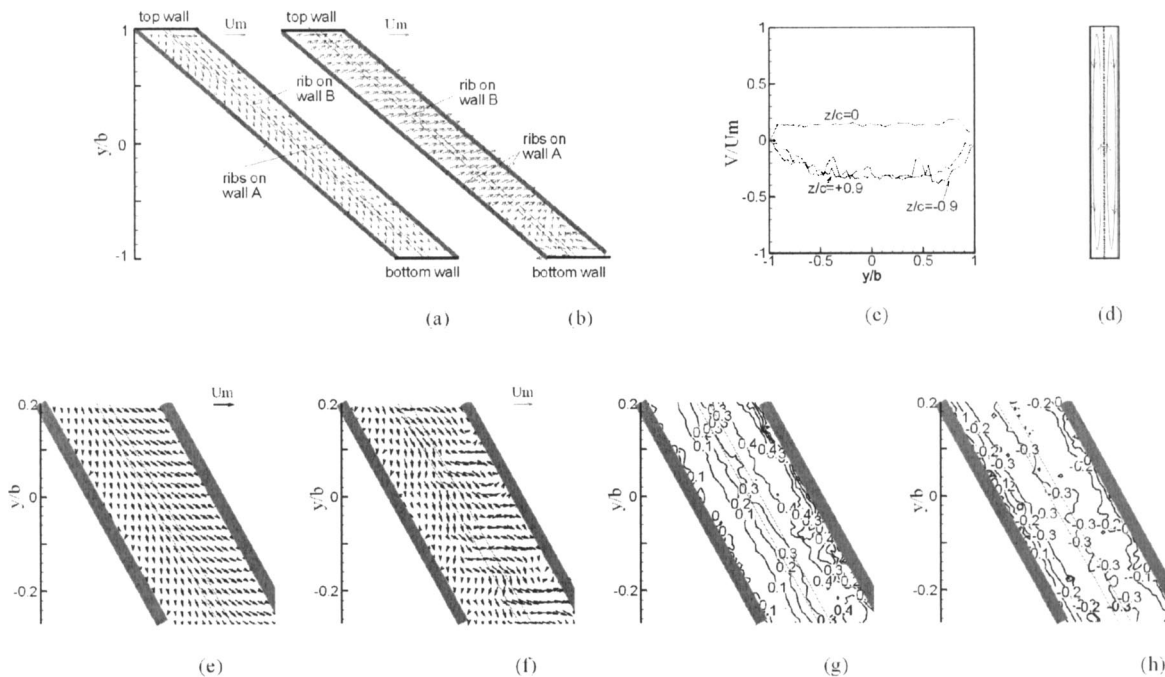


Fig. 5 Velocity vectors and component isolines in plane A of 60 deg ribs: (a) near wall A ($z/c = +0.9$); (b) velocity vectors at $z/c = 0$, U subtracted by mean velocity U_m at transverse center; (c) normalized velocity component V at three intersection lines; (d) schematic secondary flow; (e) an arbitrary sample of the instantaneous velocity field in the middle part of plane A ($z/c = +0.9$); (f) time-averaged vector field ($z/c = +0.9$); (g) normalized U velocity component U/U_m of (e); (h) normalized V velocity component V/U_m of (e)

higher than that in the symmetry plane. The U/U_m isoline distributions at $y/b = 0$ and $y/b = -0.9$ are also displaced close to the ribs but the influence is weaker. At $y/b = -0.9$, U/U_m is much lower than in the other two planes. This spanwise distribution has also been shown by plane A measurement. The altered U profiles observed by Bonhoff (45 deg square ribs in a square duct) showing two maxima and one minimum were not observed for any measured spanwise location.

The W velocity component represents the downwash or upwash flow along the ribbed walls over the cross section. This velocity component forms the secondary flow together with V , and acts as an additional heat transfer enhancement mechanism which has a significant contribution to the heat transfer distribution. The W/U_m isolines are illustrated in Figs. 6(d–f). In the plane of $y/b = +0.9$ at the upstream end of the ribs, the flow induced by the angled ribs is directed from the transverse center ($z/c = 0$) to the ribbed walls, indicating positive W/U_m in $0 < z/c < +1$ and negative W/U_m in $-1 < z/c < 0$. The downwash flow impinges on the ribbed surfaces, enhances the local heat transfer at the upstream end of the ribs. The magnitude of W/U_m is approximately only 4% of the mean velocity over the region ($-0.5 < z/c < +0.5$), but reaches 12–20% when it is closer to the wall at $z/c = \pm 0.8$ and higher value could be expected closer to the surface of the ribbed walls depending on the relative position to the ribs. In the symmetry plane ($y/b = 0$), the W components are mainly caused by the acceleration over the ribs and flow reattachment between the ribs. The magnitude is low, approximately 5–10% of the mean velocity before the rib obstacles and between the ribs where the flow reattaches on the walls. At the downstream end of the ribs ($y/b = -0.9$), upwash flow regions are formed. The fluid is conducted away from the ribbed walls, showing W/U_m with opposite sign to those at $y/b = +0.9$. Here the fluid is less efficient to remove heat from the ribbed surfaces, causing low heat transfer coefficients at the downstream end of the ribs. The magnitude of W/U_m is found to be low, less than 10% of the mean velocity in almost all regions.

The vortices downstream of each rib was clearly observed in plane C measurement. The flow fashion was similar to the ones obtained in plane B for 90 deg ribs and thus are not shown here. The flow created a separation region just behind the ribs and reattached to the top and bottom smooth walls at a distance of approximately 4–4.5 rib heights, and commenced to develop again. This flow behavior was expected to be responsible for the sawtooth distribution of the local heat transfer coefficient along the rib-roughened wall in [3]. The heat transfer coefficient there was observed to drop immediately after the ribs, due to nearly stagnant flow. It reached the highest local value at locations between a pair of adjacent ribs, where flow reattachment occurred. Then it decreased again because of the flow redeveloped.

Figure 6(g) shows the schematic pattern of the secondary flow over the y - z cross section based on the spanwise and transverse velocity components, V and W . It must be noted that it is only schematic, which does not represent symmetrical flow field everywhere. The velocity distribution on each cross section is dependent on its relative location to the ribs, as shown in the contour maps.

45 deg Ribs. The 45 deg ribs were examined with the camera focusing on separate parts and then combined to get the overall flow structure in the plane A. In general, the flow structure is similar to that for 60 deg ribs. Figure 7(a) shows the vector results between two consecutive ribs in plane A over the middle part of the 45 deg rib-roughened duct, $-0.2 < y/b < +0.2$, at the transverse location $z/c = +0.9$. The fluid again follows the ribs and flows from the upstream end of the ribs to the downstream end. At the transverse center $z/c = 0$, the flow goes up from the bottom to the top, showing a positive V component. The magnitude of the V component is slightly higher than that with 60 deg ribs.

The contour maps of the isolines of the normalized U/U_m and W/U_m in the x - z plane at $y/b = \pm 0.9$ are displayed in Figs. 7(d–g). U/U_m shows a spanwise variation similar to that with 60 deg ribs, and the effect is even more profound. Similar to 60 deg ribs,

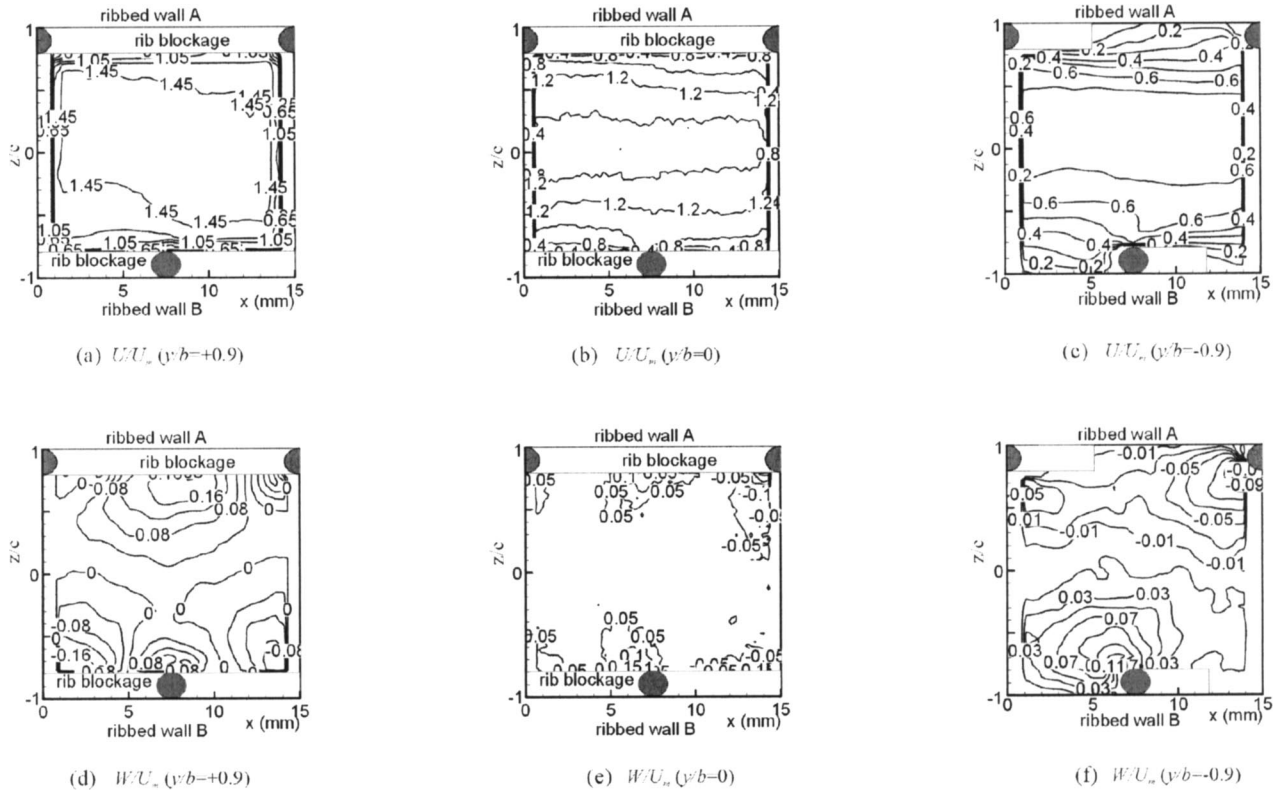


Fig. 6 Velocity isolines of U and W components in plane B of 60 deg ribs

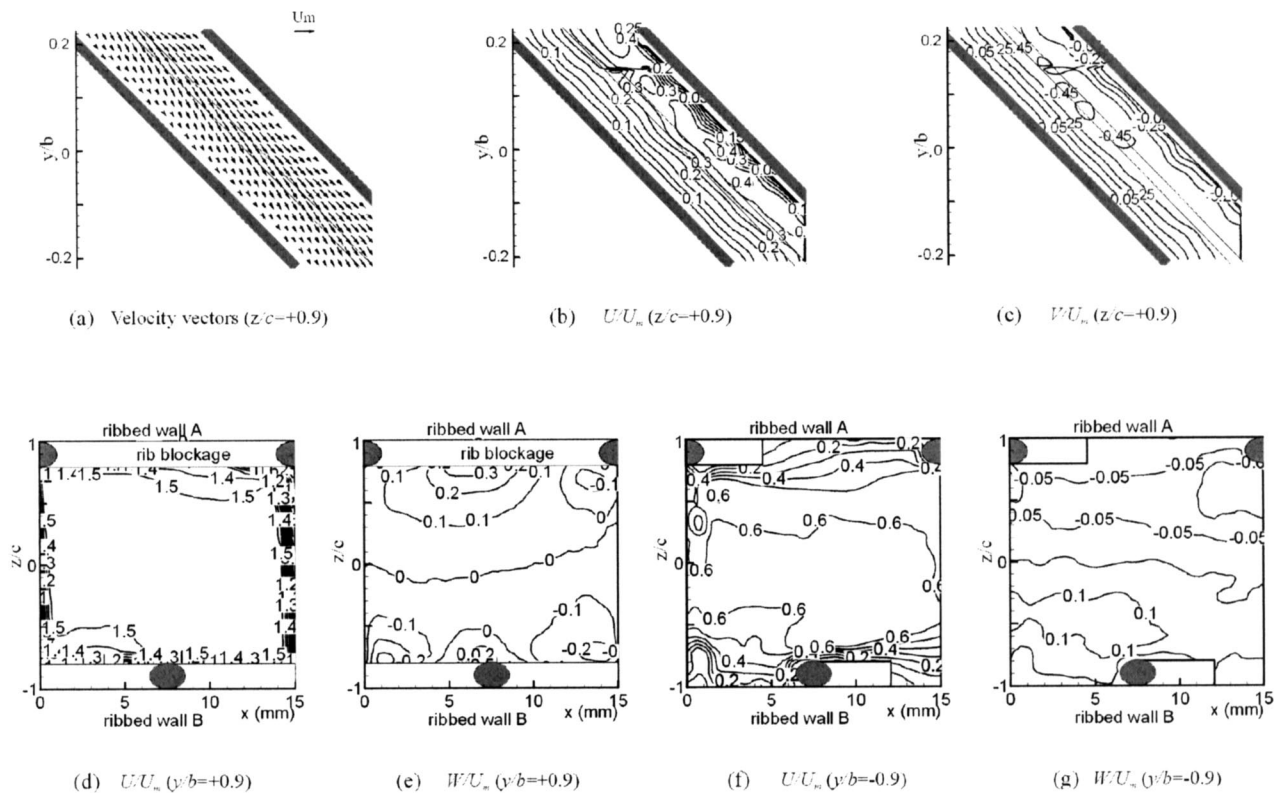


Fig. 7 Velocity vectors and component isolines of 45 deg ribs

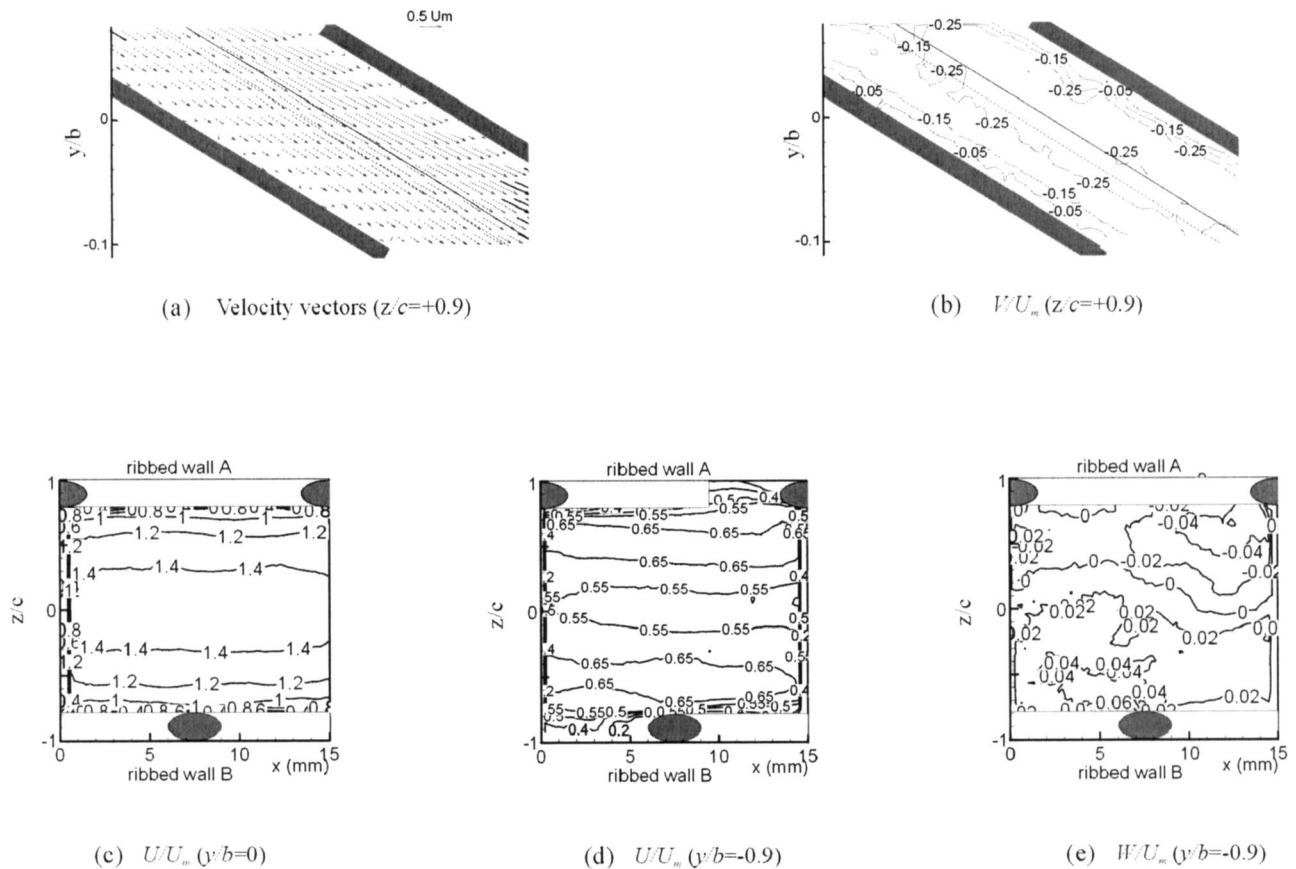


Fig. 8 Velocity vectors and component isolines of 30 deg ribs

the 45 deg ribs introduce a two-cell secondary flow, with downwash flow detected at $y/b = +0.9$ and upwash flow at $y/b = -0.9$. The magnitude of the W component at both locations is seen to be higher than for 60 deg ribs. By a combination of measured higher V and W components in planes A and B, it is thus expected that the strength of the secondary flow created by 45 deg ribs is slightly higher than that by 60 deg ribs. It would have more favorable effects on heat transfer enhancement. Unfortunately, there is no direct heat transfer data available with the same configuration to prove this speculation.

30 deg Ribs. The 30 deg ribs were examined in the same way as for the 45 deg ribs. The camera was used to capture the flow field over a part of the duct height in plane A at a time. The results obtained over $-0.1 < y/b < +0.05$ at $z/c = +0.9$ are shown in Fig. 8. The flow is seen to follow the orientation of the ribs, flowing from the upstream end to the downstream end. The magnitude of V/U_m is lower than for the other two inclined ribs considered, but higher than that caused by the 90 deg ribs.

The x - z plane measurements were made at regular spanwise locations. The streamwise velocity component U at $y/b = +0.9$ was again found higher than those at the symmetry center $y/b = 0$ and at $y/b = -0.9$, similar to the results with 60 and 45 deg ribs. Nevertheless, the difference between $y/b = 0$ and $y/b = +0.9$ was very small, and the U isolines were not deflected very much at the rib locations. The U isolines at $y/b = 0$ is shown in Fig. 8(c). Downwash flow occurs at $y/b = +0.9$ and upwash flow at $y/b = -0.9$, which suggests a similar secondary flow pattern as for the 60 deg and 45 deg ribs over the entire cross section. The strength of the secondary flow is expected to be much weaker than by the other two inclined ribs.

The isolines of U/U_m show a distinguished feature at $y/b = -0.9$. The profiles have two local maxima and decrease to a

minimum at the transverse center of the duct. This profile was observed in reference [24] in a square duct with 45 deg ribs, which was believed to occur because the two secondary vortices had their own maximal streamwise velocities in their individual center. Although no such characteristic feature was observed from measurements made at other spanwise locations further away from the bottom smooth wall, and not with the other rib arrangements either, it is speculated that if the measurement could be made close enough to the smooth wall, it would be visible.

Conclusions

The flow fields in rectangular ducts with 90, 60, 45 and 30 deg ribs were investigated using PIV, to reveal the effects of the rib inclination angle. The flow structures between two consecutive ribs in three measurement planes were obtained. It was found that the rib orientations not only affect the secondary flow style and its strength, but also alter the mean flow velocity distribution along the spanwise direction.

The results obtained for 90 deg ribs were compared with available data by LDV and showed good agreement. The streamwise velocity component in the plane A, which is parallel to the ribbed wall with a distance shorter than the rib height, showed local maxima close to the top and bottom walls. In the planes which are further away from the ribbed walls, this phenomenon disappeared. The low spanwise and transverse velocity components implied very weak secondary flow.

All three inclined rib configurations altered the spanwise profile of the streamwise velocity component, leading to high streamwise velocity component in the region of the upstream end of the ribs, and low values at the downstream end. The results in the planes parallel to the ribbed walls show that the fluid between adjacent ribs moved from the upstream end of the ribs to the downstream

end, and turned back at the transverse center. The so-called upwash or downwash flow, the W velocity component, was detected at different spanwise locations in the planes perpendicular to the ribbed walls. Two-cell secondary flows were expected to be established over the entire cross section for all angled ribs, and the one created by 45 deg ribs was found to be strongest.

Acknowledgments

Financial support for this investigation was received from the National Swedish Energy Agency (STEM) and the National Scientific Council (VR).

Nomenclature

- b = half width of the wide side wall, m
 c = half width of the narrow side wall, m
 D_h = hydraulic diameter, m
 p = rib pitch, m
 Re = Reynolds number (dimensionless), $Re = U_m D_h / \nu$
 U_m = mean velocity, m/s
 U = streamwise velocity component, m/s
 V = spanwise velocity component, m/s
 W = transverse velocity component, m/s
 x = coordinate along duct length, m
 y = coordinate along spanwise direction, m
 z = coordinate along transverse direction, m
 α = rib angle of attack, deg
 ξ = coordinate perpendicular to the ribs, m
 η = coordinate along the rib orientation, m
 ζ = coordinate perpendicular to $\xi\eta$ plane, m

References

- [1] Olsson, C. O., and Sundén, B., 1998, "Experimental Study of Flow and Heat Transfer in Rib-Roughened Rectangular Channels," *Exp. Therm. Fluid Sci.*, **16**(4), pp. 349–365.
- [2] Sundén, B., 1999, "Enhancement of Convective Heat Transfer in Rib-Roughened Rectangular Ducts," *J. Enhanced Heat Transfer*, **6**, pp. 89–103.
- [3] Gao, X., and Sundén, B., 2001, "Heat Transfer and Pressure Drop Measurements in Rib-Roughened Rectangular Ducts," *Exp. Therm. Fluid Sci.*, **24**, pp. 25–34.
- [4] Taslim, M. E., 2001, "Experimental Heat Transfer in Stationary Rib-Roughened Rectangular Channels," in *Heat Transfer in Gas Turbines* (eds., B. Sundén and M. Faghri), pp. 291–405, WIT Press, Southampton, UK.
- [5] Saidi, A., and Sundén, B., 1998, "Calculation of Convective Heat Transfer in Square-Sectioned Gas Turbine Blade Cooling Channels," ASME paper 98-GT-204.
- [6] Abdon, A., 2001, "Numerical Simulations of Cooling Concepts Related to Gas Turbine Combustors," Ph.D. thesis, Division of Heat Transfer, Lund Institute of Technology.
- [7] Han, J. C., Dutta, S. D., and Ekkad, S. E., 2000, "Gas Turbine Heat Transfer and Cooling Technology," Taylor & Francis, New York, USA.
- [8] Taslim, M. E., and Wadsworth, C. M., 1997, "An Experimental Investigation of the Rib Surface-Averaged Heat Transfer Coefficient in a Rib-Roughened Square Passage," *ASME J. Turbomach.*, **119**(2), pp. 381–389.
- [9] Kilicaslan, I., and Ibrahim Sarac, H., 1998, "Enhancement of Heat Transfer in Compact Heat Exchanger by Different Type of Rib With Holographic Interferometry," *Exp. Therm. Fluid Sci.*, **17**, pp. 339–346.
- [10] Ahn, S. W., 2001, "The Effects of Roughness Types on Friction Factors and Heat Transfer in Roughened Rectangular Duct," *Int. Commun. Heat Mass Transfer*, **28**(7), pp. 933–942.
- [11] Iacovides, H., Jackson, D. C., Kelemenis, G., and Launder, B. E., 2000, "The Measurement of Local Wall Heat Transfer in Stationary U-Ducts of Strong Curvature With Smooth and Rib-Roughened Walls," *ASME J. Turbomach.*, **122**(2), pp. 386–392.
- [12] Ekkad, S. V., and Han, J. C., 1997, "Detailed Heat Transfer Distributions in Two-Pass Square Channels With Rib Turbulators," *Int. J. Heat Mass Transfer*, **40**(11), pp. 2525–2537.
- [13] Liou, T. M., Chen, C. C., and Tsai, T. W., 2000, "Heat Transfer and Fluid Flow in a Square Duct With 12 Different Shaped Vortex Generators," *ASME J. Heat Transfer*, **122**(2), pp. 327–335.
- [14] Taslim, M. E., Li, T., and Kercher, D. M., 1996, "Experimental Heat Transfer and Friction in Channels Roughened With Angled, V-Shaped and Discrete Ribs on Two Opposite Walls," *ASME J. Turbomach.*, **118**(1), pp. 20–28.
- [15] Park, J. S., Han, J. C., Huang, Y., and Ou, S., 1992, "Heat Transfer Performance Comparisons of Five Different Rectangular Channels With Parallel Angled Ribs," *Int. J. Heat Mass Transfer*, **35**(11), pp. 2891–2903.
- [16] Abdon, A., and Sundén, B., 1998, "A Numerical Method to Calculate the Cooling Performance of a Rib-Roughened Duct," in *Advanced Computational Methods in Heat Transfer* (eds., A. J. Nowak, C. A. Brebbia, R. Bialecki, and M. Zerroukat), pp. 381–392, Computational Mechanics Publications, Southampton, UK.
- [17] Liou, T. M., Wu, Y. Y., and Chang, Y., 1993, "LDV Measurements of Periodic Fully Developed Main and Secondary Flows in a Channel With Rib-Disturbed Walls," *ASME J. Fluids Eng.*, **115**(1), pp. 109–114.
- [18] Iacovides, H., Jackson, D. C., Launder, B. E., and Yuan, Y. M., 1999, "An Experimental Study of a Rib-Roughened Rotating U-Bend Flow," *Exp. Therm. Fluid Sci.*, **19**, pp. 151–159.
- [19] Hirota, M., Fujita, H., and Yokosawa, H., 1994, "Experimental Study on Convective Heat Transfer for Turbulent Flow in a Square Duct With a Ribbed Rough Wall (Characteristics of Mean Temperature Field)," *ASME J. Heat Transfer*, **116**(2), pp. 332–340.
- [20] Kiml, R., Mochizuki, S., and Murata, A., 2000, "Function of Ribs as Turbulators and Secondary Flow Inducers," 9th International Symposium on Flow Visualization, Paper No. 164, Edinburgh, UK.
- [21] Adrian, R. J., 1991, "Particle Imaging Techniques for Experimental Fluid Mechanics," *Annu. Rev. Fluid Mech.*, **23**, pp. 261–304.
- [22] Liu, Z. C., Landreth, C. C., Adrian, R. J., and Hanratty, T. J., 1991, "High Resolution Measurement of Turbulent Structure in a Channel With Particle Image Velocimetry," *Exp. Fluids*, **10**(6), pp. 301–312.
- [23] Raffel, M., Willert, C., and Kompenhans, J., 1998, "Particle Image Velocimetry: A Practical Guide," Springer, Berlin.
- [24] Son, S. Y., Kihm, K. D., and Han, J.-C., 2002, "PIV Flow Measurements for Heat Transfer Characterization in Two-Pass Square Channels With Smooth and 90 deg Ribbed Walls," *Int. J. Heat Mass Transfer*, **45**, pp. 4809–4822.
- [25] Bonhoff, B., Parneix, S., Leusch, J., Johnson, B. V., Schabacker, J., and Böles, A., 1999, "Experimental and Numerical Study of Developed Flow and Heat Transfer in Coolant Channels With 45 deg Ribs," *Exp. Therm. Fluid Sci.*, **20**, pp. 311–319.
- [26] Schabacker, J., Böles, A., and Johnson, B. V., 1998, "PIV Investigation of the Flow Characteristics in an Internal Coolant Passage With Two Ducts Connected by a Sharp 180 deg Bend," ASME paper 98-GT-544, Stockholm, Sweden.
- [27] Schabacker, J., Böles, A., and Johnson, B. V., 1999, "PIV Investigation of the Flow Characteristics in an Internal Coolant Passage With 90 deg Rib Arrangement," *Proc. 3rd European Conference on Turbomachinery, Fluid Dynamics and Thermodynamics*, pp. 973–984, London, UK, 2–5 March.
- [28] Gao, X., 2002, "Heat Transfer and Fluid Flow Investigations in Ribbed Ducts and Impinging Jets Using Liquid Crystal Thermography and PIV," Ph.D. thesis, Division of Heat Transfer, Department of Heat and Power Engineering, Lund Institute of Technology, Sweden.
- [29] Rokni, M., Olsson, C. O., and Sundén, B., 1998, "Numerical and Experimental Investigation of Turbulent Flow in a Rectangular Duct," *Int. J. Numer. Methods Fluids*, **28**, pp. 225–242.
- [30] Rau, G., Cakan, M., Moeller, D., and Arts, T., 1998, "The Effect of Periodic Ribs on the Local Aerodynamic and Heat Transfer Performance of a Straight Cooling Channel," *ASME J. Turbomach.*, **120**(2), pp. 368–375.
- [31] Liou, T. M., Wu, Y. Y., and Chang, Y., 1993, "LDV Measurements of Periodic Fully Developed Main and Secondary Flows in a Channel With Rib-Disturbed Walls," *ASME J. Fluids Eng.*, **115**(1), pp. 109–114.
- [32] Jia, R., 2002, "Numerical Study of Cooling Processes Relevant for Gas Turbine Combustor and Blades," Licentiate Thesis, Division of Heat Transfer, Lund Institute of Technology, Sweden.
- [33] Naimi, M., and Gessner, F. B., 1997, "Calculation of Fully Developed Turbulent Flow in Rectangular Ducts With Two Opposite Roughened Walls," *Int. J. Heat Mass Transfer*, **18**, pp. 471–481.

Aerodynamic Entropy Generation Rate in a Boundary Layer With High Free Stream Turbulence

Philip C. Griffin and Mark R. D. Davies

Stokes Research Institute, Department of Mechanical & Aeronautical Engineering, University of Limerick, Plassey Technological Park, Limerick, Republic of Ireland

[DOI: 10.1115/1.1780170]

1 Introduction

The loss mechanism under consideration in this study is that fraction of turbomachinery blade profile loss [1] due to viscous dissipation and turbulent phenomena in the blade boundary layer. In the consideration of profile loss it is customary to neglect any end wall effects and as such the flow is approximately two-dimensional. Hence loss measurements can be based on cascade tests and boundary layer calculations. It has been proposed in [1] that the concept of entropy generation be used as the key measure of lost performance in turbomachinery, as opposed to the more traditional loss calculation methods based on stagnation pressure and kinetic energy losses. Assessment of loss in terms of the entropy generation rate is not dependant on whether it is examined from the perspective of a stationary or rotating blade row, thereby enabling direct comparison between measurements from cascades and rotating facilities.

Previous researchers [2–5] at the author's university have measured transitional and turbulent boundary layer losses. This paper, however, is mainly focused on loss in the laminar boundary layer and how it is influenced by FST. This is important in turbomachinery because laminar boundary layers are subjected to extremes of FST of varying intensity. As the flow under consideration is assumed to be adiabatic, the only contributory factor to loss is that due to viscous dissipation and Reynolds stresses. The entropy generation rate is therefore obtained directly from the boundary layer velocity profile; a first integration through the boundary layer thickness gives the entropy generation rate at a chordwise point, a second integration in the streamwise direction yields the entropy generation rate over the entire suction surface length. The procedures for acquiring such have been described in [2], [4] and [5]. In short, the contributions to the entropy generation rate (\dot{S}_{gen}'') per unit area in an incompressible, two-dimensional boundary layer are given by the sum of the viscous dissipation and turbulence production terms:

$$\dot{S}_{gen}'' = \frac{1}{T} \int_0^\delta \left[\underbrace{\mu \left(\frac{\partial \bar{u}}{\partial y} \right)^2}_{(I) \text{ Viscous Dissipation}} + \underbrace{\tau_{xy}' \left(\frac{\partial \bar{u}}{\partial y} \right)}_{(II) \text{ Reynolds Stress}} \right] dy = \frac{\text{Strain Work}}{T}. \quad (1)$$

For the case of increased FST it will be shown that it is necessary to include the Reynolds stress term in the calculation of laminar boundary layer loss. However, the very thin boundary layer present in this investigation precluded the use of multi-sensor hot-wire probes. As it was not possible to directly measure, the Rey-

nolds stress in the turbulent boundary layer, an approximation was required. This approximation is based on the assumption that in the near-wall region of a turbulent boundary layer, the total shear stress is constant and equal to the wall value. Therefore, the required element of the Reynolds stress tensor is approximated as:

$$\mu \frac{\partial \bar{u}}{\partial y} \Big|_{y=0} - \mu \frac{\partial \bar{u}}{\partial y} \cong \tau_{xy}' = -\overline{\rho u' v'}. \quad (2)$$

This relationship is only valid in the absence of large streamwise pressure gradients and holds approximately true for the first 10% of a turbulent boundary layer. Fortunately this constitutes the most loss-affected region of the turbulent boundary layer [4]. Additionally, studies on flat-plate boundary layers by [6] have confirmed that increased FST only alters the velocity defect region of the turbulent boundary layer. Their investigation illustrated that at FST levels of up to 20%, the near-wall region agrees very closely with the classical universal velocity profile for a turbulent boundary layer. By combining Eqs. (1) and (2), the entropy generation rate becomes:

$$\dot{S}_{gen}'' = \frac{\mu}{T} \left(\frac{\partial \bar{u}}{\partial y} \Big|_{y=0} \right) \int_0^\delta \frac{\partial \bar{u}}{\partial y} dy. \quad (3)$$

However, as the constant stress approximation is not valid in the presence of strong pressure gradients (adverse or favorable), calculation of the entropy generation rate in laminar and transitional boundary layers only involved integration of the first term in Eq. (1). Therefore, all laminar and transitional loss measurements presented here are slightly underestimated as they do not explicitly account for the Reynolds shear stress.

2 Experimental Methods

The turbine cascade and associated instrumentation have previously been described in detail in Refs. [2–5]. An illustration is given in Fig. 1. The cascade consists of seven aluminum blades, each of 92.6 mm chord, 300 mm span and spaced 70.44 mm apart. Boundary layer velocity data was acquired at a sampling frequency of 20 kHz (over a 0.2 sec duration) by traversing a single sensor hot-wire probe (Dantec type P11) operating at 250°C over-heat normal to the surface. Traversing was initially carried out in 10 μm increments as very fine resolution is required within the first 0.5 mm from the wall as the majority of entropy is generated here. Hence motion of the sensor normal to the surface was achieved using a precision traversing mechanism synchronized with the data acquisition system for automatic measurement. In addition, data was also acquired from an array of 28 hot-film sensors (spaced in 3.5% increments of suction surface length) located at mid-span of the central blade in the cascade. A perforated plate was used to raise the turbulence intensity at the inlet to the blade passage from 0.8 to 5.0% [3].

3 Error Analysis

The standard error analysis technique of Kline and McClintock [7] was used to find the uncertainty in \dot{S}_{gen}'' . Firstly, based on all possible sources of error in the hot-wire measurement technique the error in the boundary layer velocity gradient and subsequent wall shear stress estimate was estimated as $\pm 10\%$ [4]. The primary source of error comes from the low velocity hot-wire calibration needed in the near-wall region. The error shown is believed to be greatly over estimated, because the wire calibration at higher velocities is extendible to low velocities, provided that the flow velocity is not so low that natural convection effects are significant. Repeat experiments with different calibrated hot-wire sensors have shown a lower uncertainty than that estimated. Based on the estimated error of $\pm 10\%$ in the measurement of the velocity gradient, an estimate of the error of \dot{S}_{gen}'' was found to be $\pm 20\%$ using the method described in [7]. Overall, the calculated

Contributed by the Fluids Engineering Division for publication in the JOURNAL OF FLUIDS ENGINEERING. Manuscript received by the Fluids Engineering Division June 27, 2002; revised manuscript received March 5, 2004. Associate Editor: T. B. Gatski.

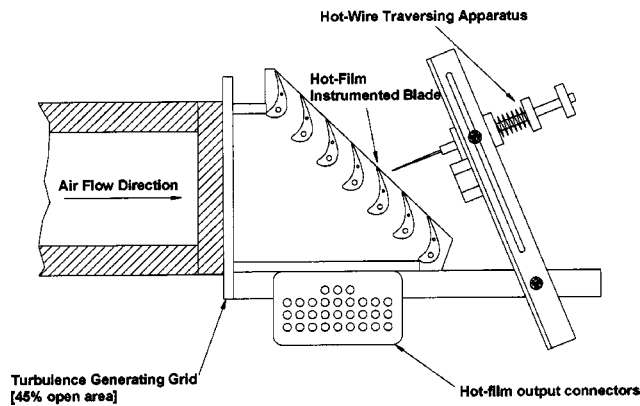


Fig. 1 Incompressible turbine cascade and hot-wire traverse assembly

maximum error in the \dot{S}_{gen}'' values is of the order of $\pm 10\%$, half that of \dot{S}_{gen}''' as the integration step averages out the errors.

4 Experimental Results and Discussion

Figure 2 illustrates a distribution of the pressure coefficient along the blade suction surface for both turbulence levels at $Re_c = 76,000$, in which peak suction occurs at 35% of suction surface length. Figure 3 shows a typical distribution of the mean and turbulent velocity components for the high turbulence case in the laminar boundary layer. Clearly visible are increased fluid strain rates under conditions of high FST as well as appreciable velocity fluctuations across the boundary layer. These effects are not due to an earlier transition as the skew distribution shown in Fig. 4(b) illustrates an unambiguous transition for the high turbulence case at 54% suction surface length.

As this laminar boundary layer possesses both laminar and turbulent characteristics we have named it a *hybrid* boundary layer. In a classical turbulent boundary layer the fluctuating velocities are at a maximum very close to the wall, however in a perturbed laminar boundary layer maxima are encountered further out from the wall ($\eta > 0.1$). These findings have previously been observed in similar boundary layers by [8] and [9]. The measured local FST in the laminar region was found to equal that convected from the grid at the boundary layer edge, according to:

$$Tu_\delta = Tu_\infty \frac{U_\infty}{U_\delta}$$

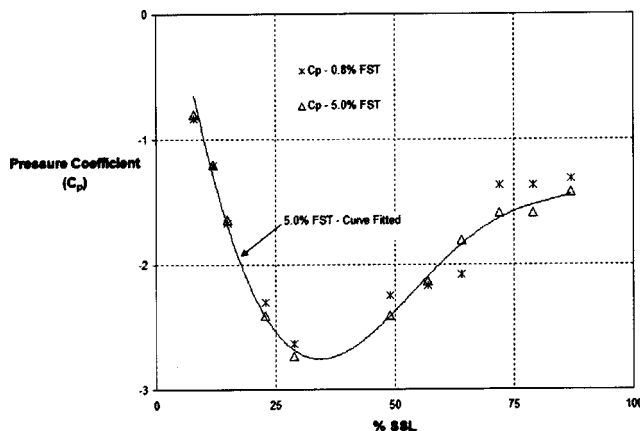


Fig. 2 Measured suction surface pressure distribution (expressed as the pressure coefficient C_p) for $Re_c = 76,000$, for both 0.8% and 5.0% FST

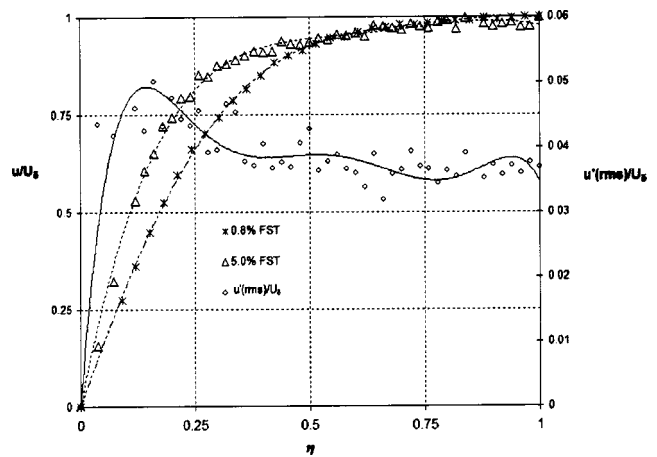


Fig. 3 Comparison between measured boundary layer velocity profiles at 5.7% SSL, $Re_c = 76,000$ both turbulence levels, $\delta = 500 \mu m$, $U_\delta = 15$ m/s. Also shown is the distribution of percentage turbulence.

There is therefore very little damping of the FST.

Using Eq. (3), velocity data is transformed into loss data. Often it is more convenient to express the measured values of \dot{S}_{gen}'' in terms of a non-dimensional dissipation coefficient defined as [1]:

$$C_d = \frac{T \dot{S}_{gen}''}{\rho U_\delta^3} \quad (4)$$

The distribution of C_d is plotted in Fig. 4(a) for both high and low FST levels at $Re_c = 76,000$. Significant losses are observed in the laminar and transitional regions with increased FST. Losses in the pre-transitional boundary layer are substantially increased in the presence of FST primarily due to changes in the mean velocity profile. This loss is even greater if the induced Reynolds stresses are considered. If a CFD code is to accurately model flows under these conditions it must account fully for the affects of a turbulent free stream. These phenomena are neglected in the conventional modelling of laminar boundary layers which would likely require the use of different turbulence models for the laminar and turbulent boundary layers. In contrast, the turbulent boundary layer is largely unaffected by FST with a near constant value $C_d \approx 0.003$ (inclusive of Reynolds stress effects) for both FST levels at the same Reynolds number. This view is supported in [10], noting that FST only effects the low loss outer boundary layer.

The overall loss generated in the entire suction surface boundary layer can best be viewed when Eq. (3) is integrated in the streamwise direction:

$$\dot{S}'_{gen} = \int_0^{SSL} \dot{S}_{gen}'' dx \quad (5)$$

Table 1 summarizes the relative distribution of the blade suction surface loss between the laminar, transitional and turbulent regions. The total loss for the 5.0% FST test case is almost 45% higher than its low turbulence counterpart due to increased losses in the laminar and transitional regions for the former. Greater losses are observed in the turbulent boundary layer of the high FST case, due to an earlier transition and hence larger coverage of the suction surface by a turbulent boundary layer. Interestingly, the relative distribution of loss between the laminar, transitional and turbulent regions remains unchanged. The fact that the laminar boundary layer accounts for the majority of the suction surface loss may appear contrary to common perception. However, as noted by [4], the very thin laminar boundary layer coupled with a high freestream velocity due to acceleration of the flow over the fore section of the blade, generates very large velocity gradients.

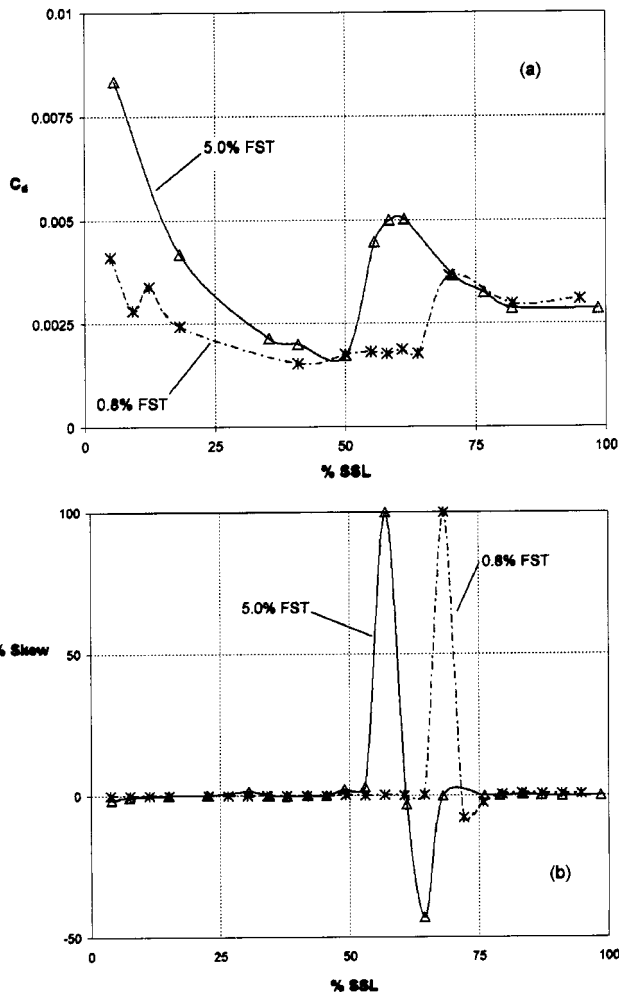


Fig. 4 (a) Distribution of the dissipation coefficient C_d derived from measurements of \dot{S}'_{gen} at $Re_c=76,000$ for both 0.8% and 5.0% FST. (b) The corresponding hot-film skewness distribution.

Furthermore, the validity of the results has been verified by [11] in which a comparison is made between the integrated boundary layer entropy generation rate and that estimated by Eq. (6) from stagnation pressure losses in the turbine blade wake (inclusive of trailing edge loss and turbulent phenomena upstream of the turbulent boundary layer):

$$\dot{S}'_{gen} = -\rho R \int_0^\delta \bar{u} \ln\left(\frac{p_{02}}{p_{01}}\right) dy. \quad (6)$$

Figure 5 shows frequency spectra at different wall-normal positions in the laminar boundary layer for both FST levels including those of the free stream ($\eta > 1$). Evident in all spectra is the similarity to the classical Kolmogorov $-5/3$ power slope characterizing the inertial subrange [12,13]. This represents the intermediate scales of turbulence; those lying between the larger energy containing and smaller dissipative scales. Adherence to the Kolmogorov $-5/3$ power-law slope indicates a flow with an equilibrium of production and dissipation of turbulent kinetic energy [12]. It is also apparent that the high free stream turbulence spectra contain greater spectral energy over the same range of frequencies than their low turbulence counterparts. For both cases the highest spectral power is observed moving into the boundary layer, with the highest encountered in the region corresponding to the maximum value of $\sqrt{u'^2}/U_\delta$ at $\eta=0.15$ in Fig. 3. In addition,

Table 1 Relative contributions to the measured entropy generation rate per unit span at both turbulence levels at $Re_c=76,000$

% SSL Coverage	0.8% FST	5.0% FST
Laminar	0–65%	0–54%
Transition	65–80%	54–70%
Turbulent	80–100%	70–100%

Suction Surface Loss Determined from Boundary Layer Hot-Wire Measurements

Measured Loss \dot{S}'_{gen} ($Wm^{-1} K$)	0.8% FST	% of Total	5.0% FST	% of Total
Laminar	0.0068	60%	0.0094	58%
Transition	0.0031	27%	0.0043	26%
Turbulent	0.0014	13%	0.0026	16%
Total	0.0113		0.0163	

Suction Surface Loss Determined from Wake Pressure Loss

Measured Loss \dot{S}'_{gen} ($Wm^{-1} K$)	0.8% FST	5.0% FST
Total	0.0129	0.0239

the boundary layer spectra exhibit greater spectral power in the lower frequency range, which increases towards the wall. This has been previously observed by [9] and is due to the receptivity of the boundary layer to disturbances in the free stream [14]. The boundary layer can be considered as a ‘noise amplifier’, which selectively amplifies low frequency fluctuations from the free stream. The maximum amplification was not observed in the near-wall region (i.e. at $\eta < 0.05$, where Tollmien-Schlichting instabilities would prevail), but further out.

5 Conclusions

An increase in the free-stream turbulence level from 0.8% to 5.0% resulted in almost a 45% increase in suction surface boundary layer loss for a comparable Reynolds number. Laminar and transitional losses were most influenced by the freestream turbulence. As the perturbed laminar suction surface boundary layer exhibits significant turbulent characteristics it has been termed a

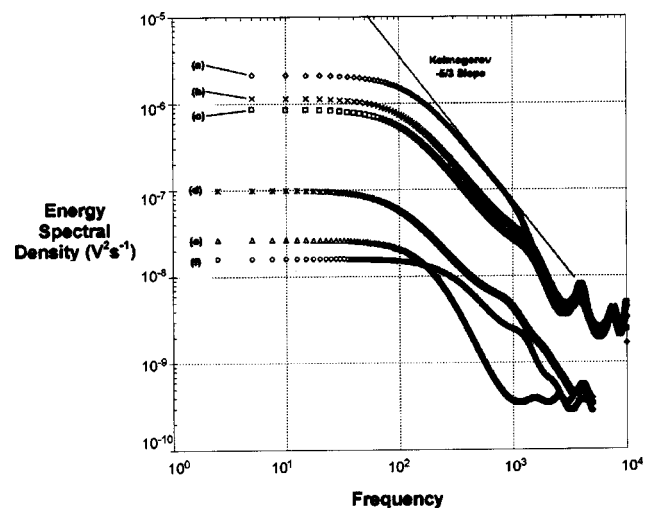


Fig. 5 Energy spectra of the fluctuating hot-wire and film voltage signals (analogous to u') at different wall-normal positions in the boundary layer for 5.7% SSL with $Re_c=76,000$. (a) $\eta=0.1$, 5.0% FST; (b) $\eta=0.4$, 5.0% FST; (c) $\eta > 1$, 5.0% FST; (d) $\eta=0.4$, 0.8% FST; (e) Wall, 5.0% FST; (f) $\eta > 1$, 0.8% FST.

hybrid boundary layer. In contrast, the local turbulent boundary layer loss was unaffected by an increase in freestream turbulence, as a constant value of $C_d \approx 0.003$ was observed for both freestream turbulence levels. The measured entropy generation rate compares favourably with that determined from the pressure loss in the turbine blade wake. The discrepancy at high FST arises due to the Reynolds stresses in the laminar and transitional boundary layers which were not included in the hot-wire determination. Therefore, if CFD codes are to accurately model boundary layers under these conditions, they must account for the turbulent phenomena. It is not clear, which, if any of the existing models will work.

Nomenclature

C_d	= Dissipation coefficient (Eq. 4) –
C_p	= Pressure coefficient = $(p - p_\infty) / (0.5 \rho U_\infty^2)$ –
Re_c	= Reynolds number based on blade chord and inlet free-stream velocity –
\dot{S}_{gen}''	= Entropy generation rate per unit area $Wm^{-2} K$
\dot{S}_{gen}'	= Entropy generation rate per unit length $Wm^{-1} K$
p_{01}	= Stagnation pressure at cascade inlet Nm^{-2}
p_{02}	= Stagnation pressure at cascade outlet Nm^{-2}
R	= Gas constant $J Kg^{-1} K^{-1}$
Tu_δ	= Local percentage turbulence intensity %
Tu_∞	= Inlet percentage turbulence intensity %
T	= Bulk fluid temperature K
u	= Instantaneous x -direction velocity ms^{-1}
\bar{u}	= Mean velocity in x -direction ms^{-1}
$\sqrt{u'^2}$	= RMS average of x -direction fluctuating velocity component ms^{-1}
U_δ	= Local free-stream velocity ms^{-1}
U_∞	= Inlet free-stream velocity ms^{-1}
y	= Wall normal coordinate m

δ	= Boundary layer thickness m
η	= Dimensionless wall-normal coordinate = y/δ –
μ	= Dynamic viscosity Nsm^{-2}
τ'_{xy}	= Turbulent shearing stress Nm^{-2}

References

- [1] Denton, J. D., 1993, "Loss Mechanisms in Turbomachines," ASME J. Turbomach., **115**, pp. 621–656.
- [2] Davies, M. R. D., and O'Donnell, F. K., 1999, "Local Measurement of Loss Using Heated Thin Film Sensors," ASME J. Turbomach., **121**, pp. 814–818.
- [3] Griffin, P. C., Davies, M. R. D., O'Donnell, F. K., and Walsh, E., 2002, "The Effect of Reynolds Number, Compressibility and Free Stream Turbulence on Profile Entropy Generation Rate," ASME Paper no. GT-2002-30330.
- [4] O'Donnell, F. K., 2000, "The Measurement of Aerodynamic Entropy Generation in a Turbine Blade Boundary Layer," Ph.D. Thesis, University of Limerick, Limerick, Ireland.
- [5] O'Donnell, F. K., and Davies, M. R. D., 2000 "Turbine Blade Entropy Generation Rate, Part II: The Measured Loss," ASME Paper no. 2000-GT-266.
- [6] Thole, K. A., and Bogard, D. G., 1996, "High Freestream Turbulence Effects on Turbulent Boundary Layers," ASME J. Fluids Eng., **118**, pp. 276–284.
- [7] Kline, S. J., and McClintock, F. A., 1953, "Describing Uncertainties in Single Sample Experiments," Mechanical Engineering, Jan 1953, p. 3.
- [8] Volino, R. J., Schultz, M. P., and Pratt, C. M., 2001, "Conditional Sampling in a Transitional Boundary Layer Under High Free Stream Turbulence Conditions," ASME Paper no. 2001-GT-0192.
- [9] Westin, K. J. A., Boiko, A. V., Klingmann, B. G. B., Kozlov, V. V., and Alfredsson, P. H., 1994, "Experiments in a Boundary Layer Subjected to Free Stream Turbulence. Part 1. Boundary Layer Structure and Receptivity," J. Fluid Mech., **281**, pp. 193–218.
- [10] Klebanoff, P. S., 1955, "Characteristics of Turbulence in a Boundary Layer With Zero Pressure Gradient," NACA Report no. 1247.
- [11] Griffin, P. C., 2003, "The Effect of Freestream Turbulence on Aerodynamic Entropy Generation Rate," Ph.D. Thesis, University of Limerick, Limerick, Ireland.
- [12] Hinze, J. O., 1975, "Turbulence," 2nd Edition, McGraw-Hill, New York.
- [13] Mathieu, J., and Scott, J., 2000, "An Introduction to Turbulent Flow," Chapter 2, Cambridge University Press, U.K.
- [14] Boiko, A. V., Grek, G. R., Dovgal, A. V., and Kozlov, V. V., 2002, "The Origin of Turbulence in Near Wall Flows," Springer-Verlag, Berlin-Heidelberg.

Discussion: Criticisms of the “Correction Factor” Verification Method [1]

Robert Wilson

Assistant Research Engineer, Member ASME

Jun Shao

Graduate Research Assistant

Fred Stern

Professor Mechanical Engineering and Research Engineer, Fellow ASME

IIHR-Hydroscience & Engineering The University of Iowa Iowa City, Iowa

The technical brief by Roache [1] presents seven criticisms of the correction factor verification method proposed by the authors and colleagues in [2–4]. The authors acknowledge Dr. Roache’s careful review and insightful comments of our work. We have addressed Dr. Roache’s first criticism and revised the correction factor uncertainty estimates; however, we rebut the other criticisms.

1. The uncorrected U_k and corrected U_{k_c} solution uncertainty estimates given by Eqs. (33) and (34) in [2] are deficient for correction factor $C_k \leq 1$ and $C_k = 1$, respectively, in only providing 50% uncertainty estimate (confidence level), as pointed out by Dr. Roache. In [4], Eq. (33) in [2] was revised for proper behavior for $C_k < 1$: increasing factor of safety for decreasing C_k (i.e., distance from the asymptotic range) similarly as is case for $C_k > 1$. Subsequently, revisions were also made for proper behavior for $C_k = 1$ for both Eqs. (33) and (34) in [2]: provision for 10% factor of safety in the limit $C_k = 1$ while smoothly merging with previous correction factor uncertainty estimates for $|1 - C_k| \geq 0.125$ (uncorrected solution) and 0.25 (corrected solution) given in [2] and [4]. Incorporating both revisions the uncorrected U_k and corrected U_{k_c} solution uncertainty estimates are given by:

$$U_k = \begin{cases} [9.6(1 - C_k)^2 + 1.1] |\delta_{REk_1}^*| & |1 - C_k| < 0.125 \\ [2|1 - C_k| + 1] |\delta_{REk_1}^*| & |1 - C_k| \geq 0.125 \end{cases} \quad (1)$$

$$U_{k_c} = \begin{cases} [2.4(1 - C_k)^2 + 0.1] |\delta_{REk_1}^*| & |1 - C_k| < 0.25 \\ [|1 - C_k|] |\delta_{REk_1}^*| & |1 - C_k| \geq 0.25 \end{cases} \quad (2)$$

C_k is the correction factor and $\delta_{REk_1}^*$ and p_k are the one-term Richardson extrapolation (RE) estimates for error and order of accuracy defined by

$$C_k = \frac{r_k^{p_k} - 1}{r_k^{p_{k_{est}}} - 1} \quad (3)$$

$$\delta_{REk_1}^* = \frac{\varepsilon_{k_{21}}}{r_k^{p_k} - 1} \quad (4)$$

$$p_k = \frac{\ln(\varepsilon_{k_{32}}/\varepsilon_{k_{21}})}{\ln(r_k)} \quad (5)$$

r_k is the k th input-parameter (e.g., grid spacing or time step) uniform refinement ratio. ε_k are solution changes between medium (2) and fine (1), and coarse (3) and medium input parameter values corrected for iterative errors. $p_{k_{est}}$ is an estimate for the limiting order of accuracy of the first term in the RE expansion as spacing size goes to zero and the asymptotic range is reached so that $C_k \rightarrow 1$. Usually approximation is made that $p_{k_{est}}$ is the theoretical order of the numerical method $p_{k_{th}}$, e.g., =2 for a second-order accurate method. Replacing equation (5) by

$$p_k = \frac{\ln(\varepsilon_{k_{32}}/\varepsilon_{k_{21}})}{\ln(r_{k_{21}})} - \frac{1}{\ln(r_{k_{21}})} [\ln(r_{k_{32}}^{p_k} - 1) - \ln(r_{k_{21}}^{p_k} - 1)] \quad (6)$$

enables use of equations (1) and (2) for nonuniform refinement ratio. Equation (6) corrects equation (31) in [2] for a typographical sign error.

2. The observed order of accuracy is not discarded, but used in defining the correction factor C_k (3), which is then used in defining a corrected one-term RE error estimate ($= C_k \delta_{REk_1}^*$) and uncertainty estimates for uncorrected U_k (1) and corrected U_{k_c} (2) solutions, as shown above and in detail in [2]. Correction factors provide a quantitative metric for defining distance of solutions from the asymptotic range and approximately account for the effects of higher-order terms in making error and uncertainty estimates. Correction factors originally based on confirmation studies for 1-D wave [2] and 2-D Laplace equation analytical benchmarks, which showed that the one-term RE error estimate (4) has correct form, but one-term RE order-of-accuracy estimate (5) is poor except in asymptotic range. Multiplication of (4) by C_k (3) provides improved error and uncertainty estimates. For uncorrected solutions, uncertainty estimate U_k (1) based on the absolute value of the corrected error estimate plus the amount of the correction. For corrected solutions (i.e., corrected error estimate is used both in sign and magnitude to define numerical benchmark $S_c = S - C_k \delta_{REk_1}^*$), U_{k_c} (2) based on the absolute value of the amount of the correction.

3. Reference [4] shows that the correction factor approach is equivalent to the GCI, but with a variable factor of safety (FS), which increases with distance of solutions from the asymptotic range. C_k (3) provides metric for estimating distance of solutions from the asymptotic range: =1 when solutions are in asymptotic range; <1 when $p_k < p_{k_{est}}$; and >1 when $p_k > p_{k_{est}}$. For GCI approach, FS is constant for all C_k : 1.25 for careful grid studies otherwise 3. For C_k approach, FS varies linearly with C_k with slope 2 (uncorrected solution) and 1 (corrected solution) and symmetric about $C_k = 1$. The intersection points between C_k and GCI approaches depends on value FS used in GCI, e.g., for FS=1.25 intersection points are $C_k = (0.875, 1.125)$ and $(0.75, 1.25)$ for uncorrected and corrected solutions, respectively. When solutions are between the intersections points (closer to the asymptotic range), GCI approach is more conservative than C_k approach. When solutions are outside the intersection points (further from the asymptotic range), GCI approach is less conservative than C_k approach. The previously mentioned analytical benchmarks confirmed the FS slope predicted by correction factors and admittedly may not be best for all cases (an interesting topic for future research). Variable FS that increases with distance from the asymptotic range is a “common-sense” advantage of correction factor approach compared to GCI, especially for practical applications where solutions are often further from the asymptotic range. In retrospect, correction factor approach has similarities to that proposed by Celik and Karatekin [5], who in present notation propose $U_{C\&K} = |C_k \delta_{RE}^*|$ (equivalent equation (9a) of [5]). $U_{C\&K}$ is similar to correction factors for $C_k > 1$ in providing variable FS

Contributed by the Fluids Engineering Division for publication in the JOURNAL OF FLUIDS ENGINEERING. Manuscript received by the Fluids Engineering Division Sept. 9, 2003; revised manuscript received March 5, 2004. Associate Editor: Joe Katz.

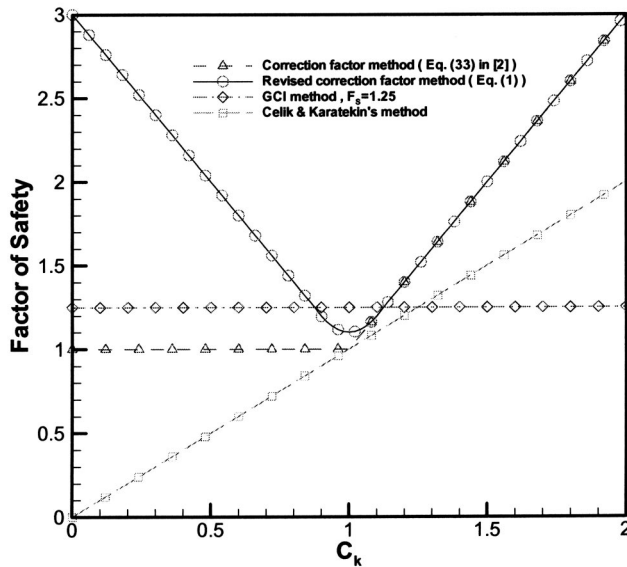


Fig. 1 Factors of safety for correction factor, GCI, and Celik & Karatekin [5] verification methods

which increases with distance from the asymptotic range; however, less conservative than correction factors which includes the amount of the correction. Also, for $C_k=0$ $U_{C\&K}$ suffers 50% uncertainty and for $C_k < 1$ gives an unacceptable result of $FS < 1$. Figure 1 compares FS predicted by correction factors, GCI, and $U_{C\&K}$.

4. Our claim of GCI being more conservative for solutions closer to asymptotic range and *more importantly* less conservative for solutions further from the asymptotic range in comparison to correction factors is based on our comparison of factor of safety for both approaches, as discussed above as well as comparisons between two approaches for analytical and numerical benchmarks and practical applications. The cases in [3,4] are practical applications with solutions further from the asymptotic range, especially [3]; therefore, correction factor uncertainties are more conservative than GCI. For the Series 60 model ship [3], verification results were obtained on four grids wherein for the finer three grids $p_G=4.4$ ($C_G=3.7$) and for the coarser three grids $p_G=2.3$ ($C_G=1.3$) for the total resistance coefficient. In the former case, the GCI approach with $F_S=1.25$ estimates uncertainties which are smaller than the correction factor approach by a factor of roughly five. If $F_S=3$ is used, the GCI approach estimates uncertainties which are smaller than the correction factor approach by a factor of roughly 2. For the 5415 surface combatant [4], verification results were obtained on three grids and both correction factor and GCI give similar results for the total resistance coefficient since $C_k=0.8$ is near the intersection of the two approaches. Ebert and Gorski [6] showed that the correction factor approach is reasonable for $p_k > p_{k_{est}}$, but not for $p_k < p_{k_{est}}$ where C_k uncertainty estimates indicated insufficient conservatism. Present revisions no longer have this deficiency, as previously discussed.

For analytical benchmarks, as already mentioned, 1-D wave and 2-D Laplace equations originally used to test verification methods. Analytical benchmarks are ideal for confirmation of verification procedures since the exact solution known analytically and modeling errors are zero such that numerical errors can be determined exactly; however, analytical benchmarks are restricted to simple problems. For the 1-D wave equation, verification results obtained on 10 grids with C_k values for maximum wave amplitude in the range $0.5 \leq C_k \leq 1$. For the uncorrected simulation, both U_k and GCI (with $F_S=1.25$) banded the true

error with the latter more conservative. The corrected simulation, U_{k_c} banded the true error, whereas GCI (extended for use with corrected solutions) failed to band the true error for the two coarsest grids. Verification results on 6 grids for the 2-D Laplace equation with constant Dirichlet boundary conditions showed C_k values at a fixed point in the range $0.8 \leq C_k \leq 1.0$. For the uncorrected simulations, both U_k and GCI (with $F_S=1.25$) banded the true error with the latter more conservative for solutions closer to the asymptotic range and less conservative for solutions further from the asymptotic range. For the corrected simulation, both U_{k_c} and GCI banded the true error. More recently, verification results were obtained for the Blasius boundary layer analytical benchmark [7], on 5 grids with C_k values for the axial velocity profile at quarter-plate in the range $0.75 < C_k < 5.0$. For the finest grid triplet, both C_k and GCI approaches band the true error, but for the coarser grid triplets, the GCI approach failed to band the true error for the inner part of the boundary layer. Results also showed difficulties for complex nonlinear analytical benchmarks such as the necessity of restricting the analysis to the region of flow for which boundary layer theory is valid.

In preparation of the present discussion, additional comparison of verification procedures used analytical benchmark data for 2-D Laplace equation with linear/logarithmic varying Dirichlet boundary conditions from [8] and numerical benchmark data for k - ϵ model turbulent flow backward facing step from [5]. Numerical benchmarks use grid-independent solutions to estimate the numerical benchmark S_C and numerical error δ_{SN}^* as the difference between the fine S_{k_1} and grid independent solutions $\delta_{SN}^* = S_{k_1} - S_C$. Numerical benchmarks are not restricted to simple problems; however, are less-ideal than analytical benchmarks for confirmation of verification procedures since assumptions must be made that benchmark solution is without numerical error and modeling errors are same for all solutions both of which are suspect for complex problems. Results for the former are similar to previously discussed 2-D Laplace equation results. Note that for both 1-D wave and 2-D Laplace equation cases the $U_{C\&K}$ approach fails to bound the true error since $C_k < 1$ for reasons discussed previously. Results for the latter, show that for the uncorrected solution both correction factor and $U_{C\&K}$ approaches with $p_{k_{est}}=1$ bound the estimated error with correction factors more conservative, whereas the GCI approach (with $F_S=1.25$) fails to bound the estimated error (based on previously published "grid independent" solutions with same turbulence model) for the finest and a medium grid. For the corrected simulation, both correction factor and GCI approaches fail to band the estimated error. Results were also obtained for the correction factor approach with $p_{k_{est}}=2$; since, [5] uses the hybrid numerical method with variable p_{th} between 1 and 2. For the uncorrected simulation, correction factor trends are similar to GCI, but more conservative. For the corrected simulation, the correction factor approach bands the estimated error, except on the finest grid. In [5], $U_{C\&K}$ and GCI (with $F_S=3$) are compared showing latter more conservative than former; however, for such careful grid study GCI with $F_S=1.25$ is more appropriate.

Data and figures showing comparisons of correction factor, GCI, and Celik and Karatekin verification methods for aforementioned analytical and numerical benchmarks are available from the authors upon request.

The overall results show that when solutions are closer to the asymptotic range both correction factor and GCI approaches provide reasonable results, although the GCI approach may be over conservative in comparison to the correction factor approach. When solutions are further from the asymptotic range, as is often the case with practical applications, correction factors have the advantage of increased factor of safety and GCI approach may be under conservative in comparison to the correction factor approach. The Celik and Karatekin [5] approach is reasonable for $C_k > 1$ although less conservative than correction factor approach and not reasonable for $C_k \leq 1$.

5. Strictly speaking, the corrected solution (i.e., simulation corrected using deterministic estimate of sign and magnitude of numerical error) will not satisfy the same conservation properties (e.g., mass and momentum) as the uncorrected solution. However, if solutions close to the asymptotic range one would expect the correction and the lack of conservation for the numerical benchmark solution to be small. Situations that might prevent correction of the solution include variability in the observed order of accuracy, lack of complete iterative convergence, and solutions further from the asymptotic range. Situations also exist when it is useful to make use of the corrected solution. Confirmation of verification procedures using numerical benchmarks in which the corrected solution is assumed without numerical error and modeling errors are assumed same for all solutions [9] and for practical applications as aid in assessing modeling errors when monotonic convergence established for multiple grid triplets and/or iterative convergence and resource issues for very fine grids [3,4]. Furthermore, the concept of deterministic error estimate for simulations seems appropriate and been advocated by others. We agree with the caveat that it is only useful as a deterministic estimate under certain circumstances (i.e., solutions sufficiently close to the asymptotic range) and in this case, the uncertainty estimate based on an estimate of the error in that estimate. We never claimed using the corrected solution addresses the criticism that the numerical error is deterministic and not stochastic.

We disagree with Dr. Roache's formulation for estimating the uncertainty of corrected solutions; since, the amount of conservatism is a function of grid refinement ratio and for $r_k < \sqrt{2}$ gives the unacceptable result that the uncertainty in the corrected solution is larger than the error in the uncorrected solution. Therefore, we recommend the revised correction factor uncertainty estimates for the corrected solution U_{k_c} (2). The revised uncertainty estimates given by equation (2) may improve the Eca and Hoekstra [8] results showing that uncertainty estimates for the corrected solution from the correction factor approach do not bound the error for the 2-D Laplace equation analytical benchmark. The data presented in [8] are insufficient to reproduce all their results. However, we are able to reproduce a subset of their results, which show that correction factor corrected solution uncertainty estimates bound the error, as we have also shown for the 2-D Laplace equation.

6. We agree that analytical benchmarks are useful to confirm verification procedures; however, we disagree that the ensemble of problems in [10] or data of [9] provide statistical evidence for establishing 95% confidence level. We find no statistical distributions in [9] or [10] while [10] assumes normal distributions with the claim that twice the standard deviation leads to a 95% confidence level with no supporting evidence. Truncation errors are systematic errors with strong spatial and temporal correlations; therefore, we do not expect errors for single problems (i.e., indi-

vidual user, code, model, grid-type, etc.) to display normal distributions. One must consider issues of replication level, as with experimental uncertainty analysis. Recently, authors have proposed a method for establishing probabilistic confidence intervals for CFD codes [11] using N-version testing [12] wherein multiple codes or users, models, grid types etc. for specific benchmark applications are used to establish normal distributions.

7. We do not understand how you can accuse us of ignoring issues related to erroneous identification of monotonic convergence when we specifically provided discussion in [2–4], including reference to [13]. We have also extensively discussed in [2–4] a minimum of three solutions are required for verification studies and desirability and issues for obtaining more than three solutions, including reference to [8]. We are indebted to Dr. Roache for pointing out the possibility of the oscillatory divergence convergence condition and to Professor Celik for pointing out his discussion in [5] of oscillatory convergence.

References

- [1] Roache, P., 2003, "Criticisms of the 'Correction Factor' Verification Method," *J. Fluids Eng.*, **125**, pp. 732–733.
- [2] Stern, F., Wilson, R. V., Coleman, H., and Paterson, E., 2001, "Comprehensive Approach to Verification and Validation of CFD Simulations-Part 1: Methodology and Procedures," *ASME J. Fluids Eng.*, **123**, pp. 793–802.
- [3] Wilson, R. V., Stern, F., Coleman, H., and Paterson, E., 2001, "Comprehensive Approach to Verification and Validation of CFD Simulations-Part 2: Application for RANS Simulation of a Cargo/Container Ship," *ASME J. Fluids Eng.*, **123**, pp. 803–810.
- [4] Wilson, R., and Stern, F., 2002, "Verification and Validation for RANS Simulation of a Naval Surface Combatant," *Standards for CFD in the Aerospace Industry*, AIAA paper 2002-0904 Aerospace Sciences Meeting, Reno, Nevada.
- [5] Celik, I., and Karatekin, O., 1997, "Numerical Experiments on Application of Richardson Extrapolation With Nonuniform Grids," *ASME J. Fluids Eng.*, **119**, pp. 584–590.
- [6] Ebert, M. P., and Gorski, J. J., 2001, "A Verification and Validation Procedure for Computational Fluid Dynamics Solutions," NSWCCD-50-TR-2001/0006, Hydromechanics Directorate Report, NSWC, Carderock Division, West Bethesda, MD.
- [7] Weymouth, G., 2002, "RANS CFD Prediction of Pitch and Heave Ship Motions in Head Seas," M.S. Thesis, the University of Iowa, Iowa City IA.
- [8] Eca, L., and Hoekstra, M., 2000, "An Evaluation of Verification Procedures for Computational Fluids Dynamics," 1st Report D72-7, Instituto Superior Tecnico Lisbon, Portugal.
- [9] Cadafalch, J., Perez-Segarra, C. C., Consul, R., and Oliva, A., 2002, "Verification of Finite Volume Computations on Steady State Fluid Flow and Heat Transfer," *ASME J. Fluids Eng.*, **124**, pp. 11–21.
- [10] Roache, P. J., 1998, *Verification and Validation in Computational Science and Engineering*, Hermosa Publishers, Albuquerque, NM.
- [11] Stern, F., and Shao, J., 2003, "Statistical Approach to CFD Code Certification," AIAA paper 2003-410, *Applied Aerodynamics Special Session on CFD Uncertainty*, 41st Aerospace Sciences Meeting, Reno, NV.
- [12] Hensch, M., 2002, "Statistical Analysis of CFD Solutions From the Drag Prediction Workshop," AIAA Paper 2002-0842, 40th AIAA Aerospace Sciences Meeting and Exhibit, Reno, NV.
- [13] Coleman, H., Stern, F., Di Mascio, A., and Campagna, E., 2001, "The Problem With Oscillatory Behavior in Grid Convergence Studies," *ASME J. Fluids Eng.*, **123**, pp. 438–439.

**Erratum: “An Experimentally Validated Model for Two-Phase Pressure Drop in the Intermittent Flow Regime for Circular Microchannels,”
[Journal of Fluids Engineering, 2002, 124, pp. 205–214]**

S. Garimella, J. D. Killion, and J. W. Coleman

1. By convention, most of the equations in this paper treat pressure drop as a negative value. For consistency, the following equations should have the negative signs added as shown below:

$$\left(\frac{dP}{dx}\right)_{\text{slug}} = -\frac{0.3164}{\text{Re}_{\text{slug}}^{0.25}} \frac{\rho_L U_{\text{slug}}^2}{2D_h} \quad (1)$$

$$\left(\frac{dP}{dx}\right)_{f/b} = -\frac{0.3164}{\text{Re}_{\text{bubble}}^{0.25}} \frac{\rho_V (U_{\text{bubble}} - U_{\text{interface}})^2}{4R_{\text{bubble}}} \quad (2)$$

$$\Delta P_{\text{one transition}} = -\rho_L \frac{(U_{\text{slug}} - U_{\text{film}})^2}{2} \quad (3)$$

$$\Delta P_{\text{one transition}} = -\rho_L \left(1 - \left(\frac{R_{\text{bubble}}}{R_{\text{tube}}}\right)^2\right) (U_{\text{slug}} - U_{\text{film}})(U_{\text{bubble}} - U_{\text{film}}) \quad (4)$$

2. In addition, Eq. (33) above had a factor of 2 in the denominator, which should be removed, as shown above.
3. The value of the coefficient, a , in Eq. (35), currently listed as 2436.9 in the text following the equation, should be changed to $a = 2.4369$.

**Erratum: “An Experimentally Validated Model for Two-Phase Pressure Drop in the Intermittent Flow Regime for Noncircular Microchannels,”
[Journal of Fluids Engineering, 2003, 125, pp. 887–894]**

S. Garimella, J. D. Killion, and J. W. Coleman

1. By convention, pressure drop is treated as a positive value. Therefore, Eq. (11) should be as follows, i.e., without the negative sign on the right-hand side:

$$U_{\text{interface}} = \frac{(dP/dx)_{f/b}}{4\mu_L} (R_{\text{tube}}^2 - R_{\text{bubble}}^2) \quad (5)$$

2. The expression for pressure drop due to the film-slug transition, Eq. (19) had a factor of 2 in the denominator, which should be removed, as shown below:

$$\Delta P_{\text{one transition}} = \rho_L \left(1 - \left(\frac{R_{\text{bubble}}}{R_{\text{tube}}} \right)^2 \right) (U_{\text{slug}} - U_{\text{film}})(U_{\text{bubble}} - U_{\text{film}}) \quad (6)$$

3. The value of the coefficient, a , in Eq. (21), currently listed as 2436.9 in the text following the equation, should be changed to $a=2.4369$. For Eq. (24), the coefficient should be: $a=0.9965$ instead of 996.5.